Progress in Paper Physics Seminar 2011

Conference Proceedings

Editor U. Hirn

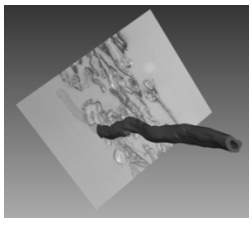
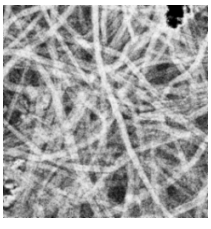
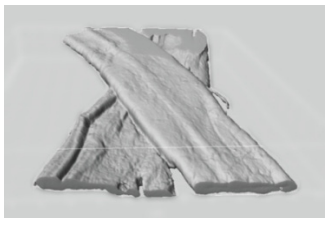
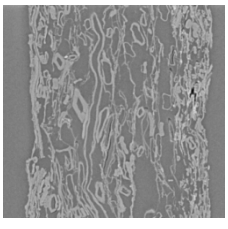
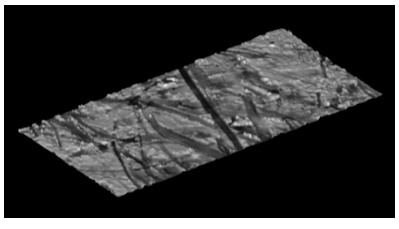

Scientific Committee

Organizing Committee

U. Hirn (Editor)
Progress in Paper Physics Seminar 2011 Conference Proceedings

Graz, 2011

www.ub.tugraz.at/Verlag

print ISBN **978-3-85125-163-0**
e-ISBN **978-3-85125-164-7**
DOI **10.3217/978-3-85125-163-0**

Presentations

Keynote Lectures

Fiber Properties and Refining

Fiber Network Modeling

Printing and Paper Optics

Paper and Web Mechanics

New Cellulose Based Products

Theory of Paper Strength

Web Consolidation and Drying

Fiber – Fiber Bonding

Paper Structure

Posters

Pulping and Stock Preparation

Fiber Suspensions and Paper Making

New Pulp and Paper Products

Paper Properties

Paper Mechanics

Keynote Lectures

Trends in European Pulp and Paper Research

WERNER FÖRSTER and SAMUEL SCHABEL

Papiertechnische Stiftung (PTS), Hess-Straße 134, D-80797 München
werner.foerster@ptspaper.de
Technische Universität Darmstadt, FG Papierfabrikation und Mechanische Verfahrenstechnik PMV, Alexanderstraße 8, D-64283Darmstadt
schabel@papier.tu-darmstadt.de

1 Abstract

While the pulp and paper industry in Europe has been characterised by stable growth and steady development for many years, new developments during the last decade and even more during the upcoming years will require significant re-orientation. As a resource and energy intensive industry it is fiercely affected by the grand societal challenges of the 21st century: mitigation of climate change, energy, shortage of resources, the strong need for developments towards a sustainable industry. Also the transformation of the economies and societies globally and in particular in Europe and the increasing competition on different fields of technology by emerging economies are "push factors" for such a change. But also "pull factors" such as new developments in the fields of bio-and composite materials, nano-science and process technology drive the pulp and paper industry to new directions.

Some of the large international companies have already transferred such new challenges and opportunities into new strategies and orientation of their business. Also European and national research framework programmes are addressing the grand challenges, request the strengthening of Europe´s competitiveness and foster the forming of a European Research and Innovation Area . Large European research organisations are reflecting the trends towards more multi-disciplinary and multi-national research in new fields. The European Forest-based Sector Technology Platform published five strategic objectives for research and innovation for 2030:

- *Green carbon:* Capture and removal of green carbon in endless cycles from sustainably managed forests. Future biorefinery processes will help to use the entire potential of forest-based raw materials and by-streams for a broad range of high added-value products.
- *Energy efficiency:* Improvements in processes and investments in more energy efficient production.
- *Key enabling technologies:* Extracting an increasing number of products from wood with technologies like nanotechnology.
- *Resource efficiency:* Recycling encompasses resource efficiency. The paper industry in Europe is a leader with recycling more than 72 % of the paper put on the market. But there is still room for significant improvement, f. i. by designing paper products optimised for recycling.
- Sustainable products: Wood-based products can replace other equipment such as alkaline batteries and smart combinations of wood-based and other materials will produce chances for more sustainable consumer products and construction materials.

These strategic objectives will drive the pulp and paper sector in Europe in new directions in the upcoming years and lead to new structures and alliances in research and development. Since this industry is based on renewable resources there are many opportunities. The only unfeasible choice is: business as usual.

Session 1

Fiber Properties and Refining

Energetic optimization for assessing the shortening kinetics of fibres in pulp refining

ROUX Jean-Claude, BLOCH Jean-Francis, NORTIER Patrice

Lab. of Pulp and Paper Science and Graphic Arts
UMR 5518 CNRS, Grenoble INP – Pagora
461 rue de la papeterie, 38400 Saint-Martin d'Hères
France
Jean-Claude.Roux@grenoble-inp.fr

The subject concerns the influence of refining on pulp fibres in the low consistency regime. In a previous article [1], we demonstrated that only the refining intensities based on physics [2], [3] should be used with statistical confidence to evaluate the °SR kinetics of the evolution of pulps. The other definitions of refining intensity developed in the context of paper industry should be used with care [4], [5]. In this research, in order to quantify the kinetics of the shortening of fibres, the net tangential force per crossing point was chosen as the refining intensity I [6]. The evolution of the average weighted fibre length was analysed versus the net specific energy consumed, for a given refining intensity.

1.1 Materials

In this research, four refining trials were undertaken on a semi-industrial pilot plant (a single disc refiner), running in hydracycle mode, considering an unbleached Kraft pulp of Canadian softwood (Figure 1). The values of the specific energies do correspond to industrial values. Moreover, the refining trials were undertaken on the pulp at both constant net power and rotation speed. The initial pulp had the following characteristics: average weighted fibre length: L_{f0} = 1.85 mm, water retention value WRV_0 = 91 g of water/100g of dry pulp, drainage index °SR= 13.4, mass fraction of fine elements =2.9%.

1.2 Methods

The parameters of the refiner studied were: the bar width, a, and the applied net power P_{net} whereas, for all trials, the angular parameters of plates were kept constant (sum of grinding angles $\alpha+\beta$, sector angle θ).

The numerical values of the parameters for the refiner were chosen in order to have a sufficient range of refining intensities and net specific energies. The experimental conditions are presented in Table 1.

1.3 Results and discussion

For a given refining intensity, it was found that a polynomial model of the third order could fit the evolution of the fibre length for the whole range of net specific energies investigated (Figure 2). Why it is really better criterion; why a second order is not good enough? It was found fit better than a linear regression since the shortening effect on fibres is a non linear phenomenon as depicted in the Figure 2. Consequently, linear methods may lead to erroneous estimation of the industrial conditions to be carried out. Hence, for a given experimental curve, it was possible to estimate a net specific energy which corresponded to the maximum kinetics of the fibre shortening. These events occurred at about the same fibre length (1.45 mm) for all the refining intensities analyzed. However, a single refining intensity (I = 3.14 N) enabled the shortening effect to simultaneously fulfil two criteria, namely: reaching the optimum kinetics and consuming the minimum of net specific energy. The proposed analysis maximized the shortening index ($-dL_f/dE_m$) and allowed the determination of the best refining intensity for the shortening effect on fibres. It must be noted that the best refining intensity is not the maximum value but an optimized quantity that was determined through the proposed methodology. This optimized refining intensity did also depend on the range of net specific energies investigated. This methodology may be applied to any other type of pulps on different refining devices.

REFERENCES

[1] J.-C. Roux, J.-F. Bloch, R. Bordin, P. Nortier. The net normal force per crossing point: a unified concept for the low consistency refining of pulp suspensions. 14th Fundamental Research Symposium, Oxford, FRC, 51-83 (2009).

[2] F. Meltzer. Key figures for the assessment of the refining process. Chapter 2. Refining Technology, Leatherhead, editor C.Baker, (2000).

[3] R.J. Kerekes and J.J. Senger. Characterizing refining action in low-consistency refiners by forces on fibres. *Journal of Pulp and Paper Science* 32(1):1-8 (2006).

[4] W. Brecht and W.H. Siewert. Zür theoretisch technischen Beurteilung des Mahlprozesses moderner Mahlmaschinen. *Das Papier* 20(1):4-14 (1966).

[5] J. Lumiainen. New theory can improve practice. *Pulp and Paper International* 32(8):46-54, (1990).

[6] J.-C. Roux. Review Paper on pulp treatment processes. 12th Fundamental Research Symposium, Oxford, FRC, 19-80 (2001).

Trial number	P_{net} (kW)	a (mm)	I (N)	Final SEC E_m (kWh/t)	$\alpha+\beta$ (°)	θ (°)
1	11	4.8	3.14	267	0	22.5
2	14.9	4.8	4.26	276	0	22.5
3	7.2	4.8	2.06	300	0	22.5
4	11	3.2	1.38	375	0	22.5

Table 1: Engineering parameters chosen for the experimental trials where P_{net}, a, I, E_m, $\alpha+\beta$ and θ represents respectively the net power, the common bar width, the refining intensity, the specific energy consumption, the sum of the grinding angles and the sector angle.

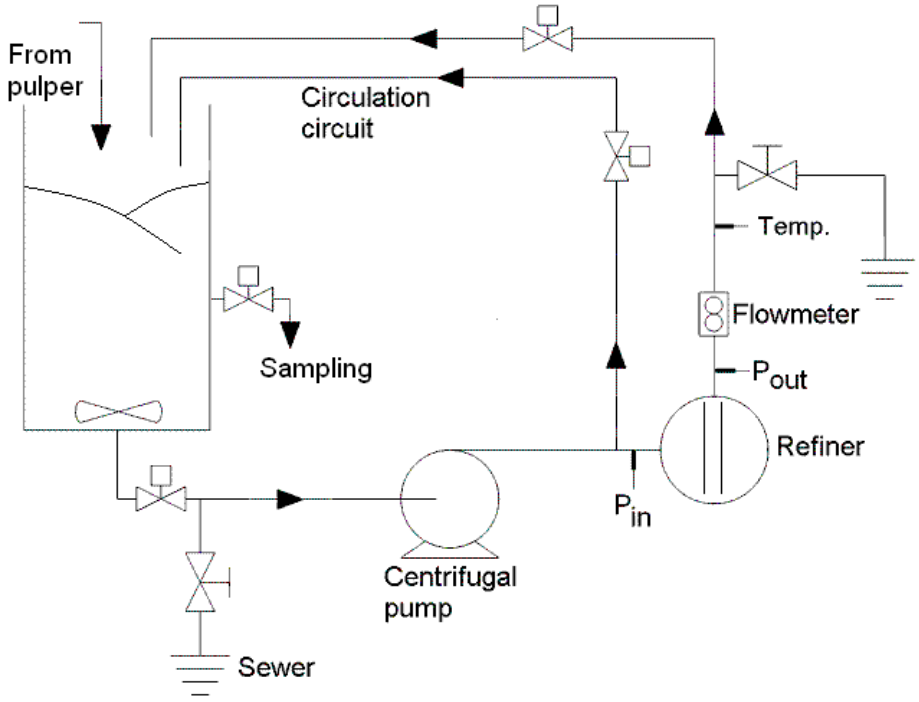

Figure 1. Semi-industrial refining plant

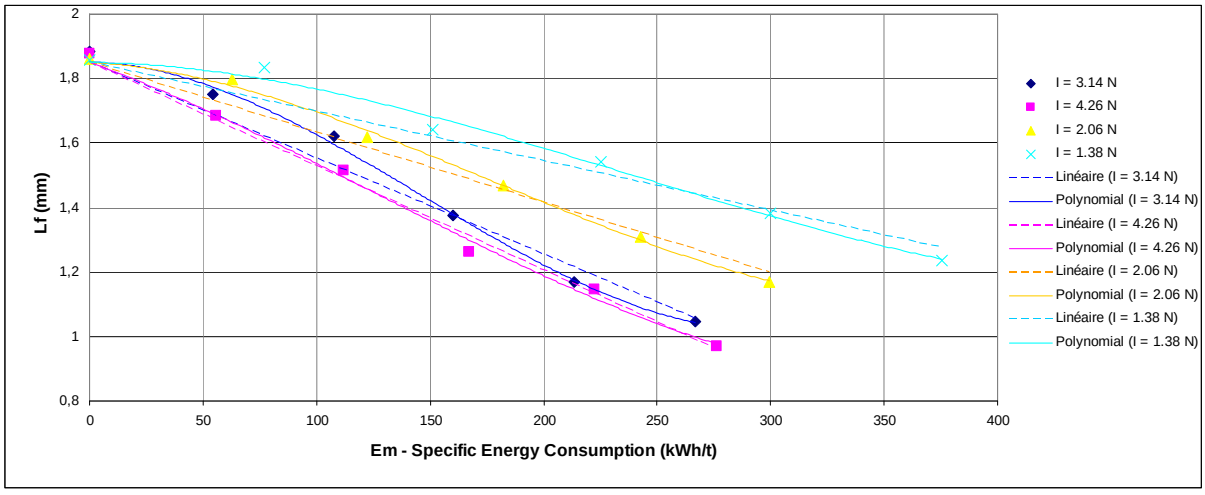

Figure 2. Kinetics of the evolution of fibre length L_f (mm) vs. the net refining energy E_m (kWh/T) and the refining intensity I (N). The tendency curves are presented for both first and third orders.

THE ROLE OF MULTIPLE LOADING CYCLES ON PULP IN REFINERS

JENS HEYMER[1], JAMES A. OLSON[1] and RICHARD J. KEREKES[2]

[1] Department of Mechanical Engineering,
[2] Department of Chemical and Biological Engineering,
University of British Columbia, Pulp and Paper Centre, 2385 East Mall, Vancouver, BC, V6T 1Z4, Canada
jheymer@chbe.ubc.ca

INTRODUCTION

In a recent study of compression of pulp pads, Goosen et al. (2007) [1] found that without fibre redistribution between loading cycles there was little tensile strength increase of pulp. However, when fibre networks were redistributed after each loading cycle, substantial strength increases were obtained. They proposed a model for this strength increase based on the observations of Dunford and Wild (2002) [2] and Wild et al. (2006) [3] that only a few cycles were needed to flexibilize single fibres, not thousands of cycles as is common in fatigue phenomena.

The findings for compression refining raise the question of whether the same holds true for industrial refiners. Specifically, is the role of multiple bar crossings in refiners one of overcoming heterogeneity of refining rather than imposing fatigue weakening. The objective of this paper is to answer this question.

ANALYSIS

In compression refining, an expression was derived by Goosen et al. (2007) [1] that related tensile strength increase ΔT to the number of loading cycles imposed on the pulp pad, N_C and the probability that each cycle was successful in creating a refining result, P_C. The analogous expression for a pulp refiner is

$$\Delta T = 1 - \left(1 - P_B\right)^{N_B} \qquad (1)$$

where N_B is number of available bar crossings a fibre may experience during its passage through a refiner, and P_B is the probability that each crossing inflicts a successful refining result.

The number of available bar crossings, N_B is in essence the number of bar crossings seen by a point moving along the edge of a bar through the refiner. Thus, N_B can be readily determined from the geometry and operating conditions in a refiner as giving by the expression below:

$$N_B = \frac{CEL \cdot 2 \cdot D \cdot G}{Q} \qquad (2)$$

Here CEL is the cutting edge length, D is the groove depth, G is the groove width, and Q is the volumetric flow rate of the suspension through the refiner.

The probability P_B is the likelihood of a successful refining result at each bar crossing. In refiners, this is a composite of the probability of capture of fibres in a groove and transport into the adjacent gap, and the probability that once in the gap, pulp is subjected to a force of sufficient intensity to create a refining result.

EXPERIMENTAL PROGRAM

We evaluated *Eq. 1* employing data obtained on a 22" Beloit Double Disc pilot refiner and an Escher–Wyss laboratory refiner. The trials examined five different plate patterns over a range of different energies and intensities shown in *Table 2*. The power cited is the net power. The consistencies are nominal values. The rotational speed for the double disc refiner was 900 rpm and for the Escher-Wyss refiner was 1000 rpm. The plate dimensions used are summarized in *Table 1*. The trials were conducted using a Northern bleached softwood kraft pulp.

RESULTS AND DISCUSSION

The increases in tensile strength for the refining conditions tested are shown in *Table 2*. These data were fitted for *Eq. 1* by regression analysis. An example of the fit of tensile strength (ΔT) development as a function of bar crossings N_B is shown in *Fig 1*.

Table 1. Summary of refiner plate geometries.

Plate	Bar Width [mm]	Groove Width [mm]	Groove Depth [mm]	Bar Angle [°]	*CEL* ·10³ [m/s]
1	3.0	3.0	4.0	17.3	20.05
2	2.5	2.5	5.0	21.5	24.10
3	1.0	2.5	1.0	21.3S*	233.2
4	3.0	8.0	4.0	21.25	7.00
5	6.0	12.0	8.0	16.0	0.52

* 21.3° Bar Angle for Stator and 26.5° for Rotor

As is evident in *Fig. 1*, the fit is very good. The fits for the other 17 cases were similarly good, having an average R^2 = 0.942. The values of P_B along with N_B for each case are shown in *Table 2*.

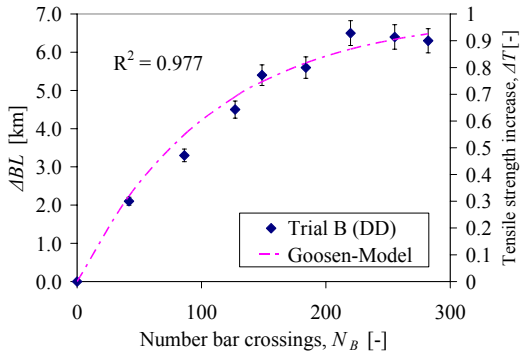

Figure 1. Measured tensile strength increase plotted against number of bar crossings showing model fit for cumulative probability for P_B = 0.72%.

The values of P_B in *Table 2* fall in the range 0.12 to 6.7%. This is smaller than previous of Goosen et al. (2007) [1] who found a value of $P_C \approx 6\%$ for compression refining of a pulp pad. In earlier work, Kerekes and Olson (2003) [4] estimated upper limits of probability of fibre capture. They estimated a 20% probability based on the zone in a groove from which fibres could be captured, and 5% based on the amount of fibre that could physically fit into a typical gap. The lower average values found in this study suggest that probability of a successful refining event at a bar crossing depends on loadings once captured as well as capture probability.

Table 2. Summary of experimental trials.

Trial	Type	Plate	C_F [%]	$Power_{Net}$ [kW]	SEL [J/m]	N_B** [-]	ΔBL** [km]	P_B [%]	$P_B \cdot N_B$ ** [-]	l_{LW}** [mm]
A	22" Beloit Double Disc	1	2.84	65	3.25	94	6.2	1.48	1.39	2.05
B		1	4.55	64	3.20	149	5.4	0.72	1.07	2.07
C		1	1.55	34	1.70	89	5.7	1.57	1.40	2.14
D		1	2.48	34	1.70	161	6.2	1.05	1.69	2.15
E		1	4.22	34	1.70	282	5.0	0.38	1.07	2.22
F		2	4.19	64	2.67	274	4.9	0.38	1.04	2.29
G		2	2.54	26	1.08	246	5.4	0.80	1.97	2.33
H		2	4.52	26	1.08	474	5.2	0.24	1.14	2.31
I		3	2.70	33	0.14	413	4.6	5.99	24.74	2.23
J		3	4.40	34	0.14	702	3.1	1.00	7.02	2.23
K		4	2.56	16	0.07	777	3.2	0.26	2.02	2.33
L		4	4.51	55	7.86	163	1.4	3.63	5.92	1.17
M		4	3.15	56	8.00	115	1.4	6.70	7.71	1.34
N	Escher-Wyss	5	1.50	0.7	1.50	830	3.4	0.12	1.00	2.10
O		5	3.00	1.4	3.00	824	3.3	0.68	5.60	1.97
P		5	4.00	2.3	5.00	657	2.8	0.33	2.17	1.75
Q		5	3.00	2.3	5.00	492	2.7	0.26	1.28	1.82

** at 120 kWh/t

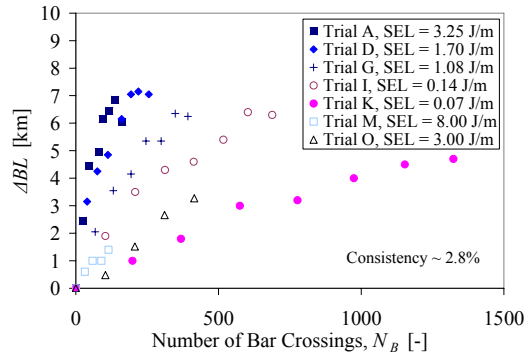

Figure 2. Increase in tensile strength as a function of total number of refining events experienced by pulp on passage through a refiner at differing levels of intensity.

The product of P_B and N_B represents the total number of successful refining events experienced by pulp on passage through a refiner. Values of $P_B \cdot N_B$ are shown in *Table 2* and in *Fig. 2*. These data indicate that tensile strength increases with $P_B \cdot N_B$. Most important for this study, the values are mostly around one, i.e. $P_B \cdot N_B \approx 1$, in the normal range of intensity (SEL = 1 – 3 Ws/m.). This supports the postulate stated earlier that only one or a few loading cycles are needed for refining, however, when SEL is very small, $P_B \cdot N_B$ must be much larger to compensate for the low forces in the gap. When SEL is very large, even large values of $P_B \cdot N_B$ fail produce substantial strength increase as is evident in *Fig. 2*. This is due to fibre shortening. The length weighted average fibre length, l_{LW}, in this case was reduced from 2.30 mm (unrefined) to

1.34 mm at 120 kWh/t energy input, as can be seen in *Table 2*.

CONCLUSIONS

The findings of this study support the postulate that only one or a few loading cycles of appropriate intensity are required to treat fibres for strength increase in chemical pulps. The level of intensity must be sufficient to create a refining effect but not so excessive as to shorten fibres. Consequently, the role of many bar crossings in refiners is primarily one of exposing many fibres to a few loading cycles rather than imposing many loading cycles on a given fibre to create fatigue weakening. In short, the role is one of overcoming heterogeneity in treatment of fibres.

These results further suggest that heterogeneity in treatment is governed by the probability of fibre capture and transport into gaps and probability of suitable forces applied to fibres within gaps. In a subsequent publication, we explore this combined probability by means of a comminution analysis to measure refining heterogeneity from fibre length changes.

REFERENCES

[1] Goosen, D. R. Olson, J. A. Kerekes, R. J. (2007), The Role of Heterogeneity in Compression Refining, Journal of pulp and paper science, VOL 33; Numb 2, pages 110-114.

[2] Dunford, J., and Wild. P.M. (2002): Cyclic transverse compression of single wood-pulp fibres. J. Pulp Paper Sci. 28(4), 136.

[3] Wild, P., Omholt, I., Steinke, D., Schuetze, A. (2006), Experimental Characterization of Wet Single Wood-pulp Fibre Under Transverse Compression, Journal of Pulp and Paper Science 31(3):116-120.

[4] Kerekes, R.J. and Olson, J.A. (2003), Perspectives on Fibre Length Reduction in Refining, PIRA International Conference on Scientific and Technical Advances in Refining and Mechanical Pulping", Paper 2, Stockholm, Sweden.

How the cell wall irregularities impact on mechanical properties of softwood fiber

ROOPE ESKOLA[1]*, JARI HÄMÄLÄINEN[2], TEEMU LEPPÄNEN[3]

[1]University of Eastern Finland,
P.O.Box 1627, FI-70211 Kuopio, Finland.
roope.eskola@uef.fi
[2]Lappeenranta University of Technology,
P.O.Box 20, FI-53851 Lappeenranta, Finland.
jari.hamalainen@lut.fi
[3]Magister Solution Ltd,
Hannikaisenkatu 41, FI-40100 Jyväskylä, Finland.
teemu.leppanen@metso.com

*Corresponding author

Keywords: Fiber, cell wall, pit, modeling.

ABSTRACT

A numerical model is presented that describes the effect of irregularities such as crossfield pits on the stress behavior of the cell wall of Norway spruce fiber. The effects of anisotropic material and the shape of the pits have been studied via finite element analysis. Partial one pit models are used to initially obtain a wider knowledge base and then a full width scale model of fiber wall can be built up from these partial models. The material of fiber is considered to be a continuous anisotropic elastic material.

1 INTRODUCTION

The aim of this work is to develop a mathematical model to examine how irregularities in the cell wall structure can affect at the mechanical behavior of wood fibers. Mechanical behavior of fibers is an important issue because the properties of the fibers have a direct impact on the mechanical properties of fiber networks [1]. There are many situations where it is vital to have a reliable knowledge of the mechanical properties of fiber network. For instance, in the case of paper, mechanical properties are crucial in both manufacturing and end use situations.

Firstly, the irregularities in Norway spruce (*Picea Abies)* fiber were studied and subsequently the effects of irregularities were investigated with finite element analysis. Norway spruce is commonly used for mechanical pulp processing and paper making. The fiber consists of four distinct layers the P, S1, S2 and S3. These are primary (P) wall and three layers of the secondary (S1, S2, S3) wall [2, 3]. The cell wall structure of a softwood fiber is shown in Figure 1.

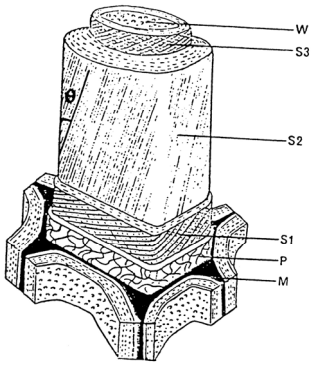

Figure 1. Schematic illustration of the structure of the softwood fiber [3].

The lignin rich middle lamella (M) is the layer which glues the fibers together. Letter W in Figure 1 points to the lumen in the fiber. However layers M, W, P and S1 are often lost during the pulping processes. In contrast, the S2 layer is usually the thickest layer and it also dominates the mechanical properties of the fiber [1, 3]. The mechanical properties of biopolymer composite material in the S2 layer are very complex. Nevertheless it can be assumed to represent a continuous anisotropic material [2]. The structure of fibers is not a perfect cylindrical tube and there are irregularities, for example, there may be a large number of pits. The pits in the softwood fiber are presented in Figure 2.

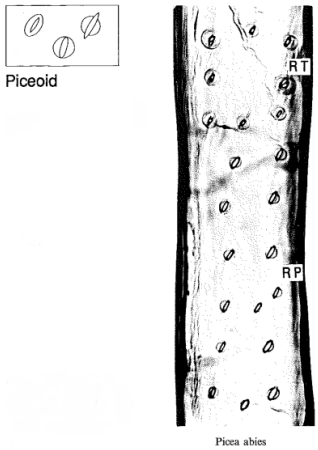

Figure 2. Pits in Norway spruce fiber [4].

Sirviö and Kärenlampi have studied the parameters for pits of Norway spruce fiber [5]. In this study the parameters taken from their measurements are size, shape and orientation of the pits. Sirviö and Kärenlampi concluded that irregularities, such as pits, do have an impact on the mechanical properties and behavior of the fiber structure.

In this work, the cell wall structure and irregularities in the cell wall have been gathered from the literature. Mathematical models were developed and these models are then used to determine the impact of the pits on the mechanical behavior of the fiber.

2 METHODS

2.1 Structure of Norway spruce fibers

Softwoods like Norway spruce are composed two types of cells, which are termed tracheids and parenchyma cells [6]. However 95 % cells of softwood are tracheids and thus it is common to concentrate on tracheids as was the case also in this study. In this text, the word *fiber* is often used instead of more the correct term *tracheid*. The term fiber is preferred because it is widely used in the field of papermaking and it describes the property of tracheids to act as reinforcement elements in the paper.

Norway spruce fiber is a layered, composite tube structure, as shown in Figure 1, the length of the fibers is approximately 3 mm and width approximately 30 µm [1]. The cell wall thickness of the fibers ranges from 1 - 3 µm and it consists of several biopolymers such as lignin, hemicellulose and cellulose [3]. Distribution of cell wall polymers is shown in Figure 3.

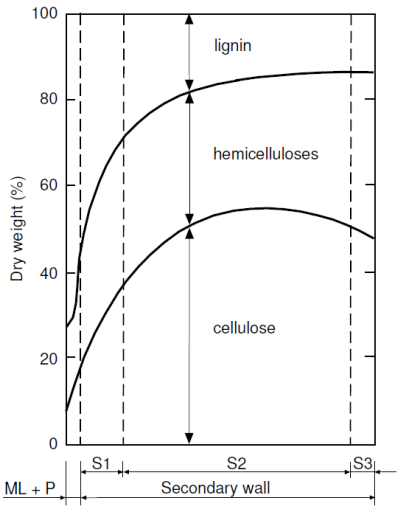

Figure 3. Distribution of cell wall polymers [3].

It can be seen from Figure 3 that the most of cellulose of fiber is located in the S2 layer. Cellulose has major impact on the properties of fiber because it is stiffer and stronger than hemicellulose or lignin [7]. Cellulose is present in molecular chains, i.e., microfibrils which are embedded in a matrix of hemicellulose and lignin [2]. Microfibrils act as tiny reinforcement fibers within the cell wall. Most 80 – 95 % of the material of fiber is contained in the S2 layer, where microfibrils are run in parallel and in steep spirals around the fiber axis. Microfibrils have a high longitudinal modulus compared to their transverse modulus. Hence the direction of microfibrils primarily defines the properties of the fiber. The angle between the microfibrils direction and longitudinal fiber axis is termed the *micellar angle*. The micellar angle varies between fibers but is close to unity in a single fiber. The micellar angle has been widely investigated and it is known that micellar angle of Norway spruce fibers can be approximated to 10 degrees [8]. Figure 4 reveals fibers with averaged micellar angle plotted against the distance from the pith, i.e., center of log.

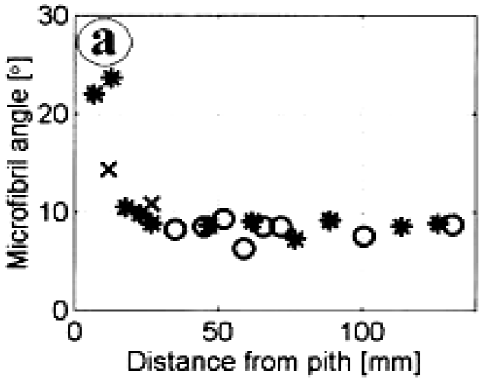

Figure 4. The plot of averaged micellar angle of Norway spruce fibers [8].

2.2 Irregularities in Norway spruce fibers

Firstly, structure of the fibers is not a perfect cylindrical tube and the geometric shape of the cross section of the fibers can be observed as round, square or hexagonal [8]. The longitudinal shape can also be more or less curled. However in this study only the part of the cell wall is being modeled and thus the shape of fiber is not so crucial in this case.

Secondly there are different kinds of irregularities in the cell wall. Irregularities can be man made or natural irregularities but in this paper natural irregularities will be considered. In softwood fibers, the most typical natural irregularities are pit openings [5]. There are three types of pits found in softwood fiber:

- Bordered pits leading from one fiber to another
- RP-pits leading from a fiber to an adjacent ray parenchyma cell
- RT-pits leading from fiber to an adjacent ray tracheid.

Pits are like pores or tiny holes in the cell wall which are intended for transport of water from one fiber to next fiber. In Norway spruce, RP-pits and RT-pits, shown in Figure 2, are identical in shape and size. Accordingly they are often treated as one class, called crossfield pits (CF-pits) [5]. As in this study CF-pits are considered. The size, shape and orientation of CF-pits can be determined from the

measurements of Sirviö and Kärenlampi. The distributions of these parameters for pits in spruce fibers are shown in Figure 5. The variable *w* refers to width, *l* to length and subscript index *p* to pit and *f* to fiber.

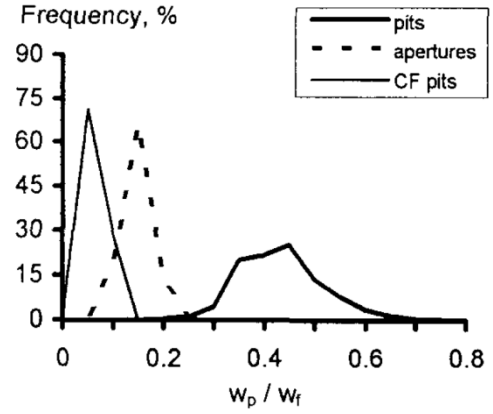

(a) Distribution of size.

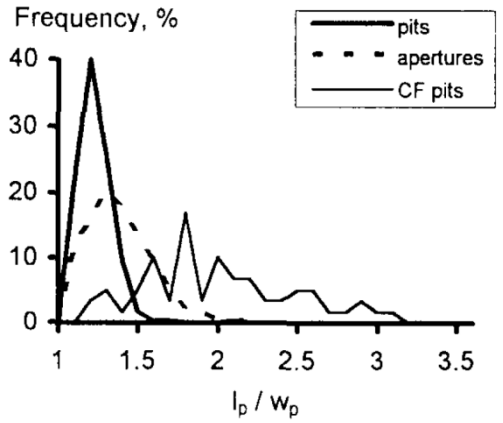

(b) Distribution of shape (length/width).

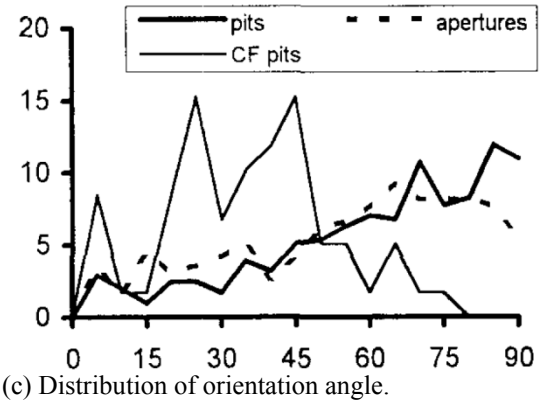

(c) Distribution of orientation angle.

Figure 5. Distributions of parameters for pits of Norway spruce fibers [5].

The size parameter for CF-pits is close to 0.05, as shown in Figure 5(a). Accordingly, the width of CF-pit can be considered to be 1.5 µm, when the width of a fiber is 30 µm. The shape parameter of CF-pits can be selected to be 2 from Figure 5(b), without introducing any major error. In addition, orientation angle θ of CF-pits can vary between 0 – 80 degrees, as shown in Figure 5(c). Sirviö and Kärenlampi [5] considered the parameters as an elliptical shape but in this case the shape of CF-pits is considered to be oval. Thus the size of the oval shape CF-pits can be considered as width 1.5 µm and length 3.0 µm. The CF-pit geometry used is shown in Figure 6.

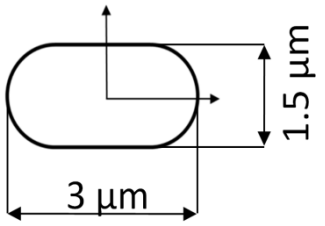

Figure 6. CF-pit geometry used.

Once the structure and irregularities of Norway spruce fiber have been studied then modeling can be conducted.

2.3 Modeling

The main goal of this study was to determine how CF-pits affect the stress behavior of Norway spruce fiber under loading. The effect of pit shape, orientation and anisotropic material were tested via finite element analysis. Firstly partial models of one pit will be considered and subsequently a full width scale model of cell wall of fiber will be presented.

Finite element analysis was implemented with ABAQUS software. Quadratic shell elements were used and further only the thickest and structurally dominating cell wall layer S2 was considered in these models. The geometries of the partial models are shown in Figure 7(a) and Figure 7(b). The parameters of geometries are presented in Table 1.

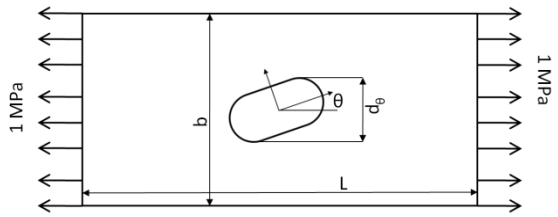

(a) CF-pit model, oval shape.

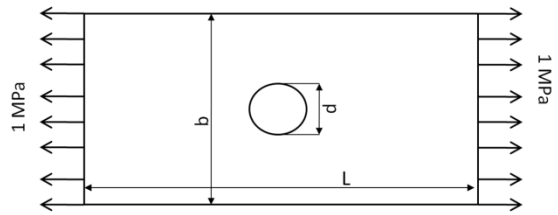

(b) CF-pit model, round shape

Figure 7. Geometries of partial models.

Table 1. Parameters of the geometries.

Parameter	Specification	Value
L	length	10 μm
b	width	6 μm
d_θ	oval shape	1.5 – 3 μm
d	round shape	0 – 3 μm
h	thickness	1 μm
θ	angle	0 – 90°

Parameter d_θ varies because orientation angle θ has an influence on the effective width of the oval shape pit. The effective width d_θ of oval shape pit can be calculated from the equation

$$d_\theta = 1.5\mu m(1+\sin\theta) \quad (1)$$

A diagram of the effective width of the plate versus the orientation angle θ is shown in Figure 8.

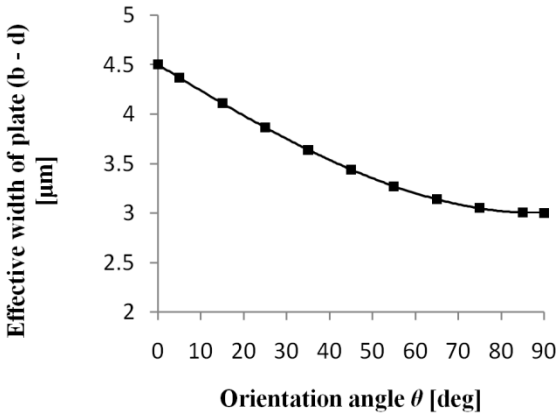

Figure 8. Dependence between effective width of the plate and the orientation angle.

The oval shape model is used to determine how the CF-pit affects the maximum stress of cell wall of fibers. A round shape model is used to determine the stress difference between oval and round shape pits. The results of the round shape model are also compared to results of a fatigue notch factor based analytical calculation. Note that equations (2) and (3) are clarified later on in this chapter.

The material of present in the cell wall is very complex biopolymer composite. It is anisotropic material which has a much higher longitudinal stiffness than in the radial or tangential directions [6]. This complex composite material of fiber can be homogenized to a continuous material. Homogenization of material can be done when linear elastic material is considered. The behavior of fiber can be assumed to be linear when temperature and moisture are constant, and strains are small, and loading time is short. Limitations of linear elastic behavior of fiber are based on the behavior of the temperature dependent lignin and the moisture dependent hemicellulose [7]. Persson [6] has developed the anisotropic elastic material model for the earlywood fiber which has a micellar angle of 10 degrees. The mechanical properties of Persson's material model are shown in Table 2.

Table 2. Stiffness parameters of S2-layer which micellar angle is 10 degrees [6].

Coefficient	Value	Specification
E_{11} [MPa]	38700	longitudinal
E_{22} [MPa]	8500	transverse
E_{33} [MPa]	4900	thickness
G_{12} [MPa]	5440	
G_{13} [MPa]	2090	
G_{23} [MPa]	1633	
υ_{21} [-]	0.115	
υ_{31} [-]	0.0229	
υ_{32} [-]	0.417	

An isotropic material is also used to determine the effect of the anisotropic material. Young's modulus of the isotropic material used is E = 40 GPa and the Poisson's ratio υ = 0.3.

The equation of calculation based on fatigue of notch factor is

$$\sigma_{\max} = \sigma_{nom} \cdot K_t = \frac{P \cdot K_t}{(b-d)h} \quad (2)$$

where $P = \sigma_{load} \cdot b \cdot h$. Thus can be written

$$\sigma_{\max} = \sigma_{nom} \cdot K_t = \frac{\sigma_{load} \cdot K_t \cdot b}{(b-d)} \quad (3)$$

where σ_{load} is the pressure load, b is width of plate, d is diameter of notch and K_t is fatigue of notch factor. Fatigue of notch factor can be determined from Figure 9.

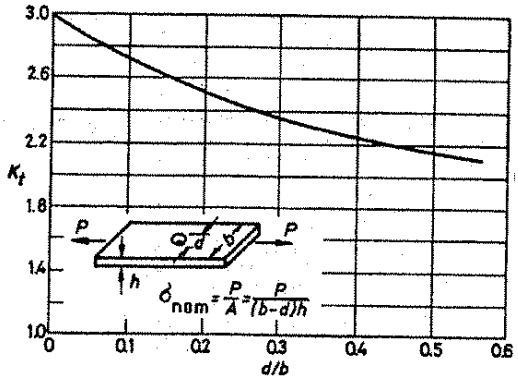

Figure 9. Fatigue of notch factor diagram [9].

The geometries are described by using the modeling unit in ABAQUS software. A finite element mesh is created by using quadratic shell elements. The size of elements was fixed to be 0.25 μm and the shape to be square. The meshed plate of

oval shape model, $\theta = 45$ degree, is shown in Figure 10.

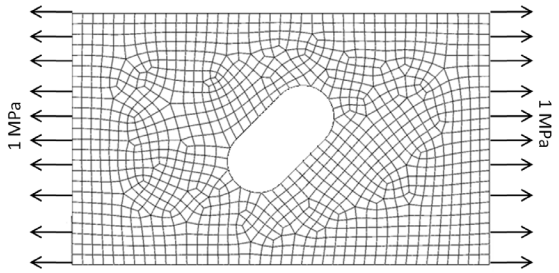

Figure 10. Meshed oval shape model, orientation angle $\theta = 45°$.

Rigid body motion in the model was eliminated by using automatic stabilization in the ABAQUS software. A stabilization factor of 10^{-7} was used for automatic stabilization "Specify dissipated energy fraction".

Primarily, Von Mises maximum stresses are considered for the results obtained from the models. Von Mises maximum stress can be calculated by using the equation

$$\sigma_{max} = \sqrt{\frac{(\sigma_1 - \sigma_2)^2 + (\sigma_2 - \sigma_3)^2 + (\sigma_1 - \sigma_3)^2}{2}} \quad (4)$$

where σ_1, σ_2 and σ_3 are components of the stress tensor. Maximum stresses are expected to be located the boundary of a pit.

Secondly, factor K_t is also considered in the results. Factor K_t describes how strongly a notch can increase the maximum stress. It is defined as maximum stress divided by the nominal stress of the effective zone of the notch.

Finally the results of model which describes how pits can affect the behavior of fiber are presented. One pit models were used to build up a model which consist 25 partial models. Thus, the dimension of a full width scale model is 30 µm x 50 µm. The creation of the model is visualized in Figure 11. Only the material model of S2 layer is used in the calculation of the full width scale model.

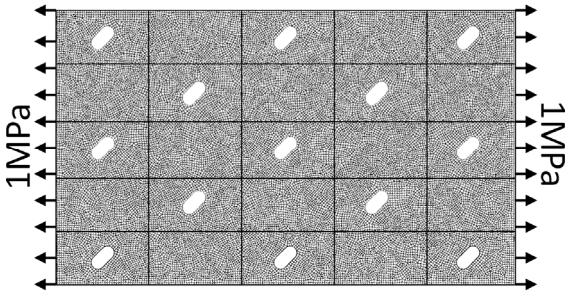

Figure 11. Full width scale model of a fiber wall.

3 RESULTS

The results are primarily presented via diagrams. K_t factors of models are plotted versus effective width of plate in Figure 15 and Von Mises maximum stresses are plotted versus effective plate width in Figure 14. Moreover three figures of stress fields and one dissimilar diagram of K_t are presented. Firstly, the Von Mises stress field of an oval shaped model (θ = 45 degree) is shown in Figure 12.

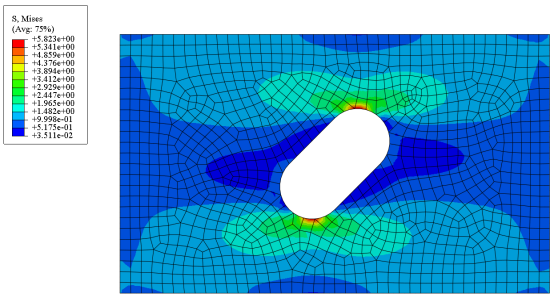

Figure 12. Stress field in the oval shaped model, orientation angle $\theta = 45°$.

The model can be verified by comparing results of FEM model to the results of the analytical calculations. The results are shown in Figure 13.

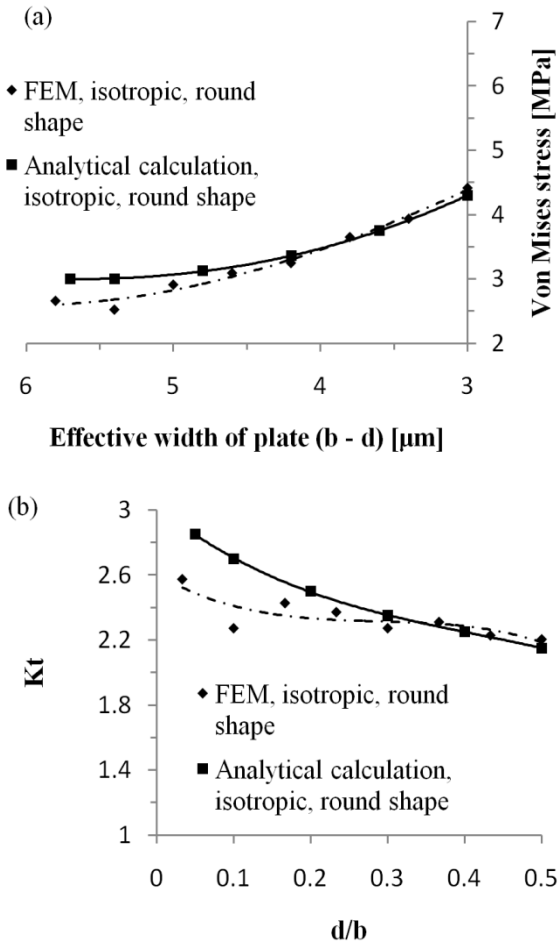

Figure 13. Verification of FEM model, (a) Von Mises stresses, (b) K_t factors.

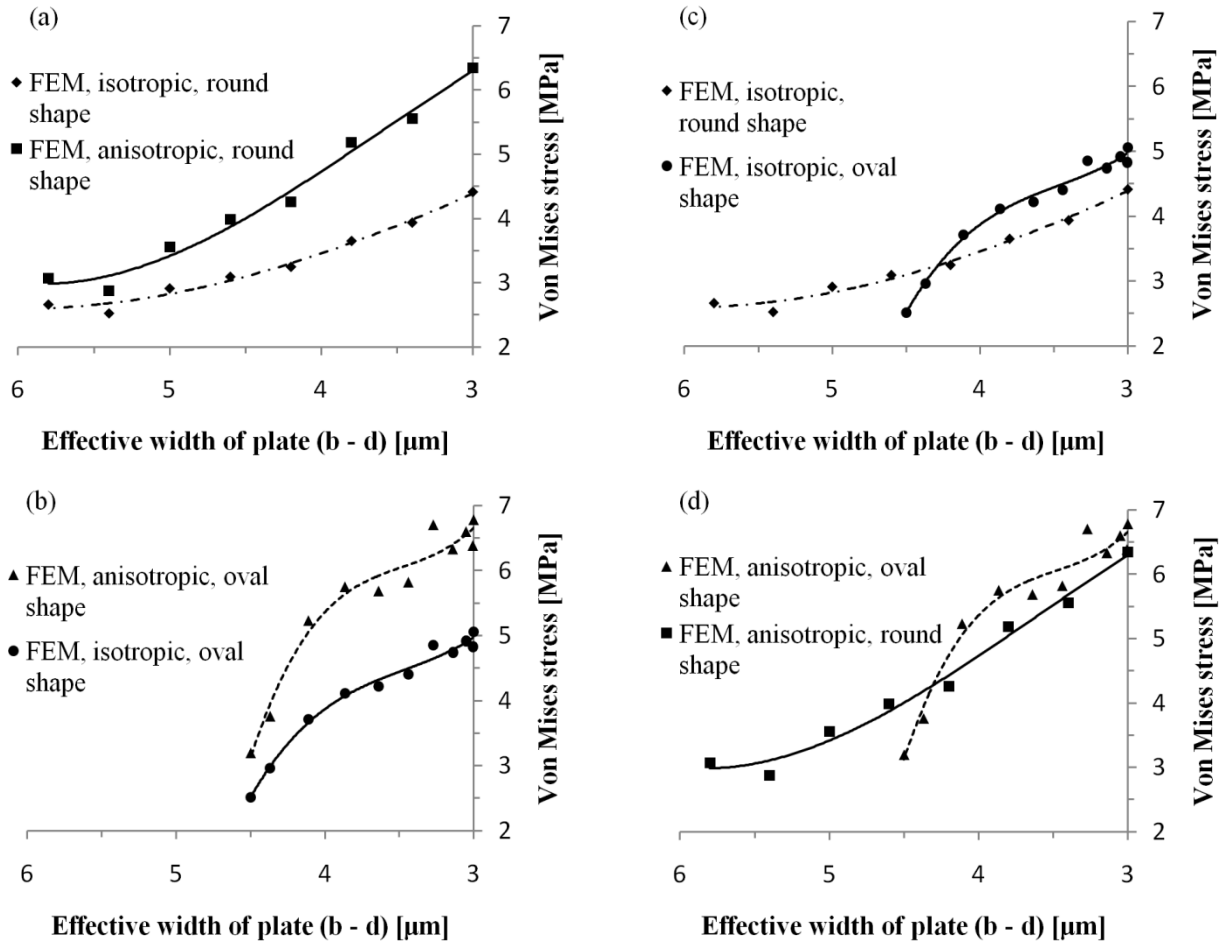

Figure 14. Maximum stresses of partial models versus effective width of plate. The effect of the material can be seen from Figures 14(a) and 14(b). The effect of the shape of notch can be seen from Figures 14(c) and 14(d).

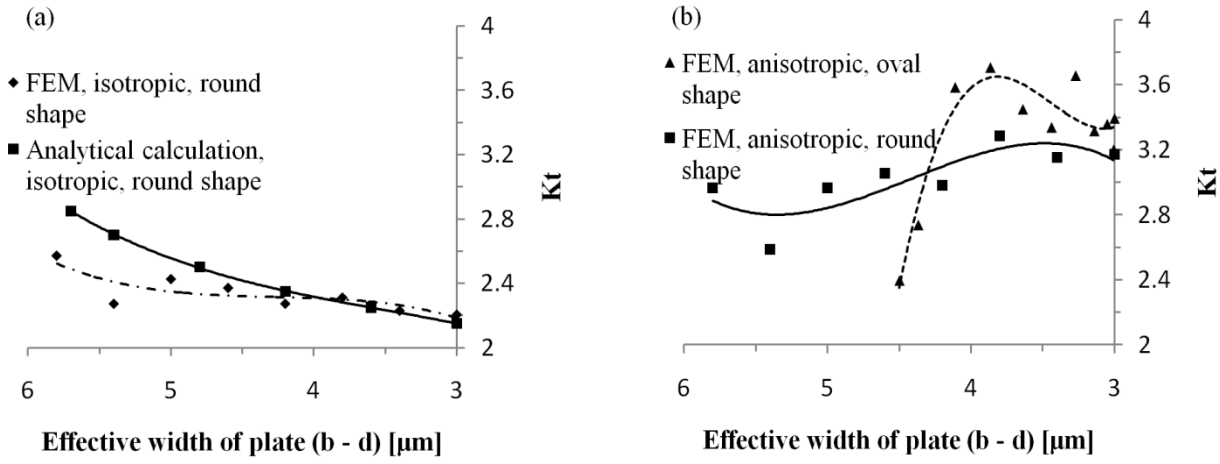

Figure 15. K_t factors of partial models versus effective width of plate. The effect of the oval shape can be seen from Figure 15 (b). Furthermore Figure 15(a) shows the same results as 13(b) but these are now plotted versus the effective width of plate.

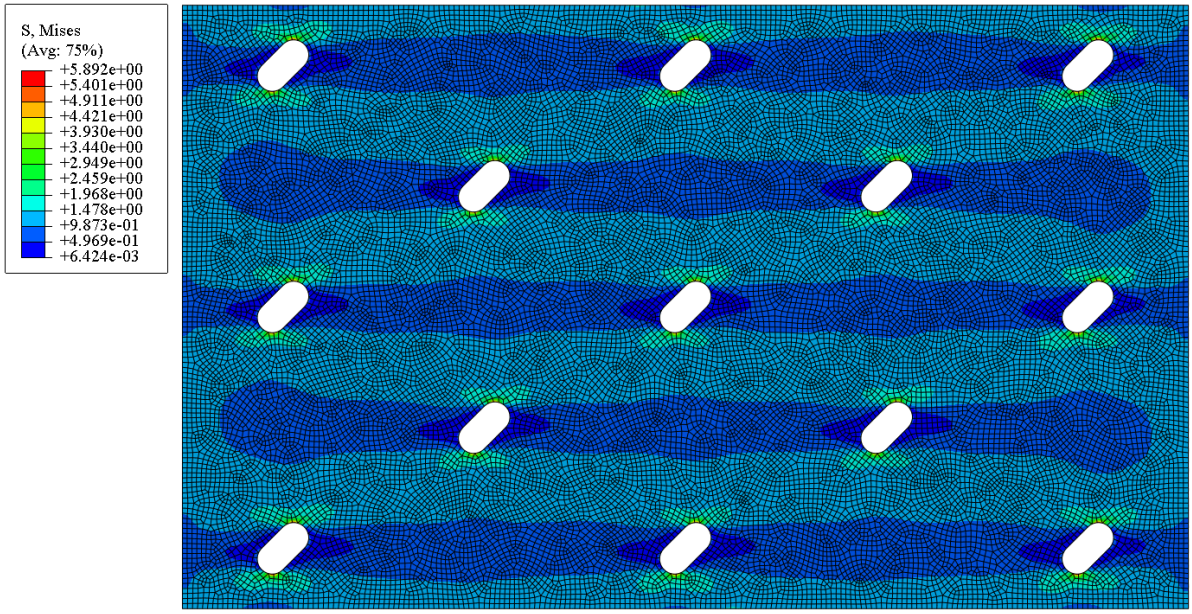

(a) Von Mises stress of full width scale model, oval shape notch, orientation angle $\theta = 45°$, $d_\theta = 2.56$ µm.

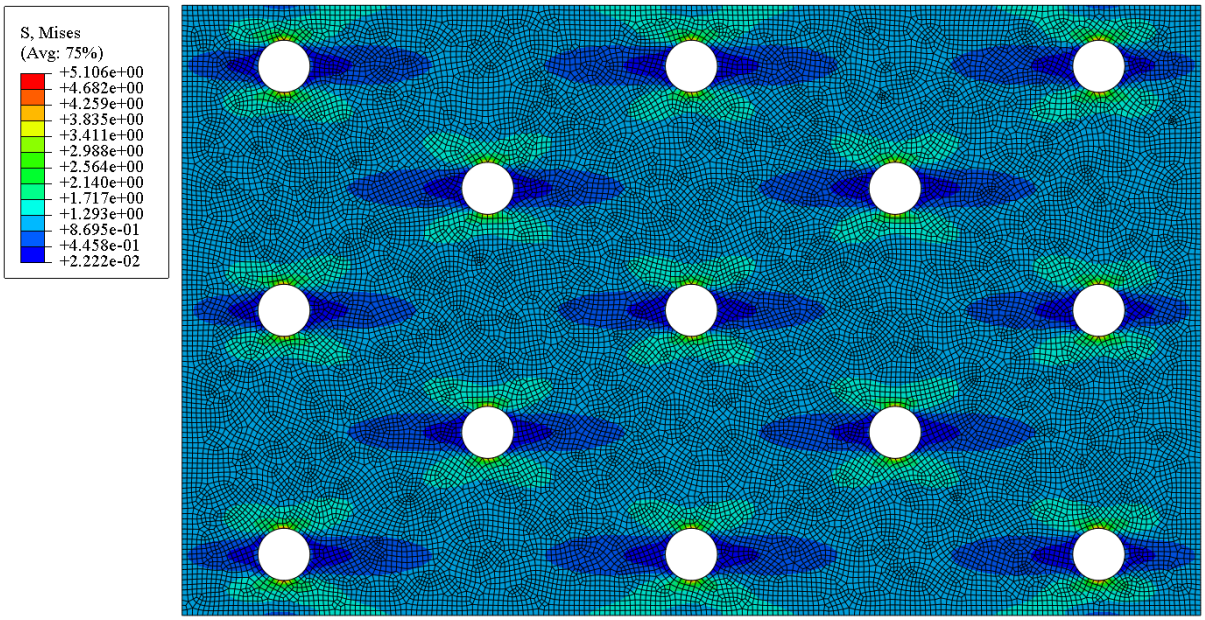

(b) Von Mises stress of full width scale model, round shape notch, $d = 2.56$ µm

Figure 16. Stress fields of full width scale models.

4 DISCUSSION

This paper has examined structure and irregularities in fibers from Norway spruce. Mathematical models were developed and then used to examine the stress behavior of the fibers. The effect of material properties and the shape of the pits have been examined.

Firstly, the behavior of models will be considered, for instance, maximum stress is located at the edge of pit as expected, this is demonstrated in Figure 12. Hence, the stress field looks reasonable, symmetric and continuous. Accordingly the behavior of stabilization can be assumed to acceptable. Similarly, from Figures 13(a) and 13(b) one can see that the finite element model gives very similar values as the analytical calculation and in fact it is reasonable that the analytical calculation will estimate slightly higher stresses because the safety of the calculations is better.

Secondly, the results of models show that a change of material properties from being isotropic to anisotropic has a major impact on the maximum stress at the edge of pit. The effect of this kind of material change is shown in Figures 14(a) and 14(b). In both models, i.e., round and oval shaped models, the stress difference between the material

models increases when the effective width of plate decreases.

Furthermore, the effect of the shape of the pit is shown in Figures 14(c) and 14(d). The results reveal that there are differences in the stresses with the different shapes. However, the difference is less than what was expected. It was anticipated that the oval shape would increase the stress maximum even more. The effect of this shape of pit is also considered in Figure 15(b) where factors K_t of oval and round shaped model are presented. From Figure 15(b) one can see that the effect of the oval shape is largest when the orientation angle θ is 15 – 25 degrees.

Finally, it can be seen from Figures 16(a) and 16(b) that pits really do have an effect on the accumulation of stresses when full width fiber wall is subjected to loading. The maximum stresses at edge of the pits, need to be taken into account if the starting point of yielding or fracture are considered.

In conclusion, the effect of pits and pores in an anisotropic material has been found to be interesting issue in the point of view of pulping where pores arise in the cell wall of fibers. As a result future work will be able to develop better mathematical models which can predict the elasticity of fiber and take into account the effects of man made and natural irregularities.

REFERENCES

[1] K. Niskanen (editor). Papermaking Science and Technology, Part 16. Paper Physics, Fapet Oy, (1998)

[2] D.H. Page. A method for determining the fibrillar angle of wood tracheids. *J. of Microscopy* **90**(2):137-143 (1969)

[3] J. Sundholm (editor). Papermaking Science and Technology, Part 5. Mechanical Pulping, Fapet Oy, (1998)

[4] M.-S. Ilvessalo-Pfäffli. Fiber Atlas, Identification of Papermaking Fibers. Springer-Verlag, (1995)

[5] J. Sirviö and P. Kärenlampi. Pits as natural irregularities in softwood fibers. *J. Wood and Fiber Science* **30**(1):27-39 (1998)

[6] K. Persson. Micromechanical modelling of wood and fibre properties (In Sweden). PhD thesis. Lund University (2000).

[7] J.E. Berg. Wood and fiber mechanics related to the thermomechanical pulping process (In Sweden). PhD thesis, Mid Sweden University (2008).

[8] M.-P. Sarén, R. Serimaa, S. Andersson, T. Paakkari, P. Saranpää and E. Pesonen. Structural variation of tracheids in Norway spruce. *J. of Structural Biology* **136**:101-109 (2001)

[9] H. Outinen and T. Salmi. Lujuusopin perusteet. Pressus Oy, 2004

Session 2

Fiber Network Modeling

Elasticity and Stiffness of Paper: A model based study of the influence of fibers

S. LAVRYKOV, K. M. SINGH[1] and B.V. Ramarao

Department of Paper and BioProcess Engineering
Empire State Paper Research Institute
SUNY College of Environmental Science and Forestry, Syracuse, NY 13210
bvramara@esf.edu

[1]International Paper Co.
6283 Tri Ridge Blvd, Loveland, OH 45140

Keywords: Stiffness, Elastic Modulus, Network Simulation, Structure, Fibers, Paper Properties.

ABSTRACT

The stiffness of paper is effected by the elastic modulus, sheet density and its thickness, all of which are in turn strongly dependent on the fiber network constituting paper. Improvement of stiffness can be achieved only through an understanding of the impact of the large variety of papermaking variables.

In this paper, we developed a fibrous network model to represent paper structure with fibers considered to be solid deformable blocks modeled by cubical elements. The compression of randomly placed fibers was simulated using the finite element method. Bonding between fibers was simulated using elements of zero thickness.

The resulting fiber network was analyzed to determine its elastic modulus and deformation under small strains. The influence of fiber refining, fiber dimensions, bond stiffness and other papermaking variables on the elastic modulus were evaluated. .

1 INTRODUCTION

Stiffness is an important property that governs the performance of the paper. Stiffness S^b is defined by

$$S^b = MR = \frac{E_s t^3}{12} \quad (1)$$

where M is the bending moment (N), R is the radius of curvature, E_s is the elastic modulus (Pa) and t is the thickness of the sheet (m). Bending stiffness depends on the width of the sheet and therefore, the above definition is given for a sheet of unit width. Stiffness is thus a function of the nature of the fibers, their bonding and the resultant sheet structure. A very large number of variables thus affect stiffness including fiber characteristics, spatial distribution and the drying process. A good simulation of sheet structure built from 'first principles' to account for the nature of the fibers, the state of interfiber bonding, the stresses in the free fiber regions and so on will enable better design of sheets for stiffness properties.

In order to investigate the impact of varying fiber dimensions or other similar properties on paper properties, a number of computer based simulations of paper forming have been developed. The earliest computer simulation of paper structure was based on dropping lines at random and investigating the statistics of the resulting structure [1, 2]. Although the two-dimensional structure properties can be studied with these simulations, generalizing them to a three dimensional structure of paper needs to account for the bending of fibers over one another and for the collapse of the cell wall and the lumen regions. One of the earliest computer simulations to fully develop a three dimensional structure for paper sheets was given by Hamlen [3]. The structure of paper was simulated by first dropping fibers along the edges of a unit rectangular cell. Once the fibers came into contact, he used beam deflection theory to simulate the bonding between fibers in a paper sheet. This was a good approximation to the real fiber structure during the consolidation process of a paper sheet. Hamelin then determined the three-dimensional permeability tensor. Niskanen et al. [4] developed an extension of Hamlen's simulation technique by laying the fibers at random and then 'pressed' uniformly to achieve realistic sheet densities. This was known as the KCL-PAKKA model for paper structure [19]. The mechanical properties of such generated structures have been extensively investigated and showed good correspondence with experimental measurements. However, the fibers were limited to assume MD and CD orientation. Many transport properties were over predicted by their simulations. Koponen et al. [5] used the Lattice-Boltzmann simulation technique for the creeping flow equations to determine the permeability of the structures generated by the KCL-PAKKA model. When compared with actual experimental values, predicted permeabilities from the simulations were orders of magnitude higher although the mechanical properties such as stiffness and elasticities were in good correspondence [6]. Thus the stochastic

simulation technique does not adequately capture the physics of the forming of the paper structures at least as far as transport properties are concerned.

The elastic behavior of paper can be understood from a combination of experimental, semi-empirical, and analytical approaches [7]. Models representing paper as a 2-D planar network of randomly laid fibers or as a 2-D laminated composite have been presented. A 3-D network model was presented by Heyden and Gustafsson [8]. In this model a cubic unit cell, with dimensions 1.2–4.8 times the fiber length is considered and fibers are deposited randomly. The fibers are modelled as linear elastic Bernoulli beams of constant curvature and bonds are assumed to be either perfect in transferring stress or none at all. The stress–strain curve was simulated. No experimental results were presented to validate the model. Their model is useful for understanding fiber fluff and very low density paper behavior but not applicable for a majority of paper and paperboard microstructures. Inelastic behavior of paper has been modelled using a mesoelement approach by Ramasubramanian and Perkins [9]. A fiber was defined as the representative volume element (RVE) and many crossings of other fibers were considered to affect the boundary. Network geometry, fiber length and orientation distributions, sheet density, and fiber and fiber-to-fiber bond constitutive behavior were taken into account. Fiber behavior can be different in tension and compression thereby the possibility of fiber buckling under compression is included. Monotonic increase in load was simulated. A two-dimensional stochastic computational network model to simulate uniaxial tension tests was presented by Bronkhorst [10]. A two-dimensional stochastically generated network consisting of fibers in a 10 mm x 10 mm area was studied. The fiber-to-fiber bond was assumed rigid and the fibers behavior was modeled with continuum plasticity models. A finite element model of the structure with isotropic elastic–plastic beams, and in uniaxial tension was developed. Bronkhorst's structure is only two-dimensional and hence cannot be used for a simulation of stiffness where the three dimensional structure is critical in determining both the elasticity and sheet caliper.

Three-dimensional networks of paper structure have been developed in a number of ways earlier, but all of them approximate fiber bending in important but limiting ways. Kahkonen's [11] simulation laid fibers on a substrate by sedimenting randomly oriented fibres and bending them in an approximate manner thus providing three-dimensionality to the structure. The rigidity of this structure was investigated using network theory. Recently, Drolet and Uesaka [12] constructed the three dimensional sheet structure assuming stiffness elements representing fibers during compression and unloading. The structure was used to simulate the impact of sheet surface on printing. Similar work has also been published by Provatas and co-workers [17, 18]. Another simulation of paper structure was developed by Vincent et al., [13, 14]. In their simulation, fibers were bent over each other according to two fixed bending angles which were 'tuned' by matching the apparent density of the resulting structure to observed values. Since the apparent density is a key variable for stiffness and elasticity, simulations which can predict this apriori are necessary.

The present simulation computes the bending of each fiber according to its mechanics. Each element in the fiber is described by its own stress-strain relation and governs its deformation. As a result, the simulation allows fibers to curl, bend and drape over each other in accordance to the stresses in forming and pressing. In addition to applied pressure, the simulation considers the forming stresses arising from fluid drag on the fibers. Once the fiber network is formed, its deformation under different kinds of loads is simulated. Our initial calculations focused on the linear and small deformation regime for the network, thus yielding information on the elastic moduli. When this is combined with the sheet density and thickness, the stiffness could be predicted using Eq (1). Specific focus is placed on refining and its effect on stiffness. Pulp refining is simulated by altering fiber properties to reflect: internal fibrillation changing the wet fiber flexibility, external fibrillation changing fiber thickness, width and specific surface area, cutting resulting in fiber shortening and fines generation and kink and curl removal. Stiffness depends on the elastic modulus which depends on the relative bonded area (RBA) besides other parameters. The RBA is directly proportional to the sheet density, so much so that we are able to use density as a surrogate for the RBA. The elastic modulus is determined from the sheet structure, as a function of fiber geometry, bond stiffness and other parameters. The elastic modulus for refined sheets is well simulated when compared to experimental data in the literature. An interesting question is whether it is possible to create sheet structures which will minimize critical inputs e.g. fiber mass but maximize the stiffness, by manipulating the density distribution in the sheet. For this purpose, we investigate the effect of different types of profiles of sheet structure on stiffness and in particular the impact of lower sheet density in the central region of paper on its stiffness.

Another important factor for the elastic modulus is the drying shrinkage. Papers dried under restraint do not shrink and residual stresses are built into the fibers at the time of drying. The resultant sheets have higher moduli of elasticity and the fiber segments are referred to as being 'activated'. It is not clear, however, what affect the geometry of

paper network and the properties of papermaking fibers have on the relationship between paper elasticity and drying restraints. Our model can estimate the elastic properties of paper as a function of the drying shrinkage. The qualitative features obtained from the model calculations are consistent with experimental observations and independent of details of the elastic properties of fibers.

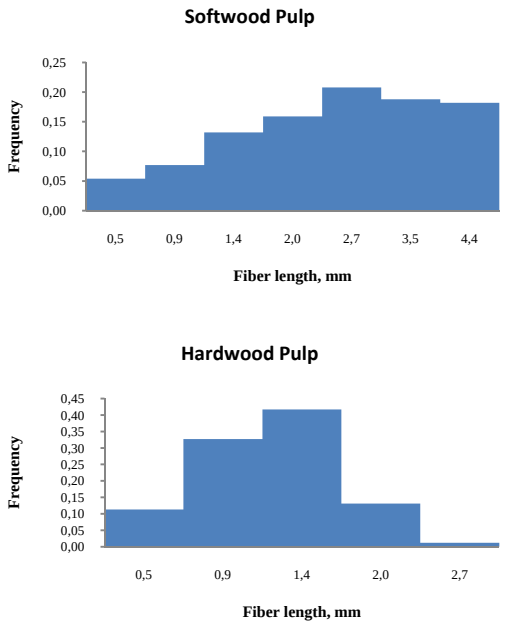

Figure 1. Fiber length distribution for softwood and hardwood pulps.

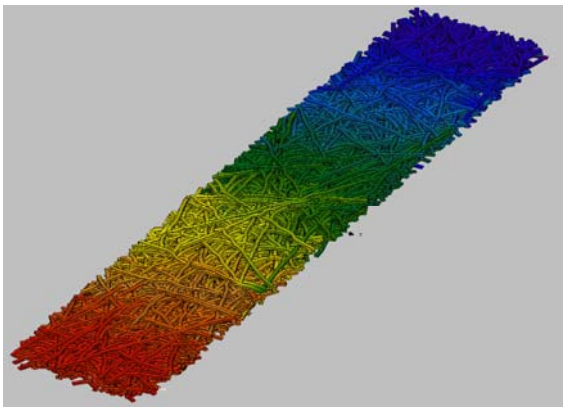

Figure 2. Strip of simulated paper 1mm x 5 mm; 64 GSM (SW Pulp).

2 MATERIALS AND METHODS

We report here the simulation of two different sets of pulp samples. The first is softwood pulp while the second is a bleached kraft hardwood pulp. The fiber length distributions for these samples were drawn from a Kajaani FS-100 analysis. Fig 1 shows these distributions.

3 RESULTS

Fig 2 shows simulated constructions of the 3D paper structures. The size of the paper strip was 5mm x 1 mm and was sufficient to yield good results for both the elastic modulus and the stiffness. Fig 3 shows another view of the pore fiber network structure. When fibers are compressed to form the network structure, residual stresses remain in them. These are also shown in this figure. The simulation calculates these values so that they can be used to study effects of different drying strategies (inducing differential residual stresses) and also the impact of different density distribution within the sheets. Fig 4 shows our calculations for the elastic modulus of the sheets as a function of sheet caliper. Since the BW is assumed a constant in these simulations, increased caliper refers to lower density of the sheets. As can be expected, the elastic modulus decreases with caliper (i.e. density). When stated explicitly, the elastic modulus can be given as a function of density as:

$$E_s = a\rho^2 + b\rho \qquad (2)$$

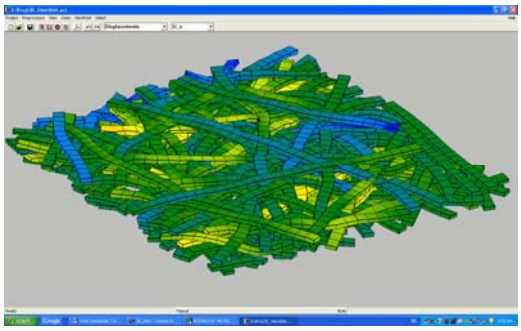

Figure 3. Fiber network shown with residual stresses in the fibers.

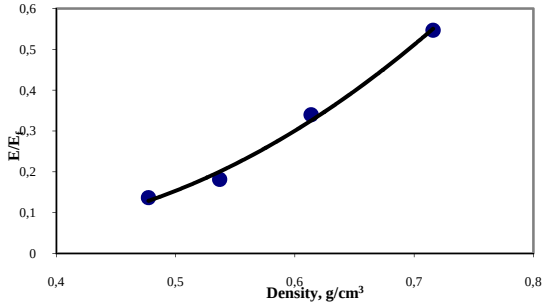

Figure 4. Network elastic modulus ratio as a function of sheet density. BKSW pulp fibers.

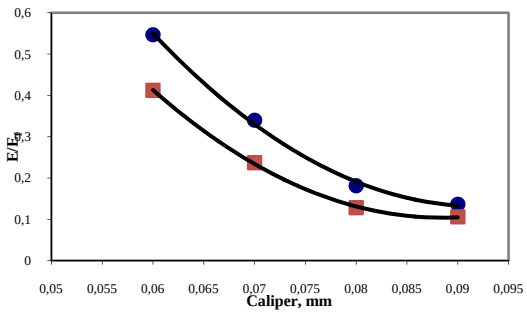

Figure 5. Elastic modulus of sheets as a function of thickness. Upper data correspond to softwood and lower to hardwood pulps.

An expression for the elastic modulus of a sheet as a function of the modulus of the individual fibers is that given by Page [see e.g. Seth and Page, 15]

$$E_s = \frac{E_f}{3}\left[1 + \frac{w}{l_f RBA}\sqrt{\frac{E_f}{2G_f}}Tanh\left(\frac{l_f RBA}{w}\sqrt{\frac{2G_f}{E_f}}\right)\right] \qquad (3)$$

The sheet modulus decreases with caliper in Fig 5. The dependence is not linear. The simulated sheets consisted of equal numbers of fibers giving constant basis weight but were pressed to different calipers yielding higher density as caliper decreased. The decrease in modulus as caliper increases is caused by decreased density. This curve is non-linear as can be expected from the quadratic density dependence of E (c.f. Eq. (2) above). The decrease in the observed sheet modulus follows the same trend that is predicted by our simulations.

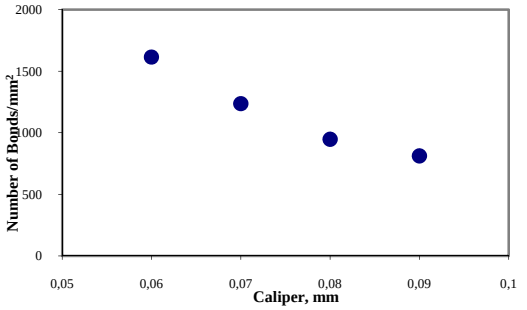

Figure 6. Relative bonded area of sheets as a function of sheet caliper (BKSWP). RBA is shown in scaled terms representing number of bonding elements per unit area of sheet.

The relative bonded area is displayed in Fig 6 as a function of caliper. The RBA increases with decreasing caliper, an indication of increased modulus and possibly higher strength of the sheets. Fig 7 shows the corresponding elastic modulus shown as a function of RBA, establishing the direct relation between these two parameters.

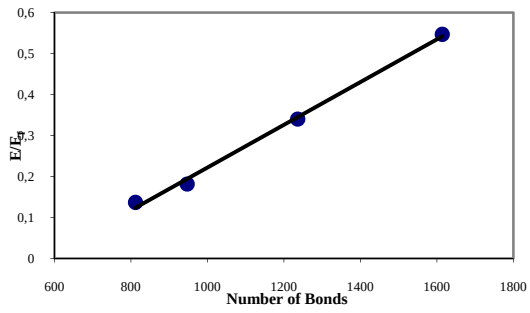

Figure 7. Relative bonded area of sheets as a function of sheet caliper (BKSWP). RBA is shown in scaled terms representing number of bonding elements per unit area of sheet.

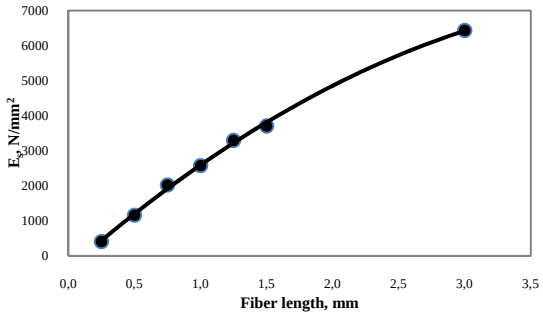

Figure 8. Sheet elastic modulus as a function of fiber length (BKHWP).

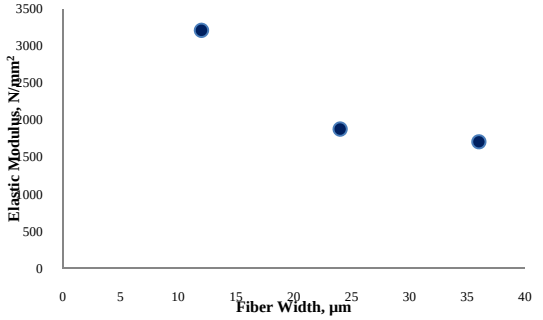

Figure 9. Sheet elastic modulus as a function of fiber widths (BKHWP).

Figs 8 thru 10 show the effects of varying fiber length, width and thickness. Increasing fiber length causes an increase in the modulus. This prediction is counter to some recent observations by Hjelt et al [20] who found experimentally that fiber lengths did not affect the elastic modulus of sample handsheets. This effect needs to be explored in more detail in order to determine its cause as well as whether other effects possibly mask the fiber length. The effect of increasing either the width or the thickness is relatively simple to understand, there being lesser numbers of fibers of increased

width or thickness in a chosen grammage sheet, thus resulting in lower elastic modulus.

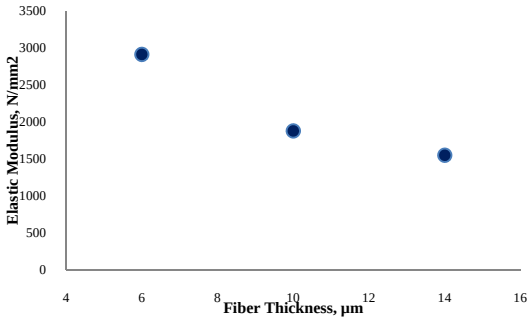

Figure 10. Sheet elastic modulus as a function of fiber thickness (BKHWP).

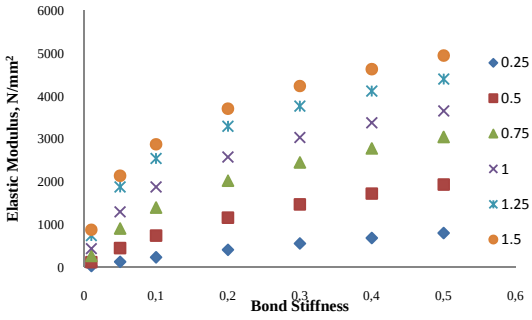

Figure 11. Sheet elastic modulus as a function of inter-fiber bond stiffness (shown as a bond shear modulus scaled to the fiber elastic modulus). Each data set corresponds to a different fiber length.

Fig 11 shows the effect of bond stiffness on the elastic modulus. Inter-fiber bonds are represented by elastic springs connecting nodes of the bonding elements. The spring constants correspond to elastic modulus of the bonds. The simulation shows that the impact of the bond stiffness decreases when bond stiffnesses are greater than about 0.5. This confirms the experimental observation that increased bonding generally has small to negligible influence on sheet elasticity.

Figure 12 shows the sheet density calculated with different wet pressing pressures for the pulps of three different refining levels described above. Experimental results of handsheets made from BKPSW pulps refined to different levels are shown in this figure. A good correspondence between the simulations and experimental results can be observed although the simulation densities are slightly higher. This is perhaps a consequence of the uncertainty in the fiber elastic modulus.

5 ACKNOWLEDGEMENTS

The member companies of the Empire State Paper Research Institute are gratefully acknowledged for the financial support of this project.

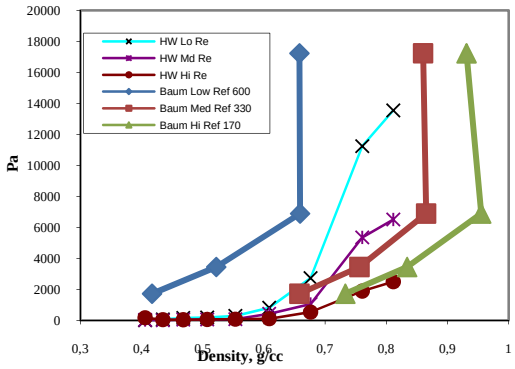

Figure 12. Plot of sheet density as a function of wet pressing pressure (sample handsheets simulated). Simulation results for Bleached kraft hardwood pulp (Refining – 650, 350, 150 ml CSF). Experimental data for pulps obtained by Baum et al [16] are shown.

4 CONCLUSIONS

A number of important papermaking variables have not yet been considered in our simulation. These are relatively simple to include. These include fiber orientation particularly in machine made sheets. Most machine made sheets show a density gradient with the layers close to the wire having higher densities compared to the top side. This densification usually is a consequence of the hydraulic pressure distribution in the press section. When fillers and fines are present, a reverse situation is obtained, due to scouring and resuspension in the mat in the forming section. The shape of these gradients is also dependent on the former: e.g. Fourdrinier vs. twin wire formers. These effects can be built into the simulation and actual density gradients can be mirrored. Fillers decrease tensile strength of sheets by interfering with the fiber bonding and drape of fibers over each other. Although sheet caliper increases, the higher density of the fillers takes over and can effectively reduce stiffness. The effect of fillers on stiffness can be quite complex and depends on the state of bonding, filler size and their state of agglomeration. The simulation provides an excellent tool to study these and guide the development of the furnish and papermaking conditions.

Fiber segments are activated during drying as a consequence of sheet restraints. Differences in fiber orientation and density gradients contribute to these and result in dimensional instability such as curl and hygroexpansion. These effects can be well simulated by our formulation.

REFERENCES

[1] O. Kallmes and H. Corte. The structure of paper. I. The statistical geometry of an ideal dimensional fiber network. *Tappi J.***43** (9):737-752 (1960).

[2] H. Corte and O.J. Kallmes. Statistical Geometry of a Fibrous Network. Formation and Structure of Paper, Trans. 2nd Fund. Res. Symp. Oxford 1961, London, BPBMA, 13-46 (1962).

[3] R.C. Hamlen. Paper Structure, Mechanics and Permeability: Computer Aided Modeling. PhD thesis, University of Minnesota (1991).

[4] K. Niskanen, N. Nilsen, E. Helleng and M. Alava. KCL-PAKKA: Simulation of the 3D structure of Paper. The Fundamentals of Papermaking Materials, Trans. 11th Fund. Res. Symp. Cambridge 1997, Leatherhead Surrey, PIRA International, 1273-1291 (1997)

[5] A. Koponen, D. Kandhai et al. Permeability of three dimensional random fiber webs. Phys. Rev. Let. **80**(4): 716-719 (1998).

[6] H. Kettunen and K. Niskanen. On the relationship of fracture energy to fiber debonding, Tappi 1999 International Paper Physics Conference, Atlanta, Tappi Press, 125–143 (1999).

[7] K. Niskanen and P. Karenlampi. In-Plane tensile properties. In: Paper Physics, Book 16, Papermaking Science and Technology, Niskanen K. Ed., pub. Fapet Oy, PO Box 146 FIN-00171, Helsinki, Finland, 138-191 (1998).

[8] S. Heyden and P.J. Gustafsson. Stress-strain performance of paper and fluff by network modeling. The Science of Papermaking, Trans. 12th Fund. Res. Symp. Oxford 2001, Bury, UK, PPFRS, 1385-1401 (2002).

[9] M.K. Ramasubramanian and R.W. Perkins. Computer simulation of the uniaxial elastic-plastic behavior of paper. J. Eng. Mater. Technol. **110**(2): 117-123 (1988).

[10] C.A. Bronkhorst. Modeling paper as a two-dimensional elastic-plastic stochastic network. Int. J. Solids Struct. **40**(20): 5441-5454 (2003).

[11] S. Kahkonen. Elasticity and stiffness evolution in random fibre networks. PhL thesis, University of Jyvaskyla (2003).

[12] F. Drolet and T. Uesaka. A stochastic structure model for predicting sheet consolidation and print uniformity. Advances in Paper Science and Technology, Trans. 13th Fund. Res. Symp. Cambridge 2005, Bury, UK, PPFRS, 1139-1154 (2005).

[13] R. Vincent, M. Rueff and C. Voillot. 3-D computational simulation of paper handsheet structure and prediction of apparent density. *Tappi J.* **8** (9):10-17 (2009).

[14] R.Vincent, M.Rueff and C.Voillot. Prediction of handsheet tensile strength by computational simulation of structure. *Tappi J.* **9** (1):15-19 (2010).

[15] R. S. Seth, D.H. Page. The stress-strain curve of paper. The Role of Fundamental Research in Paper Making, Trans. 7th Fund. Res. Symp. Cambridge 1981, London, Mech. Eng. Publ., 421-452 (1983).

[16] G.A. Baum, C.C. Habeger and E.H. Fleischman. Measurements of the orthotropic elastic constants of paper. The Role of Fundamental Research in Paper Making, Trans. 7th Fund. Res. Symp. Cambridge 1981, London, Mech. Eng. Publ., 453-478 (1983).

[17] N.Provatas, M. Kataaja. Fiber deposition models in two and three spatial dimensions. *Colloids and Surfaces, A: Phys. and Eng. Asp.* **165** (1-3):209-229 (2000).

[18] N.Provatas and T. Uesaka. Modelling Paper Structure and Paper-Press Interactions. *JPPS* **29** (10):332-340 (2003).

[19] N. Nilsen, M. Zabihian and K. Niskanen. KCL-PAKKA: a tool for simulating paper properties. *Tappi J.* **81** (5):163-166 (1998).

[20] T. Hjelt, E. Saharinen, S. Heinemann and J. Sirviö. Pure effect of fiber length on paper strength. Progress in Paper Physics Seminar 2010, FP Innovations, Montreal, Canada (2010).

Multi-scale simulation of paperboard edge wicking using a fiber-resolving virtual paper model

A. MARK[1,⋆], R. SANDBOGE[1], A. BERCE[1],
F. EDELVIK[1], E. GLATT[2], S. RIEF[2],
A. WIEGMANN[2], M. FREDLUND[3],
J. AMINI[3], R. LAI[4], L. MARTINSSON[5],
U. NYMAN[6], J. TRYDING[6]

[1]Fraunhofer-Chalmers Centre, Gothenburg, Sweden
[2]Fraunhofer ITWM, Kaiserslautern, Germany
[3]Stora Enso, Karlstad, Sweden
[4]Eka Chemicals, Bohus, Sweden
[5]Albany International, Halmstad, Sweden
[6]Tetra Pak Packaging Solutions AB, Lund, Sweden

⋆Correspondence to:
andreas.mark@fcc.chalmers.se

Keywords: Multi-scale simulation, Edge soaking, Porous flow, Immersed boundary, Pore-morphology method

ABSTRACT

When liquid paperboard based package material is made aseptic, unsealed edges of the board are exposed to a liquid front which in some circumstances may soak the material to some extent. This is not desired since it may lead to aesthetic as well as functional defects. In order to make a priori predictions of the edge wicking properties of a given paper material, something which is of great interest to paperboard industry as well as packaging manufacturers, micro simulations are required.

To calculate the penetration of fluid in the open edge of a paper sheet a multi-scale framework is developed. On the fiber micro-scale, virtual paper models are generated in PaperGeo [6]. In IBOFlow [7] a pore morphology method is used to calculate capillary pressure curves, and the active pores one-phase flow simulations are performed for relative permeabilities. The result is a database of capillary pressure curves and relative permeabilities as functions of saturation and porosity. The database is used as an input for a two-phase flow simulation on a 2D virtual macro sheet to calculate the penetration of fluid in the paper. The multi-scale framework is validated against pressurized edge wick measurements with good agreement.

1 INTRODUCTION

When liquid paperboard based package material is made aseptic, unsealed edges of the board are exposed to a liquid front which in some circumstances may soak the material to some extent. This is not desired since it may lead to aesthetic as well as functional defects. The susceptibility of a paperboard material to edge soaking, or edge wicking, is highly dependent on the physical properties of the paper network structure and of the additives used in the pulp. In order to make a priori predictions of the edge wicking properties of a given paper material, something which is of great interest to paperboard industry as well as packaging manufacturers, simulations that take the micro-structure into account are required.

A review of wetting of paperboard has been performed by Rentzhog [10]. She found four mechanisms for water transport in paper proposed in the literature [3, 12, 13]: Diffusion transport of vapor in the pores, capillary transport of liquid in the pores, surface diffusion in the pores and water transport through the fibres. She also reported that to predict the actual water penetration in paper it is necessary to take the external pressure, capillary pressure, counter pressure of air, swelling of the fiber network and liquid transport through the vapor phase, into account.

From previous work, we conclude that the micro-structure of the paper is of great importance for the edge wick performance. Therefore it is necessary to develop numerical methods based on micro-structure models to increase the understanding of the important effects of edge wicking.

In this work, edge wicking simulations have been performed on micro (fiber resolving level) scale for a virtual paper model generated in PaperGeo, the virtual paper structure generator in GeoDict [6]. The virtual paper consists of a stochastic distribution of paper fibers of varying size and cross-section. In the virtual paper model, statistical properties of the fibers are given, such as average major/minor axes, oscillation amplitudes, average volume fraction of fibers. These parameters were originally taken from tomographic images of the paper and were subsequently fine-tuned using air permeability simulations and measurements both in the paper plane and the out of plane direction.

On the paper scale, simulations have been performed using a mixture model. On this scale, liquid saturation level and pressure as a function of time were simulated in a homogenized 2D virtual paper with varying anisotropic paper porosity. To close the models on the macro-scale, micro simulations on the fiber scale are

required. On the fiber scale, the pressure drop and relative permeabilities have been simulated by IBOFlow (Immersed Boundary Octree Flow Solver) [9, 8] for different saturation levels and porosities. The pressure drop in different micro-structure realizations was simulated geometrically by a pore-morphology model. In these simulations Laplace law was used to calculate the surface tension as a function of contact angle. The liquid penetration of different channel sizes at different pressure drops is the key to predict the soaking process.

The outline of the rest of the paper as follows: In Section 2 the micro and macro-scale models along with their couplings are presented, then the experimental methods are described in Section 3. In Section 4 the numerical results are presented along with a comparison with the experiments and in the last section the paper is summarized and some future work is outlined.

2 GOVERNING EQUATIONS

Due to the large difference in scales from the fiber to the paper level, we use a multi scale ansatz for simulation of edge wicking. On the macro-scale, the fluid flow is modeled by a porous mixture model, where Darcy's [2] law is employed to derive a pressure equation. The resulting velocity field transports the saturation. To close these models the permeability and capillary pressure as a function of saturation are required, which makes the model non-linear. The permeability and capillary pressure are calculated on the fiber micro-scale on a virtual model of the paper. On this scale the fluid flow is modeled by the full Navier-Stoke's equation. The simulation framework is FCC's in-house, incompressible Navier-Stokes software, IBOFlow [7]. IBOFlow is a segregated solver that utilizes the SIMPLEC method [5] for coupling of the velocity and pressure fields. All variables are stored in a collocated arrangement and Rhie-Chow interpolation [11] is used to prevent pressure oscillations. It is based on a finite volume discretization on a Cartesian octree grid that can be dynamically refined and coarsened. The flow around the fibers are resolved and immersed boundary methods [9, 8] are used to model the presence of fibers in the flow.

2.1 Macro-scale model

A porous media model based on [4] is derived for a two phase fluid system of water and air, with application to flow in paper. The model is based on Darcy's law [2] and mass conservation of water and air, which are used to derive a pressure equation. Mass conservation of air and water is given by the continuity equation,

$$\Phi \frac{\partial (\rho_\alpha S_\alpha)}{\partial t} + \nabla \cdot (\rho_\alpha \vec{u}_\alpha) = q_\alpha \quad , \alpha \in \{w, a\} \tag{1}$$

where $\Phi = \Phi(x)$ is the porosity of the porous medium ($\Phi = 1$ corresponds to all volume is fluid), ρ_α is the density, S is the saturation, $\vec{u}$ is the velocity, and q is the source mass flow rate, for water $\alpha = w$ and for air $\alpha = a$. Darcy's law [4, 2] for each phase relates the velocity to the gradient of the pressure linearly,

$$\vec{u}_\alpha = -\frac{\kappa_{kr}}{\mu_\alpha} \vec{\kappa} \left(\nabla p_\alpha - \rho_\alpha \vec{g} \right) \tag{2}$$

where $\vec{\kappa} = \vec{\kappa}_{i,j}$ is the absolute permeability tensor of the porous medium, κ_{kr} is the relative permeability, μ_α is the viscosity, P_α is the pressure, g is the gravitational acceleration. The fluids fills the void of the porous medium, represented by Φ, $S_w + S_a = 1$ and the pressure difference between the two phases is given by the capillary pressure $p_c(S, \vec{x}) = p_a - p_w$. The capillary pressure under capillary equilibrium is for a narrow tube or a pore of circular cross-section given by the Young Laplace equation

$$p_c = \Delta p = \frac{2g\gamma \cos\Theta}{r} \tag{3}$$

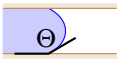

where Θ is the contact angle, γ is the surface tension, and r is the radius of the tube.

Let us introduce a weighted pressure $p = S_w p_w + S_a p_a$ which is continuous between the phases and neglect gravity as the length and time-scales are small. This along with the capillary pressure definition gives a reformulated Darcy's law

$$\vec{u} = -\vec{\kappa} \left(\tilde{\lambda} \nabla p + \left[S\tilde{\lambda} - \lambda_w \right] \nabla p_c + \tilde{\lambda} p_c \nabla S \right) \tag{4}$$

where λ_w is the water mobility, $\tilde{\lambda}$ is the total mobility and S is the water saturation. Darcy's law and the assumption of a divergence free fluid velocity field (incompressible flow) then gives an equation for the weighted pressure

$$-\nabla \cdot \left(\vec{\kappa}\, \tilde{\lambda} \nabla p \right) = -\nabla \cdot \left[\vec{\kappa} \left(S\tilde{\lambda} - \lambda_w \right) \nabla p_c + \tilde{\lambda} p_c \nabla S \right]. \tag{5}$$

Now let the saturation be transported by the Darcy's velocity

$$\Phi \frac{\partial (S)}{\partial t} + \vec{u} \cdot \nabla S = 0 \tag{6}$$

where the convective term is discretized by the shock capturing CICSAM scheme [14]. The macro model has been implemented in IBOFlow. One should notice that the capillary pressure, permeabilities and phase mobilities are also dependent on the local porosity, which is captured in the micro models. The complete set of equations describing the two phase porous flow is complete by incorporating the micro simulations of permeability and capillary pressure.

2.2 Micro-scale model

On the micro-scale the virtual paper consists of a stochastic distribution of paper fibers of varying size and cross section. Each fiber is considered as a hollow non-straight slender body with an ellipsoidal cross-section. In the virtual paper model, statistical properties of the fibers are given, such as average major/minor axes, oscillation amplitudes, average volume fraction of fibers. These parameters were originally taken from tomographic images of the paper and were subsequently fine-tuned using air permeability simulations and measurements both in the paper plane and the out of plane direction. GeoDict is employed to generate a number of virtual papers representing the different parts of the constructed CTMP lab sheets.

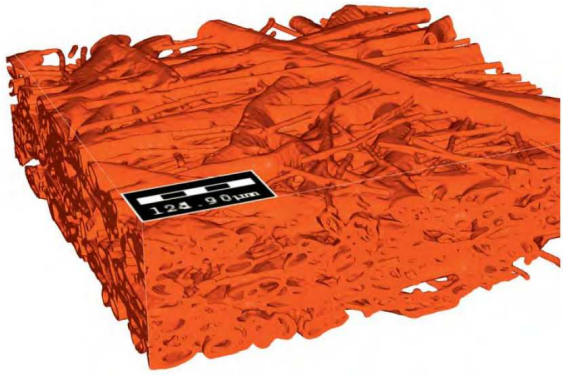

Figure 1: Stochastic realization of the micro-structure of a CTMP lab sheet in PaperGeo.

The motion of the fluid is governed by the Navier-Stokes equations:

$$\nabla \cdot \vec{u} = 0 \tag{7}$$

$$\rho_f \frac{\partial \vec{u}}{\partial t} + \rho_f \vec{u} \cdot \nabla \vec{u} = -\nabla p + \mu \nabla^2 \vec{u} \tag{8}$$

In the equations above, $\vec{u}$ is the fluid velocity, ρ_f is the fluid density, p is the pressure and μ is the dynamic viscosity.

A possible approach would be to solve these equations for the two-phase flow of water penetrating the fiber structure, e.g. by the Volume of Fluid (VoF) method in IBOFlow, to calculate the permeability. However, this would be computationally very expensive and we adopt a different strategy for which a series of one-phase flow simulations are done instead.

First, the capillary pressure is modeled by a pore-morphology model [1]. Larger and larger spheres are inserted and propagated through the paper structure. For each sphere radius we can calculate a saturation and the relationship between a pore size and the capillary pressure is then given by (3). As a result we get a capillary pressure curve for each virtual paper sample. Secondly, we perform one-phase flow simulations for the channels that are open for a certain capillary pressure. For each paper sample this results in a relationship between permeability and saturation. By simulating different paper samples with varying porosity, the porosity dependency is also captured.

3 EXPERIMENTS

Figure 2: SEM micrographs of CTMP performed at Albany International.

3.1 Manufacturing of lab sheets

Paper lab sheets are manufactured using a STFI dynamic sheet former with circulating pulp, moving head box and a stationary forming fabric. CTMP (Chemo Thermo Mechanical Pulp) pulp with and without AKD sizing chemicals was used. The lab sheets were dried and pressed by a rotating cylinder. The grammage of the resulting CTMP lab sheet was $\sim 60 g/m^2$, see Figure 2 for an SEM image.

3.2 Pressurized edge wick test case

In Figure 3 the pressurized edge wick equipment is shown. The purpose of the equipment is to simulate the environmental conditions in the deep bath of a filling machine. The diameter of the pressure-vessel is $250 mm$ and its height is $190 mm$. The vessel is filled

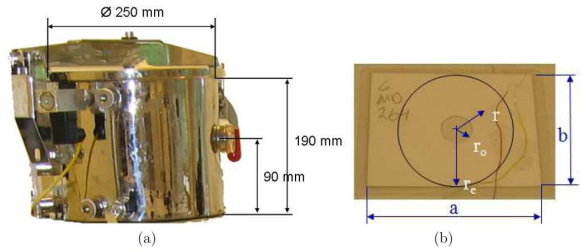

Figure 3: (a) The pressurized edge wick equipment (b) A test sample of size of $a = 62\,mm$ and $b = 50\,mm$. The punched hole has a radius of $r_o = 6\,mm$.

Figure 4: A sample from the pressurized edge wick experiments.

with water to a height of $90\,mm$. The water temperature is set to a predefined level. The paper samples (see Figures 3b and 4) consist of a punched hole with radius $r_0 = 6\,mm$ where the liquid is free to penetrate into the polyethylene laminated paperboard. The size of the paper sample is $62 \times 50\,mm^2$. The outer edge is also covered with laminated polyethylene. In the beginning of the test the sample holder is lowered in the water and the lid is closed. The pressure inside the vessel is instantly increased to $15\,kPa$ and held constant for the $20\,s$ test time. Thereafter the pressure is turned off and the rod lift up the sample holder above the water level. Then the lid is opened and the sample is removed and weighed again. The edge wick index for the sample is defined as the difference in weight before and after the test, Δm, divided by the area of the open edge of the hole,

$$EWI = \frac{\Delta m}{2\pi r_0 h} \quad [kg/m^2], \tag{9}$$

where h is the thickness of the paper. In this work the pressurized edge wick experiment is performed on a number of constructed CTMP lab sheets with and without AKD.

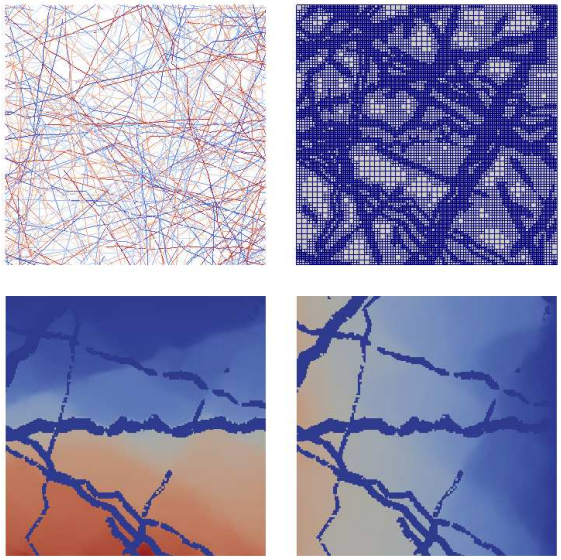

Figure 5: Micro simulation. Top left: Centrelines of fibers. Top right: Adaptive grid around the fibers. Bottom left: Pressure drop for the machine direction simulation. Bottom right: Pressure drop for the cross direction simulation.

4 NUMERICAL RESULTS

4.1 Micro simulations

On the micro-scale two different types of simulations are performed to calculate the in-plane permeabilities and capillary pressure curves. The in-plane permeabilities are simulated in IBOFlow for different virtual realizations of small pieces $1 \times 1\,mm^2$ of the paper structure. The fibers are treated as immersed boundaries and automatically a grid is generated with a number of refinements around the fibers, see Figure 5. The permeabilities are simulated in both the machine (MD) and cross (CD) directions. In Figure 5 the pressure drop for the different directions are shown.

By using the techniques described in Section 2.2 the capillary pressure curves are calculated geometrically using a pore-morphology model and Laplace's law. The capillary pressure as a function of porosity and water saturation for a given contact angle Φ is shown in Figure 6. Based on the results from the pore morphology model the relative permeabilities as a function of porosity and water saturation are calculated by one-phase IBOFlow simulations on the open pores. The results are presented in Figure 6.

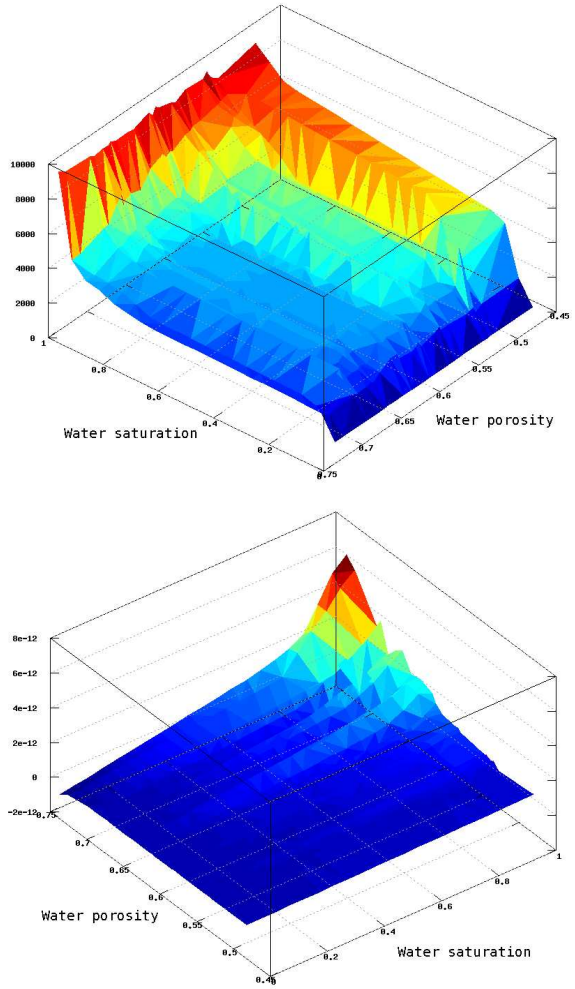

Figure 6: Top: The capillary pressure as a function of porosity and water saturation for the contact angle 95^o. Bottom: The relative permeability as a function of porosity and water saturation.

4.2 Macro simulations

On the macro-scale, the pressurized edge wick experiment is simulated in IBOFlow. The corresponding dimensions and a smoothed random paper porosity between 0.6 and 0.75 are set, see Figure 7. The pressure in the hole is set to $15kPa$ and for the external boundaries ambient pressure outlet boundary conditions are used. To capture the compression of the air when the water enters the paper, the pressure on the outlet is increased according to the ideal gas law. It is unknown how much of the air that is contained inside the paper. In the simulations it is assumed that 80% of the air is compressed and the other part leaves the domain. The simulated Darcy's velocity field is shown in Figure 7.

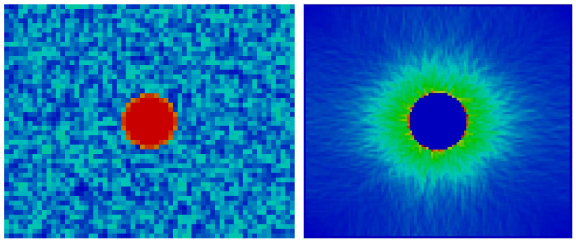

Figure 7: Simulation of the pressurized edge wick experiment. Left: Paper porosity between 0.6 and 0.75. The hole has porosity one. Right: The simulated velocity field.

To determine the required time and spatial resolution to obtain grid and time independent solutions a convergence study for the contact angle 110^o and constant porosity 0.75 is performed. In Figure 8 the edge wick index is plotted as a function of time for three different grid sizes, with time step of $1\,ms$. To see the difference between the grid sizes, only the first 3 seconds are displayed. From the Figure it is concluded that a grid size of $0.5\,mm$ is sufficient for a converged solution. Similarly, simulations are also done for different time step lengths where the grid size is held constant to $0.5\,mm$. From Figure 9 it is concluded that a time step length of $1\,ms$ is sufficiently small to reach a time step independent solution.

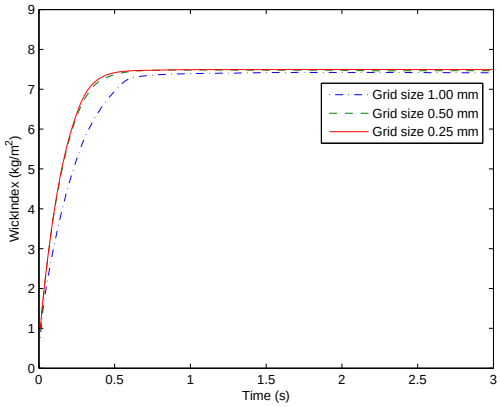

Figure 8: Grid study where the edge wick index is plotted as funtion of time for three different grid sizes. Contact angle 110^o.

4.3 Experimental validation and contact angle study

To validate the multi-scale model the pressurized edge wick experiment is simulated for different contact angles with a constant porosity 0.75. The resulting edge

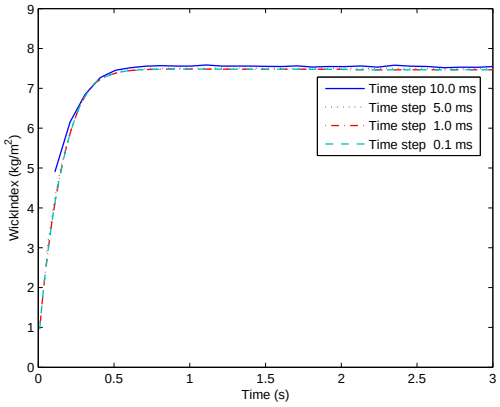

Figure 9: Time step study where the edge wick index is shown for 4 different time step lengths. Contact angle 110^o.

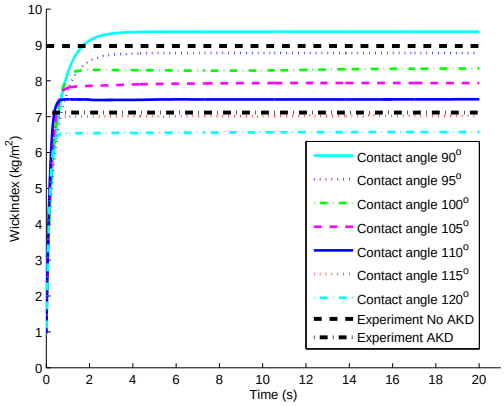

Figure 10: The pressurized edge wick experiment is simulated for different contact angles and compared to the performed experiments.

wick index is compared to the performed experiments. The lower and upper bound for contact angles are found by experiments to 90^o and 120^o. In Figure 10 the edge wick index is plotted as function of time for different contact angles in the range between 90.0^o, where no capillary pressure is present, and 120^o, where the lab sheet is highly hydrophobic. Contact angle experiments on the test sheet verify this range with values in the lower part without AKD and in the higher part with AKD. The experimental wick index for the lab sheet without AKD is higher compared to the one with AKD, which is expected due to the properties of the AKD sizing chemical. The simulations show a qualitatively correct behavior of how the edge wick index depends on contact angle and for contact angles supported by experiments we obtain a good agreement with the pressurized edge wick experiments.

5 CONCLUSIONS

To calculate the penetration of fluid in the open edge of paper board a multi-scale framework is developed. On the fiber micro-scale virtual paper models are generated in PaperGeo [6]. In the fluid flow software IBOFlow [7] a pore-morphology method is used to calculate capillary pressure curves and on the active pores one-phase flow simulations are performed for relative permeabilities. The result is a database of capillary pressure curves and relative permeabilities as a function of saturation and porosity. The database is used as input for a two-phase flow simulation on a 2D virtual macro sheet to calculate the penetration of fluid in the paper. A micro database for a new virtual paper including simulation of 25 different representations takes approximately one day to calculate. The pressurized edge wick macro simulations takes 10 minutes. This large saving in time and computer resources shows the necessity and advantage of the multi-scale approach. Further, to make the software more user friendly a GUI has been developed. The multi-scale framework is validated against pressurized edge wick measurements, which shows good agreement.

The simulations will be used to gain an understanding on how the pore size distribution and sizing affects the edge wicking performance. To fulfill this extended goal, improved models for the contact angles that possibly depend on saturation and time will be developed. The general framework will be extended such that a multi-layer board consisting of single layer sheets can be handled including a diffusion model for the layer interaction. For validation of the fluid penetration both the single layered test sheets and a multi-layer board will be used to compare simulations and pressurized edge wick measurements.

6 ACKNOWLEDGEMENTS

This work is part of the ISOP (Innovative Simulation of Paper) project which is performed by a consortium consisting of Albany International, Eka Chemicals, Stora Enso, Tetra Pak, Fraunhofer ITWM and Fraunhofer-Chalmers Centre. It was supported in part by the Swedish Foundation for Strategic Research (SSF) through the Gothenburg Mathematical Modeling Centre (GMMC).

References

[1] J. Becker, V. Schulz, and A. Wiegmann. Numerical determination of two-phase material parameters of gas diffusion layer using tomography images. *J. Fuel Cell Sci. and Tech.*, 5(4), 2008.

[2] B. Bird, W. Stewart, and E. Lightfoot. *Transport Phenomena*. Wiley International, 1960.

[3] J. Bristow. The pore structure and the sorption of liquids. in paper structure and properties, 1986. pages 183–201.

[4] Z. Chen, G. Huan, and Y. Ma. *Computational Methods for Multiphase Flows in Porous Media*. SIAM ISBN-13: 978-0-898716-06-1, ISBN-10: 0-89871-606-3, 2006.

[5] J.P. Van Doormaal and G.D. Raithby. Enhancements of the SIMPLE method for predicting incompressible fluid flows. *Num. Heat Transfer*, 7:147–163, 1984.

[6] GeoDict. `http://www.geodict.com`.

[7] IBOFlow. `http://www.iboflow.com`.

[8] A. Mark, R. Rundqvist, and F. Edelvik. Comparison between different immersed boundary conditions for simulation of complex fluid flows. *Fluid Dynamics & Materials Processing*, 7(3), 2011.

[9] A. Mark and B.G.M van Wachem. Derivation and validation of a novel implicit second-order accurate immersed boundary method. *J. Comput. Phys.*, 227:6660–6680, 2008.

[10] M. Rentzhog. Experimental techniques and significance of board structure for edgewise liquid penetration, 2008. Technical report, Stora Enso.

[11] C.M. Rhie and W.L. Chow. Numerical study of the turbulent flow past an airfoil with trailing edge separation. *AIAA J1*, 21:1527–1532, 1983.

[12] P. Salminen. Studies of water transport in paper during short contact times, 1988. PhD. Thesis, Åbo Akademi, Åbo, Finland.

[13] H. Tufvesson. The mechanisms of edge wicking, 2006. Lic. Thesis, isrn/kth/fpt/r-2006/28-se, Royal Institute of Technology, Sweden.

[14] O. Ubbink. Numerical prediction of two fluid systems with sharp interfaces, 1997. PhD. Thesis, Department of Mechanical Engineering, Imperial College of Science, London, United Kingdom.

Micromechanical network model for the evaluation of quality controls of paper

H. ANDRÄ[1], F. EDELVIK[2], M. FREDLUND[3], E. GLATT[1], M. KABEL[1,*], R. LAI[4], A. MARK[2], L. MARTINSSON[5], U. NYMAN[6], S. RIEF[1]

[1]Fraunhofer ITWM, Kaiserslautern, Germany
[2]Fraunhofer-Chalmers Centre, Gothenburg, Sweden
[3]Stora Enso, Karlstad, Sweden
[4]Eka Chemicals, Bohus, Sweden
[5]Albany International, Halmstad, Sweden
[6]Tetra Pak Packaging Solutions AB, Lund, Sweden

[*]Correspondence to:
matthias.kabel@itwm.fraunhofer.de

Keywords: Stochastic fiber network model, beam elements, micromechanics.

ABSTRACT

In this paper, we discuss the challenges in modelling and simulating infinitesimal and large deformations of cellulose fiber networks, mainly in the context of the prediction of quality controls for paper.

Understanding the influence and sensitivity of macroscopic production parameters like grammage and thickness of paperboard and understanding the influence of the fiber suspension on the quality of paper is important for the development of better papers and for preserving raw materials and energy.

The new simulation framework consists of the virtual stochastic paper structure generator PaperGeo, that was integrated in the GeoDict [i] software suite, and the finite element solver FeelMath (Finite Elements for Elastic Materials and Homogenization) for solving the equations of elasticity. The fibers and the contacts are modelled by using geometrically exact beams of Simo-type [1].

The microstructural model and the fiber network model are validated against standard measurements of existing papers in the following way: At first we perform tensile and bending tests to measure the macroscopic stress-strain relations. In the next step we apply a representative macroscopic stress or strain onto the boundaries of realizations of the stochastic fiber network model and compute by homogenization the effective (stiffness) coefficients. Finally we compare the numerical results with the measurements.

This procedure can also be used for an identification of elastic parameters on the microscale and to study the sensitivity of the effective (macroscopic) stiffness with regard to the parameters of the microstructure

[i] www.geodict.com

1 INTRODUCTION

Although paper seems to be homogeneous to the human eye, a high resolution X-ray computer tomography reveals its fibrous structure on the microscale (see Figure 1). To perform multiscale simulations for the prediction of paperboard properties, by taking realistic paper microstructures from micro-computer tomography images (µCT) of paper into account, represents a new approach to product and process development in paper industry.

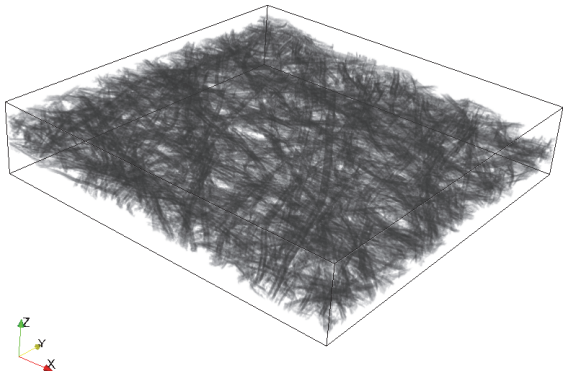

Figure 1. X-ray computer tomography of paper (sample size: 2 mm x 2 mm).

To this aim, we first present a stochastic fiber network model of the microstructure of paper (see Figure 2). It takes into account parameters of the cellulose fiber (density, length distribution) as well as of the paper making process (fiber orientation distribution, grammage, thickness of the paperboard), where the latter parameters are computed by image processing algorithms from µCT images.

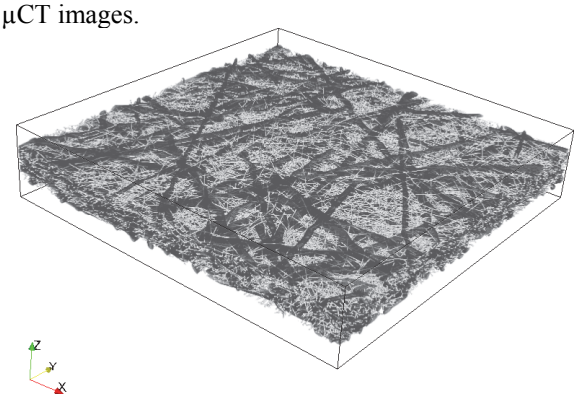

Figure 2. Realization of the stochastic fiber network model.

As a first validation of our stochastic fiber network model we will show, that the calculated and measured (in-plane and out-of-plane direction) permeabilities coincide, assuming for the calculations, that the fibers are rigid.

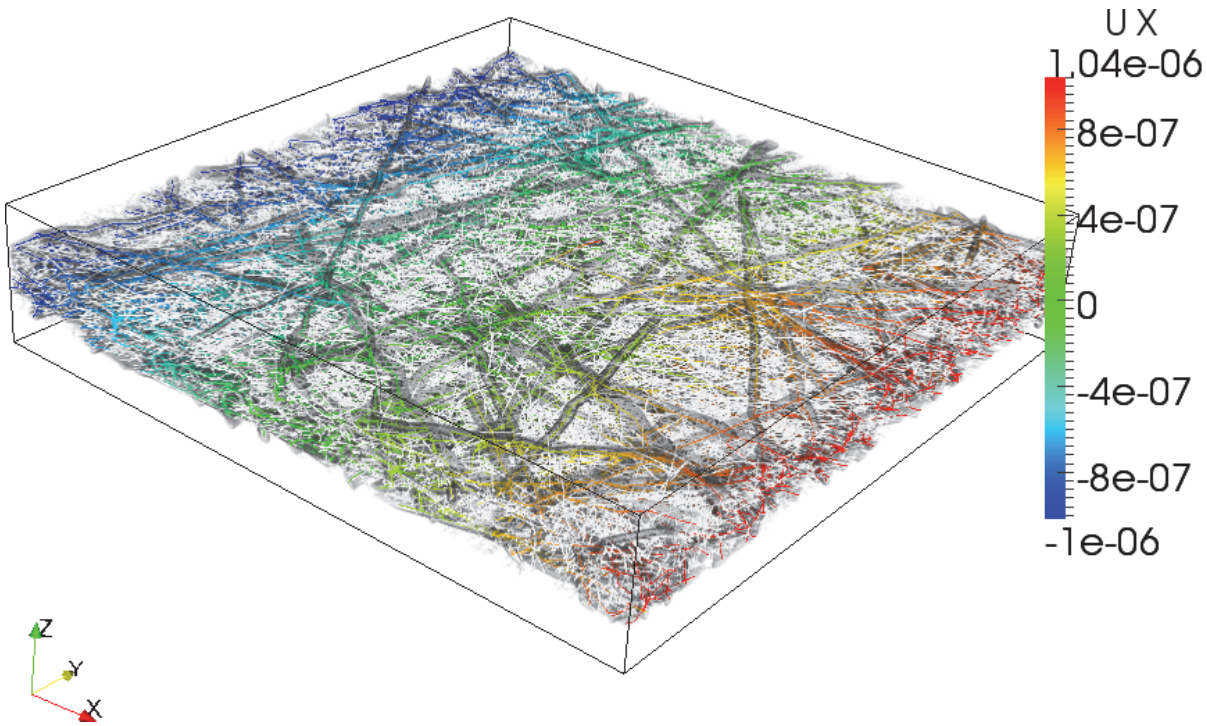

Figure 3. Deformation of the fiber network under tensile load.

In the second part we will concentrate on the problems arising in simulating the mechanical properties of fiber networks. At first one has to solve problems like the (contact) detection of bonding areas for huge networks and the elimination of weakly or not connected fibers from the fiber network model. Additionally, discretization of thin plate-like fiber networks naturally leads to very ill-conditioned linear systems because of the small effective bending stiffness. Last but not least, while the elastic properties of single fibers is often present in the literature [2], this is not the case for the fiber bonds, which are investigated in few publications [4].

At the end, we will show some results of a straightforward approach for the tensile stiffness (SCAN-P 38) and the bending resistance (SCAN-P 29:95) and compare them with measurements (see Figure 3). This approach models the tensile, shear and torsional stiffness of fiber bonds by 1D beam elements and has been integrated into the finite element elasticity solver FeelMath. The macroscopic properties (tensile and bending stiffness) of the paperboard are determined by using the strain energy equivalence principle, i.e. a classical result from homogenization theory [3].

2 GOVERNING EQUATIONS

2.1 Fiber model

Let $S \in [0, L]$ denote the coordinate along the center line of the undeformed beam. The deformation of the beam is described by the rotation of the cross-sections, i.e. by an orthogonal transformation $\Lambda(S)$, and by the position $\phi_0(S)$ of the centroids of the cross-sections. At an equilibrium configuration the spatial form of the local balance of momentum reduces to

$$\frac{\partial}{\partial S} n + \bar{n} = 0,$$

$$\frac{\partial}{\partial S} m + \frac{\partial \phi_0}{\partial S} \times n + \bar{m} = 0.$$

In the above equations n is the spatial stress resultant and m is the spatial couple stress over a cross-section.

Using the strain measures

$$\gamma = \frac{\partial \phi_0}{\partial S} - t_3,$$

$$\omega,$$

where the vector ω is defined by

$$\frac{\partial \Lambda}{\partial S} = \begin{pmatrix} 0 & -\omega_3 & \omega_2 \\ \omega_3 & 0 & -\omega_1 \\ -\omega_2 & \omega_1 & 0 \end{pmatrix} \Lambda,$$

the stress can be calculated by

$$\begin{pmatrix} n \\ m \end{pmatrix} = c \begin{pmatrix} \gamma \\ \omega \end{pmatrix},$$

with

$$c = \begin{pmatrix} \Lambda & 0 \\ 0 & \Lambda \end{pmatrix} C \begin{pmatrix} \Lambda^t & 0 \\ 0 & \Lambda^t \end{pmatrix}$$

being the spatial elasticity tensor.

The material elasticity tensor C of a homogenous isotropic material is

$$C = \mathrm{diag}\left(GA \quad GA \quad EA \quad EI_x \quad EI_y \quad GI_p\right).$$

Here, GA denotes the shear stiffness, EA the axial stiffness, EI_x and EI_y the principal bending stiffness values and GI_p the torsional stiffness of the beam. For anisotropic cellulose fibers, the 6 elastic stiffness parameters can be chosen independently.

2.2 Stochastic fiber network model

The stochastic fiber network model of the fibrous microstructure of paper, which is generated by GeoDict, cannot be used directly for structural mechanics simulations, because it typically has many fibers and other material objects which do not contribute to the elastic stiffness.

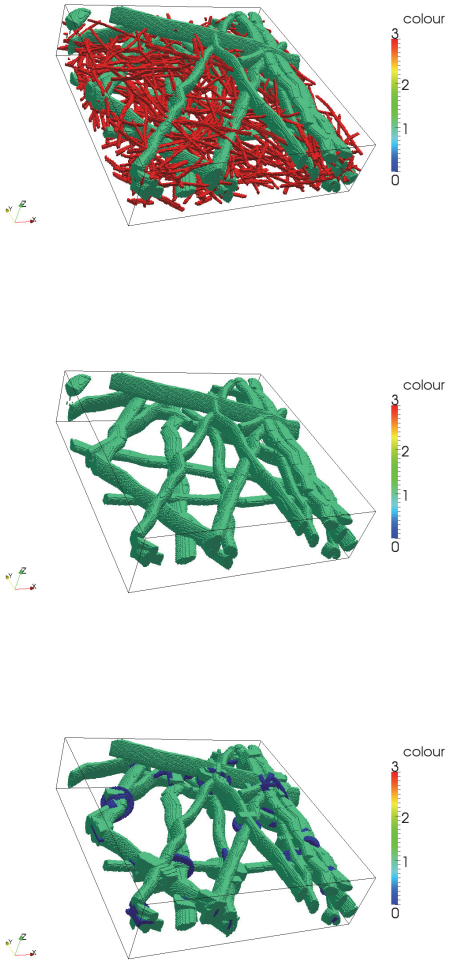

Figure 4. Top: Generated fiber network. Middle: Removed thin fibers. Bottom: "Static" connected component.

Therefore, we prepare the geometry in three steps (see Figure 4): Firstly, we remove very thin fibers, secondly, we detect bonds between the fibers and finally we remove the fibers which are not connected to the fiber network and would be movable as rigid bodies.

The crucial part in this procedure is the bond detection, which is performed by a highly efficient voxel-based discretization method for contact detection. By keeping track of the boundary voxels of the single fibers it is possible to drastically reduce the number of voxels for which we have to check if they are part of the fibers (see Figure 5).

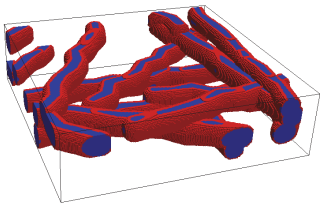

Figure 5. The blue voxels belong to a fiber. The red ones are part of the boundary of the fibers.

The (significant) contribution of the removed thin fibers to the (bending) stiffness of the paper is modelled by an increased stiffness of the bonds. Future work will incorporate fines.

2.3 Homogenization

Using the mathematical theory of homogenization [3], it is possible to determine the macroscopic properties of paper by solving boundary value problems on a representative volume element (RVE) [5].

For the tensile stiffness we simply prescribe the displacement of the centerline on the boundary faces of the RVE. After solving the resulting boundary value problem and applying the energy equivalence principle

$$\frac{1}{2} E \varepsilon_{\text{tensile}} : \varepsilon_{\text{tensile}} = \frac{1}{2} \int_{\cup \text{Fibers}} \left(n \cdot \gamma + m \cdot \omega\right) ds,$$

the effective (i.e. macroscopic) tensile stiffness is given by the equation

$$Et = \frac{t}{\varepsilon_{\text{tensile}} : \varepsilon_{\text{tensile}}} \int_{\cup \text{Fibers}} (n \cdot \gamma + m \cdot \omega) ds,$$

where $\varepsilon_{\text{tensile}}$ is the strain of a homogeneous material (replacing the fibers), E is the effective Young's modulus and t is the thickness of the paper sheet.

Nearly the same holds true for the bending resistance. Only this time we do not prescribe the position of the centroids but the rotation of the cross-section on the boundary faces of the RVE. The bending stiffness is then given by

$$EI = \frac{I}{\varepsilon_{\text{bending}} : \varepsilon_{\text{bending}}} \int_{\cup \text{Fibers}} \left(n \cdot \gamma + m \cdot \omega \right) ds,$$

with I being the moment of inertia of the paper sheet. In the above equations we have used the standard tensor notations

$$n \cdot \gamma = \sum_{i=1}^{3} n_i \gamma_i,$$

$$m \cdot \omega = \sum_{i=1}^{3} m_i \omega_i,$$

$$\varepsilon : \varepsilon = \sum_{i,j=1}^{3} \varepsilon_{ij} \varepsilon_{ij}.$$

The possibility to directly prescribe the rotation of the boundary faces is one of the main advantages of the Simo-beam element applied in the context of fiber network simulations.

Assuming small deformation the bending resistance, which can be measured by a bending test according to SCAN-P 29:95, can be estimated by

$$F_B = \frac{3EI}{H^2} \varphi,$$

where H denotes the test span length and φ the bending angle [6]. Given the grammage w of the paper sheet also the bending resistance index can be calculated as

$$F_B^w = \frac{F_B}{w^3}.$$

3 NUMERICAL RESULTS

The simulations were performed on multiple realizations of the stochastic fiber network model (see Figure 6) for a lab sheet, which was manufactured using a STFI dynamic sheet former with circulating pulp, moving head box and a stationary forming fabric. CTMP (Chemo Thermo Mechanical Pulp) pulp was used. The lab sheets were dried and pressed by a rotating cylinder. The grammage of the resulting CTMP lab sheet was 60g/m².

The size of the statistic volume element was chosen to be 0.5 mm x 0.5 mm x 200 µm, where the size is sufficient w.r.t. the desired accuracy.

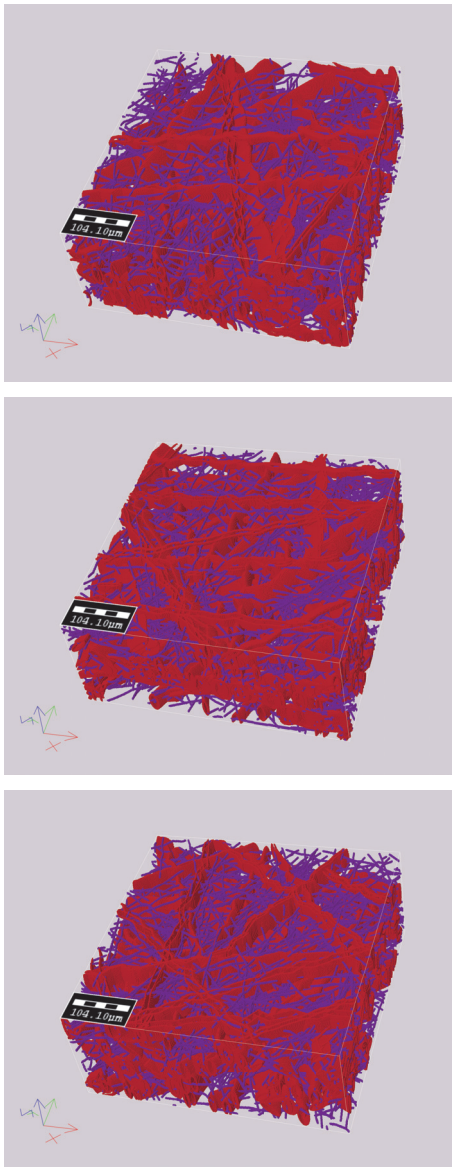

Figure 6. Three different realizations of the examined CTMP-paper.

3.1 Permeability

Under the assumption that the fibers are rigid, the calculated and measured (in-plane and out-of-plane direction) velocities coincide very well for the fiber network model. However, the tomography calculated velocities show large discrepancy to the measured values (see Table 1), because the resolution of the tomography is not high enough to detect the fillers and fines.

	Average in-plane velocity [m/s]	Average out-of-plane velocity [m/s]
Measurement	0.2	0.15
Tomography	1.4	0.42
Model	0.2	0.17

Table 1. Measured and calculated average velocities of the examined CTMP-paper.

3.2 Tensile stiffness

For the structural mechanic simulations we generated a fiber network according to the description in section 2.2 (see Table 2).

	#Fibers	#Segments
Fiber geometry	1702	12196
Cleaning	110	1803
Greatest connected component	108	1798
With bond elements	1690	4034
After refining	1690	11390

Table 2. Number of fibers and segments for the fiber network.

For parameter studies it is necessary to perform the simulation on many realizations and for different choices of the material elasticity tensor C. Therefore it is of great importance to be able to solve a single problem in moderate CPU time. This is the most important advantage of the geometrically exact beam elements compared to a straightforward approach, which discretizes the fibers in 3D elements (see Table 3).

	Runtime [s]
Reading fiber geometry	0.62
Preparing fiber geometry for structural mechanic simulation	47.59
Solving nonlinear equation (Newton-Raphson method)	12.35

Table 3. Runtime for calculating the tensile stiffness of one fiber network.

A first parameter study in which we varied the stiffness of the fibers and the bonds shows that the stiffness of the bonds has only small influence on the (macroscopic) tensile stiffness of the paper sheet (see Figure 7).

The measured tensile stiffness of 213.4 kN/m can be obtained for a fiber stiffness of approximately 20 GPa, which lies in the range of measured fiber properties [2].

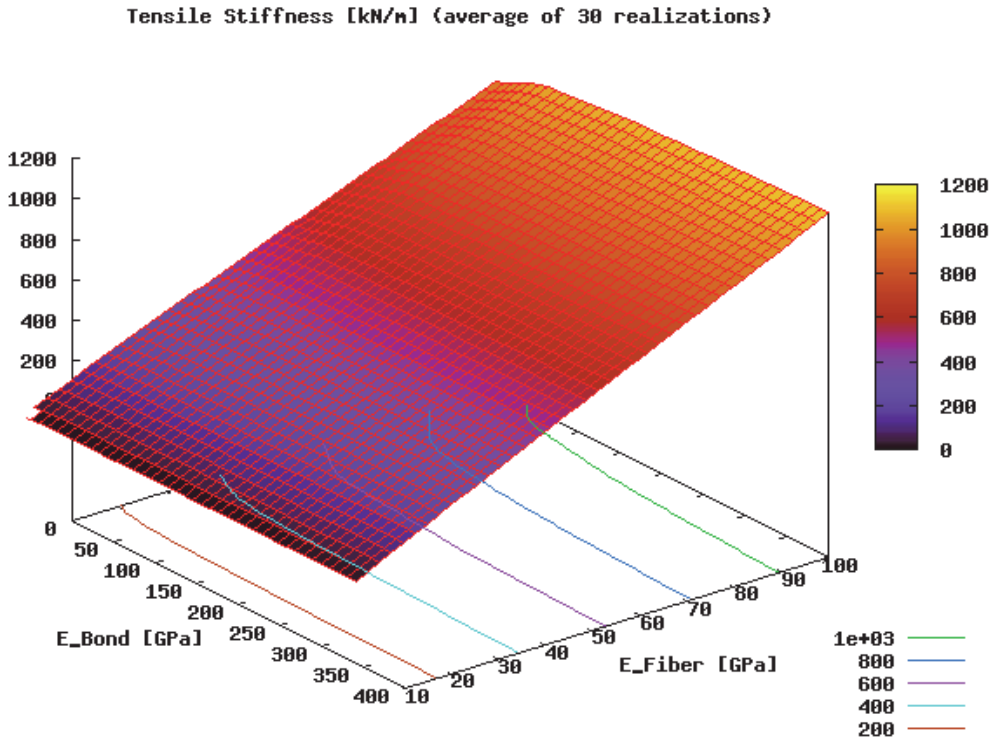

Figure 7. Average of the calculated tensile stiffness for 30 realizations with varying stiffness of the fibers and bonds.

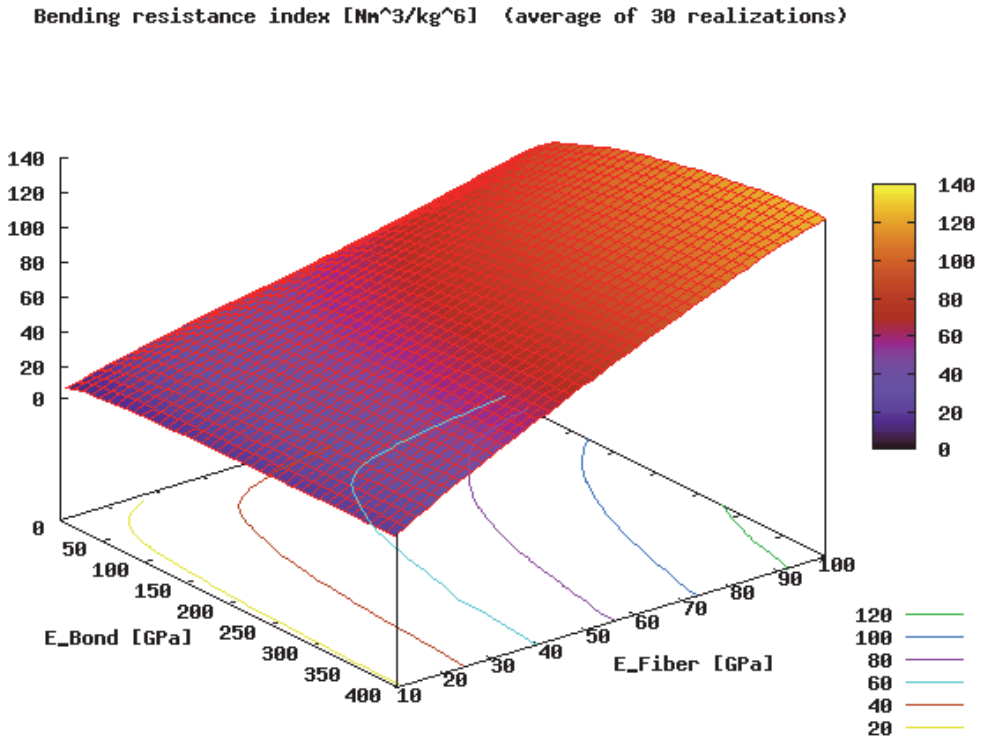

Figure 8. Average of the calculated bending resistance index for 30 realizations with varying stiffness of the fibers and bonds (test span length H=20mm, bending angle of 15°).

3.3 Bending resistance index

Performing the same parameter study for the bending resistance index reveals a greater dependence on the stiffness of the bonds. For the measured bending resistance index of 96.6 Nm^3/kg^6 there exists a lot of possible combinations of fiber and bond stiffness values (see Figure 8).

Using the same set of material parameters for different paper dimensions and comparing the results to measurements reveals, that almost all measurements lie inside the confidence interval (see Figure 9).

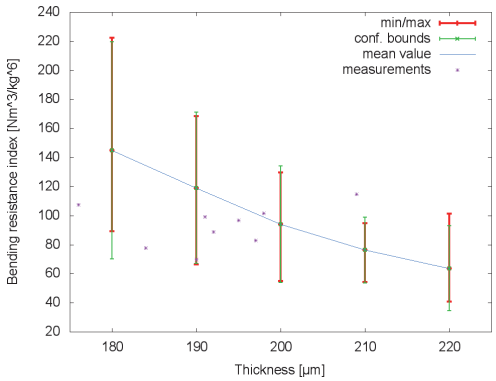

Figure 9. Bending resistance index for changing paper thickness (30 realizations).

4 CONCLUSION AND OUTLOOK

A simulation framework for the microstructure simulation of paper is developed. The simulation framework includes the virtual stochastic paper structure generator PaperGeo of GeoDict and a fiber model based on the geometrically exact Simo-beam element implemented in FeelMath. The tensile stiffness, shear stiffness and torsional stiffness of the fiber bonds are modelled by 1D beam elements of the same type.

Using the technique of homogenization, agreement with the results of standard measurement procedures (tensile stiffness (SCAN-P 38) and bending resistance index (SCAN-P 29:95)) is obtained by using realistic stochastic fiber network models for tested paper. These in turn were obtained by analysing the µCT images with image processing algorithms. The simulations were performed for multiple realization of the stochastic geometry and statistically analyzed.

First parameter studies reveal, that the tensile stiffness only slightly depends on the stiffness of the bonds. Additionally, the fine fibers have a greater impact on the bending stiffness than on the tensile stiffness.

The main disadvantage of discretizing the fiber geometry by Simo-beam elements is that changes of the shape of the cross-sections are not included in the Simo-beam model. Therefore, it is not

possible to simulate (strong) compression of fiber networks.

In a future publication we will present the simulation of damage processes and the z-strength test. In this respect, we take advantage of the fact, that the Simo-beam elements are well suited for large deformations.

5 ACKNOWLEDGEMENTS

This work was part of the ISOP project with industrial partners Albany International, Eka Chemicals, Stora Enso and Tetra Pak. It was supported in part by the Swedish Foundation for Strategic Research (SSF) through the Gothenburg Mathematical Modelling Centre (GMMC).

REFERENCES

[1] J.C. Simo and L. Vu-Quoc. On the dynamics in space of rods undergoing large motions - a geometrically exact approach. *Comput. Meths. Appl. Mech. Engrg.* **66**:125–161 (1988).

[2] D.H. Page, F. El-Hosseiny, K. Winkler and A.P.S. Lancaster. Elastic modulus of single wood pulp fibers. *Tappi* **60**(4):114–117 (1977).

[3] N. Bakhavalov and G. Panasenko. Homogenization: Averaging Processes in Periodic Media. Mathematical Problems in the Mechanics of Composite Materials. Kluwer Academic Publishers, (1989).

[4] A. Torgnysdotter and L. Wagberg. Study of the joint strength between regenerated cellulose fibres and its influence on the sheet strength. *Nordic Pulp & Paper Research Journal* **18**:455–459 (2003).

[5] R. Hill. Elastic properties of reinforced solids: Some theoretical principles. *Journal of the Mechanics and Physics of Solids* **11**:357–372 (1963).

[6] T. Beléndez, C. Neipp and A. Beléndez. Large and small deflections of a cantilever beam. *European Journal of Physics* **23**(3):371 (2003).

Session 3

Printing and Paper Optics

Inkjet pigment penetration on different surface sized papers

TIAGO G. COSTA, JOSÉ A.F. GAMELAS*, ISABEL M. MOUTINHO, ANA F. LOURENÇO, M. MARGARIDA FIGUEIREDO, PAULO J. FERREIRA

Chemical Engineering Department, University of Coimbra, Pólo II – R. Sílvio Lima, 3030-790 Coimbra, Portugal
*jafgas@eq.uc.pt

Keywords: image analysis, ink pigment, inkjet printing, paper, surface sizing

ABSTRACT

In the present study, the effect of paper surface sizing on inkjet pigment penetration was evaluated by studying four different paper samples: one taken as reference without surface sizing (paper RP), one surface sized with cationic starch (RPS1), one with a mixture of cationic starch and poly(styrene-co-maleic anhydride) (RPS2), and one with a mixture of cationic starch and poly(styrene-co-acrylate) (RPS3). The evaluation was based on the grey level analysis of a black printed area on the top surface of the paper samples and on internal layers below that printed area (obtained by delamination of the paper sheets). From the grey level distribution curves it was possible to confirm that the majority of the ink was retained at the top surface, as expected. The penetration degree of the ink pigment was RPS1 ≤ RPS3 < RPS2 << RP. The ink penetration into the paper sheets was less pronounced for the papers with a higher surface polar character. The highest ink penetration was observed for the reference sample due to the very low polarity and higher porosity of its surface.

1 INTRODUCTION

The interaction of ink components with the paper surface and the corresponding degree of penetration into the paper structure has important effects on printing quality. During the printing process with pigment-based inks, the pigment should separate from the ink vehicle (usually water in inkjet printing and vegetable or mineral oils in offset printing) and should also be preferentially retained at the paper surface. On the other hand, the penetration of the ink vehicle should be minimized, in order to prevent the reduction of the paper sheet strength properties or the loss of opacity. Weak ink pigment retention at the paper surface (with correspondingly high penetration into the paper sheet) produces low optical densities and high print through and, consequently, a low printing quality [1-3].

Several studies have been made regarding the penetration of the offset pigments and oils into the paper structure [3-5]. Typically, two methods have been applied in those studies: one based on the analysis of images from scanning electron microscopy in the z direction of the paper sheet, and one based on sheet splitting techniques (delamination) and reflectance measurements on the surfaces of the obtained layers. Recently, a study evaluating the penetration of inkjet pigments into the paper structure has been published [6].

Surface sizing is used to control some relevant paper surface properties such as porosity, roughness and surface chemistry, in order to promote an adequate interaction with inks and to improve the final printing quality [7-9]. This operation may involve application of cationic starch alone or by combining it with synthetic polymers. The study of the effect of surface sizing, particularly the interaction of the sizing formulations with the base paper and with the inks is of utmost importance. In the present study, the effect of surface sizing agents on the penetration degree of a black inkjet ink was considered by varying the surface sizing materials and, after printing, by determining the grey level values of the printed areas and of the corresponding areas in the layers below [10].

2 EXPERIMENTAL

2.1 Materials

Four paper samples were studied: a calendered uncoated base paper (RP) produced with a *E. globulus* Kraft pulp, and three samples obtained after surface sizing the base paper in laboratory, with cationic starch (formulation S1) and with two mixtures of cationic starch and a copolymer (in a proportion of 90/10 w/w), as summarized in Table 1. The copolymers have the structures depicted in Figure 1, as deduced from elemental analysis measurements [9].

Table 1. Paper surface sizing

Chemical formulations used in the surface sizing	Paper samples
---	Reference paper, RP
cationic starch, **S1**	RPS1
cationic starch/ poly(styrene-co-maleic anhydride) 90:10 (w/w), **S2**	RPS2
cationic starch/ poly(styrene-co-acrylate) 90:10 (w/w), **S3**	RPS3

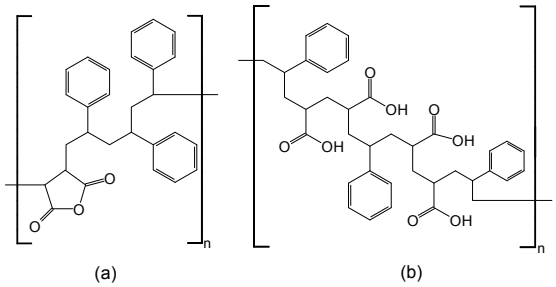

Figure 1. Chemical structure of poly(styrene-co-maleic anhydride) (a), and poly(styrene-co-acrylate) (b).

The surface sizing formulations were applied using a Mathis laboratory coating device, SVA-IR-B, as previously reported [11]. The total surface sizing pick-up (in both paper surfaces) was 3.5 ± 0.3 g/m^2. The surface sized samples were not calendered.

The contact angles with water and organic liquids with known surface tensions (formamide, ethylene glicol, propylene glycol) were measured with the DataPhysics OCA20 equipment using the sessile drop method, and the surface energy parameters were then determined by using the Owens and Wendt model [12]. Air permeance was determined by the Bendtsen method. Topographical parameters were determined using the AltiMet Profilometer Altisurf 500 coupled with the paperMap software. For each paper sample, six replicates were evaluated.

2.2 Print assessment methods

A black rectangle of 29×19 mm^2 was printed on each paper sample using a HP Deskjet 6540 operating at the maximum printing quality mode. A pigment-based black ink was used (HP C8765E). After printing, each paper sheet was split into different layers, by delamination, as follows:

(1) each sample was coated on both sides with a 125 μm thickness sheet of plastic using the Leitz PH 9 Photo Laminator 4B device;
(*2*) the paper sheet was then divided in two layers originating two new surfaces, the upper layer (1A) and the layer below (1B);
(*3*) steps 1 and 2 were repeated for the upper layer, originating again two new surfaces, (2A) and (2B);
(*4*) the same procedure was repeated several times in order to generate surfaces 3B, 4B, 5B, 6B and 7B.

This procedure is schematically detailed in Figure 2. The thickness of the samples obtained by the paper samples delamination process was measured using an Optical Microscope Olympus BH-2.

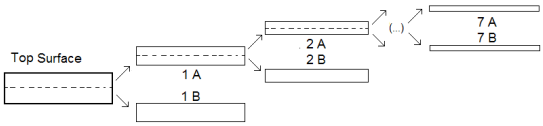

Figure 2. Schematic representation of the paper delamination process.

Images of the top surface, containing the printed area and of the corresponding surfaces obtained by delamination (namely 1B, 2B, 3B, 4B, 5B, 6B and 7B) were acquired in the reflective mode using an Epson Perfection V500 Photo scanner. The resolution for the image acquisition was 2400 dpi and the assessed area was 31×22 mm^2, slightly larger than the black printed rectangle area, in order to use the unprinted areas for the background correction, as explained below. Figure 3 shows the images corresponding to the reference paper.

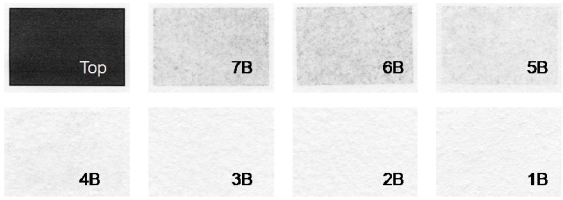

Figure 3. Images for the reference paper of the printed area (top) and of the corresponding surfaces obtained by delamination.

The 8 bits (tiff) digital images from the scanner were exported to the ImageJ software in order to obtain the grey level histograms. Typically, for each digital image, four grey level measurements were made in randomly selected regions (A, B, C and D) of the 29×19 mm^2 printed area, as illustrated in Figure 4. An average histogram such as the example depicted in Figure 5(a) was obtained. Background correction was applied by taking four measurements in the "white" regions outside the printed area (E, F, G and H), and subtracting the resultant average histogram (such as the example in Figure 5(b)) from the histogram of Figure 5(a). The final result is a histogram similar to that plotted in Figure 5(c).

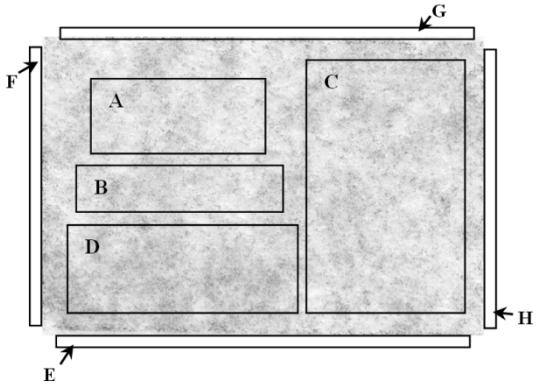

Figure 4. Illustration of the areas used for the scanning assessment.

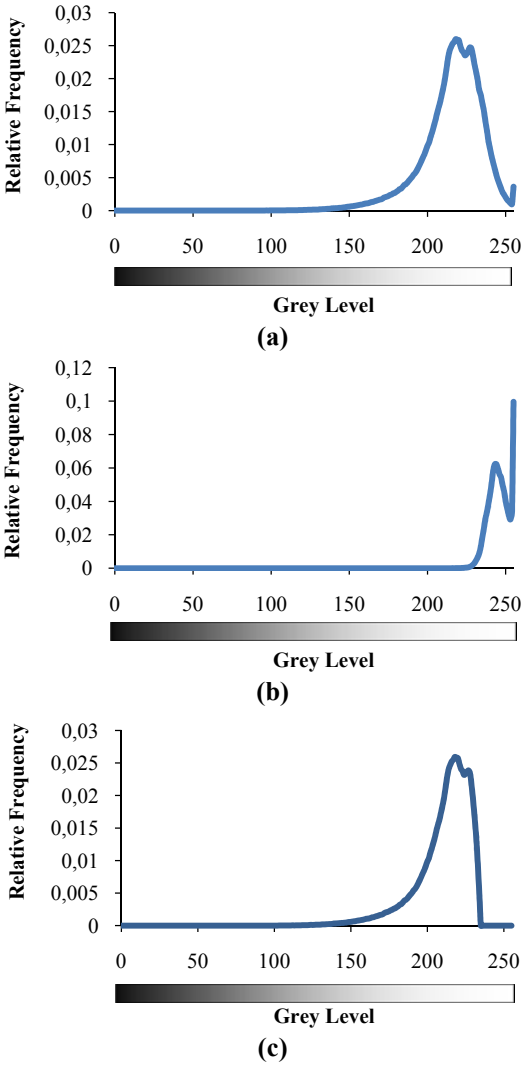

Figure 5. Grey level histograms for the uncoated base paper (inner layer surface 3B): (a) printed area; (b) white area; (c) as (a) subtracted from (b).

This procedure was repeated for each paper sample in two additional printed areas. Several statistical parameters including the mean, median, standard deviation and skewness, were computed by processing the data of the histograms in Matlab R2007B.

3 RESULTS AND DISCUSSION

3.1 Grey level histograms analysis

Grey level distribution curves were obtained for the four paper samples studied, at the top surface and at the surfaces obtained by the delamination process (surfaces 1B to 7B as detailed in Figure 2). Figures 6, 7 and 8 include the curves corresponding to the uncoated base paper (sample RP), the paper sized only with cationic starch (sample RPS1) and the paper sized with cationic starch and copolymer (sample RPS2), respectively. The most relevant statistic parameters such as the mean, median and standard deviation of each histogram are listed in Table 2 for all the samples and for all the layers.

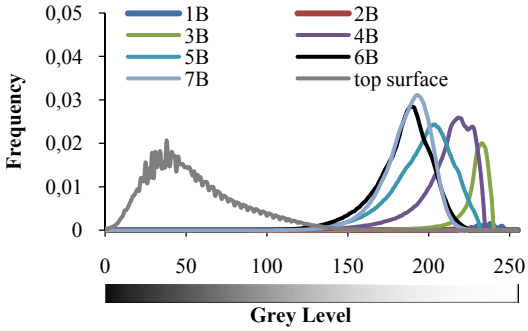

Figure 6. Grey level histograms for the uncoated base paper (RP).

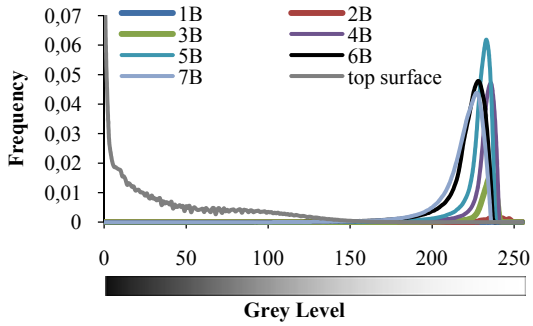

Figure 7. Grey level histograms for the paper surface sized with cationic starch (RPS1).

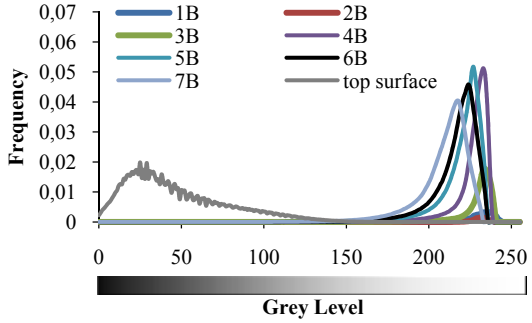

Figure 8. Grey level histograms for the paper surface sized with cationic starch/poly(styrene-co-maleic anhydride) (RPS2).

From these figures, it is obvious that the grey level distribution curves corresponding to the top surfaces are towards the left and approach the "black" levels (grey levels near 0) whereas those corresponding to the inner layer surfaces are towards the right and approach the "white" levels (grey levels near 255). This drastic reduction in colour intensity means that the penetration is not extensive and thus most of the ink pigment is retained at the surface. As expected, the inner layers furthest from the top surface show grey level distribution curves closest to the "white" level.

Table 2. Results for the grey level parameters at different depths of printed paper samples

		Depth		Mean	Median	Standard Deviation
		%	µm			
RP	Top	0	0	54	49	28.4
	7B	21	24	188	189	14.8
	6B	32	36	184	187	17.8
	5B	40	46	196	199	19.3
	4B	50	58	211	215	17.5
	3B	58	66	228	231	11.0
	2B	68	78	217	218	5.4
	1B	81	93	234	235	7.3
RPS1	Top	0	0	41	26	38.8
	7B	15	17	219	222	14.0
	6B	23	25	221	225	14.5
	5B	32	34	228	231	10.6
	4B	44	48	231	234	9.8
	3B	55	59	232	234	9.1
	2B	63	68	239	239	5.4
	1B	78	84	221	217	8.1
RPS2	Top	0	0	47	39	30.8
	7B	20	24	209	213	15.3
	6B	28	34	217	220	14.0
	5B	35	42	220	224	13.6
	4B	45	54	227	230	11.2
	3B	57	69	229	232	11.5
	2B	67	81	231	231	4.7
	1B	78	94	232	233	6.7
RPS3	Top	0	0	45	35	34.9
	7B	13	22	217	220	13.0
	6B	25	35	220	224	13.5
	5B	34	47	227	229	10.4
	4B	43	58	230	232	8.4
	3B	53	67	234	235	5.3
	2B	65	76	230	231	3.7
	1B	78	88	232	233	5.9

Besides this common general behaviour, important differences in the performance of the paper samples regarding ink penetration can be detected in the histograms. For instance, clear differences can be found when comparing the data obtained for the reference paper (Figure 6) to those from the surface sized samples (cationic starch (Figure 7) and cationic starch/poly(styrene-co-maleic anhydride) (Figure 8)). Besides some discrepancies among the grey level distributions at the top surface, it is noteworthy that the curves corresponding to the various surfaces of the internal layers are closer to each other and more shifted towards the "white" level for the sized papers. Moreover, differences can also be detected between the samples sized with different formulations.

Comparing the results for the top surface (Figure 9), it is apparent that the frequency near zero level ("black") is considerably higher for the paper sample RPS1, suggesting, in this case, a higher retention of ink at this surface in comparison to the other samples. Similarly, the mean grey level value at the top surface is also considerably lower for RPS1 than for the other samples (Table 2). The largest mean grey level value is obtained for sample RP.

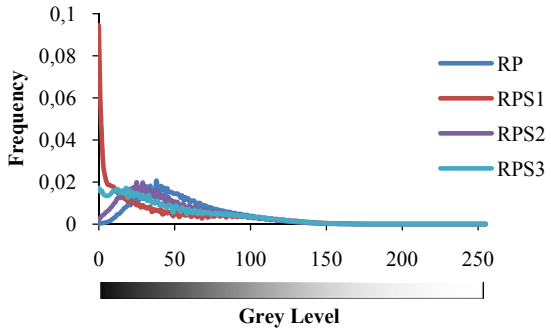

Figure 9. Grey level histograms at the top surface for the distinct samples.

This is in agreement with the grey level distribution curves obtained for the inner layer surface closest to the top surface, 7B (Figure 10), which clearly show that the sample in which the ink has penetrated most is the reference paper, with RPS1 the one whose curve is more displaced to the "white" levels. The samples RPS2 and RPS3 show an intermediate behaviour between samples RP and RPS1. In general, the histograms at the inner layer surfaces 6B to 1B exhibit the same trend to those of the surface 7B along the several paper samples.

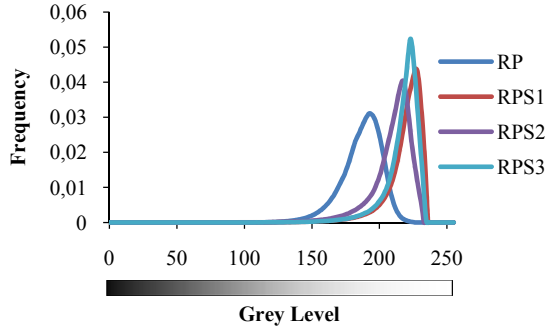

Figure 10. Grey level histograms at the surface 7B for the several samples.

3.2 Relation between ink pigment penetration and surface treatment

In order to compare the ink pigment penetration for the distinct samples, a plot of the mean grey level values as a function of depth is presented in Figure 11. From this plot it can be concluded that the degree of ink penetration is as follows: RPS1 ≤ RPS3 < RPS2 << RP.

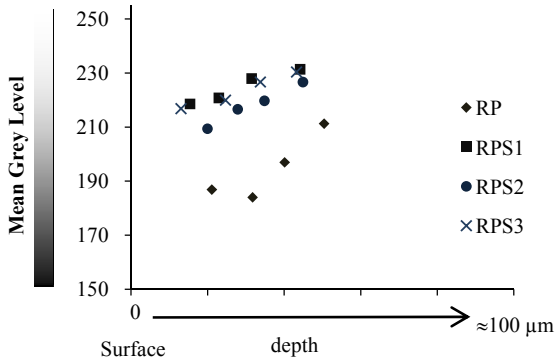

Figure 11. Graphical representation of the mean grey level values along the z direction of the paper sheets (values obtained at the top surface layer were excluded for better visualization of the differences among the inner layers).

As mentioned in the experimental section, for each surface sized paper sample two additional black printed areas were analysed and the results of the replicates are not markedly different to the initial results. However, larger variations were obtained between the replicates of RP.

For a better understanding of the differences in the ink pigment penetration among the several paper samples studied, some specific parameters of the paper sheets were additionally determined, as detailed in Table 3.

Table 3. Surface energy, air permeance and topographical parameters for the different paper samples

Sample	Surface Energy Polar Component (mN/m)	Polar/Total Surface Energy	Air permeance, Bendtsen (ml/min)	Average roughness, R_a (µm)
RP	<0.1	<0.01	744±57	2.42±0.16
RPS1	75.1	0.96	309±33	2.38±0.10
RPS2	21.0	0.61	258±27	2.35±0.10
RPS3	41.1	0.85	267±29	2.36±0.09

The RP sample has a surface energy polar component near 0 since no surface treatment was used to increase the polar character of the surface. When comparing the surface sized samples, surface energy polar components are high and have the following trend: RPS2 < RPS3 < RPS1 (Table 3). These results are certainly related to the presence of the copolymers and cationic starch at the sheet surface. It should be kept in mind that the surface sizing agents are located mostly at the top surface, as previously confirmed by FT-IR [11]. Polymers containing high amount of OH groups, such as cationic starch, or the copolymer poly(styrene-co-acrylate), when located at the sheet surface (samples RPS1 and RPS3), increase its polar character. For the paper sample RPS2, the presence of the less polar copolymer, poly(styrene-co-maleic anhydride), is obviously responsible for the lower polar component of the paper surface energy.

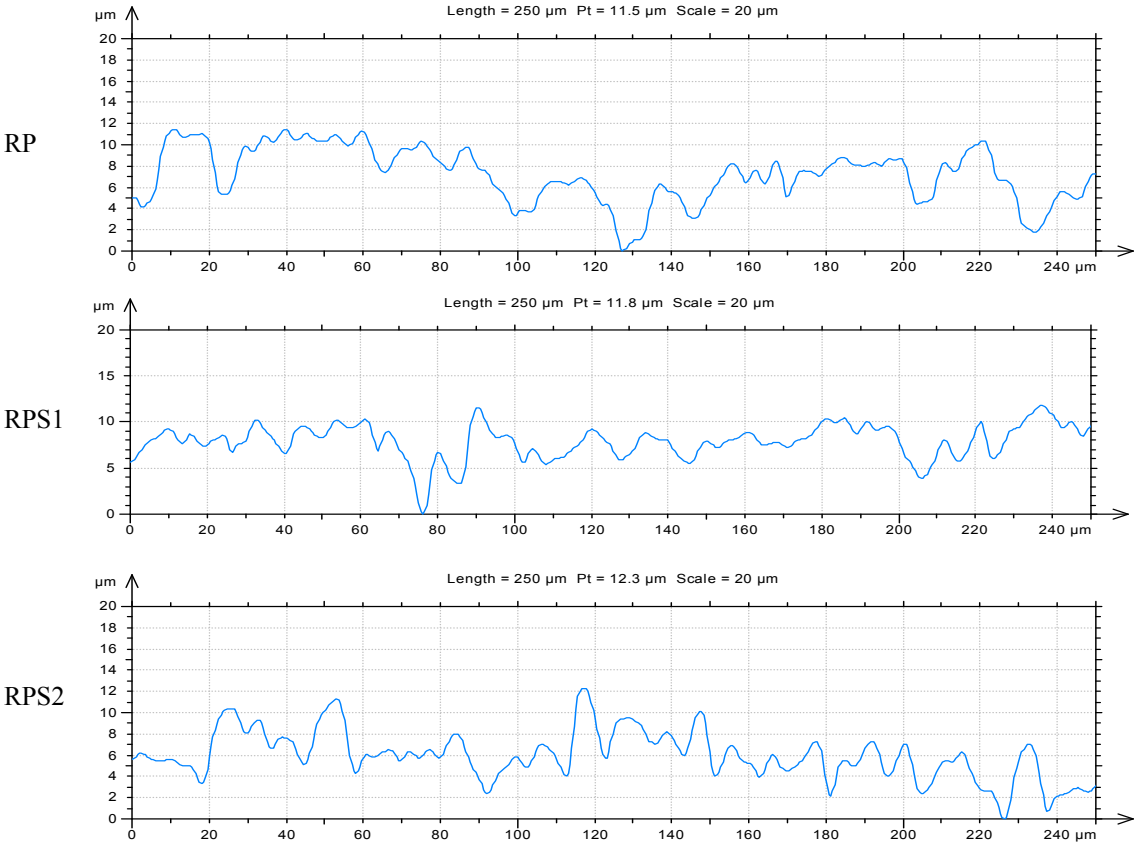

Figure 12. Profilometry of RP, RPS1 and RPS2.

The values obtained for the air permeance (Table 3) suggest a much higher surface porosity for the reference paper. On the other hand, no significant differences are found between the surface sized samples, indicating a similar porosity.

Topographical studies by profilometry indicate that in average the roughness (Table 3 (R_a) and Figure 12) of the reference paper sample and the surface sized paper samples are similar. However, considering the several replicates of each paper sample, a higher variation was obtained for the roughness parameters between the replicates of RP. This may be the reason why the replicates of RP showed greater variation among themselves for the ink pigment penetration, as mentioned above. Notwithstanding, according to the results obtained, the topography should not influence differently the ink pigment penetration into the several samples studied.

From the ink pigment penetration studies, RPS1 and RPS3 are those samples in which the ink penetrates less in the z direction of the sheet, with sample RP showing the opposite trend.

There is a significant difference between the ink pigment penetration in the RP sample and the corresponding penetration in the other surface sized paper samples. This large difference could be due to the existence of significant differences in some chemical and physical parameters of the RP and the other paper samples, namely the surface polar character and porosity. In fact, besides presenting an apolar and hydrophobic surface, the RP sample also exhibits by far the highest air permeance (highest porosity). These characteristics contribute to the significantly higher ink pigment penetration observed for sample RP.

Among the surface sized samples, no significant differences were found in the porosity and topographical parameters values. However, the polar character of the surfaces varied along the surface sized samples, and it was found that the increase in the ink penetration degree follows the order of decreasing surface polarity. This trend is presumably due to the presence of oxygen-containing polar groups at the surface of the carbon black particles present in the black ink formulation. These polar groups when interacting with the polar cationic starch or poly(styrene-co-acrylate) macromolecules should be responsible for the high retention of ink pigments at the paper surface and, thus, to the lower ink penetration observed for paper samples RPS1 and RPS3. As for sample RPS2, the surface energy polar component is lower than those of RPS1 and RPS3 and so the ink pigment is less retained at the surface, as confirmed by the grey level histograms.

4 CONCLUSION

The ink pigment penetration in different paper samples, containing different surface sizing agents (including the paper sample without surface sizing), was evaluated and compared. From the grey level histograms and the corresponding mean grey level values of the printed samples, it was verified that most of the ink, as expected, was retained at the surface in all cases. Nevertheless, the influence of the surface sizing agents on the ink penetration could be observed. The sample surface sized only with cationic starch (RPS1) was the one in which ink penetrated the least, i.e. was more retained at the surface. This was attributed mainly to the large polar component of the surface energy of the RPS1 sample, making the retention of ink polar groups at the surface higher (thus, lowering the ink penetration degree). The sample without chemical surface sizing (RP) was the one in which ink penetrated the most, showing more ink in the internal layers, located down to about 50 μm (in the z direction) from the printed sheet surface. This behaviour was related to the very low polarity and the higher porosity exhibited by sample RP. The other samples, RPS2 and RPS3, surface sized with a mixture containing both cationic starch and copolymers had an intermediate behaviour between samples RP and RPS1.

Finally, it should be stressed that this work demonstrates that the analysis of the grey level histograms at different depths of printed paper sheets is most helpful to study the influence of the surface sizing treatment on the printing quality.

REFERENCES

[1] A. Hladnik, M. Cernic and V. Bukosek. Role of paper coating pigments and additives in darkfastness of ink jet prints. *J. Imaging Sci. Techn.* **52**(1):010507-010507-7 (2008).

[2] H. Nilsson and A. Fogden. Inkjet print quality on model paper coatings. *Appita J.* **61**(2):120-127 (2008).

[3] ∅. Eriksen and ∅.W. Gregersen. The influence of ink pigment penetration and paper structure on print through. *Nord. Pulp Pap. Res. J.* **20**(2):242-246 (2005).

[4] ∅. Eriksen and ∅. Gregersen. Ink pigment location measured as the position of clay in yellow coldset ink. *Nord. Pulp Pap. Res. J.* **21**(4):460-465 (2006).

[5] ∅. Eriksen and ∅.W. Gregersen. The influence of ink oil on print through. *Nord. Pulp Pap. Res. J.* **22**(3):364-370 (2007).

[6] T.G. Costa, J. A. F. Gamelas, I. M. Moutinho, M.M. Figueiredo and P.J. Ferreira. The influence of paper surface sizing on inkjet pigment penetration. *Appita J.* **63**(5):392-398 (2010).

[7] J. Sequera. Encolado superficial para hacer papeles más competitivos. *El Papel* 50-52 (1999).

[8] M. Prinz and W.-S. Schultz. Sizing agents for surface and wet end application. *Prof. Papermaking* 1, 44-49 (2007).

[9] I.M.T. Moutinho, P.J.T. Ferreira and M.L. Figueiredo. Impact of surface sizing on inkjet printing quality. *Ind. Eng. Chem. Res.* **46**(19):6183-6188 (2007).
[10] G. Chinga, ∅. Eriksen, and M. Eilertsen. On the suitability of desktop scanners for assessing print-through. *J. Pulp Pap. Sci.* **33**(3):1-8 (2007).
11] P.J. Ferreira, J.A. Gamelas, I.M. Moutinho, A.G. Ferreira, N. Gómez, C. Molleda and M.M Figueiredo. Application of FT-IR-ATR spectroscopy to evaluate the penetration of surface sizing agents into the paper structure. *Ind. Eng. Chem. Res.* **48**(8):3867-3872 (2009).
[12] D.K. Owens and R.C. Wendt, *J. Appl. Polym. Sci.* **13**(8):1741-1747 (1969).

Micro-fluidics in Printing Nip - Liquid Transfer on Random Fibre Network Surface

M. HOLMVALL[A,1], F. DROLET[B], T. UESAKA[A], AND S. LINDSTRÖM[A,2]

[a] Mid Sweden University, Fibre Science and Communication Network, Sundsvall, Sweden
[b] FPInnovations, Pointe-Claire, Quebec, Canada
tetsu.uesaka@imiun.se

1 INTRODUCTION

Ink transfer from printing plate to paper surface determines almost every aspect of print quality, such as print density, print uniformity, image sharpness, and colour fidelity. Therefore, ink transfer in a printing nip has been a central theme in printing research. The difficulty in investigating this problem, particularly by experimental means, is that the phenomena take place *in the order of milliseconds*, and in a small *confined area (nip)* where no direct observation is possible. Although considerable efforts have been put for understanding the roles of ink properties and paper surface texture, the results are still of phenomenological nature [1-2]. It is only recently that serious analyses of fundamental mechanisms have been started using the first principle approach [3]. In this paper we have investigated ink transfer on random fibre network surface by using a phase-field model with immersed, moving boundary conditions. The objective is to understand the dynamics of liquid transfer in the nip and the role of paper surface structures.

2 NUMERICAL METHODS

When a half-tone dot is printed on paper surface, the liquid (ink) is first compressed under the nip, decompressed, and then splits itself, leaving one portion on the paper surface and the other on printing plate. Important features of this problem are that (1) the ink is small (i.e., micro-fluid) so that surface tensions effects and interfacial phenomena play crucial roles, and (2) the solid-fluid boundaries are moving. In order to investigate this process, we need to track the motion of interface(s) between the liquid and gas (air) and to precisely take into account interactions of the liquid with irregular solid surfaces (random fibre network surfaces) that are moving during the process. For this purpose we have modelled the liquid and gas as a single but non-uniform fluid, called binary fluid, by employing a phase-field model (or diffused interface model) [4-5]. The resulted Navier-Stokes equations for a binary fluid were solved by a finite difference scheme, together with a recently developed immersed, moving boundary method [6, 8]. Fibre networks were created by using Drolet-Uesaka's model [7] that can take compression and shear forces at its nodes to deform the fibre network. Currently the only missing component in the model is the feature of complete, two-way coupling between the fluid phase and solid phase (fibres). Therefore the simulation results may be interpreted as the liquid-transfer to a *semi-rigid surface*.

3 RESULTS AND DISCUSSIONS

A series of simulations were performed for different surface roughness values, the processes of liquid transfer were monitored, and the amount of liquid transfer was determined for each case. The simulation conditions are those corresponding to flexo-post printing of corrugated board. Figure 1 is one of the examples of how the ink is transferred to paper surface. The ink droplet is first compressed, and fills some surface pores at a maximum compression. When receding, it emptied out some gaps and finally split into two by negative pressure (tack force). An important observation may be that there is no extensive penetration of liquid during this transfer process so that the interactions between the liquid and paper surface are limited on the very surface. Another observation is that relatively large pores tend to be emptied out in the decompression (receding) stage.

4 CONCLUSIONS

In a dynamic situation of liquid transfer, such as printing, liquid doesn't easily *flow* into pores but instead behaves like an elastic gel. If any penetration occurs, it will be only after the liquid transfer. This physical picture may be very different from the one drawn from the models based on Lucas-Washburn equation.

REFERENCES

[1] Fetsko, J.M. and W.C. Walker, *Measurements of ink transfer in printing coated paper*. Am. Ink Maker, 1955. 33(12): p. 38-44, 69-71.

[2] Mangin, P.J., et al., *Ink transfer equations - Parameter estimation and interpretation*. Advances in Printing Science and Technology, ed. W.H. Banks. Vol. 16. 1981, London, UK: Pentech Press.

[3] Dubé, M., et al., *Hydrodynamics of fluid transfer*. J. Pulp and Paper Sci., 2008. 34(3): p. 174-181.

[1] Current affiliation: SCA R&D, Sundsvall, Sweden

[2] Current affiliation: Royal Institute of Technology, Stockholm, Sweden

[4] Jacqmin, D., *Calculation of two-phase Navier-Stokes flows using phase-filed modeling.* J. Comput. Phys., 1999. 155: p. 96-127.

[5] Jacqmin, D., *Contact-line dynamics of a diffused fluid interface.* J. Fluid Mechanics, 2000. 402: p. 57-88.

[6] Homvall, M., S. Lindström, and T. Uesaka, *Simulation of two-phase flow with moving immersed boundaries.* J. for Numerical Methods in Fluids, 2010. Accepted, October 2010.

[7] Drolet, F. and T. Uesaka, *A stochastic structure model for predicting sheet consolidation and print uniformity, in Advances in Paper Science and Technology, C.F. Baker, Editor. 2005, The Pulp and Paper Fundamental Research Society: Lancashire, U.K. p. 1139-1154.*

[8] Holmvall, M., F. Drolet, T. Uesaka, and S. Lindström, *Transfer of a Microfluid to a Stochastic Fibre Network.* J. Fluids and Structures, 2011. Published online.

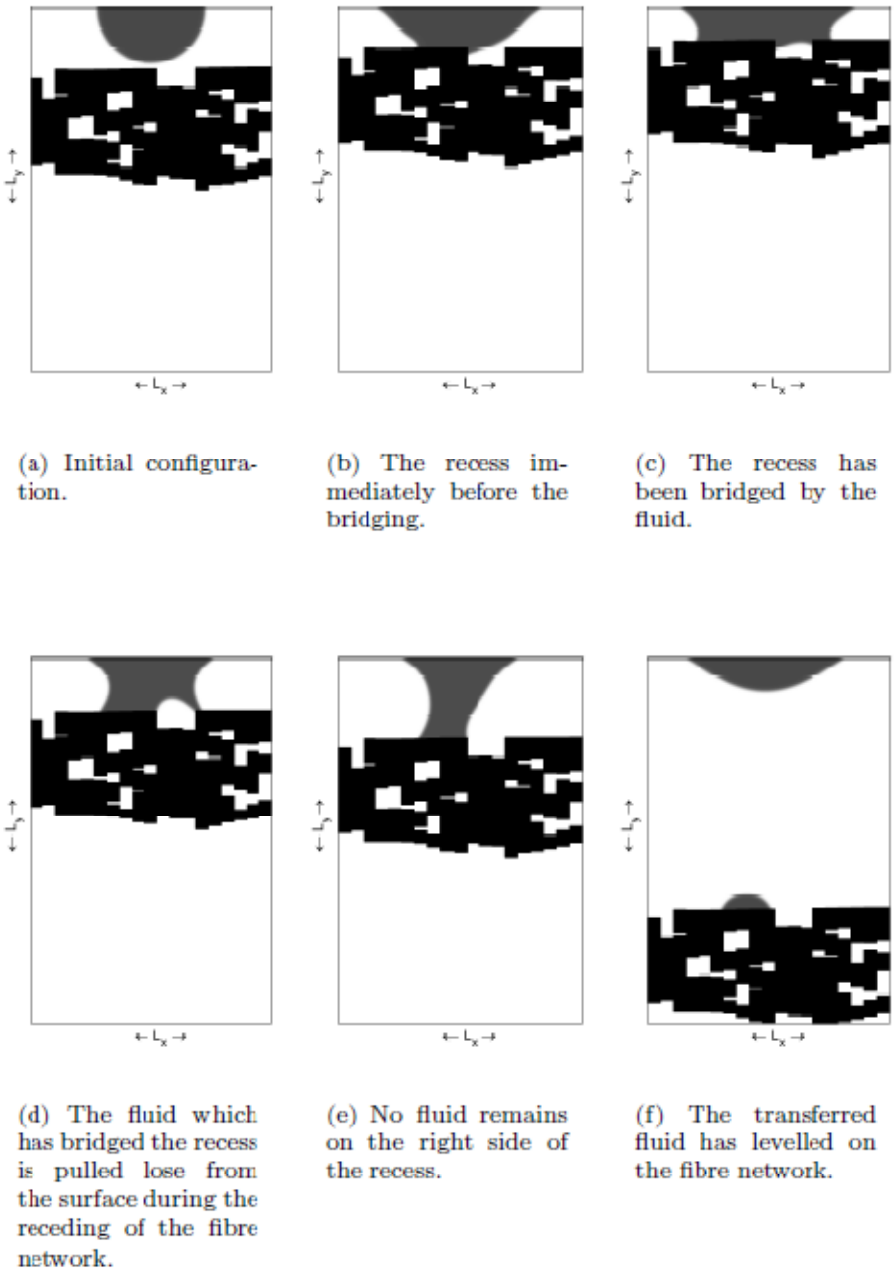

(a) Initial configuration.

(b) The recess immediately before the bridging.

(c) The recess has been bridged by the fluid.

(d) The fluid which has bridged the recess is pulled lose from the surface during the receding of the fibre network.

(e) No fluid remains on the right side of the recess.

(f) The transferred fluid has levelled on the fibre network.

Figure 1. Liquid transfer on paper surface

A NOVEL METHOD FOR THE DETERMINATION OF LINTING PROPENSITY OF PAPER

ALESSANDRA GERLI, LEENDERT C. EIGENBROOD and SANNA NURMI

Global Graphic Customer Support Center
Nalco Europe B.V.
Ir. G. Tjalmaweg 1, 2342 BV, Oegstgeest,
The Netherlands
agerli@nalco.com

Keywords: Linting, IGT Printability Tester, Commercial Printing Press, Newsprint, Supercalendered Paper, Machine-Finished Paper.

ABSTRACT

A novel method was developed for the determination of linting propensity of paper based on printing with an IGT printability tester and image analysis of the printed strips. On average, the total fraction of the surface that is removed as lint during printing is of the order of 0.01-0.1%. This value is lower than those reported in laboratory linting tests performed by others, and more representative of commercial offset printing applications. Newsprint paper produced on a roll/blade former machine was evaluated for linting propensity using the novel method and also printed on a commercial coldset offset press. A very good correlation was found between laboratory and commercial printing results, showing that linting was higher for the bottom side of paper than for the top side, and it could be reduced on both sides by application of a dry-strength additive. In a second case study, four paper reels were produced on a hybrid former machine by varying the wet-end conditions with the goal of matching the low linting propensity of the paper produced on a machine with gap former configuration. It was found that the retention program, by improving fiber fines retention, substantially reduced the linting propensity of the paper produced on the hybrid former machine. The papers were also printed on a commercial coldset offset press. An excellent correlation was found between the total lint area removed from the bottom side of the paper samples during laboratory printing and lint collected on halftone areas of the first upper printing unit after 45,000 copies. Finally, the method was applied to determine the linting propensity of highly filled supercalendered paper produced on a hybrid former machine. In this case, the linting propensity of the bottom side of paper was found to correlate with its ash content.

1 INTRODUCTION

Current papermaking trends towards increase of use of recovered fiber and substitution of fiber for filler have significantly contributed to the reduction of surface strength of paper, affecting both papermaking and printing operations. Linting is the term generally used to define the slow detachment of loosely bonded fibers and fines from the paper surface during offset printing and their accumulation on the printing blanket [1]. The detached material can travel further into the inking system, eventually preventing the transfer of ink to the paper. This causes deterioration of the image quality to the point that the printing press needs to be stopped for maintenance/washing. Offset processes are especially prone to linting since they subject the surface of paper to significant stress forces as the tacky ink splits at the exit of the printing nip. Linting issues have become more severe with increasing use of heatset web offset to print uncoated mechanical papers.

Linting has been the subject of intense investigations for more than 40 years because of its economical impact on both paper machine and printing press operations [2]. It has been shown that pulp quality [3-5], paper machine configuration and operational parameters [5-6], and printing press variables [7-10], all influence linting. In parallel, much research effort has been spent in identifying reliable laboratory methods to predict the linting behavior of a paper on a printing press. The availability of such a method is critical for anticipating print runnability issues and quickly defining the best papermaking strategy to improve the surface strength of paper. For detailed information on most commonly used lint tests, the reader is referred to the comprehensive reviews on the subject by Mangin [11] and Aspler [12]. Most tests are based on detachment of fibers from the paper surface and analysis of the collected debris. Detachment can be performed, for example, with a weakly adhesive tape [13,14], or in a laboratory-printing nip using a viscous fluid.

One of the most popular printing tests that use a viscous fluid to exert a pulling action force on the surface of paper is the IGT test. In the standard method [15-17], the inked printing disc is placed under pressure against paper mounted on a circular sector. The sector is run against the disc under acceleration from zero to some preset end velocity. Surface strength of paper (pick resistance) is derived from the distance between the starting point of the print and the position of the print where the first damage occurs. For mechanical grade papers like newsprint, the visual assessment of the picking point on paper using a transparent oil is difficult. As an alternative, the lint accumulated on the printing disc has been collected for further quantification [18-19] or analyzed directly on it using a CCD-camera [2]. One draw-back of the IGT test, as performed following the standard procedure, is that

the stresses applied on the surface of the paper need to be very high to remove a sufficient amount of lint to measure. Therefore, it was pointed out that the test allows evaluating more the bonding potential of fiber than the true paper linting tendency [11, 14].

A novel method was developed in the Nalco Company laboratory for the determination of the linting propensity of mechanical papers. Paper strips are printed in accelerating speed mode using an IGT printability tester. The use of a red ink instead of oil allows determination of the lint by quantifying the area and number of particles removed from the printed strips using image analysis. Printing conditions (ink viscosity, final printing speed and printing pressure) are chosen, such as to remove a limited amount of lint particles from the test strips and still achieve differentiation among samples. On average, the total fraction of the surface that is removed as lint is of the order of 0.01-0.1%. This value is lower than those reported in laboratory linting tests performed by others [20] and more representative of commercial offset printing applications. Nalco has now used the test for more than three years to predict the linting propensity not only of paper grades containing marginal amounts of filler such as newsprint and directory papers, but also grades containing significant amount of filler such as SC-B and SC-A papers. Three representative mill case studies are presented in this paper. They cover the practical application of this novel method and its validation through correlation with commercial printing press results.

2 EXPERIMENTAL

2.1 Paper Properties

Paper sheets were conditioned in a constant temperature and humidity room (23°C, RH 50%) for 24 h before testing.

Caliper

Sheet caliper was measured by using an L&W Micrometer (Lorentzen & Wettre, Kista, Sweden) at eight random positions on every sheet using a foot pressure of 50 ± 2 kPa. A total of five sheets per sample were analyzed. Caliper and grammage values were used in the calculation of sheet bulk.

Permeability

Sheet permeability was measured by using an L&W Bendsten tester (code SE 114), equipped with a 10 cm^2 measuring head. Eight measurements per sheet were performed and a total of five sheets per sample were analyzed. Measurements were carried out at a standard pressure of 1.47±0.02 kPa according to the ISO 5636 method (ISO 5636-3 "Paper and board-determination of air permeance [medium range]-Part 3: Bendtsen method second edition").

Bendtsen Roughness

Bendtsen roughness was measured by using an L&W Bendsten tester. Sheet samples were held between the measuring head and a glass plate. Four measurements per sheet side were performed and a total of five sheets per sample were analyzed. Measurements were carried out at a standard pressure of 1.47±0.02 kPa according to the ISO 8791-2 method (ISO 8791-2 "Paper and board-determination of roughness/smoothness (air leak methods)- Part 2: Bendtsen method ").

Parker Print-Surf Roughness

Sheet roughness was measured by using a Parker Print-Surf (PPS) roughness tester. Sheet samples were fixed between the measuring head and the base with a clamp pressure of 1 MPa (soft backing). Four measurements per sheet side were performed and a total of five sheets per sample were analyzed.

Beta-Formation

Beta-formation was measured by using an Ambertec beta-formation tester (Ambertec, Espoo, Finland). The instrument determines the deviation from the mean weighted sheet basis weight. Normalized formation values were obtained by dividing the standard deviation of the basis weight (formation) by the square root of the basis weight. Two measurements per sheet were performed, and a total of five sheets per sample were analyzed. Each measurement consisted of 400 measured points. The pulse counting time was 0.4-0.6 seconds.

Tensile Strength

Tensile properties were measured using an Instron Model 1011 electromechanical tensile tester (TestResources Inc., Shakopee, MN, USA). The span length used was 140 mm. The tensile load was applied at a constant speed of 25 mm/min. Measurements were carried out in both CD and MD directions. Two measurements per sheet (CD and MD direction) were performed and a total number of five sheets per sample were analyzed.

Z-Filler Distribution Analysis

The paper sample was sandwiched between two laminator foils and inserted in a hot laminator. After lamination, the sample was split manually in two halves. The procedure was repeated until enough splits were made. The basis weight of each split was determined by subtracting the weight of the foil from the weight of foil and paper. The splits were subsequently ashed, and the z-filler distribution profile depicted by plotting the % ash content of the individual layer versus the relative basis weight (% basis weight at which splitting occurred).

2.2 Fiber Fines Determination

The paper samples were disintegrated at 1.2% consistency for 45,000 revolutions using a standard

Figure 1. Example of montage obtained with ImageJ, including the original scanned image of the printed strip and the processed image. Quantification of lint particles removed from the printed strip was carried out in 20 adjacent segments, each corresponding to a different/increasing printing speed.

L&W disintegrator after being soaked overnight. The stock was diluted with deionized water to 0.5% consistency for fines fractionation, added of Nalco 460-S5440 dispersant solution at 1 %, and additionally disintegrated for 1 min. The total fines content was determined following TAPPI Method T 262 cm-94: "Fine fraction of paper stock by wet screening". The solid collected from the filtrate was ashed and the fiber fines content determined from the weight difference of the solids before and after ashing. The procedure was repeated three times for each sample and the results averaged.

2.3 IGT Printing

Printing tests for the determination of linting propensity of paper were performed using an IGT AC2 model electrically driven printability tester used in combination with an IGT AE inking unit. 8 μm of ink (Huber ink 404.800.002 Nr. 2, medium tack, supplied by IGT Testing Systems, Amsterdam, The Netherlands) was added to the top roller of the inking unit. Following ink distribution, the printing disc (32-mm-wide-rubber-coated Shore A) was inked for 45 seconds and inserted after being weighed on the upper printing shaft of the printability tester. A print was made on the test strip in accelerating mode, using a printing force of 400 kN. The end-speed selected was 2 or 4 m/s. The printing disc was re-weighed after printing. The inking unit was cleaned after each print run. Images of the printed samples were obtained by scanning the printed strips in reflected mode at 600 dpi using a flatbed scanner (Epson Perfection XL10000).

3 RESULTS AND DISCUSSION

3.1 Test Method Development

The method that was developed is based on the IGT linting test [21], but using a new way of analyzing the linting propensity of the printed strips. Printing is performed in accelerating speed mode using medium viscosity ink. End-speed of 2 or 4 m/s were found to be suitable for mechanical grade papers to remove a limited amount of lint particles from the test strips and still achieve differentiation among samples. In a second step, gray images of the printed strips are acquired using a flatbed scanner. Image processing is carried out using the ImageJ program [22,23]. ImageJ is a freely available Java-based software that has sets of ready-made tools for image manipulation and plugins to extend its core functionality. A macro was developed for automatic determination of the number of lint particles and their area. It includes the following steps: alignment of the images, selection of the printed area, exclusion of a fixed area on the edges and automatic thresholding. A maximum entropy threshold algorithm available as plugin in ImageJ was found suitable to detect the small defects corresponding to the particles removed as lint on the original images. Additional steps include inversion of the binary images and their segmentation in 20 parts, each corresponding to a different/increasing printing speed. A representative montage obtained for a printed strip is shown in Figure 1. Quantification of the number and area of the lint particles in each of the 20 adjacent segments allows distinguishing between unbound particles, loosely or more strongly bound particles. Thus, the true linting propensity of a paper can be derived.

3.2 Case Study I: Newsprint Paper

A trial with a dry-strength agent was run on a newsprint machine with the goal of improving the surface strength of paper. The mill reported for their paper recurrent linting issues and eucalyptus vessel picking problems during printing press operations. The problems were the most severe when the paper was printed in heatset offset, but also occurred during coldset printing utilized for most of the production. The machine is a high-speed roll/blade gap former provided with a 3-nip press with a shoe press in the third nip. The furnish composition was 50% TMP/50% DIP. Three reels of paper, a reference reel and two reels produced

	Dry-Strength Additive	Basis Weight	Ash	Bulk	N. Beta-Formation	Ash		PPS Roughness		Bendtsen Roughness		Tensile Index	
	Kg/t	g/m^2	%	cc/g	√g/m	%		µm		mL/min		Nm/g	
						Top	Bottom	Top	Bottom	Top	Bottom	MD	CD
Sample A	0	41.4	8.9	1.48	0.407	8.8	10.1	3.90	3.44	138	136	58.7	15.1
Sample B	1	41.8	8.9	1.50	0.415	7.7	10.2	3.94	3.57	144	149	62.0	14.7
Sample C	2	41.2	8.9	1.50	0.420	8.6	9.5	4.06	3.56	143	141	65.0	14.4

Table I. Properties of the newsprint paper samples evaluated for linting propensity.

	Area of White Spots on Magenta, mm^2		Number of White Spots on Magenta	
	Top Side	Bottom Side	Top Side	Bottom Side
Sample A	0.078	1.356	7.00	62.50
Sample B	0.046	0.544	4.75	32.00
Sample C	0.014	0.493	3.00	32.75
	Area of White Spots on Black, mm^2		**Number of White Spots on Black**	
	Top Side	Bottom Side	Top Side	Bottom Side
Sample A	0.105	1.203	25.25	97.75
Sample B	0.168	0.720	27.25	66.25
Sample C	0.068	0.240	18.75	34.50

Table II. Total area and number of white spots quantified by image analysis on magenta (total area analyzed = 51.3 cm^2) and black (total area analyzed = 54.9 cm^2) solid prints of the test target printed on a commercial coldset offset press.

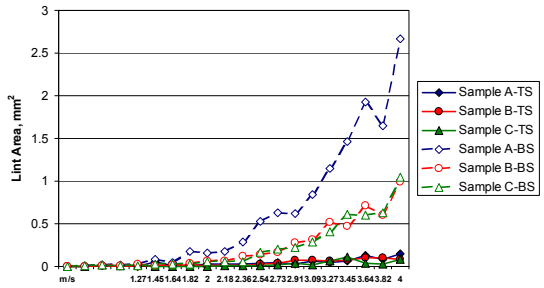

Figure 2. Lint area as a function of printing speed removed from the top (TS) and bottom (BS) sides of sample A (reference), sample B (1 kg/t of dry-strength additive) and sample C (2 kg/t of dry-strength additive).

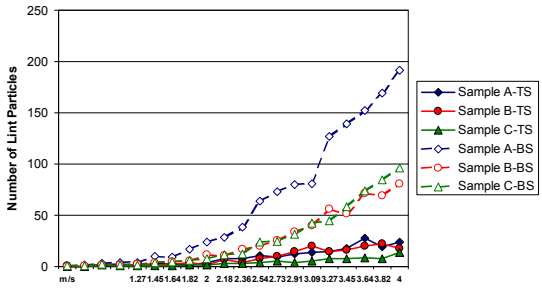

Figure 3. Number of lint particles as a function of printing speed removed from the top (TS) and bottom (BS) sides of sample A (reference), sample B (1 kg/t of dry-strength additive) and sample C (2 kg/t of dry-strength additive).

with the dry-strength agent at different dosages, were collected and characterized for sheet properties and linting propensity using the new method. The sheet property data and the amount of filler on the two sides of paper derived from z-filler distribution analysis are illustrated in Table I. Figure 2 shows the area of particles removed as lint from the top and bottom sides, as a function of the printing speed. The number of particles versus printing speed is plotted in Figure 3. The data show that the bottom side of paper has significantly higher linting propensity than the top side, consistently with what the mill was reporting for commercial printing press operations. On average, the total fraction of the area that was removed as lint was of the order of 0.01% on the paper top side and 0.11% on the paper bottom side. Addition of the dry-strength agent significantly reduced the linting propensity on both top and bottom sides. For all three samples, slightly higher filler content was found for the paper bottom side when compared to the paper top side (Table I). A higher filler amount, generally speaking, reduces strength and facilitates fiber/fines removal. Thus, one could easily conclude that the bottom side surface is weaker due its higher filler content. However, in additional investigations performed on paper produced on the same machine, it was found that the bottom surface gave more linting than the top side, even when its ash content was lower. The mill sent the three paper reels to a printing house for qualitative assessment of linting. The paper was printed in coldset offset using a CMYK printing sequence. The printed samples showed a significant amount of white spots on solid black, cyan and magenta prints. The spots were likely produced by lint particles on the plate or blanket that prevent printing. Solid black and magenta prints had uniform color, whereas the solid cyan print was largely not uniform. As a result, solid black and magenta prints were chosen for image analysis quantification of the total number of white spots and their area.

	Paper Machine	Basis Weight g/m^2	Ash %	Bulk cc/g	N. Beta-Formation √g/m	PPS Roughness µm		Bendtsen Roughness mL/min		Tensile Index Nm/g		Fiber Fines %
						Top	Bottom	Top	Bottom	MD	CD	
Sample D	Gap	51.5	7.2	1.6	0.541	3.81	3.93	116	137	55.8	16.8	24.1
Sample E	Hybrid	51.8	6.0	1.6	0.426	4.28	3.49	152	111	45.4	17.5	21.2
Sample F	Hybrid	51.8	8.9	1.6	0.450	4.10	3.44	136	99	43.9	16.9	20.9
Sample G	Hybrid	52.3	6.4	1.6	0.450	4.17	3.51	141	110	46.8	17.3	22.2
Sample H	Hybrid	52.4	6.2	1.6	0.431	4.03	3.48	137	104	46.7	17.5	20.1

Table III. Properties of the machine-finished paper samples evaluated for linting propensity.

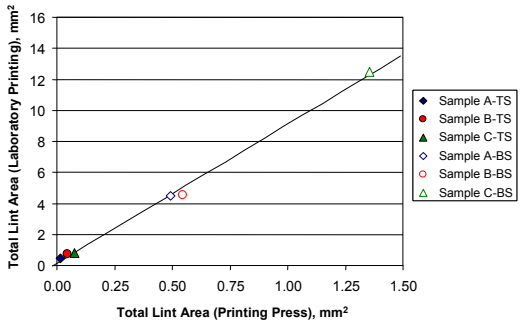

Figure 4. Correlation between total area removed as lint from the test strips during laboratory printing and total area of white spot defects on magenta solid color of the printing press test target.

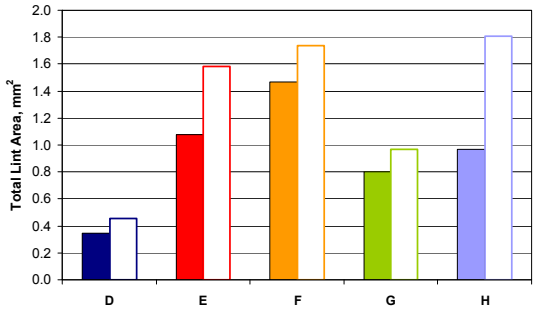

Figure 5. Total lint area removed during laboratory printing from the top (solid-color bar) and bottom (empty-color bars) sides of the machine-finished paper samples produced on the gap former (sample D) and hybrid former (samples E, F, G, and H) machines. The paper samples were printed in accelerating speed mode using 2 m/s as end-velocity.

The results found matched the laboratory printing results. In particular, it was found that addition of the dry-strength additive reduced significantly the number of white spots on both black and magenta solid prints (Table II). More white spots were found on the paper bottom side when compared to the paper top side. The correlation found between the total area removed as lint from the test strips during laboratory printing and the total area of white spot defects on magenta solid color of the printing press test target was excellent (Figure 4, $r^2 = 0.998$).

3.3 Case Study II: Machine-Finished Uncoated Mechanical Paper

A wet-end chemistry trial was run on a hybrid former machine producing machine-finished uncoated mechanical paper. The goal was to be able to reduce the linting propensity of the paper produced, matching the good quality of paper of the same grade produced on a paper machine with gap former configuration. Both machines were provided with a 3-nip press. The furnish composition was for both machines a mixture of kraft, thermo-mechanical and groundwood pulps. One paper reel produced on the gap former machine (sample D) and four paper reels produced on the hybrid former machine using different wet-end conditions (samples E, F, G, and H) were characterized for sheet properties and linting propensity. The sheet property data are illustrated in Table III. Paper samples E and F were produced at standard first pass retention. The ash was increased to produce sample F. As a result, the retention program addition levels were increased to maintain retention. Samples G and H were produced at higher retention. The filler (ground calcium carbonate) addition point was at the fan pump for all the samples. For sample H, it was moved from the fan pump to after the blend chest. Addition of the filler back into the system (sample H), allowed reduction of the retention program dosage while maintaining retention.

The five samples were analyzed for linting propensity using the novel method. The total lint area values (sum of lint areas on the 20 adjacent segments on the printed strips) found for top and bottom sides of the five samples are combined in Figure 5. Sample D, the reference paper, showed the lowest linting value. Sample G was the best among the samples produced on the hybrid former machine. For the gap former machine, linting propensity on the two sides of paper (sample D) was similar. For the hybrid former machine, the bottom side of the paper samples (samples E to H) had higher linting propensity than the top side.

In order to get insights into the structural features of the sheet that may induce differences in linting behavior between top and bottom sides of paper, the z-filler distribution was determined for the five paper samples. The z-filler distribution of sample D produced on the gap former machine is shown in Figure 6 and those of samples E to H produced on the hybrid former are compared in Figure 7. Among the samples produced on the hybrid former machine, sample G had the lowest filler two–sidedness.

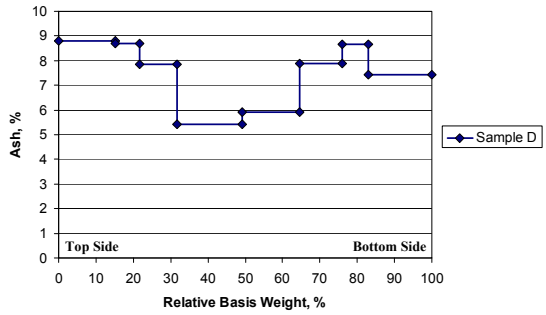

Figure 6. Z-filler distribution of sample D, produced on the gap former machine.

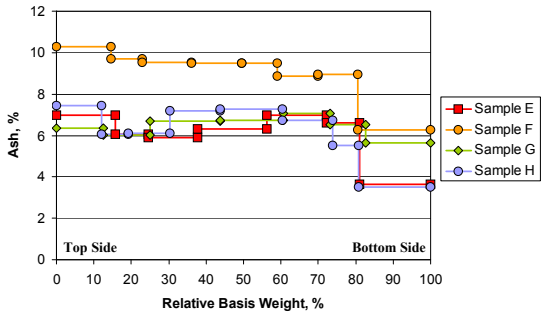

Figure 7. Z-filler distribution of samples E, F, G, and H, produced on the hybrid former machine.

Lower filler two-sidedness is likely the result of improved first pass retention. The bottom side of samples E to H had higher linting propensity despite its ash content was lower. There are two possible explanations for this finding. If the distribution of fiber fines follows that of filler, then higher amount of fiber fines on the top side of the samples may counteract the weakening effect of higher amount of filler and lead to an overall strengthening effect on the top side. Additionally, the third press nip may play an important role in reducing the linting tendency of the top side of paper. Paper samples E to H were produced on the same day with no variation of press loads. The higher roughness of their top side compared to the bottom side (Table III) is indicative of a higher imprint by the felt in the third nip associated with improved top surface consolidation. Images of the surfaces of all five sheets were taken with a scanning electron microscope. The images clearly showed that both top and bottom surfaces of the sheets are well consolidated, but the top side had improved consolidation with no open cavities between fibers. As an example, images of the top and bottom surface of sample G are given in Figure 8. Studies were published before, showing that high concentration of fiber fines at the surface, as long as they are well consolidated, may reduce linting [9, 24, 25]. This prompted examining the fiber fines content of the five samples. The results are provided in Table III.

A good correlation ($r^2 = 0.969$) was found between linting propensity of the bottom side, determined with the novel method, and the fiber fines content of the five samples. Interestingly, sample D, produced on the gap former, had the lowest linting propensity among all the samples and also had the highest fiber fines content. Among the samples produced on the hybrid former machine, sample G with the lowest linting propensity also had the highest amount of fiber fines. Thus, the results indicate that the retention program, by improving fiber fines retention, substantially reduced the linting propensity of the paper produced on the hybrid former machine. Samples G and H were both produced at high first pass retention. For sample H, produced with filler added back in the system, mechanical entrapment of the filler partly contributed to higher first pass retention values, such as reduced dosages of retention chemicals were needed to maintain retention. Clearly, these conditions caused reduced chemical retention of fiber fines with increasing linting as a result.

The five reels of papers were also printed on a commercial coldset offset press using the CMYK sequence. The bottom side of the paper samples (Table III) were printed toward the top press blanket, and the top side toward the bottom press blanket. The lint accumulated on the first and fourth printing units after 15,000 and 45,000 copies was collected using tape pulls from the halftone and

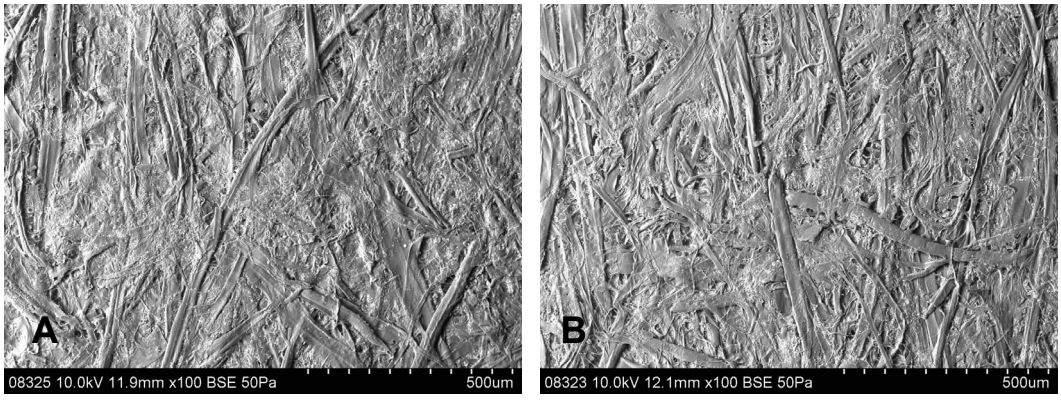

Figure 8. Scanning electron microscope images of the top (A) and bottom (B) side of sample G. The top, lower linting surface, is more consolidated than the bottom one.

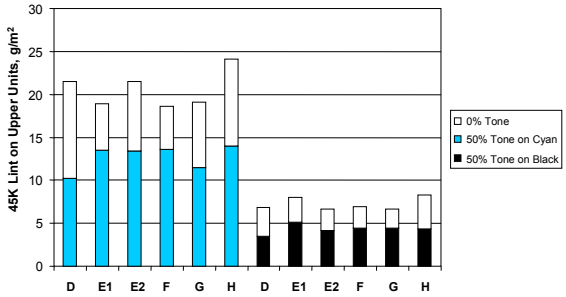

Figure 9. Amount of lint collected after 45,000 copies on the upper cyan and black printing units in the unprinted and halftone areas. The bottom side of the paper samples was printed toward the upper printing units.

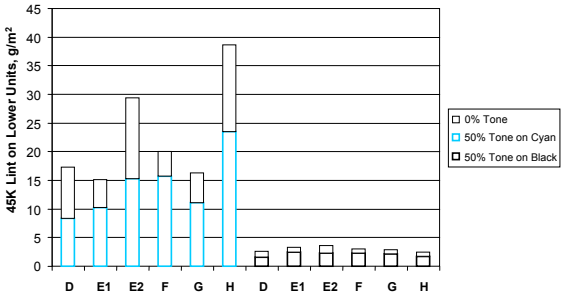

Figure 10. Amount of lint collected after 45,000 copies on the lower cyan and black printing units in the unprinted and halftone areas. The top side of the paper samples was printed toward the lower printing units.

unprinted areas. The lint collected after 45,000 copies is illustrated in Figures 9 and 10 for the top and bottom side blankets, respectively. A higher amount of lint was collected on the cyan units (upper and lower) than on the black units (upper and lower) in both halftone and unprinted areas after 15,000 or 45,000 copy printing. Sample E was printed twice (trial runs E1 and E2 in Figures 9 and 10), before and after changing of the printing plates for damage. The printing plates were also replaced after running sample G. The reproducibility of the amount of lint collected after 45,000 copies was excellent for the halftone areas of the cyan upper unit (coefficient of variation = 0.4%). The repeatability was less positive for the lint collected on the halftone areas of the black upper unit (coefficient of variation = 15.2%). The repeatability was poor for linting collected in unprinted areas of the cyan upper unit (coefficient of variation = 28.0%). For printing toward the bottom press blankets, the repeatability was overall very poor in both halftone and unprinted areas. Samples D, E1, and G linted more on the bottom side than on the top side, as was discovered in the laboratory results. For samples E2, F and H linting on the top side was higher. Since the side of paper that gave more linting changed when printing was repeated (trial runs E1 and E2), it is clear that not only the structural characteristics of the paper, but also printing press operation variables played a major role in determining which side of paper is linting more.

An excellent correlation (r^2 = 0.991) was found between the total lint area removed from the bottom side of the paper samples during laboratory printing and the lint collected on the halftone areas of the upper cyan unit after 45,000 copies (Figure 11). This is the printing unit for which the lint amount estimation was very good. Sample F produced with higher ash content gave relatively less linting after 15,000 copies than after 45,000. Thus, the correlation found between laboratory results and lint collected on halftone areas of the first unit after 15,000 copies was less (r^2 = 0.62; r^2 = 0.87 excluding sample F). Poor correlations were found

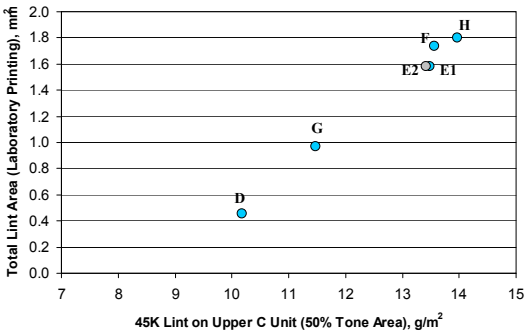

Figure 11. Correlation between total area removed as lint from the bottom side of the paper samples during laboratory printing and lint collected on the upper first printing unit (cyan) used to print this side of paper.

between laboratory results and lint collected on black units and in unprinted areas. On the other hand, the coefficient of variation for the repeatability of the lint collected in these areas was also very high.

Overall, both laboratory and commercial printing data showed that the reference sample D produced on the gap former machine had the lowest linting propensity. Additionally, higher first pass retention conditions used to produce sample G were found to be the most promising to reduce the linting propensity of the paper produced on the hybrid former machine.

3.4 Case Study III: Supercalendered Paper

The method that was developed can also be applied to mechanical papers containing high amount of filler, such as supercalendered grades. A mill producing SC-A paper was concerned about linting/dusting issues for the paper produced on one of their machines and asked to investigate papermaking factors that could be addressed to reduce it. Three paper samples produced on this machine were analyzed for sheet properties, z-filler distribution profile and linting propensity. Table IV illustrates the sheet properties data for the three

	Basis Weight g/m²	Ash %	Bulk cc/g	N. Beta-Formation √g/m	Ash %		PPS Roughness µm		Tensile Index Nm/g	
					Top	Bottom	Top	Bottom	MD	CD
Sample I	55.2	32.1	0.89	0.407	43.3	25.2	1.25	1.22	43.4	14.7
Sample J	46.8	22.9	0.99	0.425	42.7	17.7	1.37	1.34	53.6	16.7
Sample K	56.7	31.5	0.89	0.460	28.5	29.9	1.24	1.26	45.3	14.8

Table IV. Properties of the supercalendered paper samples evaluated for linting propensity.

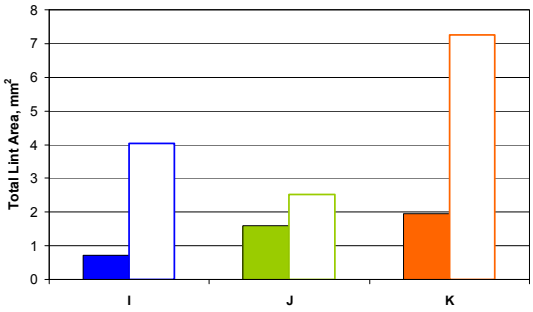

Figure 12. Total lint area removed during laboratory printing from the top (solid-color bar) and bottom (empty-color bars) sides of the supercalendered paper samples. The paper samples were printed in accelerating speed mode using 2 m/s as end-velocity.

samples and the amount of filler on the two sides of paper derived from z-filler distribution analysis. It was found that the bottom side of the paper samples had higher linting propensity than the top side (Figure 12), consistently with what the mill was reporting for printing press operations. The linting propensity of the bottom side was found in this case to correlate with the amount of filler on the bottom surface, the higher the filler the higher the linting propensity (r^2 = 0.889). The sample that had the highest linting propensity (sample K) was the one with the lower filler two-sidedness and worse beta-formation. Thus, improved control of the z-filler distribution profile through adjustment of mechanical, operational and chemical parameters was proposed to minimize linting/dusting propensity issues.

4 CONCLUSIONS

A novel method was developed to determine the linting propensity of mechanical papers. Paper strips were printed with a medium viscosity red ink in accelerating speed mode, using an IGT printability tester. Quantification of the number and area of the lint particles in 20 adjacent segments on the printed strips allowed distinguishing between unbound particles, loosely or more strongly bound particles. Thus, the true linting propensity of a paper can be derived. The method was validated through correlations with commercial printing results and used successfully in the last years to guide papermakers on the best approach to address linting issues. Three mill case studies were presented. In the first case study, the method was used to assess the impact of a dry-strength agent on the linting propensity of newsprint paper. The results showed that addition of the dry-strength agent significantly reduced the linting propensity on both top and bottom sides. The same paper reels were printed on a commercial coldset offset press. The total area removed as lint from the test strips during laboratory printing correlated with the total area of white spot defects on magenta solid color of the printing press test target. In the second case study, four reels of machine-finished uncoated mechanical paper were produced on a hybrid former machine using different machine wet-end conditions. The goal was to be able to reduce the linting propensity of the paper produced, matching the good quality of paper of the same grade produced on a paper machine with gap former configuration. The laboratory linting results and quantification of the fiber fines content of the sheets indicated that the retention program, by improving fiber fines retention, substantially reduced the linting propensity of paper. Additionally, the papers were printed on a commercial coldset offset press. An excellent correlation was found between the total lint area removed from the bottom side of the paper samples during laboratory printing and the lint collected on the halftone areas of the upper first printing unit. Finally, in a third case study, the method was used to determine the linting propensity of highly filled SC-A paper. Linting propensity of the bottom paper surface was found to correlate with its ash content. Since mechanical, operational and chemical parameters influence the z-filler distribution profile, their control is critical in the case of highly filled grades to address linting.

ACKNOWLEDGEMENTS

The authors would like to acknowledge Björn Kamlin for his initial work on the ImageJ macro for linting evaluation, Dr. Richard Cloud for taking the scanning electron microscope images of the sheets and Eduard Visscher for his contribution on paper property measurements.

REFERENCES

[1] Suontausta, O., *Pulp and Paper Testing, Papermaking Science and Technology Series*, Levlin, J.-E. and Söderhjelm, L, Eds., TAPPI PRESS, Atlanta, GA, USA, Chap. 9.

[2] Song, H., Ankerfors, M., Hoc, M. and Lindström, T., *Nord. Pulp Pap. Res. J.* 25 (4):519 (2011).

[3] Pamiri, R., Begin, B., Deshaies, S., and Mozaffari, S., *Pulp Pap. Can.* 105(6):23 (2004).

[4] Wood, J.R. and Karnis, A., *Pulp Pap. Can.* 97(3):17 (1992).

[5] Ionides, G., *Paperi Ja Puu* 66(4): 298 (1984).

[6] Wood, J.R., McDonald, J.D., Ferry, P., Short, C.B. and Cronin, *Pulp Pap. Can.* 99(10):53 (1998).

[7] Heintze, H.U., *Pulp Pap. Can.* 107(2):30 (2006).

[8] Wood, J.R., Imada, S.E., Beaulieu, S. and Kerr, R.B., *Pulp Pap. Can.* 96(10):344 (1995).

[9] Wood, J.R., Imada, S.E., Beaulieu, S. and Kerr, R.B., *Pulp Pap. Can.* 96(11):368 (1995).

[10] Sudarno, A., Batchelor, W., Banham, P. and Gujjari, C., *Tappi J.* 6(9): 25 (2007).

[11] Mangin, P.J., *1987 Proceedings of the Technical Association of the Graphic Arts*, Rochester, NY, p. 397.

[12] Aspler, J.S., *2003 Proceedings of the Technical Association of Graphic Arts*, Montreal, Canada, p. 52.

[13] Brouilette, F., Morneau, D., Chabot, B. and Daneault, C., *Pulp Paper Can.* 107(2):47 (2006).

[14] Gratton, M.F. and Frigon, P., *Preprints of the 92nd PAPTAC Annual Meeting*, p. A175 (2006).

[15] ISO 3783:1980 "Paper and Board – Determination of resistance to picking – Accelerating speed method using the IGT tester (electrical model)".

[16] Aspler, J. S., Davis, S., Ferguson, S., et al., *Tappi J.* 68(5):112 (1985).

[17] Gerli, A., Eigenbrood, L., Nurmi, S., *Tappi J.* 10(2):17 (2011).

[18] Mangin, P.J. and Dalphond, J.E., *Pulp Paper Can.* 93(12):176 (1992).

[19] Mangin, P.J. and Dalphond, J.E., *Pulp Paper Can.* 94(1):23 (1993).

[20] Sudarno, A., Gujjari, C., Rand, S., et al., *Proceedings of the 59th Appita Annual Conference and Exhibition: Incorporating the 13th ISWFPC (International Symposium on Wood, Fibre and Pulping Chemistry),* Auckland, New Zealand (2005).

[21] IGT Testing Systems "W44 Linting Rubber 85 Shore A" Testing Method, http://igt.nl.

[22] ImageJ, National Institutes of Health, Bethesda, Maryland, http://rsb.nih.gov/ij.

[23] Burger, W. and Burge, M.J., *Digital Image Processing, An Algorithm Introduction using Java*, Springer, 2008.

[24] Miyanishi, T. and Miyagi, M., *Tappi J.* 75(5): 75 (1992).

[25] Hoc, M., *Tappi J.* 72(4): 75 (1989).

Paper dust determination via acoustic waves – a new high precision method

ANDREAS KORNHERR, PAUL ACHATZ and GERHARD DREXLER

Mondi Uncoated Fine Paper
Haidmuehlstrasse 2-4
A – 3363 Ulmerfeld-Hausmening
andreas.kornherr@mondigroup.com

1 INTRODUCTION

Paper is a complex compound material which consists of an organic fiber matrix with embedded inorganic filler particles and various organic additives. Such compound materials always show some tendency towards the emission of various fragments, particles and residues, i.e. loose material which is removed from the paper surface when exposed to mechanical stress [1]. This characteristic can be troublesome for paper handling as well as for printing and other technical processes. In general one distinguishes between paper dust arising during paper production and paper dust at the end customer or printer. Especially the elimination of particulate matter emissions or abrasions during the printing process, in order to avoid deposition of such particles on the various flexible and fixed parts of a printing device [2], is a tremendously important quality characteristic of high grade office and communication papers. Furthermore, it has to be ensured that all possible health risks arising from an increased concentration of respirable small dust particles due to the handling of paper can be completely excluded for human beings [3].

Both paper quality and health issues were the main driving forces for the Mondi R&D team to fill this gap by developing a new method allowing for both quantitative and qualitative information about particulate matter being emitted under reproducible (lab) conditions.

2 METHOD

This new patented method [4] is based on a joint research project between Mondi – the international paper and packaging group – and Prof. Georg Reischl from GPR Aerosol Inc. Consulting & Instrument Development. The so-called ADT (Acoustic Dust Tester) uses acoustic waves to impose defined mechanical stress on clamped paper sheets, thus triggering paper dust emissions under controlled conditions. The released paper dust is analyzed according to total particle concentration, particle number size distribution as well as structural and chemical properties of the emitted particles. The sheets under investigation are fixed on both sides in a metallic frame, which is then inserted into the measurement chamber from a carousel slide tray for A4 paper sheets (see Fig. 1). After this, the measurement chamber is sealed and flushed with purified air until all particles have been removed from the chamber. Subsequently, the paper is exposed for 5 minutes to a well defined mechanical stress induced via acoustic waves created using two separate loud speakers, one on each side of the paper sheet. The shape of the acoustic waves as well as the amplitude can be adjusted according to the sheet properties. Accordingly, not only low paper grammages but also higher grammages and even paper board, plastic foils or textiles can be investigated with the ADT method.

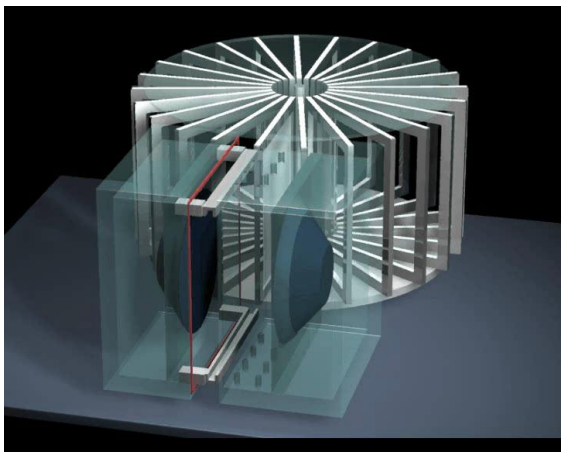

Figure 1. Scheme of the ADT measurement chamber with the two loudspeakers and the carousel slide tray for A4 paper sheets.

The exit air from the measurement chamber is led to various aerosol characterizing and sampling instruments, e.g. a condensation particle counter and an electro-mobility spectrometer. Due to the high precision of this method not only micro- but also nanoparticles [5] can be detected for the first time.

3 FIRST RESULTS

In the course of a benchmark a number of different paper samples were tested including both standard paper brands as well as lab handsheets. One of the major advantages of the method under consideration lies in its small sample size – only 15-20 sheets are necessary to derive a statistically reliable value. Thus it is possible to probe different recipes in the lab which affect paper dusting (new modified filler types or higher filler content, new sizing agents, binders, fiber quality, etc.) and directly measure their influence not only on mechanical and optical paper properties but also on the overall dusting propensity. During the development of the ADT method a series of internal

Figure 2. Complete ADT measurement device from left-to-right, top-to-bottom: carousel slide tray, measurement chamber with built-in loudspeakers, cylindrical sampling unit, flow control unit with gas purification and particle analyser.

studies comparing the new method with conventional dust measurements were conducted showing an excellent correlation regarding the dusting propensity of various paper samples during the printing or copying process.

Therefore we are convinced that the new method which delivers very accurate data is also of high importance to predict the dusting behaviour of paper sheets in a printer. This is in contrast to most other measurement methods where some hundred up to hundred thousand sheets are required for long-time tests. As a result, both time and costs for the evaluation of the dusting property of paper brands can be dramatically reduced.

In September 2010 Mondi started a large cooperative project together with the Austrian KC (Kunststoff-cluster – Plastics Cluster) and OFI (Österreichisches Forschungsinstitut – Austrian Research Institute for Chemistry and Technology) in order to develop the ADT method into an industry standard for the testing of various paper, packaging and even textile materials. Accordingly, this new method is not only of high interest for the paper industry but will certainly also have a high impact on the quality control and product development of many other industrial branches.

REFERENCES

[1] A. Kornherr. Papierstaub unter der Lupe. *Papier aus Österreich* **6**: 32-33 (2008)

[2] F. Eder. Requirements for Office Communication Papers of Today and Tomorrow. *Advances in Printing Science and Technology* **27**: 17-26 (2001)

[3] E. Roblegg, F. Sinner and A. Zimmer. Health Risks of Nanotechnology. *EURO-NanoTox-Letters* **1:** 1-18 (2009)

[4] A. Kornherr, P. Achatz, G. Drexler. Acoustic waves for the precise determination of particulate matter emitted from paper surfaces *ipw* **6**: 13-16 (2011)

[5] G.P Reischl. Measurements of Ambient Aerosols by DMA Method; Concepts and Realization Criteria for the Size Range between 2 and 500 nm. *Aerosol Sci. Technol.* **14**: 5-24 (1991)

Kubelka Munk model in paper optics: successes, limitations and improvements

LI YANG

Innventia
Drottning Kristinas väg 61, Stockholm, Sweden
li.yang@innventia.com

1 INTRODUCTION

Paper optics deals with phenomena of light paper interaction which consists of fundamental physical events, namely light scattering, absorption, and fluorescent emission. Due to complexity of the interaction, theoretical models are needed in order to obtain the fundamental optical properties of the paper (intrinsic coefficients of light absorption and scattering, quantum efficiency, etc) from measurements, such as reflectance factor, transmittance and so on [1,2]. Moreover, the optical properties may even provide information on paper's structure and material distributions [3].

Kubelka-Munk (K-M) model [4,5] is the long standing and the most widely used optical model in paper industries [3,6]. The fundamental equations provided by the model are,

$$K = 2a, \qquad S = s \tag{1}$$

They are linear relationships, with K and S standing for the phenomenal coefficients of light absorption and scattering while a and s for their respective intrinsic coefficients.

For the K-M model, there has been countless number of successful applications in the industries, not least in product development. Nevertheless, there have also been notorious examples to which the K-M model applied less successful or not at all [7,8]. It has been observed that, contradicting to Eq. (1), the phenomenal scattering coefficient S depends on both a and s, when applied to media of strong light absorption, such as dyed sheet [9-11].

In the original work of Kubelka and Munk [4] there were clearly stated assumptions under which the model applies, such as completely diffused light distribution, medium layer of homogeneous material distribution, and no surface reflections etc. Unfortunately, these were frequently overlooked or ignored by users who used the model as a universal tool of paper optics. With these in mind, one can easily understand the notorious failure of the model when applied to the absorbing medium. For example, because of strong light absorption of the dye, light distribution in the dyed sheet becomes no longer complete diffuse even if the illumination is complete diffuse. The observation that light scattering decreases with calendering can be attributed to the involvements of surface reflection and multiple internal reflections at the paper-air interface which were not accounted for by the original model.

There have been continuous efforts in solving the problems. Some of the efforts are mentioned here.

1.1 Revised K-M model

The presumptions or limitations of the K-M model can be released or completely removed, based on through physical analysis This has actually been demonstrated by the author and his colleagues in a series of works under the name of revised K-M model [12-15].

The revised model keeps the simplicity of the original K-M, a two-flux approach. But instead of being two true light fluxes propagating upward and downward, these two fluxes are collective (average) representations for all fluxes towards upper- and lower-hemispheres. In this way, the revised model is capable of dealing with various layered media: of non-complete diffuse light distribution [12], having absorbing components [13,14], including interfacial reflections and even with non-uniform material distributions [15] can also be accommodated by the revised K-M model.

1.2 Other Approaches

A straight forward way for accommodating the non diffuseness of light distribution is to solve the Radiative Transfer Equation in a multiple flux scheme, known as DISORT (Discrete Ordinates Radiative Transfer). Historically, this type of method has widely been applied in studying atmospheric radiative transfer for climate and weather forcasting. There are even open source computer programs downloadable from internet. Since 1970's, this method has even been applied to other medium systems [16,17], like paper and prints. In recent years, this method is investigated and implemented in Matlab [18].

Monte Carlo simulation is another techniques used for studying paper and print [19,20].

2 THE REVISED K-M MODEL

The fundamental idea behind our proposed revision is illustrated in Fig. 1. B and C are an arbitrary pair of positions on the path of the light propagation. Because of light scattering, there are many positive paths, as indicated by the dotted lines. The average path length (L) for the photon noted by the solid line, differs from the direct path (R). We define therefore their ratio as,

$$\mu = \frac{L}{R} \tag{2}$$

For a linear optical medium in which statistics applies, this relationship holds independent of the medium thickness. Evidently, the true path length due to the light scattering has an influence on the

final probability of a photon being absorbed. This feature was overlooked in the original KM theory.

In the revised model [13,14], Eq. (1) is replaced by

$$K = \alpha\mu a, \qquad S = \frac{\alpha}{2}\mu s \tag{3}$$

where α is the quantity governed by the light distribution and $\alpha=2$ for diffuse light distribution.

The explicit expression for $\mu = \mu(s,a)$ reveals that both K and S depend simultaneously on the light absorption and scattering or a and s. This is the essential difference compared to the original K-M model which is only a special case of Eq. (2), when $\alpha=2$ and $\mu=1$.

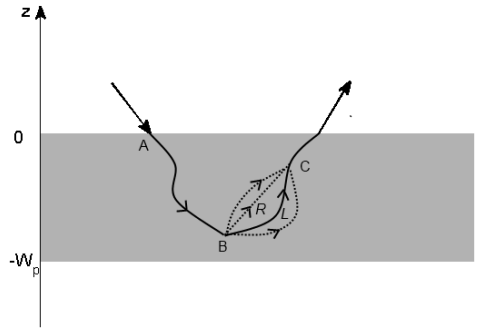

Figure 1. Illustration for light propagation in the medium layer with the dotted lines for the possible paths while the solid lines for the average paths.

In the following subsections, we demonstrate why the phenomenal scattering coefficient, S, decreases with increasing light absorption in dyed-sheet and how a medium with partial-diffuse light distribution can be accommodated by the revised model.

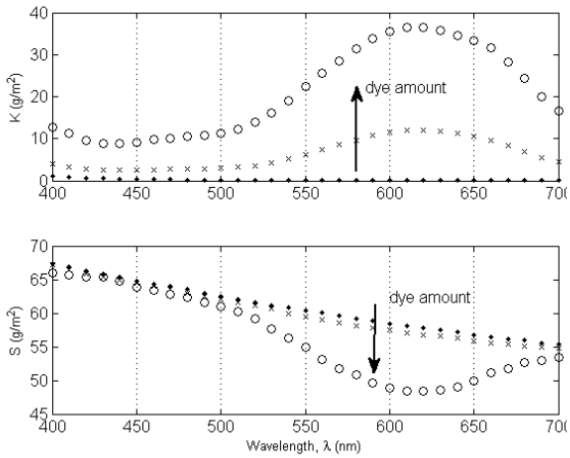

Figure 2. The coefficients of absorption (K) and scattering (S) for dyed sheets, calculated from experimental spectra. The results for white paper are denoted by the dots.

2.1 Example 1: The Dyed Sheet

Dyed sheet is the most notorious example that demonstrates the failure of the Kubelka-Munk model. According to Eq. (1), one would expect that the phenomenal scattering coefficient, S, remains unchanged upon dyeing, because dye molecules are of little light scattering. However, experiments showed a significant drop at wavelengths where the light absorption is strong, see Fig. 2.

The contradiction of the K-M prediction to the experiment can easily be understood by the revised K-M model. As depicted in Fig. 3, the quantity, μ, decreases with increasing dyeing. Furthermore, as shown in Fig. 4, the experimental features can well be reproduced with the revised model.

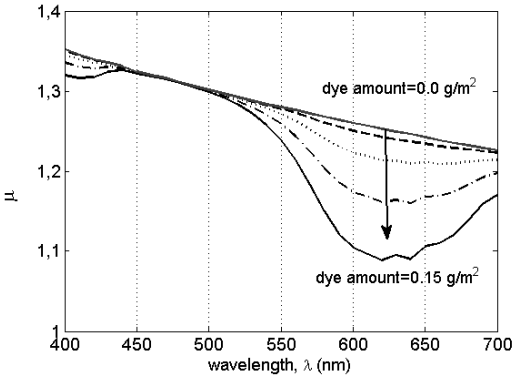

Figure 3. Variations of the quantity, μ, with respect to the amount of dye (cyan) in the dyed sheets.

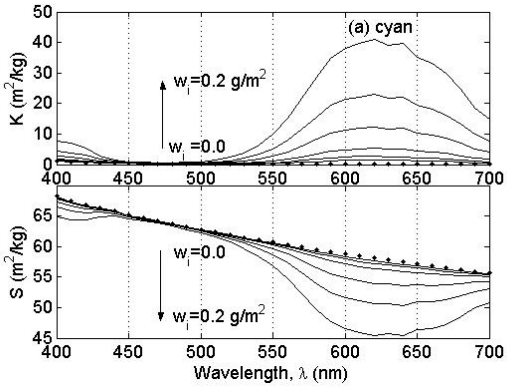

Figure 4. Simulations of the dyed sheets with the revised K-M model.

2.2 Example 2: Partial-diffuse Light Distribution

Independent measurements of reflectance and transmittance of stacked sheets, comprising one, two, and three paper sheets, were conducted [12]. The optical geometries are $45^o/0^o$ for the reflection but $D/0^o$ for the transmission. As the paper is of little light absorption, it is reasonable to expect that the light distribution in the samples is complete diffuse in the transmission measurements, but not in the samples of the reflection measurements.

Considering the fact that the quantity α in Eq. (3) depends strongly on the light distribution, one can easily see that there are different values, $\alpha_r \neq \alpha_t$,

for the reflective and the transmission, respectively. In other words, it is incorrect to use the S and K distributions in the reflection and transmission. This explains the large deviations (Fig. 5a) between the calculations and the measurements. Nevertheless, when the light distribution is appropriately dealt by the revised model, the agreement between the experiments and the calculations are significantly improved, as shown in Fig. 5b.

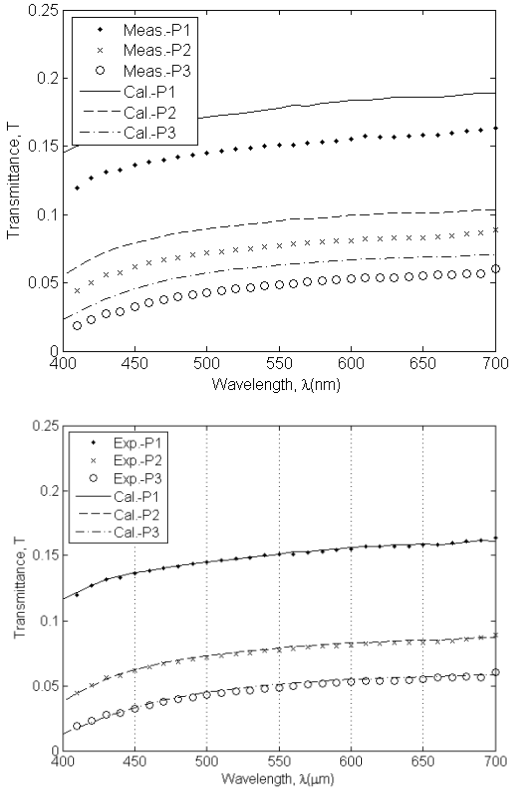

Figure 5. Transmittance values of stacked paper sheets. a) The calculations were made directly employing the S and K values obtained from the refection spectra (upper panel); b) calculations with the revised K-M model (lower panel) incorporating the effects of non-complete light distribution.

3 CONCLUSION

We demonstrated how to remove the limitations possessed of the original K-M model, in the remaining scheme of two-flux approach.

REFERENCES

[1] S. Chandrasekhar, Radiative Transfer (1960).

[2] W. Wendlandt and H. Hecht, Reflectance Spectroscopy (1966).

[3] N. Pauler, Paper Optics, AB Lorentzen & Wettre Corporate (2002).

[4] P. Kubelka and F. Munk, Ein Beitrag zur Optik der Farbanstriche (in German), *Z. Tech. Phys.* **12**: 593–601 (1931).

[5] P. Kubelka, New contributions to the optics of intensely light-scattering materials. Part I, *J. Opt. Soc. Am.* **38**: 448–457 (1948).

values that are obtained from the reflectance values to compute the transmittance values due to different

[6] M. Leskelä, Optical Properties, in *Paper Physics*, 116-137 (1998).

[7] J. H. Nobbs, Kubelka–Munk theory and the prediction of reflectance, *Rev. Prog. Color. Relat. Top*. **15**: 66–75 (1985).

[8] B. Philips-Invernizzi, D. Dupont, and C. Caze, Bibliographical review for reflectance of diffusing media, *Opt. Eng.* **40**: 1082–1092 (2001).

[9] J. A. Van den Akker, Theory of Some of the Discrepancies Observed in Application of the Kubelka–Munk Equations to Particulate Systems, in Modern Aspects of Reflectance Spectroscopy, pp. 27–46, (1968).

[10] M. Rundlöf and J. A. Bristow, A note concerning the interaction between light scattering and light absorption in the application of the Kubelka–Munk equations, *J. Pulp Pap. Sci.* **23**: J220–223 (1997).

[11] W. E. Vargas and G. A. Niklasson, Applicability conditions of the Kubelka- Munk theory, *Appl. Opt*. **36**: 5580–5586 (1997).

[12] L. Yang and R.D. Hersch, Kubelka-Munk model for imperfectly diffuse light distribution in paper, *J. Imaging Sci. Technol.*, **53**: 030201-030207 (2008).

[13] L. Yang and S.J. Miklavcic, Theory of light propagation incorporating scattering and absorption in turbid media, *Opt. Lett.* **30**: 792-794 (2005).

[14] L.Yang and S.J. Miklavcic, Revised Kubelka-Munk theory: III A general theory of light propagation in scattering and absorptive media, *J. Opt. Soc. Am. A* **22**: 1866-1873 (2005).

[15] L. Yang, B. Kruse and S.J. Miklavcic, Revised Kubelka-Munk Theory. II Unified framework for homogeneous and inhomogeneous optical media, *J. Opt. Soc. Am. A* **21**: 1942-1951 (2004).

[16] P. S. Mudgett and L. W. Richards, Multiple Scattering Calculations for Technology, *App. Opt.* **10** (7): 1485-1502 (1971).

[17] P. S. Mudgett and L. W. Richards, Multiple Scattering Calculations for Technology II, *J. Colloid Interface Sci*. **39** (3): 551-567 (1972).

[18] P. Edström, Efficient Reflectance Calculations and Parameter Estimation Methods for Radiative Transfer Problems in Paper Industry Applications, PhD thesis, Mid Sweden University, Sweden (2008).

[19] L. Coppel, Whiteness and Fluorescence in Paper: Perception and Optical Modelling, Lic thesis, Mid Sweden University, Sweden (2010).

[20] M. Sormaz and T. Stamm and S. Mourad and P. Jenny, Stochastic modeling of light scattering with fluorescence using a Monte Carlo-based multiscale approach, *J. Opt. Soc. Am. A* 26: 1403-1413 (2009).

Effect of Moisture on Paper Color

SHAKESPEARE TARJA and
SHAKESPEARE JOHN

Honeywell
Process solutions
Sensor Technology Center
Viestikatu 1-3, FI-70600 Kuopio, Finland
tarja.shakespeare@honeywell.com
john.shakespeare@honeywell.com

Keywords: Color, fluorescence, moisture, paper

ABSTRACT

The optical properties of paper are important in our everyday lives, such as in print media and packaging. To achieve the desired ISO whiteness (especially for high white fine papers) the furnish employed needs to contain well-bleached fibers, and large dosages of FWAs are typically added both at the wet-end and at the size press. Paper makers want to minimize their production cost and thus it is imperative to minimize the dosage of high-cost FWAs while still meeting the quality criteria of whiteness and appearance [1]. This provides a set of challenges not only to the color instruments in the mill's quality laboratories [2] but especially for on-line color measurement and/or automated color instruments which must estimate a stack color based on a single sheet color measurement of paper.

COLOR

It is commonly overlooked that the color of manufactured paper can change from influences other than paper aging. Transformations of lignin and its derivatives are the main cause of color changes during aging of paper. Changes of illumination light conditions and observer are also important factors for paper color [2]. However, there is also a shorter time-scale variation due to changes in temperature and in the moisture content of the paper.

Thermochromic colorants are known to change paper color as a function of sheet temperature. This issue affects correlation between off-line and on-line color measurements. The opacity of paper also depends on the moisture content in the paper. The drier sheet provides better opacity. That fluorescent emission is also moisture dependent seems to be unexpected by many paper makers.

At several mills it has been noticed that dry (4-5 % moisture) copy paper generally produces less fluorescence than the typical 6-7% moisture content copy paper conditioned at ambient conditions of 25 °Celsius and 50% RH (relative humidity) in the quality laboratory. The difference is larger for the overly dry fine papers, Figure 1. The chemical activity of a colorant obviously changes with temperature, which consequently affects its light absorption and/or fluorescent emission properties.

However, similar results can be achieved also when keeping the ambient temperature constant but varying the moisture content of the copy paper keeping the ambient temperature constant, Figure 2. Thus thermal activity alone does not explain the observed difference between the on-line and off-line fluorescent efficiency results.

FWAs

Fluorescent whitening agents (FWAs) used in the paper industry are mainly derivatives of stilbene. FWAs used with bleached cellulose are anionic. FWA molecules are adsorbed at suitable sites of the surfaces of fibers and fillers. Their bonding mechanism to fibers is similar to that of anionic direct dyes.

The excitation maximum in the UVA band is similar to all commonly used FWAs in the paper industry and it locates at about 360-380nm. It varies in the UVB (below 300nm) where CIE standard illuminants are not defined and it is assumed that irradiance below 300nm is not used in color measurement instruments. The emission maximum of an FWA is between 420nm and 450nm, Figure 3.

The probability of excitation of FWA molecules within the paper is defined by the length of the optical path of photons at the FWA's excitation band in the UVA and incident number of photons. Thus a shortening of the optical path at UVA will mean a reduced probability of FWA activation. At the excitation band of an FWA its wavelength dependent Kubelka-Munk absorption coefficient behaves as for an absorbent dye.

With currently favored CIE Whiteness (D65/10) 160 to 180 levels the total dosage of FWAs often exceeds 12kg/ton on a dry basis. At these dosage levels FWAs molecules are agglomerated causing self-stimulation and excitation and emission wavelengths. This and other challenges of high dosage of FWAs are not discussed here.

MOISTURE

Printing papers are manufactured and consumed within a very specific range of moisture (4% - 6%) for good runnability and jam-free operation and to sustain the intense heat associated with the laser printing mechanism of printers, copiers and high-speed production equipment. Printers emphasize that all necessary precautions must be taken to ensure that proper moisture content is present in the paper at time of manufacture and that it remains consistent and uniform during storage, processing and imaging of the business. The appearance characteristics are more easily controlled and maintained by printers when paper RH is about 40% [3].

At equilibrium for any given ambient conditions, the actual moisture content of various papers will differ due to type and quality of used fibers, fillers, adhesives/binders and the past moisture history of the paper/fibers. The rate of approach to such equilibrium will depend among other things on the openness of the paper structure.

The paper being measured on-line is at a different temperature (usually rather higher, 60° to 110° Celsius) and/or moisture content (often lower, sometimes higher) to that which pertains later during measurement in the laboratory. It is therefore unreasonable to expect an exact agreement between on-line and off-line measurements.

OPTICS

The mechanical structure of paper with the effect of colorants defines its optical properties. Small pores act as scattering sites in the paper, and their light scattering decreases when the pore size (diameter) decreases below half the wavelength, but remains larger than 200nm. This applies whether the pores are bounded by fibers, fines, fillers, or coating layers [4, Chapter 4]. This is in agreement with the observation that light scattering increases in the system with decreasing particle size, though there is a sharp decrease when the characteristic particle size decreases below half the light wavelength of interest. Here the interest is opacity.

The refractive index of many paper making materials is 1.55 while water has an index of 1.34. The refractive index of cellulose $C_6H_{10}O_5$ is 1.490 at 380m and 1.480 at 440nm [5]. It is known that the opacity of paper will decrease non-linearly with moisture causing it to have a more transparent appearance at higher than about 10-15% moisture content.

Wood fibers are hygroscopic in nature. The cellulose fibers change in dimension as a function of moisture content, such as that caused by a change in ambient RH. The thickness of fibers will change 2-5 times more than their length. Fibers also change dimensions while being placed into the fiber network, paper. The paper shrinks by an amount determined by the equilibrium between tensile and compressive forces at bonded interfaces. The molecular bonding between fibers is primarily due to hydrogen bonds but van der Waals forces are also important. This structural elasticity of fiber network means the pore size distribution changes as a function of moisture content. Thus when the paper shrinks the pores size distribution changes.

UVA LIGHT SCATTERING

A question is what causes the UVA light scattering to be significantly affected by reducing moisture content of the paper from 6% to 4% moisture?

This question may be discussed as effect of i) effective refractive index of fiber network structure and ii) effective refractive index of materials for the UVA light scattering for emission efficiency of FWAs as function of moisture content.

If the commonly used half wavelength theory is followed this leads to interest of the scale of pores below 200nm (half of excitation wavelengths 360-380nm). This is in contrast to the situation for measurements of visible light, where pores larger than 200nm are most significant, with a major interest being in opacity, which is measured as a weighted sum of visible wavelengths with average 550nm.

Fibers absorb water in two main ways as free water and as bound water. When the solids content of paper is above 60% all free water is gone followed by freezing bound water and then nonfreezing bound water [4, Chapter 7]. Park has demonstrated that for bleached softwood fibers at 14% and at 5-6% moisture content all free water is gone, about 9% of the remaining moisture is freezing bound water and rest about 91% nonfreezing bound water [6].

The nonfreezing bound water is defined to be the first 1-3 layers of water molecules adjacent to a cellulose surface, being bound to the hydrophilic surfaces of the paper fibers as well as trapped inside the pores of fibers [6]. The first monolayer of water molecules on cellulosic surfaces is virtually immobile [4, Chapter 7].

Effective refractive index of fiber network structure

When the moisture content of paper reduces from 6-7% moisture down to 3-5% moisture the fiber network structure shrinks causing the pore size distribution to change. At a fixed moisture content of paper the light scattering coefficients were measured versus equivalent spherical void diameter for 460nm and 680nm illumination [4, Chapter 4]. The 460nm light scattering coefficient curve has a definite optimum between 200nm - 300nm void diameter and was reduced as pore size increased or reduced. The 680nm light scattering curve does not have as clear an optimum; larger pores reduce scattering only a little.

Conclusion is the pore diameter for light scattering at the excitation band of the FWA is changed as moisture content of paper changes, such as by shrinking.

Effective refractive index of materials

The refractive index of many materials is a function of wavelength increasing with shorter wavelengths. For some polymers (optical adhesives) it also depends on their moisture content.

It may be assumed that when only bonded water exists with fibers and fillers the refractive index may vary very little. However the situation may change when approaching monolayer of water on cellulosic surface.

CONCLUSIONS

Sufficient information to allow the papermaker to optimize production of high white paper does not appear to be available. We postulate the light scattering in UVA affecting FWAs' excitation and emission efficiency would follow the half wavelength theory, but no studies were found in a search of the literature.

A study of variation of refractive index of papermaking fibers as a function of moisture content is needed. At the same time it would be possible to study any association with scattering power at UVA and visible wavelengths. Also a study is needed on the variation of larger (more than 100nm) pore size as a function of moisture content and resulting effects on visible and UVA wavelengths

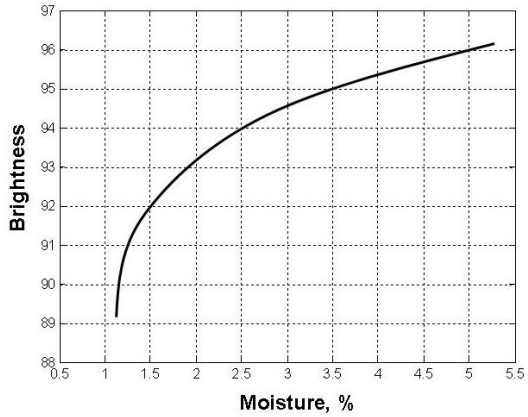

Figure 1. On-line measured brightness of white fluorescent paper versus on-line %moisture content when the off-line measured brightness of preconditioned paper has been constant..

REFERENCES

[1] L. Coppel. Whiteness and Fluorescence in Paper. Licentiate Thesis. Mid Sweden University. (2010).

[2] B. Jordan, J. Zwinkels and P. McGarry. The influence of the illuminant of the luminescent radiance factor spectrum of a reference fluorescent paper. TAGA 2003 Proceedings, (2003).

[3] Paper Moisture and Relative Humidity. Glatfelter's Technical bulleting, Issue 2005-2, (2005).

[4] K. Niskanen (Ed.). Paper Physics, Paperi ja Puu Oy, (2008).

[5] http://www.filmetrics.com/refractive-index-database/Cellulose

[6] S. Park, R. Venditti, H. Jameel and J. Pawlak. Hard-to-remove water in cellulose fibers characterized by thermal analysis: A model for the drying of wood-based fibers. Tappi J. 6(7):10-16 (2007)

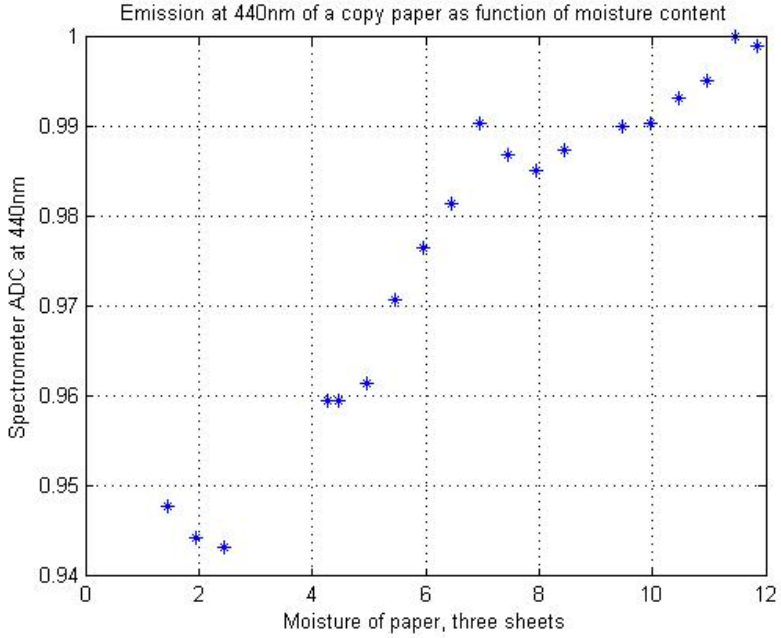

Figure 2. Fluorescent emission of a copy paper versus %moisture content when the ambient temperature has been kept constant at 22°C.

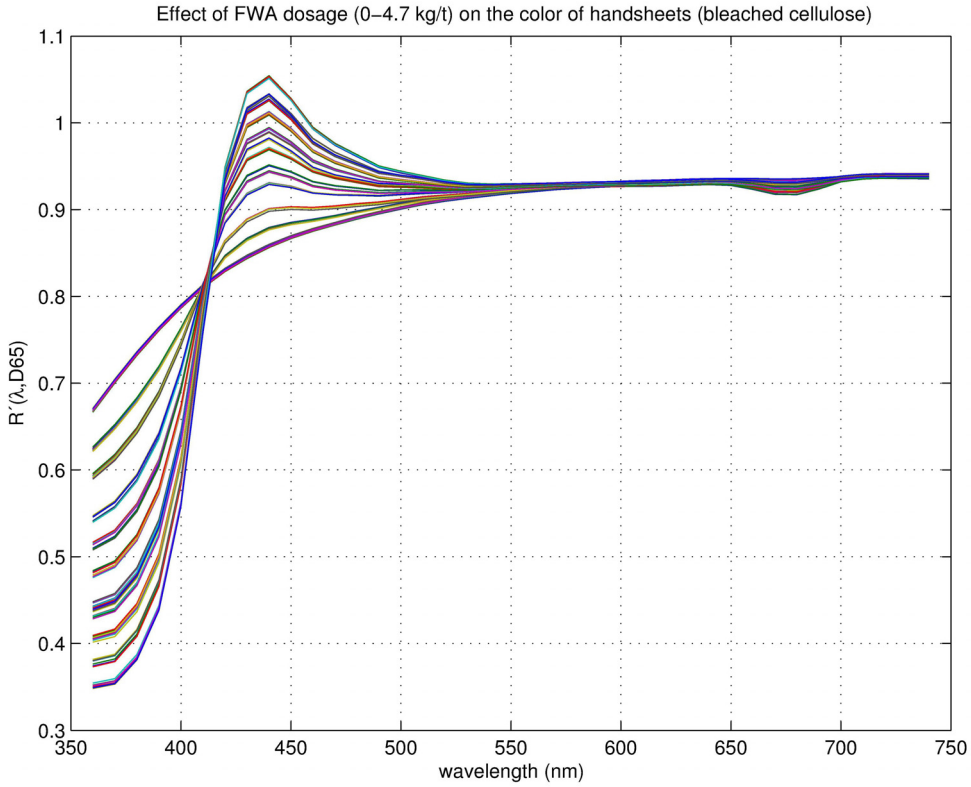

Figure 3. Apparent reflectance of bleached cellulose hand sheets at different FWAs dosage levels.

Theory of print through caused by ink oil: Its application to low basis weight newsprints.

ILYA VADEIKO

FPInnovations
570 Saint-Jean Blvd., Pointe-Claire,
QC H9R 3J9, Canada
Ilya.vadeiko@fpinnovations.ca

Keywords: print through, scattering coefficient, Kubelka-Munk, porosity, caliper, newsprint

ABSTRACT

We developed a fundamental approach to quantifying the contribution of coldset ink oil to print through in newsprint. In a previous report, we showed that the propensity of newsprint to lose opacity due to ink oil can be well characterized by a parameter we called the Oil Gain Factor (OGF). In this paper, we demonstrated how the OGF is related to the light scattering coefficient of paper. We obtained a general solution for the reflectance of paper containing ink oil. The latter allowed us to demonstrate that the OGF is inversely proportional to the pore volume to the power 3/2. In addition, we developed a novel method for characterizing paper surface pores using non-contact laser surface profilometry. We related the print through two-sidedness to differences in the characteristic depth of surface pores. We also demonstrated that higher print through of low basis weight newsprints is well explained by changes in paper caliper and porosity.

1 INTRODUCTION

The average basis weight of newsprint is decreasing for both economic and environmental reasons. As a result, print through (PT), which is the undesired appearance of an image on the reverse side of the print, has become more important. Nearly all newspapers and a significant amount of low-end commercial and directory publications, are printed with non-drying oil-based coldset inks. With these inks, the print through is controlled by three factors [1,2]: the initial opacity of the unprinted paper, the penetration of ink pigments into the sheet, and the loss of opacity due to ink vehicle oil that fills paper pores and reduces the effective scattering area of air-fibre interfaces. The non-drying ink oil may cause up to 70% of the measured print through[3].

Since the pioneering work of De Grace[2] discussing the relationship between print through and paper properties such as opacity and the amount of fines, several other research groups have studied the relationship in detail[4,5,6,7]. In our previous work[8], we proposed that the effect of ink oil on print through directly correlates with the pore volume of the paper. The pore volume was calculated as the product of the paper's porosity and caliper. In this report, we continue the fundamental analysis of the phenomenon and provide a consistent theory describing the print through caused by ink oil. Based on the Kubelka-Munk theory, we link the Oil Gain Factor (OGF)[8] with the scattering coefficient of paper and then link it to the pore structure. The results of our theoretical analysis are verified in the experimental part of the work.

1.1 EXPERIMENTAL

We tested newsprints of different basis weights from four Canadian mills labelled A to D. Mills A and B use approximately 25% and 55% of deinked pulp (DIP), respectively. Mills C and D produce newsprint from 100% TMP. The basic paper properties of samples are reported in Table 1. In the paper ID, the letter denotes a paper mill and the number identifies the basis weight of the paper in g/m^2.

Paper ID	Ash, %	Caliper, µm	PPS, µm		Porosity, %
			Side 1	*Side 2*	
A40	--	--	--	--	--
A43	0.61	70.8	3.42	3.71	55.6
A45	0.52	71.2	3.44	3.62	54.4
A48	1.12	74.4	3.42	3.36	53.6
B40	2.84	59.7	3.16	3.46	49.3
B43	2.45	63.3	3.08	3.43	50.8
B45	2.50	66.5	3.08	3.36	51.3
B48	1.55	74.2	3.45	3.72	52.7
C40	≈0	66.1	3.48	3.12	54.8
C43	≈0	71.1	3.66	3.42	54.6
C45	≈0	73.9	3.57	3.55	54.5
C48	≈0	79.4	3.55	3.42	55.4
D40	--	--	--	--	--
D43	≈0	71.2	4.10	3.64	51.6
D45	≈0	75.4	4.16	3.79	51.9
D48	≈0	78.9	4.02	3.81	53.0

Table 1 Basic physical properties of the samples

Principal differences between the newsprints produced at different mills can be understood from the plot of paper air permeability versus basis weight in Figure 1. The newsprint from mill B contains the highest level of DIP and therefore the sheet is denser and less permeable. The sheet from mill A is similar as it also contains some DIP. The newsprints from mills C and D are very similar to each other. They are bulkier, more open and therefore more permeable, because they contain 100% stiff and less compressible TMP fibres.

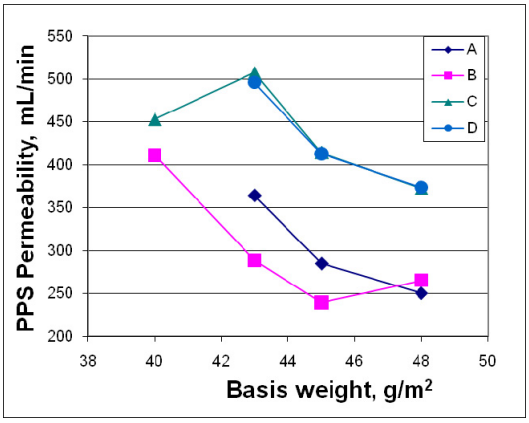

Figure 1. Air permeability vs. basis weight

The results of optical and print testing are presented in Table 2. The printing results in the table correspond to a commercial target of 1.0 of corrected print density (PD). Details about testing methods and measurement procedures can be found in our previous report [8].

Paper ID	Opacity, %	IR, g/m^2		Total PT		PTO		OGF, (g/m^2)$^{-1}$	
		Side 1	*Side 2*	*Side 1*	*Side 2*	*Side 1*	*Side 2*	*Side 1*	*Side 2*
A40	--	--	--	--	--	--	--	--	--
A43	93.63	3.06	2.98	0.090	0.096	0.032	0.043	0.010	0.015
A45	95.05	3.56	3.07	0.088	0.088	0.038	0.045	0.011	0.015
A48	95.80	3.58	3.19	0.078	0.080	0.034	0.042	0.010	0.013
B40	93.17	3.17	2.88	0.132	0.117	0.067	0.053	0.021	0.018
B43	94.14	3.36	3.12	0.109	0.103	0.058	0.051	0.017	0.016
B45	94.89	3.64	3.33	0.108	0.099	0.058	0.051	0.016	0.015
B48	95.84	3.3	3.32	0.085	0.082	0.044	0.040	0.013	0.012
C40	93.71	2.97	2.85	0.102	0.089	0.049	0.033	0.016	0.012
C43	93.57	2.93	2.69	0.097	0.083	0.040	0.026	0.014	0.010
C45	95.03	3.2	3.07	0.092	0.077	0.041	0.027	0.013	0.009
C48	95.95	3.41	3.56	0.076	0.071	0.033	0.027	0.010	0.008
D40	--	--	--	--	--	--	--	--	--
D43	93.61	3.45	3.44	0.109	0.102	0.052	0.047	0.015	0.014
D45	94.59	3.74	3.88	0.109	0.103	0.053	0.045	0.014	0.012
D48	94.05	3.7	3.69	0.100	0.090	0.044	0.041	0.012	0.011

Table 2 Optical and printing test results (PD=1.0)

2 INTERPRETATION OF PRINT THROUGH DUE TO OIL USING THE KUBELKA-MUNK THEORY

The Kubelka-Munk theory of light reflectance and transmittance in a macroscopic layer of material has been successfully applied in paper physics to the analysis of print through [1, 9]. It is well known that as ink oil penetrates into the structure of paper, it reduces the light scattering area of the fibre-air interfaces. The magnitude of that effect can be expressed in terms of the scattering coefficient. Although Larson and Trollsås did analyze the change in the scattering coefficient of paper due to ink oil based on the Kubelka-Munk theory[9], they did not provide any explicit relationship between the amount of oil penetrated into the paper and the reduction of the scattering coefficient. In this section, we will address the issue.

A coldset ink consists of two main components: pigments and vehicle oil. Several studies of ink penetration into the paper showed that the pigments remain concentrated within a thin layer of printed surface while the oil penetrates deep into the structure of paper[6, 10, 11, 12]. Since the print through phenomenon is observed from the reverse side of the print, we can follow the idea of penetration depth introduced by Larsson and Trollsås [9] and assume that the printed paper can be split into two parts: a thin layer of thickness W_p containing the pigment particles and the rest of thickness $L = W - W_p$ containing just the vehicle oil. Therefore, we can represent the reflectance of the reverse side of printed paper as the reflectance of a sheet of thickness L measured on the background of a thin paper layer containing the pigments.

2.1 GENERAL SOLUTION OF KUBELKA-MUNK EQUATION FOR EXPONENTIAL OIL DISTRIBUTION

The oil mainly reduces the scattering coefficient S_0 of paper and has little effect on the absorption coefficient K. The change in the scattering coefficient for commercial levels of ink on paper was found to be relatively small, in the range of 13-17% [9]. We can therefore assume that

$$\delta S(z) \equiv \frac{S_0 - S(z)}{S(z)} << 1 \qquad (1)$$

Generally speaking, the ink oil can be distributed non-uniformly along the thickness direction of the paper (coordinate z). Therefore, the scattering coefficient of paper with the oil $S(z)$ may depend on the coordinate z.

The Kubelka-Munk equation of light reflectance from a thin layer of scattering material can be represented in the following form:

$$\frac{dr(z)}{dz} = \left[r^2 - 2\left(1 + \frac{K}{S(z)}\right) r + 1 \right] \cdot S(z) \quad (2)$$

Here, $r(z)$ is the reflectance of paper in the thin layer, K is the absorption coefficient. We will consider $z = 0$ as the back side of the paper and $z = L$ – the front surface where the reflectance affected by the oil is measured. Eq.(2) is a first order nonlinear differential equation that is called in the literature the Riccati equation. It can be transformed to a linear second order differential equation if we make a substitution:

$$r = -\frac{y'}{y},\ y'' + 2\left(1 + \frac{K}{\tilde{S}(\tilde{z})}\right) y' + y = 0 \quad (3)$$

Here the prime denotes a derivative with respect to a new variable $\tilde{z} \equiv \int S(z)dz$ and $\tilde{S}(\tilde{z}) = S(z)$. We require that the origin of $\tilde{z}$ coincides with that of original variable z:

$$\tilde{z}(z = 0) = 0. \qquad (4)$$

The linear form of Eq.(3) is advantageous, because it allows applying the perturbation theory to find solutions of the equation. Using the assumption Eq.(1) that the relative change of the scattering coefficient is a small dimensionless parameter, we will seek the solution in the form of perturbation series. Substituting $y = \sum_{n=0}^{\infty} y_n$ in Eq.(3) we find

$$y_n'' + 2\left(1 + \frac{K}{S_0}\right) y_n' + y_n = -\frac{2K\,\delta\tilde{S}}{S_0} y_{n-1}' \quad (5)$$

where y_n is a term of the order of $\left(\delta\tilde{S}\right)^n$. The solution reads:

$$y_n = \frac{a-1}{b} \int_0^{\tilde{z}} \delta\tilde{S}\, y_{n-1}' \left[e^{-\lambda_+(\tilde{z}-\zeta)} - e^{-\lambda_-(\tilde{z}-\zeta)} \right] d\zeta. \quad (6)$$

where $\lambda_\pm = a \pm b$ and $a \equiv 1 + K/S_0$, $b \equiv \sqrt{a^2 - 1}$. The first term of the series y_0 is the solution of the homogeneous part of Eq.(5), i.e. the standard Kubelka-Munk solution.

Previous studies of ink oil penetration into the paper showed that the concentration of oil decays exponentially with the distance from the paper surface [10]. Whatever effect the oil has on the paper scattering coefficient, it should be related to the amount of oil in the paper. Therefore, we assume that in the leading term δS is also decaying exponentially:

$$\delta S(z) = \alpha\, e^{-2\beta S_0 z} \qquad (7)$$

where α is a small parameter describing the magnitude of the oil effect on paper's opacity, and β is a dimensionless parameter describing the exponential decay of oil concentration in the paper. The exponent in Eq.(7) was chosen in such a way that the parameter β can be compared to the parameter b. Since in the print through tests the printed side of paper surface corresponds to $z = 0$, the deviation of the scattering coefficient reaches its maximum there $\delta S(0) = \frac{S_0}{1+\alpha}$. At large paper depths $z \to \infty$ where the oil is not present, the scattering coefficient approaches paper's own value $S \to S_0$.

The exponential form of the scattering coefficient in Eq.(7) permits a simple transformation to the new variable $\tilde{z}$:

$$z \to \tilde{z} \equiv \int S(z)dz = \frac{S_0}{\beta} \ln\left(\frac{e^{\beta z} + \alpha}{1 + \alpha}\right) \qquad (8)$$

Substituting Eqs.(7), (8) in the general solution Eq.(6), we can find the reflectance coefficient. We will consider two opposite scenarios: $\beta \ll b$ – ink oil is distributed almost uniformly, $\beta \gg b$ – ink oil is localized near the printed surface. In the first case of almost uniform oil distribution, the leading term of print through due to oil reads

$$PTO \approx \frac{a-1}{b-\beta}\ \alpha\, e^{-2\beta S_0 L}. \qquad (9)$$

In the opposite case, when oil remains close to printed surface, i.e. $\beta \to \infty$, the leading term reads

$$PTO \approx \frac{(a-1)}{\beta - b}\alpha e^{-2b\,S_0\,L} \cdot \frac{2b^2}{(b+\beta)\beta}\frac{a+\beta+Rg(\beta-a)\big(2(\beta+a)-Rg\big)}{(b+a-Rg)\big(1-Rg(a-b)\big)} \quad (10)$$

Taking into account that $\beta \approx b$ and $Rg \to 0$ for black prints, Eq.(10) can be simplified further

$$PTO \approx \frac{a-1}{\beta - b}\alpha e^{-2b\,S_0\,L}\left[2\frac{a+\beta}{a+b}\left(\frac{b}{\beta}\right)^2\right] \quad (11)$$

2.2 RELATIONSHIP BETWEEN PAPER PROPERTIES AND THE PRINT THROUGH

In the previous paper, we demonstrated that the print through due to ink oil increases linearly with the amount of oil on paper. This has been verified with newsprints produced at different mills from different blends of TMP and recycled pulp [8]. The slope of the line is the Oil Gain Factor (OGF):

$$PTO = OGF \cdot \Delta M_I \quad (12)$$

where ΔM_I is the amount of ink (in grams) transferred onto one square meter of paper. The value of OGF for all the newsprints studied in this paper is provided in Table 2.

Since we are studying the effect of ink oil on the print through, we will convert the total mass of ink to the volume of just vehicle oil. For that, we will denote the mass fraction of oil in the ink by μ and the oil density by ρ_O. The expression Eq.(12) can then be transformed to the following form

$$PTO = OGF \cdot \frac{\rho_O}{\mu}\Delta V_O \quad (13)$$

where ΔV_O is the volume of oil per square meter of paper and $\mu\,\Delta M_I = \Delta M_O = \rho_O\,\Delta V_O$ is the mass fraction of the oil in the ink. Since the ink oil applied on paper fills some paper pores, we can assume that $\Delta V_O = -\Delta V_p$, where V_p is the pore volume normalized to a square meter of paper.

It has been demonstrated in the literature[10,11,12] that the vehicle oil of coldset inks can penetrate deep into the paper structure. Since the effect of the oil on print through is measured from the reverse side of the print, we can assume that when looking from that side the oil distribution inside the paper can be considered been close to uniform[10]. Although the oil concentration may decay exponentially[11] as measured from the printed side, from the reverse side the exponent's tails is well approximated by a constant level. In addition, that trend also agrees with our assumption that the amount of oil in the bulk of the paper is relatively small and therefore its effect on paper's scattering coefficient can be considered as a small correction. In the previous subsection, we found a simple approximation for the print through caused by near uniform distribution of ink oil in the paper Eq.(9). Taking $\beta \to 0$, substituting that expression for PTO on the left side of Eq.(13), and rearranging the terms, we obtain:

$$OGF \approx \left(\sqrt{\frac{K}{2}}\frac{\mu}{\rho_O}\right)\cdot\frac{1}{S_0^{3/2}}\frac{\Delta S}{\Delta V_p} \quad (14)$$

Here, the coefficient in the brackets only depends on ink properties and the light absorption coefficient. If the relationship between S_0 and paper pore volume were known, Eq.(14) would provide a way of relating the Oil Gain Factor to the pore volume.

It is widely accepted in paper physics that the scattering coefficient is proportional to the specific surface area of paper pores, i.e. unbonded fibre surface. A good analysis of different experimental attempts to prove that linearity using mercury porosimetry and BET nitrogen adsorption technique is provided by Lehtonen and Dyer [13]. The theoretical foundation for the linear relationship was first approached by Scallan and Borch [14, 15]. For simplicity, let us consider the paper as a continuous medium of fibre material containing N pores of similar shape. In that case, the total surface area would be N times the surface area of a single pore. On the other hand, N times the volume of a single pore gives the total pore volume in the paper. Therefore, we may assume that in the first approximation the total surface area of paper pores should also be proportional to the total pore volume of the paper. So, the total pore volume should also be proportional to the scattering coefficient. Previous experimental works show evidence supporting our conclusion. For example, a paper studying light scattering in clay coatings [16] indicated that the scattering coefficient in that case was proportional to the porosity of the coating with a very high degree of accuracy. Another experimental work [17] studying the relationship between paper pores and scattering coefficient also demonstrated that the latter is well approximated by a linear function of paper porosity. Therefore, we suppose that the scattering coefficient S_0 of paper is proportional to the pore volume:

$$S_0 = \nu\, V_p \quad (15)$$

where ν is a parameter that may depend on the average pore diameter or higher order moments of the pore size distribution. Therefore, $\frac{\Delta S_0}{\Delta V_p} = \nu$ and we finally find:

$$OGF = \left(\sqrt{\frac{K}{2\nu}}\frac{\mu}{\rho_0}\right)\cdot\frac{1}{V_p^{3/2}} \quad (16)$$

Eq. (16) satisfies some basic physical requirements. OGF quickly increases as the pore volume approaches zero and it vanishes as it approaches infinity. That means that a paper with a small pore volume will exhibit a rapid increase of print through due to ink oil as the amount of ink on paper increases. On the other hand, a paper with a very large pore volume should be less prone to the effect of ink oil on loss of opacity. It is important to understand that the pore volume V_p and porosity are not the same. The thicker the paper, the larger its pore volume becomes even if the porosity remains constant.

In conclusion, Eq.(16) constitutes the main theoretical result of this paper and provides a simple analytical expression for the dependence of OGF on paper pore volume. It indicates that the paper with larger pore volume should demonstrate slower decrease in print through due to ink oil, because its OGF is smaller. In our previous study [8], we demonstrated that OGF may be strongly two-sided, indicating that we cannot ignore the effect of two-sidedness in pore structure on the distribution of ink oil inside the paper. Therefore, before testing Eq.(16) on some paper samples studied in this work, we will investigate how the surface structure of paper pores may be characterized and related to the distribution of ink oil in it.

3 NEW APPROACH TO CHARACTERIZATION OF PAPER SURFACE PORES

The structure of paper is often two-sided, suggesting the existence of structural characteristics that can distinguish between the average bulk and surface properties of paper. The pore structure is no exception. Rigorously measuring and characterizing the properties of surface pores still represents a difficult and important challenge. Most of the experimental methods for measuring porosity of paper such as mercury intrusion cannot disentangle the information about the bulk from its surface component. On the other hand, air leak surface tests such as PPS roughness cannot separate the surface topography from the pore structure of surface layers, which can be different for different sides of the same paper. In our previous work on the contribution of oil to print through [8], it became evident that many papers have a large two-sidedness in terms of surface pore structure revealed by the amount of oil penetration into the paper. Hence, it is of great importance to be able to measure those differences in the surface pore structure.

Surface pores can be analyzed with a non-contact laser profilometer that measures the depth and size of surface openings. The properties of the surface pores are more apparent if the 2D map of z-direction heights is represented in a histogram form. An example of such histogram for a newsprint paper is shown in Figure 2. The depth is calculated from the average surface level which is taken to be zero. In what follows, we will denote the distribution of surface heights with $\Omega(z)$, where z is the pore depth or the surface elevation.

We first notice a strong skewness of the histogram in Figure 2. In order to characterize the skewness, we propose to divide the histogram in three parts. In the center of the plot, in the interval from -15 <z <15, the distribution can be approximated well with a Gaussian function. To the left of that interval (z < -15), $\log(\Omega)$ decreases linearly with the pore depth (solid line in Figure 2), therefore the distribution follows an exponential law. The third component of the histogram, which falls in the interval z > 15, corresponds to another functional form that we will not analyze in this paper. Here, we will primarily focus on the interval z < -15, because it best characterizes the properties of deep surface pores.

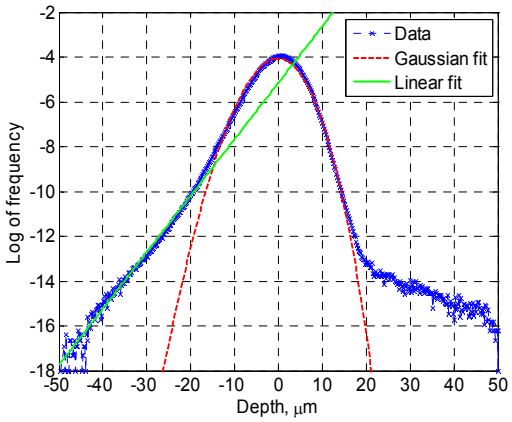

Figure 2. Histogram of surface pore depth

3.1 DERIVATION OF THE DISTRIBUTION OF SURFACE PORE HEIGHTS

In order to better understand the exponential distribution of surface pores, we begin with a short review of the theory of Planar Poisson Line Process (PPLP) that is often used to describe a single layer of paper as a random fibre network [18]. Several assumptions are usually made about the distribution of fibres in the plane in order to allow for some statistical estimates of the network properties (see [19]). One of the main ones is the assumption that the probability of more than two fibres intersecting at a point is negligible. The distribution of fibres in the plane is characterized by the intensity of the Poisson process denoted with τ. The intensity τ is equal to the average total fibre length per unit area. In our analysis, the most important characteristic is the area of the plane not covered with any fibres. According to Miles [19], if the fibres have an average width $\overline{\omega}$, the non-covered fraction of the

plane is equal to $\exp\left(-\tau\,\bar{\omega}\right)$. When the structure is formed of n layers, the probability to find a pinhole would be $\exp\left(-n\,\tau\,\bar{\omega}\right)$.

Let us now describe the surface profile in terms of idealized multi-planar fibre network. First, we define the layers in the paper structure. We represent the thickness h_i of the i[th] layer of the structure as

$$h_i\left(x,y\right)=\bar{h}_i+\tilde{h}_i\left(x,y\right) \qquad (17)$$

where $\bar{h}_i$ is an average thickness and $\tilde{h}_i$ is a random variable with zero average. Note that in our idealized multi-layer model of paper, the boundaries of the layers do not necessarily coincide with the fibre surfaces. If two fibres from adjacent layers are not in contact, the boundary should be drawn through the middle of the pore between them. If there is a pinhole at a particular point (x,y) of the layer, its thickness $h_i\left(x,y\right)$ at that point is determined by the boundaries with adjacent layers. A schematic example of the layers is shown in **Figure 3**.

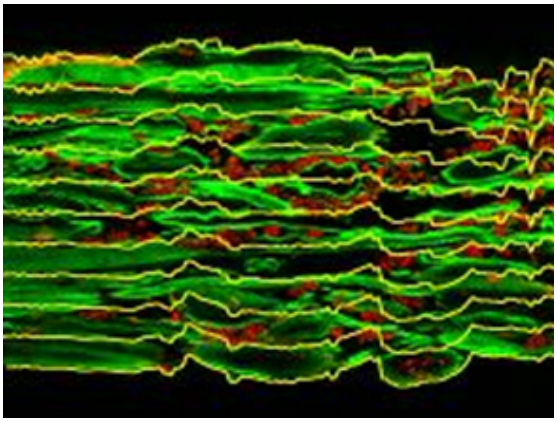

Figure 3. Confocal microscope image of a paper cross-section. Green color represents fibres, red – fillers, and yellow—layer boundaries.

The parameter $\tilde{h}_i$ in Eq.(17) takes into account many factors such as: fluctuation of fibre thickness along the fibre length and from fibre to fibre, overlap of two fibres in the same layer (we assume that only two fibres can intersect in a single layer), fibre flexibility determining the bending around an intersection point, etc.

Secondly, we assume that all layers are statistically similar and that their average thickness is $\bar{h}$. The similarity between different layers also implies that the probability density function of $\tilde{h}_i$ is common to all of them and can be simply denoted by ρ_h. Since the paper structure is often two-sided, we will always divide it into the top and bottom halves and consider all properties of each half independently. For the laser based non-contact surface profilometry, the probability of hitting a fibre surface at some depth z measured from a reference plane can be defined as follows

$$\Omega\left(z\right)=e^{-n\tau\bar{\omega}}\left(1-e^{-\tau\bar{\omega}}\right)\mathrm{P}\left(\tilde{h}\right) \qquad (18)$$

where we assume that the intensity of the Poisson process τ is the same for all surface layers. The principal idea of the multi-layer approach to the analysis of surface profiles is schematically demonstrated on a paper cross-section in Figure 4. Arrows of different colors point at fibres located in different layers of the structure. The pore depth $|z|$ corresponds to the length of the arrow. The number of arrows of the same color qualitatively represents the frequency of points of given depth. The sheet structure is divided in two halves by the middle yellow line.

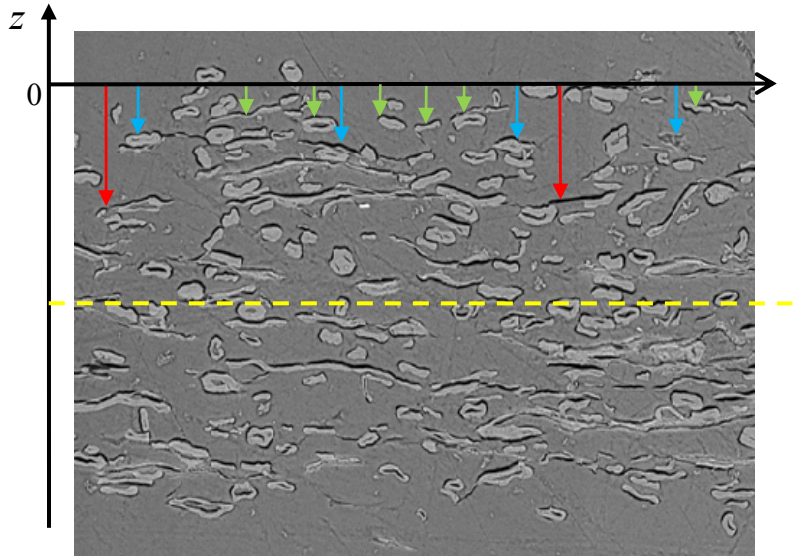

Figure 4. SEM image of paper z-direction cross-section

The first factor in Eq.(18) is the probability that the first n layers have a void (pinhole) at the point of interest in the x-y plane whereas the second term is the probability of finding a fibre in layer $n+1$. The function $\mathrm{P}\left(\tilde{h}\right)$ in Eq.(18) is the probability density describing accumulated layer thickness fluctuations from the $N-n$ layers underneath point z, where N is the total number of layers in the given half of the paper structure. The parameter N can be evaluated by dividing half of the paper caliper by the average layer thickness $\overline{h}$. Taking into account that the middle plane has the coordinate $z_0 = -N \cdot \overline{h}$, we can represent z in Eq.(18) in terms of $\tilde{h}$ as follows:

$$\begin{aligned} z(x,y) &= -N \cdot \overline{h} + \sum_{i=1}^{N-n} h_i(x,y) - \Delta\tilde{h}_{N-n} \\ &= -n \cdot \overline{h} + \tilde{h}(x,y) \end{aligned} \tag{19}$$

where $\tilde{h} = \sum_{i=1}^{N-n} \tilde{h}_i - \Delta\tilde{h}_{N-n}$. Here, $\Delta\tilde{h}_{N-n}$ is the distance from the top surface of the fibre at the point (x,y) to the layer's boundary. As we mentioned before, the layer boundary is not necessarily passing by the fibre surface. Since all fluctuations $\tilde{h}_i$ follow the same distribution function ρ_h (the assumption made earlier), according to the Central limit theorem, as $(N-n)$ increases – we approach the surface of paper, $\mathrm{P}\left(\tilde{h}\right)$ should approach a Gaussian function with zero average and

$$\sigma(N-n) = \sqrt{2(N-n)+1} \cdot \sigma_h . \tag{20}$$

From a physical standpoint, the multi-planar structure of paper implies that inside the paper structure $\tilde{h}$ cannot exceed $\overline{h}$. Therefore, for the internal layers $\mathrm{P}\left(\tilde{h}\right)$ should be zero outside of some interval $\left[-\overline{h}, \overline{h}\right]$.

Now, we can rewrite Eq.(18) in a form that would emphasize the leading term with respect to z:

$$\Omega(z) = \exp\left(-|z|\frac{\tau\,\overline{\omega}}{\overline{h}}\right) \cdot \Omega_0\left(\tilde{h}\right) \tag{21}$$

where $\Omega_0\left(\tilde{h}\right) = \left(1 - e^{-\tau\,\overline{\omega}}\right) \cdot \exp\left(\frac{\tilde{h}}{\overline{h}}\tau\,\overline{\omega}\right) \mathrm{P}\left(\tilde{h}\right)$.

The first term of Eq. (21) describes an exponential dependence of the probability density function on the pore of depth z and the second term $\Omega_0\left(\tilde{h}\right)$ is a modulating function. It is important to note that the amplitude of the modulating function $\Omega_0\left(\tilde{h}\right)$ is limited, because $\left|\tilde{h}\right| < \overline{h}$. Hence, Eq.(21) shows that the probability density function of the depth of surface pores deeper than one fibre layer should follow the exponential distribution. This confirms the observation that $\log(\Omega)$ is a linear function with the slope:

$$\gamma \equiv -\partial_z \log(\Omega) = \frac{\tau\,\overline{\omega}}{\overline{h}} \tag{22}$$

We can also note, that as we approach the surface layer, i.e. $n \to 0$, $\mathrm{P}\left(\tilde{h}\right)$ becomes the leading term of Eq.(18). As we discussed earlier, according to the central limit theorem $\mathrm{P}\left(\tilde{h}\right)$ should approach a Gaussian distribution with $\sigma(N) = \sqrt{2N+1} \cdot \sigma_h$. This is in agreement with the observation that in the interval z=(-15, 15) the pore depth distribution is approximated well by the Gaussian function (see Figure 2).

In Eq.(22) which is the main result of this section, $\overline{\omega}, \overline{h}$ are the average fibre width and average layer height that should be fairly similar on the opposite sides of the paper. They are determined by the furnish and paper consolidation. On the other hand, the parameter τ describes the number of fibres or so called coverage in each layer of the paper structure and can be fairly different on opposite sides. It is affected by the type of paper machine clothing used on each side and by differences in water drainage.

3.2 TWO-SIDEDNESS OF PAPER SURFACE PORES

Our analysis of surface topography of numerous newsprints produced at different mills showed that the distribution of surface heights can be qualitatively split into three different domains: the Gaussian central region of the distribution characterizing the morphology of the top fibre layer; the exponential region characterizing deep pores formed by several surface layers of fibres, and the region of high values of z characterizing the elevated points on the surface. An example was discussed in the previous subsection (see Figure 2). In that subsection, we also established the fact that the depth of the deep pores of a multi-planar fibre network should follow the exponential distribution with parameter γ, Eq.(22). As we will see below, γ provides important information about the properties of surface layers of paper and will be used to explain the print through two-sidedness.

In our work on the print through of different newsprints, we observed a significant two-

sidedness for many of the papers (see OGF values in Table 2 and Figure 5). For example, at 2 g/m^2 of ink on paper, the two-sidedness in print through due to ink oil on sample A43 could easily reach 0.01, a difference that is visually perceptible.

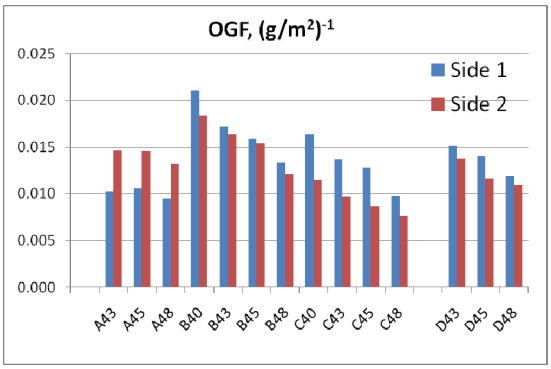

Figure 6. OGF of tested samples.

In order to relate the print through two-sidedness to the difference in the surface pore structure, we measured surface profiles on each side of the newsprints studied in this work and calculated γ from the distribution of surface heights. The results are presented in Figure 6.

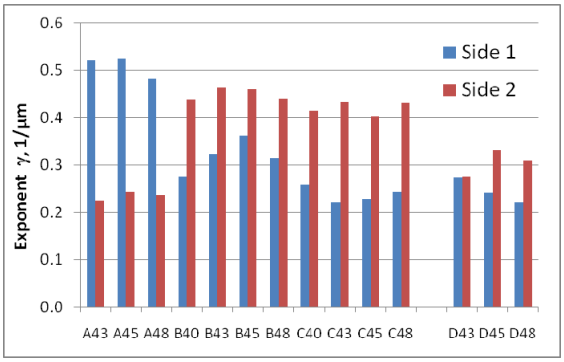

Figure 5. Exponent γ of surface pore depth distribution

One can see a significant two-sidedness of surface pore structure for most of the samples. The value of γ, averaged over all samples and sides, is $\overline{\gamma} \approx 0.35\ \mu m^{-1}$. We can estimate the average pore diameter that would correspond to that exponent (see Miles [19]). Assuming that the typical fibre aspect ratio of TMP fibres $\frac{\overline{\omega}}{\overline{h}} \approx 2$, we obtain

$$\overline{D} = \frac{1}{\tau} = \left(\frac{\overline{\omega}}{\overline{h}}\right) / \gamma \approx 6\ \mu m . \qquad (23)$$

That estimate matches well the average pore diameter of typical newsprint as measured by mercury intrusion porosimetry.

Since we followed the macroscopic approach of Kubleka-Munk theory to the light scattering in paper, we cannot directly evaluate the microscopic effect of ink oil on the scattering of pores of different diameter. That would require us to consider the pores as scattering centers randomly distributed in the paper (see for details Ref. [20]). Therefore, we cannot find an explicit relationship between OGF and the average pore diameter.

On the other hand, it is natural to assume that the easier the oil penetrates inside the paper, the higher OGF (paper's propensity to PTO) should be. The penetration of ink oil is dependent on the characteristic depth of surface pores on the printed side. The characteristic depth is a reciprocal of γ of that side. We can therefore assume that the ratio between OGF values of opposite sides of the paper should correlate with the ratio of the corresponding characteristic depths. The ratios are plotted against each other on Figure 7. We observe a good correlation between OGF two-sidedness and the differences in the characteristic depth. So, the observed two-sidedness in print through due to ink oil can be well explained by differences in the pore structure of surface layers.

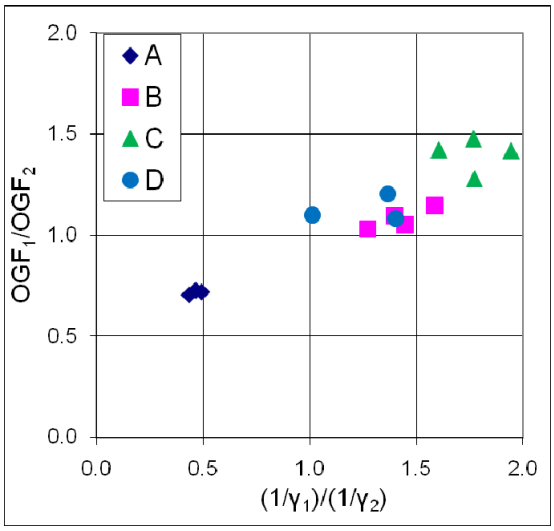

Figure 7. Correlation between paper characteristic surface pore depth and OGF two-sidedness. Subscript indices denote the paper side.

4 RELATIONSHIP BETWEEN PAPER PORE STRUCTURE AND OGF

In previous sections we analyzed how the print through due to ink oil can be linked to the scattering coefficient of paper and its pore structure. We also demonstrated that the two-sidedness in OGF often observed in newsprint, can be explained by the differences in the surface pore structure. We showed that if the ink oil is distributed uniformly along the thickness of a homogeneous paper structure, OGF should be inversely proportional to a power of pore volume (see Eq.(16)). Since such ideal conditions are never met and the paper usually shows some pore two-sidedness, we proposed in our previous report [8] to average the OGF over both sides of the paper:

$$\langle OGF \rangle = \frac{OGF_1 + OGF_2}{2} . \qquad (24)$$

The pore volume per square meter of paper can be calculated as a product of paper porosity and caliper. The pore volume V_p normalized to a square meter of paper will be measured in microns. The plot of $\langle OGF \rangle$ versus V_p is shown in Figure 8.

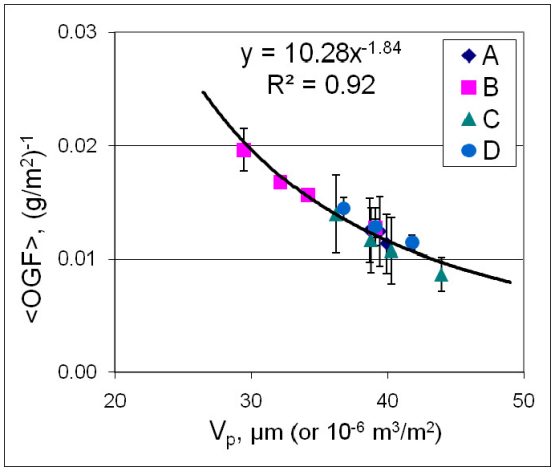

Figure 8. Average OGF vs. paper pore volume. Error bars denote deviation of the actual $OGF_{1,2}$ from the average value.

Taking into account that we studied newsprints of basis weights varying from 40 to 48 g/m^2 produced at four paper mills from very different pulps, we can note that the observed correlation between $\langle OGF \rangle$ and V_p is very good. The best fit solid line shown on the plot is described by the equation:

$$\langle OGF \rangle = 10.28\, V_p^{-1.84} \qquad (25)$$

The exponent -1.84 is also relatively close to the theoretical value of -1.5 predicted in Eq.(16). According to Table 2, the propensity for print through caused by ink oil (OGF) increases significantly with decreasing basis weight of the newsprint for most of the samples. According to Eq.(25), this is explained by decreasing pore volume in the lower basis weight newsprints. We also note that the effect can be mitigated in lower basis weight newsprints if their porosity is increased as is the case for sample A (see Table 1 and Figure 8).

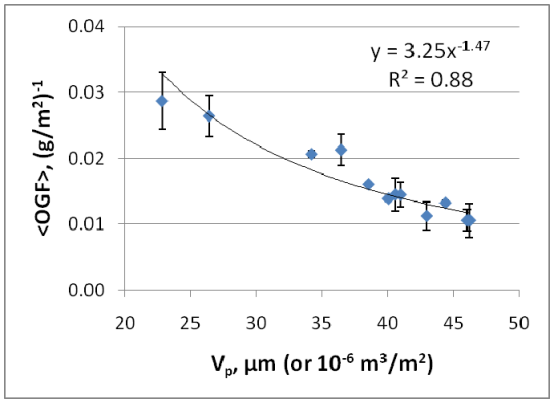

Figure 9. Average OGF vs. paper pore volume. Results of the tests on 12 newsprints studied in the previous report[8] (North American coldset ink).

In our earlier work[8], we presented the results obtained for 12 different newsprints from six Canadian mills and one Asian mill. We fitted a power function to the data as shown by a solid line in Figure 9. As one can see, the obtained exponent of -1.47 is again very close to the predicted value of -1.5.

In addition to the standard printing tests with North American coldset ink, we also tested in the same study the print through effect using a typical Asian ink. We replotted those results together with a power-law fitting function in Figure 10. And again, we noted a very good agreement between the measured exponent (-1.66) and the predicted value of -1.5 .

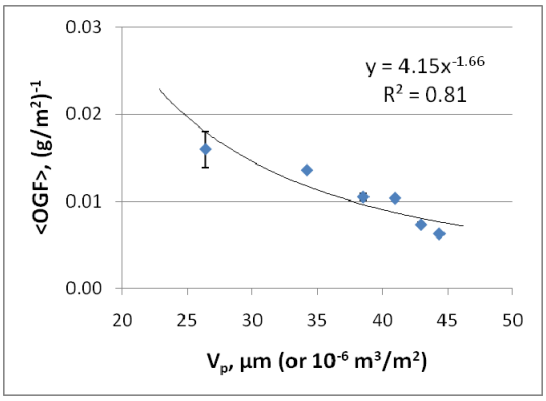

Figure 10. Average OGF vs. paper pore volume. Results of the tests on 12 newsprints studied in the previous report [8] (Asian coldset ink).

The observed deviation of the exponent from the theoretical value predicted in Eq.(16) can be attributed to several factors. We believe that the main factor explaining the deviation is the effect of surface pores and therefore non-uniform distribution of ink oil throughout the paper thickness. Our assumption of near uniform homogeneous distribution of ink oil across the thickness of paper can only be valid to some extent (see Ref.[21]). The OGF two-sidedness is well reflected by the large error bars for some of the points in Figure 9. Another reason can be sought in the fact that the actual pore size distribution of different newsprints is not the same and that difference should have an impact on the light scattering. All the results presented in this paper are based on macroscopic average characteristics of the pore size distribution such as pore volume. Higher order parameters of the distribution are not taken into account. And finally, as we demonstrated in the previous work using two different inks applied on the same samples, the rheological properties of ink oil are also important and have their effect on OGF. This can readily be seen from the differences in fitting coefficients between Figure 9 and Figure 10. This is also not taken into account in the present work.

5 CONCLUSIONS

In this paper we analyzed the effect of ink oil on the print through phenomenon in newsprints. We provided a general solution for the reflectance of newsprint paper containing small quantities of the vehicle oil Eq.(6). We also analyzed the case of exponential oil distribution and found approximate expressions for PTO as a function of the light scattering coefficient in two opposite limits (see Eqs.(9) and (11)). In particular, in the most common case of near uniform oil distribution, the print through due to oil is inversely proportional to the power 3/2 of S_0. Based on the analysis of different theoretical and experimental results reported in the literature, we then proposed that S should be proportional to the paper pore volume V_p. That allowed us to derive the relationship between the Oil Gain Factor and V_p .

In the experimental part of our work, we studied print through in newsprints of different basis weights produced at four Canadian paper mills. Previously, we found that the component of print through due to oil increases linearly with the amount of ink on paper. The slope of that line representing the propensity of paper to lose opacity due to ink oil, is the Oil Gain Factor (OGF). As in the earlier work, we found that OGF can be highly two-sided for some papers. Using non-contact surface profilometry to measure the depth of surface pores and applying the theory of random fibre networks, we were able to show that the depth of surface pores can be well characterized by a new parameter that can be extracted from surface profilometry data. We demonstrated that two-sidedness in OGF can be related to the differences in the characteristic depth of surface pores on opposite sides of the paper.

In order to mitigate the two-sidedness in OGF, we proposed to take an average over both sides of the paper. We demonstrated that the averaged OGF is inversely proportional to the pore volume of paper and the exponent is close to -3/2 as predicted theoretically.

6 ACKNOWLEDGEMENTS

The author would like to thank Tony Manfred and Jöelle Grenon of FPInnovations for performing the tests used in this work. The author would also like to thank François Drolet, Pierre Lepoutre, Xuejun Zou, and Joe Aspler also from FPInnovations for fruitful discussions, improving many aspects of the paper and reviewing its final version.

REFERENCES

1 Bristow, J.A., Print through and ink penetration – a mathematical treatment, Adv. Printing Sci. and Technol. Edited by W.H. Banks, Pentech Press, London, 19:137 (1987).

2 De Grâce J. H., The print-through propensity of newsprint. *J. Pulp Paper Sci.* **19**:J208 (1993).

3 Erkisen O. and Gregersen, O., The influence of ink oil on print-through, *Nordic Pulp and Paper Res. J.* **22**:364 (2007).

4 S.R. Corson, A.G. Flowers, D.G. Morgan, and J.D. Richardson, Paper structure and printability as controlled by the fibrous elements, *Tappi J.* **3**(6): 14 (2004).

5 A.R. Dickson, N.J. Doodley, and C.M. Sloane, The Print-Through of Newsprint with Different Sheet Structures, Proc. 59th Appita Ann. Conf. Exhibition **1**: 275 (2005).

6 O. Eriksen and O. Gregersen, The Influence of Ink Pigment Penetration and Paper Structure on Print Through, *Nordic Pulp Paper Res. J.* **20**(2): 242 (2005).

7 G. Chinga-Carrasco, M. Axelsson, O. Eriksen and S. Svensson, Structural Characteristics of Pore Networks Affecting Print-Through, *J. Pulp Paper Sci.* **34**(1): 13 (2008).

8 I. Vadeiko and T. Manfred, Predicting Sheet Structure Effect on Ink Oil Contribution to Print Through of Newsprint, TAGA 63nd Annual Technical Conference, March 6 - 9, 2011, Pittsburgh, PA, TAGA Proceedings (2011); (in press)

9 L.O. Larsson and P.O. Trollsås, Print-through as an ink/paper interaction effect in newsprint, in The Fundamental Properties of Paper Related to Its Uses: 600 (1973).

10 R. Marton and R. Koeppicus, Printing Ink Penetration Into the Structure of Paper, in The Fundamental Properties of Paper Related to Its Uses: 613 (1973).

11 P. Varjos, K. Kataja, M. Lipponen, P. Qvintus-Leino, Absorption studies of coldset ink components into paper, 11th International Printing and Graphics Arts Conference, Vol.1, Bordeaux Lax, France, Association Technique de l'Industrie Papetiere, Paris (2002).

12 U. Mattila, K. Tahkola, S. Nieminen and M. Kleen, Penetration and Separation of Ink Resin and Oils in Uncoated Paper Studied by Chromatographic Methods, International Printing and Graphic Arts Conference (2002), Bordeaux du Lac, v.1, Session III.

13 L.K. Lehtonen, T.J. Dyer, Light-scattering coefficient as a measure of specific surface area in mechanical pulp laboratory sheets, *Paperi ja Puu (Paper and Timber)* **87**(8): 517 (2005).

14 A.M. Scallan and J. Borch, In "The Fundamental Properties of Paper Related to its Use," (F. Bolam, Ed.), Tech. Section Brit. Paper and Board Makers' Assoc., London **1**: 164 (1973).

15 A.M. Scallan and J. Borch, An Interpretation of Paper Reflectance Based Upon Morphology I. Initial Considerations, *TAPPI J.* **55**(4): 583 (1972).

16 B. Alince and P. Lepoutre, Porosity and Optical Properties of Clay Coatings, *J. Colloid Interface Sci.* **76**(2): 439-444 (1980).
17 B. Alince, J. Porubska and T.G.M. Van De Ven, Light Scattering and Microporosity in Paper, *J. Pulp Paper Sci.* **28**(3): 93 (2002).
18 W. W. Sampson, Modelling Stochastics Fibrous Materials with Mathematica, Springer-Verlag, London (2009).
19 R.E. Miles, Random Polygons Determined by Random Lines in a Plane, Proc. Nat. Acad. Sci. USA **52**: 901-907, 1157-1160, (1964).
20 E.W. Arnold, Light Scattering in Fibrous Sheets, *TAPPI J.* **46**(4): 250 (1963).
21 L.M. Lyne and V. Madsen, An Apparatus for the Measurement of Liquid Penetration into Porous Webs at a Press Nip, Pulp and Paper Magazine of Canada, T-523 (1964).

Session 4

Paper and Web Mechanics

Explicit Analysis of the Lateral Mechanics of Web Spans

B. FU, R. MARKUM, A. REDDY,
S. VAIJAPURKAR, and J. K. GOOD

Oklahoma State University
Mechanical and Aerospace Engineering
218 Engineering North
Stillwater, Oklahoma 74078-5016
james.k.good@okstate.edu

Keywords: Webs, Lateral Mechanics, Slippage.

ABSTRACT

All previous analyses of webs being steered through process equipment have required enforcement of assumed boundary conditions. An example is the normal entry boundary condition which has been employed in many web/roller analyses.

Explicit finite element analyses show much promise for studying all types of web handling problems. The primary benefit of this type of analysis is that only very basic assumptions are required, average web velocity and tension for example.

The use of Laser Doppler Velocimetry to infer the internal moment in a web in a noncontact measurement will be demonstrated. This and lateral deformation data will be used to validate models.

1 INTRODUCTION

The assumptions made for the analysis of single span web systems may not be valid when multiple span web systems are taken into account. For example, the cantilever support assumed by Shelton [1] at the upstream roller in a single span would require infinite friction between the web and the upstream roller as the web exits the roller. Since infinite friction cannot exist, some slippage will result. This condition is shown in Figure 1(a) for a two span web system. Three rollers are shown in a single plane but in reality the web wraps around each roller 90°. Whenever Roller 3 (R3) is misaligned, a bending moment is developed in the entering Span B. The bending moment is maximum as the web exits Roller 2 (R2) and decreases linearly to zero as the web approaches R3 [1]. The value of the bending moment in the web at the exit of R2 increases with the increased misalignment of R3. This moment must be reacted by frictional forces associated with slippage of the web on R2. When the moment is small this slippage will occur near the exit of the web from R2 and the lateral deformations will be confined to Span B as shown in Figure 1(a). As the moment becomes larger the slippage will occur over a larger portion of the total contact area between the web and R2. There is a limit to the moment that can be reacted by friction which is called the critical moment, M_r. Closed form solutions to calculate the critical moment have been developed and reported by Dobbs and Kedl [2], Good [3] and Shelton [4] using different assumptions and models. In these references whenever the misalignment of R3 produces a moment in the web at the exit of R2 that surpassed M_r, the condition of moment transfer from Span B into Span A begins. Once this occurs there are bending moments and lateral deformations introduced into web Span A. This behavior is shown in Figure 1(b). The machine direction (MD) tension distribution at each roller associated with the misalignment and hence the induced bending moments is also shown.

The focus of this research is to study the transfer of moment from one span (entering span) to an upstream span (pre-entering span). The moment transfer is induced by a misaligned downstream roller in the entering span. In the laboratory Laser Doppler Velocimeters (LDV) were used to measure a change in MD strain across the web width due to the misalignment. In-situ moment values in the moving web spans could be inferred from these strain differences. To study the moment transfer, moment values were inferred using this method in several MD locations in two web spans for varied levels of misalignment at the downstream roller. Lateral displacements of the web were also measured using Keyence edge sensors. The roller misalignment was increased in steps until moment started transferring into the pre-entering span. The experiments were designed and the measurements were conducted by Reddy [5].

Unlike the previous finite element (FE) simulations on misalignment [6], commercial FE software Abaqus/Explicit[1] was employed in this work. Explicit FE analysis involves the solution of the equations of motion through time:

$$[M]\{\ddot{u}\} + [C]\{\dot{u}\} + [K]\{u\} = \{F(t)\} \qquad \{1\}$$

where [M], [C], and [K] are the mass, damping, and stiffness matrices formed using the finite element method. The response of the web to the applied loads ($F(t)$) and constraints comes in the form of accelerations $\{\ddot{u}\}$, velocities $\{\dot{u}\}$, and deformation $\{u\}$ which are all time variant. In the simulations of this study, the web and rollers were modeled. The simulation was started by bringing the web tension, velocity, and the roller misalignment from zero to their final values. This occurred in the first 5 seconds of the simulation. During this period, contact pressures are developing between the web and the 4 rollers and Poisson contraction is

[1] Dassault Systems, Simulia, Rising Suns Mills, 166 Valley St., Providence, RI, 02909-2499, USA

attempting to occur due to the rising web tension. The web is now traveling in the MD and is attempting to achieve normal entry at each of the rollers, including the misaligned Roller 3. During the remainder of the simulation, steady state lateral deformation of the web will be achieved. The web attempts to steer into the misaligned roller so that the directions of velocity of the web surface and the misaligned roller can match, due to assumed Coulomb friction. If the velocities can match in direction and magnitude, normal entry of the web to the downstream roller may result. In the remainder of the simulation the web achieves a steady state lateral deformation. When this occurs the output can be compared to available test data. In this study the test data used for comparison will include lateral deformations at discrete MD locations and measured internal moments at several locations.

No lateral deformation or slope of the web was enforced as a constraint at any roller in these simulations. The lateral tracking of the web over the rollers is dictated only by the friction forces that develop between the web and rollers.

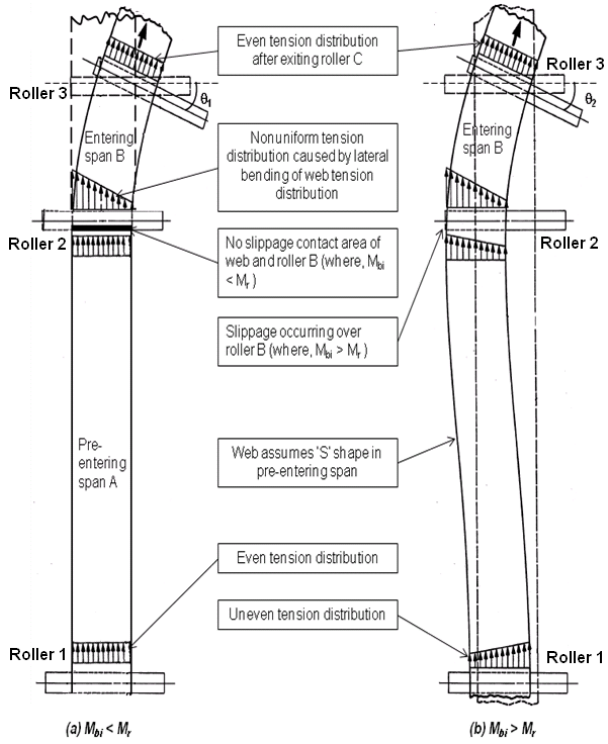

Figure 1. Schematics of lateral deformation and tension distribution before and after slippage at R2 due to misalignment at R3.

2 EXPERIMENTAL PROCEDURE

Good *et al.* [8] demonstrated how the LDV can be used to measure a strain change between in two points in a web. In that publication the change in strain was measured down the length of the web such that a change in web tension could be inferred. In this study a change in strain across a web width will be measured from which the internal moment in the web can be inferred. The LDV is a device that is capable of measuring velocity directly. Most of these devices output a TTL (Transistor Transistor Logic) pulse train from which the length of a moving strained or unstrained surface can be inferred, similar to the output of an encoder which might touch a web via a contact wheel. The method requires that the moving surface be opaque and have some surface roughness. The LDVs (Model LS200) used herein were produced by BETA LaserMike[2].

A set-up of two LDVs was used to acquire the data induced in web spans due to a misaligned downstream roller. The LDVs were mounted above the web span side by side in the cross machine direction (CMD) to measure the length of the web moving beneath them as shown in Figure 2. The length of deformed web measured by the LDVs was used to calculate a relative strain across the web width. When the downstream roller is aligned, the difference of pulses from the LDVs (LDV_a - LDV_b) must be zero because of zero bending moment in the web. Whenever there is some misalignment in a span, one edge of the web becomes longer when compared to other edge due to the bending moments and strains that result. The difference in the counts output by LDVs is directly proportional to the bending strain in the web at an MD location.

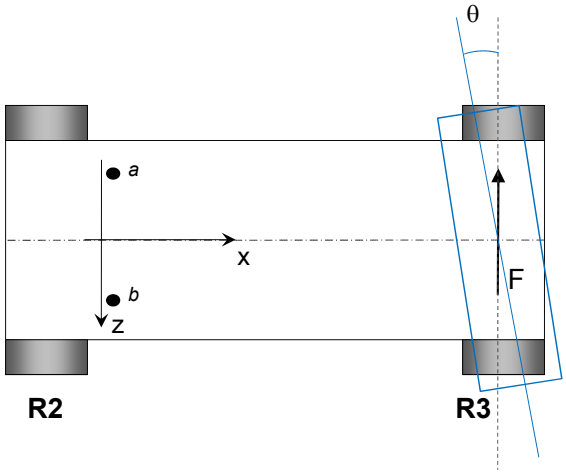

Figure 2. Schematic plot of LDVs install positions

The LDVs were set at various 'x' positions in the spans where moments were intended to be measured, see Figure 2. Each LDV was targeted at a distance of 63.5 mm above and below the central axis of the web, thus the distance between the two LDV measurements is 127 mm. The strains at locations *a* and *b* and their difference will be:

$$\varepsilon_a = \frac{Mz_a}{EI} + \frac{T}{AE},\ \varepsilon_b = \frac{Mz_b}{EI} + \frac{T}{AE},\quad \varepsilon_a - \varepsilon_b = \frac{M(z_a - z_b)}{EI} \qquad \{2\}$$

[2] Beta LaserMike Americas, 8001 Technology Blvd., Dayton, OH, 45424 USA

where M is the moment, T is the web tension, E is Young's modulus, I is the area moment of inertia, A is the cross sectional area and z_a and z_b are the distances to a and b shown in Figure 2. Thus the moment can be inferred experimentally using:

$$M = EI\frac{\varepsilon_a - \varepsilon_b}{z_a - z_b} \quad \{3\}$$

where,

$$\varepsilon_a - \varepsilon_b = \frac{LDV_a - LDV_b}{LDV_a} \quad \{4\}$$

and LDV_a and LDV_b were the TTL pulses counted at locations a and b.

The LDVs yield an output of 1000 TTL pulses per 0.3048 m (1 ft) of passing web or 100,000 pulses for 30.48 m (100 ft) of web. At each 'x' position in the span, ten measurements were made as 30.48 m of web were allowed to pass the LDVs. This length of web was chosen to increase the precision of the strain difference measurement as determined by expression {4}. This will produce an accuracy of approximately 1/100,000 or 10 μS which was found to be satisfactory in this study. Greater accuracy could have been obtained by making measurements over yet longer lengths of web but to achieve that accuracy would require the web and the operating parameters to remain constant while the length of web selected passed the measurement site.

To study the moment transfer in a multi-span web system, a machine (test rig) was needed which would allow the misaligning of a downstream roller and to allow the moment to transfer upstream into the pre-entering span from the entering span. To investigate the moment distribution in web spans, the LDVs needed to move to multiple test locations in the entering span, around the upstream roller (R2) and in the pre-entering span while maintaining the required standoff distance (304.8 mm). A schematic showing dimensions and locations of edge sensors and LDVs is shown in Figure 3. The finished assembly of the new test rig and the winder setup is shown in Figure 4.

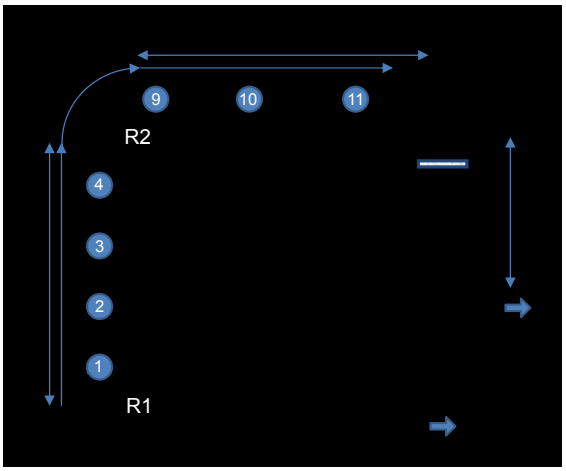

Figure 3. Schematic plot of test rig design

In this design, the web passes from the pre-entering Span A around R2 into entering Span B. The LDVs were positioned on a rotating arm as shown in Figure 4 which slides on a set of rails traversing Span A, R2 and Span B. The misalignment of R3 is precisely set with the help of a micrometer and was measured using a linear variable differential transformer (LVDT). R3 sits on a carriage that slides on the horizontal rails to adjust the desired length of Span B. A web guide was installed just before the web enters the pre-entering Span A. The web guide ensured that the lateral web position was maintained at the entry of the test section (Spans A and B). At the right in Figure 4 an unwind/rewind system is shown that was responsible for maintaining the web tension and velocity at a constant level during a test. Note the two Keyence edge sensors (LS-3100) which were used to measure the lateral deformation of the web near the exit of Span A and after the web exits Span B. A National Instruments 6602 counter/timer was used to simultaneously acquire the TTL pulses from the LDVs. A LabVIEW™[3] VI triggered two counters that began counting pulses from LDV_a and LDV_b. Whenever one of the two counters reached 100,000 pulses the counters were triggered off. The count values and the count difference were stored, the counters were cleared, and the counters were triggered on again in a repeating cycle. The count difference could then be used in expressions {3} and {4} to establish the moment.

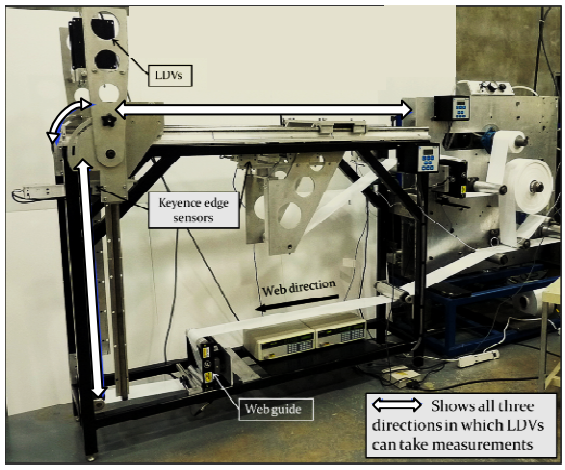

Figure 4. Finished assembly of the test rig and the winder setup

Using this apparatus, LDV measurements were recorded at a total of eleven locations in the pre-entering Span A, on the roller R2, and entering in the Span B as shown in Figure 3. Table 1 provides all of the positions at which LDV data was recorded. As shown in Figures 3 and 4, the two Keyence edge sensors were installed to measure the lateral displacements at 165.1 mm before the web enters R2 and 101.6 mm after the web exits from

[3] LabVIEW is a trademark of National Instruments Corporation, Austin, TX, USA.

R3, respectively. Three different misaligned angles of R3 were used in the tests: 0.223°, 0.446°, and 0.502. Based on Good [3], the moment transfer should begin when R3 is misaligned 0.446°.

LDVs locations	Distance from exit of R1 (mm)	LDVs locations	Distance from exit of R1 (mm)
1	50.8	7	1148.59
2	279.4	8	1171.09
3	558.8	9	1221.89
4	838.2	10	1552.09
5	1111.25	11	1933.09
6	1126.21		

Table 1. Locations in pre-entering and entering spans and on R2 where LDV data was acquired.

3 FINITE ELEMENT SIMULATION MODEL

A four-roller FE model was setup to model Spans A and B in the test setup using Abaqus/Explicit as shown in Figure 5. The modeled web has the same dimensions as the web that Reddy used in the measurements, which are 152.4 mm (6 in) in width and 0.0508 mm (0.002 in) in thickness. An oriented polyester film was employed. Reddy measured Young's modulus (E) for this web at 3.93 GPa and Poisson's ratio (v) was set to 0.3, not unlike the properties of paper. The free web span length modeled starting from Roller 1 (R1) and moving to the upstream end of the web is more than three times the entering span length (850.9 mm) between R2 and R3. It will be shown later that allowing this length of web to pass the four rollers was sufficient to achieve steady state lateral behavior.

During the simulations, R3 was misaligned at a specified angle as shown in Figure 5 which induced lateral motion in the web. In these simulations, the web was given a velocity of 31.75 mm/s at the downstream end. A tension load of 57.83 N, the same as that used in the experiments, was applied on the upstream end of the web. Both this velocity and load were brought from zero to their final values linearly with time at the beginning of the simulation and then kept constant through the remainder of the simulation. In the experiments, R1 and R3 had high coefficient of friction coatings (Dow 236). Although lab tests have shown that these coatings can produce friction coefficients in excess of 4, the friction coefficients at R1 and R3 was set to 0.9 in the simulations. This was done because Coulomb friction coefficients in excess of unity can produce odd model behaviors. As long as the friction coefficients are set high enough to confine the transient behavior to Spans A and B between R1, R2, and R3 the simulation and test behaviors should be similar. Reddy measured a friction coefficient of 0.33 between the aluminum roller surfaces and the polyester web and this friction coefficient was assigned to the contact properties for R2 and Roller 4 (R4).

The aluminum rollers were modeled as analytical rigid parts. In Abaqus, analytical rigid parts do not require meshing and are continuously defined geometric shapes. Membrane elements (M3D4R) [7] were used to generate the web model in these simulations.

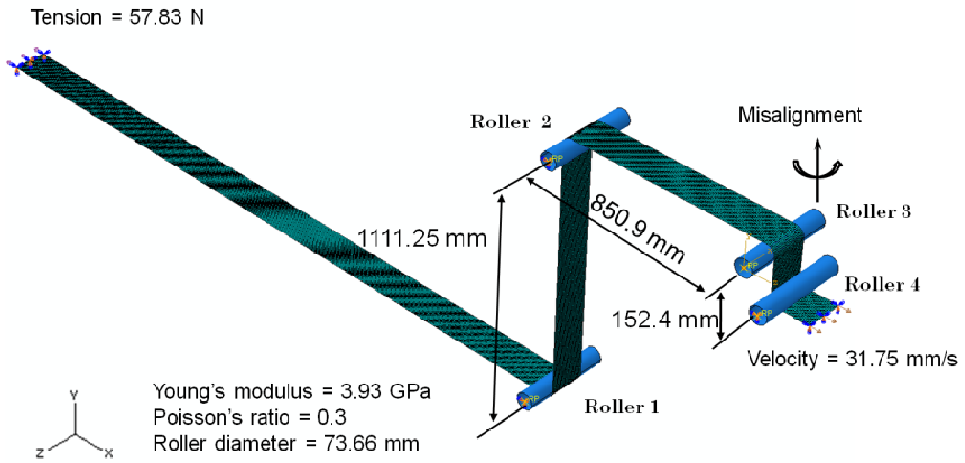

Figure 5. Four-roller FE model set up

4 SIMULATION AND EXPERIMENTAL RESULTS

Simulations were done using the model created with consideration of dynamic equilibrium. To explore the behavior of moment transfer, several direct output variables from simulations have been studied, the lateral displacements and MD stresses are examples. The slope of the lateral deformation, velocity and moment distribution can be calculated using the lateral displacements and MD stresses. To demonstrate that steady state conditions have been reached, the lateral displacements of the web acquired at the entry points of the four rollers and the corresponding calculated velocities are shown in Figure 6. This data was collected on the web centerline (the elastic axis). At the start of the simulation the lateral deformations of the web are

all zero entering each of the four rollers. As the simulation progresses note that the lateral deformation remains zero as the web enters R1. This is an indication that the moment interaction has been confined to Spans A and B. As the simulation progresses note the positive lateral deformation of the web at R2 followed by negative deformations at R3 and R4. The signs of these deformations are with respect to the coordinate axes shown in Figure 6 where a positive misalignment angle is shown. The shape of the deformed web is consistent with the illustration of lateral deformation under moment transfer conditions shown in Figure 1(b). The web displacements achieve steady state at 120 sec which is confirmed by the lateral velocities which are approaching zero as shown in Figure 6. The results presented hereafter were harvested from the last step of the simulations.

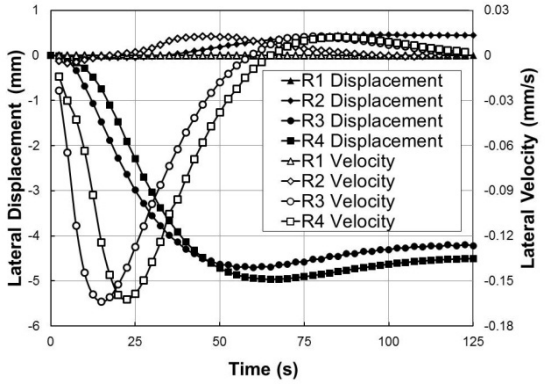

Figure 6. Web lateral displacements and velocities at the entry of each roller for a misalignment of 0.446°

The lateral displacements from the simulation output were compared directly with the lateral displacements measured during tests. Reddy measured these lateral displacements [5] and the data is shown in Tables 2 & 3 for three misalignment angles of R3. The lateral displacements from the three simulations along the centerline of the web are shown in Figure 7. The web coordinate referred to on the abscissa axis has an origin at the upstream end of the web model. This is a curvilinear coordinate that follows the web path. The experimental results agree with the simulation results very well. These deformations were measured several times (N>100) while the LDV data was being acquired. The standard deviation of this data was typically 0.06 mm. The accuracy of the Keyence LS 3100 sensor is specified as 3 μm. The standard deviation of the edge deformation data is high compared to the accuracy of the instrument and thus it must be concluded that the standard deviation of the data is a measure of the slit edge quality. Also shown are the lateral deformations that were calculated using the closed form expressions developed by Good [3] which also agree well with the results from the Abaqus simulations and the experimental data. To determine whether normal entry was achieved the slopes were calculated using the lateral displacements shown in Figure 7 and overlaid in the charts of Figure 7. The slopes were calculated using a finite difference method to estimate the first order differentiation of lateral displacements with respect to the MD coordinate. The slope is not a direct output for the membrane element because an out-of-plane rotation (in fact any rotation) is not a defined degree of freedom. Vertical lines have been added in Figure 7 to help interpret the locations of where the web enters and exits R2 and R3 and to aid in determining the lateral displacements and slopes of web at these locations.

Lateral deflection (Sensor 1)	Misalignment angle (°)		
	0.223	0.446	0.502
Experimental (mm)	0	0.483	0.719
Abaqus (mm)	6.045e-3	0.416	0.714
Good [3] (mm)	0	0	0.460

Table 2. Lateral deflections: upstream edge sensor

Lateral deflection (Sensor 2)	Misalignment angle (°)		
	0.223	0.446	0.502
Experimental (mm)	-2.294	-4.270	-4.735
Abaqus (mm)	-2.441	-4.503	-4.780
Good [3] (mm)	-2.377	-4.755	-4.862

Table 3. Lateral deflections: downstream edge sensor

From Figure 7, it is apparent that the web exits R2 with zero lateral displacement and small negative slope for the 0.223° case. This slope becomes negative before the web exits R2 and is an indication of local web slippage at the exit of R2. The negative slopes increase at the exit of R2 as the misalignment at R3 increases as shown in Figure 7 (b) and (c). Moment transfer was predicted to begin when R3 was misaligned 0.446° using closed form expressions from Good [3]. It is obvious that moment transfer has already begun at this misalignment as shown in Figure 7 (b). The lateral displacement of the web entering R2 is no longer zero for this or the larger misalignment angle shown in Figure 7 (c). The web achieved normal entry to R3 in all three cases, note the web slope matches the misalignment of R3 in each case in Figure 7. As the web transits R3 the slope remains nearly constant until the exit zone is reached where a transition to web twist occurs.

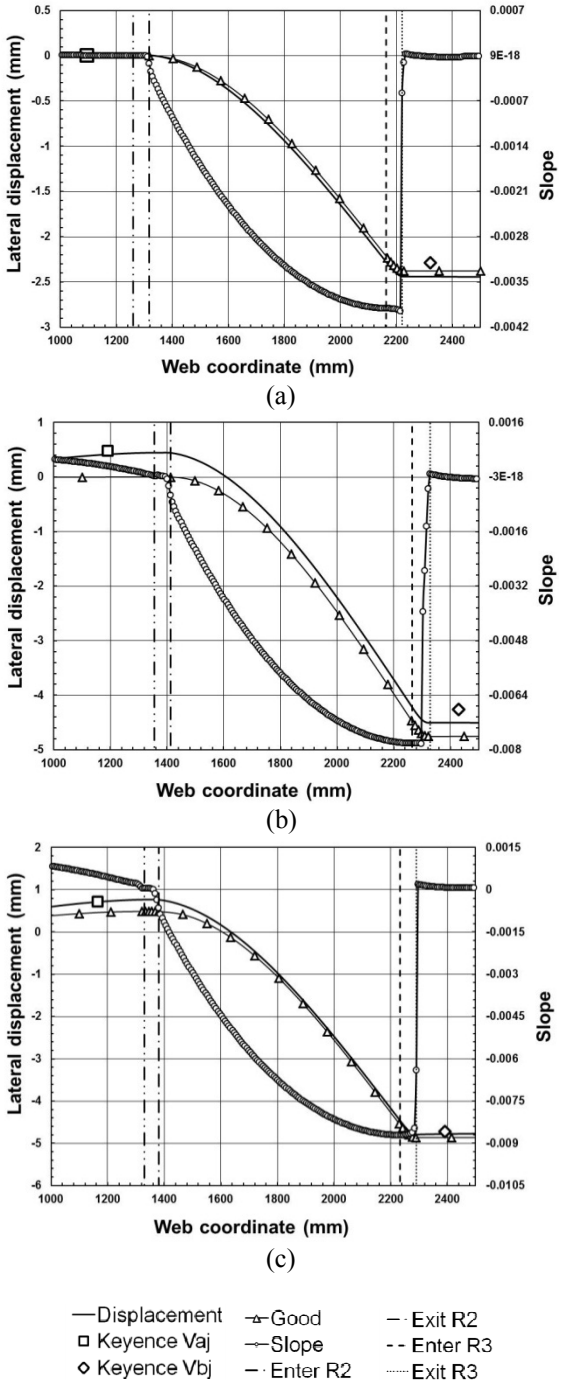

Figure 7. Lateral displacement comparison between simulations and experiments, and the calculated slope curve for each misaligned angle: (a) 0.223° (0.00389 radians) (b) 0.446° (0.00778 radians), and (c) 0.502° (0.00876 radians).

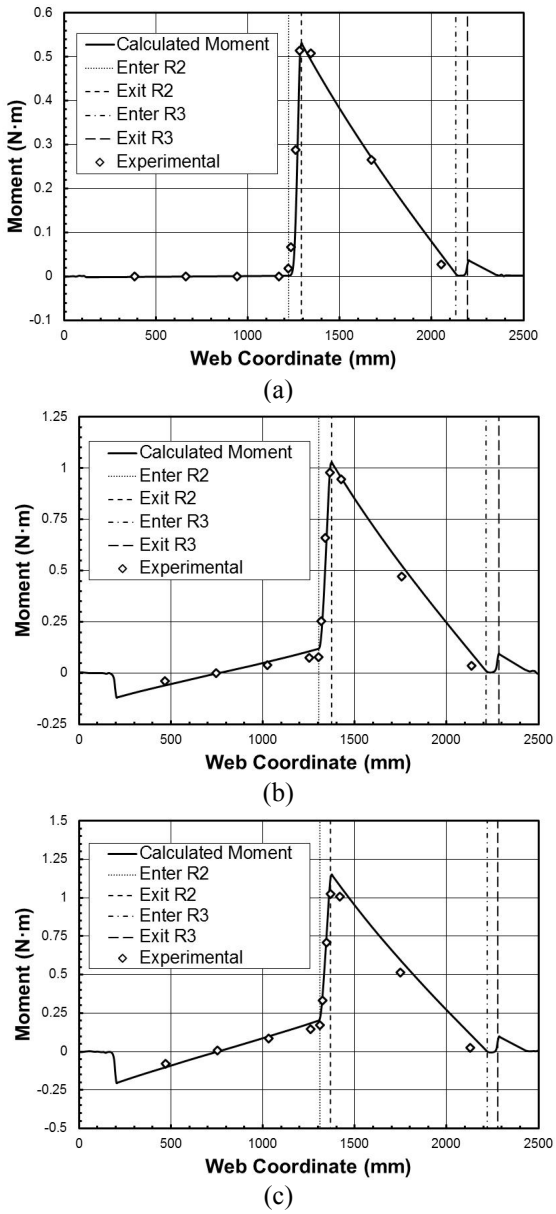

Figure 8. Moment comparison between simulations and experiments: (a) 0.223°, (b) 0.446°, and (c) 0.502°.

Next, the calculated moments using simulation outputs and experimental results from the LDVs in the web spans for each case were compared in Figure 8. In the simulations, MD stress values were harvested for each integration point in each element in the CMD at a particular MD location. These stresses were then used to estimate the internal moment in the web at that MD location using the expression:

$$M = \int \sigma_{MD} z dA = \sum_{i=1}^{n} \sigma_{MDi} z_i A_i \qquad \{6\}$$

where σ_{MDi}, z_i, and A_i are the MD stress levels at the integration points, the distances between the integration points and the elastic axis, and the cross-section areas, respectively.

As mentioned previously, the LDV measurements used to infer the internal moment were taken at

different locations in the pre-entering Span A, the web on R2 and the entering Span B. The inferred moments are shown as discrete data points at the MD locations where the LDV data was collected (refer to Figure 3 and Table 1). Each inferred moment shown as a data point was the mean of 10 sets of LDV measurements. The standard error of this data in units of the inferred moment was 0.01 N-m or less. The simulation results agree with experimental results very well at each point. The moment reaches its peak value at the exit of R2 and then decreases almost linearly as the web approaches R3 in the entering Span B. Finally, the moment decreases to zero when the web arrives at the misaligned R3 and is consistently zero on the roller until the web exits from it. It is worthy to note that the moment at the entry point of the web to R3 is not exactly zero, but it is a very small value. This provides additional evidence to support Shelton's assumption [1] of zero moment at the entry of the misaligned downstream roller.

To further explore the boundary conditions, the curvatures in Spans A and B were studied. The curvature was determined using a finite difference estimate of the second derivative of the lateral displacements of the elastic axis from the simulations with respect to the MD coordinate. The curvature and the moment are related by the well-known Bernoulli-Euler relationship for small deformations:

$$\frac{1}{R} = \frac{d^2 w}{dx^2} = \frac{M}{EI} \qquad \{7\}$$

where *1/R* is the web curvature, *R* is the radius of curvature, and *w* is the lateral deformation of the web. The curvature could also be inferred by using expression {7} in conjunction with the moments that were shown in Figure 8. The curvatures derived by the two different means are shown in Figure 9. The Bernoulli-Euler expression is considered valid for cases where the shear deformations are small and where the beam deformations are small. For the span length to width ratio of Span B (850.9/152.4=5.6) the shearing deformation accounts for less than 5% of the total lateral deformation. The maximum lateral deformations in this study are two orders of magnitude smaller than the span length of Span B (5.0/850.9=0.006). Thus the Bernoulli-Euler expression should be valid. As shown in Figure 9 (a), the web enters roller R2 with zero curvature for the 0.223° case with no moment transfer. These curvatures were not equal to zero as shown in Figures 9 (b) and 9 (c). In the free spans, the curvatures derived from the two methods agree. Several sharp disparities in the curvature derived from the second derivative of the lateral deformation are noted at the exits of R2 and R3 in Figure 9 (a) and at the entry of R2 in Figures 9 (b) and 9 (c).

The deviation of the curvature inferred from slope and from bending moment was studied further. The Euler-Bernoulli expression {7} requires plane sections to remain plane after deformation. If the deformations were large expression {7} should be expanded to:

$$\frac{1}{R} = \frac{d^2 w/dx^2}{[1+(dw/dx)^2]^{3/2}} \qquad \{8\}$$

Expression {8} was used to develop the curvature for the 0.446° case using the lateral deformations produced by the simulation. That curvature and the curvature calculated using moments inferred from MD stresses {6} are shown in Figure 10. If the curvature calculated using expression {7} from Figure 9 (b) is compared with the curvature in Figure 10 from expression {8} there is no distinguishable difference and provides validation of the small deformation assumption. In the pre-entering and entering spans, both methods shown in Figure 10 show a linear characteristic and agree with each other very well. The two methods yield nearly zero curvature as the web enters R3, which is consistent with the previous conclusion. The only significant differences occurs when the web exits rollers R2 and R3. To investigate the planarity of the web after deformation, the MD displacements across the web width are shown at three different selected locations in Figure 10. The MD displacements indicate a planar deformation midway in the entering span. When the web exits from R2 and R3, the MD displacements along CMD are shown to be non-planar in Figure 10. The Bernoulli-Euler expression {7} is known to error in beams when shear stresses are sufficient to cause non-planarity called warpage in deformed sections. It was argued earlier that shear stresses in the entering span should be small because of the aspect ratio chosen. Since the MD deformations across the web width are planar in the free span in Figure 10 this argument is validated. However the distribution of the friction forces between the web and roller which react the moment are not necessarily linear and will be examined next.

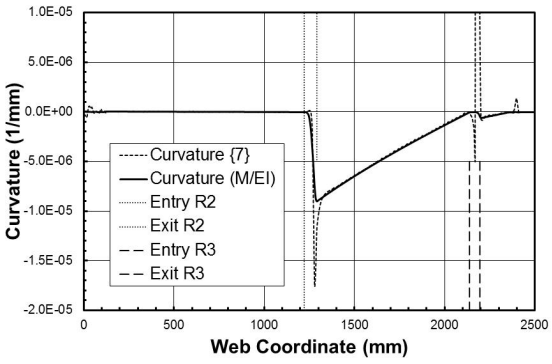

(a)

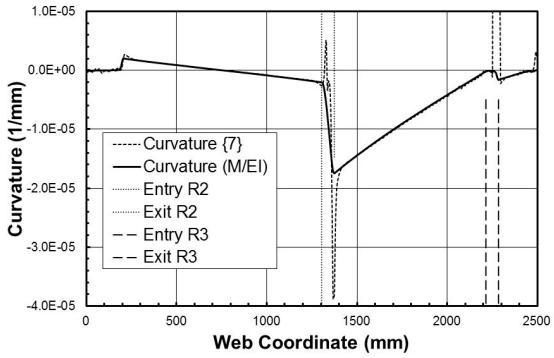

(b)

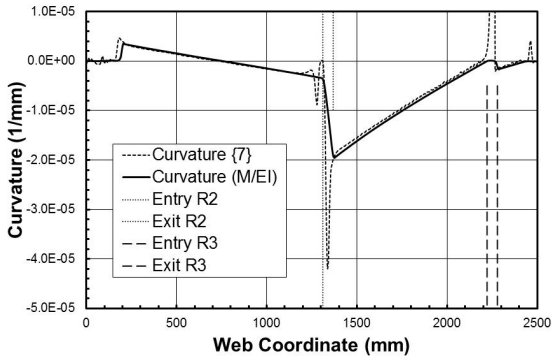

(c)

Figure 9. Curvature curves for each misaligned angle: (a) 0.223°, (b) 0.446°, and (c) 0.502°.

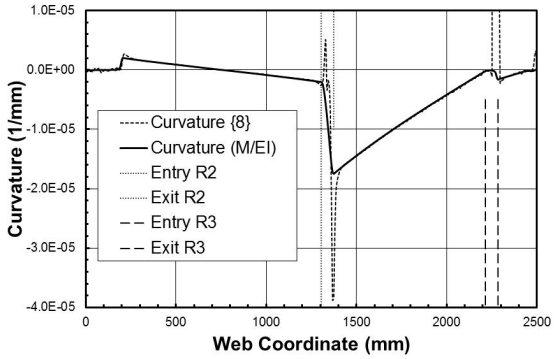

(a)

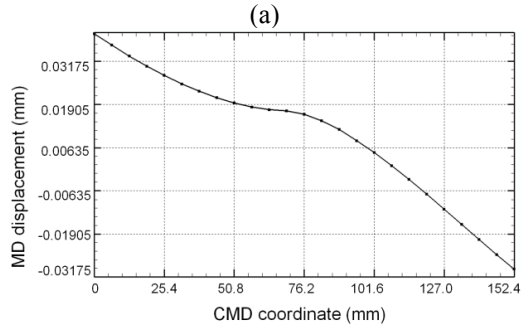

(b) Exit R2

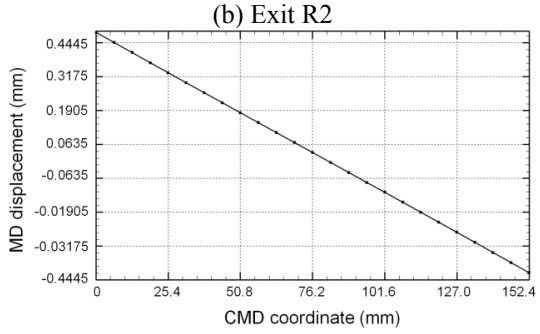

(c) Midspan Entry to Span B

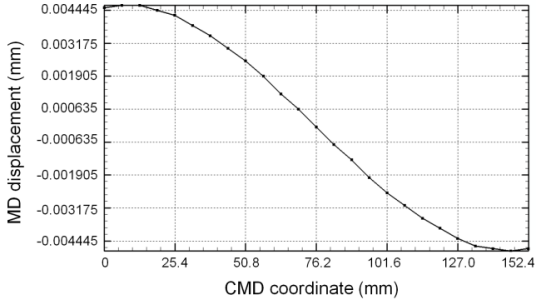

(d) Exit R3

Figure 10. Curvatures comparison and section shapes at different locations for a 0.446° misalignment.

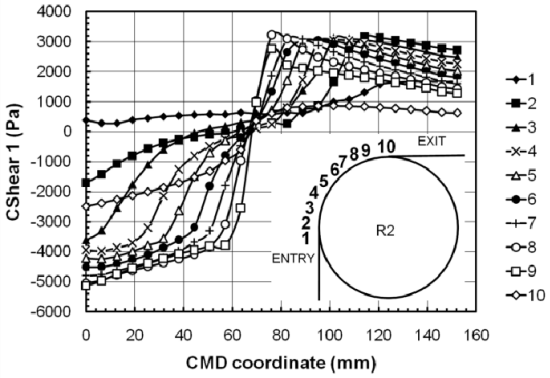

Figure 11. CShear1 stress distribution on R2 from 0.446° misalignment case.

As shown in Figure 8, the misalignment of R3 leads to the upstream moment, which causes web slippage on R2. Due to the frictional contact, MD frictional shear contact stresses are generated which resist slippage of the web on R2. In Abaqus, the output CShear1 is the contact shear stress between the roller and web in the MD. Figure 11 shows the CShear1 stress distribution on R2 for the 0.446° case. CShear1 stresses were harvested from each node of the web contacting roller R2. Figure 11 displays the Cshear1 stresses along CMD at different MD locations. These distributions of contact shear stress are obviously nonlinear across the web width and are responsible for the non-planar MD deformations that were shown in Figure 10. These contact shear stresses can be integrated to produce the moment (M_{rl}) that is applied to the web by the friction forces in the MD:

$$M_{r1} = \sum_{i=1}^{n} CShear1_i \, z_i \, A_{si} \qquad \{9\}$$

where A_{si} is the elemental contact area between the web and roller. Using this expression the moment caused by the web slippage in the MD is calculated to be 0.86 N-m. Since the web slips and rotates on R2, the CMD contact shear stresses also contribute to the reaction moment. In Abaqus, this contact shear stress is defined as CShear2. The moment calculated using CShear2 is about 0.045 N-m. The combined reaction moment due to friction on R2 is 0.905 N-m. Figure 8 (b) shows the calculated moments at the entry and exit point of R2 are about

0.12 N-m and 1.03 N-m, respectively, and the difference of these two is 0.91 N-m which agrees with the calculation using CShear stresses. From Good's closed form solution [3] the moment reacted by friction is:

$$M_r = \frac{\mu TW}{4}\theta = \frac{\mu TW\pi}{8} \qquad \{10\}$$

where θ is the angle of wrap of the web about R2 which is $\pi/2$ in this case, W is the web width and μ is the coefficient of friction (0.33). Using expression {10} produces an M_r of 1.14 N-m which is the same moment that Good would have predicted at the exit of R2 when the misalignment of R3 was 0.446°, thus moment transfer into the upstream span should have just begun. Expression {10} produces a moment that can be reacted by friction that is 26% higher than that calculated from Abaqus. This error is offset somewhat in that, by allowing no slippage at the exit of R2, Good predicts a moment at that location (1.14 N-m) which is 10.7% higher than predicts by Abaqus (1.03 N-m). It is due to this offset of error that the lateral deformations predicted by Good [3] compare so well with the Abaqus results and the test data in Figure 7.

5 CONCLUSIONS

Explicit finite element simulations have been conducted that prove the value of this method for addressing lateral mechanics problems in web handing. The simulations produced lateral deformations very similar to results produced by the closed form method developed by Good [3] and in lab measurements. The method developed by Good required assumptions of normal entry to rollers R2 and the misaligned roller R3. His method also enforced normal exit of the web from rollers R1 and R2. Good's method [3] also required the assumption that the moment in the web at the entry of R3 is zero per Shelton [1]. Good's method also relies on an expression {10} for the web moment that can be sustained by friction on roller R2. None of these assumptions were enforced in the Abaqus simulations. It could also be argued that the simulations have provided a method for substantiating the assumptions made in the previous analyses. Good's assumption of normal exit from roller R2 is obviously not exact as was shown in Figure 8 for all misalignments. The assumption of normal exit by Good's method did not produce lateral deformations with significant error for this study. The assumption of zero moment at the entry of the misaligned roller [1] is also not exact, but it is extremely close and still considered valid. The moments shown in Figure 7 indicate that zero moment occurs slightly after the web contacts the misaligned roller. Both Shelton [1] and Good [3] incorporate a basic assumption that a web can be modeled as a beam in which plane sections are assumed to remain plane before and after deformation. The curvatures inferred from moment and from second derivatives of lateral deformation shown in Figure 9 indicate that this assumption appears valid in broad areas of the free spans but as the web encounters rollers where slippage occurs these curvatures diverge. Again the lateral deformations predicted by closed form methods such as that of Good [3] agree with the Abaqus simulations. However assuming the web behaves as an Euler or Timoshenko beam may not produce acceptable results for all cases.

It has been shown that the Laser Doppler Velocimeters can be used to infer internal moments in the web that match nicely with moments from the simulations. This is the first non-contact measurement of internal moments for webs in free spans and on rollers.

6 ACKNOWLEDGEMENTS

The authors thank the industrial sponsors of Web Handling Research Center at Oklahoma State University for providing the funding which made all the work possible.

REFERENCES

[1] J. J. Shelton. Lateral dynamics of a moving web. PhD thesis, Oklahoma State University (1968).

[2] J. N. Dobbs and D. M. Kedl, Wrinkle dependence on web roller slip. Proceedings of the Second International Conference on Web Handling, Oklahoma State University (June 1995).

[3] J. K. Good. Shear in multispan web systems. Proceedings of the Fourth International Conference on Web Handling, Oklahoma State University (June 1997).

[4] J. J. Shelton. Interaction between two web spans because of a misaligned downstream roller. Proceedings of the Eighth International Conference on Web Handling, Oklahoma State University (June 2005).

[5] A. Reddy. Analysis of moment transfer in multi-span web systems. M.S. thesis, Oklahoma State University (2010).

[6] J. A. Beisel and J. K. Good. The instability of webs in transport. *J. Appl. Mech*. **78**(1):011001-1–011001-7 (2011).

[7] Abaqus Analysis User's Manual, Section 25.1, (2010).

[8] J. K. Good, B. K. Kandadai, and R. Markum. A new method for measurement of wound-in-tension in webs wound into rolls. *J. Pulp Pap. Sci.* **35**(1):17–23 (2009).

Movement of Layers and Induced Tension in the Nip Area between Drum and Paper Layers

PETER HOFFMANN[1], SAMUEL SCHABEL[2]

[1] Stora Enso Research
Krefelder Straße 560
41066 Mönchengladbach
peter.hoffmann@storaenso.com

[2] Fachgebiet Papierfabrikation und Mechanische Verfahrenstechnik Technische Universität Darmstadt
Alexanderstraße 8
64283 Darmstadt
schabel@papier.tu-darmstadt.de

Keywords: layer movement, induced tension, winding

Abstract

During paper manufacture and processing production losses occur during winding of machine-wide paper rolls and finished rolls due to winding faults. During the winding process at least one drum (steel or rubber-covered) is in contact with the winding roll and creates a nip area where tension and shifting of layers are induced. This process in the nip area with several layers of paper is not known in detail but the knowledge would be helpful to improve winding processes.

1. INTRODUCTION

Nip induced tension at a stack of paper and at wound rolls began appearing in the literature a long time ago. Winding models were created and helpful to understand the nip effect [1-8], but a calculation of induced tension is possible only in a narrow area.

In this presentation basic models were established where the deformation process in the nip area, movement of layers as well as induced tension were theoretically and experimentally investigated on a stack of 500 layers of LWC rotogravure paper and then transferred to the winding process (surface winding). Tests were carried out with a steel drum and, partially, with a rubber-covered drum.

2. EXPERIMENTS AND RESULTS AT A PAPER STACK

Deformation at the paper stack and winding roll for determination of a modulus of elasticity theoretically resulted, as a contact problem, in a smaller modulus as compared to compressibility measurements. Measurement of pressure distribution in the nip zone resulted in a higher distribution than assumed according to *Hertz*.

When rolling a drum over the surface of a loose paper stack results in shifting of layers within the stack. The shifting was calculated from geometric dimensions of deformation in connection with a static friction zone. The deformation caused a change in length of the half nip width. The half from this change of length move in rolling direction and the other half is fastened in the center of the nip and released during the rolling motion. Movement of the first layer results from the sum of movements of individual layers (Figure 1).

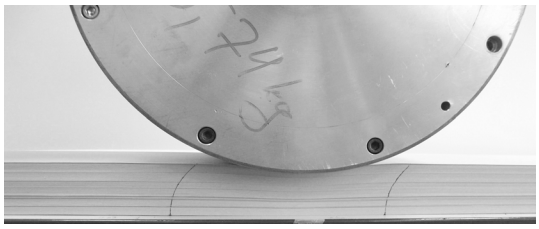

Figure 1: Layer movement at a loose paper stack

A measurement of induced tension on the first layer showed a difference between the loose stack and the situation when all layers are fixed (Figure 2). Change of length with reference to deformation in the nip area showed that only part of the deformation is transferred into tension. That means slippery effects are acting at the entrance of the nip area.

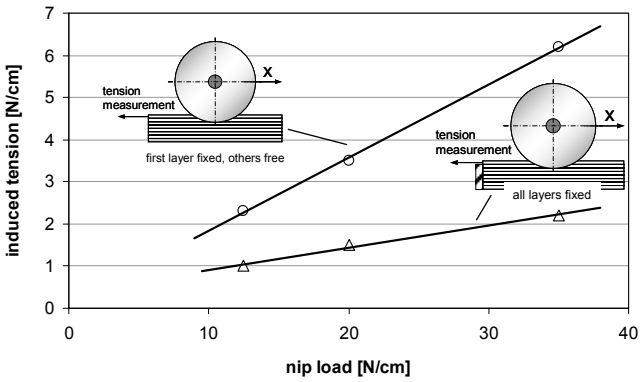

Figure 2: Tension measurement at the first layer

If more layers of the paper stack are fastened, rolling of the drum induces tension within the layers, and highest tension occurs in the first layer. Subsequent layers show a reduction of induced tension; no more forces are measurable after the 10th layer. If pretension was exerted on the layers this resulted in a different induced tension, depending on the start point of the drum.

Induced tension occurs after a longer drum travel distance when all layers are fastened. Change of length resulting from deformation was summed up in dependence of the drum travel distance. This showed a direct dependence on the start point of the drum. The transferable tangential force is distributed to the underneath layers and reversal of force direction was found after the 8th layer (Figure 3). The sum of induced tension at the first 8 layers was identical with the induced tension in the first layer at the loose stack.

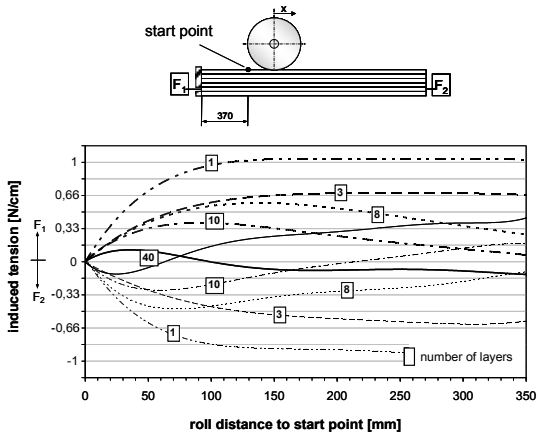

Figure 3: Measurement of tension in different layers with pretension 2,5 N/cm

The tension-free 8th layer was assumed to be the instantaneous centre level. Layers above this level are "pushed" towards machine direction, hence inducing a change in length which is fastened in the center of the nip and released during the rolling motion as tension.

Induced tension in the nip area at the paper stack was calculated by a differential equation for the case that one and more layers are fastened in steps. The process is according to the shaping process during „rolling of sheet metal"[9], taking into consideration shape alterations (Figure 4).

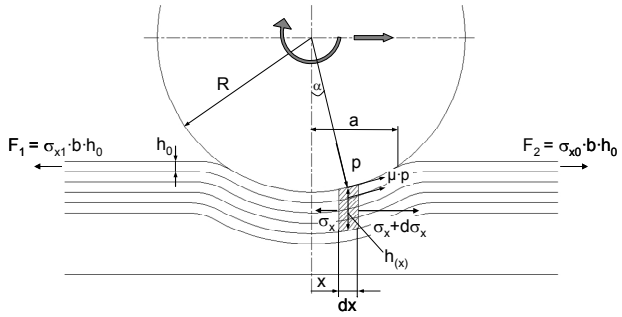

$$\frac{d}{dx}\left(\sigma_x \cdot h_{(x)}\right) + p \cdot \sin\alpha + 2 \cdot \mu \cdot p \cdot \cos\alpha = 0$$

Figure 4: Shaping process at a stack and differential equation

The equation shows the balance of force for the hachure volume element with the stress σ_x. The pressure distribution was statically measured with a foil sensor and showed a higher distribution according to *Hertz* (Figure 5).

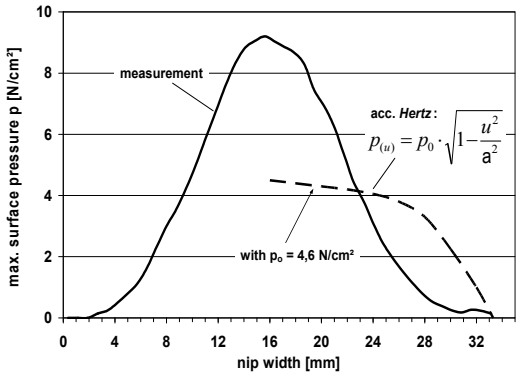

Figure 5: Pressure distribution in the nip

The solution of the equation has one constant only but two conditions are required i.e. for the nip entrance one condition and one for the middle of the nip.

The calculation with the data (Table 1) and the pressure distribution yields two solutions which show a place of relative calmness at their transition point. Friction shear force tensions change their algebraic sign in this location. Solutions were identical for a quantity of 8 – 10 layers of the penetration depth (Figure 6). The figure showed that the nip induced tension is complete in the middle of nip area.

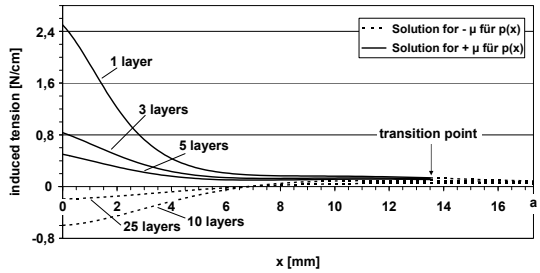

Figure 6: Solution for different layers

Drum radius	R = 150 mm
Drum weight	150 N
Half nip width	a = 17,4 mm
Paper thickness	h_0 = 40 µm
Paper width	b = 120 mm
Friction coefficient	µ = 0,26
Penetration depth	1 mm

Table 1: Test parameters

Progression of compressive load and shear force load during drum movement was recorded by two piezo-foil sensors on the drum surface. Dynamic measurements of a compressive load signal and a sum signal from compressive and shear force load were conducted where the shear force portion was measured for determination of difference (Figure 7).

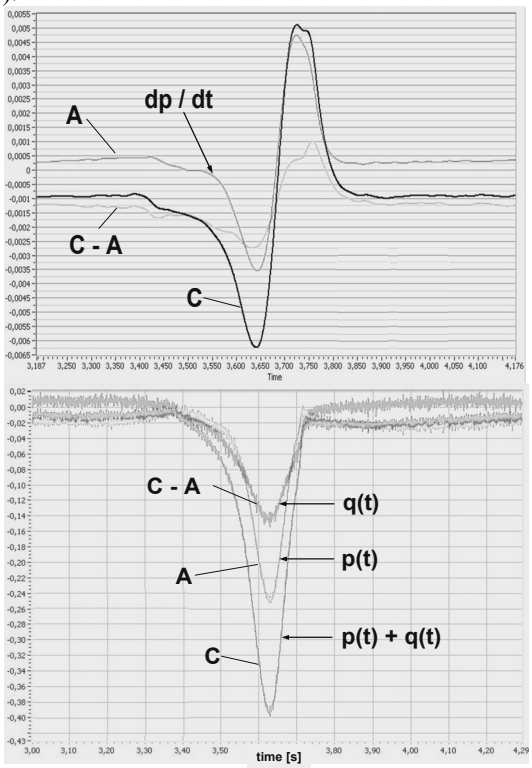

Figure 7: Dynamic measurement of pressure (A) and shear force (C-A) (top side-raw signal, bottom side-integrated signal)

Measurements at the lose paper stack showed a symmetric distribution of the shear force. Measurements at the fixed paper stack showed a rise in the shear force portion upon entering the nip area and zero occurred only in the compressive load zone. Upon entrance into the nip area the combination drum – winding roll yielded a steep rise in the compressive load portion with subsequent reversal, which leads to the conclusion that similar processes take place during winding and on a paper stack.

3. EXPERIMENTS AND RESULTS AT WINDING

Results from the paper stack tests were transferred to the winding process. Mechanisms of induced tension and movement of layers are similar to those in the paper stack. First, movements during the winding process are against machine direction of winding roll and lead to increased tension, referred to the winding roll as a spiral. Progression of movement of one layer shows that after two or three revolutions of the winding roll movement of this layer against machine direction comes to an end during one revolution. After further revolutions the movement migrates in direction of the winding roll and then again reaches the initial position (Figure 8). The trial was done on a wound roll with a new "window" after each one revolution.

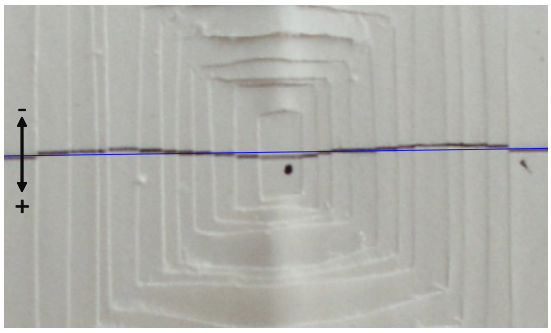

Figure 8: Layer movement at winding roll (-) in opposite machine direction and (+) in machine direction, Nip load 130 N/cm

The evaluation (Figure 9) showed an increase of layer shifting with higher line load.

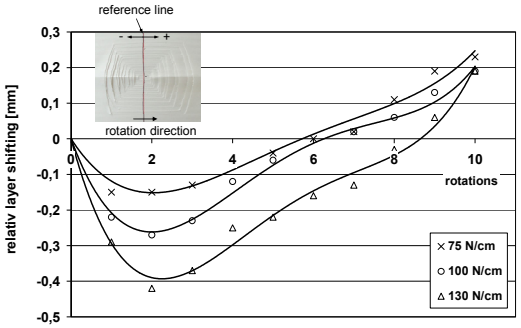

Figure 9: Layer shifting with line load (75 – 130N/cm)

Further movement in the winding roll occurs up to the depth where layers are deformed. Calculation of the deformation yielded a parabolic which explains the movements as a J-shaped line. With reference to the winding roll, movement towards the winding roll direction is a reduction in tension.

The static condition of one layer during a revolution as well as reversal of direction leads to the conclusion that an instantaneous centre exists. While tension reversal on a paper stack led to a tension-free layer, reversal on the winding roll causes maximum tension.

Circumferential velocity of the winding roll was determined considering an instantaneous centre course where the velocity is equal to that of the drum. It is larger than the circumferential velocity of the drum (Figure 10).

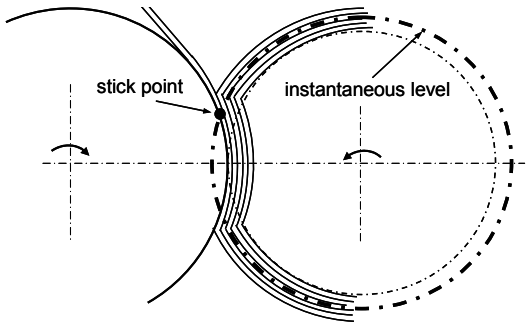

Figure 10: Instantaneous level for one revolution.

Regarding tension progression a differential equation with the winding parameters was established similar to that for the paper stack (Figure 11).

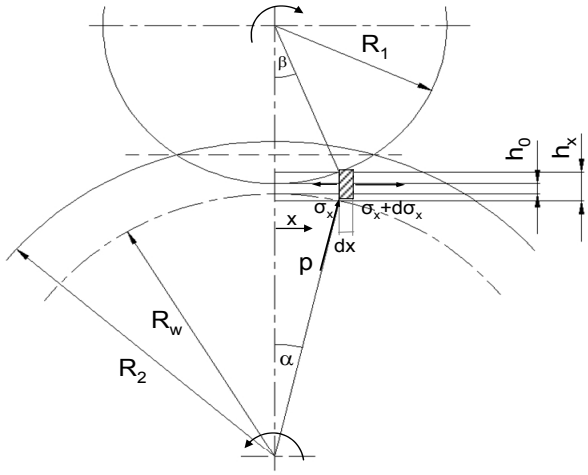

Figure 11: Shaping process at wound roll

Similar as for the stack two resolutions are necessary. Both solutions yielded a common intersection which is in agreement with the position of the instantaneous centre (point x_0 in Figure 12). With the data in Table 2 and the measured pressure distribution the calculation results showed that a reduction of tension occurs in front of or at the entrance into the nip area, both for the arriving web tension as well as for the layers on the winding roll up to the third layer. The induced tension including the web tension is named WOT (wound on tension). In the middle of the nip the WOT is complete similar to the paper stack.

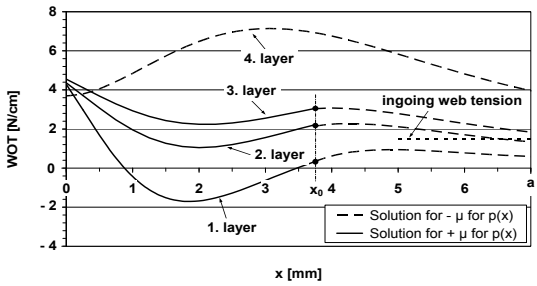

Figure 12: Calculation of wound on tension

Drum radius	R = 150 mm
Roll radius	R_w = 150 mm
Half nip width	a = 7 mm
Paper thickness	h_0 = 40 µm
Web tension	1,5 N/cm
Friction coefficient	µ = 0,26
Penetration depth	0,32 mm
Line load	75 N/cm

Table 2: Test parameters

At a winding equipment the WOT was measured and controlled with the "Gap"–test (Figure 13).

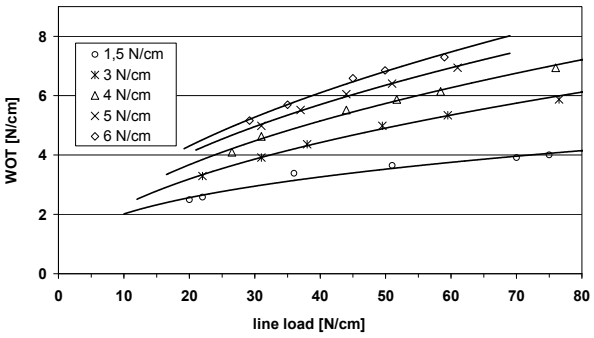

Figure 13: WOT – measurement with web tension (1,5 – 6 N/cm)

This measurement is helpful in practice for the winder parameters to avoid winding faults.

4. CONCLUSION

The movement of layers and the induced tension in the nip was experimentally and theoretically analysed on a stack of paper and in winding. The movement on the stack was calculated from the geometric dimension of deformation in the nip area. The induced tension was calculated from the shaping process and showed two solutions which are equal on one point. This point is identical with the instantaneous level on a stack and a course in winding. The level is a tension free layer on a stack and the course a maximum tension in winding. Additional to the theoretical understanding of the nip process usable results for practice could be developed.

REFERENCES

[1] Pfeiffer, J.D. "Mechanics of a rolling nip on paper webs", Tappi Journal, Vol. 51, No. 8, S.77-85, 1968

[2] Rand, T. and Erikson, L.G. "Physical properties of newsprint rolls during winding", Tappi Journal, Vol 56, 1973

[3] Pfeiffer, J.D. "Nip forces and their effect on wound rolls" Tappi Journal, Vol. 60, No. 2, S.115-117, 1977

[4] Good, J.K. and Wu, Z. "The mechanism of nip induced tension in wound rolls" Journal of Applied Mechanics, Vol. 60, 1993

[5] Güldenberg, B. "Einfluss der nipinduzierten Effekte auf den Wickelprozess von Papier", Dissertation University Bochum, 2000

[6] Jorkama, M. and von Hertzen, R. "The mechanism of induced tension in winding" Journal of pulp and paper science, Vol. 28, No.8, 2002

[7] Jorkama, M. and von Hertzen, R. "Contact mechanical approach to the winding nip "Proceedings of the 8th International Conference of Web Handling, Oklahoma, 2005

[8] Desch, M. Kaulitz, T. Dörsam, E. "Industrial use for the nip induced effect to separate sheets" Proceedings of the tenth International Conference of Web Handling, Oklahoma, 2009

[9] Szabo, I. "Höhere technische Mechanik", 5.Auflage, Springer-Verlag Berlin 2001

Transverse Compression of Paper and Coating

RAMIN FARNOOD, MARK KORTSCHOT, TURN LU, and STEVEN NUNNARI

Department of Chemical Engineering and Applied Chemistry, University of Toronto.
200 College Street, Toronto, ON, M5S 3ES, Canada Canada
ramin.farnood@utoronto.ca

ABSTRACT

Paper and coated paper undergo transverse compression during the manufacturing and end-use. For example, in the calendering process, paper is compressed in a rolling nip to impart the desired surface finish, and in the printing nip, paper compression affects the contact area and hence the ink transfer process. Although, mechanics of paper compression in a rolling nip have been studied intensively, we lack the fundamental understanding that would allow us to relate the physical properties of paper constituents to changes in both thickness and roughness after calendering as a function of the compressive loads under various strain rates.

At the University of Toronto, we have been investigating the above phenomenon using a combination of theoretical models and experimental tools [1-7]. In particular, we have developed a unique microcompression device that is capable of measuring the stress-strain response of thin films (with thickness ~20 um or larger) at high speeds (~1-2 msec) over small areas (~0.5 mm^2) [1]. Using this device, compressive stress was applied to both uncalendered and calendered newsprint samples in the z-direction to investigate the stress-strain properties of paper at various compressive cycle times between 5 ms and 5000 ms. The van Haag model was adopted to interpret the stress-strain behavior of paper. It was found that the initial compressive modulus of paper was a strong function of the rate of compressive strain.

Using this apparatus, compression of free layers of coating formulations normally used to coat paper was also examined. Tests were conducted at high speeds, with a pulse duration of 2 ms during the compressive stroke. The compressive modulus of the coating did not correlate strongly with the modulus of its constituent latex. Latex content, however, strongly affected coating compressive modulus. A sharp increase in the compressive modulus was observed at the coating critical pigment volume concentration (CPVC) – essentially the latex concentration at which the coating layer porosity is reduced to zero. Pigment size distribution and pigment morphology also affected the compressive modulus of coating in a manner consistent with packing theory.

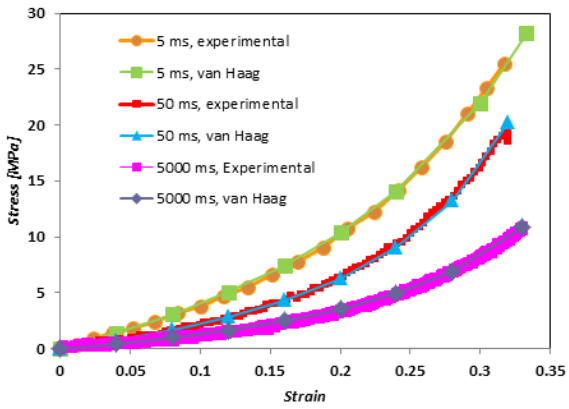

Figure 1. Stress strain curves at three compression cycle times (5, 50 and 5000 ms) for uncalendered samples. The curves are fitted with van Haag model at initial modulus of 39.6, 18.5 and 10.5 MPa, and strain limit of 0.53, 0.46 and 0.49, respectively.

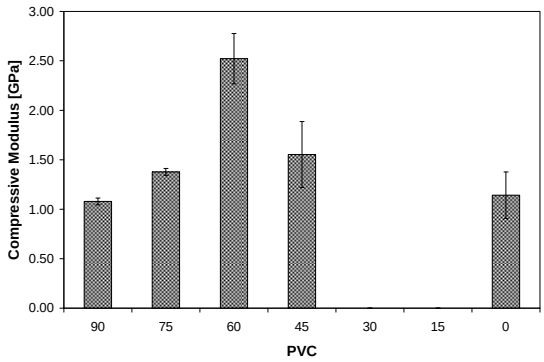

Figure 2. The compressive modulus measured as a function of PVC under dynamic conditions. The sharp transition occurring at a PVC of approximately 60 denotes the CPVC.

REFERENCES

[1] S.J. Nunnari, R.R. Farnood and M.T. Kortschot. High speed microcompression of paper coatings. *J. Mater. Sci.* **44**(10) 2507-2512 (2009).

[2] P. Azadi, S. Nunnari, R. Farnood, M.T. Kortschot and N. Yan. High speed compression of highly filled thin composite: Effect of Binder Content and Stiffness. *Prog. Org. Coat.* **64**(4) 356-360(2009).

[3] V. Litvinov and R. Farnood. Phenomenological modelling of the compression of coated papers in a Soft Rolling Nip. *J. Mat. Sci.* **45** (1) 216-226 (2010).

[4] P. Azadi, R. Farnood and N. Yan. Modeling the effect of pigment morphology on the dynamic compression of coating layers using DEM. *Comp. Chem. Eng.* **32** (12) 3084–3089 (2008).
[5] P. Azadi, R. Farnood and N. Yan. Discrete element modeling of the mechanical response of pigment containing coating layers under compression. *Com. Mat. Sci.* **42** (1) 50–56 (2008).
[6] K. Kwong and R. Farnood. Modelling the compression of three-dimensional fibre networks using dynamic finite element analysis. *J. Pulp Pap Sci.* **33**(2) 79-84 (2007).
[7] V. Litvinov and R. Farnood. Modeling thickness and roughness reduction of paper in calendering. *Nordic Pulp Pap. Res. J.* **21**(3) 365-371 (2006).

Discriminating between different mechanosorptive creep hypotheses

S. B. LINDSTRÖM, E. KARABULUT,
A. KULACHENKO and L. WÅGBERG

Fiber and Polymer Technology / KTH
SE-10044 Stockholm, Sweden
stefan.lindstroem@gmail.com

INTRODUCTION

The creep rate of some hygroscopic materials has a strong dependence on fluctuations in the ambient relative humidity (RH). Wood [1], paper [2] and individual wood fibers [3] are known examples. This phenomenon, known as *mechanosorptive creep*, threatens the integrity of any hygroscopic material structure under constant load, and particularly shortens the storage-life of corrugated boxes [4].

Previously, many models for describing the generic mechanisms of mechanosorptive creep, as well as mechanisms particular to paper, have been proposed. Mechanosorptive creep in cellulose-based materials has been attributed to physical ageing of glassy materials [5], macroscopic moisture gradients and associated enhanced stresses [6], various fiber-level processes introducing stress concentrations [7,8,9] and more [6,10]. This work is focused on testing the predictions of the previously proposed models, and particularly identifying the length-scale at which the dominant mechanosorptive creep mechanism is found; sample size-level, fibril-level, or subfibril-level. To avoid the complexity of hierarchical microstructures typical to wood or paper, we use nanofibrillated cellulose (NFC) films and aerogels [11] as model systems.

MATERIALS AND METHODS

Solvent-cast films have been prepared using an aqueous dispersion of TEMPO-oxidized cellulose nanofibrils, by evaporating the water at room temperature. The thickness and area density ranges are $h \square [11,20]$ µm and $b \square [17,30]$ g/m^2, respectively. The porosity is about 5 %, and Fig. 1 shows a field-emission scanning electron micrograph of an NFC film cross-section exposed by manually tearing the film. The preparation procedure for aerogels (h=150 µm, b=53.1 g/m^2 and h=170 µm, b=26.7 g/m^2) is described elsewhere [11]. The PerkinElmer DMA7e^{TM} dynamic mechanical analyzer is used for mechanical testing.

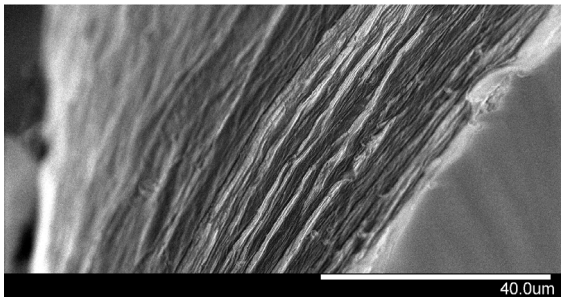

Figure 1. The cross-section of a solvent-cast cellulose nanofibril film with basis weight b=21.4 g/m^2. The exposed cross-section is prepared by manually tearing the film.

RESULTS AND DISCUSSION

Creep curves are obtained at 60 MPa tensile stress for 3 mm long and about 6 mm wide samples. At a constant relative humidity, after the initial elastic deformation, and about 25 min transient response, the creep strain ε of the NFC films develops logarithmically with time: $\varepsilon=\Gamma\log_{10}(t/\tau)$. Here, τ is a constant and Γ is the logarithmic creep rate. In our experiments Γ is determined at t_1=40 min. To compare the mechanosorptive creep curves, a normalized creep strain $\varepsilon_n=[\varepsilon(t)-\varepsilon(t_1)]/\Gamma$, which accounts for variations in Γ between samples, is considered.

First, we address the question of whether mechanosorptive creep is primarily explained by the sorption-induced, through-thickness stress gradient [6], a nonlocal effect, or by one of the previously proposed local mechanisms originating directly from the moisture change [5,6,7,8,9]. For this purpose, the film thickness and ramp rate of the ambient relative humidity are varied to decouple the moisture gradient and the rate of moisture change. The cyclic moisture creep curves are obtained at 60 MPa tensile stress, while the RH is varied between 40 % and 80 %. This induces a through-thickness stress variation amplitude of about 20 MPa for the ideal RH step, but at most 5 MPa amplitude for the slowest RH ramp rate. In each experiment, the moisture equilibration time, as computed from the measured diffusivity and film thickness, is much shorter than the half-period of RH cycling. The normalized creep curves for different RH ramp rates and different sample thicknesses are plotted in Fig. 2. These cyclic moisture creep curves overlap each other, indicating that the through-thickness moisture gradient has a negligible effect on mechanosorptive creep.

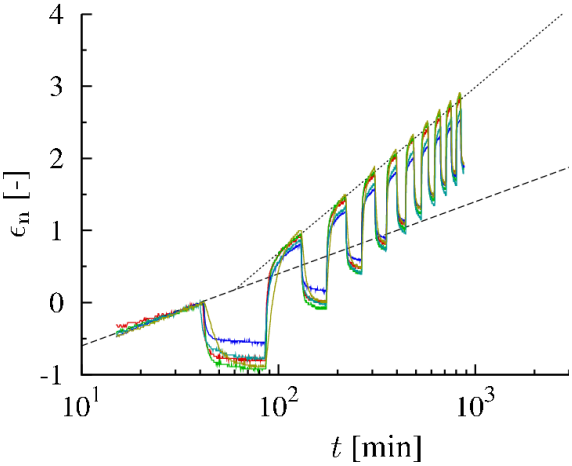

Figure 2. Normalized creep strain ε_n during moisture cylcling between 40 % and 80 % RH. The experiments represent a range film thicknesses h [11,20] µm and RH ramp rates. The accelerated creep is 2.3 according to definition (see Ref. [13]).

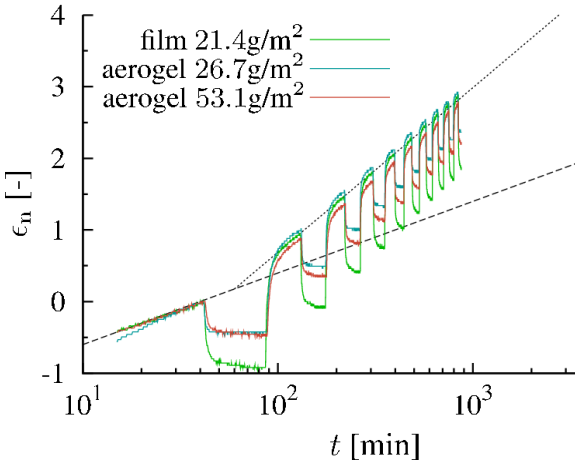

Figure 3. Normalized creep strain ε_n during moisture cylcling between 40 % and 80 % RH. The accelerated creep of NFC aerogels are compared with that of an NFC film. The accelerated creep is 2.3.

In another investigation, we compare the mechanosorptive creep of films and aerogels. This is to reveal the importance of the geometrical constraints of the structure. The microstructure of the film is severely constrained, which produces relatively large interfibril bond stresses during hygroexpansion or -contraction. In contrast, the high porosity aerogel has a much more forgiving structure by virtue of bending deformations of the longer unbonded fibril segments [11]. Comparing the mechanosorptive creep of films and aerogels estimates the importance of the heterogeneity-driven [6,8] accelerated creep.

Cyclic moisture creep experiments were conducted at 2.0 and 4.1 MPa for the low and high density NFC aerogel, respectively, to maintain a constant specific stress. The normalized cyclic moisture creep curves of the aerogels are plotted together with the corresponding experiment of the b=21.4 g/m^2 NFC film in Fig. 3. The curves overlap each other, demonstrating that mechanosorptive creep is unaffected by significant differences in the fibril-level microstructures.

CONCLUSIONS

Cellulose nanofibril films exhibit a significant mechanosorptive creep. Since mechanosorptive creep is observed in NFC films, it is concluded that features particular to microfibrils or wood fibers, including anisotropic swelling, are not necessary for the phenomenon to occur. Moreover, as long as there is sufficient time for the sample to equilibrate during each step of an RH cycle, the mechanosorptive log time creep rate does not significantly depend on the sample thickness. Mechanosorptive creep is thus not sensitive to the moisture gradients at the scale of the sample thickness. NFC aerogels also exhibit machanosorptive creep, and their accelerated creep is essentially the same as that of NFC films; the fibril-level structure has a negligible effect on the mechanosorptive creep rate. Thus, the primary mechanism of mechanosorptive creep is found at length-scales smaller than the fibril diameter.

REFERENCES

[1] L. D. Armstrong and G. N. Christensen. Influence of moisture changes on deformation of wood under stress. *Nature* **191**(4791):869–870 (1961).

[2] V. L. Byrd. Effects of relative humidity changes during creep on handsheet paper properties. *Tappi* **55**(2):247–252 (1972).

[3] A.-M. Olsson, L. Salmén, M. Eder and I. Burgert. Mechano-sorptive creep in wood fibres. *Wood Sci. Technol.* **41**:59–67 (2007).

[4] C. H. Leake and R. Wojcik. Humidity cycling rates: How they influence the container life spans. *Tappi* **76**(10):26–30 (1993).

[5] Z. V. Padanyi. Physical aging and the glass transition: Effects on the mechanical properties of paper and board. *10th Fund. Res. Symp.*, vol. 1, Oxford, UK, 521–545 (1993).

[6] C. C. Habeger and D. W. Coffin. The role of stress concentrations in accelerated creep and sorption-induced physical aging. *J. Pulp Paper Sci.* **26**:145–157 (2000).

[7] C. Söremark and C. N. Fellers. Mechano-sorptive creep and hygroexpansion of corrugated board in bending. *J. Pulp Paper Sci.* **19**(1):J19–J26 (1989).

[8] J. Alfthan and P. Gudmundson. Linear constitutive model for mechano-sorptive creep in paper. *Int. J. Solids Struct.* **42**:6261–6276 (2005).

[9] J. Strömbro and P. Gudmundson. An anisotropic fibre-network model for mechano-

sorptive creep in paper. *Int. J. Solids Struct.* **45**:5765–5787 (2008).
[10] C. C. Habeger, D. W. Coffin and B. Hojjatie. Influence of humidity cycling parameters on the moisture-accelerated creep of polymeric fibers. *J. Polym. Sci. B Polym. Phys*, **39**:2048–2062 (2001).
[11] H. Sehaqui. Nanofiber networks, aerogels and biocomposites based on nanofibrillated cellulose (NFC) from wood. PhD thesis, KTH, Sweden (2011).
[12] C. Aulin, M. Gällstedt and T. Lindström. Oxygen and oil barrier properties of microfibrillated cellulose films and coatings. Cellulose **17**(3):559–574 (2010).
[13] J. Z. Wang, D. A. Dillard, M. P. Wolcott, F. A. Kamke and G. L. Wilkes. Transient moisture effects in fibers and composite-materials. *J. Compos. Mater.* **24**(9):994–1009 (1990).

Session 5

New Cellulose Based Products

Swelling of nanofibrillated cellulose

MARJO MANNINEN, KAARLO NIEMINEN, THAD MALONEY

Aalto University, School of Chemical Technology,
Department of Forest Products Technology
P.O. Box 16300, 00076 Aalto, Finland
marjo.manninen@aalto.fi

1 INTRODUCTION

Swelling is a fundamental material property of particular importance, relevant to many aspects of material behavior. For pulp fibers, the degree of swelling is linked to many important properties including dewatering, recycling and strength development. For water-saturated materials, the water held within an individual particle is a measure of the particle level swelling.

Nanofibrillated cellulose (NFC) is a highly swollen cellulosic material and it has a viscous gel-like appearance even at low concentrations. NFC consists of nano-scale microfibrils and microfibril bundles that are released from the fiber cell wall by mechanical and chemical treatments. Many of the interesting properties of NFC and its behaviour in different processes are likely to be related to its large water binding capacity. Thus it is important to be able to determine the swelling of the material and gain knowledge about the factors controlling the interactions with water. The aim of this work was to develop a method for measuring the swelling of NFC.

The swelling of pulp fibers can be measured with solute exclusion test, which was first introduced by Stone and Scallan in the 1960s [1]. The principle of the solute exclusion test is to add a non-interacting probe molecule solution into the pulp sample and measure the dilution of the molecule solution. The probe molecule is so large it cannot penetrate into the cell wall, thus water in the cell wall is inaccessible to it. The inaccessible water in pulp fibers reaches a maximum at a probe molecule size of approximately 30 nm [2], thus 2×10^6 Dalton dextran molecule, with a spherical diameter in solution of approximately 56 nm, is commonly used in FSP measurements. The dilution of the probe molecule solution expresses the amount of accessible water and the inaccessible water equals the total water of swelling and defines the fiber saturation point (FSP). FSP is expressed as grams of water per gram of dry pulp.

In the solute exclusion test, one important assumption is that the probe molecule does not adsorb or otherwise interact with the cellulosic material. However, Fig. 1 shows that the apparent FSP varies in a complex pattern as a function of dextran concentration. We believe there are two important interactions that must be accounted for to derive a meaningful swelling value. Firstly, we believe that the dextran interacts with the nanofibrillated cellulose, contrary to the test's basic assumptions. Second interaction that should be accounted for is the osmotic pressure balance between the external dextran solution and the inside of the swollen particle. The increased osmotic pressure squeezes water out of the cellulosic material and decreases the FSP. The slope of the FSP vs. dextran concentration curve at the higher dextran concentrations depends on the elastic response of the material. These two different effects, the adsorption of dextran and elastic response of the material, make the FSP curve distorted and thus the measured FSP depends on the final concentration of the dextran solution.

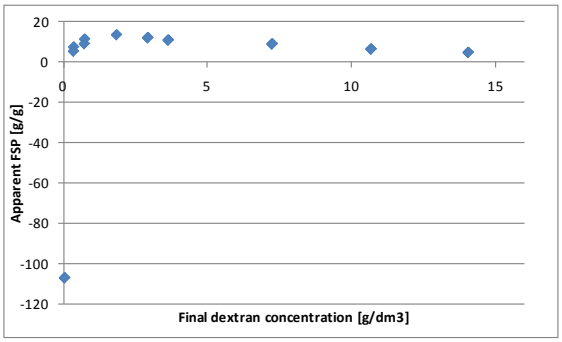

Figure 1. Apparent fiber saturation point (FSP) of Masuko grinded nanofibrillated cellulose (NFC) measured at varying dextran concentrations.

When both these interactions are accounted for, a new material property FSP at zero external osmotic pressure (FSP_0) can be obtained. The FSP_0 is the amount of water contained in the material, when no external osmotic pressure is affecting it.

2 EXPERIMENTAL

The starting material of NFC was ECF bleached, never-dried chemical birch pulp. The acid groups in the pulp fibers were converted to either H^+- or Na^+-form. NFC was produced with MasukoSupermasscolloider MKZA 10-15J at approximately 2 % solid content. The energy consumption of grinding was 6.6 and 7.8 kWh/kg for H^+- and Na^+-forms, respectively. Data from measurements performed with never-dried, oxygen delignified softwood pulp [3], not in any specific ionic form, was also used. In some test points, the softwood pulps were also refined at never-dried and once-dried forms with Voith Sulzer refiner at 200 kWh/t. The FSP of NFC and pulp fibers was measured with solute exclusion at dextran (2×10^6 Dalton dextran, Sigma-Aldrich) concentrations varying from 0.02 to 4 %.

A new method for determining FSP_0 was developed and a new swelling equation was derived. The derived equation was based on the following assumptions: some of the dextran adsorbs onto the cellulosic material, partition effects are negligible (i.e. dextran does not enter into the pores), the material responses elastically to the changes in the external osmotic pressure and the elastic modulus is constant over the range of the experiment. The swelling equation accounting for the adsorption of dextran and elastic response of the material is as follows,

$$c_i \cdot w_{dex} = \frac{w_p \cdot \gamma \cdot \alpha \cdot c_f}{1+\alpha \cdot c_f} + c_f \cdot w_t + \frac{c_f^2 \cdot \frac{R \cdot T}{M_n} \cdot w_p \cdot 0.67}{E_i} + \frac{c_f^2 \cdot \frac{R \cdot T}{M_n} \cdot w_{ino}}{E_i} - c_f \cdot w_{ino}$$

where c_i and c_f are the concentrations of the dextran solutions before and after mixing with the cellulosic materials, respectively, w_{dex}, w_p, w_t and w_{ino} are the masses of the dextran solution, dry cellulosic material, total amount of water and amount of water at 0 external osmotic pressure, respectively. γ is the saturation value of adsorption, α is a parameter, R is the gas constant, T is the temperature, M_n is the molar weight of dextran and E_i is the isotropic elastic modulus. FSP_0 is w_{ino}/w_p.

3 RESULTS AND DISCUSSION

The model fit of the FSP measured from NFC is presented in Fig. 2. The figure also shows how the adsorption of dextran and the elastic response of the material to external osmotic pressure distort the measured FSP. The effect of dextran adsorption is clearly seen when the adsorption is accounted for in the model. The intercept of the curve in which the data is corrected for adsorption estimates the FSP_0 and the slope of the curve describes the isotropic elastic modulus. When the elastic response is also accounted for, the FSP becomes independent of dextran concentration. It should also be noted that the FSP_0 is higher than the originally measured FSP.

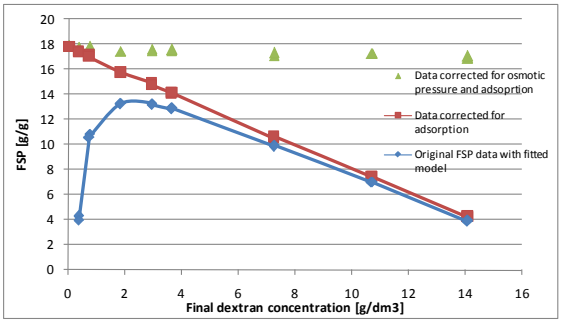

Figure 2. Model fit of FSP measured from NFC and how FSP_0 can be obtained when the adsorption of dextran and the elastic response to external osmotic pressure are accounted for.

The two important values, isotropic elastic modulus (Ei) and fiber saturation point at 0 external osmotic pressure (FSP_0) derived from the new swelling equation are shown in Table 1. Also a rough estimate of the amount of dextran adsorbed (γ) can be obtained. Data from another study [3] was also fitted to the model in order to evaluate if the changes in the fibers due to hornification and refining can be detected with this method.

Table 1. Isotropic elastic modulus (E_i), FSP at 0 external osmotic pressure (FSP_0) and amount of dextran adsorbed onto the cellulosic material (γ) of bleached never-dried hardwood fibers (NDHW), nanofibrillated cellulose (NFC) and oxygen delignified never-dried (ND) or dried (D) softwood (SW) fibers, determined from the swelling equation.

Sample	E_i [Pa]	FSP_0 [g/g]	γ [mg/g]
NDHW fibers, H^+-form	165	1.80	0.46
NDHW fibers, Na^+-form	208	1.83	0.45
NFC from NDHW, H^+-form	25	11.6	1.98
NFC from NDHW, Na^+-form	24	17.5	4.66
NDSW fibers [3]	698	1.48	0.04
DSW fibers [3]	1420	1.05	0.11
NDSW fibers, refined 200 kWh/t [3]	167	2.44	0.42
DSW fibers, refined 200 kWh/t [3]	364	1.61	0.03

The swelling of fibers, determined as FSP_0, shows that the Na^+-form is more swollen than the H^+-form, as was expected. The values calculated for the never-dried and dried softwood pulps show that due to hornification upon drying, the swelling of the material decreases and the material becomes stiffer, i.e. the elastic modulus increases, thus the results are logical. Refining changes the cell wall structure of the fibers and makes the fibers more flexible and this is seen as an increase in the FSP_0 and a decrease in the elastic modulus with refined fibers. Refining the dried fibers partly restores the effects of hornification, but the properties are not at the same level as those of the never-dried refined fibers, however they clearly differ from those of the unrefined ones.

The FSP_0 of the highly swollen NFC is much higher than that of the pulp fibers. The elastic modulus of NFC is also significantly lower when compared with the parent fibers and thus NFC is more conformable under external osmotic pressure. Measurements done with different ionic forms showed that the ionic form had a significant effect on the FSP, as expected, but surprisingly there was no effect on the elastic modulus. More dextran is adsorbed onto NFC than onto pulp fibers; one reason could be the larger specific surface area of NFC.

The very high FSP_0 values obtained for NFC could in part be due to the size of the probe molecule in relationship to the size of the NFC particle. The size of the probe is 56 nm and the diameter of the NFC type used in this study is typically approximately 5-20 nm. The particular probe was chosen because it is the probe conventionally used in FSP measurement, which was used as the starting point of the method development. We also wanted to start with a big enough probe in order to ensure that the probe will not penetrate into the material. However, because of the different dimensions of NFC compared with pulp fibers, the probe used here could be too large. Thus, the FSP_0 results can include also interstitial water, which is within the NFC network structure or between fibrils along the NFC backbone, rather than in the particle per se. The exact interpretation of FSP_0 for NFC is ambiguous at this point. In future work the size of the dextran probe molecule will be considered.

Previously reported elastic moduli of fibers vary greatly depending on the type of modulus defined; our method determines an isotropic elastic modulus and it is sensitive to the conditions at the outer fiber interfaces. The technique used also effects the obtained elastic modulus, and values reported previously are much higher than those measured in this work. For example, the elastic modulus of wet unbeaten softwood kraft measured with AFM micro-indentation gave value of 7 MPa for transverse microcompression [4]. Scallan and Tigerström [5] proposed a method to calculate elastic modulus of water swollen cell wall. In that method a change in the osmotic pressure is generated by changing the counter-ions of the acid groups from H^+-form to Na^+-form and the increase in the swelling is measured with solute exclusion. This stress-strain phenomenon was used as a basis for deriving the elastic modulus. With that method, the values calculated for materials measured in this study were 0.016 and 5.58 MPa for NFC and pulp fibers, respectively. Our method is sensitive to the conditions of the outer interface of the fiber material, for example to polymer chains that extend to the solution. This may explain the low modulus values compared with other techniques that have often yielded results for wet fibers in the range of 10^6 Pa.

REFERENCES

[1] Stone, J., Scallan, A., The Effect of Component Removal Upon the Porous Structure of the cell Wall of Wood. II. Swelling in Water and the Fiber Saturation Point, *Tappi J.* **50**(10):496-501 (1967).

[2] Stone, J., Scallan, A., A structural model of the cell wall of water swollen wood pulp fibers based on their accessibility to macromolecules, *Cell. Chem. Technol.* **2**(3):343-358 (1968).

[3] Auranen, J., New elasticity measurement technique for swollen fibre material, Master's Thesis, Helsinki University of Technology (2009).

[4] Nilsson, B., Wågberg, L., Gray, D., Conformability of Wet Pulp Fibres at Small Length Scales, Mid Sweden University, report number R-00-6 (2000).

[5] Scallan, A., Tigerström, A., Swelling and Elasticity of the Cell Walls of Pulp Fibers, *J. Pulp Pap. Sci.* **18**(5):188-192 (1992).

Elastic properties of cellulose nanopaper versus conventional paper

DENOYELLE T., KULACHENKO A., SYLVAIN G. AND LINDSTRÖM S.

Royal Institute of Technology
Osquars Backe 1
artem@kth.se

Keywords: Nanopaper, nanocellulose, elastic properties.

1 INTRODUCTION

In most of the engineering applications, materials are utilized within their elastic limit, in other words, well below the point where the unrecoverable inelastic deformations appear. Naturally, the elastic properties are usually the key parameters in evaluating the potential of new materials.

Recent studies have demonstrated a great mechanical performance of "nanopaper" [1, 2]. By nanopaper, we refer to a thin membrane made of nanocellulose fibrils (also called nanofibers). Nanofibers are about 1000 times shorter and thinner than the ordinary paper fibers. At the same time, nanopaper is significantly denser than the ordinary paper. Since there are no well established standards to assess the quality of nanofibers, it is instructive to investigate how the properties of nanofibers translate into the properties of nanopaper and how it is compared to the corresponding relation between conventional fibers and paper.

Paper is essentially a network of fibers. The elastic modulus of paper depends on a number of factors, such as fiber orientation, fiber stiffness and network interconnectivity which often expressed through density.

The contribution of these factors to paper stiffness has been reported widely in the literature. Cox [3] connected the elastic modulus of two-dimensional fiber network to the elastic modulus of a single infinitely long fiber. According to Cox theory, the upper estimate of the elastic modulus of a randomly oriented fiber network equals to one third of the fiber's elastic modulus. The ratio between density of the network and cellulose fiber is usually used to relate this prediction to the three-dimensional paper structure.

The follow up studies argued about difficulties of applying the Cox theory to paper. The theory does not account for non-uniform shear transfer along the fibers (Shear-lag phenomenon) but most importantly it is unable to describe the presence of fiber defects, which may develop during the fiber extraction process and during drying of paper sheets [4]. Drying affects the properties of the fibers. Depending on the drying conditions, the free segments between the bonds along the fiber may develop different elastic properties.

Being much denser, nanopaper should intuitively be more predictable in this respect, since the segment length is much shorter and the nanofiber are stiffer and have a simpler structure compared with the ordinary fibers.

Although, nanocellulose fibrils were reported to have elastic modulus as high as 134 GPa [5, 6], the reported modulus of isotropic sheets made of nanocellulose varies between 8 to 15 GPa in the literature [1, 2], which is significantly lower than the theoretical maximum of 44 GPa. We aim to provide tools explaining this difference.

We revisited the previous studies regarding the contribution of different network factors on the elastic modulus. A combination of numerical and experimental approach is used in the analysis.

2 METHODS

The fundamental limitations of the Cox and Shear-lag theory have been described by Åström et al [7]. In essence, Cox theory ignores the length of the fibers, and both theories consider only straight fibers as well as neglect the compliance of the fiber joints. The variation of the properties along the fibers is neither taken into account.

The limitation of these models has been overcome by network models [7, 8] in which the fibers are represented explicitly, as a chain of beam elements in the finite-element analysis, for example. Heyden [8] presented a comprehensive study of the effect of various network parameters on the elastic properties. One of the limitations of the previous model is the inability to consider dense networks partly because of limited computational tools and also because the fibers had to share the nodes in the points of contacts. Increasing the density required very fine and non-uniform mesh to meet this condition. We avoided this limitation by using a bonded contact formulation to describe the bonds between the fibers. In this approach, fibers are connected in both translational and rotational degrees of freedom at the points of contacts and do not need to share a node. This enabled us to consider a broad range of densities in the analyses.

We start the analysis with experimental work. In this work, we accurately measured the stiffness of the nanopapers by PerkinElmer DMA7e dynamic mechanical analyzer in order to quantify the effect of the drying constraints and assess the applicability of the models.

3 RESULTS

3.1 Effect of drying constraints.

We investigated the effect of drying constraints experimentally. We created two identical circular samples of nanopaper with nanofibrilated cellolose produced with an oxidation pre-treatment

(TEMPO). The samples were dried differently. The first sample was dried under the pressure between the plates at the temperature of 50 C. The other sample was dried freely in the room temperature. The freely dried sample showed significant out-of-plane distortion, while the constrained sample was practically flat. Small pieces of material (6x6 mm in size) were then extracted from each sample and tested in the dynamic mechanical analyzer (DMA) under varied humidifies. The thickness of the films was measured by scanning electronic microscope. Both films showed nearly identical density of 1570 kg/m^3. Figure 1 shows the elastic moduli of two differently dried nanopapers under stepwise elevating relative humidity. The mean stress level was 3 MPa with the dynamically varying amplitude of 2.4 MPa. The sample dried under constraints showed 12% higher elastic modulus, but the difference was not dramatic as in the case of sparse conventional paper, where it can be above 50%.

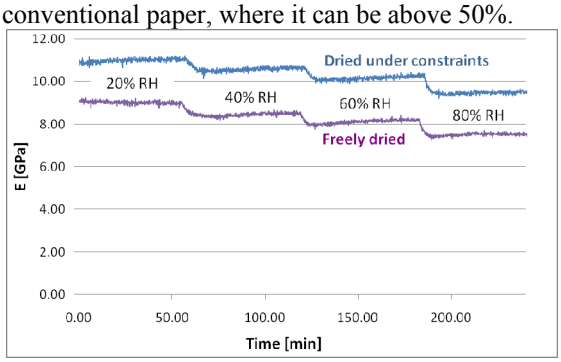

Figure 1. Elastic modulus as a function of relative humidity.

Concluding that drying does not significantly alter the elastic properties of a dense nanopaper, we proceed with numerical studies.

One of the most influential factors for the network stiffness is the fiber's length-to-width ratio. In case of uniform elastic properties along the fiber, Shear lag theories describe the dependency on the ratio very well and the effect of the ratio is theoretically observed even at high densities. According to experimental results, the effect of the length-to-width ratio is weak in conventional paper (unless the ratio is very small). In nanopaper, the effect of the ratio is hard to test experimentally, since the ends of the fibrils cannot be identified on the SEM or AFM images of the film surface. Separating nanofibrils is also difficult since even at lowest concentrations they seem to assemble into films.

Our results suggest, however, when the length-to-width ratio exceeds 200, it no longer affects the elastic modulus.

3.2 Effect of the fiber curl.

Heyden [8] reported the effect of the fiber curl on the modulus. The denser network is less sensitive to changes in fiber curl (Figure 2).

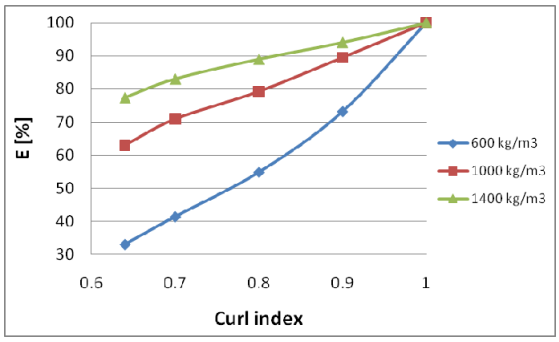

Figure 2. Dependence of the elastic modulus on the curl index.

Figure 3 shows how the elastic energy is re-distributed between different deformation modes in the fibers.

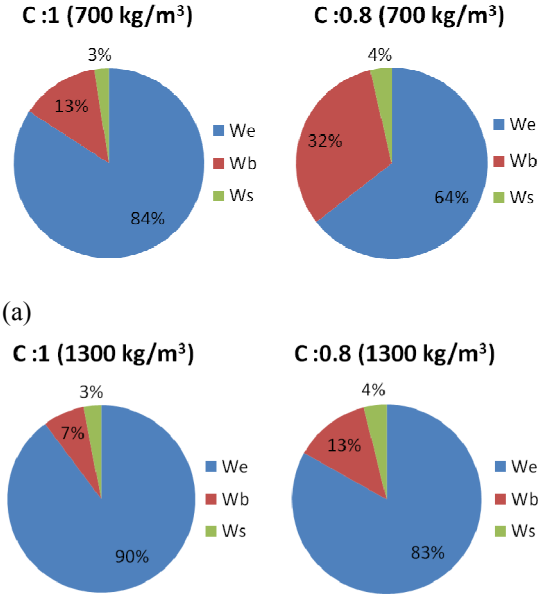

Figure 3. Partition of elastic energy stored in the fibers between axial strain energy (W_e), bending strain energy (W_b) and transverse shear strain energy (W_s) for the network density of: a) 700 kg/m^3; b) 1300 kg/m^3.

Increasing curl index increase the amount of energy stored in the bending-type deformation. The sparse the network, the more energy is shifted from the axial elongation into bending.

3.3 Effect of number of bonds.

The structure of nanopaper in the thickness directions has a layered arrangement. Figure 4 shows a SEM macrograph of the nanopaper cross-section. A two-dimensional fiber network model should adequately represent an individual layer.

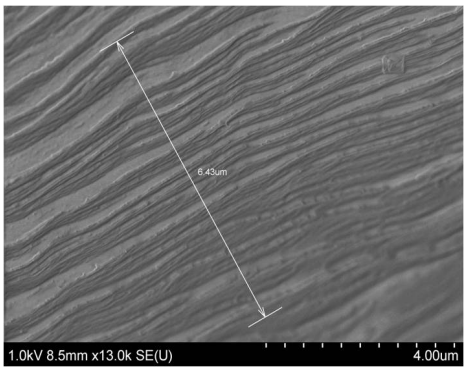

Figure 4. SEM micrograph of the cross-section of nanopaper (the marked distance is 6.5 microns).

During deposition, we assumed that all the fibers crossing in the plane form a bond. In reality, not all the bonds can equally bear the load. Figure 5 demonstrates the development of elastic modulus as the amount of bonds is decreased by removing them randomly while maintaining the same density.

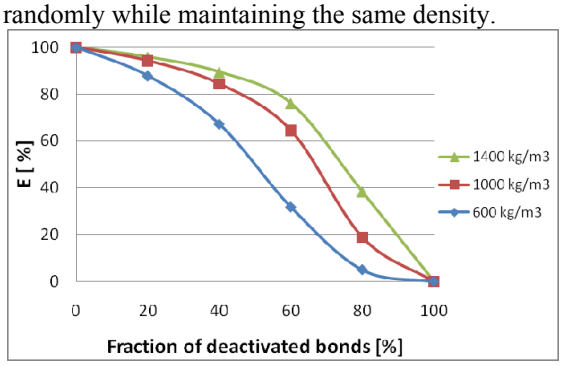

Figure 5. Dependence of the elastic modulus on the fraction of active bonds in the network.

The sparse network is more susceptive to bond removal. In a dense network, however, the removal of 40% bonds causes only 10% decrease of the modulus. Bond removal increases the stress variation inside the network, however.

3.4 Effect of bond stiffness.

We varied the bond opening stiffness which is likely to depend on the transverse properties of the nanofibers. Beam-to-beam contact is a point-wise contact, in other words, the contact area is not resolved. This means that the actual stiffness is defined in the units of N/m. The bond stiffness for the reference case was set to be elastic modulus of the fiber times fiber width. With this value, the elastic energy stored in the bonds turned out to be less than 1 percent of the total elastic energy.

Increasing the bonds stiffness does not affect the modulus of the network. Results in Figure 6 show that scaling the bond stiffness by a factor of 100 did not change the stiffness of the network. On the other hand, only significant decrease of the bond stiffness from the reference level changed the modulus. The effect is sensitive to the length to width ratio. Smaller ratio is more sensitive to the bond stiffness.

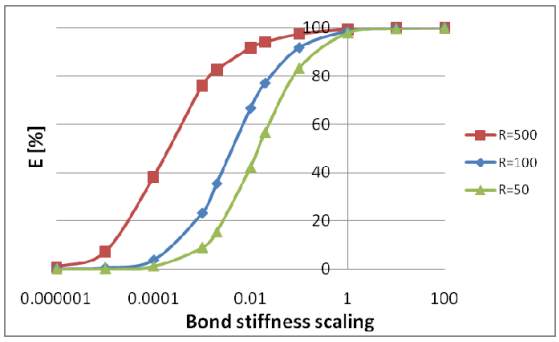

Figure 6. Elastic modulus as a function of bond stiffness.

4 CONCLUSIONS

The elastic properties of nanopaper are not significantly affected by the drying process compared to conventional paper, presumably because the nanofibers have a simple structure compared to ordinary paper fibers, and they form extremely dense networks with very short free segments. Neither bond stiffness nor fraction of inactive bonds showed a significant effect on the elastic modulus of the dense network. This means that after estimating the length-to-width ratio of the nanofibers, it is possible to connect the elastic properties of the nanofibers and nanopaper by a simple empirical relation.

REFERENCES

[1] K. Syverud and P. Stenius. Strength and barrier properties of mfc films. *Cellulose*. **16**(1):75-85 (2009).

[2] M. Henriksson, L.A. Berglund, et al. Cellulose nanopaper structures of high toughness. *Biomacromolecules*. **9**(6):1579-1585 (2008).

[3] H.L. Cox. The elasticity and strength of paper and other fibrous materials. *British Journal of Applied Physics*. **3**(3):72-79 (1952).

[4] D.H. Page and R.S. Seth. The elastic modulus of paper. The effects of dislocations, microcompressions, curl, crimps, and kinks. *Tappi*. **63**(10):99-102 (1980).

[5] I. Sakurada, Y. Nukushina, and T. Ito. Experimental determination of the elastic modulus of crystalline regions in oriented polymers. *Journal of Polymer Science*. **57**(165):651-660 (1962).

[6] F. Tanaka and T. Iwata. Estimation of the elastic modulus of cellulose crystal by molecular mechanics simulation. *Cellulose*. **13**(5):509-517 (2006).

[7] J. Åström, S. Saarinen, et al. Microscopic mechanics of fiber networks. *Journal of Applied Physics*. **75**(5):2383-2392 (1994).

[8] S. Heyden. Network modelling for the evaluation of mechanical properties of cellulose fluff. Ph.D. thesis, Lund University (2000).

Intriguing Structural and Strength Behavior in Foam Foarming

T. HJELT[1], K. KINNUNEN[1], J. LEHMONEN[1], N. BELETSKI[1], E. HELLÉN[1], V. LILJESTRÖM[2], R. SERIMAA[2], A. MIETTINEN[3], AND M. KATAJA[3]

[1] VTT TECHNICAL RESEARCH CENTRE OF FINLAND ADRESS POB 1000, 02044 VTT, FINLAND
[2] DEPARTMENT OF PHYSICS
POB 64, 00014 UNIVERSITY OF HELSINKI, FINLAND
[3] DEPARTMENT OF PHYSICS
POB 35, 40014 UNIVERSITY OF JYVÄSKYLÄ, FINLAND
TUOMO.HJELT@VTT.FI

Using foam instead of water as the material carrier phase is an alternative way to build up fibrous structures. The method is currently used in non-woven industry. The foam forming process for paper making has been successfully demonstrated on a production machine in the middle of the 1970s.

In foam forming, mixture of stock and foam is transformed through headbox to the wire, where the foam is removed using vacuum. This forming method gives many positive effects: Firstly, fibers are locked between foam bubbles, and thus they do not flock during transportation to the wire. This gives better formation and allows one to use higher consistency stock. Secondly, the capillary forces affecting fibers during dewatering are smaller compared to water forming. When combining the forming process with air drying, this leads to very bulky structures.

The plane directional tensile strength of foam formed bulky structures decreases as expected due to increasing porosity. However the z-directional strength decreases as a function of bulk much less than in normal water-formed papers. We have studied this using sheets of pine kraft pulp formed in both water suspension and in foam. The samples were dried in the same way in both cases. In order to study the high z-directional strength observed in the foam-formed sheets, we have recorded the 3D fiber network structure by X-ray tomography and studied the relative proportion of fiber segments tilted in z-direction. The experimental network structure (Figure 1) can be also used as a starting configuration for fiber network simulations.

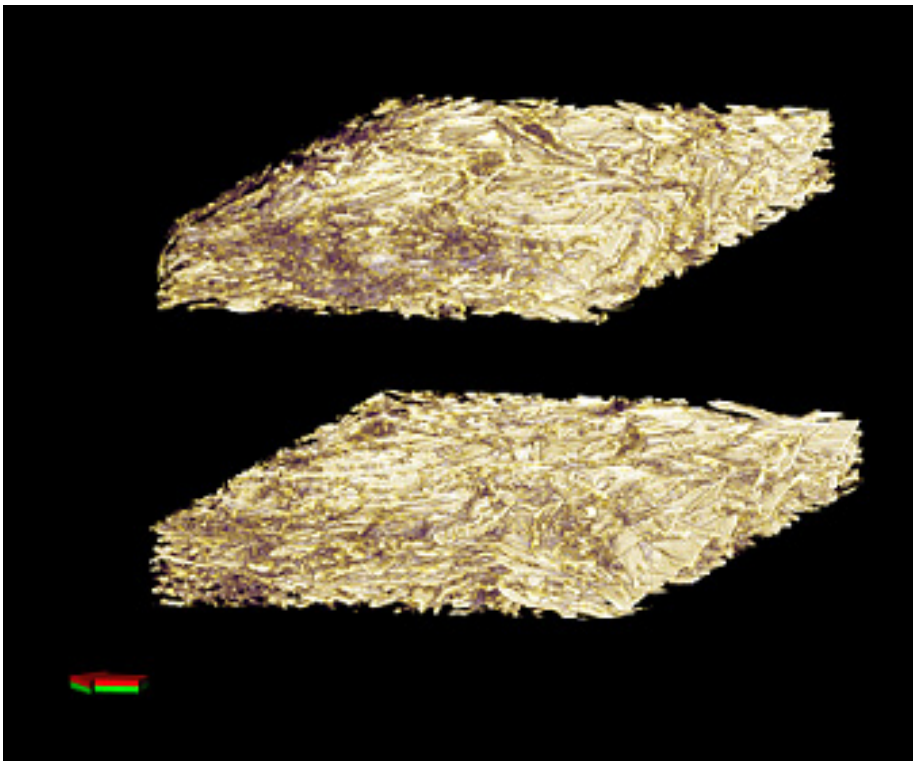

Figure 1. X-ray microtomography figures of the foam formed (top) and the water formed (bottom) samples.

Paper Characteristics Influencing the Deep Drawing Ability of Paper

PAUL-PHILIPP POST[1)], DOMINIK HUTTEL[2)], PETER GROCHE[2)] and SAMUEL SCHABEL[1)]

[1)] Chair of Paper Technology and Mechanical Process Engineering / [2)] Institute for Production Engineering and Forming Machines
Technische Universität (TU) Darmstadt
Alexanderstr. 8, 64283 Darmstadt, Germany
post@papier.tu-darmstadt.de
huttel@ptu.tu-darmstadt.de

Keywords: Deep drawing, bulge test, material characterization, forming, biaxial tension, paperboard

ABSTRACT

The mechanical properties of handsheets made from differently treated pulps were determined in uniaxial tensile tests and by a biaxial bulge test method. The bulge test system, which was specially adjusted for paperboard testing, is introduced in the first part of this paper.

Experimental investigation showed that the bulge test method was technically feasible and produced reproducible results. Comparison of bulge test and tensile test flow curves proved the theory that biaxial load leads to higher breaking strains.

A hydroforming processes for paperboard was designed. Wet handsheets made of beaten, curled kraft pulp showed the best overall forming ability while freely shrunken samples reached the highest breaking strain. Tests revealed that besides the *elongation the level of yield stress considerably influenced the forming results*

1 INTRODUCTION

Paperboard is an attractive, contemporary material used mainly for packaging. It is also increasingly attracting attention in furniture, automotive and construction industries. Paperboard has a comparatively low density, beneficial strength properties and particularly favourable environmental characteristics. However, converting of paperboard to three-dimensional structures is mainly done by folding and wrapping processes that are hardly able to produce complex three-dimensional structures. Primary shaping (pulp molding) and forming (deep drawing) are in use only for special applications. The converting of paperboard thus significantly differs from the converting predominantly used for metal or plastics.

The widespread use of deep drawing processes in paper converting is currently restrained by a lack of understanding of the factors that influence the forming results. This implies that simulation possibilities for design and layout of new geometric shapes do not exist. Suitable material laws that could be used for description of the material behaviour under multiaxial load are not available. In addition, the production of complex three-dimensional structures is also constrained by the typically poor ductility of paperboard.

Following a period of stagnation the research on deep drawing processes of paperboard has recently been intensified. The Technische Universität Dresden deals with mechanical deep drawing using punches and moulds [1]. Besides TU Darmstadt the Kungliga Tekniska högskolan of Stockholm is engaged in research concerning hydro-mechanical deep drawing [2]. This technique has widespread use in other industries and the authors believe that it also has great potential with regard to sustainable production of complex, three-dimensional paperboard carrying structures.

2 OBJECTIVES OF THE STUDY

For a targeted research of the paperboard hydroforming process it is necessary to create test and simulation methods adjusted to deep drawing. On the long run it is essential to get fundamental knowledge on the interrelationship between material properties, process design and process variables occurring in deep drawing. This shall lead to efficient as well as environmentally and economically sound production processes.

In this study a bulge test method suitable for paperboard testing is presented. The obtained mechanical properties were compared to those obtained from standard tensile tests. For this a bulge test system known from sheet metal testing was adapted, analyzed and optimized. The test data was used to evaluate the influences of different raw material compositions as well as laboratory treatments on the deep drawing ability of paper.

In the observed forming process both, the achievable deformation degree and the workpiece quality, strongly benefit from a high breaking strain. Therefore in particular those factors that influence paper's elongation were investigated in detail. This included the intentional creation of curled fibres as well as an analysis of the effects of free shrinkage.

3 BACKGROUND

3.1 Tensile tests

Tensile tests are commonly used to subject samples to uniaxial tension and thus to determine Youngs's modulus, yield strength, breaking strength and elongation at break. There are several standards describing the measurement procedure.

3.2 Bulge tests

Bulge tests are widely used in iron sheet testing as they induce a state of stress close to the load spectrum in deep drawing. This multi-dimensional state of stress can not be sufficiently reproduced by standard tensile tests. Consequently, the bulge test allows better predictability of the forming results. **Figure 1** compares flow curves derived from both test methods. Metal usually reaches higher breaking strains and stresses when subjected to biaxial load.

Recently there has been extended effort to adapt the bulge test to other materials. This has been successful for example for magnesium and aluminium alloys, thin films and wafers [3-4].

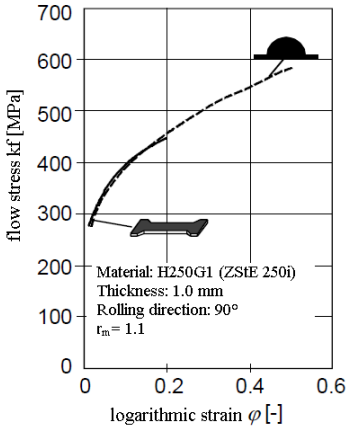

Figure 1: Comparison of bulge test and tensile test flow curves for sheet metal [5]

For testing, a sheet is usually clamped between a lower and an upper die and then pressurized fluid is applied in the lower chamber (cf. **Fig. 3**). This forces the sheet to bulge. During testing, clamping forces have to be high enough to prevent movement of additional material to the stretch region. When the elongation of the material exceeds the fracture strain the sheet will burst.

Today, the bulge profile is usually measured optically during testing. Subsequently, the flow curve can be calculated from the bulge profile and the pressure data. This requires a proper material model that accurately describes the behaviour of the test structure. Panknin [6] determined the flow curve in a bulge test with the equation:

$$\frac{\sigma_t}{r_t} + \frac{\sigma_r}{r_r} = \frac{p}{S} \qquad (1).$$

The variables he used are shown in **Table 1**.

Table 1: Variables for calculation of flow curves from bulge tests

σ_t	tangential stress	σ_r	radial stress
r_t	radius in tangential direction	r_r	radius in radial direction
p	pressure	r	bulge radius
S	surface thickness		

Figure 2 gives a schematic illustration of the bulge test and the prevailing state of stress.

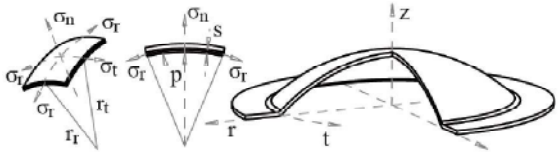

Figure 2: Schematic illustration of bulge test

In case of axial symmetry at the pole of the dome it can be shown that $r_t = r_r = r$ and $\sigma_t = \sigma_r = \sigma$. This simplifies equation (1) to:

$$\frac{2\sigma}{r} = \frac{p}{S} \quad \rightarrow \quad \sigma = \frac{pr}{2S} \qquad (2).$$

Considering that at the inner surface it holds $\sigma_n = p$ and at the outer surface $\sigma_n = 0$ the mean normal stress is $\overline{\sigma_n} = p/2$. In combination with the maximum shear stress theory the yield stress can be obtained:

$$k_f = (\sigma_{max} - \sigma_{min}) \rightarrow \; k_f = \frac{p}{2} * \left(\frac{r}{S} + 1\right) \qquad (3).$$

Equation (3) is based on Tresca. Von Mises leads to an equivalent result [6].

The yield strain can be determined to:

$$\varphi_v = \ln\left(\frac{S_0}{S}\right) \qquad (4).$$

In practice, the change in sheet thickness occurring during bulge testing is seldom measured directly. Instead, volume constancy is assumed (which usually also is the case in tensile testing). The permissibility of this assumption can be evaluated by a comparison of the yield curves derived from tensile and bulge tests.

As the surface of the sphere section is known ($A = 2\pi rh$), the strain can be calculated as follows:

$$\varphi_n = \log\left(\frac{S_0}{S_n}\right) = \log\left(\frac{S_0 * A_n}{A_0 * S_0}\right) = \log\left(\frac{A_n}{A_0}\right) \qquad (5).$$

It is standard practice to use flow curves derived from bulge tests for simulation of deep drawing processes with sheet metal. The advantage is that the state of stress prevalent in bulge testing is similar to that in the deep drawing process. Therefore the prediction of the deep drawing behaviour can be improved.

4 PAPERBOARD BULGE TEST

To adapt the bulge test to paperboard some modifications had to be made. This especially included replacing the pressurized oil by pressurized air and adding a membrane separating the pressure medium from the paper. Also dimensional changes were made to adapt the test

device to the size of Rapid Köthen handsheets. **Figure 3** shows a schema of the modified bulge test.

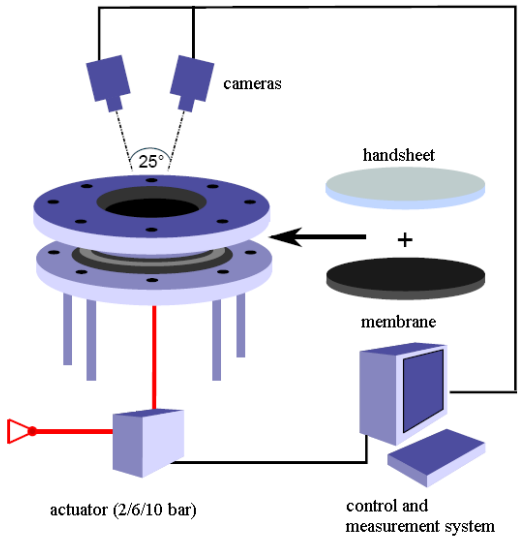

Figure 3: Paperboard bulge test (PBT)

A handsheet and a membrane are fixed under a clamp ring. The membrane separates the sheet from a pressure chamber where controlled pressure is applied. Pressure is increased till sample failure. During pressure increase the sheet deformation is observed with an optical 3D extensometer (GOM ARAMIS, commercially available). Consequently, the test can also be referred to as a bursting strength tester extended by strain measurement.

The membrane should have properties assuring the smallest possible impact on both paperboard behaviour and results of the measurement. The membrane used was made of silicone, with a linear elastic behaviour in the relevant strain area and a small Young's modulus (4 N/mm²) compared to the paperboard test specimen (1000 - 7000 N/mm²).

The membrane had the same diameter as the handsheet (200 mm). The area actually subjected to bulging had a diameter of 140 mm. To minimize effects of the fixed boundary a smaller diameter of 80 mm was used to calculate the bulge radius (using a best sphere fitting method). Thinning of paperboard was averaged inside the inner diameter of 30 mm.

The design of the clamping system and the transition radius at the edge of the blank holder can be adjusted depending on the properties of the tested paper.

A closed loop pressure control with three different controllers was used. The controllers had an accuracy of 1% and maximum working pressures of 2, 6 and 10 bar. Two separate pressure cycles were installed. One for the bulge test pressure and one for the blank holder system. Fluctuations in pressure supply were minimised by an air accumulator in combination with back-pressure valves. To assure a fixed position of the test specimen a radial crimp was integrated in the blank holder system.

5 EXPERIMENTAL STUDY

5.1 Sample preparation

To cover a wide range of commonly used raw materials and fibre treatment methods the handsheets used in this study were made resp. tested under variation of the following parameters:

- type of fibre
  - mechanical pulp (spruce)
  - hardwood pulp (beech)
  - softwood kraft pulp (mixture of 40-60 % spruce and 40-60 % pine)
- freeness
  - unbeaten
  - 25 SR
  - 50 SR
  - 70 SR
- fibre length
- softwood pulp sheets were manually cut into small stripes to decrease fibre length
- grammage
  - mass of handsheets: 8/16/24 g
  - equivalent grammage: 252/505/707 g/m²
- moisture
  - 7/10/15/20 %
- fibre curl
- shrinkage.

A Jokro-mill was used for beating. Sheets were formed in the Rapid Köthen sheet former using tap water. Finished sheets were stored at 23 °C and 50 % relative humidity (RH). Pulps were analysed with a Kajaani FiberLab system.

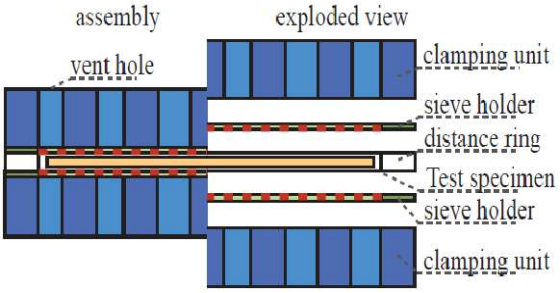

Figure 4: Drying frame for free shrinkage during drying

Free shrinkage

A drying frame (see Figure 4) was constructed to produce freely dried sheets. The sheets were first dried for 1 min using the pressurized Rapid Köthen dryer and then transferred to the drying frame that consisted of two supported sieves that could be separated by adjustable spacers. The sieves prevented the sheet from curling and bulging.

Moisturization

To adjust the moisture to the desired values the sheets were sprayed with water using a plant

sprayer and then kept in plastic bags for at least 24 hours for homogenization.

Fibre shortening

Normally fibre shortening always involves at least some part of fibrillation. It is difficult to shorten the fibres and keep all other fibre properties unchanged. However, at laboratory scale it is possible to use a guillotine and cut paper sheets into small stripes. This shortens the fibres while it hardly effects the fibrillation, specific fibre volume etc. [7]. To investigate the pure effect of fibre length on the forming ability of paperboard softwood pulp was cut into stripes of 1 mm width and analysed with Kajaani FiberLab. **Table 2** shows the fibre lengths before and after cutting.

Table 2: Fibre length of differently treated pulps

	uncut	cut
L*n* (mm)	1.24	0.73
L*l* (mm)	2.01	1.15
L*w* (mm)	2.5	1.51

	uncut, 70 SR	cut, 70 SR
L*n* (mm)	0.91	0.62
L*l* (mm)	1.74	1.06
L*w* (mm)	2.29	1.42

L*n*: arithmetic av. fibre length, **L*l*** length weighted av. fibre length **L*w*** weight weighted av. fibre length

Fibre curl

A laboratory kneader (Janke & Kunkel) was used to increase fibre curl. The rotation speed of the faster shaft was 84 rpm, the slower shaft rotated at 42 rpm. Pulp consistency was 25 %, treatment took place at room temperature. 20 minutes of kneading increased the fibre curl of the used softwood pulp from ~18 % to ~25 % (FiberLab measurement).

5.2 Tensile tests

Tensile tests were carried out according to DIN EN ISO 1924-2 at 23 °C and 50 % RH. The tensile testing machine used was a Zwick Z010 which was equipped with a 2.5 kN load cell with an accuracy of <0.3 %. The test strips were 15 mm wide, the free clamping length was 100 mm. The initial strain rate was 20 mm/min which was later adjusted due to characteristics of the bulge test. A preload of 1 N was applied. The measured flow curves served as a reference for evaluation and calibration of the bulge test.

5.3 Bulge tests

To provide a foundation for the research it was first necessary to adapt the bulge test to the requirements of paper testing. This included the structural design, but also required to conduct test trials. These were used to detect and eliminate possible sources of error and to assess the comparability of the test results with tensile tests and forming tests.

It soon became clear that the bulge test was a suitable method for paperboard testing. The test results proved to be useful for the evaluation of the hydro-mechanical deep drawing abilities of paperboard specimen. The determination of flow curves required the application of a stochastic pattern on the samples. In most cases it worked fast, repeatable and reliable. Only in some cases atypical failure behaviour of the test specimen occurred.

Failure behaviour

Figure 5 compares a typically failed sample (a) to two unusually failed samples (b, c). The typical failure behaviour of paperboard samples in the bulge test is rupture beginning from the middle. Unusual failure behaviour includes cracks that develop from a point far out of the sample's center (b) as well as punching out of the matrix at the edges (c).

The transition radius at the edge of the blank holder was determined to have decisive influence on the failure behaviour. However, several modifications and adjustments could by now not completely prevent unusual failure of some specific test specimen. "Brittle" papers like unbeaten, dry groundwood as well as high-strength papers (softwood, 70 SR) could not always be tested sufficiently. However, the great majority of samples showed the expected failure behaviour.

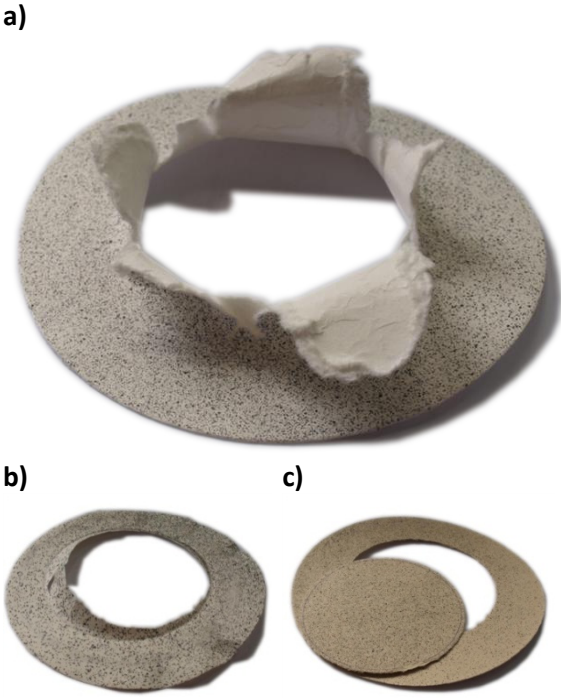

Figure 5: typical compared to unusual failure behaviour

Strain rate

The bulge test measurement is pressure-controlled. Pressure is linearly increased till failure of the sample. Consequently, a stronger test specimen with a higher Young's modulus is

subjected to a lower strain rate than a weak test specimen. As the mechanic properties of paper are strain rate dependent this implies some error when comparing results from fixed strain rate tensile tests to those from bulge testing. However, the pressure control allows varying the pressure path and thus the strain rate can be adjusted iteratively.

5.4 Experimental results

Comparison of paperboard bulge test (PBT) and tensile test (TT) flow curves

As expected, the flow curves for multi-dimensional and one-dimensional load varied. The fracture strain reached in bulge testing was in every case the same or higher than in tensile testing. However, the breaking stresses did not show a completely unified picture. In some cases they were a little lower in PBT than in TT.

Deviations between the PBT and TT flow curves especially occurred in cases of high breaking stress. The cause for this could be a higher probability of local defects due to the bigger area subjected to bulge testing compared to tensile testing. The authors also assume that further optimisation of the clamping system is necessary.

Figure 6 shows exemplary results of tensile and bulge tests of two different kinds of test specimen. Test sheets were made of softwood pulp which was beaten to 25 SR. The upper curves were detected at 7 % moisture content, the lower curves at 20 %.

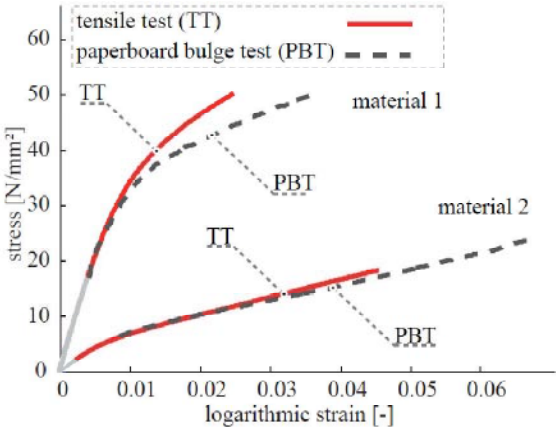

Figure 6: Comparison of flow curves for two exemplary materials.

Characteristics of the tested handsheets

The test results of the handsheets (according to section 5.1) did not show any major surprises. As it could be expected from paper physic's current knowledge, beating, wetting, free shrinkage and a bigger share of curled fibers had a strong positive impact on the specimen's fracture strain. This attribute was regarded as the most important factor affecting the forming abilities of paper. Also a higher basis weight and enlarged fiber length increased the elongation at break and therefore the aptitude for deep drawing.

Figure 7 exemplarily shows the influence of beating on the tested raw materials. Beating led to larger maximum elongations of the test specimens. However, **Figure 9a)** shows that this effect was less pronounced at increased moisture content. At 20 % moisture content beating could only slightly further increase the breaking strain. **Figure 7** also displays the general differences between the used raw materials. The softwood (SW) pulp showed the highest elongation at break. Also the results of the other screening measurements indicated that this pulp was the most promising raw material for further investigations.

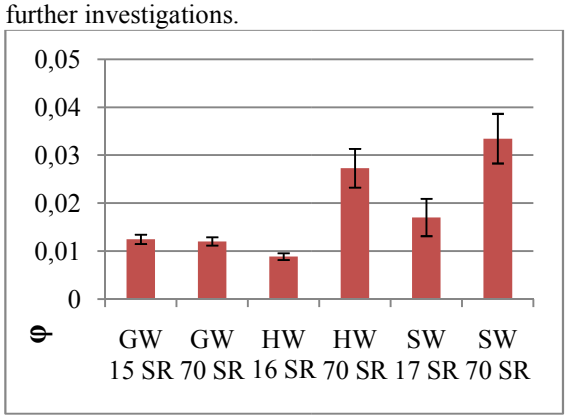

Figure 7: influence of beating on different raw materials at 7% moisture content (GW = groundwood, HW = hardwood, SW = softwood)

Figure 8 shows the changes in breaking strain occuring through different pulp treatment procedures. Curling of the fibres significantly increased the elongation at break. Also most of the freely dried handsheets showed a (very) high breaking strain. However, in this case the standard deviation was extremely high. Consequently some further investigations of the drying frame and the test method are necessary. Shortening of the fibres by ~50 % had no major influence on the breaking strain. There was only a tendency towards smaller strain values.

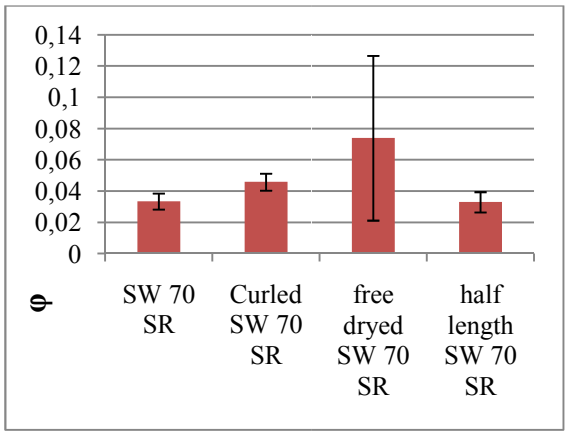

Figure 8: Effects of different pulp treatment mthods on breaking strain

Figure 9 a) / b) summarizes the influence of moisture and beating on the used softwood pulp. It can be seen that the positive effect of moisture on breaking strains reached an optimum at 15 % moisture content. Further increase did not lead to

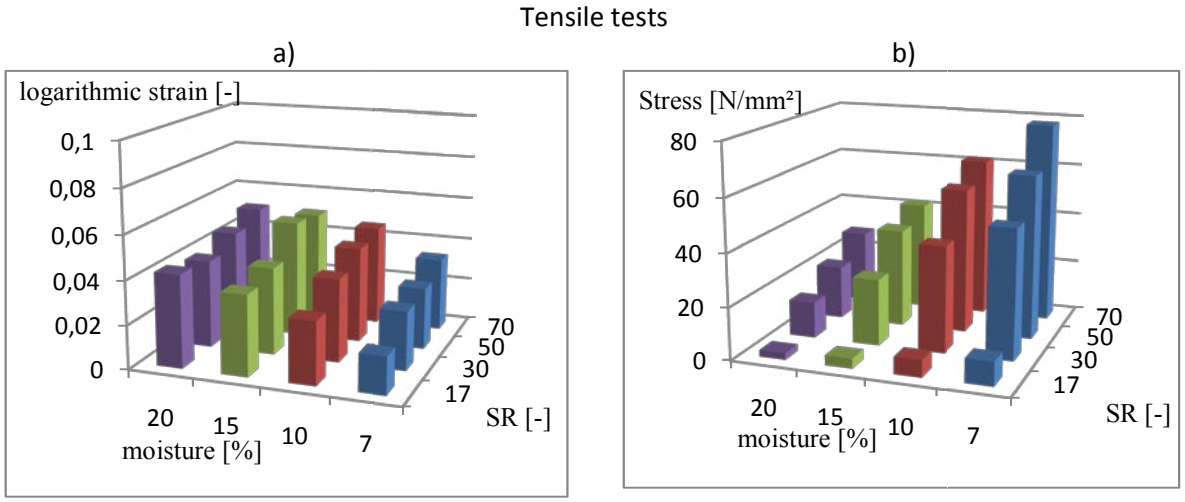

Figure 9: Tensile test

higher breaking strains (except with unbeaten pulp). The tensile strength increased with increasing SR and decreased with increasing moisture.

5.5 Forming process

To investigate the behaviour of the paperboard material in conditions of a forming process a demonstrator geometry was developed. The aim was to enhance the formability of the paperboard by a uniform distribution of the occurring elongation. A hydroforming process which was developed and optimized for paperboard was used for the investigations. The assembly of the tool as well as the geometry information are summarized in **Table 3** and **Figure 10**.

Table 3: dimensions of the mould

dm1: 20 mm	Rm1: 50 mm	hm1: 8mm
dm2: 40 mm	Rm2: 50 mm	hm2: 13 mm
dm3: 57 mm	Rm3: 25 mm	-
dm4: 72 mm	Rm4: 16 mm	-

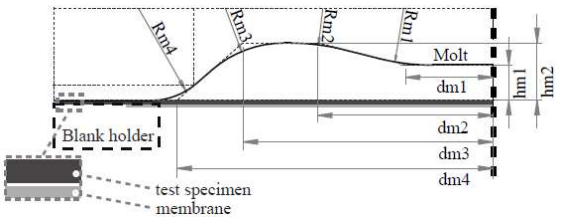

Figure 10: Demonstrator mould and assembly

The forming process was performed with different material conditions and process settings. The blank holder force as well as the fluid pressure for the hydroforming process was varied. Two different dominating failure criteria occurred: wrinkles and surface imperfections/cracks. **Figure 11** shows the two failure criteria as well as a finished product. However, optimisation of the process settings and raw material made it possible to produce drawn parts without any of the two failure types. The best overall results showed sheets that were made from softwood pulp which was beaten to 25 SR and curled, formed at a moisture content of 15 %.

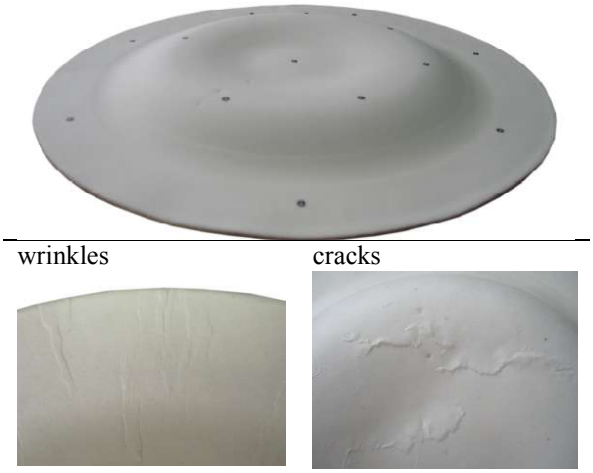

Figure 11: Optimised demonstrator model and failure criteria

Figure 12 compares two different material settings. The handsheets used are made of 25 SR softwood pulp and only differ in moisture content. With regard to better recognisability, cracks are marked in red colour and wrinkles in blue. It is obvious that the occurrence of cracks rose with increasing blank holder force as well as increasing moisture content. On the other hand wrinkles only appeared at small blank holder forces. However, at 20 % moisture content even small blank holder forces led to cracks while at the same level of blank holder force no cracks appeared with 15 % moisture content. This fact made it necessary to reconsider the initial strategy of mainly focusing on a high breaking strain of the material

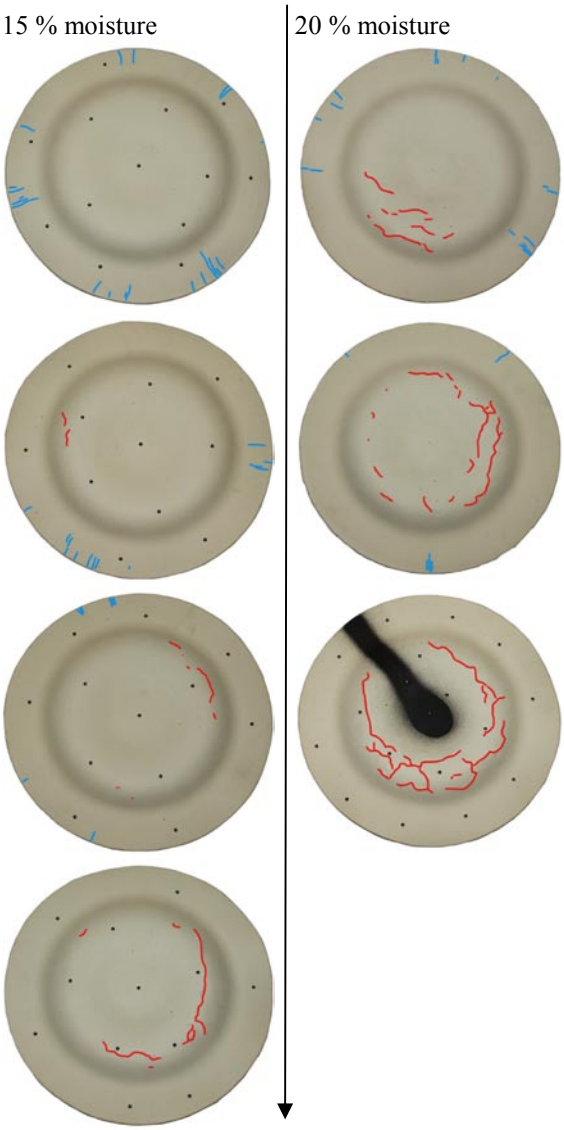

Figure 12: influence of moisture content and blank holder force on finished part quality

Figure 13 compares the flow curves of 25 SR softwood handsheets at 15 % and 20 % moisture content. The mean fracture strain is nearly the same, though the deviations at 20 % are higher. The main difference is that the yield stress of the drier material is higher. This abviously leads to a better formability as shown in the experiment.

As a result of this the yield stress level has to be taken into account when setting up the "forming ability benchmark" of the material that could be used as a pre-selection method to determine promising material conditions for forming of paperboard.

Taking a closer look at the test samples in comparison with the flow curves it can be shown that the yield stress of the dryer material is higher as the one with 20% moisture content. This leads to a better formability as shown in the experiment.

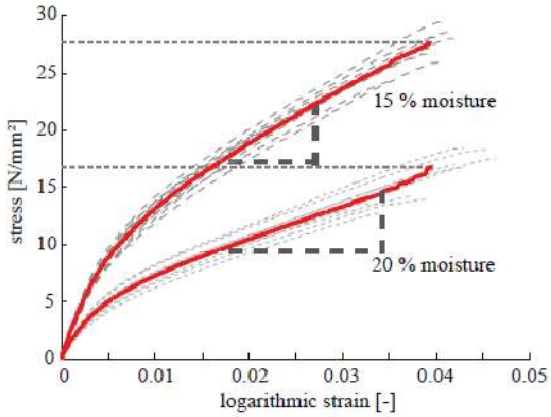

Figure 13: Flow curves of softwood, 25 SR, 20 % and 15 % moisture content

As a result of this the level of the yield stress has to be taken into the "forming ability benchmark" of the material. Altogether this could be used as a pre-selection method to determine promising material conditions for forming of paperboard.

CONCLUSIONS AND PERSPECTIVES

The paperboard bulge test proved to be an appropriate test procedure for evaluation of the material behaviour of paperboard under multiaxial load. The assumption that multiaxial load leads to higher fracture strains, as it is the case in sheet metal forming, could be validated also for paper. Furthermore, it could be shown that the maximum elongation is not the only material parameter which affects the forming behaviour. The level of yield stress is also important. Together they can be used to predetermine promising materials for forming paperboard. Of the tested materials, wet handsheets made of beaten, curled kraft pulp showed the best overall forming ability while freely shrunken samples reached the highest breaking strain.

Nevertheless, the occurrence of the shown untypical failure types, as well as the deviations of the stress-strain curves for some material settings, need further investigations.

Improvement of the material properties will stay in focus of the research project. However, further research will also deal with the transition radius at the edge of the blank holder and the crimp of the paperboard bulge, which are believed to cause differences in the stress strain curves derived from bulge and tensile tests. Also the drying frame as well as the drying procedure will be topic of further investigations. Planned optimization steps of the forming process include the installation of a heating unit and a deeper investigation of friction behaviour and surface finish.

The gained material data will be used to optimize the present FEA (finite element analysis) modeling. Improved FEA investigations not only allowed predictions of the producibility of certain geometric shapes, they could also be used to optimize and develop the forming process.

ACKNOWLEDGEMENTS

The authors would like to thank the German Research Foundation (DFG) for its financial support of the project GR 1818/37-1.

REFERENCES

[1] M. Hauptmann. Die gezielte Prozessführung und Möglichkeiten zur Prozessüberwachung beim mehrdimensionalen Umformen von Karton durch Ziehen. PhD thesis, Technische Universität Dresden (2010).

[2] L. Mozetic. Design and Development of Laboratory Equipment for Forming of Double-Curved Paperboard Surfaces. MSc thesis, KTH Stockholm (2008).

[3] S. Kaya, T. Altan, P. Groche and C. Klöpsch. Determination oft he flow stress of magnesium AZ31-O sheet at elevated temperatures using the hydraulic bulge test. *International Journal of Machine Tools and Manufacture*. 48(5):550–557 (2008).

[4] R. Edwards, G. Coles, W. Sharpe. Comparison of tensile and bulge tests for thin-film silicon nitride. Experimental Mechanics. 44(1):49–54 (2004).

[5] T. Hallfeldt. Untersuchungen zur Beschreibung des Tief- und Streckziehverhaltens höherfester Feinbleche aus Stahlwerkstoffen. PhD thesis, Leibniz-Universität Hannover (2001).

[6] W. Panknin. Der hydraulische Tiefungsversuch und die Ermittlung von Fließkurven (The hydraulic bulge test and the determination oft he flow stress curves). PhD thesis, Universität Stuttgart (1959).

[7] S. Heinemann. Neue Überlegungen zum Zusammenhang zwischen Faserlägenverteilung und Blatteigenschaften. Österreichische Papierfachtagung, Graz, 2010.

Crash of a molded pulp package

PROF. DR.-ING. B. KÜNNE, DIPL.-MATH.
D. STRACKE, DIPL.-ING. B. PALM

Department of Machine Elements / TU Dortmund
Leonard-Euler-Str. 5 / 44227 Dortmund
Germany
bjoern.palm@tu-dortmund.de

Keywords: Crash, molded pulp, tensile energy absorption, loading rate, viscoelastic

ABSTRACT

Parts for packaging made of molded pulp have many advantages. These are on the one hand recyclability and on the other hand absorbability. For this reason parts made of molded pulp are designated for packaging functions with short lifecycles. To optimize this product the material has to be studied before further simulation. As the main demand for packaging parts is to protect the packed goods during a drop the high speed deformation characteristics have to be explored. A first qualitative analysis is carried out.

1 INTRODUCTION / MOTIVATION

How can the goal of optimizing these packaging parts be achieved considering their main functionality namely to secure the goods from being damaged during transportation?

Today's transported goods have to withstand all kind of influences occurring during their journey. The mechanical applied load is one group of these influences. One of the most important mechanical functions of packages is to protect the goods from being damaged due to a drop. Therefore the package has to cushion the goods. For reasons of easy stocking packings are mostly rectangular. So the different shaped goods are fixed by cushion edges inside the box. These edges are made from either synthetic materials or from materials based on wood fibres.

In times of waste reduction it gets more and more important to raise the recyclability of the produced goods and to lower the energy amount that is necessary for production. By these means cushion packages made from wood fibres benefit from their way of production that resembles to the paper making process. Besides the renewable raw material only water is necessary for this kind of production process. Therefore packaging products made of wood fibres should be privileged.

To get a better understanding of the used material the production process of molded pulp products is described below. Chemically or mechanically separated cellulose fibres from wood are used as raw material. After the defibration in water the pulp is applied to a mesh which has the shape of the product to be formed. The water flows through the mesh while the fibres remain on the mesh surface and form the expected product. By applying a pressure difference between both sides of the mesh the water flows through the mesh either by suction or by pressing. After the forming process the part can be pressed while still being wet to increase strength. To finish the product it has to be dried, assuring a controlled drying process to keep the shape.

The quasi-static mechanical behaviour of molded pulp products is state of the art [8, 9, 10, 11, 12]. But former experiments of Baar [2] have shown a dependency between the material behaviour and the loading rate. That leads to the conclusion that it is not suitable to extrapolate the data of quasi-static experiments to crash speed.

The main requirements of packaging products are to cushion a drop and to protect the packed good. In this case the properties of packages made of molded pulp should be looked at. There mainly exist two possibilities of influencing the crash behaviour: changing the shape or changing the mechanical properties of the material. In this study the mechanical behaviour will be discussed. To improve the mechanical characteristics of the molded pulp material with focus on its crash performance the high speed deformation properties have to be studied and improved.

1.1 Interaction of mechanical values

To preserve packed goods from being damaged by falling down, the package has to cushion the goods. Therefore it is important to know the maximum acceleration which the goods can withstand. Using this information one can calculate the maximum force the goods can withstand on the one hand and the distance in which the content of the package has to be stopped on the other hand. The energy that is needed to stop the goods from falling can be calculated using this force and this distance. The tensile energy absorption of the molded pulp material has to exceed the energy which is needed to stop the falling goods. However the maximum stress is limited because the acceptable acceleration is limited. So problems can occur since those bounded values are proportional to the tensile energy absorption that has to be maximized.

2 DETERMINING FACTORS

2.1 Test speed

Baar's [2] experiments have been carried out with a maximum loading rate of about 0.004 m/s. Today's standards dealing with packaging tests like ISO 4180 [4] require a minimum test speed of 2 m/s to 3 m/s. UPS mentions in its package adviser [1] a speed of about 2.8 m/s that results from a falling

height of 0.8 m. Older standards like EN 24180 [3] ask for a test speed of 5 m/s. That shows a clear necessity for exploration of the mechanical behaviour at those speeds.

2.2 Humidity

Packages do not only have to withstand mechanical loads, they also have to cope with climatic changes. These changes consist of high and low temperatures as well as an alternating humidity. Rising humidity increases the amount of water inside the material as it is highly hygroscopic. An increasing amount of water inside the material loses the chemical fibre assembling mechanism (hydrogen bonds). As Baar's experiments have shown a significant effect of the humidity on the mechanical behaviour the humidity factor has to be taken in account. As the humidity of the climate can easily vary conditions for testing of paper are regulated in DIN EN 20187 [13]. This standard gives a value of 50% as normal and a range from 30% to 90%. Theses boundaries have to be included in the tests.

2.3 Wet compression

Tests of Baar [2] and Stumpf [5] have shown a clear dependency of the mechanical values and the degree of wet compression. It seems like the contact area between two fibres widens during compression what results in an enlarged hydrogen bond. For that reason the factor wet compression will be taken into account.

2.4 Thickness

Depending on the thickness of the material it is obvious that the force during the tensile test will vary. That is because the thickness is directly connected with the number of fibres that withstand the load. And the number of fibres is expected to be connected with the force. It has to be mentioned that this is only true for constant basic conditions such as constant compression.

3 RESPONSE VALUES

3.1 Force

The maximum force a test piece can withstand is one of the basic response values of a tensile test. In comparison to stress no more values have to be added and it can be measured directly. This is important to get basic knowledge about the interactions of this response value and the determining factors. The disadvantage of the value force for further applications is the dependency on the geometry. For designing the stress is more meaningful.

3.2 Stress

Because stress cannot be measured directly it has to be calculated from force and cross-section area. Although the cross-section area may change during the tensile test it is measured before the test and therefore expected to be constant. This is because of the lack of a possibility to measure the lateral strain in both dimensions fast enough.

3.3 Strain

The maximum strain of the tested material characterises the way until it breaks. In this study it is measured globally. This means it is measured between the clamps in which the test piece is fixed. The basic test length where the test begins has always been kept the same.

3.4 Tensile energy absorption

The energy absorption is a dimension of the capacity of a material to break down tensile energy. The inserted energy is absorbed by elastic and inelastic deformation. In ISO 1924-3 [6] the energy absorption is defined as:

$$E_{\mathrm{abISO}} = \frac{\int F \mathrm{d}l}{w_0 \times l_0}$$

That means the tensile energy absorption is the quotient of the integral of the force F over length l and the product of the width w_0 and the length l_0 of the sample before the test. Graphically it is the area below the tensile force curve. This notation is suitable for standard paper weights because in this case the thickness of the material always keeps the same. But it is not comparable with other thicknesses. As the thickness varies on the one hand because of heterogeneity of the material and on the other hand because of selective variation it is absolutely necessary to keep the value independent from the thickness. Therefore a different notation for the tensile energy absorption should be used to make the results transferable to other material geometries. Herrlich [7] defines the tensile energy absorption per volume as integral of stress and strain as follows:

$$E_{\mathrm{abHerrlich}} = \int \sigma \mathrm{d}\varepsilon$$

This way of calculation takes the thickness into account because the stress σ includes the thickness. It is displayed by the area under the stress-strain curve like it is shown in figure 1.

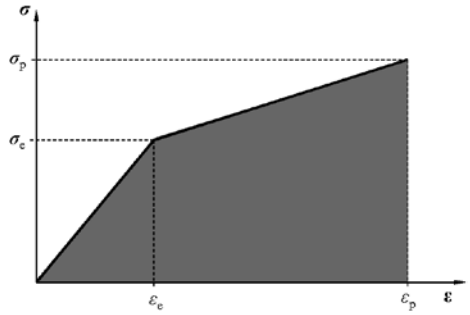

Figure 1. Tensile energy absorption

Since the energy absorption is one of the most important factors concerning a package crash, the kinetic energy during a drop has to be absorbed to protect the good.

4 SCREENING

The first test series realized with the raw material cellulose was based on a full factorial 2^4 experimental design in order to determinate the expected two factor interactions and higher degree interaction effects. The experimental data was analysed by means of regression analysis with the statistical software *JMP*. This analysis resulted in a high significance of the factors loading rate and relative humidity. Furthermore a significant three factor interaction of the factors concentration, maximum molding pressure and relative humidity could be recognized. According to the model an increasing loading rate results in a raise of the tensile energy absorption. The raw material mechanical wood pulp was under examination in a second test series. In the process of this series the determining factors were selected as analogous to the first series of tests, while a central composite design was used to compute the model. The regression analysis leaded to a high significance of the factors resource concentration and maximum molding pressure and also a two factor interaction between molding pressure and loading rate.

With the help of these experiments a significant dependency of the targeted values and the loading rate could be shown. This dependency now has to be modelled and verified in further tests with higher loading rates.

5 TEST RESULTS

Subsequently the experiments were concentrated on the raw material cellulose. After the previously realized full factorial 2^4-screening experiment a full factorial 3^4-experimental design was used in order to get a broad overview of the existing interaction effects. Due to the screening tests the determining factors concentration, maximum molding pressure, relative humidity and loading rate were selected. The total of five response values were observed, namely Young's modulus, force, tensile energy absorption, maximum stress and strain at maximum stress. To keep scattering under control and get an overall better quality of the ascertained values two iterations of the tests were run. That led to a total amount of $2*3^4 = 162$ experiments being conducted. The experimental design was generated with the statistical software *JMP* that was also used in the evaluation process.

All samples were prepared according to the experimental design; precisely a climatic chamber in which the patterns were sealed for 24 hours [2] to create the designated humidity level was used. After that we ran the tension tests. Force and distance were measured with a high dynamic measuring amplifier using a sampling rate of 96 kHz. All measuring was done unfiltered in order to maintain the possibility to filter afterwards appropriately. We used LabVIEW to grab the measured values. Afterwards these values were analysed in LabVIEW. Young's modulus was calculated by measuring multiple gradients of the linear part in the stress-strain-diagram and building the mean value of these gradients. Also using the stress-strain-diagram we calculated the tensile energy absorption by numerical integration.

The full factorial experimental design makes it possible to observe all possible factor interactions. An extensive regression analysis using the statistical software JMP was made for model generation and validation. All five response values were transformed by a Box-Cox-Transformation to stabilize variance and to gain better results in the further process. Relevant outliers were detected by measuring the Cooks distance after which those were excluded from the following steps.

The common further procedure in analysing the four response values was to create a model based on the least square mean error method. Now a regression analysis was carried out. The following was investigated:

- Coefficient of determination
- Analysis of variance
- Residual analysis

5.1 Tensile Energy absorption

The generated model for the response value energy absorption yielded in:

R^2 (coefficient of determination)	0.8
P (analysis of variance)	< 0.0001
P (Shapiro-Wilk-W-Test)	0.5067

and is illustrated in figure 2.

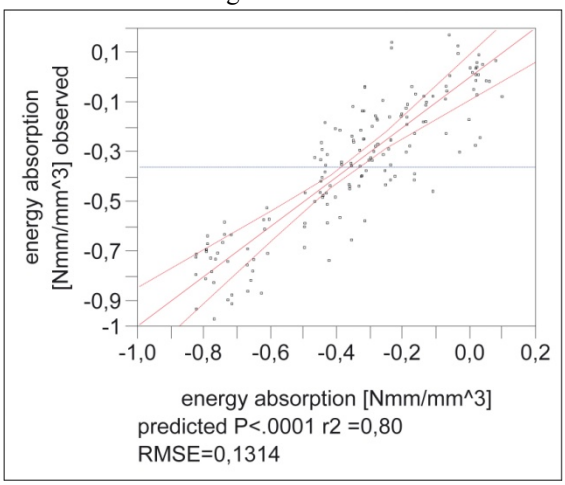

Figure 2. Comparison of observed and predicted response value tensile energy absorption

Because of the Shapiro-Wilk-Test one can say that the residuals originate from a Gaussian distribution (see figure 4). Approximately 80% of the energy

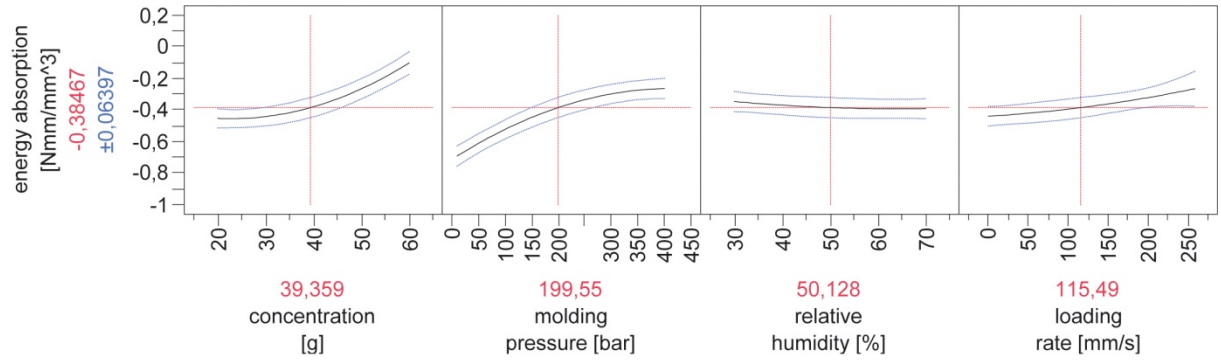

Figure 3. Influence of the determining factors on tensile energy absorption

absorption variation can be explained by the four determining factors, the remaining 20% are statistically unexplained.

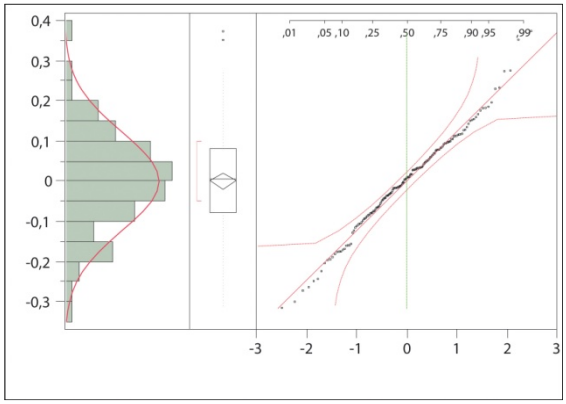

Figure 4. Distribution of residuals (tensile energy absorption)

The analysis showed six highly significant factors, namely molding pressure, concentration, loading rate, concentration squared, molding pressure squared and concentration times molding pressure. While molding pressure is the factor with the highest impact on the response value, loading rate comes at third place.

Considering the previous results one can postulate that the found model is capable of describing the observations. In figure 3 we see the determining factors influence on the energy absorption qualitatively.

As you can see a rise of the loading rate leads to increasing energy absorption. The same counts for molding pressure and concentration, while the relative humidity is anti-proportional to energy absorption.

5.2 Force

Examination of the response value force led to these parameters:

R^2 (coefficient of determination)	0.95
P (analysis of variance)	< 0.0001
P (Shapiro-Wilk-W-Test)	0.0526

Figure 5 shows the models accuracy graphically. It is obvious that the model has a huge potential in describing the observed processes. The Shapiro-

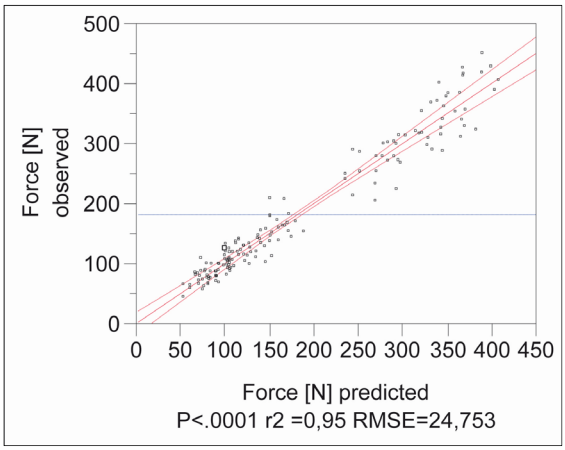

Figure 5. Comparison of observed and predicted response value force

Wilk-Test shows, that the residuals are normally distributed (figure 6).

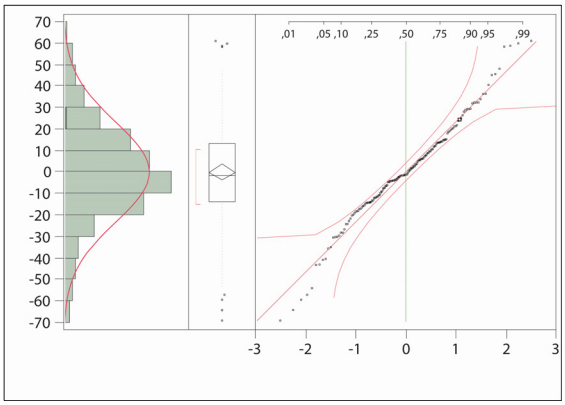

Figure 6. Distribution of residuals (force)

We observed eight highly significant factors, which are as follows:

- Concentration
- Concentration * Concentration
- Loading rate
- Molding pressure
- Relative humidity
- Concentration * Loading rate
- Relative humidity * Relative humidity
- Concentration * Relative humidity
- Concentration * Molding pressure * Relative humidity * Loading rate

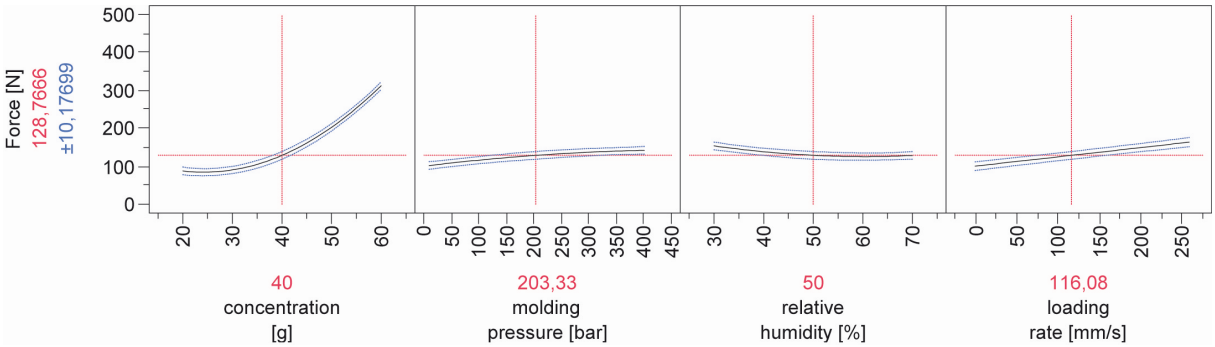

Figure 7. Influence of the determining factors on force

Concentration and Concentration squared are the most influencing factors according to a Pareto-Diagram. Right after these two there is loading rate as third most significant factor.

The determining factors exert these influences on the response value force

All determining factors except relative humidity are proportional to the measured force (see figure 7). An isolated increasing of one of those factors leads to an increase of the response value as well. On the other hand it is shown that a decreasing of relative humidity leads to a higher breaking force.

5.3 Maximum Stress

The analysis of this response value led to the following important values (see figure 8):

R^2 (coefficient of determination)	0.86
P (analysis of variance)	< 0.0001
P (Shapiro-Wilk-W-Test)	0.4044

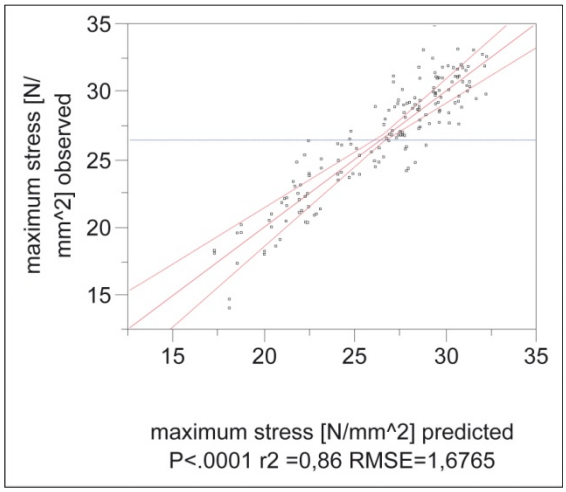

Figure 8. Comparison of observed and predicted response value maximum stress

The Shapiro-Wilk-Test shows that the residuals originate from a Gaussian distribution (figure 9).

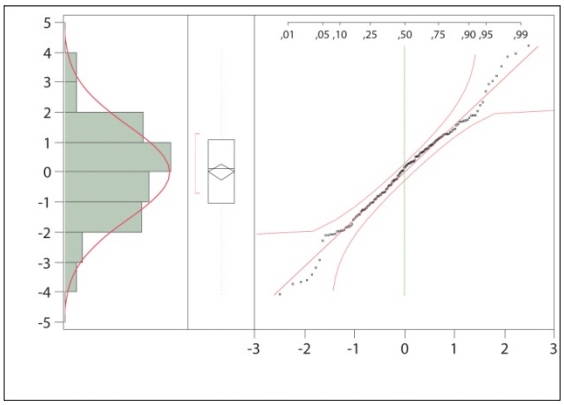

Figure 9. Distribution of residuals (maximum stress)

Thus the used least square mean error method is also a maximum-likelihood estimation. About 86% of the maximum stress variation can be explained by the determining factors.

A total of six highly significant factors were calculated in the model. Concentration, concentration squared, molding pressure, molding pressure squared and loading rate were found. Additionally relative humidity plus a four factor interaction of concentration, molding pressure, relative humidity and loading rate is observable. A Pareto-Diagram shows that molding pressure is the factor with highest impact. Now loading rate follows up as determining factor with the second highest impact.

Concentration, molding pressure and loading rate seem to be proportional to the maximum stress (see figure 10). At very low concentration the four factor interaction of all four determining factors affects the negative gradient in the concentration diagram. Relative humidity once again is inversely proportional to the maximum stress.

5.4 Strain at maximum stress

The linear regression analysis of the generated model with this response value yields to the following values (see figure 11):

R^2 (coefficient of determination)	0.75
P (analysis of variance)	< 0.0001
P (Shapiro-Wilk-W-Test)	0.1483

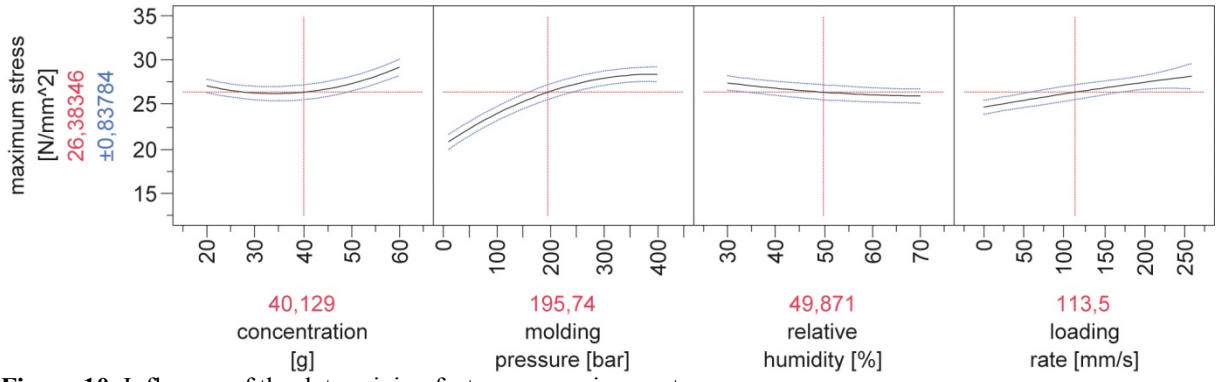

Figure 10. Influence of the determining factors on maximum stress

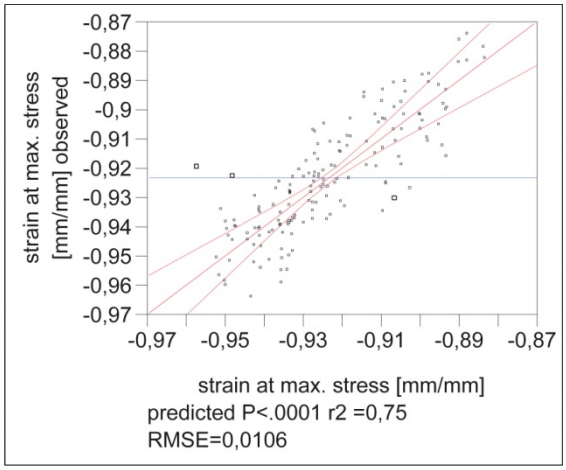

Figure 11. Comparison of observed and predicted response value strain at maximum stress

Three factors can be identified as being highly significant, namely concentration, relative humidity and a two factor interaction between both. Apart from that the following factors are significant:

- ... Concentration * Relative humidity
- ... Concentration * Concentration
- ... Concentration * Molding pressure * Loading rate
- ... Molding pressure * Relative humidity * Loading rate
- ... Molding pressure * Loading rate
- ... Concentration * Molding pressure * Relative humidity * Loading rate.

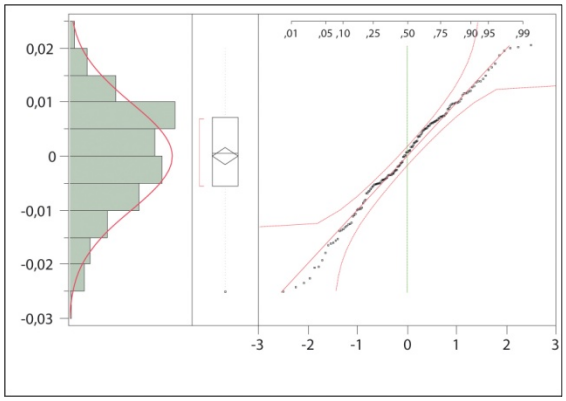

Figure 12. Distribution of residuals (strain at maximum stress)

Concentration has the highest impact on the response value. The distribution of residuals is shown in figure 12.

Now concentration, relative humidity and loading rate are proportional to the strain at maximum stress. The negative gradient in the loading rate is affected by the factor interactions. In this case molding pressure is anti-proportional to the strain.

5.5 Young's modulus

The experiments showed the following model parameters (see figure 14):

R^2 (coefficient of determination)	0.82
P (analysis of variance)	< 0.0001
P (Shapiro-Wilk-W-Test)	0.4095

The residuals are normally distributed, as the Shapiro-Wilk-Test shows (see figure 15).

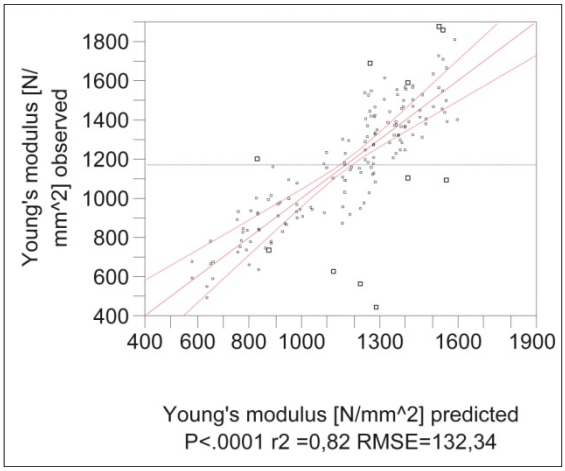

Figure 13. Comparison of observed and predicted response value Young's modulus

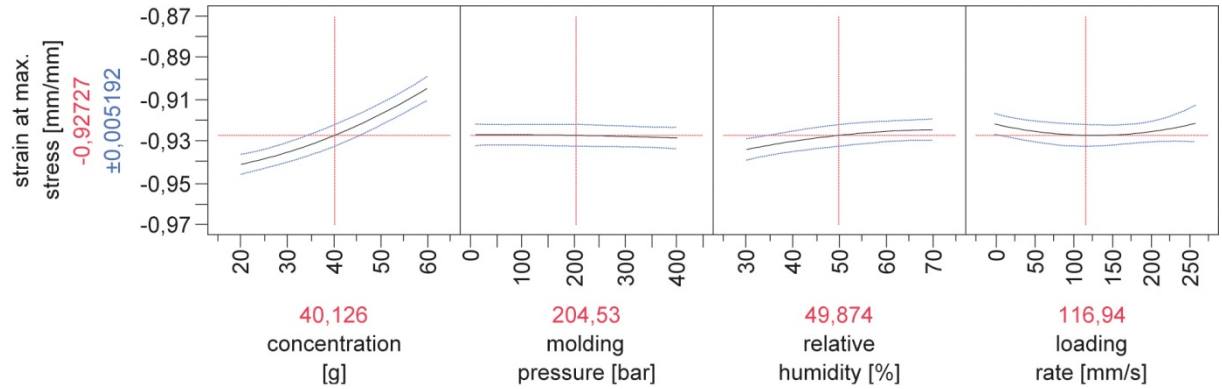

Figure 14. Influence of the determining factors on strain at maximum stress

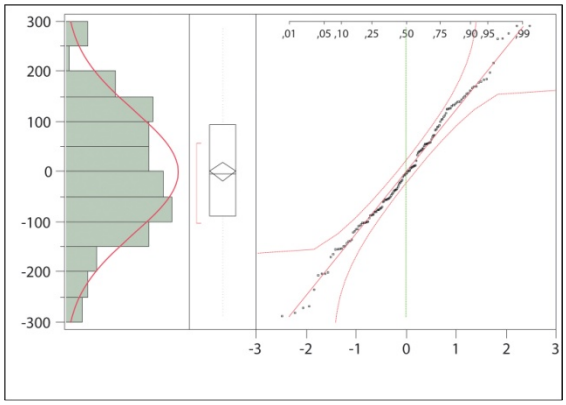

Figure 15. Distribution of residuals (Young's modulus)

A total of nine significant factors were found, namely:

- Molding pressure
- Molding pressure * Molding pressure
- Concentration
- Concentration * Concentration
- Relative humidity
- Relative humidity * Relative humidity
- Loading rate * Relative humidity
- Loading rate * Concentration
- Loading rate * Molding pressure

Once again molding pressure is the most influencing factor. Loading rate has no significant independent influence on Young's modulus, only by two factor interaction with any of the three remaining determining factors.

Figure 16 shows a nearly constant trend in the loading rate diagram. In the other three diagrams the quadratic influence of the factors is obvious. While concentration and molding pressure are proportional to Young's modulus, relative humidity is found to be anti-proportional again.

6 INTERPRETATION/CONCLUSION

The results will now be interpreted in a broader context. All response values are influenced by the determining factor loading rate. An increase in loading rate results in higher response values namely tensile energy absorption, force, maximum stress and strain at maximum stress. This underlines the necessity of studying the mechanical behaviour of molded pulp material at high deformation speeds. It is one possible way of predicting the behaviour of the material in crash situations. The results build the base for an extensive simulation.

6.1 Concentration

The maximum reached force is significantly depending on the concentration. The concentration defines the amount of fibres per volume of suspension respectively per area after forming given a constant volume of suspension. Therefore a linear relation between Force and concentration can be expected. But the results show a clearly not linear relation between those two factors. The trend of the curve is nearly quadratic. In contrast to homogeneous materials like steel the molded pulp material seems to be highly inhomogeneous.

One reason for this behaviour might be the different properties in the boundary area and the inner area of the test piece cross-section area. These properties can be mechanical e.g. differences in fibre bonds or a not equally distributed humidity along the sample cross-section area. This characteristic will be part of further examinations conducted at the department.

As the response values maximum stress, strain at maximum stress, tensile energy absorption and Young's modulus show a similar quadratic trend it is obvious that the reason for it is the same as in regard to force.

6.2 Molding pressure

The dependency of force, maximum stress tensile energy absorption and Young's modulus regarding molding pressure converges asymptotically towards a constant value. The reason for this behaviour is some kind of pressing limit. At this pressing limit no further compression of the fibre assembly and of the fibres can be achieved. There is no more space between the fibres and the fibres themselves are flattened. More pressing would not change the fibre arrangement.

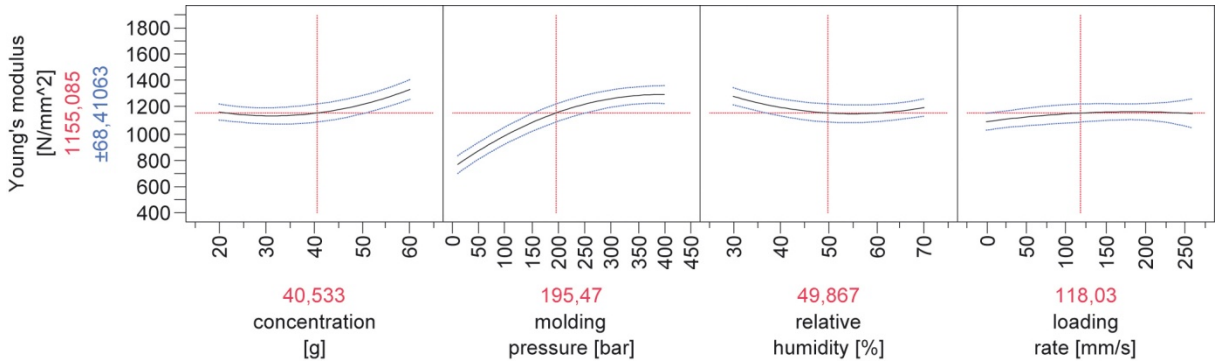

Figure 16. Influence of the determining factors on Young's modulus

The influence of the molding pressure on the strain at maximum stress can be seen in interactions with other determining factors exclusively.

6.3 Relative humidity

The response values force, maximum stress and Young's modulus show a significant decline when relative humidity is increasing. Young's modulus is declining even quadratically. The reason for that can be found in the chemical fibre bonds. A rising humidity leads to a rising amount of water content inside the material. This water moistens the bonds between the fibres and therefore weakens the material. At the same time the material gets more ductile leading to an increase in strain at maximum stress.

6.4 Loading rate

An increase in loading rate yields in a linear ascent of force, tensile energy absorption and maximum stress. This can be seen from the linear factors in the respective model equations. On the other hand there are no direct dependencies on loading rate for the response values strain and Young's modulus. There can only be observed two to four factor interactions with concentration, molding pressure and relative humidity.

It can be concluded that loading rate has no direct and independent influence on the targeted values Young's modulus and strain at maximum stress and thus only very small interactive dependencies of higher degrees are obvious. One possible explanation for the significance of the interaction apart from the insignificance of the one factor dependency is the variation of the test results. If the dependency of the factors is smaller than the variation of the test results the statistical analysis will not recognize the significance. To get a clearer view of the relation between these factors further tests have to be conducted.

The clear dependency of the targeted values and the loading rate leads to the conclusion that the material behavior of molded pulp is definitely time dependent.

It is known from paper that the material is viscoelastic. That means that under a defined force the material weakens over time. Principally there always exist creeping deformations. In most cases these creeping deformations are very small in respect to other deformations like elastic and plastic deformations. The results show that in case of molded pulp creeping seems to have a wider, not negligible, influence. The goal is to perform a deep analysis of these important influences. This is necessary for understanding the processes that take place in the molded pulp material. With the help of this knowledge it will be possible to perform a goal-oriented optimization of the molded pulp material regarding the high speed deformation. This optimization will allow an improvement of the crash performance of molded pulp packages according to their requirements.

REFERENCES

[1] UPS (Hrsg.): *Verpackungsleitfaden: Transportverpackung für den Einzelversand.* http://www.initiative-gut-verpackt.de/download/UPS-Verpackungsleitfaden_2004.pdf. Version: 2004. Leitfaden

[2] BAAR, Alexander: *Modellierung der Werkstoffeigenschaften von Papierfaserprodukten als Grundlage für deren konstruktive Gestaltung.* Soest, Technische Universität Dortmund, Fachgebiet Maschinenelemente, Diss., 2006. https://eldorado.tu-dortmund.de/bitstream/2003/22145/1/Diss_Baar_Bib.pdf

[3] Standard DIN EN 24180-2 Februar 1993. *Versandfertige Packstücke; Allgemeine Regeln für die Erstellung von Prüfplänen*

[4] Standard DIN EN ISO 4180 Dezember 2010. *Verpackung - Versandfertige Packstücke - Allgemeine Regeln für die Erstellung von Prüfplänen*

[5] STUMPF, Christian: *Systematische Optimierung der mechanischen und hygroskopischen Eigenschaften von Faserformprodukten.* Dortmund, Technische Universität Dortmund, Fachgebiet Maschinenelemente, Diss., 2010

[6] Standard ISO 1924-3 Juni 2007. *Papier und Pappe – Bestimmung von Eigenschaften bei zugförmiger Belastung - Teil 3: Verfahren mit*

konstanter Dehngeschwindigkeit (100 mm/min)

[7] HERRLICH, Norbert: *Kunststoffpraxis: Konstruktion*, Weka Media Gmbh & Co. KG, Kissing, 2004

[8] CHEN, J.; WANG, M.; WANG, H.; JI, X.; JI, H.; FAN, Jinghong: An experimental and numerical investigation of cushioning mechanism of mold pulp structure. In: *Advances in Heterogeneous Material Mechanics (ICHMM-2008).* Huangshan, China: DEStech Publications, Juni 2008, S. 988–992

[9] GAVAZZO, G. B.; LANOUETTE, R.; VALADE, J. L.: Study of the important variables of a pulp molding process Étude des variables importantes d'un procédé de moulage de pâte. In: *ATIP* 57 (2003), Nr. 4, S. 47–52 & 54

[10] WANG, H.; JI, H.; MIAO, H.; CHEN, J.; WANG, H.: Research on compression mechanical behaviors and constitutive relation of molded pulp material. In: *Jixie Qiangdu/Journal of Mechanical Strength* 31 (2009), Nr. 3, S. 382–386

[11] JI, H. W.; SHAO, W. Q.;WANG, H. M.; LAN, J.: Mechanical Properties of Molded Pulp under Various Loading Conditions. In: *Chinese Packaging Engineering* (2007), Nr. 08

[12] LIN, D. M.; CHEN, Y. M.; ZHANG, X. C.: Nonlinear elastic viscoplastic model of molded pulp material and its experimental verification. In: *Zhongguo Zaozhi Xuebao/Transactions of China Pulp and Paper* 23 (2008), Nr. 2, S. 91–95

[13] Standard DIN EN 20187 EN 20187 November 1993. *Papier, Pappe und Zellstoff - Normalklima für die Vorbehandlung und Prüfung und Verfahren zur Überwachung des Klimas und der Probenvorbehandlung*

Session 6

Theory of Paper Strength

The Hyperbolic Theory of Light Scattering, Tensile Strength and Density in Paper

GERARD J. F. RING

Department of Paper Science and Engineering
University of Wisconsin-Stevens Point
Gerry.Ring@uwsp.edu

Keywords: Apparent sheet density, fiber bonding, cellulose, densification, light scattering coefficient, tensile strength, shear-lag theories, relative bonded area, solid foam, tensile energy, hydrogen-bonds, Ingmanson-Thode, process pathway, sheet structure, Kallmes-Bernier-Perez, Page, papermaking, wet pressing, refining, Shallhorn-Karnis, pore structure

ABSTRACT

The hyperbolic theory of light scattering, tensile strength and density in paper describes a sheet of paper as a matrix of cellulose having a characteristic material strength and having both open and closed pores dispersed through the cellulose forming a solid foam.

Two principle hyperbolic equations are presented: an equation describing the conservation of tensile strength and an equation describing the conservation of mass as functions of light scattering. From these two equations, three additional equations are derived: an equation relating tensile strength to sheet density, an equation relating light scattering to total pore volume, and an equation relating tensile strength to total pore volume.

The conservation of tensile strength equation varies with processing for a given cellulose pulp. Variable refining levels at constant levels of wet-pressing produce separate curves for each wet-pressing level. Correspondingly, variable wet-pressing levels produce separate curves for each level of constant refining. Hydrolyzing pulps or cutting fibers to shorten the average degree of cellulose polymerization shifts the curves to lower tensile strengths. The conservation of mass equation results in a single curve regardless of processing or reduction in the degree of cellulose polymerization.

The concept of relative bonded area (RBA) measurement using light scattering as developed by Ingmanson and Thode is shown to be invalid for paper by this hyperbolic theory. The validity of relative bonded area by any technique is also questioned.

In addition, the Page tensile strength equation is demonstrated not to be a function of fiber properties but only a function of pore volume. Shear lag theories where either a critical fiber length or a critical RBA is used to produce a weak bonding equation and a strong bonding equation are shown to be suffering from a subtle mathematical error. Once this error is removed the weak bonding equations are eliminated and the strong bonding equations become identical to the Page equation.

1 INTRODUCTION

The hyperbolic theory of light scattering, tensile strength and density (HSTD) in paper describes the tensile failure of paper as a function of only two variables: pore volume and the strength of cellulose at its maximum density. The customary fiber properties (measured after pulping) of length, coarseness, fiber strength, and fiber-to-fiber bonding strength are not necessary in HSTD theory. Also not necessary are fiber conditions such as the degree of crimping, kinking, and curling [1]. HSTD theory treats paper, not as a structure composed of hydrogen-bonded fibers, but as a cellulosic material with air pores randomly dispersed throughout [2]. By this definition, paper is an example of the general category of colloidal materials known as solid foams [3].

HSTD theory will demonstrate that shear lag models such as the Kallmes-Bernier-Perez [4-7], the Shallhorn-Karnis [8], and the Page [9] equations cannot be applied to paper. Shear lag theory has been used to assess the tensile failure of fiber-reinforced composite materials, which are formed by dispersing individual fibers in an initially-liquid, continuous resin matrix [10, 11]. Once solidified, shear stresses in the matrix material result in tensile stresses in the fiber components. Fibers will break by tensile failure if their length is longer than a critical length. Fibers shorter than a critical length will pull out of the matrix material. The bond strength between the matrix and the fiber is determined by the cylindrical geometry of the fiber and is a function of the product of the bond shear strength, fiber perimeter, and fiber length. When fibers are longer than the critical length, the composite tensile failure is described by a non-linear equation incorporating both fiber strength and bond shear strength referred to as well bonded. When fibers are shorter than the critical length, tensile failure is described by a linear equation incorporating only bond shear strength referred to as loosely-bonded.

Papermaking fibers are assumed to function as both reinforcing fiber and matrix in shear lag analysis. There is no liquid matrix material to adhesively bond to the individual fibers. Solid fibers cohesively bond together through hydrogen bonds leaving unbonded fiber surfaces. As a result, pores are formed between bonded fibers. The ratio of bonded area to total fiber area is termed relative bonded area (*RBA*) [12].

HSTD theory will show that the concept of *RBA* as an estimate of partial bonding between fibers is not applicable to paper. Furthermore, it will be shown that the mathematical definition of *RBA* is actually a parameter that transforms shear lag tensile strength equations into HSTD hyperbolas.

Shear lag models ignore the effects of processing on pulp fibers. In contrast, HSTD theory incorporates both pulp refining and wet pressing as "sheet densification pathways" described by light scattering versus tensile strength hyperbolas (TS hyperbolas). A hyperbolic pathway describes the change of state that a sheet undergoes as a particular process produces a denser and stronger sheet. Refining pathways may or may not be collinear with wet-pressing pathways. The hyperbolic process pathways of light scattering versus sheet density (DS hyperbolas) for a given pulp are all collinear. When the TS and the DS hyperbolas are equated a tensile density hyperbola (TD hyperbola) is produced. All three hyperbolas describe the TDS process space where the TD hyperbolas lie on a plane normal to light scattering surfaces. Through the light scattering and density relationships, pore volume (V) can be related to light scattering resulting in a TDV process space.

2 TENSILE/LIGHT-SCATTERING (TS) HYPERBOLAS

2.1 Basic Theory

Tensile strength measurements in paper are mathematically related to measured light scattering coefficients by a rectangular hyperbola that is origin shifted into the third quadrant. This hyperbola has the form:

$$\begin{aligned}&\left(T - T\left\langle \text{disp}\right\rangle\right)\left(s - s\left\langle \text{disp}\right\rangle\right)\\ &= \gamma\, T\left\langle \text{disp}\right\rangle s\left\langle \text{disp}\right\rangle \rightarrow \text{constant}\end{aligned}. \qquad (1)$$

The variables are defined as T, tensile strength and s, the specific light scattering coefficient. The constants are defined as $T\langle\text{disp}\rangle$, the shift of the origin on the T-axis; $s\langle\text{disp}\rangle$, the origin shift on the s-axis; and γ, a dimensionless constant. The three-part overall constant of equation (1) is significant since it allows for the separation of dimensionally consistent variables with their respective constants. Figure 1 illustrates an example hyperbola with its corresponding second branch in the first quadrant.

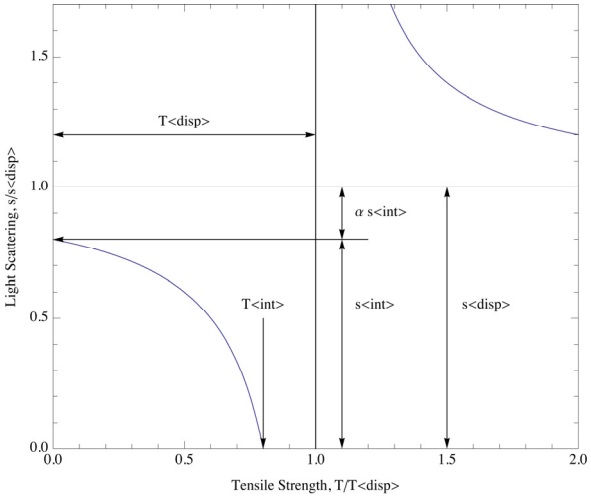

Figure 1. Origin-shifted, rectangular TS hyperbola.

Solving equation (1) as a function of T requires the definition of a hyperbolic parameter, $\Phi\langle\text{disp}\rangle$, which combines the specific light scattering coefficient, s, with its constant, $s\langle\text{disp}\rangle$, into a normalized difference:

$$\Phi\left\langle \text{disp}\right\rangle = \frac{s\left\langle \text{disp}\right\rangle - s}{s\left\langle \text{disp}\right\rangle}. \qquad (2)$$

By inserting equation (2) into equation (1) the following results:

$$\frac{T}{T\left\langle \text{disp}\right\rangle} = 1 - \frac{\gamma}{\Phi\left\langle \text{disp}\right\rangle}. \qquad (3)$$

Note that $\Phi\langle\text{disp}\rangle$ is linearly related to s and when $s = 0$, $\Phi\langle\text{disp}\rangle = 1$, but when $T = 0$, $\Phi\langle\text{disp}\rangle = \gamma$.

The intercepts of equation (1), $T\langle\text{int}\rangle$ and $s\langle\text{int}\rangle$, are related to the displacement values as

$$T\left\langle \text{int}\right\rangle = \left(1 - \gamma\right) T\left\langle \text{disp}\right\rangle$$

and

$$s\left\langle \text{int}\right\rangle = \left(1 - \gamma\right) s\left\langle \text{disp}\right\rangle. \qquad (4)$$

A useful re-expression of equation (1), produced by substituting $s\langle\text{int}\rangle$ for $s\langle\text{disp}\rangle$ and incorporating the dimensionless constant, α, defined by

$$\alpha = \frac{s\left\langle \text{disp}\right\rangle - s\left\langle \text{int}\right\rangle}{s\left\langle \text{int}\right\rangle},$$

is

$$\left(T - T\left\langle \text{disp}\right\rangle\right)\left(s - \left(1 + \alpha\right)s\left\langle \text{int}\right\rangle\right) = \alpha\, T\left\langle \text{disp}\right\rangle s\left\langle \text{int}\right\rangle. \qquad (5)$$

Making

$$\gamma\, s\left\langle \text{disp}\right\rangle = \alpha\, s\left\langle \text{int}\right\rangle,$$

and

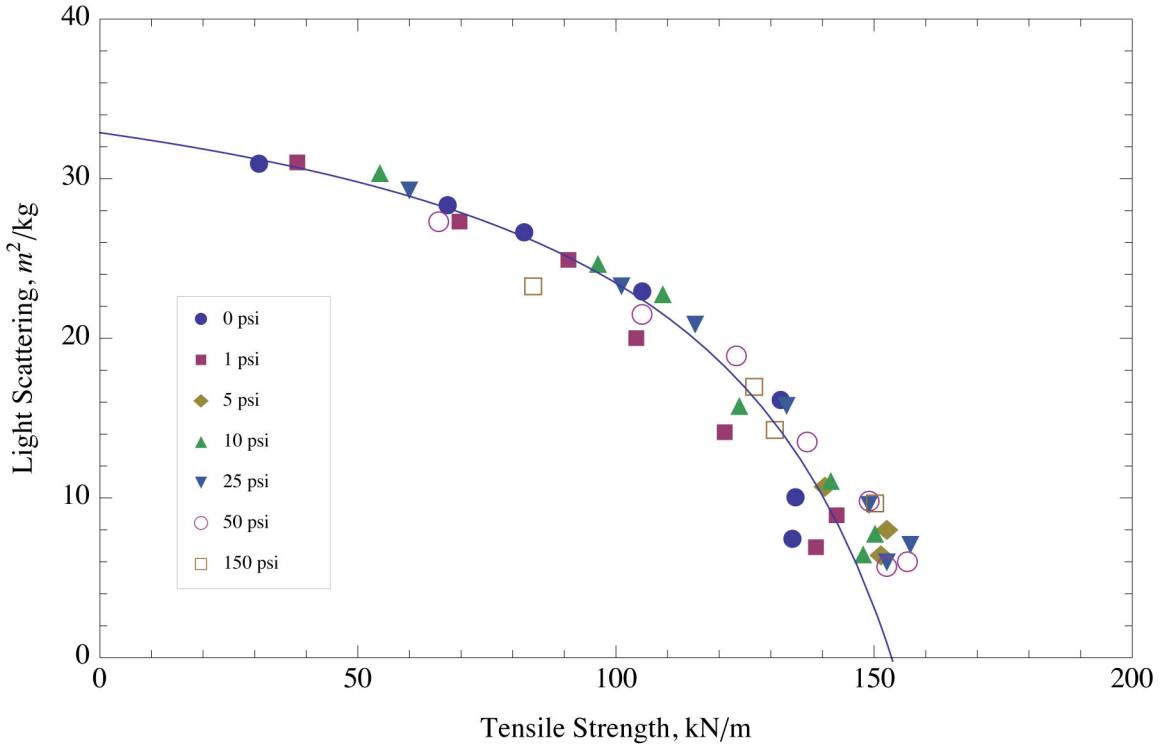

Figure 2. TS hyperbola for Ingmanson/Thode data.

$$\gamma = \frac{\alpha}{1+\alpha}. \tag{6}$$

In similar fashion to equation (2), a hyperbolic parameter, $\Phi\langle \text{int} \rangle$, can be defined for equation (5):

$$\Phi\left\langle \text{int} \right\rangle = \frac{s\left\langle \text{int} \right\rangle - s}{s\left\langle \text{int} \right\rangle}. \tag{7}$$

Note that $\Phi\langle \text{int} \rangle$ is also linearly related to s and when $s = 0$, $\Phi\langle \text{int} \rangle = 1$. But, when $T = 0$, $\Phi\langle \text{int} \rangle = 0$. Solving equation (5) for $T/T\langle \text{disp} \rangle$ yields:

$$\frac{T}{T\left\langle \text{disp} \right\rangle} = \frac{\Phi\left\langle \text{int} \right\rangle}{\alpha + \Phi\left\langle \text{int} \right\rangle}. \tag{8}$$

Equation (8) can be rewritten in a linear form, ($1/T$ versus $1/\Phi\langle \text{int} \rangle$):

$$\frac{1}{T} = \frac{1}{T\left\langle \text{disp} \right\rangle} + \frac{\alpha}{T\left\langle \text{disp} \right\rangle \Phi\left\langle \text{int} \right\rangle}. \tag{9}$$

$\Phi\langle \text{disp} \rangle$ is linearly related to $\Phi\langle \text{int} \rangle$ in the following manner from equations (2), (4), and (7):

$$\Phi\left\langle \text{disp} \right\rangle = \gamma + \left(1-\gamma\right)\Phi\left\langle \text{int} \right\rangle.$$

2.2 Relative Bonded Area

The most direct application for TS hyperbolas is the concept of measuring relative bonded area (*RBA*) in paper via the Ingmanson/Thode procedure [13]. *RBA* is hypothesized to be the ratio of bonded fiber surface area to the total fiber surface area available for bonding in a sheet of paper. Ingmanson and Thode proposed using light scattering as a simpler alternative to more involved experimental techniques such as BET etc. [14]. However, the technique has been criticized because it results in an optical bonded area that is substantially greater than the actual bonded area [15, 16]. This criticism arises from the concern that unbonded fiber-to-fiber distances less than the wavelengths of light (~ 600 nm) do not scatter light. Essentially, their technique involves measuring the specific light scattering coefficient, s, as a function of tensile strength, T, and determining the value of the total area available for bonding by assuming that this area is proportional to the extrapolated light scattering coefficient when tensile strength fell to zero, $s_{T=0}$, namely the intercept on the s axis.

Rewriting equation (5) for the specific light scattering coefficient, s, in terms of tensile strength, T, yields

$$s = s\left\langle \text{int} \right\rangle \left[1 - \alpha \left(\frac{T}{T\left\langle \text{disp} \right\rangle - T} \right) \right]. \tag{10}$$

Equation (10) is shown in Figure 2 as the regression line plotted through the data originally published by Ingmanson and Thode to establish the veracity of their technique. This data represents an unclassified, never-dried, bleached sulfite pulp that was ball milled from 0 to 250 min and wet pressed at 0 psi to 150 psi (0-1 MPa) [17]. Table I presents the hyperbolic constants calculated from this data.

Table I. TS hyperbolic constants for Ingmanson/Thode data.

$s\langle \text{int} \rangle$	32.9 m^2/kg
$s\langle \text{disp} \rangle$	41.9 m^2/kg
$T\langle \text{int} \rangle$	153 kN/m
$T\langle \text{disp} \rangle$	195 kN/m
α	.273
γ	.214

Using the definition of *RBA* given by Ingmanson and Thode where $s_{T=0}$ is the scattering coefficient corresponding to $T = 0$ and the total fiber surface area available for bonding, the following normalized difference occurs:

$$RBA = \frac{\text{bonded area}}{\text{total bonding area}} = \frac{s_{T=0} - s}{s_{T=0}} = \Phi\langle \text{int} \rangle = \frac{s\langle \text{int} \rangle - s}{s\langle \text{int} \rangle}$$

.

Consequently:

$$RBA \neq \Phi\langle \text{disp} \rangle = \frac{s\langle \text{disp} \rangle - s}{s\langle \text{disp} \rangle}.$$

2.3 The Page and the Well-bonded Shallhorn-Karnis Equation

The Page equation [9], characterized as equivalent to the well-bonded shear lag equations of the Kallmes-Bernier-Perez theory [11, 18], is actually a TS hyperbola in the form of equation (10). Shallhorn and Karnis have also demonstrated that their well-bonded equation is formally identical to the Page equation and will not be discussed separately [8, 19]. Because the Kallmes-Bernier-Perez equation is more complex, it will be discussed in the following section.

The traditional representation of the Page equation is

$$\frac{1}{T} = \frac{9}{8Z} + \frac{k_1 A \rho}{PL\, b(RBA)},$$

where

- A = average fiber cross section
- ρ = density of the fibrous material
- b = shear bond strength per unit bonded area
- P = perimeter of the fiber cross section
- L = average fiber length, and
- Z = fiber strength (zero-span tensile).
- k_1 = 12

By setting

$$T\langle \text{disp} \rangle = \tfrac{8}{9} Z, \qquad (11)$$

and

$$\alpha = \frac{k_1 A \rho\, T\langle \text{disp} \rangle}{PL\, b}. \qquad (12)$$

The following equation results

$$\frac{1}{T} = \frac{1}{T\langle \text{disp} \rangle} + \frac{\alpha}{T\langle \text{disp} \rangle\ RBA}. \qquad (13)$$

Equation (13) equals equation (9) since *RBA* = $\Phi\langle \text{int} \rangle$.

In HSTD theory, T<disp> does not represent the zero-span tensile strength, *Z*, but the tensile strength of a specimen tested at a standard span length (100 mm for handsheets). And, as will be demonstrated in the TD Hyperbolas section, the density of this test specimen is also at a maximum. Using equation (11) and the values from Table I, the calculated value of *Z* based on T<disp> is 219 kN/m while the range of *Z* values reported for Ingmanson/Thode's unclassified pulps ranged from 226 to 260 kN/m [17].

Figure 3 illustrates the plotting of equation (13) or equation (9) through the same data presented in Figure 2 and using the TS hyperbolic parameters presented in Table I. The coefficient of determination (r^2) for the curve plotted through the inverse transformed data is 0.943. This means that 94.3% of the total variability in the transformed data is explained by equation (9). Since, equation (9) is a function of only tensile strength (T) versus light scattering (s) there is very little unexplained variability in this data to assign to other possible variables such as the fiber properties in the Page equation. It should be noted that the inverse transformation of the data affects the residuals of the linear regression [20]. As seen in Figure 3, the residuals for the transformed data are greater at larger inverse values. The transformed data clusters tightly on the regression line for low inverse values but spreads noticeably at higher values. Page incorporated this double inverse plot in his original publication to demonstrate experimental verification of his theory but excluded the last two points. Page reported r^2 = 0.951 without the excluded data points [9]. Because the residuals of the transformed data expand for larger inverse values, equation (9) should be used judiciously when estimating TS hyperbolic parameters for small data sets. When estimating hyperbolic parameters, all three untransformed hyperbolas (TS, DS and TD) should be used instead.

The equivalence of the regression line through the Ingmanson/Thode data and the Page equation leads to the conclusion that *RBA* is not an independent measurement of the extent of fiber-to-fiber bonding, and should not be referred to as "relative bonded area". Rather, *RBA* should be referred only as a hyperbolic parameter or $\Phi\langle \text{int} \rangle$ in the TS hyperbola. In addition, the assumption that the product of the fiber shear bond strength, *b*, and *RBA* can estimate the shear stress, τ, between two fibers is incorrect, or more explicitly $\tau \neq b\ RBA$.

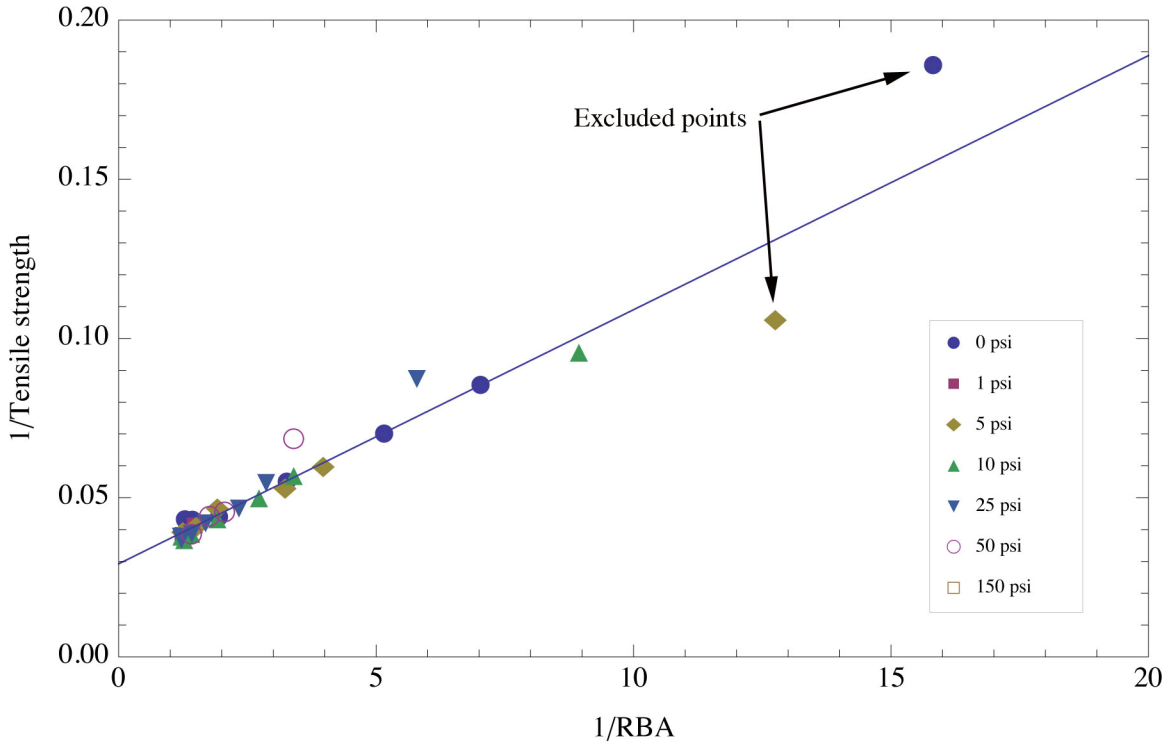

Figure 3. TS hyperbola for Ingmanson/Thode data in Page equation format.

The discussion below demonstrates that this incorrect assumption leads to another problem in the implementation of shear lag theory to paper.

2.4 The Kallmes-Bernier-Perez Equations

The Kallmes-Bernier-Perez (KBP) theory, also a shear lag model, attempts to describe the tensile behavior of planar, randomly formed fiber webs under uniform strain more comprehensively than the Page equation [4-7]. Fibers are assumed to be cylindrical in shape with well-defined surface areas. For this reason, a critical relative bonded area can be defined directly from the critical fiber length. However, this section will show that the well-bonded KBP equation is also a TS hyperbolic equation. In addition, it will be shown that a subtle mathematical error is made when *RBA* is used instead of $\Phi\langle\text{disp}\rangle$. The need for a loosely bonded equation disappears when this error is removed.

The KBP equation for well-bonded sheets ($RBA > RBA_{crit}$) related to equation (3) is

$$T_{wb} = \frac{8}{9} Z \left[1 - \frac{j k_2 A \rho^{8/9} Z}{\left(1 - f_i\right) PL\, b\, RBA} \right] \qquad (14)$$

$$= T\langle\text{disp}\rangle \left[1 - \frac{\gamma}{RBA} \right]$$

The linear KBP equation for loosely bonded sheets ($RBA < RBA_{crit}$) is

$$T_{lb} = \frac{\left(1 - f_i\right) PL\, b}{k_3 A \rho} RBA = \frac{k_2}{k_3} \frac{T\langle\text{disp}\rangle}{\gamma} RBA. \qquad (15)$$

Williams defined the parameter j as a proportionality constant incorporating the shift from the KBP designation of fiber area to that of Page (k_1/k_2) [18]. The parameters k_2 and k_3 are numerical constants and the hyperbolic parameter, γ, similar to α in equation (12), is defined as

$$\gamma = \frac{j k_2 A \rho^{8/9} Z}{\left(1 - f_i\right) PL\, b} = \frac{j k_2 A \rho T\langle\text{disp}\rangle}{\left(1 - f_i\right) PL\, b} \qquad (16)$$

where f_i is an arbitrary parameter incorporated into the KBP equation to account for the fraction of fibers initially inactive or presumably incapable of bearing a tensile load. However, f_i, similar to the other fiber property parameters used in the definitions of α (equation (12)) and γ (equation (16)), has no physical meaning independent of the primary hyperbolic relationship between light scattering and tensile strength. Combining equation (12) and equation (16) and equating the result to equation (6) demonstrates this fact:

$$\gamma = j \times \frac{k_2}{k_1} \times \frac{\alpha}{\left(1 - f_i\right)} = \frac{\alpha}{1 + \alpha}.$$

Since j must equal k_1/k_2, f_i must equal $-\alpha$.

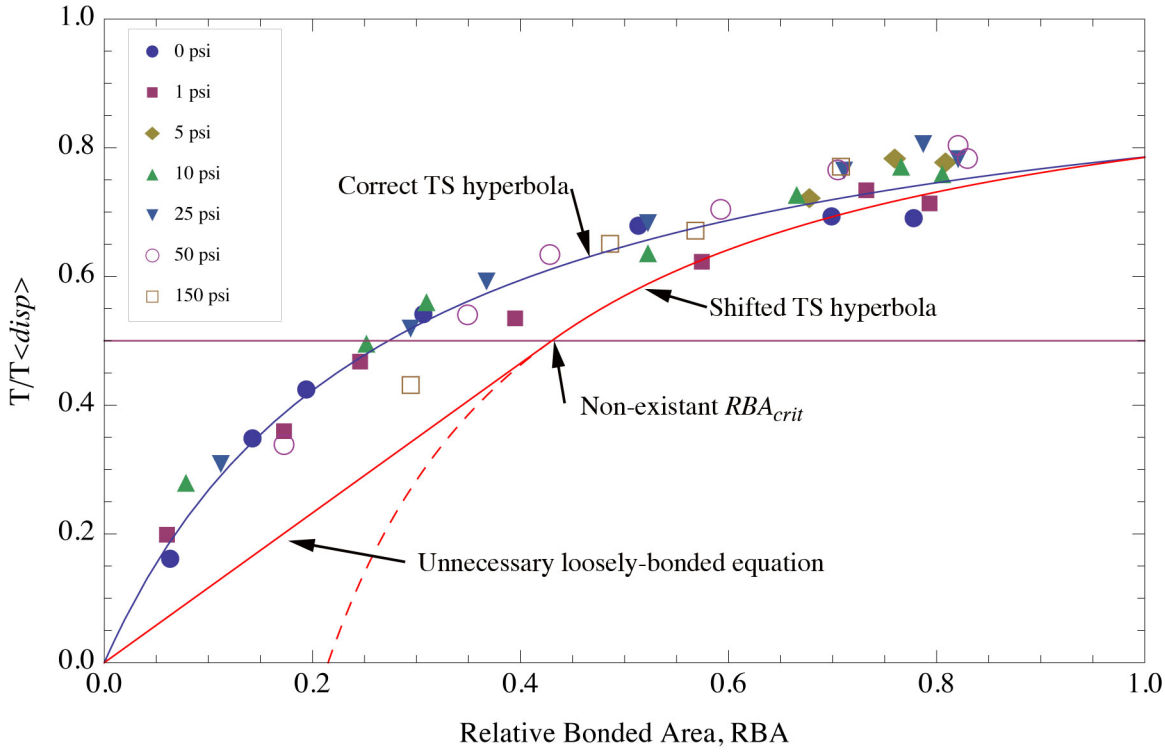

Figure 4. Incorrect use of RBA instead of $\Phi\langle\text{disp}\rangle$.

Equation (14) differs from hyperbolic equation (3) by the fact that RBA equals $\Phi\langle\text{int}\rangle$ not $\Phi\langle\text{disp}\rangle$, which reveals a hitherto unknown problem with the KBP and Shallhorn-Karnis equations, namely that *RBA* as measured by light scattering has been incorrectly applied in these equations. However, measuring *RBA* by any other technique, such as the nitrogen adsorption BET technique, would also have a problem, because when $T = 0$, *RBA* should equal γ not 0. The severity of this problem will be illustrated below.

Equation (14) and equation (15) must be equal at the critical relative bonded area, RBA_{crit}. This occurs when the slopes of both equations are equal. Thus,

$$\frac{dT_{wb}}{dRBA} = \frac{dT_{lb}}{dRBA} = \frac{\gamma T\langle\text{disp}\rangle}{RBA_{crit}^2}.$$

Resulting in $RBA_{crit} = 2\gamma$ at $T = .5T$<disp> and

$$\frac{T_{lb}}{T\langle\text{disp}\rangle} = \frac{RBA}{4\gamma}.$$

Figure 4 plots equation (8) as the regression line through the Ingmanson/Thode data using the same hyperbolic parameters from Table I. Also plotted are the well-bonded equation (14) and the loosely bonded equation (15). It is obvious that equation (8) is the correct TS hyperbola fitting the data appropriately, while equation (14) does not. Using *RBA* instead of $\Phi\langle\text{disp}\rangle$ in equation (14) results in a shifted TS hyperbola that does not equal the correct TS hyperbola of equation (3). It can be speculated that this non-fitting of the well-bonded KBP equation to the data was the reason that an arbitrary parameter, f_i, was incorporated to describe the nebulous "fraction of inactive fibers" [21].

Figure 4 also demonstrates that there is no critical RBA or fiber length eliminating the need for a loosely bonded equation. The Ingmanson/Thode never-dried pulp data show that both refining and wet pressing, densify the sheet in a continuous manner. The Kallmes-Bernier-Perez, the Shallhorn-Karnis, and the Page equations are all the same TS hyperbola when the proper hyperbolic parameter is used.

2.5 Process Pathways

Paper produced from beaten pulp is stronger than paper that is wet pressed to the same density [11]. This is particularly true for pulp that has been dried before papermaking. Page hypothesized that previously dried pulp had set in kinks, crimps and curls that were pulled out during refining to make fibers better able to take the applied tensile load [22]. However, this hypothesis assumes that the fiber property variables in the Page equation are functional and that crimped fibers behave as shorter fibers. HSTD theory contradicts this hypothesis, because the α hyperbolic parameter is constant during either a refining process or a wet-pressing process. If refining were lengthening crimped fibers, that increase in effective fiber length is not a casual factor in the observed differences between wet pressing and refining. This statement is demonstrated in Figure 5 by plotting three separate TS hyperbolas through Page's 1985 data.

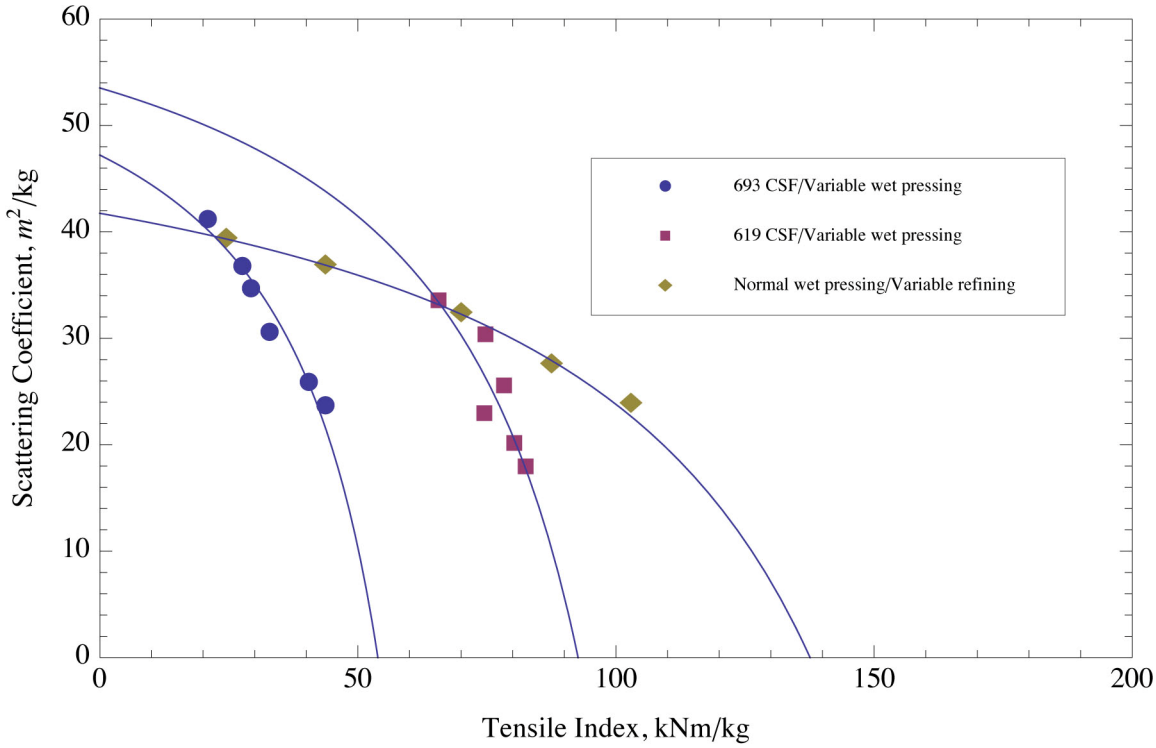

Figure 5. Process pathways through Page 1985 data.

The three TS hyperbolas are: variable wet pressing at a freeness of 693 CSF, variable wet pressing at a freeness of 619 CSF, and variable refining at standard wet pressing. Table II lists the TS hyperbolic constants determined by fitting equation (10) through the data. Notice that the hyperbolic constant term is different for each process.

Table II. TS hyperbolic constants for previously dried process pathways.

Process	***α***	***s*<int>**	***T*<disp>**	***constant***
		m^2/kg	kNm/kg	
Variable wet pressing, 693 CSF	.381	47.2	74.4	1,338
Variable wet pressing, 619 CSF	.330	53.5	123	2,172
Variable refining, standard wet pressing	.396	41.7	192	3,170

Because HSTD theory is restricted to the variation of tensile strength as a function of pore volume, the simple explanation for the divergent pathways in Figure 5 resides with fiber fibrillation occurring during refining. Since wet pressing does not fibrillate fibers, the effect of wet pressing is to densify the sheet by reducing pore volume. This direct densification process will be limited by the amount of air that is trapped in "blocked" pores.

Through fibrillation, refining will open the cellulose structure allowing blocked pores to collapse more completely during wet pressing and more importantly during drying where considerable surface tension forces will collapse the fibrillated cellulose material.

By examining Figure 5 further, additional conclusions can be drawn about *RBA* and shear lag models. At each intersection of a constant wet pressing pathway and a constant refining pathway a material state exists that can either be refined or wet pressed further. However, each of these states has two different *s*<int> values defined by each TS hyperbola. This fact presents a contradiction in the concept of *RBA*, because either a wet pressing or a refining process determines the value of relative bonded area rather than a fiber property such as a well-defined maximum surface area. Furthermore, there are two values for α at each crossing point, which means that each crossing point would have different potential values for fiber properties. Since neither of these two possibilities can be true, both *RBA* and shear lag models are not applicable to paper structure.

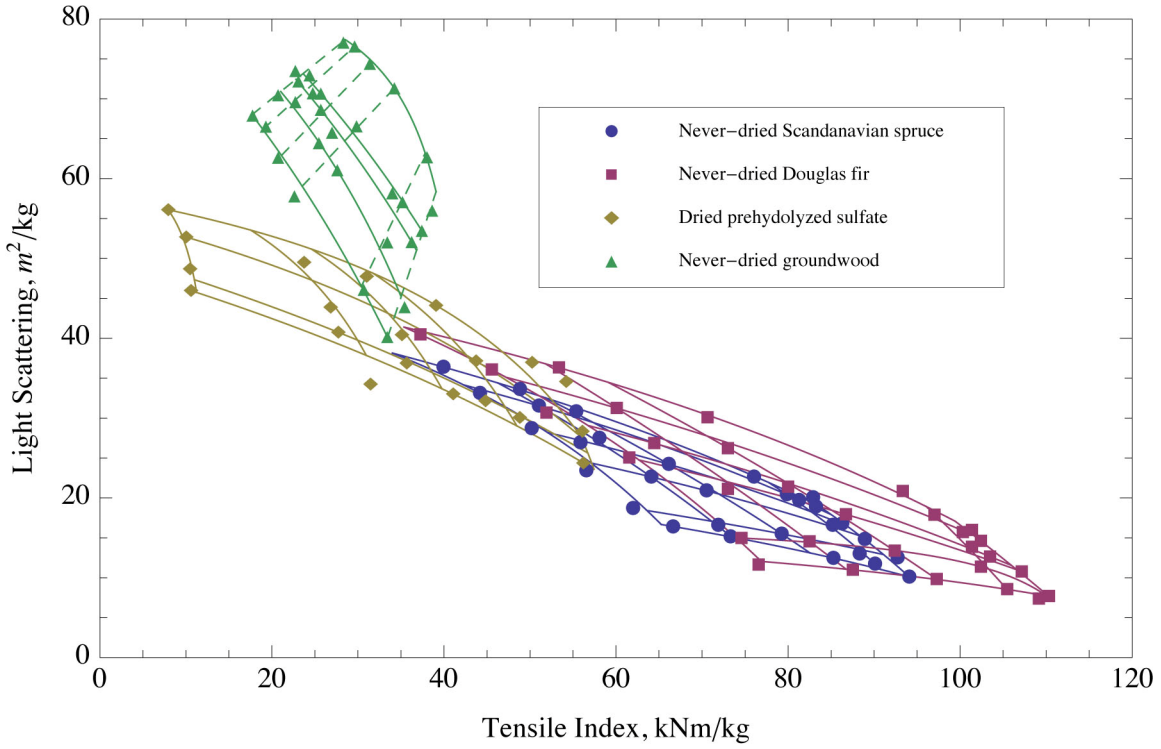

Figure 6. Rennel's 1969 data.

Rennel studied the effect of both wet pressing and refining on fiber bonding and sheet strength for four pulps and produced depictions of TS hyperbolic process pathways [23]. Figure 6 presents all four of his pulps plotted together with TS hyperbolas. The four pulps were never-dried Douglas fir, never-dried Scandinavian spruce, dried pre-hydrolyzed sulfate, and never-dried groundwood pulp. The pulps were wet pressed at intervals from .25 to 15 MPa, and refined in a PFI mil at intervals from 0 to 32,000 revs. Rennel's more extreme experimental conditions when compared to Ingmanson and Thode's produced distinct, separated TS hyperbolic process pathways that form a grid for each pulp. The never-dried Douglas fir and Scandinavian spruce are virtually identical and have over lapping grids. The dried pre-hydrolyzed sulphate pulp's grid is shifted to lower tensile strengths from chemical shortening of the cellulose polymers. While, the never-dried groundwood pulp is shifted to lower tensile strengths due to mechanical fiber fracturing, which ostensibly also results in shortening of the cellulose polymers. The groundwood pulp's grid has higher scattering coefficient values due to the presence of lignin in the high yield pulp.

The groundwood pulp is significant because refining does not fibrillate a high-yield pulp but rather breaks the fibers into smaller particles. For this reason, refining does not produce TS hyperbolic process pathways, but rather pathways that are linear functions of light scattering and tensile. Only wet pressing produces TS hyperbolic process pathways for groundwood. Figure 7 illustrates the plotting of the five, groundwood wet-pressing hyperbolas using equation (8). According to the theory of Shallhorn and Karnis all five of these pathways should be linear following the loosely-bonded shear lag equation [8]. It is rather obvious that there is no evidence of short fiber pullout since each TS hyperbola passes through each data set with no discontinuities. Furthermore, the highest degree of refining (revs = 32,000) that produces the shortest groundwood fibers follows the most non-linear TS process pathway that is also entirely in the supposedly well-bonded region ($T >$ .5 T<disp>).

Seth explored the effect of guillotining paper into thin strips in order to reduce fiber length without apparently changing any other fiber property [24]. By cutting never-dried, unbleached, softwood Kraft pulp sheets having a 2.7 mm initial fiber length into 2.5 mm, 2.0 mm and 1.0 mm strips, paper with fiber length averages of 2.7, 2.17, 1.91 and 1.47 mm respectively were produced. Figure 8 shows Seth's data as a set of TS hyperbolic wet-pressing pathways using equation (10). The data in each pathway represents wet pressing pressures ranging form 70 kPa to 7 MPa with no refining. The TS hyperbolic parameters are given in Table III. The results for the 2.17 and the 1.91 mm sheets are virtually identical.

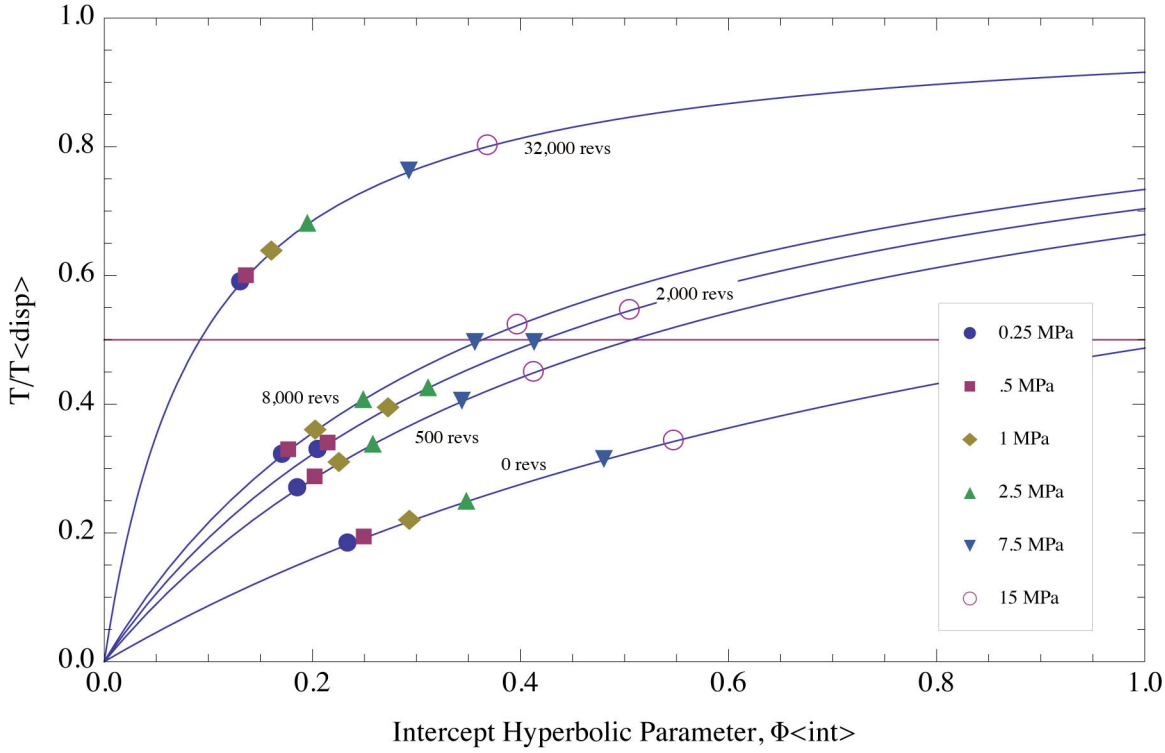

Figure 7. Rennel's groundwood TS wet pressing hyperbolas.

Figure 8 demonstrates the same shift to lower tensile strengths for Seth's cut fibers that was demonstrated in Rennel's pre-hydrolyzed sulfate and groundwood pulp when compared to non-hydrolyzed sulfate pulps in Figure 6. Cutting fibers should not change the total fiber area, but Figure 8 demonstrates that a reduction in *RBA* would be calculated as a function of fiber length at constant tensile strength. HSTD theory would explain these results in terms of improved formation due to shorter fiber length reducing the average pore size between fibers. Seth reported that improved formation did occur as fiber length was reduced [24].

Table III reveals that the hyperbolic constants for these "no refining" processes was remarkably constant in contrast to the results in Table II. It appears that refining increases the hyperbolic constant because the value of *T*<disp> is increased through more effective pore elimination via fiber fibrillation when compared to wet pressing.

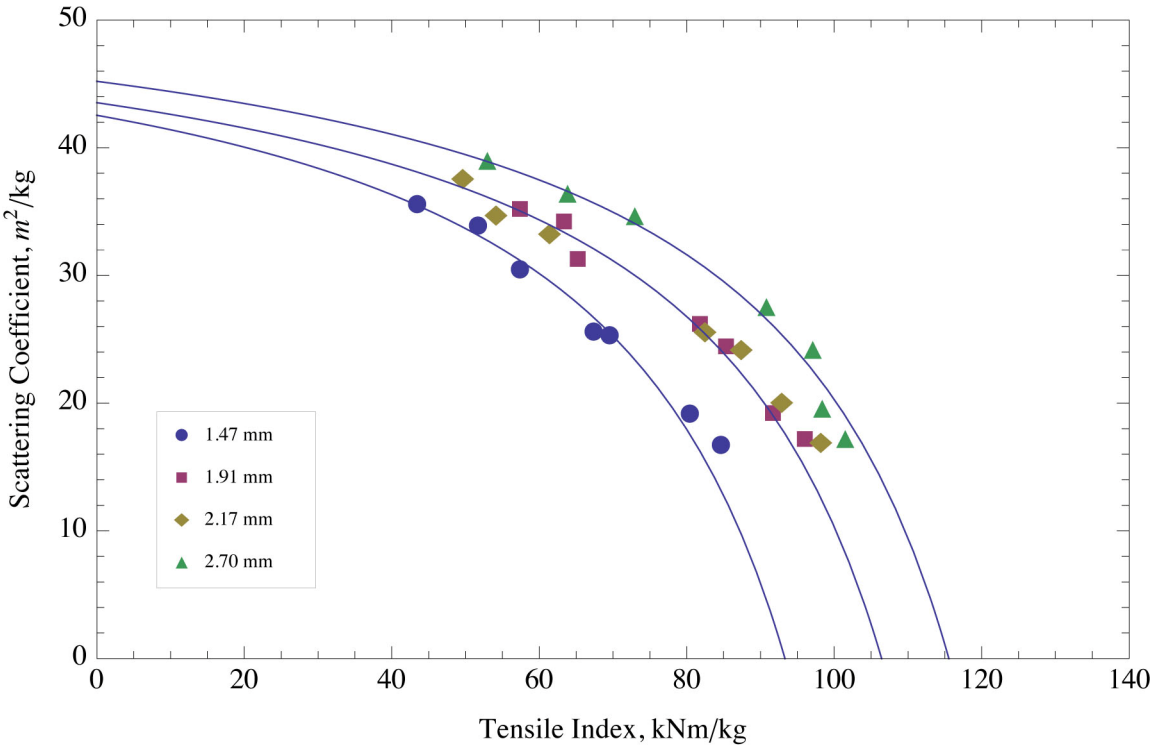

Figure 8. Effect of guillotining paper to shorten fiber length from Seth's data.

Table III. Hyperbolic constants for Seth's data.

Fiber length	α	s<int>	T<disp>	*constant*	$A\rho/Pb$
mm		m^2/kg	kNm/kg		x 10^4
1.47	0.296	42.5	121	1,522	3.00
1.91	0.260	43.5	134	1,516	3.08
2.17	0.261	43.5	134	1,516	3.52
2.70	0.236	45.2	143	1,525	3.71

The data in Table III appears to display an inverse relationship between fiber length and α that would support the original assumption of fiber property functionality in shear lag analysis expressed by equation (12). However, this correlation is specious since it also requires the acceptance of a pseudo-correlation between α and the remainder term in Table III, $A\rho/Pb$, consisting of fiber properties that would not be affected by Seth's guillotining. This observation explains why credible values for the bond shear strength, b, using these models, have never been calculated [25, 26]. When five of the six fiber properties displayed in equation (12) are measured independently, the sixth fiber property will be dependent upon these five. Fundamentally, hyperbolas have only one independent variable and one dependent variable. With the TS hyperbolas, tensile strength is dependent upon light scattering. The shear-lag theories incorporated fiber properties into the hyperbolic constant that forced the value of the last fiber property (inevitably the fiber bonding strength) to have a dependent value. For this reason, the shear-lag equations such as the Page equation were over determined in their incorporated variables.

3 DS HYPERBOLAS

Light scattering and sheet density follow a hyperbolic relationship similar to equation (1). Analogous versions of all TS hyperbolas can be written for the DS hyperbola. The relevant DS hyperbola similar to equation (10) is:

$$s = s_D \left[1 - \beta \left(\frac{D_{sheet}}{D_{\max} - D_{sheet}} \right) \right], \qquad (17)$$

where s_D is the intercept light scattering value, D_{sheet} is the apparent density of paper, and D_{max} is the density of cellulose. Because the density of cellulose is a known physical property of cellulose $D_{max} \approx 1{,}500$ kg/m^3. Only two significant figures were chosen for D_{max} due to the uncertainties implicit in the measurement of D_{sheet} [27].

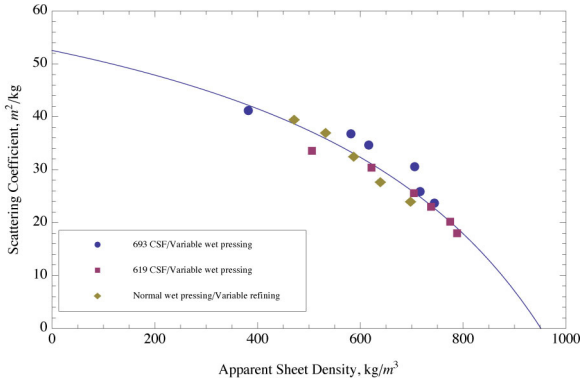

(a) DS hyperbola for Page data.

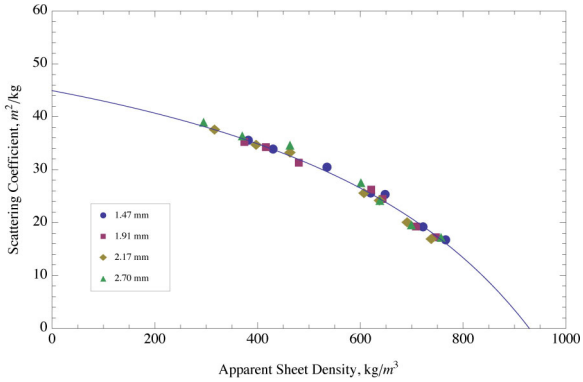

(b) DS hyperbola for Seth data

Figure 9. DS hyperbolas.

Table IV. DS hyperbolic constants for Page and Seth data.

	β	s_D
		m^2/kg
Page	0.577	52.5
Seth	0.615	44.9

Figures 9a and 9b and Table IV reveal that for a particular pulp undergoing either a wet pressing or a refining process, the data is co-linear. The explanation for this fact is that the hyperbolic constant ($\beta D_{max}\, s_D$) for DS hyperbolas is equivalent to mass. This can be shown by a simple exercise in dimensional analysis. The dimensional analysis of the DS hyperbolic constant with customary units is:

$$\beta D_{\max} s_D \Rightarrow \left(\frac{kg}{m^3}\right)\left(\frac{m^2}{kg}\right) \equiv \frac{M}{L^3} \times \frac{L^2}{M} = L^{-1}$$

The dimension of reciprocal length makes no sense for the DS hyperbola. The customary units of the light scattering coefficient are calculated by dividing the scattering power, sW, which is determined from reflectance measurements according to the Kubelka-Munk theory, by the basis weight, W, to yield kg/m^2 [14]. If the units of the light scattering coefficient were substituted with units of area (m^2) as suggested by the linear correlations between BET surface area and the lights scattering coefficient [14, 17] dimensions of ML^{-1} would result that still don't make sense. However, when light scattering's customary units

are replaced with volume the following analysis occurs:

$$\beta D_{\max} s_D \Rightarrow \left(\frac{kg}{m^3}\right)\left(m^3\right) \equiv \frac{M}{L^3} \times L^3 = M \Rightarrow \text{Mass}$$

A similar dimensional analysis of the TS hyperbolic constant *(α T<disp> s<disp>)* further demonstrates that the dimensions of volume for the light scattering coefficient are more natural than the dimensions of the customary units. For tensile strength, using the standard tensile strength dimensions compatible with the units of kN/m^2 instead of the units of tensile index (kNm/kg) is necessary. Hence with customary units the final dimensions of the constant are meaningless:

$$\gamma T\langle disp\rangle s\langle disp\rangle \Rightarrow \left(\frac{kNm}{kg}\right)\left(\frac{m^2}{kg}\right)$$

$$\equiv \frac{ML^2T^{-2}}{M} \times \frac{L^2}{M} = M^{-1}L^4T^{-2}$$

But with corrected units, the resultant dimensions are those of energy, which is very significant since the phenomenon of stretching a material until rupture involves the storage of tensile energy in the material until rupture occurs.

$$\gamma T\langle disp\rangle s\langle disp\rangle \Rightarrow \left(\frac{kN}{m^2}\right)\left(m^3\right)$$

$$\equiv \frac{MLT^{-2}}{L^2} \times L^3 = ML^2T^{-2} \Rightarrow \text{Energy}$$

Further justification for the equivalence of light scattering and pore volume will be given in the section on TDS and TDV process space below.

4 TD HYPERBOLAS

When equation (17) is combined with equation (10), a TD hyperbola results:

$$\frac{T}{T\langle disp\rangle} = \frac{\frac{\left(s<\text{int}>-s_D\right)}{\alpha s<\text{int}>} + \frac{\beta s_D}{\alpha s<\text{int}>}\left(\frac{D_{sheet}}{D_{\max}-D_{sheet}}\right)}{1+\frac{\left(s<\text{int}>-s_D\right)}{\alpha s<\text{int}>} + \frac{\beta s_D}{\alpha s<\text{int}>}\left(\frac{D_{sheet}}{D_{\max}-D_{sheet}}\right)}$$

.(18)

Figure 10 shows the TD hyperbolas for both Page and Seth. The effects of the applied processes can be seen clearly. The slopes of the wet-pressing processes are less than the slopes of the refining process. And, the effect of fiber cutting is to reduce the position of the hyperbola to lower tensile values.

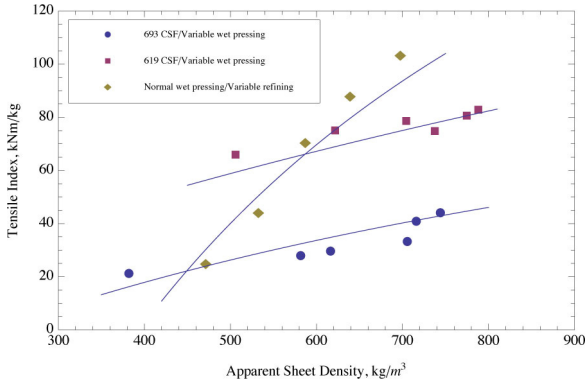

(a) TD hyperbolas for Page data.

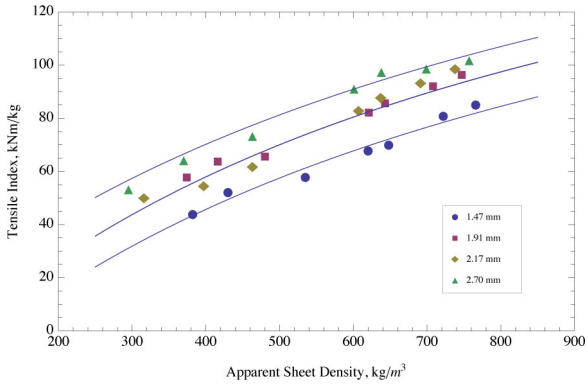

(b) TD hyperbolas for Seth data.

Figure 10. TD hyperbolas.

5 TDS AND TDV PROCESS SPACE

The TS, DS, and TD hyperbolas (equations (10), (17), and (18)) can be combined to form the TDS process space as shown in Figure 11. The purpose of TDS space is to illustrate that any final sheet state defined as $s = f(T,D)$ can be achieved by first refining and then wet-pressing. Neither refining nor wet-pressing alone can produce all states.

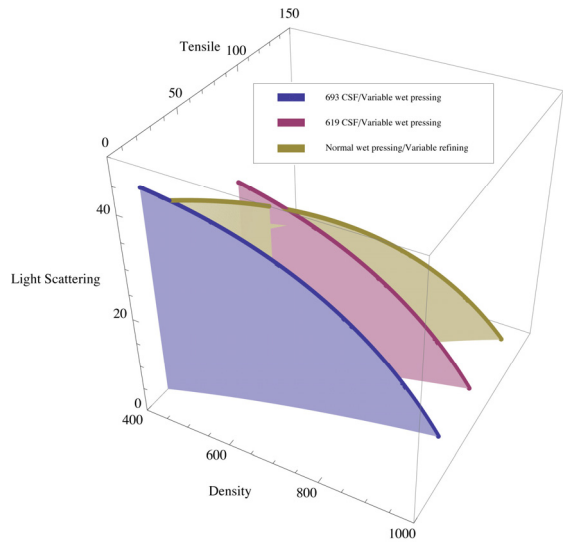

Figure 11. TDS process space for Page data.

The TDV process space can be produced by conversion of the light scattering variable into that of pore volume through equating the DS hyperbola (equation (17)) to a simple mass balance for a porous material:

$$D_{sheet}\left(V_{cellulose}+V_{pore}\right)=D_{\max}V_{cellulose}=M_{cellulose}$$

.

This results in the following hyperbola:

$$s=s_D\left(1-\beta\frac{V_{cellulose}}{V_{pore}}\right). \qquad (19)$$

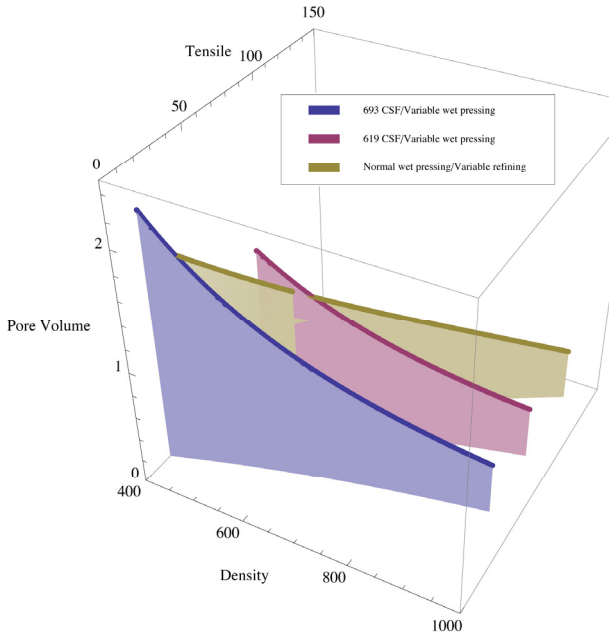

Figure 12. TDV process space from Page data.

Combining equation (19) with equation (10), a final TV hyperbola in quadrant 1 results:

$$\frac{T}{T\left\langle disp\right\rangle}=1-\frac{\alpha s\left\langle \text{int}\right\rangle V_{pore}}{\left(\left(1+\alpha\right)s\left\langle \text{int}\right\rangle-s_D\right)V_{pore}+\beta s_D V_{cellulose}}. \qquad (20)$$

Equation (20) is the mathematical equivalent of the statement made in the introduction: "The hyperbolic theory of light scattering, tensile strength and density (HSTD) in paper describes the tensile failure of paper as a function of only two variables: pore volume and the strength of cellulose at its maximum density." But, the included constants for the TS and the DS hyperbolas build in the capability to describe multi-path processes as depicted in Figure 12.

6 CONCLUSIONS

The Ingmanson/Thode method of calculating relative bonded area (*RBA*) using light scattering is a widely accepted technique [12]. It is also a very intuitive concept that pulp fibers in the papermaking process will share a planar bond area. However, HSTD theory demonstrates that the specific light scattering coefficient is responding not to the planar area of unbonded fibers surfaces, but to the volume of pores within the sheet structure. This conclusion is supported by the observation that the specific light scattering coefficient is directly related to the pore structure of paper [28, 29].

Placing an emphasis on pore volume rather than fiber surfaces shifts the focus of paper's structure from an assemblage of bonded fibers to that of a cellulose matrix with dispersed pores. Such a structure would be identical to a "solid foam" colloidal material. The papermaking process can then be divided into two sequences: a fiber-dominated sequence and a matrix-dominated sequence. The fiber-dominated sequence starts with stock preparation and continues through forming. Fibers are internally and externally fibrillated in stock preparation by refining. Fiber length controls both the flocculation of fibers in the headbox and the stock's response to shearing forces on the wire during formation. The pore structure of the sheet is finalized on the wire when consolidation occurs at the dry line on the forming unit, where the porous cellulose matrix is created. Water in the largest pores is removed from the matrix by vacuum over the flat boxes. The sheet is then densified in the wet press, and finally brought to moisture equilibrium in the dryer section where additional densification occurs through hydrogen bonding of cellulose molecules. At this point the sheet can be referred to as a hydrogen-bond dominated material [30, 31].

It is remarkable to observe these operations on a small Fourdrinier paper machine. From the headbox to the dryer section no fiber properties are changed, but sheet strength can be affected greatly by the manner in which the paper machine is set up. Formation is a primary factor that is affected by the machine's jet to wire ratio. Poor formation means that the presence of relatively large pores creates weak points or Griffith cracks [2] that result in runnability problems due to frequent sheet breakage. Tight draws between sections pulls the sheets in the machine direction affecting the shape of the pores producing differences in the sheets tensile strength in the machine direction compared to the cross-machine direction.

Formation can be considered the most important of all paper properties. Formation is the term used to describe the uniformity of the fiber distribution in a paper sheet [32]. It can also be described by the uniformity of the pore size distribution [33]. Such paper properties as tensile strength, burst strength tear strength and the uniformity of optical properties are related to formation. Good formation is a function of the design of the paper machine and the skill of the papermaker in setting up the machine. Recently, we have demonstrated in a patent application that maintaining a constant fiber length distribution, with differing mixtures of three different pulps produces constant sheet properties for tensile, burst and tear [34]. The explanation for this result is that constant fiber length distributions result in constant formation due to identical table activity for all pulp mixtures. The principles behind controlling fiber length distribution in pulp mixtures has been published previously [35].

The mathematical definition of *RBA* is the difference between the light scattering intercept and the specific light scattering coefficient normalized into a dimensionless variable as defined by equation (7). As a simple ratio, RBA appears to function as the percentage of effective bonding between two fibers, and there is significant experimental evidence supporting this observation [36]. However, when RBA is used in a shear-lag tensile strength equation to modify the shear strength terms, the equation is transformed into a TS hyperbola that is only a function of light scattering and tensile strength. Significantly, this transformation makes the Page, the Kallmes-Bernier-Perez, and the Shallhorn-Karnis equations identical. Furthermore, RBA is one half of the TS hyperbolic equation where the specific light scattering variable is algebraically separated from the tensile variable. In addition, the equivalence of the TS hyperbola with the well-bonded shear lag equations eliminates the need for the loosely-bonded shear-lag equations. The later statement also means that there is no critical fiber length to determine a fiber pull out versus a fiber breakage event. The absence of a critical fiber length means that shear-lag theory does not apply to paper. Rather tensile fracture of paper occurs because shear stresses intensify inside the cellulose material around the pores.

Since the DS hyperbola is related to the mass balance for a porous material, the dimensions of the specific light scattering coefficient must be expressed as volume. It should also be stated that if nitrogen-adsorption BET surface area (m^2) is used to measure RBA instead of specific light scattering coefficients (m^2/kg), the same dimensional enigma that was discussed in the DS hyperbola section will occur between RBA and the DS hyperbola. Replacing the dimensions of area with volume for the specific light scattering coefficient also eliminates the concept of a maximum bonded fiber area.

Because wet pressing and refining can generate different TS hyperbolas the term “process pathway” was used. There is a similarity between the TS hyperbolas and the isotherm hyperbola of the ideal gas law in thermodynamics. Both equations describe the densification of a material under specified conditions. And both can be related to the constancy of energy during a process. The TS hyperbola describes the ability of paper to store tensile energy during stretching while the isotherm hyperbola describes stored mechanical energy in a compressed gas. This analogy is limited because a sheet of paper cannot re-expand.

However, TS and TD hyperbolas can be referred to as ideal equations of state. Similar to the ideal gas equation where no distinction is made for different types of gas molecules, there are no specific variables to predict the behavior of different types of pulp fibers and/or additives. And, also similar to the ideal gas equation, real equations of state for paper might be derived based on these ideal hyperbolas. Equation modifications for lignin and hemicellulose content, molecular chain length, and moisture content could be added. Finally, it might be possible to merge these hyperbolas with the theories describing the elastic properties of paper to predict a complete stress strain curve from the initial straining to rupture.

REFERENCES

1. Seth, R.S., *Pulp Paper Can.* 107(1): 34(2006).
2. Gordon, J.E., *The New Science of Strong Materials or Why You Don't Fall through the Floor,* 2nd ed, Princeton University Press, Princeton, New Jersey, 1976.
3. Myers, D., Surfaces, Interfaces, and Colloids - Principles and Applications, V C H Publishers, New York, 1991.
4. Kallmes, O., Bernier, G., and Perez, M., *Paper Tech. Ind.* 18(7): 222(1977).
5. Kallmes, O., Bernier, G., and Perez, M., *Paper Tech. Ind.* 18(8): 243(1977).
6. Kallmes, O., Bernier, G., and Perez, M., *Paper Tech. Ind.* 18(9): 283(1977).
7. Kallmes, O., Bernier, G., and Perez, M., *Paper Tech. Ind.* 18(10): 328(1977).
8. Shallhorn, P.M. and Karnis, A., "Tear and Tensile Strength of Mechanical Pulps," in *TAPPI/CPPA Intern. Mech. Pulping Conf.* Toronto, 1979, pp. 25-36.
9. Page, D.H., *Tappi J.* 52(4): 674(1969).
10. Cox, H.L., *Br. J. App. Phys.* 3(3): 72(1952).
11. deRuvo, A., Fellers, C., and Kolseth, P., in *Paper: Structure and Properties* (Bristow, J.A. and Kolseth, P., Eds.), Marcel Dekker, New York, 1986, pp 267-279.
12. Uesaka, T., in *Handbook of Physical and Mechanical Testing of Paper and Paperboard* (Mark, R.E., Ed.), Marcel Dekker, New York, 1984, pp 379-402.
13. Ingmanson, W. and Thode, E.F., *Tappi J.* 42(1): 83(1959).
14. Swanson, J.W. and Steber, A.J., *Tappi J.* 42(11): 986(1959).
15. Haselton, W.R., *Tappi J.* 37(9): 404(1954).
16. Haselton, W.R., *Tappi J.* 38(12): 716(1955).
17. Thode, E.F. and Ingmanson, W., *Tappi J.* 42(1): 74(1959).
18. Williams, D.G., *Tappi J.* 66: 100(1983).
19. Niskanen, K. and Kärenlempi, P., in *Paper Physics* (Niskanen, K., Ed.), Fapet Oy, Helsinki, Finland, 1988, pp 138-191.
20. Weisberg, S., *Applied Linear Regression,* 1rst ed, John WIley & Sons, New York, 1980.
21. Kubát, j., Page, D.H., Kallmes, O.J., et al., in *Consolidation of the Paper Web* (Bolam, F., Ed.), Br. Pap. Board Ind. Fed., London, 1966, pp 804-813.
22. Page, D.H., *Svensk Papperstid.* 88: R30(1985).
23. Rennel, J., *Pulp Paper Mag. Can.* 70(10): 73(1969).

24. Seth, R.S., *Mat. Res. Soc. Sym. Proc.* 197: 125(1990).
25. He, J., Batchelor, W.J., and Johnston, R.E., *Appita J.* 57(4): 292(2004).
26. Seth, R.S. and Page, D.H., *Tappi J.* 79: 100(1996).
27. Fellers, C., Andersson, H., and Hollmark, H., in *Paper: Structure and Properties* (Bristow, J.A. and Kolseth, P., Eds.), Marcel Dekker, New York, 1986, pp 151-167.
28. Alava, M. and Niskanen, K., "The Physics of Paper", Institute of Physics Publishing, 2006.
29. Alince, B., Porubska, J., and van de Ven, T.G.M., *J. Pulp Pap. Sci.* 28: 315(2002).
30. Nissan, A.H., *Lectures on Fiber Science in Paper,* Tappi Press, Atlanta, GA, 1977.
31. Nissan, A.H. and Batten, G.L., Jr., *Tappi J.* 73(2): 159(1990).
32. Peel, J.D., in *Paper Science and Paper Manufacture* (Smook, G.A., Ed.), Angus Wilde Publications, Vancourver, B.C., 1999, pp 26-46.
33. Deng, M. and Dodson, C.T.J., *Paper: An Engineered Stochastic Structure,* TAPPI Press, Atlanta, 1994.
34. Ring, G.J.F., US Patent App., 20080066883 (2008).
35. Ring, G.J.F. and Bacon, A.J., *Tappi J.* 80(1): 224(1997).
36. Page, D., H., Tydeman, P.A., and Hunt, M., in *Formation and Structure of Paper* (Bolam, F., Ed.), Br. Pap. Board Ind. Fed., London, 1962, pp 171-193.

An Epidemiological Approach Applied on the Break Behaviour of the Dry Paper Web

FRANK W. A CAMPO

Stora Enso Research Mönchengladbach
Krefelder Straße 560
41066 Mönchengladbach
Germany
frank.acampo@storaenso.com

KEYWORDS: web break, web strength, bond strength, reinforcement pulp

An approach from mathematical epidemiology is applied to the break behavior of the dry paper web. A differential equation is derived which describes the effect of the energy released by breaking bonds when the web breaking process has become global. An analysis of this differential equation yields results about the role of reinforcement fibers:

- *The strong bonds between reinforcement fibers will not be able to stop a globalized breaking process or to slow it down. It is the plastic deformation of the reinforcement fiber network which has the capability to do so.*
- *Reinforcement fibers may prevent a local breaking process from becoming global by confining it into a local cell.*

The hypothesis is proposed that it is not a weak spot, which triggers the paper break, but that the final breaking process starts in an area in which the bond breaking process has already become global, regardless, if this area has originally been weak or not.

1 INTRODUCTION

There are different scales in the description of paper breaks. In the most macroscopic one paper is regarded as homogeneous and its breaking behavior is described by parameters and methods developed for homogeneous materials. In a closer view paper is regarded as a collection of fibers connected by bonds, and in the most microscopic view the behavior of single fibers and bonds under load is analyzed.

The role of bonds and the way they are analyzed is different in these approaches. In the homogeneous scope they do not play any role, and in the most microscopic one they are treated as individuals. In the intermediate scale a vast quantity of them has to be handled and there are two common ways to do so. In one of them, which did rapidly develop in the last decade in parallel with the rapid development of computational power, fiber networks and their breaking behavior are simulated and analyzed in detail with finite element methods [1-4]. In the other one a more traditional stochastic approach is used: paper is regarded as a collection of bonds with stochastically distributed properties, and the breaking of paper is analyzed as a stochastically ruled process. It is this way to look to paper breaks which is in the focus of this paper.

One feature which complicates the stochastic modelling is the redistribution of load after a bond break: If a bond breaks, the energy stored in it is distributed to the bonds around it. Already Page gave attention to this phenomenon when deriving his famous formula for paper strength [5], but his approach was mechanistic rather than stochastic. In a stochastic approach developed at the end of the nineties the redistribution process is modeled by means of two dimensional lattices of links with stochastically distributed link strength [6, 7].

In this article an approach from mathematical epidemiology is used to analyze paper breaks and the energy redistribution process. In the approach the bond breaking process is regarded as a disease spreading in a population. The resulting differential equation yields results about the way in which reinforcement fibers strengthen the dry fiber network. It is the plastic deformation of the network which plays a major role here, not the bond strength. Furthermore, the reinforcement fiber network may prevent a bond breaking process from becoming global by confining it into small cells.

2 THE EPIDEMIOLOGICAL APPROACH

2.1 Motivation

In mathematical epidemiology the development and spread of diseases is described and analyzed with mathematical methods. In the simplest model there is a population containing healthy, infected and immunized people, and there is some probability for healthy individuals to become infected. If they are infected, they die or become immunized after some time with some probability, and as long as they are infected they can infect other individuals.

The connection to paper and paper breaks is not obvious, but it exists. Paper consists of fibers which are connected by bonds. If the paper is loaded, there is some risk for the bonds to break (it is the bonds which fail in dry paper breaks, not the fiber shafts). Each bond has its own strength, and it will break if its local load exceeds its strength. If it breaks, the load taken up by it is distributed to the bonds in its neighborhood, which increases the risk for them to become overloaded and to break. The total process can thus be regarded as a “break disease” which spreads in the population of bonds. The

correspondences are summarized in the table below.

epidemiological term	paper physics term
individual	bond
infective load	bond load
resistibility	bond strength
infection	break
germs spread by infected people	energy released by breaking bonds

Because our purpose is the modeling of paper breaks, we do not have to deal with the effects of recovering from infection and immunization, and because the paper is assumed to be dry we can neglect the effect of fiber-fiber friction.

2.2 Formalization

In order to make the epidemiological approach working we have to formalize it. We are dealing with a basic population Z of individuals. At every time t each individual $z \in Z$ is subjected to some infective load (tensile) which we denote by $i(t)(z) \geq 0$. The way the functions $i(\bullet)(z)$ develop with time depends on external as on internal factors. The externally applied tension may vary, which directly influences the functions $i(\bullet)(z)$. But there are internal factors, too. How the network deforms under the external load and in particular how it consumes tensile energy by plastic deformation also affects the functions $i(\bullet)(z)$.

Each individual $z \in Z$ has its own resistibility $r(z) \geq 0$ which is stochastically distributed in Z with probability density p. If the infective load of an individual is greater/equal than its resistibility, $i(t)(z) \geq r(z)$, the individual becomes infected (the bond breaks) and spreads some additional infective risk around it (germs in infection, released energy in bond breaks).

In the case of our "break disease" it makes sense to assume that the increase in infective load caused by a newly infected individual depends on its previous resistivity: in the case of break, a strong bond will release and redistribute more energy around it than a weak one. Therefore, we describe the increase in infective load caused by the infection of an individual $z \in Z$ by a function s which has the resistivity $r(z)$ as argument (we write $s(r(z))$). s is assumed to be non-negative and strictly monotonically increasing: $s(0) = 0$, and $s(\rho_2) > s(\rho_1)$ for all $\rho_2 > \rho_1 \geq 0$.

The additional infective risk caused by an infection of z is distributed in the neighborhood of z. In order to model this spatial distribution we use a weight function γ: if z becomes infected, each individual $\zeta \in Z$ realizes an additional infective risk of $\gamma(\zeta - z) \cdot s(r(z))$.

The reader should be aware that the argument $\zeta - z$ of the weight function γ is a vector. The increase in infective risk faced by $\zeta \in Z$ depends thus on its distance from z and on its relative direction to z. The model includes thus isotropic and anisotropic cases, and it works in two dimensions (bonds spread over an area) as good as in three dimensions (bonds spread in a volume). Because γ is a weight function, it is everywhere greater/equal zero, and it is normalized by $\int_Z \gamma(\zeta - z)\, d\zeta = 1$, $z \in Z$ arbitrarily.

At time t some individuals are infected, some not. After an additional time period Δt the infective risk has been increased by the infective risk spread by all newly infected individuals, thus by the individuals contained in the set

$$I(t, t+\Delta t) \equiv \{ z \in Z : i(t)(z) < r(z) \leq i(t+\Delta t)(z) \}$$

In order to be able to deal with this set in our formulas we introduce the characteristic function χ_A of subsets $A \subset Z$:

$$\chi_A(z) \equiv \begin{cases} 0, & \text{if } z \notin A, \\ 1, & \text{if } z \in A. \end{cases}$$

The infective risk $e(t+\Delta t)(z)$ to which an individual $z \in Z$ is exposed at time $t+\Delta t$ is its infective risk $e(t)(z)$ at time t plus the infective risk spread by all newly infected individuals. Written as a compact formula this means:

$$\begin{aligned} & e(t+\Delta t)(z) \\ = \; & e(t)(z) + \int_{\zeta \in Z \setminus \{z\}} \gamma(z-\zeta) \cdot s(r(\zeta)) \cdot \chi_{I(t,t+\Delta t)}(\zeta)\, d\zeta \\ = \; & e(t)(z) + \int_{\zeta \in Z} \gamma(z-\zeta) \cdot s(r(\zeta)) \cdot \chi_{I(t,t+\Delta t)}(\zeta)\, d\zeta \end{aligned}$$

The infective risk $e(t)(z)$ to which an individual $z \in Z$ is exposed at time t will affect its infective load $i(t)(z)$. However, modeling this relation is not the scope of this paper.

3 THE GLOBALIZED INFECTIVE PROCESS

3.1 The Differential Equation for the Globalized Infective Process

The infective process starts with an initial infective load $i(0)(z) \geq 0$ spread over the individuals. At the beginning the infective process

will be very local: some weak individuals will become infected and will increase the infective risk around them. It may happen that the infective process stops at this stage. However, if it proceeds we can assume that after a while the infection has become global in the sense that the infective load and the infective risk do not depend on the individual $z \in Z$ any more. This will be the case if there are so many infected individuals around each uninfected individual $z \in Z$ that each uninfected individual is living in the same situation. In this stage of the infective process the dependence of $e(t)(z)$ and $i(t)(z)$ from $z \in Z$ can be skipped.

This assumption has some consequences for our formula for $e(t+\Delta t)(z)$. First, if there are sufficiently many infected individuals around every uninfected one, we can replace the weight function $\gamma(\zeta - z)$ by a global constant $\Gamma > 0$:

$$\begin{aligned} & e(t+\Delta t)(z) \\ = \; & e(t)(z) \; + \frac{\Gamma}{|Z|} \cdot \int_{\zeta \in Z} s(r(\zeta)) \cdot \chi_{I(t,t+\Delta t)}(\zeta) \, d\zeta \end{aligned}$$

$|Z|$ is the size of Z (area or volume); the normalization with $|Z|$ makes Γ independent from this size of Z.

Because $i(t)(x)$ and $i(t+\Delta t)(x)$ do not depend on $x \in Z$ any more, the remaining integral integrates $s(r(\zeta))$ over the set $I(t,t+\Delta t)$. If the function i is non-decreasing in the interval $[t,t+\Delta t]$, we can replace this integration by the weighted integration of $s(\rho)$ over the interval $[i(t), i(t+\Delta t)]$; the weight function is the probability density function p multiplied by $|Z|$. In total we get the formula

$$e(t+\Delta t) \;=\; e(t) \;+\; \Gamma \cdot \int_{i(t)}^{i(t+\Delta t)} s(\rho) \cdot p(\rho) \, d\rho$$

which yields the differential equation

$$\frac{de}{dt}(\tau) \;=\; \Gamma \cdot s(i(\tau)) \cdot p(i(\tau)) \cdot \frac{di}{dt}(\tau) \, .$$

If the function i is decreasing in the interval $[t,t+\Delta t]$, no new individuals will be infected, and we get $\frac{de}{dt}(\tau) \;=\; 0$.

3.2 How to Stop a Globalized Infective Process

In spite of its very general nature, the differential equation above allows some interesting conclusions. A differential quotient $\frac{de}{dt}(\tau) = 0$ means that the infective risk remains constant and no new individuals will be infected. In the language of paper breaks: no additional bonds will break – the breaking process stops. How can this be achieved?

According to our differential equation and our assumptions about s, $\frac{de}{dt}(\tau) = 0$ is equivalent to $p(i(\tau)) = 0$ or $\frac{di}{dt}(\tau) = 0$. $p(i(\tau)) = 0$ means that the probability density of bond strength is bi- or multimodal with a zone of zero in between. Looking to fibers we can express this as follows. Assume that we have some fiber mix with low strength and we want to strengthen it by the addition of reinforcement fibers which are evenly distributed in the fiber mix. These reinforcement fibers will be able to stop an already globalized breaking process by their bond strength if and only if this bond strength is clearly higher than the strongest bonds in the weak furnish component. We need "super bonds". This does not look realistically for wood fibers.

$\frac{di}{dt}(\tau) = 0$ means that the bond load does not increase. This can be due to external reasons, e.g. the release of an external tensile force. More interesting is the possibility that $\frac{di}{dt}(\tau) = 0$ is caused by plastic deformation of the fiber network which consumes some of the energy stored in the bonds. It is thus the plastic deformation of the fiber network and not some strong bonds which may stop a globalized bond breaking process.

Differentiating the differential equation yields

$$\begin{aligned} & \frac{d^2e}{dt^2}(\tau) \\ = \; & \Gamma \cdot \frac{ds}{dt}(i(\tau)) \cdot p(i(\tau)) \cdot \left(\frac{di}{dt}(\tau) \right)^2 \\ + \; & \Gamma \cdot s(i(\tau)) \cdot \frac{dp}{dt}(i(\tau)) \cdot \left(\frac{di}{dt}(\tau) \right)^2 \\ + \; & \Gamma \cdot s(i(\tau)) \cdot p(i(\tau)) \cdot \frac{d^2i}{dt^2}(\tau) \end{aligned}$$

If $\frac{d^2e}{dt^2}(\tau)$ is greater than zero everywhere, the function $e(\tau)$ is convex and the infective risk spread around explodes (bond breaking becomes an avalanche). In order to prevent this, $\frac{d^2e}{dt^2}(\tau)$ has to be less/equal zero which means that at least one of the summands on the right hand has to be less/equal zero.

We have already discussed the implications of $p(i(\tau)) = 0$ (existence of super bonds) and

$\frac{di}{dt}(\tau) = 0$ (external reasons or plastic deformation) and can thus assume that both terms are greater than zero. (Less than 0 is not possible due to the nature of a probability density and due to the assumption about i we made in the derivation of the differential equation.)

If $\frac{d^2i}{dt^2}(\tau)$ is less/equal zero depends either on external factors or on plastic deformation, as it was the case for $\frac{di}{dt}(\tau) = 0$, too. From the remaining terms it is $\frac{dp}{dt}(i(\tau))$ only which may become negative. In this case the probability density p is decreasing in $i(\tau)$, which means that the infection or bond breaking process has already passed the peak of the probability density function.

4 HOW TO PREVENT AN INFECTIVE PROCESS FROM BECOMING GLOBAL

Until now we have discussed how an already globalized infective or bond breaking process can be stopped (case $\frac{de}{dt}(\tau) = 0$) or at least been prevented from exploding (case $\frac{d^2e}{dt^2}(\tau) \le 0$). Both cases can be achieved by the development of the external tensile process or by plastic deformation of the fiber network. Otherwise, the outcome was not promising: stopping the process requires the addition of extremely well-bonding fibers, and keeping it non-exploding means to wait until the big bunch of bonds has already been broken. (The reader is asked to remember that we do not model any recovering or immunization process as they happen in biological diseases; the perspective is thus not so pessimistic for these.)

What remains to do is to prevent the infective process from becoming global. In the beginning of paragraph 3.1 we stated as a condition for the globalized infective process that "this will be the case if there are so many infected individuals around each uninfected individual $z \in Z$ that each uninfected individual is living in the same situation". If we want to prevent the infective or bond breaking process from becoming global (and thus nearby unstoppable according to the results of paragraph 3.2), we have to look how to keep it localized.

In epidemiology this means "quarantine" and it is done in most cases by transporting infected people to some specialized camps or hospitals and controlling their contact with the uninfected population. But this is not possible for bonds in paper. We have to ensure locality of the bond breaking process by other means.

The mathematical consequence of our assumption about the globalized infective process was the replacement of the function γ by a constant $\Gamma > 0$; after this replacement, the pessimistic differential equation resulted inevitably after some technical rearrangements of the formula. Indeed, the replacement of the weight function by a global constant is mathematically equivalent to the globalization of the infective process. If we want to prevent the infective process from becoming global, we have thus to ensure, that the replacement is not allowed.

The key herein is the "horizon" of the weight function γ. For every individual $z \in Z$ the infective risk acting on it is collected from all infected individuals, and we get the infective risk spread by them to z by weighting it with the function $\gamma(z - \bullet)$. If the values of this function decrease slowly with the distance from z, we will quickly run into the situation that every $z \in Z$ is facing the same situation because there are so many individuals affecting it. Because we want to avoid this situation we have to ensure that the function $\gamma(z - \bullet)$ drops quickly to zero as we go away from z. This happens if the energy released by a breaking bond is absorbed and taken up totally in its close neighborhood.

One possibility to achieve this is that in a furnish of weak stuff and reinforcement fibers the weak stuff is located in cells which are more or less isolated from each others by the reinforcement fibers. A bond breaking process starting in one of these cells will not become global because the reinforcement fibers prevent it from jumping over to other cells. (This is a localized version of the bimodal bond strength distribution mentioned in paragraph 3.2). This effect of stronger areas surrounding weaker cells may also explain why a more uneven formation does not necessarily impair paper strength [8, p. 172]: If areas of increased basis weight surround lighter parts of the web, they may prevent a bond breaking process starting in the lighter parts from becoming global. Also the break-preventing consequence of plastic deformation can be achieved by a network consisting of strongly bonded reinforcement fibers with cells of weaker material in between them.

If it is possible to keep a starting breaking process local by an increase in the density of bonds per unit area or unit volume depends on the details of γ. On the one hand an increase in bond density will result in a smaller effective horizon of the weight function. But on the other hand there are more bonds contained in this smaller horizon. For an analysis of these counteracting effects a scaling approach as outlined in [9] may be useful.

5 FINAL REMARKS

The concept of the different effective horizons of the weight function γ covers as extreme cases the

concepts of "equal load sharing" and "local load sharing" developed in [6] and used in [7]. In consequence the conclusions about the effect of the effective horizon of the weight function γ on the breaking process are quite similar to the conclusions about the effects of the two load sharing concepts presented in [6].

In an e-mail to the author [10] Uesaka points out, that in paper breaks a number of damaged islands grow in the paper structure which are surrounded by relatively undamaged areas; finally, one of those damaged islands triggers the global failure. This observation corresponds well with the concept developed in this article: the growing damaged islands may be areas in which the bond breaking process has already become global, and one of these "locally" global bond breaking processes finally causes the paper break. (In epidemiological terms: in order to cause a disaster it is sufficient that the disease has become global in some larger areas or cities, even if other parts of the country are not as heavily infected.)

It is common believe that a paper web will break at its weakest point. Following the reasoning about global and local paper breaking processes presented in this article I propose the hypothesis that the final breaking process starts in an area in which the bond breaking process has already become global, regardless, if this area has originally been weak or not.

REFERENCES

[1] P. Miettinen, J. Ketoja: Rheology of Simulated Wet Fibre Networks. EUROMECH COLLOQUIUM 486, Deformation and Fracture Processes in Paper and Wood Materials, June 12 – 15, 2006, Hotel Södra Berget, Sundsvall, Sweden.

[2] P. P. J. Miettinen, J. A. Ketoja, D. J. Klingenberg: Simulated strength of wet fiber networks. J. Pulp Paper Science 33(4), 198-205 (2007).

[3] S. B. Lindström: Modelling and simulation of paper structure development. Ph.D. thesis kappa, Mid Sweden University, Sundsvall, Sweden, 2008.

[4] A. Kulachenko, S. Lindström, T. Uesaka: Strength of Fiber Networks – Scale Effect. Papermaking Research Symposium, Kuopio 2009.

[5] D.H. Page: A Theory for the Tensile Strength of Paper. Tappi 52(4):674 (1969).

[6] B.Q. Wu, P.L. Leath: Failure Probabilities and Tough-Brittle Crossover of Homogeneous Materials with Continuous Disorder. Phys. Rev. B 59, 4002–4010 (1999).

[7] T. Uesaka: Prediction of Low Tail of Strength Distribution of Paper. Proc. 2007 International Paper Physics Conference, 115-122 (2007).

[8] K. Niskanen (ed.): Paper Physics. J. Gullichsen, H. Paulapuro (eds.): Papermaking Science and technology, book 16. Fapet Oy, Helsinki 1998.

[9] R. Ritala: Geometrical Scaling Analysis of a Fiber Network: Effect of Reinforcement Pulp. Nordic Pulp and Paper Research Journal, Special Issue: Börje Steemberg. 75(1987)2, 15-18.

[10] T. Uesaka: E-mail to F. W. a Campo, 2011-01-22.

Session 7

Web Consolidation and Drying

Micro-fluidics of "Water Bond"

H. S. WIKLUND and T. UESAKA

Fibre Science and Communications Network/ Mid Sweden University
SE-851 70 Sundsvall, Sweden
Hanna.Wiklund@miun.se

1 INTRODUCTION

The nature of fibre-fibre bonds has been one of the central themes of research in paper physics and paper chemistry. Particularly, in a wet state of fibre networks, liquid phase of water is present, together with gas phase, between fibres or fibrils, which create long-range interactions with its surface tension and wetting property. This is well known in the early literature by Lyne and Gallay [1] and by Campbell [2].

Accordingly, there have been active discussions on the role of water bridge. Page [3] pioneered to derive an expression for wet web strength by using his semi-empirical strength equation. Assuming fibre strength is much higher than shear bond strength in a wet state, he obtained an expression, which is essentially proportional to capillary pressure, and the proportional constant includes a phenomenological "friction coefficient" (of water bridge). Recently van de Ven [4] further examined different cases of geometry of water bridge. His final expression, again, include the phenomenological "friction" coefficient. One question that may be raised is whether shear resistance of water bridge can be treated as a friction phenomenon. The second question is if the force calculation based on static equilibrium is still applicable to realistic dynamic cases (i.e., finite shear rate).

In this study we consider a simplest case of water bridge between two rigid plates, but using the first principle, we directly calculate shear resistance of the water bridge and determine the relationship between shear resistance, the fluid and wetting properties and geometry. The method used is Lattice-Boltzmann approach based on free-energy formulation [5].

1.1 The Lattice Boltzmann Method

The binary free energy lattice Boltzmann method, first developed by Swift et al. [5], is thermodynamically consistent in equilibrium and solves the Navier-Stokes equation by following the evolution of particle distribution functions on a fixed regular lattice. A wetting boundary condition is incorporated [6] by using the Cahn-model [7].

2 RESULTS AND DISCUSSION

We have performed simulations of two smooth, non-porous and chemically homogenous plates connected by a water bridge, Fig 1. The two plates were moved horizontally at a constant velocity, u, in opposite direction of each other, causing the water bridge to shear. In our simulations the volume of the water bridge was V=16 μm^3, the distance between the two plates, h = 1μm. The surface tension of the liquid and the equilibrium contact angle were varied as σ=12mN/m, 32mN/m, 72mN/m and θ=20°, 40°, 60°. The viscosity of the liquid phase was ten times that of the surrounding gas phase and two different velocities of the plates were used u=100μm/s and 0.1μm/s.

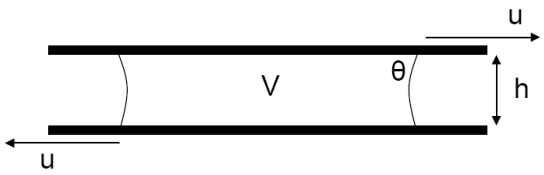

Figure 1. Schematic simulation set-up of water bridge.

Figure 2 shows a comparison of shear resistance force for the two different shear velocities. The results show that the order of magnitude of the shear force is highly dependent on the velocity, unlike typical friction phenomena (Fig. 2), indicating that the viscose force plays a mayor role in the development of shear resistance.

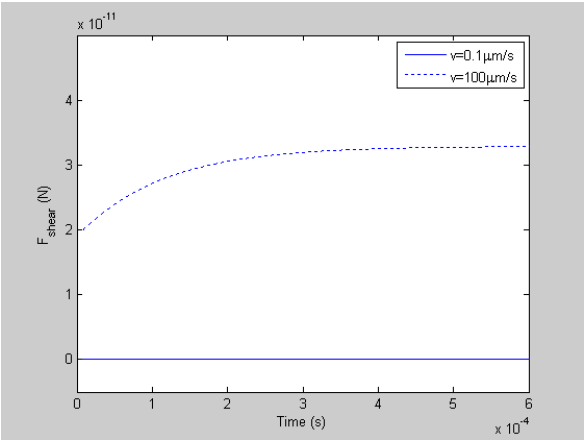

Figure 2. The shear resistance force as a function of time at different plate velocities. The surface tension was σ=72mN/m and the contact angle θ=60°. The viscosity of the liquid is ten times that of the surrounding phase.

Our results also show that the shear force as measured from our simulations is smaller in magnitude than the shear force estimated by calculations made by Page [3]. For example, in Page's calculations the estimated shear force is about half of the capillary force, while in our case

the shear force is less than one hundredth of the capillary force, even for the velocity u=100µm/s.

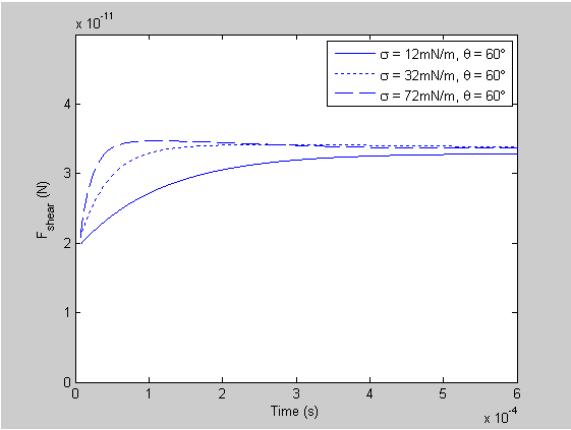

(a) The shear resistance force as a function of time at different surface tensions.

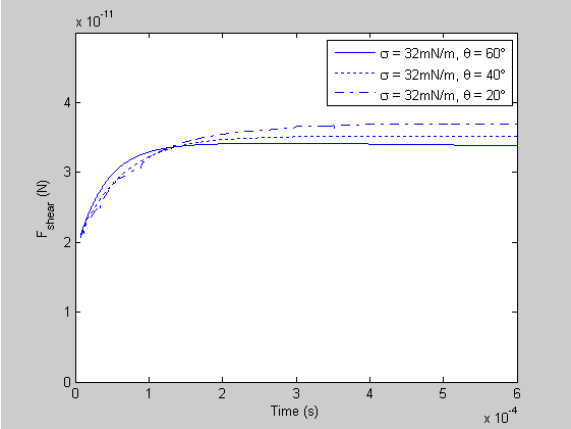

(b) The shear resistance force as a function of time at different contact angles.

Figure 3. The shear resistance force as a function of time at different surface tensions and contact angles.

In Figures 3a-b the shear resistance force as a function of time is plotted at different surface tensions and contact angles. It can be seen that in all cases the shear resistance force initially increases to later reach a maximum value. It can also be seen that the time to reach this value is dependent on surface tension, but there is only a small dependence on surface tension and a slightly larger dependence on the contact angle in the maximum value.

In Figure 4 the shear resistance force as measured from simulations, is plotted together with the shear resistance force approximated by assuming a linear flow field in the entire water bridge. The plot shows that the introduction of interfaces to the system increases the shear resistance force. About half of the shear resistance comes from the presence of interfaces. The reason for the increase is that the interfaces will cause the flow field to be distorted close to the interface and increase the shear force. This shows that although the viscose force plays an important role in determining the magnitude of the shear force resistance the contributions from interfaces in the system cannot be neglected.

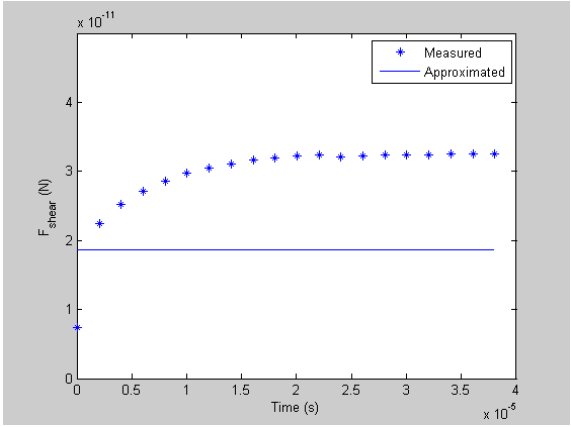

Figure 4. The shear resistance force as a function of time measured from simulation and approximated by assuming a linear velocity gradient in the entire liquid bridge.

3 CONCLUSIONS

Our results have shown that the order of magnitude of the shear force is highly dependent on the velocity, indicating that the viscose force plays a mayor role in the development of shear resistance. The results have further shown that the shear force as measured from our simulations is smaller in magnitude than the shear force estimated by calculations made by Page. We have also shown that the introduction of surfaces to the system will increase the shear resistance force and that this increase is dependent on the surface tension and the contact angle. The results thus indicate that the previous assumption that there is a relationship $F_{shear} = \mu F_{Cap}$, i.e. that the shear force is a function of the surface tension, contact angle and an undefined parameter, µ, is not sufficient if one wants to understand how the water bridge affect the shear resistance forces between two surfaces.

4 REFERENCES

[1] L. M. Lyne and W. Gallay. Studies in the Fundamentals of Wet Web Strength. *Tappi J.* **37**(12):698-704 (1954)

[2] W. D. Campbell. The cellulose-water relationship in paper making. *Forest Service Bulletin 84*. (1933)

[3] D. H. Page. A Quantitative theory of the Strength of Wet Webs. *Journal of Pulp and Paper Science*. **19**(4):175-176 (1993)
[4] T. G. M. van de Ven. Capillary Forces in Wet Paper. *Ind. Eng. Chem. Res.* **47**(19):7250-7256 (2008)
[5] M. R. Swift, E. Orlandini, W. R. Osborn and J. M. Yeomans. Lattice Boltzmann simulations of liquid-gas and binary fluid systems. *Phys. Rev. E.* **54**(5):5041-5052 (1996)
[6] A. J. Briant and J. M. Yeomans. Lattice Boltzmann simulations of contact line motion. II. Binary fluids. *Phys. Rev. E.* **69**(3):1603-1612 (2004)
[7] J. W. Cahn. Critical point wetting. *J. Chem. Phys.* **66**(8):3667-3673 (1977).

Consolidation and dewatering mechanisms in papermaking

ATSUSHI TANAKA, NIKOLAI BELETSKI,
SANNA HAAVISTO AND JUKKA KETOJA

VTT Technical Research Centre of Finland
P.O. Box 1000, FI-02044 VTT, Finland
atsushi.tanaka@vtt.fi

ABSTRACT

Consolidation and dewatering are central mechanisms when the wet web is formed on a paper machine. The later rheological behavior of the web significantly depends on these processes – the way in which water is removed from the structure and web elements are brought together to a strong, well bonded material. There have been relatively few direct studies on the effect of small-scale web elements on consolidation and runnability.

We have developed the laboratory device *VIHTORI* to visualize the dynamics of fibers, fines or other particles under controlled conditions (**Fig.1**). The glass filter is embedded inside the chamber at the bottom of the sample pocket. The controlled suction is given through the glass filter so that the sample furnish consolidates and dewaters on the filter. The combination of strong uniform light and high speed camera (max 2000 images/s with 1.3 megapixels) enables to capture the particle movements. The resolution of the system is ~15µm, so that the largest fine particles are in that range. Image analysis gives the information of consolidation / dewatering time, as well as local profiles such as particle distribution or flow velocity field (**Fig.2**).

The starting / end points for consolidation and dewatering can be determined by gray level analyses. Trials with TMP showed that both suction level and pore size of the glass filter affect the consolidation time. However, the most significant impact turned out to be given by grammage. For example, consolidation time of 60 g/m^2 furnish is 10 times longer than that of 20 g/m^2 furnish. This difference becomes even larger as the fines content of furnish is reduced (**Fig.3**).

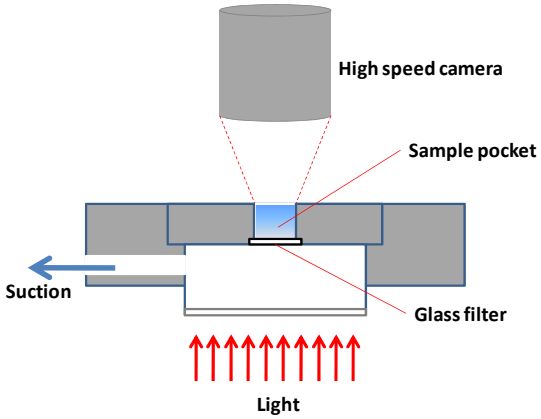

Figure 1. Schematic image of the *VIHTORI*.

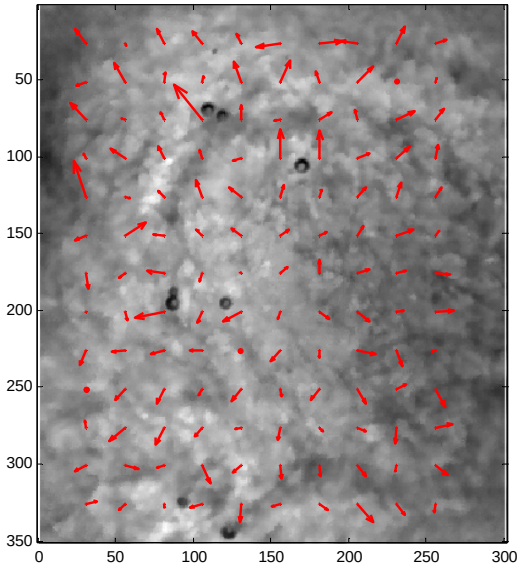

Figure 2. Flow velocity field during consolidation process (analyzed by cross correlation method).

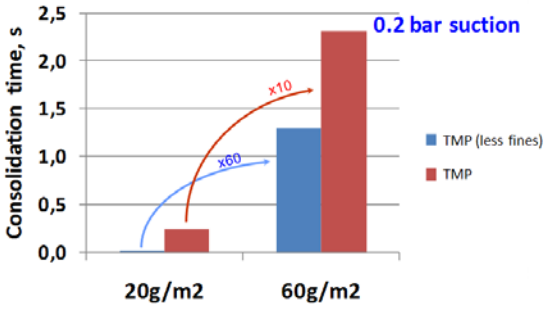

Figure 3. Comparison of consolidation time for different grammage (under 0.2 bar suction).

Paper machine simulation with a modified servohydraulic test rig

H. RUD; C. FRIETSCH; T. KASAH; J. ROLEFS; A. EICHLER; M. FEICHTINGER

Voith Paper GmbH
Linzer Strasse 55, A-3100 St.Pölten, Austria
Heimo.Rud@voith.com

Keywords: Paper machine simulation; dynamic process simulation; press nip simulation; drying test rig

ABSTRACT

Trials on real paper machines are expensive and restricted to the given machinery and boundary conditions. In order to simulate different sections of a paper machine in a more economic but nevertheless still realistic manner a paper simulation test rig was developed and applied to press section (press-nip simulation, press felt characterization), dryer section (Yankee, single tier dryer group) and calendering.

1 INTRODUCTION

Papermaking is a complex process where first a web is formed out of a suspension, which is afterwards further dewatered, dried und finally reeled up. In those steps paper quality is influenced by several physical parameters as dwell time, pressure profiles of different nips, surface temperatures of machinery as well as web properties like moisture content and web temperature.

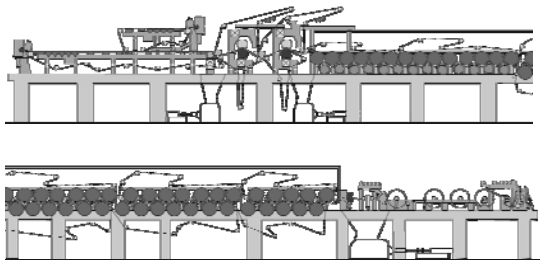

Figure 1. Packaging paper machine (schematically)

While first attempts in press simulation were restricted by the speed of the pressing devices, the development of servohydraulic test rigs in combination with fast data processing made it possible to simulate shoe press profiles in a more realistic manner [1, 2]. With these new testing devices not only the influence on paper quality parameters could be obtained, but it becomes also possible to investigate phenomena like rewetting [3, 4] or press felt densification during start up.

This paper summarises some work in paper machine simulation during recent years. In [5] we already described a method to simulate extended nip calender devices. In this paper three examples of paper machine simulation (shoe press, MG-cylinder, single tier dryer group) are given, but first the experimental set up and possibilities for sample conditioning (moisture, temperature) will be described.

2 EXPERIMENTAL SET UP

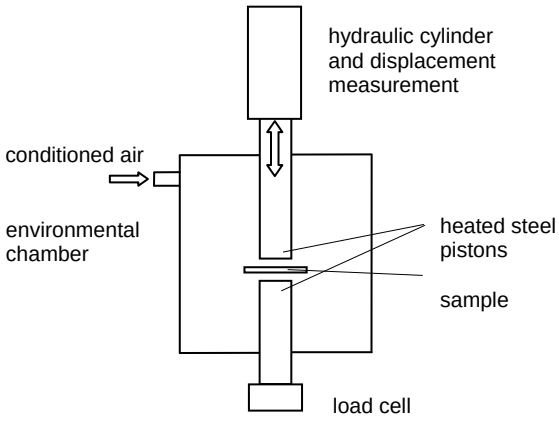

Figure 2. Schematics of the paper machine simulator

Driven by a servohydraulic system defined pulses can be applied on a stationary paper sample. In this way forces up to 25 kN at a minimum pulse duration of 8 ms can be achieved. The steel pistons are heated to control the surface temperature of the pressing elements. In addition to that an environmental chamber around the pressing elements makes it possible to simulate the conditions (heat, moisture) within a paper machine.

3 SAMPLE CONDITIONING

To simulate different sections of a paper machine not only nip pressure and dwell time have to be considered, also moisture content and sample temperature are decisive for the simulation result. The provision of paper samples with defined dry content is crucial. On one hand it is difficult to get undamaged samples from a board machine for example with low dry content, on the other hand the preparation of hand sheets is time-consuming and the sheet structure is different to machine produced paper [6]. Another way is to remoisten dry paper by putting it into a water bath for a defined time.
In Fig. 3 the dry content development for folding boxboard as function of insertion time is illustrated. Thereby the water absorption can be described with a logarithmic function.

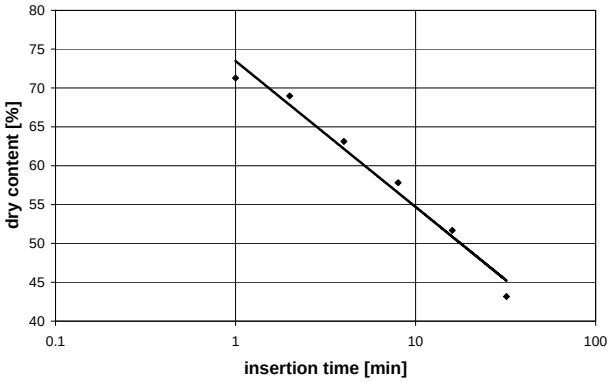

Figure 3. Dry content development during remoistening of folding boxboard

The longer the sheet is in contact with water the more water is absorbed. After taking the samples out of the water bath, surface water is removed with help of a couch roll. Anyway the initial wet or remoistened samples have to be protected against moisture loss due to evaporation. Therefore the samples are stored in plastic bags. To ensure a uniform moisture distribution the samples have to rest for 12 hours before the trials can be executed. Using the environmental chamber the sample can be warmed-up directly in the test rig. In Fig. 4 the warming-up procedure of a folding boxboard sample is illustrated.

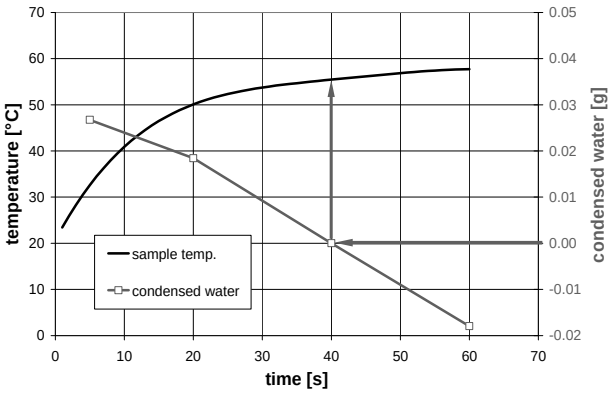

Figure 4. Sample warming up-procedure

In the first seconds of the warming up-procedure condensation takes place while the sample temperature begins to increase. With higher temperatures the condensation phenomenon is reduced due to evaporation, while the sample temperature stabilizes. The time necessary to evaporate all the condensed water has to be determined in pre-tests (point at 40 s in the example of Fig. 4).

SHOE PRESS SIMULATION

A first application of the paper machine simulator for shoe press simulation is shown in Fig. 5. By tuning the servohydraulic system a good correlation between simulated and theoretical nip profile can be achieved.

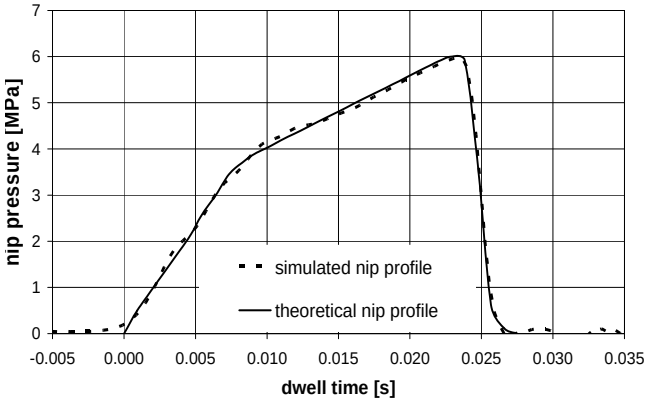

Figure 5. Shoe press simulation; measuring record

Shoe press simulations can be used for example to determine the dewatering behavior of different fabrics or to investigate the influence of nip load on paper quality parameters or the influence of furnish on dryness.

In Fig. 6 exemplarily the impact of different shoe designs (shoe length, peak pressure, nip load) of a single felted shoe press on bulk and Bendtsen roughness (top-side) is shown.

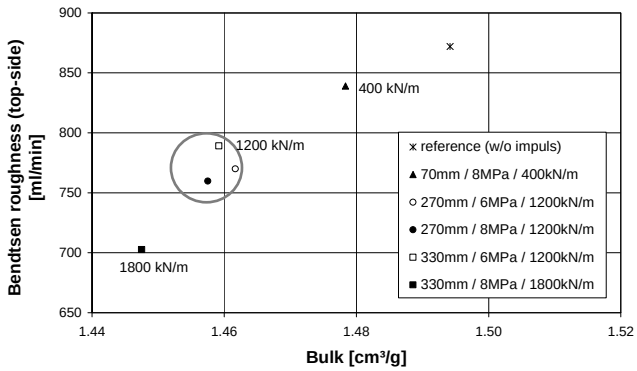

Figure 6. Shoe press simulation; influence of shoe press profile on roughness and bulk

For the shoe press simulation hand sheets (195 g/m², Rapid Köthen sheet former, initially wet TL pulp) were produced. Obviously, with higher line loads the samples get more densified. At the same

time also the top-side of the samples gets smoothed. But not only the line load alone influences the pressing process, also shoe length and maximum pressure show an impact on bulk and roughness. By comparing the 1200 kN/m shoe geometries (270mm/6MPa, 270/8MPa, 330/6MPa) the highest densification could be achieved with shorter shoe design (270mm/8MPa) and higher peak pressure.

4 MG CYLINDER SIMULATION

To illustrate the potential of the paper machine simulator for smoothing purposes a MG cylinder (Fig. 7) was simulated. The example shows the simulation of complex nip geometry. After a rather short nip of the MG smoothing press a long dwell time at low pressure (dryer fabric tension) is needed to simulate a MG cylinder.

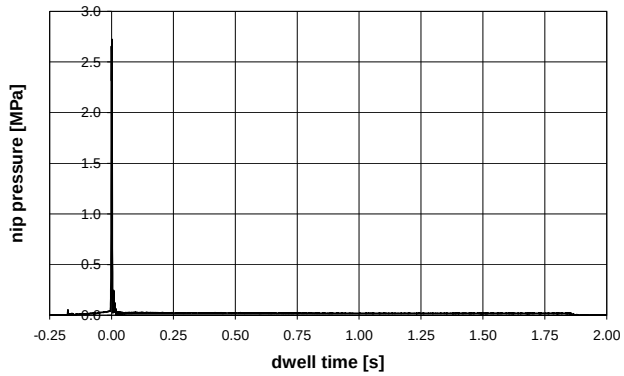

Figure 7. MG simulation; measuring record

For the trials uncalendered board from a board machine (FBB 250 g/m²; opened MG smoothing press) was taken. To have a reference for the calendering effect of the MG cylinder, also board samples with closed MG smoothing press were produced. The machine-dry and uncalendered board was conditioned to a dry content of 65% and a web temperature of 60°C. The upper steel piston representing the MG cylinder was set on a temperature of 115°C.

Fig. 8 shows the influence of the MG smoothing press on smoothness, gloss and bulk for the samples calendered in the servohydraulic test rig in comparison to the machine calendered reference samples. For both, the samples calendered on a production MG cylinder and the samples calendered in the MG servohydraulic test rig, a large influence of the smoothing press on board quality can be seen. With low bulk loss a good roughness reduction can be achieved. By comparing the test results for the test rig calendered samples with the samples from the board machine, the same effect on PPS roughness can be found. By comparing gloss and bulk development with the samples from the board machine a reduced influence of the MG smoothing press in the simulation is found. An explanation could be that for the MG-simulation remoistened board was used with less flexible fibers than in an initially wet board. Nevertheless the effect of the MG smoothing press on gloss and bulk proves the potential of the testing device.

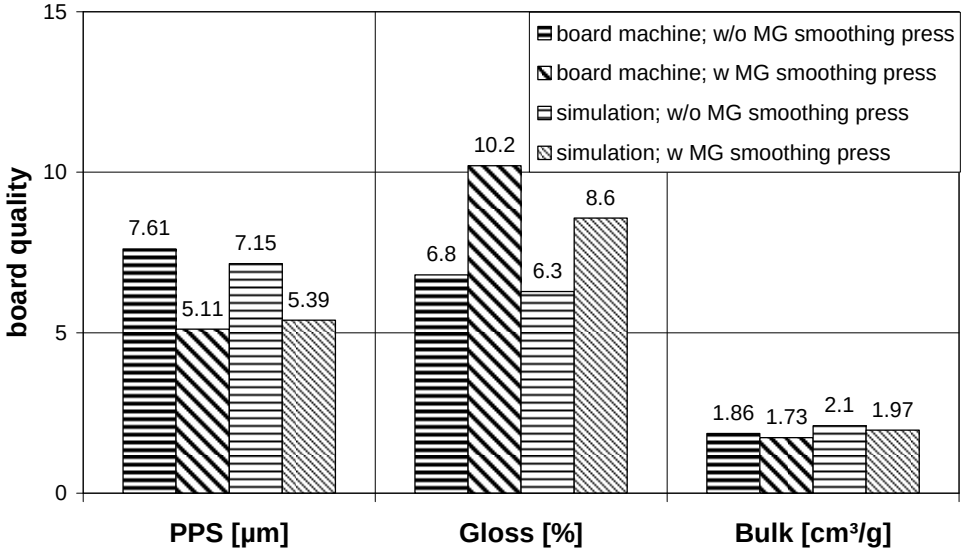

Figure 8. MG Simulation; influence of MG smoothing press on board quality

5 SINGLE TIER DRYER GROUP SIMULATION

After the press section water has to be removed from the web mostly by contact drying on steam heated cylinders. In single tier dryer groups (Fig. 9) a fabric is used to support the wet web and to improve the heat transfer from the cylinder into the web. Between the drying cylinders suction rolls and web stabilizers are used to guide the web.

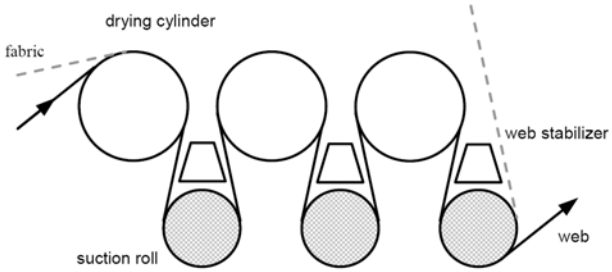

Figure 9. Single tier dryer group (schematically)

To simulate the alternating contact between drying cylinders and suction rolls a slightly modified experimental set up is used (Fig. 10).

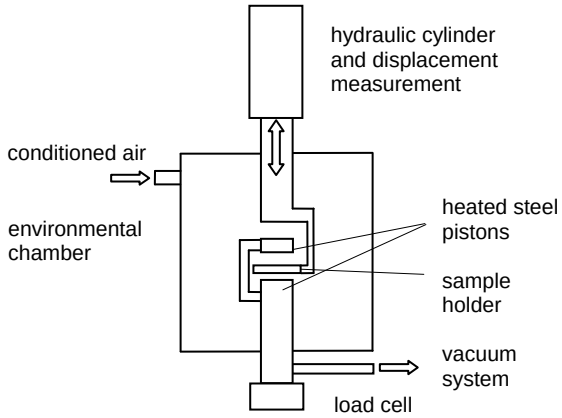

Figure 10. Modified experimental set up for single tier group simulation

To support the wet sample a fabric is fixed on a specially designed holder. The pistons are fixed and the paper sample is moved up and down between the two pistons. To simulate drying cylinder contact, the paper sample and the supporting fabric is pressed against the upper piston. The contact. with the lower piston mimics the stabilizing roll. With help of a vacuum system suction roll ventilation can be simulated For the cylinder contact a much lower contact pressure than for example for the shoe press simulation is needed (see Fig.11). The contact pressure can be calculated from fabric tension and cylinder diameter as follows:

$$contact\ \ pressure = \frac{2 \times fabric\ tension}{drying\ \ cylinder\ \ diameter}$$

Fabric tension of 3.7 kN/m results in a contact pressure of only 0.004 MPa, while the maximum pressure at the shoe press simulation was about 8 MPa.

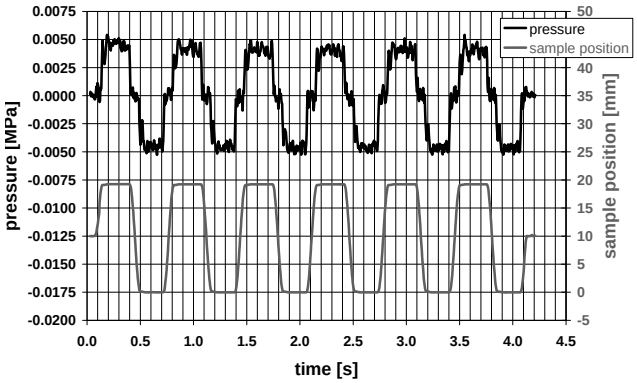

Figure 11. Single tier dryer group simulation; measuring record

Further a fast sample positioning is needed. While the contact times at the upper piston representing the drying cylinder (260 ms at 800 m/min) and the bottom piston representing the suction roll (200 ms at 800 m/min) is quite long, the paper sample has to be moved in only 90 ms from the upper position to the bottom position.

In a first attempt to test the modified test rig a single tier dryer group (6 cylinders/ suction rolls; 800 m/min) was simulated. For the trials packaging paper (TL 130 g/m²) was used. The samples were conditioned to a dry content of 55%. The upper steel piston representing the drying cylinder was set on a temperature of 120°C.

In Fig. 12 the effect of suction roll ventilation on evaporation rate is demonstrated. By weighing the samples before and after the trials, changes in dry content or evaporation rates can be determined.

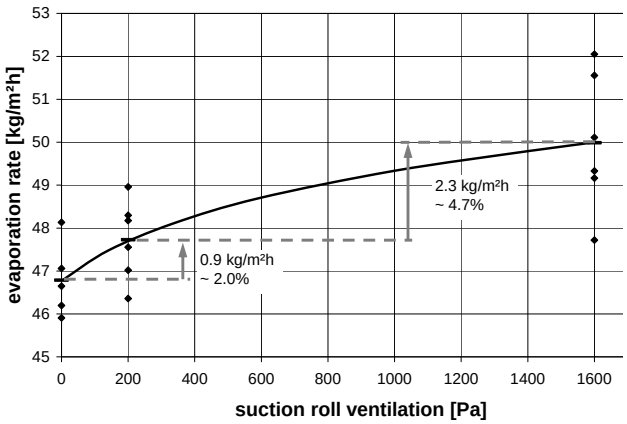

Figure 12. Single tier dryer group simulation; influence of suction roll ventilation on evaporation rate

Due to the gravimetrical measurement technique the results for the evaporation rate vary. Nevertheless a supportive effect of suction roll ventilation can be found. Thereby the evaporation rate rises from about 47 kg/m²h (no ventilation) to almost 50 kg/m²h (1600 Pa under pressure) which is an increase of almost 7%. For usual under pressure of 200 Pa still an increase of 2% can be determined.

An explanation for this behavior could be that due to higher ventilation humid air is removed from the suction roll and therefore the mass transfer is supported.

SUMMARY

Servohydraulic testing systems have become a powerful research tool in paper machine simulation. While shoe press simulation is already established, also extended nip calender simulation as well as single tier dryer group simulation becomes possible.

Emphasis was laid not only on a realistic simulation of the pressure pulse but as well on a new and reproducible method for sample conditioning (temperature, moisture) which is the prerequisite for meaningful and realistic results.

REFERENCES

[1] H. Vomhoff and B. Normann. Method for the investigation of the dynamic compressibility of wet fibre networks. Nordic Pulp and Paper Research Journal 16 (1), 57-62, (2001).

[2] P. Phelan, F. Ahrens and G. Worry. Laboratory study of shoe pressing for low basis weight paper applications. TAPPI JOURNAL, 84(4), 73 ff, (April 2001).

[3] N. Guy. Development of a method to determine the press dewatering with an existing laboratory press (STFI). Diploma thesis, Grenoble Institute of Technology, (2004).

[4] T. Saukko. Potential of the MTS press simulator for wet pressing research. M.Sc. thesis, Helsinki University of Technology, (2006).

[5] H. Rud, S. Hoche, A. Eichler and M. Feichtinger. New insights into the calendering process with a servohydraulic calender test rig. Papermaking Research Symposium, (2009).

[6] M. Dröscher. Einfluss von Temperatur und Feuchte bei der Satinage von Karton und Oberflächenbeurteilung mittels Lasertopografiemessung (in German). Diploma thesis, Graz University of Technology, (2004).

Shear strength development between couched paper sheets during drying

MAGNUS GIMÅKER[1], MIKAEL NYGÅRDS[1, 3], LARS WÅGBERG[2] and SÖREN ÖSTLUND[1, 3]

[1] Innventia AB
BOX 5604, SE-114 86 Stockholm Sweden
magnus.gimaker@innventia.com

[2] KTH Fibre and Polymer Technology,
SE-100 44Stockholm, Sweden

[3] KTH Solid Mechanics
SE-100 44 Stockholm, Sweden

1 INTRODUCTION

The out-of-plane properties (e.g., out-of-plane shear strength) of paper materials are very important for their performance during converting and end use [1]. There is, however, a lack of published data on how shear strength develops throughout the stages of paper manufacturing. The understanding of the mechanisms that give paper its strength are much better understood for the dry state than for the wet state. There is also limited understanding of how the fibre interactions develop during drying. Wet tensile strength can be used as an indirect measurement of how the interaction between fibres develops with drying. At low solids content with weak interactions between fibres the situation is however complicated by the fact that the structure of the fibre network, i.e. degree of fibre entanglement, might give a significant contribution to the tensile strength besides the actual interaction/friction between the fibres. It is therefore suggested that measuring the shear strength between couched sheets is a better estimate of the fibre interaction since it to a large extent eliminate the influence of fibre entanglement. The shear strength measurement also has the advantage that local properties can be measured easily, whereas standard tensile testing gives the strength of the weakest part of the test specimen.

2 EXPERIMENTAL

Unbeaten bleached fibres and beaten unbleached fibres were used in the study. Both sheets made of never-dried fibres and rewetted previously dried sheets were used for specimen preparation. For specimens made by rewetting, sheets with a grammage of 300 g/m^2 were first prepared and dried in the Rapid-Köthen equipment according to ISO 5264-2:2002 (except for the significantly higher grammage than the 75 g/m^2 specified by the standard). The paper sheets were then cut into 15-mm-wide strips, which were subsequently soaked in water for 2 hours. The wet paper strips were then arranged together as indicated in Figure 1, with the strips overlapping 15 mm, such that the overlap area was 15 x 15 mm. The specimens were subsequently dried between Teflon wires at 93°C and at a pressure of 95 kPa below atmospheric pressure for various durations (0.5–40 minutes) in the Rapid-Köthen dryers. The prepared specimens were then carefully transferred to the tensile tester and tested as described below.

For specimens made of never-dried fibres, sheets with a grammage of 300 g/m^2 or 500 g/m^2 were prepared in the Rapid-Köthen machine. Owing to the support of the carrier board on which the wet sheets were couched according to the Rapid-Köthen method, the wet paper sheets could be cut in half. These halves were then removed from the carrier board and arranged together according to Figure 1 with the sheets overlapping 15 or 5 mm, such that the overlap area after strip cutting was 15 x 15 mm or 15 x 5 mm. The sheets were then dried at 93°C and at a pressure of 95 kPa below atmospheric pressure for various durations (4–50 minutes) in the Rapid-Köthen dryers. After drying, the moist sheets were cut into 15-mm-wide strips and tested as described below.

Two grammages and degrees of overlap were used because at high solids contents the shear strength of the specimens made of never-dried fibres was so high that they did not break in shear but in tension at the notches, if the overlap was not decreased and the grammage increased

The prepared specimens were tested on a type 81502 horizontal tensile tester (FRANK Prüfgeräte GmbH, Birkenau, Germany) designed for testing paper materials. Configuring the samples as shown in the specimen side-view in Figure 1 ensures there will be a relatively pure shear stress field along the contact zone between the two strips when the samples are loaded in tension [2]. Immediately after testing, the shear zones were cut off from the rest of the strips and put in an IR drier (Mettler LP16) mounted on a balance (Mettler PM460) to determine the solids content of the samples.

3 RESULTS AND DISCUSSION

The results of the shear testing of never-dried and rewetted sheets, made of beaten and of unbeaten fibres, that had been couched together as described above, are shown in Figure 2. From the data it is obvious that the shear strength of all combinations of the two types of fibres (i.e., beaten and unbeaten) and the two specimen preparation methods (i.e., never-dried and rewetted sheets) was low (<120 kPa) up to a solids content of approximately 60–70%, after which the shear strength increased rapidly with increasing solids content. The kink in the shear strength versus solids content plot at 60–70% suggests that interactions important for the strength at complete dryness started to develop at this particular solids content.

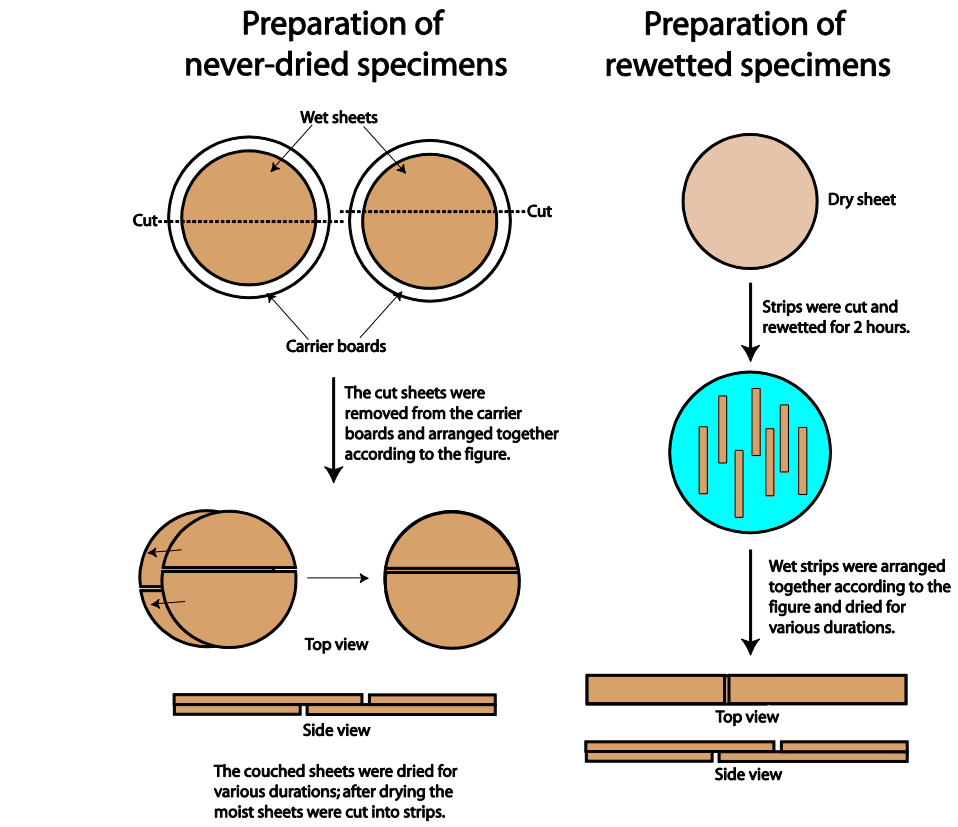

Figure 1. Schematic of how the shear testing specimens were prepared. The overlap between the strips was 15 mm except for the high-dry-content samples made of never-dried fibres, in which the overlap was reduced to 5 mm.

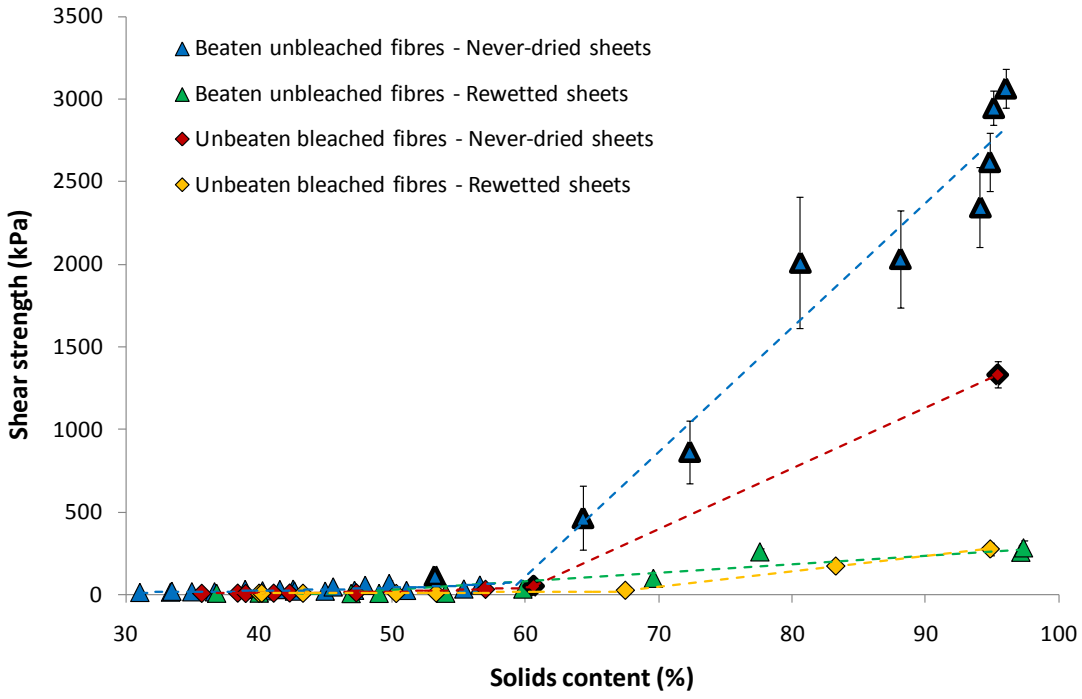

Figure 2. Shear strength of the various sheets couched together, plotted as a function of the solids content. The specimens with a 15-mm overlap between the strips are indicated by symbols with a thin outline, whereas the specimens with a 5-mm overlap are indicated by symbols with a bold outline. The regression lines included in the figure merely serve to guide the eye.

The exact nature of the fibre/fibre interactions at different dry solids contents is impossible to deduce from the present data. However, at a solids content of 60–70%, the fibres were likely so close together that significant van der Waals interaction could develop between the fibres. The interdiffusion of polymer chains between adjacent fibres might also have started to occur at this solids content. At solids contents below 60%, fibril entanglement, mechanical interlocking, capillary forces (below the fibre saturation point), and capillary condensation (above the fibre saturation point) are probably the most important interactions keeping the couched sheets together.

As seen in Figure 2, the highest shear strength, throughout the solids content range examined, was achieved with never-dried sheets made of beaten fibres, which is logical since beating is known to increase the strength of paper and never-dried fibres are known to give stronger paper than previously dried fibres. Beating is known to increase swelling [3] and never-dried fibres are known to swell more than previously dried fibres [4, 5]. Increased swelling increases the shear strength of fibre/fibre joints as determined by testing individual fibre/fibre crosses [6]. Increased shear strength of the fibre/fibre crosses should manifest itself in the shear strength of the couched papers, which explains why the never-dried sheets made of beaten fibres displayed the highest shear strength.

The specimens made from rewetted sheets had significantly lower shear strength than did those made from never-dried sheets. However, since beating increase swelling, sheet strength and fibre joint strength there should also be a difference between the rewetted sheets made from beaten and unbeaten fibres. This is not the case and it is suggested that this is due to that the reduced swelling of the rewetted sheets (compared to the virgin sheets) hinders them from developing fully intimate contact in the sheet interface, such that not only the actual fibre interactions, but also the conformability of the sheets at the macroscopic level determines the shear strength. Hence it is also suggested that the shear strength measurements only is a good measure of fibre interactions in the case of highly conformable sheets that develop full microscopic contact in the sheet interface.

van de Ven and co-workers have also studied the shear strength of couched paper sheets [7-9]. These authors, who examined blotter papers made of bleached unbeaten fibres, found that maximum shear strength was reached at a solids content of approximately 39%, after which the shear strength dropped, reaching zero at a solids content of approximately 47%. The rewetted sheets made of unbeaten fibres were not found to behave in this way in the present study. It is suggested that this discrepancy probably is due to that the blotter sheets must have been to un-conformable to allow close contact between fibres in the sheet interface and hence development of strong fibre-fibre interactions.

If further investigation and comparison with for example experiments with cellulose model surfaces show that the shear strength measurements under certain circumstances are a good estimate of the pure interactions between fibres, these measurements would be a very convenient for quantifying fibre interaction at different moisture content. This could probably contribute to a more rapid development of the understanding of how fibre interactions develop during sheet consolidation.

4 ACKNOWLEDGMENTS

The authors gratefully acknowledge the financial support for this project from BiMaC Innovation. Mr Felix Lindström is acknowledged for his skilful assistance with the laboratory work.

REFERENCES

[1] Nygårds, M., M. Just, and J. Tryding. Experimental and numerical studies of creasing of paperboard. *Int. J. Solids Struct.* **46**(11-12): 2493-2505 (2009).

[2] Nygårds, M., C. Fellers, and S. Östlund. Development of the notched shear test. Advances in Pulp and Paper Research, 14th Fundamental Research Symposium, Oxford, UK, 877-897 (2009).

[3] Stone, J.E., A.M. Scallan, and B. Abrahamson. Influence of beating on cell wall swelling and internal fibrillation. *Svensk Papperstidning*. **71**(19): 687-94 (1968).

[4] Forsström, J., B. Andreasson, and L. Wågberg. Influence of pore structure and water retaining ability of fibres on the strength of papers from unbleached kraft fibres. *Nord. Pulp Paper Res. J.* **20**(2): 176-185 (2005).

[5] Jayme, G. Mikro-Quellungsmessungen an Zellstoffen. *Der Papier-Fabrikant, Wochenblatt für Papierfabrikation*. **6**: 187-194 (1944).

[6] Torgnysdotter, A. and L. Wågberg. Influence of electrostatic interactions on fibre/fibre joint and paper strength. *Nord. Pulp Paper Res. J.* **19**(4): 440-447 (2004).

[7] Alince, B., et al. The effect of polyelectrolytes on the wet-web strength of paper. *Nord. Pulp Paper Res. J.* **21**(5): 653-658 (2006).

[8] de Oliveira, M.H., M. Maric, and T.G.M. van de Ven. The role of fiber entanglement in the strength of wet papers. *Nord. Pulp Paper Res. J.* **23**(4): 426-431 (2008).

[9] Tejado, A. and T.G.M. van de Ven. Why does paper get stronger as it dries? *Materials Today*. **13**(9): 42-49 (2010).

Session 8

Fiber – Fiber Bonding

Insights into single fiber-fiber bonds using atomic force microscopy

FRANZ J. SCHMIED[1,4], CHRISTIAN GANSER[1,4], WOLFGANG FISCHER[2,4], ULRICH HIRN[2,4], WOLFGANG BAUER[2,4], ROBERT SCHENNACH[3,4], CHRISTIAN TEICHERT[1,4]

[1]Institute of Physics, Montanuniversität Leoben, Franz Josef Strasse 18, 8700 Leoben

[2]Institute for Paper, Pulp and Fiber Technology,Graz University of Technology, 8010 Graz, Austria

[3]Institute of Solid State Physics, Graz University of Technology, Petersgasse 16/2, 8010 Graz

[4]CD-Laboratory for Surface Chemical and Physical Fundamentals of Paper Strength, TU Graz, Petersgasse 16/2, 8010 Graz

1 ABSTRACT

Paper is one of the most versatile materials in human society. It is used for delivering and storing information as well as to protect food and other goods from the environment. Although paper is already known for almost 4000 years, the process of bonding two fibers together is still an open discussion.

During the fabrication cycle of paper, single pulp fibers approach each other and form bonds during the drying process. The mechanism of forming bonds between two single fibers is up to now a speculative issue. There are several mechanisms suggested that play a significant role in forming fiber-fiber bonds that lead to a fiber network that is called paper. Lindström et al. proposed the following five bonding mechanisms [1]: (i) mechanical interlocking, (ii) hydrogen bonds, (iii) electrostatic interactions, (iv) interdiffusion, and (v) induced dipoles. In this work, a method is introduced that is based on conventional atomic force microscopy (AFM) technique to measure the desired bonding force. Besides this single quantity, the behavior prior to the failure is analyzed and correlated to the true bonded area, recorded by conventional AFM scanning. This comprehensive investigation reveals new insights into the mechanisms of fiber-fiber bonding and their contribution to the fiber-fiber bond. Furthermore, time dependent behavior, such as creep and relaxation can be studied. Additionally, a comparison between dry and wet fibers is presented, revealing the influence of drying on the fiber surface morphology.

REFERENCES

[1] [1] Lindström, T.; Wågberg, L. & Larsson, T., *Proc. 13th Fundamental Research Symp.* **2005**

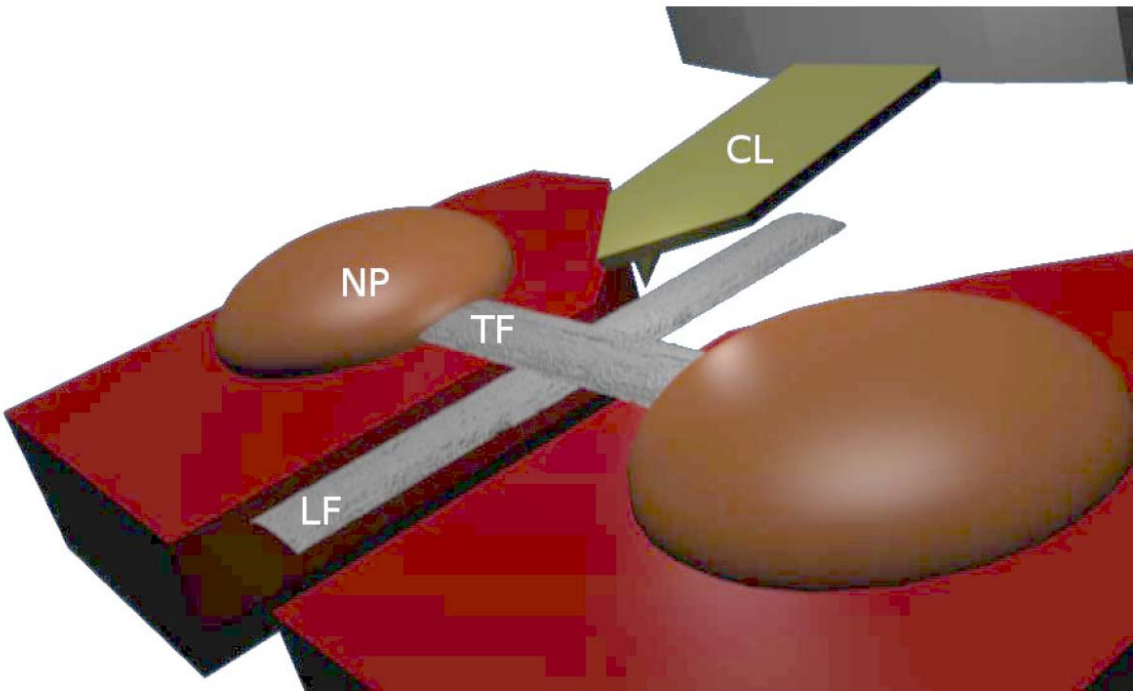

Figure 1. Measurement of Individual Fiber-Fiber Bonding Force using AFM: A single fiber-fiber crossing (TF-top fiber, LF-lower fiber) is glued to a sample holder using nail polish (NP). The cantilever CL of the AFM presses the lower fiber downwards. The cantilever force necessary to separate the two fibers is measured.

Measuring Bond Strengths of Individual Paper Fibers using Microrobotics

P. SAKETI and P. KALLIO

Micro- & Nanosystems Research Group
Tampere University of Technology
Korkeakoulunkatu 3, 33720, Tampere, Finland
pooya.saketi@tut.fi and pasi.kallio@tut.fi

Keywords: Bond Strength, Fiber-Fiber Bond, Individual Paper Fiber Bond, Measurement, Micromanipulation, Microrobotics

ABSTRACT

This paper discusses the direct strength measurement of individual fiber - fiber bonds. Conventional methods for characterizing fiber - fiber bond strengths are mainly on the hand-sheet level. Reported methods for measuring individual paper fiber bond strengths are manual, laborious and provide low throughput, or are indirect based on e.g. optical measurements. The microrobotic platform presented in this paper measures individual paper fiber bond strengths directly in a tele-operated process.

1 INTRODUCTION

An individual paper fiber bond (IPFB) is the construction unit of a paper hand-sheet. The quality of paper hand-sheets are affected by the strength of IPFBs directly. *Allison* in 1940 mentioned the following challenges to measure the IPFB strength: "Fundamental measurements of this property are impossible because of such unmeasureable and uncontrollable variables as the formation of the sheets, the nature of the actual area tested, and the several fundamental stresses empirically applied in any one standard physical test " [1]. Despite of the extensive achievements in science and technology in the last decades, the challenges mentioned by *Allison* are still valid. Because of the aforementioned complications, paper fiber specialists still rely more on bond strength estimations on the hand-sheet level rather than on the individual level. In other words, to provide statistically reliable data, it is preferred to measure the energy required to break a certain number of bonds on the hand-sheet level instead of characterizing many individual bonds [2]. A lack of high through-put IPFB strength measurement tools is one of the main reasons for the tendency of paper fiber specialists to use tests on the hand-sheet level. Recent studies, however, on internal bond strength measurement methods on the hand-sheet level such as a peel cohesion test, a delamination test, a Z-directional tensile test, a cantilever beam test, a shear cohesion test and a Scott bond test prove that the results acquired with these methods contain undesirable information[3]. In general, the results obtained with any of the aforementioned methods, include the fiber-fiber bonding energy together with other energies. For example: the Z-directional tensile test measures both intra- and inter-fiber bonding energies, the shear cohesion test couples the force required to shear the bond with the force acting on the plane of the sheet, and the dynamic nature of the Scott bond test overestimates the bond strength [3]. The need for new products in the highly competitive market motivates the paper making industry and paper fiber specialists to face the challenges of the IPFB strength measurements to get a better understanding of bonding mechanisms between two individual paper fibers.

Challenges of measuring the strength of an IPFB, is not only related to finding an adequately accurate and sensitive force-sensor but also handling and mounting the IPFB. *Mayhood et al. (1962)* modified a chainomatic balance to make an apparatus for measuring the shear strength of IPFBs and used cement to mount the IPFBs to the specimen holder [4]. *Schniewind et al. (1964)* used an Instron tensile tester for measuring the shear strength of the IPFBs and double-sided adhesive tape for mounting them [5]. *Stratton et al. (1990)* used the second generation of an IPC load-elongation recorder developed by *Hardacker (1962)* to measure the IPFB strength and used Epon 907 resin and hot melt to mount the IPFBs[6][7]. Manipulating and mounting the IPFBs in all of these reported methods are performed manually.

Advances in microrobotics and microsystems technology in the last decade provide new tools to manipulate and characterize both natural and synthetic micro- and nanoscale samples. *Sun et al. (2004)* and *Park et al. (2004)* have developed microsystem solutions to handle embryo cells [8][9]. *Carlson et al (2007)* and *Eichhorn et al. (2007)* have used microrobotics to manipulate carbon nanotubes [10][11]. *Probst (2009)* has reported a microassembly system capable of semi-automatic assembly of 3D bio-microrobotic devices from individual microelectromechanical (MEMS) components [12].

Micro- and Nanosystems research group of Tampere University of Technology has realized the need for a high throughput individual paper fibers and IPFBs characterization system and has utilized microrobotics and microsystems technology to address this need. In a previous study, a microrobotic platform to make, manipulate and break IPFBs was reported which was able to break the IPFBs in a tele-operated process with three microgrippers without using any type of adhesive [13]. The shortcoming of the reported platform was a lack of a force sensor to measure the IPFB strength. This paper introduces a microrobotic platform to measure the strength of IPFBs directly

by using two microgrippers and a force-sensor. At the moment, the force-sensor is not integrated in the third microgripper- Therefore; glue is used to attach the end of the IPFBs to the sensor. The results and knowledge acquired in this study will be used to develop and integrate a force-sensor in a microgripper to measure the strength of IPFBs with this microrobotic platform without the need for using adhesives.

The rest of the paper is organized as follows: Section 2 explains the design and implementation of the platform; Section 3 and Section 4 encompass the experiments and results, respectively. Section 5 includes the conclusions and discussions of the study and Section 6 describes the plans for future works.

2 DESIGN AND IMPLEMENTATION

The conceptual design of the platform and the main functions are illustrated in **Figure 1**. The tasks of sample storage (F1), visualization (F4), control (F6), micromanipulation (F2) and dispensing (F5) functions are discussed in previous publications about individual paper fiber flexibility measurement and IPFB making, manipulating and breaking, respectively [13][14]. The force sensing (F3) function measures the magnitude of force required to break an IPFB.

Figure 2 illustrates the implementation and configuration of the platform. In this configuration, microgrippers (1) and (2) (SmarAct Co.) have three degrees of freedom (DOF) to grasp and manipulate the IPFBs in the XYZ directions. The movement of the microgrippers is synchronized. A 3DOF glass-slide-micromanipulator (3) (SmarAct Co.) moves a glass slide (4) in the XYZ directions. The glass slide is used both for gluing and glue removal purposes. A 1DOF rotary table (5) (SmarAct Co.) and a 10mN force sensor (7) (FemtoTools Co.) are mounted on the top of a 2DOF XY-table (6) (SmarAct Co.). The rotary table is used to orient the IPFBs and the force sensor is used to measure the strength of IPFBs. The sensitivity and resolution of the force sensor are 5000 µN/V and 2 µN, respectively. A syringe pump (New Era Pump Systems Inc.) with a silicon tube (8) is used for supplying glue-removing acetone onto the glass slide (4). A motorized 12X zoom (Navitar Co.) and a manual macro video zoom lens (Optem Co.) are used to provide top-view and side-view visual feedbacks, respectively. A PCI-6259 (National Instruments) measurement board is used for acquiring data from the force sensor. The glue (BILTEMA) is used to attach the IPFBs free end to the force sensor probe.

3 EXPERIMENTS

An *untreated* softwood pulp sample is used in the experiments. To make the IPFBs, a highly dilute suspension of fibers is placed between two Teflon plates and dried for 45 minutes in 70 °C under 140

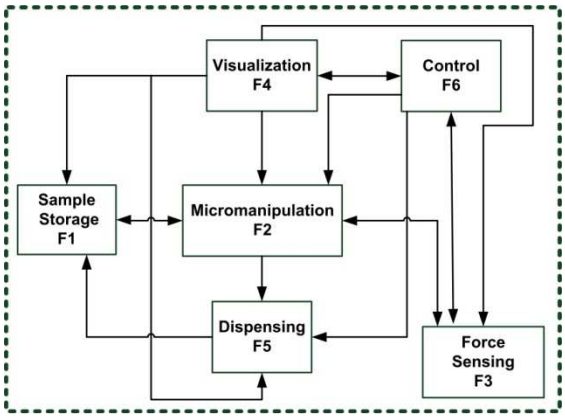

Figure 1. Conceptual design of the microrobotic platform to measure IPFB strength.

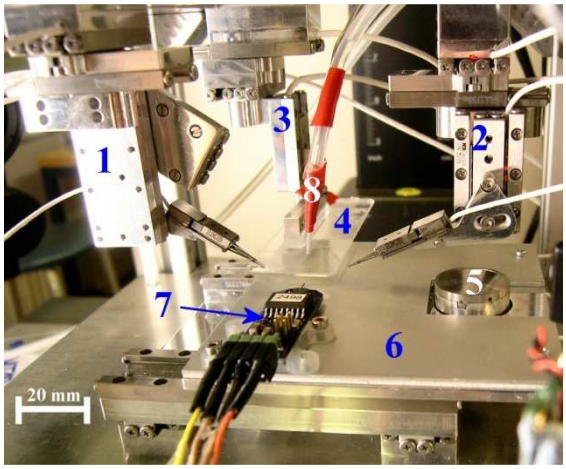

Figure 2. Implementation of the microrobotic platform. 1) and 2) XYZ-microgrippers, 3) Glass-slide-micromanipulator, 4) Glass slide, 5) Rotary table, 6) XY-table, 7) Force sensor, 8) Tube of the syringe pump.

kN/m^2 pressure. Then the Teflon plate is placed under a light microscope to identify the IPFBs; the IPFBs are moved from the Teflon plate to the rotary table using a tweezers.

From this point, the rest of the experiment is performed in a tele-operated process using the microrobotic platform. The XY-table moves the rotary table under the field-of-view (FOV). The rotary table orients the IPFBs. After imaging the bonding area of the IPFBs, one of the IPFBs is grasped and picked-up with two microgrippers in synchronized mode. Most of the IPFBs rotated 90° during the grasping and formed a vertical cross between the microgrippers, as depicted in **Figure 3**. **Figure 4** illustrates the tele-operated process of IPFB strength measurement using the microrobotic platform. A droplet of glue is placed on the edge of the glass slide. The glass slide is moved to the FOV and aligned with the force sensor probe using the visual feedback [See **Figure 4**-A]. The force sensor probe is dipped into the glue [See **Figure 4**-B] and is then aligned with the free end of the IPFB both horizontally and vertically [See **Figure 4**-C]. After waiting three minutes the glue is cured.

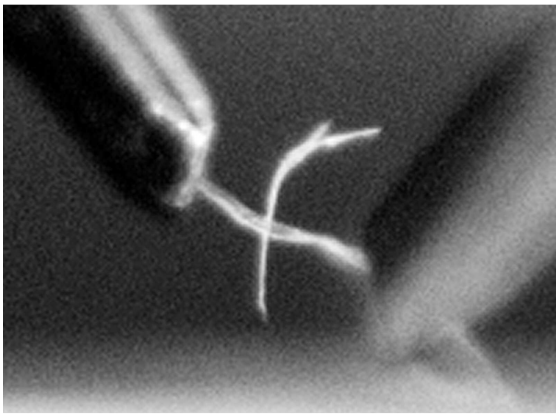

Figure 3. *Side-View:* An IPFB grasped with microgrippers standing as a vertical cross.

To measure the IPFB strength, the XY-table moves the force sensor and thus the crossing fiber in continuous 5 µm steps backwards until the IPFB is broken [See **Figure 4** -D]. To use the force sensor in the next measurement, the glue contaminated on the probe should be removed. The syringe pump infuses droplets of acetone onto the edge of the glass slide and then the force sensor probe is dipped into acetone to remove the remaining glue. As acetone is a very aggressive chemical, it is necessary to calibrate the force sensor after glue removals to verify that the performance parameters of the force sensor do not change.

4 RESULTS

In this section, the results of the IPFB strength measurements using the microrobotic platform are presented. **Figure 5** shows the force sensor data in an IPFB strength measurement. The step shape of the data is caused by the 5 µm stepwise movement used for breaking the IPFB.

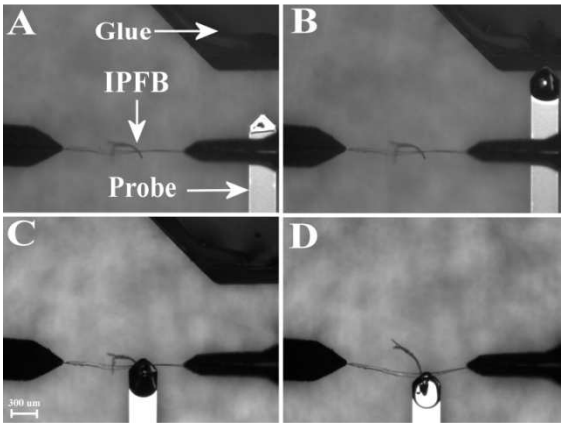

Figure 4. *Top-View:* Process of IPFB strength measurement. A) Placing the glue onto the glass slide and moving the glass slide under the FOV. B) Dipping the force sensor probe into the glue. C) Aligning the free end of the IPFB with the force sensor probe and curing the glue. D) Moving the force sensor backwards and breaking the bond while measuring the force.

The bonded areas are estimated from the top-view images before breaking the IPFBs. The performance parameters of the force sensor are inspected between and after the tests to make sure that the cleaning process does not affect them. **Table 1** shows the results of the IPFB strength measurements. Since the IPFBs stand in a vertical cross during the measurements [See **Figure 3**] and the free end of the IPFB is pulled only from one end [See **Figure 4**], the measured values indicate the IPFB strength as a combination of normal and shear forces. The IPFB strength values measured with the microrobotic platform is in the same range as the bond strength values reported previously in the literature [6].

5 CONCLUSION AND DISCUSSION

A microrobotic platform to measure IPFB strength was designed and fabricated. The IPFB strength measurements were demonstrated successfully. The tele-operated microrobotic platform minimizes the human interaction with the IPFBs in handling them which reduces the chance of introducing artifacts to them, and also minimizing human errors while measuring the IPFB strength. Even though acetone was used to remove the glue used for mounting a fiber to the sensor probe, the calibration tests indicated that there are not severe changes in force sensor performance for few measurements. However, the force sensor calibration is necessary in a regular basis in a case of a high number of tests.

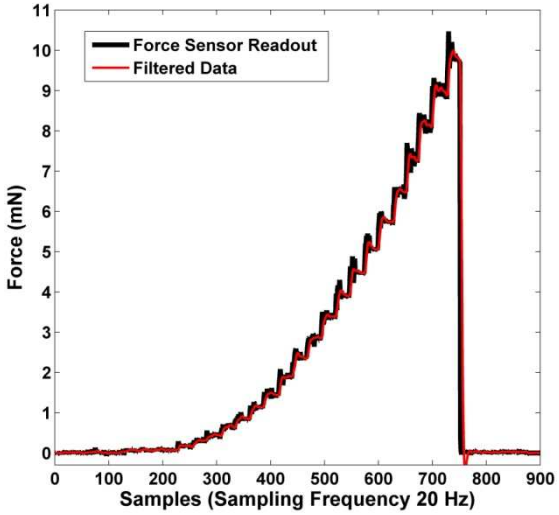

Figure 5. Measured bonding force. Black line: Force Sensor readout; Red line: Filtered data.

Table 1. Results of IPFB strength measurements.

Test No.	Force (µN)	Area (μm^2)	Bond Strength (N/mm^2)
1	2349.1	929.4	2.5
2	943.3	685.3	1.4
3	9877.0	523.4	18.9
4	9989.5	626.2	16.0
5	1726.8	1076.8	1.6

The following error sources are identified during the measurements: pulp fibers are natural fibers and they do not have as uniform properties as synthetic fibers; optically measured bonded area is not necessarily equal to the actual bonded area; the measured force during the bond strength measurement is a combination of normal force and shear force components and it is not possible to decuple them with the current configuration of the platform. In other words, the IPFB breaking mechanism is neither shear nor tension, but a combination of both which result in a peeling mechanism.

6 FUTURE WORKS

Modifying the microrobotic platform to measure the bond strength in a shear mode will help the paper fiber scientists to understand the IPFB breaking mechanisms better in the future. This issue can be addressed either by placing the force sensor in parallel with the plane of bonded area or adding a rotational degree of freedom to the microgrippers to rotate the IPFB towards the force sensor.

Gluing the IPFBs to the force sensor probe is not only time consuming but also removing the glue from the probe with acetone will eventually destroy the force-sensor if the number of experiments is high. In our former publication, a method to break the IPFBs using a third microgripper was reported [13]. **Figure 6** illustrates breaking an IPFB with a third microgripper. Integrating a force sensor into the third microgripper will eliminate the need for gluing the free end of IPFB to the force sensor probe. In addition, it will provide infrastructure to measure the strength of IPFBs automatically with high throughput.

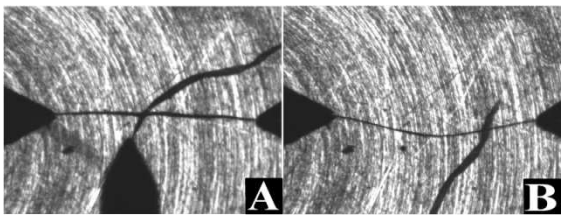

Figure 6. Breaking an IPFB with three microgrippers. A) Grasping the crossing fiber and pulling it. B) Breaking the IPFB [13].

ACKNOWLEDGEMENTS

The authors gratefully acknowledge The Finnish Funding Agency for Technology and Innovation (Tekes) for funding this project, M. v. Essen at MST-Group of Tampere University of Technology (TUT) for developing the software and user interface of the platform and Marianna Vehviläinen at Department of Material Science of TUT for providing the fiber samples.

REFERENCES

[1] H. J. Allison, Jr. The Relation between Surface Activity and Fiber-Bond Strength in Papermaking Pulp. PhD Thesis, The Institute of Paper Chemistry, Appleton, Wisconsin (1940).

[2] L. Nordman, Ch. Gustafsson and G. Olofsson. The strength of bondings in paper II. *Paperi ja Puu J.* No 8:315 – 320 (1954).

[3] A. Koubaa and Z. Koran. Measure of the internal bond strength of paper/board. *Tappi J.* **78**(3): 103 – 111 (1995).

[4] C. H. Mayhood, JR., O. J. Kallmes and M. M. Cauley. Mechanical properties of paper; Part II: Measured shear strength of individual fiber to fiber contacts. *Tappi J.* **45**(1): 69 – 73 (1962).

[5] A. P. Schniewind, L. J. Nemeth and D. L. Brink. Fiber and pulp properties; I. Shear strength of single-fiber crossings. *Tappi J.* **47**(4): 244 – 248 (1964).

[6] R. A. Stratton and N. L. Colson. Dependence of fiber/fiber bonding on some papermaking variables. SYMP on Materials Interactions Relevant to the Pulp, Paper, and Wood Industries, San Francisco, USA, 173 – 181, (1990).

[7] K. W. Hardacker. The automatic recording of the load-elongation characteristic of single papermaking fibers: IPC fiber load-elongation recorder. *Tappi J.* **45**(3): 237 – 246 (1962).

[8] Y. Sun, M. A. Greminger and B. J. Nelson. Investigating protein structure with a microrobotic system. ICRA 2004 IEEE International Conference on Robotics and Automation, New Orleans, USA, 2854–2859, (2004).

[9] J. Park et al. An integrated bio cell processor for single embryo cell manipulation. IROS 2004 IEEE/RSJ International Conference on Intelligent Robots and Systems, Sendai, Japan, 242–247, (2004).

[10] K. Carlson et al. A carbon nanofibre scanning probe assembled using an electrothermal microgripper. *Nanotechnology J.* **18**(34): 345501 (2007).

[11] V. Eichhorn, K. Carlson, K. N. Andersen, S. Fatikow and P. Boggild. Nanorobotic manipulation setup for pick-and-place handling and nondestructive characterization of carbon nanotubes. IROS 2007 IEEE/RSJ International Conference on Intelligent Robots and Systems, San Diego, USA, 291–296, (2007).

[12] M. Probst, C. Hrzeler, R. Borer and B. J. Nelson. A microassembly system for the flexible assembly of hybrid robotic mems devices. *Optomechatronics J.* **3**(2): 69 – 90 (2009).

[13] P. Saketi and P. Kallio. Microrobotic platform for making, manipulating and breaking individual paper fiber bonds. ISAM 2011 International Symposium on Assembly and Manufacturing, Tampere, Finland, (2011).

[14] P. Saketi, A. Treimanis, P. Fardim, P. Ronkanen and P. Kallio. Microrobotic platform for manipulation and flexibility measurement of individual paper fibers. IROS 2010 IEEE/RSJ International Conference on Intelligent Robots and Systems, Taipei, Taiwan, 5762–5767, (2010).

Inter-Fibre Bond Strength and Combined Normal and Shear Loading

MIKAEL S. MAGNUSSON, SÖREN ÖSTLUND

BiMaC Innovation
Department of Solid Mechanics
KTH, Royal Institute of Technology
SE-100 44 Stockholm, Sweden
mima@kth.se and soren@kth.se

1 Abstract

Despite their obvious importance for the properties of paper, relatively little is known on the deformation and damage mechanisms of inter-fibre bonds, compared to the fibres. In order to tailor the properties of fibre network materials, by biochemical and/or mechanical modifications of the fibre wall and fibre surfaces, better understanding on how to evaluate the properties of the bonds at the microscopic level is desirable. This paper reports on the development of a method including manufacturing of fibre-fibre cross test pieces, set-up and analysis of experimental results. Evaluation of the strength of modified and non-modified kraft pulp fibres has been investigated. The measured load-displacement responses have been analyzed numerically, taking into account the initial curved shape of the crossing fibres.

Of particular interest has been to estimate the state of loading in terms of normal and shear components in the bond region at failure. Different modes of bond failure have been observed in the experiments, and they are used to qualitatively discuss the mechanical behaviour of the bond region under loading.

2 Introduction

In paper physics, the inter-fibre bond strength is commonly estimated indirectly from sheet testing. Nordman *et al.* [1] proposed a method for estimating the specific bond strength based on release of energy and loss of light scatter in a sheet. Since the results of these measurements rely on the averaged energy dissipation of the whole sheet during tensile testing, the results cannot easily be used for comparison of bond strength between different types of fibres or different types of fibre modifications. Direct measurements of inter-fibre bond strength have been reported by Mayhood [2] *et al.* in 1962 and, later, others, ([3], [4], [5], [6], [7]), by testing individual fibre-fibre crosses. In this study, a similar approach is used, based on mechanical testing of fibre-fibre crosses (see Figure. 1) by applying a load on to one fibre that is bonded to another fibre, which is fixed at both ends.

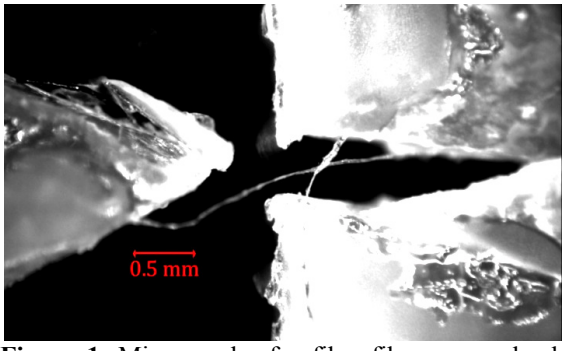

Figure 1. Micrograph of a fibre-fibre cross glued on a specimen holder.

3 Materials and Methods

In this study, fibre-fibre crosses were prepared by drying a small amount of fibres in a steel press with PTFE (Teflon) treated surfaces. Fibres where manually suspended into droplets of depolarized water under a stereo microscope with oblique illumination with typically two to ten individual fibres per droplet to keep the flocculation of the fibres low, and to prevent premature drying. After drying, the plates where examined under a stereo microscope and fibre-fibre cross samples were selected and placed onto a steel specimen holder; see Figure 2, using tweezers.

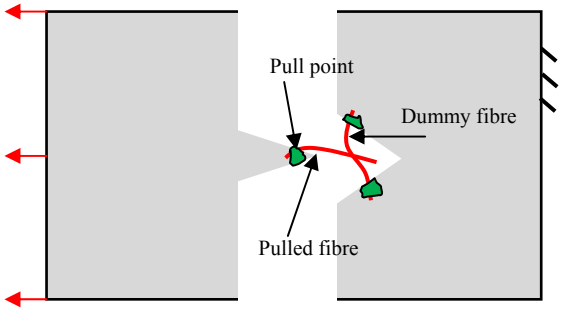

Figure 2. Schematic of the specimen holder with fibres in red and glue points in green.

The mechanical testing experiments were carried out in an Instron ElectroPulse E1000 electrodynamic tensile testing machine using a miniature Honywell Sensotec 50 g load cell to resolve forces in the mN range.

The relative orientation of the two fibres and the natural variations in the fibre geometry, respectively, give rise to different combinations of normal and shear loading in the inter-fibre bond. Thus, the measured force- displacement relation was in the analysis of the experiment treated as a structural response dependent on an unknown combination of interface normal and shear strengths, geometrical and material parameters.

Information on the structural geometry was gathered from microscope images of the specimen, where the centreline of the fibres was used in the structural model (an example is shown in Figure 3).

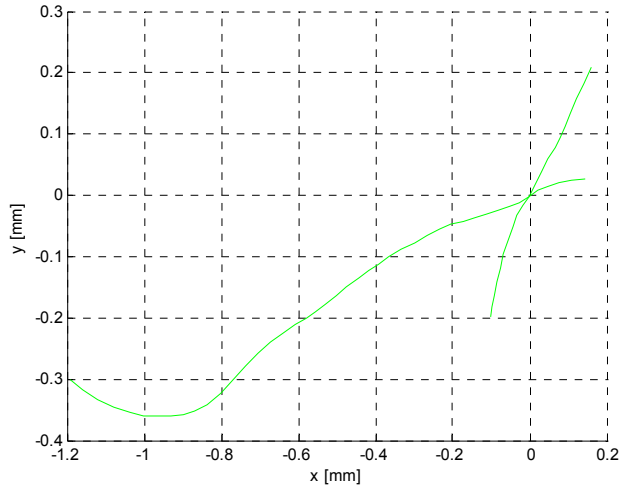

Figure 3. Centreline approximation of the captured fibre-fibre cross geometry used in the analysis

This information was used to relate the measured structural response to the response of the structural model based on the finite element method and then to evaluate the normal and shear loading components at the fibre-fibre interface. The structural model was calibrated using the point of loading where a sudden drop of stiffness occurred (as are depicted in Figure 4).

Even though pulp fibres experience large variations in material behaviour, a simple linear elastic model was able to capture the experimental load-displacement curve for the fibre-fibre crosses when the initial shapes of the fibres were taken into account since the bond strength is considerably lower than the yield strength of the fibres. The structural model was solved using three dimensional solid finite elements with finite deformations (Figure 5).

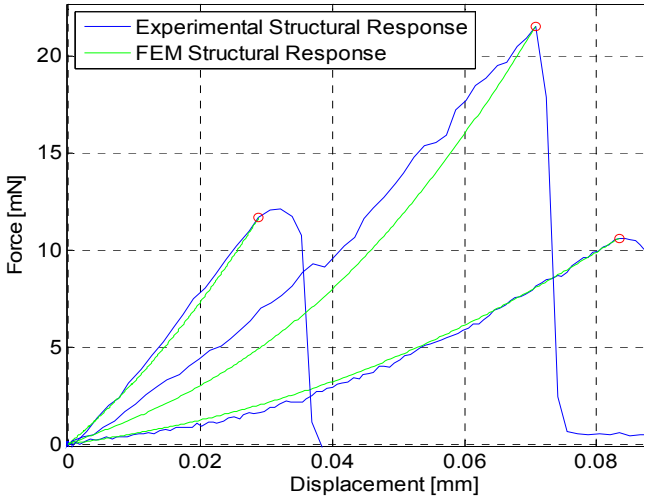

Figure 4. Comparison between the experimental and model response for three different specimens experiencing, from left to right, softening, brittle and progressive damage failure. The point used for calibrating the model is depicted in red

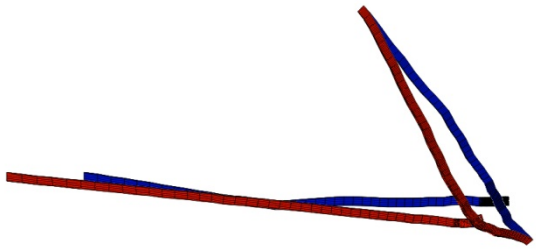

Figure 5. Example of a structural model in the undeformed (blue) and in the deformed state (red).

By this simple scheme, considering the geometry and the point at the onset of damage only, the predicted force- displacement curve show an excellent fit for most cases, and therefore, as a first approximation, we assume that the model can be used to estimate the loads transferred by the fibre-fibre interface. It should be noted however that even though the structural response (measured at the point where the load is applied) is captured very well, the bending and twisting behaviour would affect the transferred loads and not necessary coincide with that of such a simple material model.

Also, the model fibres where approximated as hollow and rectangular but non-straight elastic bodies. In reality the geometry of the cross section as well as material behaviour, such as anisotropy, are far more complex and show variations along the fibre and may also result in other modes of deformation and failure.

From the analysis of the structural fibre model, three stress components arise in the interface between the model fibres. These stresses are integrated over the interface surface to obtain the load transferred normal to the interface surface, in the direction of the pulled fibre and in the direction perpendicular to the pulled fibre. These interface traction distributions are illustrated in Figure 6.

The averages of these traction distributions serve as a first approximation of the combined normal and shear loading at bond failure, although, details in the shape and internal structure of the fibres can have a noteworthy influence on the state of loading of the bond.

Since the selection of specimens will have an influence on the state of loading, a parametric study was carried out in parallel to the experiments. By varying geometric parameters in the model structure, a better understanding on how to design the inter-fibre bond strength experiment is gained.

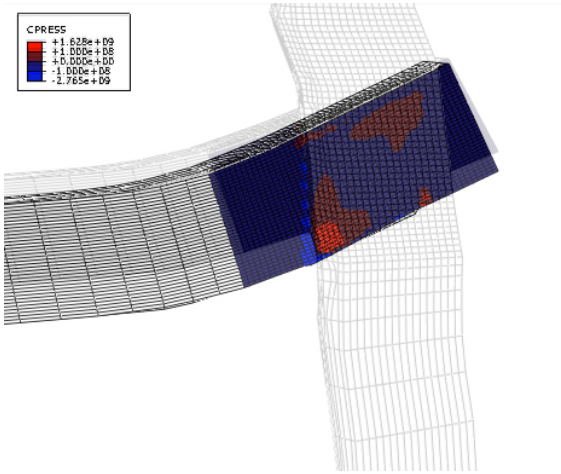

(a) Interface normal traction

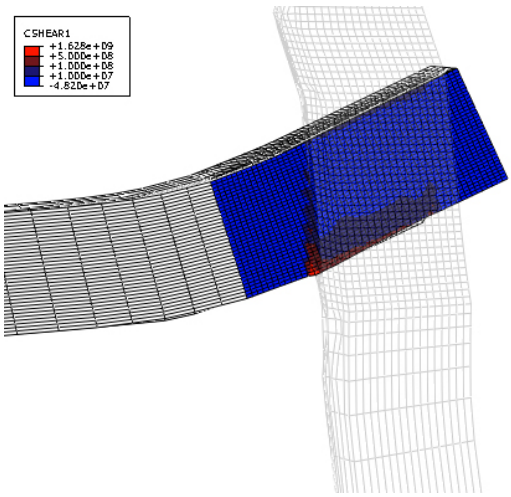

(b) Interface shear traction in the direction of the pulled fibre

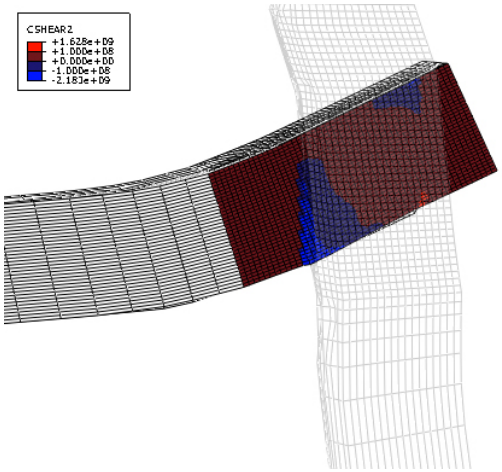

(c) Interface shear traction in the direction perpendicular to the pulled fibre

Figure 6. Example plots of the interface traction distribution, normal to the interface, (a), in direction of the pulled fibre, (b) and perpendicular to the pulled fibre, (c).

The inter-fibre bond test have, in the previously published results ([3], [4], [5], [6], [7]), all been conducted in a manner that yields an "near Mode II" or "sliding" type of loading (see Figure 7), resulting in stresses in the inter-fibre bond that are predominantly shear.

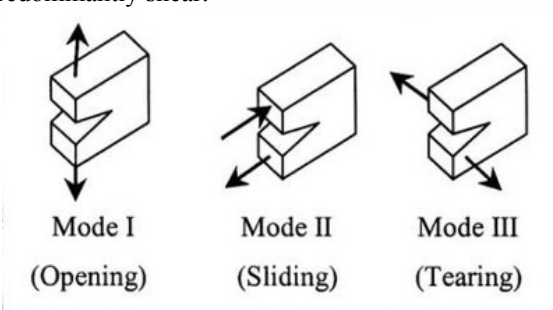

Figure 7. Illustration of Mode I, II and III fracture modes

By applying the load in an out-of-plane (near Mode I or opening mode) or in-plane perpendicular to the pulled fibre (Mode III or tearing mode) information on the strength of the inter-fibre bond in other directions could be obtained.

Lastly, the influence of chemical modification of the fibre surface are evaluated by comparison of inter-fibre bond strength of unmodified and modified fibres, respectively.

REFERENCES

[1] L. Nordman, C. Gustavsson, and L. Olofsson, *Papper och Trä, 3*, No. 47, 1952

[2] C. H. Mayhood, JR., O. J. Kallmes, and M. M. Cauley, The Mechanical Properties of Paper – Part II: Measured Shear Strength of Individual Fiber to Fiber Contacts, *Tappi J.* **45(**1):69-73 (1962)

[3] A. P. Schniewind, L. J. Nemeth, and D. L. Brink, Fiber and Pulp Properties - 1. Shear Strength of Single-Fiber Crossings, *Tappi J.* **47(**4):244- 248, (1964)

[4] D. C. McIntosh, Tensile and Bonding Strengths of Loblolly Pine Kraft Fibers Cooked to Different Yields, *Tappi J.* **46**(5):273-277 (1963)

[5] A. F. Button, Fiber-Fiber Bond Strength – A Study of a Linear Elastic Model Structure, PhD Thesis, The Institute of Paper Science and Technology, Atlanta, Georgia (1979)

[6] R. A. Stratton and N. L. Colson, "Fibre wall damage during bond failure." *Nordic Pulp and Paper Research Journal*, **8**(2):245-257 (1993)

[7] A. Torgnysdotter, Fibre/fibre joints; Their characterization and influence on different paper strength properties, PhD Thesis, Department of Fibre and Polymer Technology, Stockholm, Sweden, KTH. Royal Institute of Technology PhD Thesis (2006)

Effect of drying and refining on the fibre-fibre shear bond strength measured through acid exposure

KAUSTUBH JOSHI, WARREN BATCHELOR AND KHAIRUNNISAA ABD RASID

Australian Pulp and Paper Institute, Department of Chemical Engineering, Monash University, Australia

Warren.batchelor@monash.edu

INTRODUCTION

Previously we reported a simple concept *[1]* for measuring the fibre-fibre shear bond strength, based on the idea of weakening the fibres independently of the bonds in a sheet of paper, using acid vapour until all the fibres break across the fracture line during a tensile test. The bond strength is then calculated from the fibre strength, as measured by the zero-span test, at the point where the fibres first are weakened such that they all break. This is determined by using a confocal microscope to image each fracture line and manually counting broken and pulled out fibres. The minimum acid exposure time required for all the fibres along the fracture line to break is called the critical exposure time.

THEORY

The fibre-fibre shear bond strength, σ_b, was calculated from the fibre strength, as calculated from the measured zero-span strength, divided by the average area of a fibre-fibre bond, estimated from the fibre width.

$$\sigma_b = \frac{8 Z_c \rho X_f \overline{\cos\theta}}{3 D_w^2} \quad (1)$$

Where Z_c is the zero-span strength at the critical point, ρ is the fibre wall density, which is assumed to be 1500 kg/m^3, X_f is the fibre wall cross sectional area, D_w is the fibre width and $\overline{\cos(\theta)} = 0.841$ and is the average of the all the values of the values of $\cos(\theta)$, once the probability density function of fibre angle distribution is taken into account and where θ =0 is when two fibres are lying on top of each other. It should be noted that this has been somewhat changed from the original paper.

RESULTS AND DISCUSSION

Figure 1 shows how the appearance of the fracture line changes with increasing acid exposure. The fracture line of the sample without acid gas exposure many fibres that have pulled out across the fracture line, while after three hours acid exposure time, the fracture line appears as if it has been cut with a knife and almost all the fibres crossing the fracture line have broken.

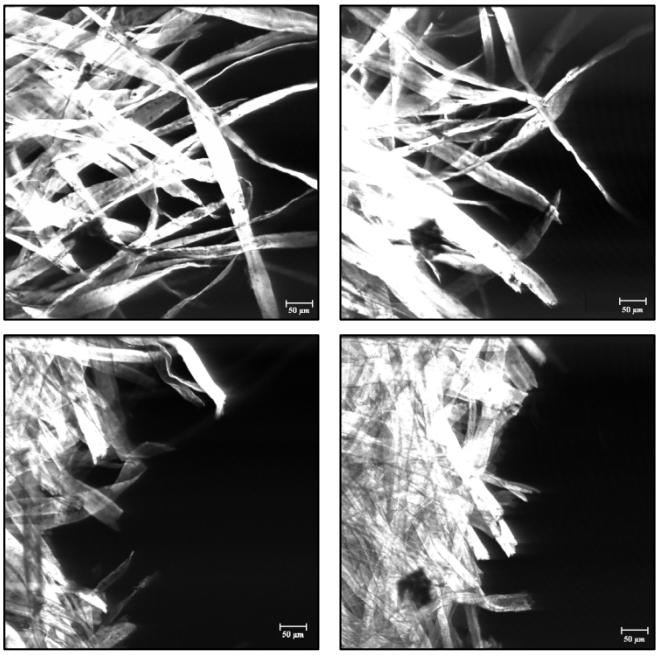

Figure 1. Fracture line images from sheets made from NIST pulp refined for 5 minutes. Top left: 0 hour; top right: 30 minutes; bottom left: 2 hours; bottom right: 3 hours of acid exposure

Two sets of experiments were made.

The NIST NBSK reference material (RM 8495) *[2]* is a dried bleached softwood pulp and was used to investigate the effect of refining. Three sets of handsheets were made, with the first set from the unrefined pulp and the second and third sets after refining for 5 and 40 minutes, respectively, in a Valley beater.

The level of refining was found to have little influence on the reduction in zero-span strength with acid gas exposure. Zero-span strength shows a sharp initial fall followed by an approximately linear reduction of fibre strength with exposure. The differences between the samples are due to fibre straightening in refining allowing more fibres to contribute to the load at failure *[3]*.

Refining reduced the critical exposure time from 6.7 hours for the paper made from the unrefined pulp to 2.06 hours for the paper made from the fibres refined for 40 minutes. The calculated bond strength increased from 13.7 MPa (unrefined) to 37 MPa for sheets made from fibres refined for 40 minutes. The bond area was calculated from the average fibre width and average crossing-angle in the sheet, with no allowance for the actual area of a crossing that will be in contact. A substantial fraction of the improvement in calculated bond strength is probably due to the bonded area of each fibre-fibre contact increasing.

A 60% yield, never-dried Radiata Pine pulp was used to investigate the effect of drying on the bond strength. The pulp was beaten in a Valley beater for 12 minutes. After refining, a 0.2mm slotted screen and 200 mesh screen for fines were used to remove shives and fines, respectively. Three sets of sheets were made. The first set was from the never-dried starting material. The second set and third set of handsheets were made from pulp from handsheets that had been dried, reslushed and made into handsheets again. For the second and third set, the initial drying was conducted at room temperature and 105^{o}C, respectively. The effect of the high temperature drying was to reduce the calculated bond strength from 25 MPa to 16 MPa in comparison to the sheets made from the never-dried fibres. Previous estimates of the reduction in shear-bond strength with drying, as calculated using the Page equation *[4]*, showed somewhat similar fraction of reduction- eg 30% reduction after air-drying unrefined fibres and a 50% reduction after air-drying refined fibres. However, when the values are converted to bond strengths using an assumed fibre perimeter and length, then the maximum calculated bond strength is 5.6MPa, for sheets made from a refined, never-dried softwood kraft.

The sources of discrepancy are two-fold. Firstly the area basis of the bond strength calculation for the Page equation is different to what has been used here, with the Page equation assuming that the entire perimeter of the fibre is involved in bonding, instead of only the width of the fibre, as has been assumed in this work. The second source of the discrepancy is that equation 1 assumes that the fibres are uniform cylinders, when the softwood fibres will be tapered at their ends. Preliminary estimates suggest that equation 1 will overestimate the bond strength, as a result of this taper, by up to 50%.

REFERENCES

1. JOSHI, K.V., BATCHELOR, W.J., PARKER, I.H. and NGUYEN, K.L., "A New Method for Shear Bond Strength Measurement", *Proc. International Paper Physics Conference*, Batchelor, W.J., Ed., Appita, Gold Coast, 7-13 (2007).
2. AMPULSKI, R.S., "Report of Investigation Reference Materials 8495 Northern Softwood Bleached Kraft 8496 Eucalyptus Hardwood Bleached Kraft", National Institute of Standards and Technology Gaithersburg, MD (2001).
3. SETH, R.S., "Zero-Span Tensile Strength of Papermaking Fibres", *Paperi Ja Puu-Paper & Timber*, 83(8):597-604 (2001).
4. GURNAGUL, N., JU, S. and PAGE, D.H., "Fibre-Fibre Bond Strength of Once-Dried Pulps", *J. Pulp Paper Sci.*, 27(3):88-91 (2001).

A Model Approach to Understand the Fiber – Fiber Bond in Paper

R. SCHENNACH[2,4], U. HIRN[1,4],
A. E. HORVATH[4], F.J. SCHMIED[3,4],
C. TEICHERT[3,4]

[1]Institute for Paper, Pulp and Fiber Technology, Graz University of Technology
[2]Institute of Solid State Physics, Graz University of Technology
[3]Institute of Physics, University of Leoben
[4]CD-Laboratory of surface chemical and physical fundamentals of paper strength

robert.schennach@tugraz.at

1 Introduction

The strength of paper depends on three properties namely the network, the strength of the single paper fibers and the strength of the bonds between individual paper fibers in the network. Of these three properties only the strength of a single fiber has been understood in quite some detail. The network is extensively investigated, however, more information about the bonding mechanism between the individual fibers would be very important for this field of paper research. The bond between two single paper fibers has also been studied over the years. However, due to a lack of appropriate analysis methods there is still hardly anything known about quantitative properties of the fiber – fiber bond. In this contribution we aim to build a model for understanding the bond between single paper fibers. Five bonding mechanisms have been established [1] in paper research and these are the starting point for the model proposed here.

2 Model

The five bonding mechanisms are mechanical interlocking, interdiffusion, hydrogen bonding, Van der Waals bonding and Coulomb interactions. In the following the mechansims will be discussed shortly.

Mechanical interlocking is most likely due to two effects. One is wrinkling of the fiber surfaces and the second is entanglement of fibrils and microfibrils from the two bonding fibers. That the latter happens can be seen in atomic force microscopy (AFM) images of the formerly bonded area between a single fiber – fiber bond, recently obtained in our group. The first will happen in the drying process, when the fibers shrink and the fiber surfaces start to wrinkle.

Interdiffusion can happen when the fiber surfaces are close together in the wet state. Then cellulose molecules or hemicelluloses from one fiber can diffuse into the second fiber. This will establish a bond. This bond will mainly be due to the interaction of the diffused species with the cellulose and hemicelluloses of the fiber. These interactions will be hydrogen bonding, Van der Waals bonding and Coulomb interactions. Therefore, one can expect that interdiffusion increases the impact of these three bonding mechanisms. The model proposed here focuses on these three bonding mechanisms.

Hydrogen bonding will occur mainly between the OH groups in the cellulose molecules in terms of intra molecular hydrogen bonds. Such bonds can also occur between hemicelluloses and between cellulose and hemicellulose molecules. Another source of hydrogen bonds can be the acid functions in hemicelluloses. For our model approach we try to get a handle on the number of hydrogen bonds that can be formed. For this purpose we use the proposed structure of microfibrils [2]. This structure suggests that the surface of a microfibril consists of a low Miller index surface of a cellulose crystal. Three such surfaces are shown in figure 1.

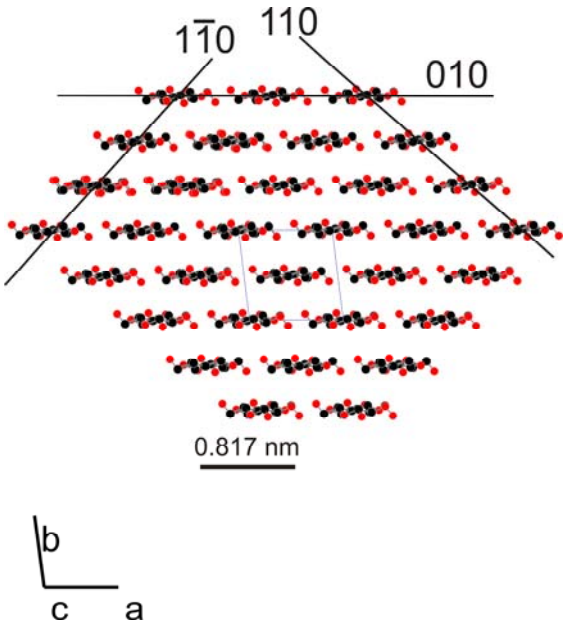

Figure 1. Crystal structure of cellulose I. Three low index surfaces are indicated. Carbon atoms are black and oxygen atoms are red. The unit cell is indicated in light grey.

One can now take a closer look at one of these surfaces and use the surface structure to count the number of possible intra molecular hydrogen bonds on this surface. If two such surfaces get into

molecular contact one will have this number of hydrogen bonds per unit area. In this way one can calculate a lower limit for the influence of hydrogen bonds on the total binding energy between two paper fibers. For the (010) plane one finds 4.7 hydrogen bonds per $(nm)^2$. In the next step this number can be multiplied with the bond energy of a typical hydrogen bond [3] in order to calculate the bonding energy due to hydrogen bonds (9.1x10-23 kJ(nm)-2).

A similar approach can be made for Van der Waals interactions. In this case one needs the number of atoms per unit cell, as Van der Waals interactions can occur between all kinds of atoms. Taking again the (010) plane of cellulose one gets about 46 atoms per $(nm)^2$. With an average Van der Waals bonding energy [4] this adds up to about 2.4x10-22 kJ(nm)-2. This result shows that the influence of Van der Waals interactions on the fiber – fiber bond is slightly higher than that of hydrogen bonds.

For Coulomb interactions the model cannot be set up from the crystal structure of the microfibrils, because there are no charged species on a cellulose molecule. However, if one measures the surface charge of a paper fiber one finds that the fibers have negative charges. These will enable Coulomb interactions with cations, as macroscopic paper is electrically neutral. From a measurement of the surface charge of a paper fiber and from the surface area of this fiber, one can calculate a charge per surface area. Considering an average bonded area in a fiber – fiber bond and an average Coulomb interaction energy [5] one can now calculate the bond energy due to Coulomb interactions. This gives a value of about 5.3x10-9 kJbond-1. Here the resulting value will be an upper limit, because the bonded area will be larger than the area in molecular contact. In addition, one will not be able to measure exclusively surface charge and the average surface area of paper fibers is also a rather crude approximation, considering that the fibers are a natural product with a wide variety of sizes.

3 Conclusions

This paper proposes a novel model to quantify the contributions of hydrogen bonding, Van der Waals bonding and Coulomb interactions to the bond energy of a single fiber – fiber bond. The model gives a lower limit for hydrogen bonding and Van der Waals bonding and an upper limit for Coulomb interactions. Further refinement of the model and newest experimental results from ongoing atomic force microscopy experiments in our group will bring a deeper insight into the bonding mechanisms in paper.

Acknowledgements

The financial support by the Austrian Federal Ministry of Economy, Family and Youth and the National Foundation for Research, Technology and Development is gratefully acknowledged.

References

[1] T. Lindström, L. Wagberg and T. Larsson, 13th Fundamental Research Symposium, Cambridge, (2005) 457.

[2] S.-Y. Ding and M. E. Himmel, J. Agric. Food Chem. 54 (2006) 597.

[3] B.G. Oliveira, F.S. Pereira, R.C.M.U. de Araújo and M.N. Ramos, Chem. Phys. Lett. 427 (1-3) (2006) 181.

[4] B. Velino, A. Millemaggi and W. Caminati, J. Mol. Spec. 215 (2002) 73.

[5] B. Bendiksen, S.E. Friberg and P.L. M. Plummer, J. Coll. Interf. Sci. 72 (3) (1979) 495.

Extending the insight into fiber-fiber bonding by the use of cellulose model films

EDUARD GILLI[1,2], MARIO DJAK[1,2], EERO KONTTURI[3] AND ROBERT SCHENNACH[1,2]

[1]Institute of Solid State Physics / Graz University of Technology
Graz, Austria
[2]Christian Doppler Laboratory for Chemical and Physical Fundamentals of Paper Strength
[3]Department of Forest Products Technology, School of Chemical Technology / Aalto University
Aalto, Finland
gilli@tugraz.at

1 INTRODUCTION

The fundamental chemical processes of fiber-fiber bonding remain not fully understood so far. This is due to different reasons, one of them being the high morphological complexity of the pulp-fiber structure. Investigating single pulp fibers or sheets by infrared spectroscopy can give some insight, but is limited in quantification and full interpretability of the data, due to many different contributing effects, such as diffuse scattering, multi-layer resonances, etc.

Therefore, we take an approach to this question from a simplified model system. The model system consists of amorphous cellulose layers on silicon substrates. A schematic image of the model system is given in Fig. 1.

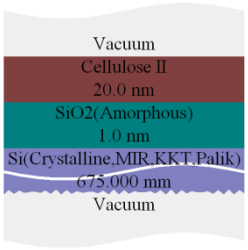

Figure 1. Schematic image of the layered model film system.

The almost complete transparency of the silicon substrates in the mid-infra-red, enable transmission as well as reflection and ellipsometry measurements. This opens new possibilities in investigation of surface treatments and chemical modifications, allowing for a quantitative analysis of the spectra, and for complete spectral simulation. The link to the macroscopic bonding strength is closed by establishing bonding between two cellulose model films. These bonded films can subsequently be tested in a z-strength test setup.

2 THE MODEL SYSTEM

The films of amorphous cellulose are prepared on silicon wafer substrates from regenerated cellulose by spin coating of trimetylsilyl cellulose (TMSC) and consecutive regeneration by acid vapor as described by Ref. [1]. Film thickness can be controlled by the concentration of the TMSC or for thicker films by consecutive spin coating and hydrolysis steps.

Surface coatings of hemicelluloses can be prepared by spin coating from solution or by adsorption from aqueous solution, the latter being observed by Quartz Crystal Microbalance with Dissipation monitoring (QCM-D).

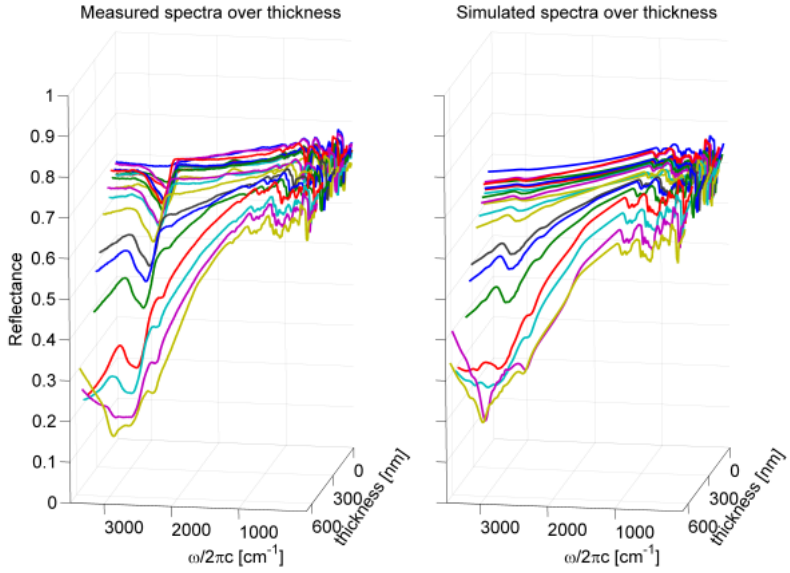

Figure 2. Measured (right) and simulated (left) s-polarized infra-red spectra of cellulose model films with a thickness between 0 and 530 nm [4].

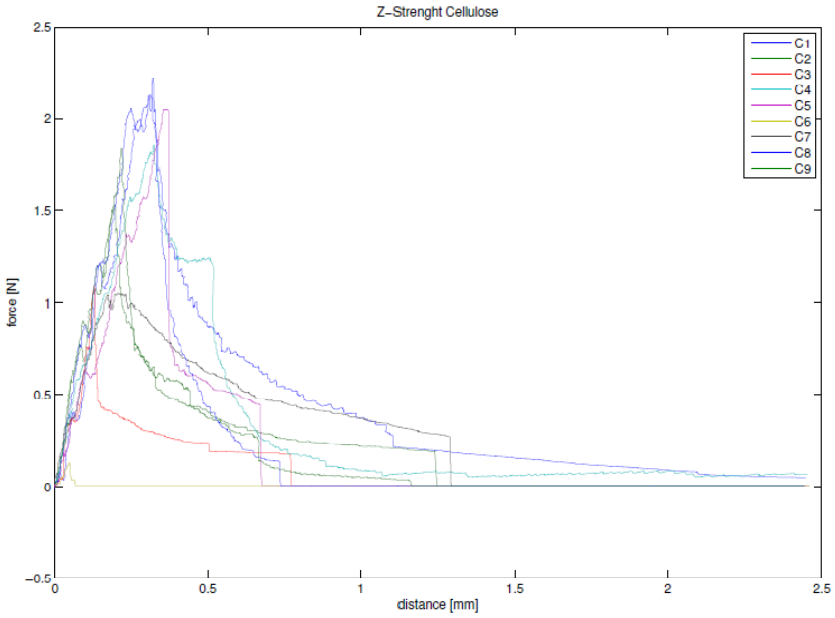

Figure 3. Force distance curves of z-strength tests with cellulose model films. The data are not calibrated.

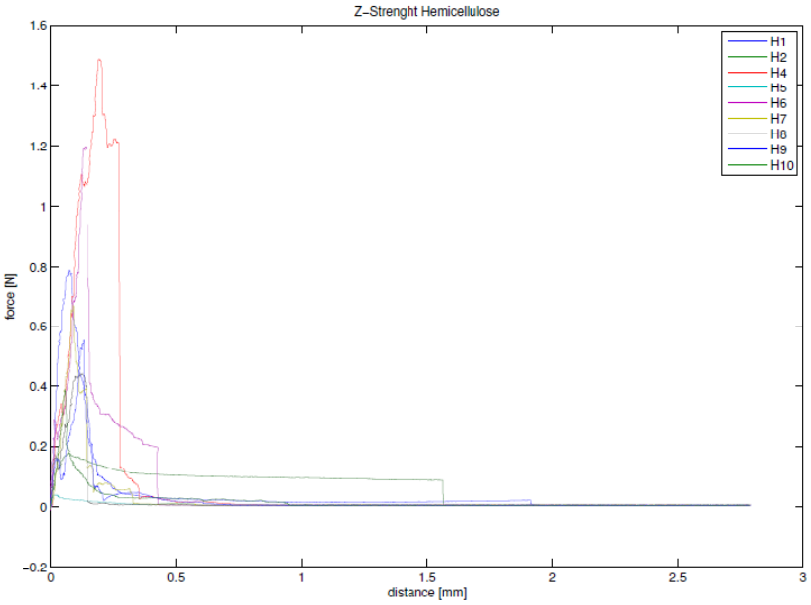

Figure 4. Force distance curves of z-strength tests with cellulose model films, coated with xylan. The data are not calibrated.

Mechanical testing of bonding strength of the model films is performed by forming bonds between two model films. This is done by allowing the films to swell in deionized water and subsequent bond forming in a Rapid Köthen sheet former between Teflon foils [2].

By the addition of various ions into the water used for film swelling, coulomb interaction between the films can be tailored.

Bonding strength between the model films is measured by the use of a modified rheometer, as a sensitive z-strength tester.

3 FILM CHARACTERIZATION BY INFRARED SPECTROSCOPY

The films can be investigated by polarization modulated infrared reflection absorption spectroscopy (pm-IRRAS) as described by Ref [3].

Figure 2, left frame depicts s-polarized reflectance spectra of a set of model films of varying thickness between 0 and 530nm, measured in the mid-infrared. The right frame of Fig. 2 depicts the corresponding simulated spectra, which can be used for example to measure the film thickness from a reflectance spectrum.

This can be carried out by optical simulation and best match optimization [4]. Additionally the high chemical sensitivity of infrared spectroscopy can be employed to characterize various functional groups relevant to fiber-fiber bonding.

4 MECHANICAL TESTING

First tests were performed in a conventional z-strength tester. This approach has not proven useful, because the achieved bonding forces are far below what one would expect from up-scaling a fiber-fiber bond. Thus, conventional z-strength testers are simply too coarse for this kind of experiment.

This can partially be attributed to the absence of hemicelluloses in the model films, but probably has its main reason in the reduced area in actual molecular contact, due to the high stiffness and, therefore, reduced conformability of the silicon substrates. For film thicknesses well below 100nm bonding could not be introduced to the films, which is also attributed to the low conformability.

A second set of test measurements has been carried out, using a modified rheometer. The resulting force-distance curves for pure cellulose films are depicted in Fig. 3.

The distance data of Fig. 3 are not yet calibrated, therefore, only the maximum force can be used for an evaluation.

Samples with an additional xylan layer, added by spin coating have been tested in the same manner. The resulting force distance curves are depicted in Fig. 4.

The resulting breaking forces are given in Tab. 1 and yield a mean breaking force of 1500±680 mN for the pure cellulose samples and 140±500 mN for the xylene coated samples.

The comparison of the two systems, therefore, reveals significantly lower breaking forces for the hemicellulose coated model films. This is absolutely counterintuitive, and further research is currently ongoing.

Sample No.	**f_{max} [mN], Cellulose**	**f_{max} [mN], Xylan on Cellulose**
1	2219	790
2	1529	177
3	1094	1488
4	1853	40
5	2049	1196
6	130	669
7	1049	444
8	2126	552
9	1835	389
Mean	1542	638
σ	678	466

Table 1. Breaking forces of model film bonds, for pure cellulose and xylan coated cellulose films.

5 ACKNOWLEDGEMENTS

The financial support by the Federal Ministry of Economy, Family and Youth and the national Foundation for Research, Technology and Development is greatfully acknowledged.

REFERENCES

[1] E. Kontturi, P.C. Thüne and J.W. Niemansverdriet. Cellulose Model Surfaces - Simplified Preparation by Spin Coating and Characterization by X-ray Photoelectron Spectroscopy, Infrared Spectroscopy, and Atomic Force Microscopy. *Langmuir* **19**:5735-5741 (2003).

[2] M. Djak, Diploma thesis, *Graz University of Technology* (2011).

[3] R. Schennach, C. Hirschmugl, E. Gilli and W.T. Tysoe. A New Method for Performing Polarization-Modulation Infrared Reflection-Absorption Spectroscopy of Surfaces. *Applied Spectroscopy* **30**(3):369-372 (2009).

[4] M. Djak, E. Gilli, E. Kontturi and R. Schennach. Thickness dependence of reflection absorption infrared spectra of supported thin polymer films. *Macromolecules* **16**(5):1775-1778 (2011).

Session 9

Paper Structure

Revisiting the voidal continuum model for tensile strength of paper: the interdependence of pore size and relative bonded area

W.W. SAMPSON[†] and J.F. WATERHOUSE[‡]

[†]Northwest Composites Centre, School of Materials, University of Manchester
Manchester, M13 9PL, UK.
w.sampson@manchester.ac.uk

[‡]102 Delbank Point
Peachtree City
GA 30269, USA

1 BACKGROUND

It is well established that the strength of paper formed from a given furnish increases with sheet density, primarily via an increase in Relative Bonded Area (RBA) and that this is associated with a decrease in the mean dimensions of inter-fibre voids within the sheet. Waterhouse [1,2] proposed a continuum model for the tensile strength of paper such that the tensile index, T (kN m kg^{-1}) can be described by a simple power law relationship with porosity, ε:

$$T = T_0 (1-\varepsilon)^{1/n} \approx T_0 \left(\rho_a / \rho_f\right)^{1/n} \qquad (1)$$

where ρ_a is the apparent density of the sheet and ρ_f is the density of the fibre; the same power-law dependency was noted also by de Ruvo *et al.* [3]. Equation (1) is plotted in Figure 1.

In an analysis of data from the literature, Waterhouse [1] found the value of the parameter n to typically vary between about 0.6 and 2; de Ruvo *et al.* [3] observed n to be between 0.46 and 2.2 for sheets densified by wet pressing and found a value of 0.26 for sheets densified by refining. Of course, least squares fits of power law expressions can be highly sensitive to outlying data and de Ruvo *et al.* note that when n = 0.26, the curve becomes very steep at higher densities; ultimately, of course, tensile index cannot exceed the zero span tensile index of the pulp, so a decreasing gradient at higher densities is expected [4].

Bither and Waterhouse [2] extended their analysis to consider the tensile strength and fracture resistance of notched samples. They considered that sheets with a given porosity may exhibit different pore-size distributions and that these may influence stress concentrations in a network under strain, thereby influencing sheet strength. Such an approach implicitly accounts for stress concentration at inter-fibre bonds since pore size is directly influenced by fibre contacts, this dependency being the basis of probabilistic models of pore size distribution [5]. Nevertheless, Bither and Waterhouse observed no direct relationship between pore size and strength.

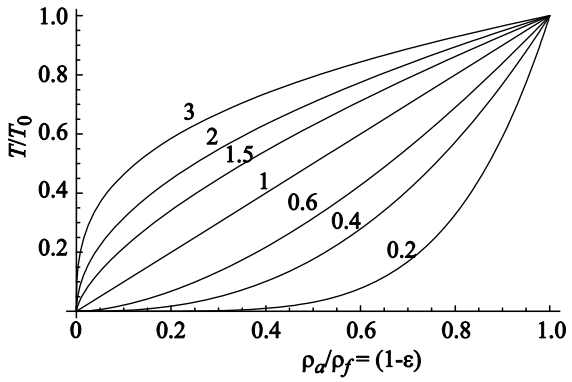

Figure 1. Graphical depiction of Equation (1). Numbers on lines represent parameter n.

Analytic models indicate that the porous structure of paper is anisotropic, with the mean in-plane dimension of voids, $\bar{d}$, being at least twice that of the plane-perpendicular dimension, or pore height, $\bar{h}$ [6]. Both properties are a function of fibre dimensions and porosity only:

$$\bar{d} = \frac{2\omega}{\log(1/\varepsilon)} \qquad (2)$$

$$\bar{h} = \frac{\varepsilon t}{1-\varepsilon} \qquad (3)$$

where ω is fibre width and t is fibre thickness. It follows that

$$\frac{\bar{d}}{\omega} \geq 2\frac{\bar{h}}{t} \ . \qquad (4)$$

Similarly, for networks with sufficiently high grammage that the reduced contact area of surface fibres can be considered negligible, the fractional contact area (FCA), *i.e.* the structural analogue of RBA, is a function of porosity only:

$$\Phi = 1 - \frac{(1-\varepsilon)(2-\varepsilon)\varepsilon}{\log(1/\varepsilon)} \qquad (5)$$

It follows then that pore dimensions exhibit a one-to-one relationship with FCA (≈ RBA); these are plotted in Figure 2. Further, since sheet strength is known to depend on RBA, a relationship between pore size and tensile strength should be expected. Here we explore this dependence by consideration of established theory and experimental data and proceed to investigate the appropriate interpretation of the parameter n in Equation (1).

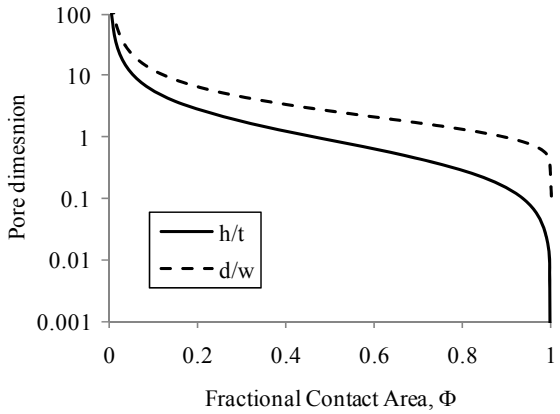

Figure 2. Theoretical relationships between pore height, in units of fibre thickness ($\bar{h}/t$), in-plane pore diameter in units of fibre width ($\bar{d}/\omega$) and Fractional Contact Area, Φ.

2 STRENGTH AND PORE SIZE

The nature of the relationship between tensile strength and pore size can be estimated by assuming the Page Equation for the tensile strength of paper to hold:

$$\frac{1}{T} = \frac{9}{8Z} + \frac{12\delta}{bP\lambda\Phi} \qquad (6)$$

where δ is fibre coarseness, P is fibre perimeter, b is the shear bond strength per unit area, λ is fibre length. Rearranging Equation (6), we obtain,

$$\frac{Z}{T} = \frac{9}{8} + \frac{12\delta Z}{bP\lambda\Phi} \quad . \qquad (7)$$

Of more practical interest is the reciprocal of this ratio, *T/Z*, which quantifies the tensile index as a fraction of the maximum strength achievable from a given fibre type. Holding all fibre variables and the bonding parameter, b constant, the influence of RBA on *T/Z* is captured via the influence of porosity, as given by Equation (5). Further, for fibres of given cross-sectional dimensions, porosity influences the mean pore dimensions, as given by Equations (3) and (4). Accordingly, given values for fibre variables and the shear bond strength per unit area, the only free parameter in our equations for *T/Z* and mean pore height is porosity. On this basis, Figure 3 shows *T/Z* plotted against $\bar{h}/t$ assuming the following values: $\delta = 2\times10^{-7}$ kg m^{-1}; P = 100 μm; b = 5 MN m^{-2}; λ = 2 mm and Z = 120 kN m kg^{-1}. Inevitably, different curves will be obtained when different values are assigned to the parameters, though for now we note the general shape of the curve and remark that this persists for other sets of parameters that we have investigated.

Urquhart [7] provides data for tensile properties and pore dimensions, as measured by fluid porometry, for handsheets made from hardwood and softwood pulps beaten in the Valley beater. The ratio *T/Z* calculated from these data is plotted against mean pore diameter in Figure 4. The broken line represents a log-linear regression on the data and is included for illustrative purposes only. Despite the inherently different fibre morphologies, a single relationship characterises the relationship between normalized tensile strength and pore size remarkably well.

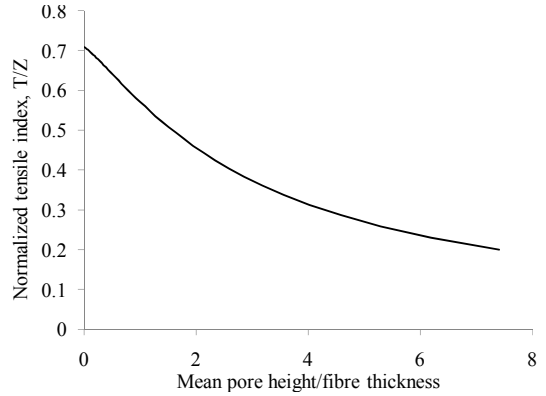

Figure 3. Estimate via the Page Equation of the relationship between *T/Z* and pore size.

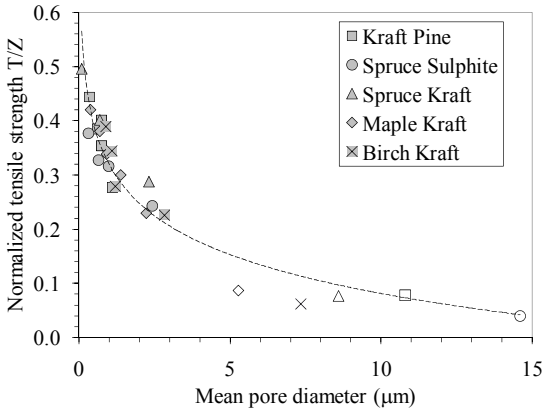

Figure 4. Relationship between *T/Z* and pore size from the experimental data of Urquhart [7]. Open symbols are unbeaten pulps.

3 POWER LAW RELATIONSHIP

Returning to Equation (1), we note that the ratio ρ_a/ρ_f represents the solid fraction of the sheets and, from inspection of Equation (5), observe that this is directly related to the fractional contact area, Φ. Further, it is reasonable to assume that $T_0 = Z$. The second term on the right hand side of Equation (6) characterises interfibre bonding and the combined influence of these parameters can be obtained as the contribution of bonding to tensile index, B (kN m kg^{-1}) from the simplified Page equation:

$$\frac{1}{T} = \frac{9}{8Z} + \frac{1}{B}$$

With others, one of us has previously investigated the influence of laboratory papermaking treatments on the shear bond strength per unit area, b and on fractional contact area, determined as the 'Contact Ratio' [8]. The experiments involved

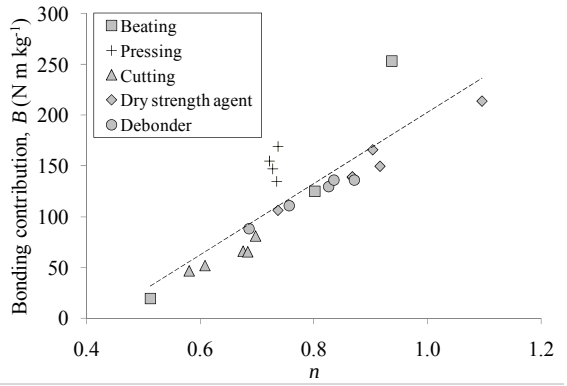

Figure 5. Relationship between the contribution of bonding to tensile index, *B* and parameter *n.*

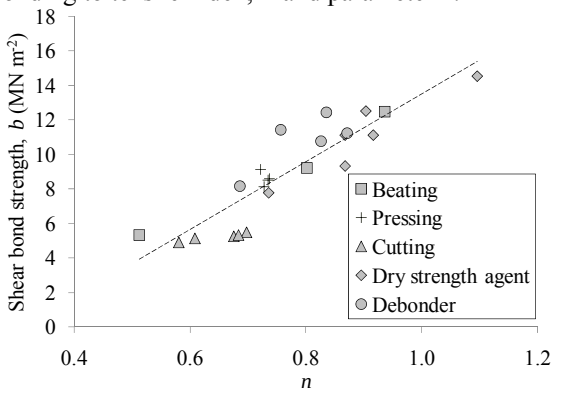

Figure 6. Relationship between the shear bond strength per unit area and parameter *n.*

laboratory beating and wet-pressing, cutting wet sheets and reslushing them in an attempt to influence fibre length independently of bonding, and adding dry-strength and debonding agents. Here we have re-examined the tensile and density data provided in [8] to provide insights into the physical meaning of the exponent *n* in Equation (1).

Although it is attractive to determine parameter *n* in Equation (1) from power-law regressions for families of data varying, *e.g.* beating or wet-pressing, this carries with it an implicit assumption that *n* is constant for the treatment under consideration. Instead, we have obtained *n* for each condition by and solving Equation (1) such that $n = \mathrm{Log}(\rho_a/\rho_f)/\mathrm{Log}(T/Z)$. Figures 5 and 6 show the contribution of bonding to tensile index, *B,* and the shear bond strength per unit area, *b,* plotted against *n* determined in this way. Both bonding parameters exhibit reasonable correlation with parameter *n*. As density was increased by wet pressing so did the fractional contact area, Φ, though wet pressing had no discernable effect on *b*, as noted in [8]. In Figure 5 we observe that wet pressing had no discernable influence on *n*, but did affect *B*. In [8], we noted also that beating increased *b* and Φ and in Figure 5 we observe that the datum for the highest beating, which has the highest value of *B*, lies away from the main body of data also. In contrast, although the data exhibit some scatter, there are no such outliers in Figure 6. Thus, whereas parameter *B* captures changes in bond strength and bonded area, the treatment suggests that parameter *n* captures changes in bond strength only.

4 SUMMARY

We have presented a preliminary analysis of the relationship between the void structure of paper and its tensile strength. Combining recent theoretical relationships for fractional contact area and pore size with the well-established Page equation for tensile strength, we have provided a relationship between pore size and normalized tensile strength. Whilst such a dependency is intuitive – pore size decreases with density whilst strength increases—experimental data suggests that the relationship is unexpectedly insensitive to pulp type.

It has previously been proposed that the relationship between tensile strength and solid fraction can be described by a power law. Our preliminary analysis of experimental data in this context suggests that the exponent in the power law may provide a rapid and convenient estimator of shear bond strength per unit area, which requires no knowledge of fibre morphology.

REFERENCES

[1] J.F. Waterhouse. The ultimate strength of paper. In **Design Criteria for Paper Performance** (P. Kolseth, C. Fellers, L. Salmen, M. Rigdahl, eds.), STFI-Meddelande, Stockholm, 1987.

[2] T.W. Bither and J.F. Waterhouse. Strength development through refining and wet pressing. *Tappi J.* **75**(11):201-208, 1992.

[3] A. de Ruvo, C. Fellers and P. Kolseth. Chapter 13 in **Paper structure and properties**, (J.A. Bristow and P. Kolseth, eds.), Marcel Dekker, New York, 1986.

[4] W.W. Sampson. Materials properties of paper as influenced by its fibrous architecture. *Int. Mater. Rev.* **54**(3): 134-156, 2009.

[5] W.W. Sampson. **Modelling Stochastic Fibrous Materials with *Mathematica***. Springer-Verlag, London, 2009.

[6] W.W. Sampson and S.J. Urquhart. The contribution of out-of-plane pore dimensions to the pore size distribution of paper and stochastic fibrous materials. *J. Porous Mater.* **15**(4):411-417, 2008.

[7] S.J. Urquhart. Informed manufacture of medical barrier grades of paper. PhD Thesis, University of Manchester, 2006.

[8] S.J. I'Anson, A. Karademir, W.W. Sampson. Specific contact area and the tensile strength of paper. *Appita J.* **59**(4):297-301, 2006.

Quantification of the web structure in relation to process conditions during wet pressing and furnish composition

HII, C.[1,*] GREGERSEN, Ø.[1]
CHINGA-CARRASCO, G.[2] ERIKSEN, Ø.[2]
TOVEN, K.[2] ROSÉN, F.[3] AND VOMHOFF, H.[3]

[1].NTNU, Trondheim, Norway
[2] PFI, Trondheim, Norway
[3] Innventia, Stockholm, Sweden
[*]corresponding author: hii@nt.ntnu.no

Introduction

The purpose of this study was to quantify the web z directional structure in relation to process conditions during wet pressing and furnish composition. Statistical analysis was used to analyze the results. The main variables and interactions were assessed in detail to determine their significance in affecting the web dryness after pressing.

1.1 Experiment

60 g/m^2 laboratory sheets were used for the wet pressing study. The sheets were made from mixtures of deinked pulp (DIP), thermomechanical pulp (TMP) and ground calcium carbonate (GCC). The wet pressing was carried out using a dynamic wet pressing simulator. Single sided dewatering was used in the wet pressing experiment. Two pulse types were evaluated, a roll press and a shoe press pulse. The length of the press pulse was set to 8-15 ms for roll pulse and 25-35 ms for shoe pulse. The pressure used for the study ranged from 4-6 MPa.

Both pre pressed and after pressed web samples were freeze dried. The freeze-drying step was important to preserve the wet web structure and minimize any shrinkage effects. The samples were then embedded in epoxy resin, ground and polished. Images were acquired using scanning electron microscope (SEM) in backscatter electron imaging mode. The ImageJ software was used for structural quantification. The web z-direction cross-sectional area as illustrated in **Figure 1** was split into 3 layers. The assessments were based on a new optimized method to divide each single layer in the z-direction of paper, taking into consideration the local solid structure. A detailed analysis was then performed on the individual layers to quantify and compare the structural characteristics. The web structures such as pore size and filler distributions were quantified.

1.2 Results and Discussion

Preliminary results have showed significant pore size changes when wet webs were pressed to >45% solids. As illustrated in **Figure 2**, the number of small pores (< 2 μm) increased while the number of big pores (8-16 μm) decreased significantly, i.e. the densification of the sheet structure was seen, as expected during wet pressing.

The differences in the fraction of fines in the dewatering layer in the pre pressed sheets also affected the web dryness after pressing. **Figure 3** shows that the dryness after pressing increased when the fines content at the wire side decreased. The fines were determined digitally from the image analysis [1]. Fines have higher water retention values than fibres, thus more fines in the dewatering layer will impede dewatering during wet pressing.

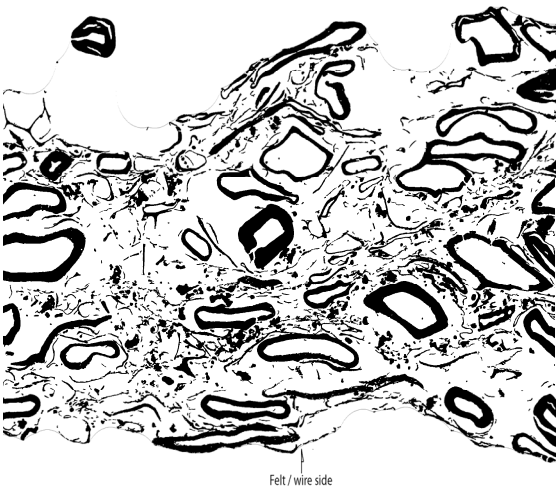

Figure 1. The cross-sectional image of a paper sample, acquired with a scanning electron microscope (SEM). The individual layers in the image are determined based on equal solid pixel per line length.

The focus of this study was on the after-pressing sheet dryness in relation to the web structure of different furnishes. Post-press sheet dryness was correlated to both the z directional structure and the furnish composition. The significance of the main variables and potential interaction terms were studied. Results from image analysis showed the following:

1. The number of small pores after wet pressing increased while the number of big pores decreased as the sheet was pressed to >45% solids content. This indicated sheet densification as expected during wet pressing.
2. Pre-pressed sheets with higher number of bigger pores yielded higher solids content after wet pressing.
3. The higher amount of fines in the layer closest to the web felt interface impeded dewatering and yielded lower solids content after wet pressing.

REFERENCE

[1] G. Chinga, O. Solheim and K. Mörseburg. Cross- sectional dimensions of fibers and pore networks based on Euclideam distance maps. Nordic Pulp and Paper Res. J. 22(4):500-507(2007).

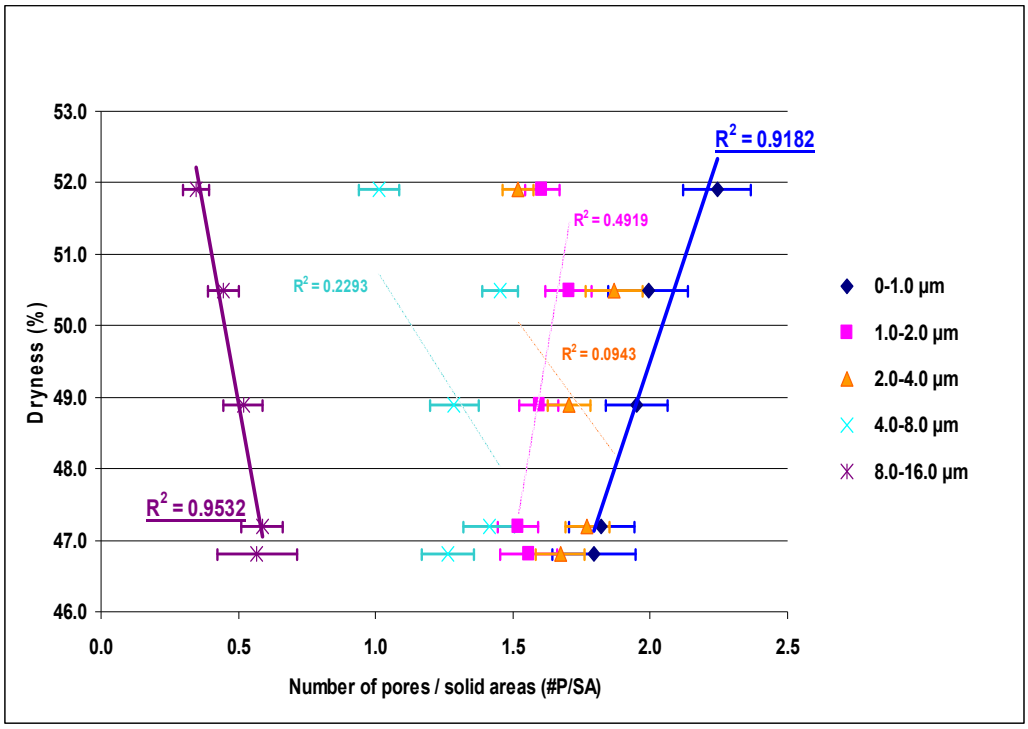

Figure 2. Dryness as a function of the number of pores with the specified pore radius per solid pixels of wet web after wet pressing. The pore radii were quantified with computerized image analysis on the cross-sectional images, acquired using a scanning electron microscope.

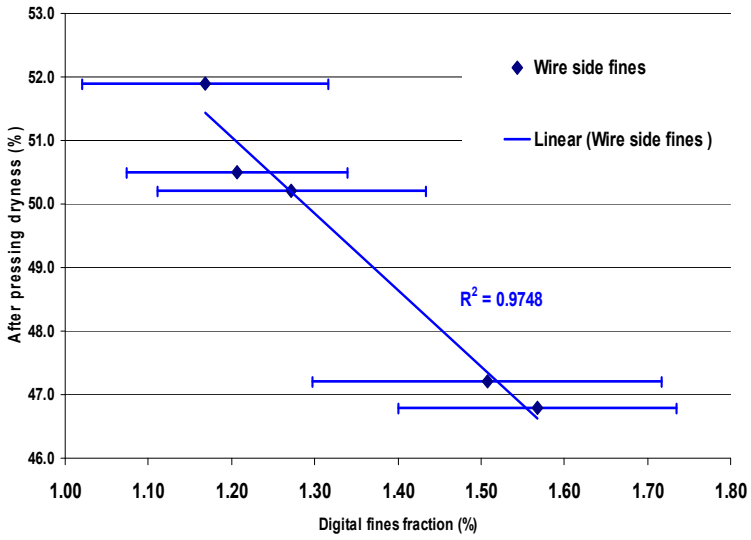

Figure 3. After pressing dryness (%) vs. digital fines fraction (%) [1] in the wire side layer in the pre pressed sheets. The sheet was divided into 3 layers in the thickness direction. The individual layers in the image were determined based on equal solid pixel per line length.

Comparison of registered paper surface representations from microtomography and photometric stereo

MARJA METTÄNEN[1], MATTI JUKOLA[1], ARTTU MIETTINEN[2], HEIMO IHALAINEN[1], TUOMAS TURPEINEN[2], JUSSI TIMONEN[2]

[1]Department of Automation Science and Engineering / Tampere University of Technology
P.O.Box 692, 33101 Tampere, Finland
[2]Department of Physics / University of Jyväskylä
P.O.Box 35 (YFL), 40014 University of Jyväskylä, Finland
marja.mettanen@tut.fi

Keywords: surface topography, photometric stereo, X-ray microtomography

ABSTRACT

Paper and cardboard samples have been imaged with a laboratory-scale photometric stereo device with a spatial resolution of approximately 7 µm and by an X-ray microtomograph with resolutions of 7.1 µm, 3.8 µm and 1.4 µm. The photometric stereo based surface gradients and topography maps are compared with the surface representations that have been estimated from the three-dimensional microtomography data. The correspondence of the spatially aligned surface reconstructions is evaluated through pointwise correlation and 2D coherence that reveals the scales at which the surface roughness is similar in two topography maps. The estimates of the orientation distribution of the topographic features are also compared.

1 INTRODUCTION

Photometric stereo is a fast non-contact solution to acquiring surface topography maps of paper samples [1]. To estimate surface topography by photometric stereo, the sample is first imaged with a camera using slanting illumination from at least two directions. Then the gradients of the surface are computed from the images, and finally the surface topography is estimated from the gradients by integration that involves noise removal and compensation of the point spread function. The method has been used successfully in relating missing ink with the depressions on the paper and cardboard surfaces [1,2,3]. The on-line applicability of the method also motivates to further investigate the practical limitations and possibilities of this image based measurement to characterize paper surface, e.g., in terms of roughness and fibre orientation.

The problem with the photometric stereo method in the measurement of paper stems from the violation of the assumptions regarding the behaviour of light on the surface of the examined material. Paper does not exactly have a Lambertian surface in the micrometre scale, and light is occasionally reflected from the internal fibre surfaces [4]. In addition, erroneous surface height estimates may occur at points of specular reflection, or at steep and deep pores on the paper surface that are unreachable by light [5,6]. The surface representation also depends on the parameter values chosen at the integration stage. The present work is aimed at comparing the photometric stereo (PS) based surface topography reconstructions of paper and cardboard samples with ones obtained through X-ray microtomography that is considered as the reference measurement.

X-ray microtomography (X-µCT) is a non-destructive method for obtaining the three-dimensional (3D) structure of a physical sample [7]. Historically the method has been available in synchrotron X-ray facilities only, but during last years, laboratory-scale devices with resolution adequate for material characterisation have become available.

The method is based on taking a series of two-dimensional (2D) X-ray projection images at a multitude of angles around the sample. A three-dimensional map of X-ray attenuation coefficients is reconstructed computationally from the 2D projection data. The attenuation coefficients distinguish different materials from each other such that their map can be treated as a three-dimensional image of the structure of the sample. A recent review of theoretical and practical structural analysis of paper using 3D tomography has been presented by Bloch and Rolland du Roscoat [8].

Surface topography maps are estimated from the 3D microtomography data by an iterative computational method referred to as the "carpet" method. It is based on the Edwards-Wilkinson equation [9] which is well known in the physics of dynamic interfaces under the influence of random forces. The carpet method has been used previously, for instance, to detect the local structures of base paper and coating layer [10].

In the current work, the surface reconstructions made of the 3D microtomography data are registered and compared with the PS based topography maps. The correspondences of the surface reconstructions are evaluated through statistical methods such as 2D squared coherence. The orientation distributions of the surface topography estimates are also compared. The long term goal of the analyses is to answer two questions. First, is it possible to optimize the photometric stereo based surface topography estimate by adjusting the illumination conditions and the integration parameters? Second, how reliably can the orientation of the surface fibres be

estimated from the images related to the photometric stereo method?

This paper is organized as follows. Section 2 introduces the measured samples and data acquisition. Section 3 describes the surface reconstruction and image registration. The comparisons of the surface representations are described in Section 4, and Section 5 concludes the work.

2 MEASUREMENT DATA

The material studied in this work contains six samples divided into two groups. The first group contains three paper samples that have been imaged from an area of 10 × 10 mm^2 with both the camera system and the X-ray microtomograph. The second group consists of two paper samples and one uncoated cardboard sample. Two separate measurement areas have been marked on each of these samples, and each area has been imaged with the microtomograph using two different resolutions, and with the camera system using a fixed resolution. Table 1 presents a summary of the acquired data.

Photometric stereo images have been taken on each of the nine measurement areas and both sides of each paper/cardboard sample. These images cover an area of 32.5 × 21.5 mm^2 except for paper samples 1-3 (see Table 1) for which the area is 10 × 10 mm^2. In the purpose-built photometric stereo imaging setup, the illumination has been implemented by four white led lights attached at increasing heights to an arm that is rotated around the sample. The system provides, for each sample, 672 images, comprising of 168 illumination angles around the sample and four illumination angles with respect to the surface normal: 82º, 73º, 59º and 46º. The surface gradients are estimated from the images by a least squares method.

The X-µCT measurement has been performed with the SkyScan 1172 device employing cone-beam geometry that allows easy tuning of image resolution. Hence, two image pixel sizes, 7.1 µm and 1.4 µm, have been used for samples 4-6 (see Table 1). The tomography scans have been performed in the absorption contrast mode using 50 kV X-ray tube voltage and 0.3 degree angular step size. The reconstruction has been done with the SkyScan's NRecon software employing standard corrections for temperature drift and rotation axis misalignment.

It is worth noting that the voxels in the X-µCT data have the same size in all three directions (x,y,z), so the resolution directly affects the size of the imaged area. The data sets with a resolution of 1.4 µm thus present an area as small as 5.0 mm by 2.7 mm. Figure 1 exemplifies the various sizes of imaged areas in the case of samples 4, 5, and 6.

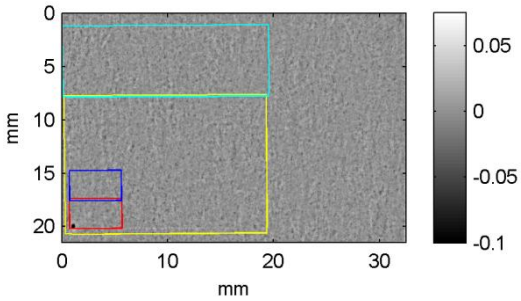

Figure 1. One of the two imaged areas of the cardboard sample. The grayscale image is the PS based topography map, the colorbar signifies the surface heights as millimeters, and the rectangles represent the X-µCT measurement areas: yellow and cyan for 7.1 µm resolution and red and blue for 1.4 µm resolution.

3 SURFACE RECONSTRUCTION AND REGISTRATION

One of the challenges in this work is the detection of the paper surface from the 3D X-µCT data. The current approach is based on the "carpet" method, where the surface is defined as a propagating interface obeying the Edwards-Wilkinson equation [11]. Let the height of the surface above the paper be h and its initial value h_0. The surface is defined by determining the static solution of

$$\begin{cases} \dfrac{\partial h}{\partial t} = \vartheta \nabla^2 h + V + \eta \\ h(t=0) = h_0, \end{cases}$$

where ϑ controls surface tension, V is constant pushing the surface towards the paper and η is the scaled gray value from the image. The carpet method is applied to each of the 3D tomography data arrays to reconstruct the surface topography maps of both the top and bottom side of the paper.

The surface topography maps reconstructed from the microtomography data are registered with the

Table 1. Summary of measurements.

Sample	X-µCT measurement area	X-µCT resolution	PS measurement area	PS resolution	Remarks
paper 1	10 mm × 10 mm	3.7 µm	10 mm × 10 mm	6 µm	one test area per sample
paper 2	10 mm × 10 mm	3.8 µm	10 mm × 10 mm	6 µm	one test area per sample
paper 3	10 mm × 10 mm	3.8 µm	10 mm × 10 mm	6 µm	one test area per sample
paper 4	5.0 mm × 2.7 mm 20 mm × 13 mm	1.4 µm 7.1 µm	32.5 mm × 21.5 mm	7.5 µm	two test areas per sample
paper 5	5.0 mm × 2.7 mm 20 mm × 13 mm	1.4 µm 7.1 µm	32.5 mm × 21.5 mm	7.5 µm	two test areas per sample
cardboard	5.0 mm × 2.7 mm 20 mm × 13 mm	1.4 µm 7.1 µm	32.5 mm × 21.5 mm	7.5 µm	two test areas per sample

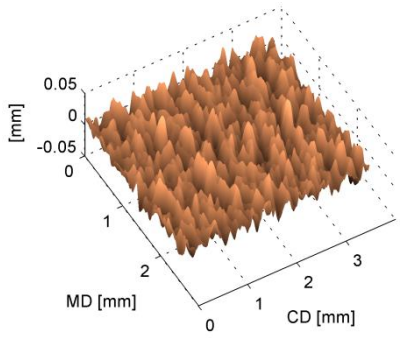

(a) Photometric stereo (spatial resolution 7.5 µm)

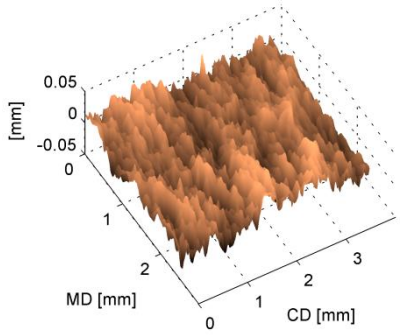

(b) Microtomography (7.1 µm per pixel)

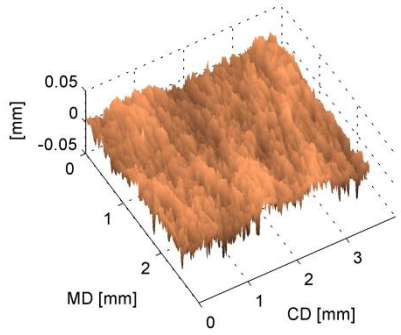

(c) Microtomography (1.4 µm per pixel)

Figure 2. Surface of the bottom side of the uncoated cardboard sample on a 3.8 mm by 2.6 mm area reconstructed from (a) PS images with all illumination angles combined, (b, c) X-µCT data of resolution 7.1 µm and 1.4 µm, respectively.

PS based surface topography maps. The surface representations, exemplified in Figure 2, often exhibit similar features that enable the detection of matching points based on cross-correlation. An affine transformation between the maps is estimated from a few hundred matching point pairs.

4 ANALYSIS AND RESULTS

Once the spatial transformation between two surface representations has been found, the images are aligned. The affine transformation is applied to the coordinates of the PS based topography map, and the pixel values of the tomography based map are interpolated to these new coordinates. The pointwise correlation coefficient between the aligned maps is typically between 0.5 and 0.7.

Coherence reveals the wavelength-dependent correspondence between the surface topography maps estimated with the different methods [12]. Coherence has been estimated pairwise between the three surface topography maps: the one based on photometric stereo and the ones based on X-µCT with resolutions of 7.1 µm and 1.4 µm. Figure 3 shows the 2D spectra of the maps presented in Figure 2(a) and 2(c), and their 2D squared coherence. The frequencies below which the coherence is high are interpreted as the limits of the scale at which the surface roughness is similar in the PS based and the tomography based topography maps. In Figure 3(c), the squared coherence is higher than 0.5 (i.e., correlation coefficient > 0.7) at frequencies below approximately 10 mm^{-1} in the cross direction (CD) and 7 mm^{-1} in the machine direction (MD), which correspond to wavelengths

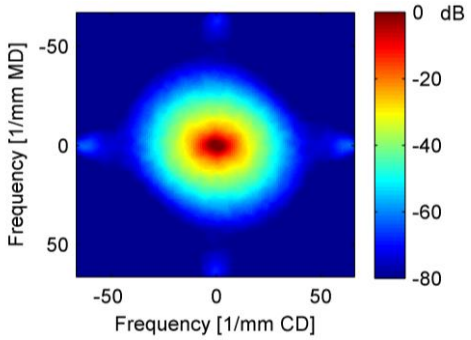

(a) Spectrum of the PS based topography map.

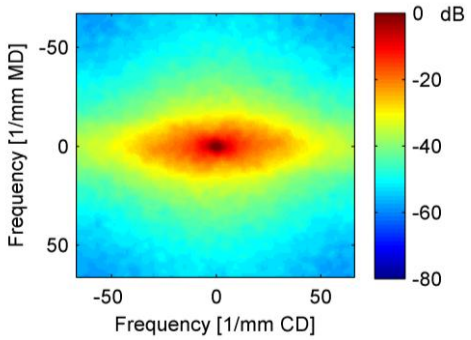

(b) Spectrum of the X-µCT based topography map.

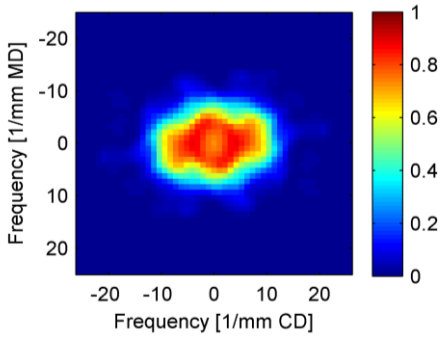

(c) Squared coherence.

Figure 3. 2D power spectra of (a) the photometric stereo based topography map (Fig. 2(a)) and (b) the tomography based surface topography map of resolution 1.4 µm (Fig. 2(c)). (c) Squared 2D coherence between the maps.

Table 2. CD and MD ([*x*, *y*]) wavelength (λ) limits below which the squared coherence falls below 0.5, using the specified illumination angles in the PS based surface topography estimation.

Illumination angle	λ limits [*x*, *y*], PS vs. 7.1 µm	λ limits [*x*, *y*], PS vs. 1.4 µm
82º	[128, 175] µm	[101, 137] µm
73º	[113, 175] µm	[96, 137] µm
59º	[113, 160] µm	[96, 137] µm
46º	[113, 175] µm	[96, 148] µm

longer than around 96 µm and 137 µm, respectively. The coarser resolution (7.1 µm) tomography based surface estimate has higher than 0.5 squared coherence with the PS based map at wavelengths longer than 113 µm in CD and 175 µm in MD. These results apply for the topography map that has been estimated by the photometric stereo method using the combination of all four illumination angles (with respect to the surface normal). Table 2 presents the corresponding results for the PS based topography maps computed with one illumination angle at a time.

The coherence behaviour described above is typical of the samples imaged for this study. The results show only slight dependence on the light configuration used in photometric stereo imaging. The similarity of the surface roughness scales is, however, dependent on the methods of estimating the surface heights from the X-µCT data and from the photometric stereo images. Further experiments are required to see if the correspondence between the surface topography estimates can be enhanced at wavelengths closer to the width of fibres.

While image alignment is a prerequisite for the joint statistical analysis of the multivariate surface height maps, it forces the maps into the same spatial resolution and may thus lose some of the details of the tomography based surface representations. The interpolation of the pixel values is thus omitted in the orientation analysis, and the same area is just selected from each map based on the correspondence of the spatial coordinates that has been discovered in the image registration phase. The orientation of the paper surface structure is estimated from the x- and y-gradients. They are computed from the tomography based surface representations by convolution with a gradient operator. In the case of the photometric stereo method, the x- and y-gradients are readily available as they have been estimated from the images taken with the camera. Surface orientation is described by the surface orientation distribution, and it can be summarized by circular statistics [13]. Figure 4 presents the orientation distributions estimated from the map shown in Figure 2(a) and from the corresponding areas of the X-µCT based topography maps. Each map has been band-pass filtered with limit wavelengths of 50 µm and 200 µm before the orientation analysis. The solid lines describe the distribution of variance with

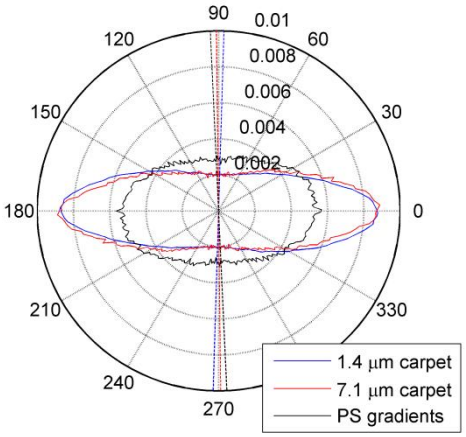

Figure 4. Orientation estimates from the cardboard surface topography maps shown in Figure 2. The solid lines represent the orientation distributions and the straight dashed lines show the main orientation direction relative to the cross direction.

respect to direction. The main orientation of the surface structures is thus perpendicular to the main axis of the ellipse.

The estimated main orientation directions relative to MD are -1.7º, 0.7º and 2.6º for the 1.4 µm and 7.1 µm carpet estimates and the PS based topography estimate, respectively. Similar discrepancies have been found with other analysis areas. The respective circular variances of the orientation distributions are 0.65, 0.66 and 0.84, which are rather high. The theoretical maximum of circular variance is 1.0 and it corresponds to a distribution with no single preferred orientation direction. The results reflect the fact that the area used for the orientation estimation is small and contains only a small number of fibres or other oriented features.

Despite the uncertainty of the surface orientation estimates, the work done so far is a good start to the effort towards our long term goals. The success of the image registration opens up the possibility of aligning the 2D and 3D data. Eventually the purpose is to compare the orientation distribution estimated from the photometric stereo images or gradients to the orientation of the surface fibres that can be determined from the reference X-µCT data. The assumption is that the orientation of the surface structures, particularly in the appropriate size scale, is related to the orientation of the surface fibres. Versatile experiments on the illumination and other details of the photometric stereo method can also be made with the purpose-built laboratory setup. For on-line applications, it is of particular interest to characterize the paper surface based on the gradient information without the integration of the surface.

5 CONCLUSIONS

The goal of this work was to assess the capability of the camera based approach of producing correct description of the paper surface. The topography

maps estimated from the camera based images were successfully registered with those estimated from the X-µCT data, and 2D coherence analysis revealed that the various topography maps present similar surface roughness on wavelengths longer than approximately 100...160 µm, depending on direction and resolution. The orientation distributions were computed from surface topography maps that had been estimated from the data of the two separate measurement devices but presented exactly the same area in different resolutions. As the variance of the orientation distributions was rather high, the main orientation direction of the topographic structures was considered similar in the compared maps.

The analysis of the valuable data set presented in this paper will continue in the near future. The next major step will be the comparison of the whole 3D X-µCT image of the sample with the photometric stereo based 2D surface topography estimate. The current work applied the carpet method for the estimation of the surface topography map from the X-µCT data, but it was not optimized for the detection of the surface fibres. The future work will focus more on the fibres in order to obtain a reliable surface fibre orientation reference. We will investigate the possibility of estimating the surface topography from the 3D tomography data so that not only the original X-ray absorbance values but also their local variance in the (x,y)-plane affect the detection of the surface.

REFERENCES

[1] P. Hansson and P.-Å. Johansson. Topography and reflectance analysis of paper surfaces using a photometric stereo method. *Optical Engineering* **39**(9):2555–2561 (2000).

[2] G.G. Barros and P.-Å. Johansson. Prediction of UnCovered Area occurrence in flexography based on topography – A feasibility study. *Nordic Pulp & Paper Res. J.* **21**(2):172-179 (2006).

[3] M. Mettänen. Measurement of print quality: Joint statistical analysis of paper topography and print defects. PhD thesis, Tampere University of Technology (2010).

[4] G. Chinga. Detailed paper surface characterization for gloss assessment. *J. Pulp Paper Sci.* **30**(8):222-227 (2004).

[5] G.G. Barros and P.-Å. Johansson. The OptiTopo technique for fast assessment of paper topography – Limitations, applications and improvements. *J. Imaging Sci. Tech.* **49**(2):170-178 (2005).

[6] T. Kuparinen. Reconstruction and analysis of surface variation using photometric stereo. PhD thesis, Lappeenranta University of Technology (2008).

[7] A.C. Kak and M. Slaney. Principles of Computerized Tomographic Imaging. IEEE Press (1988).

[8] J.-F. Bloch and S. Rolland du Roscoat. Three-dimensional structural analysis. Advances in Pulp and Paper Research, Trans. 14th Fund. Res. Symp. (S.J. I'Anson, ed.), Oxford, FRC, 599-664 (2009).

[9] S.F. Edwards and D.R. Wilkinson. The surface statistics of a granular aggregate. *Proc. Roy. Soc. (Lond.) A* **381**:17-31 (1982).

[10] G. Chinga-Carrasco, H. Kauko, M. Myllys, J. Timonen, B. Wang, M. Zhou and J.O. Fossum. New advances in the 3D characterization of mineral coating layers on paper. *J. Microscopy* **232**(2):212-224 (2008).

[11] T. Turpeinen, M. Myllys, P. Kekäläinen and J. Timonen. Dynamic interface detection using quench Edwards-Wilkinson equation. In preparation.

[12] M.B. Priestley. Spectral analysis and time series. Vol. I and II. Academic Press (1981).

[13] N.I. Fisher. Statistical analysis of circular data. Cambridge University Press (1995).

Image Analysis Technique for the Characterization of Tissue Softness

J. J. PAWLAK*, A. ELHAMMOUMI

Department of Forest Biomaterials
North Carolina State University
Raleigh, NC 27695 USA
*Email: jjpawlak@ncsu.edu

Keywords: softness, AFM, roughness, surface, compressibility

ABSTRACT

Five different consumer tissue sheets were characterized using image analysis and a panel softness test. The results showed that there is a correlation between fine scale roughness and softness, while roughness induced by patterns was not related to softness. Furthermore, the rougher the surface, the softer the tissue was found to be. This was related to the increased compressibility of the surface due to the flexible fibers extending far from the surface.

1 INTRODUCTION

Tissue softness is a critical property in bath tissues serving the at home sector of the marketplace. A wide variety of experimental techniques have been developed to create correlations between tissue softness and other properties. (Hollmark and Ampulski, 2004) Softness is not a single paper property, but a combination of many paper properties in addition to a "human factor" that takes into account a number of other variables. The most accurate means for evaluating tissue softness is through panel evaluation. This method is time consuming, expensive, and not easily accessible. Physical testing of the sheet, such as in a Kawabata evaluation (Chen et al, 2000), can lead to a good correlation to panel softness. (Lui and Hseih, 2004) Others have developed correlations between ultrasonic testing and tissue softness. (Pan, 1991) These technique require specialized equipment and it is unclear the exact nature of the relationship between these tests and actual tissue softness.

In this work, an image analysis technique has been developed for simple and effective prediction of the bath tissue softness. This work describes the technique and algorithms used to characterize tissue softness in relationship to a panel evaluation of the sheets. A variety of commercial tissue sheets are examined and simple relationships are developed between tissue softness, sheet properties, and the image analysis technique. The basis of the technique is to examine the free fiber ends extending from the surface of the paper sheet. The surface is then characterized using a number of statistical methods to develop relationships with softness and other sheet properties. This work describes a technique that will allow for the engineering and development of tissue papers with improved softness.

This work also describes a theoretical relationship between the surface softness of a paper sheet and the contact mechanics. The longitudinal compression of a single fiber is characterized using an atomic force microscope. Results indicate that the fiber flexes much like a thin column. The results are related to panel evaluations conducted to characterize the softness. Overall, this work provides a greater understanding of the relationship between fiber properties, surface structure, and tissue softness.

2 EXPERIMENTAL

Five different brands of toilet tissue were obtained from retail outlets. These samples represented three different manufacturers and four manufacturing processes. Two of the samples were from the same manufacturer and made with the same process. These samples exhibited significantly different softness related to either random or systematic variability in the process. **Table 1** provides additional detail for the samples.

Table 1: Sample Identification

Sample ID	Quality	Manufacturer ID
C	*Premimum - Name Brand*	1
M	*Premimum - Store Brand*	2
P	*Premimum - Store Brand*	2
O	*Premimum - Name Brand*	3
S	*Economy - Name Brand*	3

2.1 Basis Weight

The basis weight of each sample was found by cutting a 10 x 10 cm^2 sheet from each sample. This square was then weighed and the mass was multiplied by 100 to obtain the units g/m^2. This was performed five times per sample and the average was taken for data analysis.

2.2 Caliper

The caliper of each sample was taken using L&W 51 Micrometer, which uses 50 kPa of measuring pressure. Five measurements were taken per sheet and five sheets per sample were measured.

3 Stacking Thickness

Two methods were used to find the stacking thickness. The first involved taking individual sheets from the sample roll and placing them one on another until a height of 1 cm was reached. The number of sheets required to reach this height was then recorded and the single sheet thickness was calculated by dividing the height by the number of sheets. It is important to note that the stack was not compressed during this test. The second method involved placing the sample sheets one on another and compressing them with a metal plate until a height of 1 cm was obtained. The metal plate exerted a pressure of 81 Pa, which was enough to compress the large scale sheet deformations. The single sheet thickness was then determined by dividing the stack height by the number of sheets in the stack.

2.4 Fiber Quality

The fiber length, and width was found using an Optest Equipment Fiber Quality Analyzer (FQA). To prepare the fibers for the instrument, one sheet was placed into a blender with 1000 mL of water. The sheet was then disintegrated for 1 minute to ensure complete fiber separation. This fiber suspension was then diluted five times by removing 500 mL of suspension and then adding 500 mL of dilution water. The FQA was set to count 3000 fibers and the diluted suspension of fibers was placed into the FQA and left to run. Each measurement was done in duplicate.

2.5 Imaging

To obtain an image of the surface of the tissue paper an Olympus BH-2 optical microscope was used with a 5X objective and 10X eyepiece. A SONY digital video camera with an image size of 480 x 640 pixels was used to obtain the images. The pixel resolution was calibrated to be 3.175 μm per side. The samples were prepared by folding a tissue sample over a glass microscope slide so that tissue covered the edge of the slide. Three slides were prepared from each sample. The slides were placed into the microscope and brought into focus. The slide was then moved to show the edge of the slide where the tissue was folded over. An image was then acquired such that the fibers extending from the surface could be seen. One picture was taken every centimeter for a total of three pictures per slide. This resulted in nine pictures for each of the five samples.

2.6 Image Processing

The pictures from each sample were then converted from color to black and white using an image processing software (ImagePro 4). The black and white images were then opened as a matrix in Matlab and the values were put through thresholding to convert all the pixels to 1s and 0s (binary image). With this new matrix of binary numbers, a Sobel edge detection method was used to find the surface line of the fibers. This follows the gradient of the image's intensity to find the edge of the object. Once the edge data was saved in a new matrix, the first point that a fiber was sensed in each column was kept and any lower data points in the column were discarded. This was done to obtain a line of the highest fibers on the surface. The XY position of each data point was used to create a line of the surface. To correct for any misalignment in the image, a linear trend line was fit to the data and then used to correct the baseline of the surface profile. From the baseline corrected profiles, the variance, standard deviation, and power spectrum were calculated.

2.7 Simplified Softness Panel Test

Tissue samples were placed in a box with five slots. The box was designed to obstruct the view of the tissue sheets and prevent the study participants from possibly recognizing a brand and having their softness ratings biased. Participants were asked to feel the tissue samples and rank the tissue sheets in order of softness from least soft to most soft. Participants recorded their observations on a paper sheet and the results were tabulated.

3 RESULTS AND DISCUSSION

Dimensional properties of the tissue sample are displayed in **Table 2**. All premium brand tissue had a basis weight in the range of 38-40 grams per meter squared. The economy tissue was a single ply sheet with approximately half the basis weight of the premium sheets. It should be noted that samples M and P were both double ply tissue sheets, while the other samples were all single ply. The effective thickness of the sample were evaluated in three different manners. First, single sheets of the tissue were tested using a micrometer, which applied 50 kPa of pressure (Tappi, 1999). The results showed significant differences in the single sheet caliper. The premium tissues had a range of over 40 micrometers in thickness (~20% of total thickness), while maintaining a similar basis weight. The result is that there exists a spread of 30 kg/m^3 in density of tissue sheets when the sheets are measured at standard caliper pressure.

Table 2: Tissue properties.

Sample ID	Basis Weight	Thickness (µm)		
	g/m^2	*50 kPa*	*81 Pa*	*0 Pa*
C	40	235	500	1000
M	39	216	455	833
P	39	197	476	769
O	39	212	476	909
S	18	96	147	385

By measuring the paper sheet at two different lower levels of applied pressure, one can begin to understand the effect of surface roughness and sheet deformations on the perceived density of the sample. At 81 Pa, the large scale sheet deformations are predominately removed, but the fiber extending from the surface and the roughness is not yet compressed. Thus, once can see that the "surface" one might sense during the tactile evaluation of softness may be very different than the surface one characterizes with standard caliper measurements. **Figure 2** shows the percent reduction in density of the various paper sheets when evaluated at 81 Pa and nominally 0 Pa. Note that sample S has a density very similar to the other samples when characterized at 50 kPa caliper measure, but a much higher density at 81 Pa and a similar value once again at 0 Pa. In **Figure 2**, samples with larger reductions in density are more compressible. Thus, at 81 Pa, sample P is the most compressible, while sample S is the least compressible.

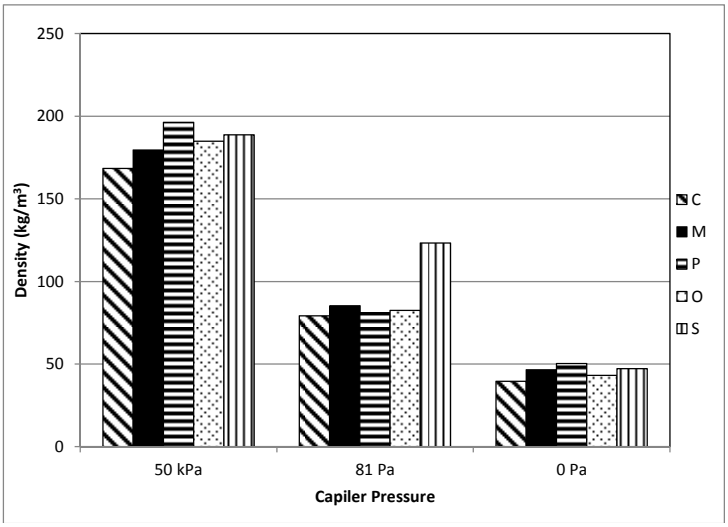

Figure 1: Tissue density when caliper is measured at various pressures.

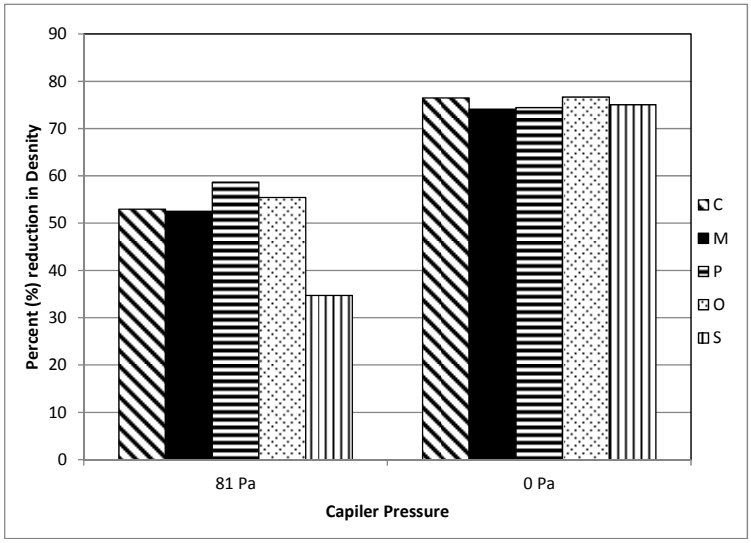

Figure 2: Percent reduction in density at various applied pressures used to measure caliper

.

The difference in density of the tissue sheets is created through a combination of process, raw materials, and converting operations. The dimensional properties for the fibers making up each sample is given in **Table 3**. Pawlak and Keller (2005) predicted that the compressive characteristics of a paper or tissue sheet would be dependent on the density of the fibrous structure and the dimensional properties making up that structure. Their work showed that shorter fiber at the same density will result in a more compressible material. **Figure 3** shows the relationship between fiber length and sheet density for the tissues. One can see that there is a correlation between the two properties with the longer fiber being made into a sheet with lower density. From a materials design standpoint, it would be logical that longer fibers need to be at a lower density to create comparable compressive characteristics according to Pawlak and Keller.

Table 3: Fiber dimensional data.

Sample ID	Mean Length (mm)			Mean Width (μm)
	Arithmetic	*Weighted*	*Weight Weighted*	
C	0.744	1.227	1.895	17.0
M	0.742	1.150	1.809	16.3
P	0.737	1.125	1.710	16.3
O	0.741	1.196	1.888	16.4
S	0.659	0.976	1.429	16.4

While density is closely correlated to the bulk softness, Pawlak (2001) showed that there is close relationship between local compressive characteristics and surface structure. It is theorized that the local compressive characteristics are more important for the creation of softness rather than bulk compressibility.

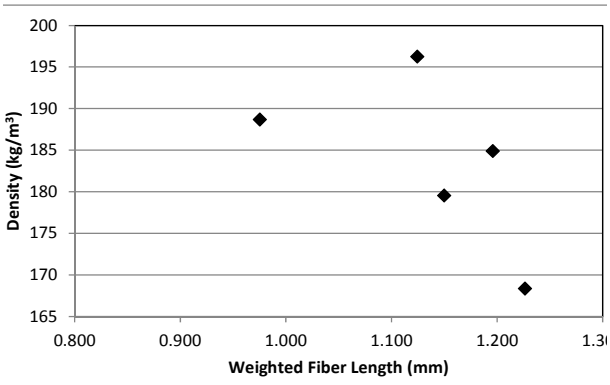

Figure 3: Relationship between weighted fiber length and tissue density measured with 50 kPa caliper.

3.1 Characterization of Surface

The surfaces of the tissue samples were characterized by a simple optical method. This involved wrapping the tissue around a glass slide and imaging the surface of the tissue folded over the slide. The fibers extending from the surface were then captured in a digital image by an optical microscope. This image was then converted into a binary image, cf. **Figure 4**.

The surface profile was then identified and shown in **Figure 5**. A total of nine images were taken for each of the five samples. The surface profile was characterized using the standard deviation and power spectrum (Norman and Wahren, 1973; Parker 1975) of the surface. The average standard deviation was determined by taking the square root of the average variance of the sample. The average power spectrum was also determined over a length of 512 pixels of the height profile data.

Figure 4: Example of binary image obtained of the surface. Note the fiber extending from the surface of the tissue. (Sample C)

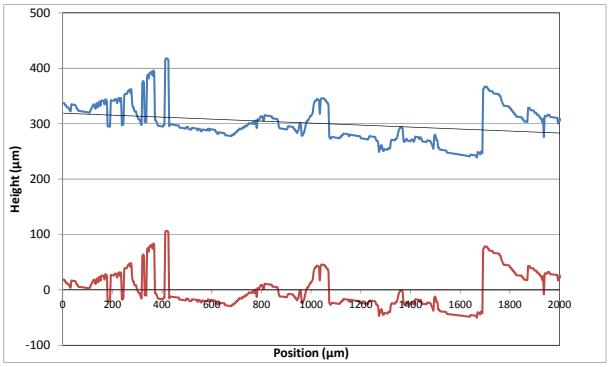

Figure 5: Line data obtained for the image shown in **Figure 4**. Note that this is a representation of the "surface" of the tissue. The top line represents the profile without a baseline correction.

Table 4: Surface height standard deviation for each tissue sample.

Sample ID	Surface Height Standard Deviation (micrometers)
C	*10.8*
M	*15.2*
P	*30.4*
O	*23.3*
S	*4.5*

Results showed distinct differences in the samples. Sample S had the lowest standard deviation of height, while sample P had the largest standard deviation in height, cf. **Table 4**. Overall, the samples created a wide range of surface roughness from 4.5 µm to 30.4 µm in standard deviation of the height. However, the standard deviation tells us little about the surface texture. This can be more effectively evaluated using a power spectrum, which characterizes the scale at which the variability occurs. **Figure 6** contains the power spectrum for each of the five samples. The area under a given curve represents the overall standard deviation in the sample. Thus, sample S with the lowest average standard deviation also has the lowest magnitude on the power spectrum graph. The shapes of the curves in **Figure 6** give an indication of how the variability in height is distributed. Samples C, P, and O all seem to have a bimodal slope in the log/log plot. This is an indication of multi-scale roughness of the sample with the finer scales having more of the overall influence on the standard deviation (i.e. more variability at small scales). Sample O shows a set of peaks, which may be directly attributable to a repeated embossed pattern on the surface of the tissue. Repeated features will show up as peaks or spikes in the power spectrum at specific wavelengths. Thus, from the power spectrum analysis one can say that the premium samples are indeed rougher and the that the roughness at small scale (fiber dimensions) is more important than the embossed pattern or large scale variability.

3.2 Softness

Softness ranking was determined by a panel test. Twenty individuals ranked the tissue samples from softest (5) to least soft (1). Of the twenty individuals, 4 observers were discarded due to errors in recording data. Of the 16 remaining rankings, the softness of the tissue sheets was evaluated. The magnitude of the softness difference was described using a total point system. For each person ranking the sample as "1", a single point is recorded, "2" receives two points, and so on. This allows for the overall difference to be described in a simple manner. **Table 5** shows the total point score for each sample. According to the panel, sample S was by far the least soft with sample O being next and the three remaining samples all being very similar to one another.

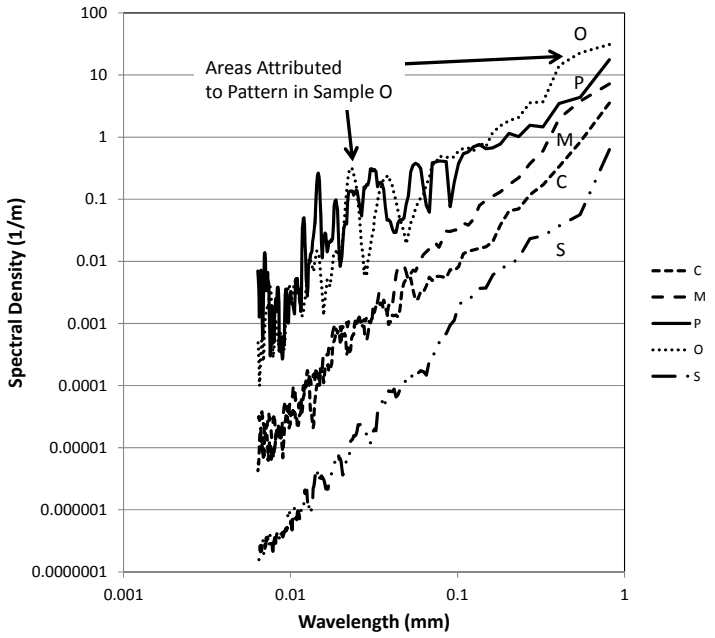

Figure 6: Power Spectrum analysis of surface height deviation of the five samples.

Table 5: Total softness points accumulated.

Sample ID	Softness Points
C	58
M	56
P	59
O	44
S	23

Figure 7 shows the percentage of respondents ranking the tissue in each level of softness. This graph gives a better idea of the overall distribution of the softness rankings. Sample S is clearly identified as the least soft of the respondents. Sample O seems to be the next lowest in softness with it receiving the next most frequent ranking of 1 and 2. Sample M seems to be ranked near the middle with the most frequent responses being in the 3-4 range. Sample C and sample P seem to be the most soft with P receiving no ranks of 1, but a higher frequency of 2 than sample C. Based on the overall softness rank and the total points accumulated, sample P would be ranked as the slightly softer tissue sample. However, is should be noted that sample P and C have very similar levels of softness.

3.3 Tissue Properties and Softness

Tissue softness is known to be a combination of various factors related to the surface as well as the bulk properties. The work above illustrates this point. Examining the data, density of the tissue sheet is not enough to predict the softness of tissue. In fact, when using traditional caliper measurement methods at 50 kPa, there is relatively little difference in the density of all the sheets. However, softness tests show that sample S is distinctly different than the other tissues. By measuring the samples over a range of pressures, the compressibility of the sheet is measured. It was shown that sample S is the least compressible of all the samples. This may not be directly attributed to the "bulk" compressibility of the structure, but more so to the surface roughness. When comparing **Figure 2** and **Table 3**, one sees that the roughest samples are also the most compressible samples. This follows directly from contact mechanics.

Figure 8 shows the predicted compressibility as a function of surface displacement and applied pressure. The material is modeled using a Greenwood-Williamson (1966) model of rough surface contact. It is readily apparent that rougher surfaces are more compressible. However, this may not translate directly into softness. Sample O, while being rough, was characterized as not being very soft. The roughness was attributed to the strong pattern embossed into the surface. This pattern showed up in the power spectrum analysis as peaks. Thus, the compressibility was increased due to the large out of plane pattern introduced, but this did not translate into softness.

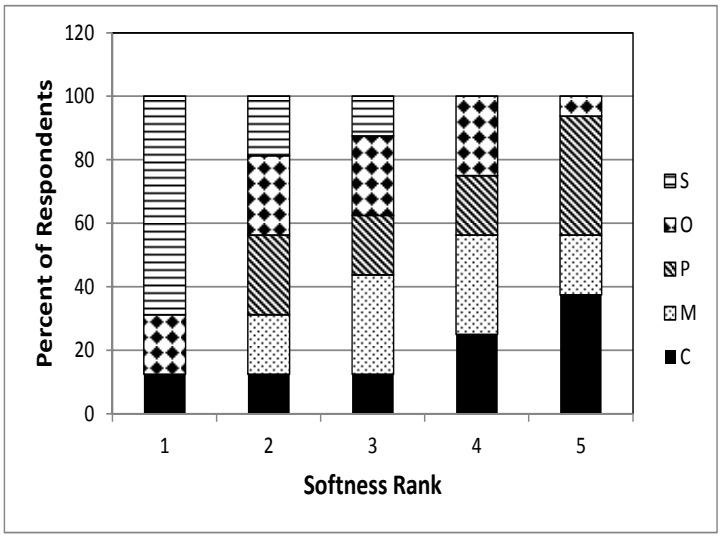

Figure 7: Percentage of respondents ranking each tissue sample. (1 corresponds to the least soft and 5 to the most soft.)

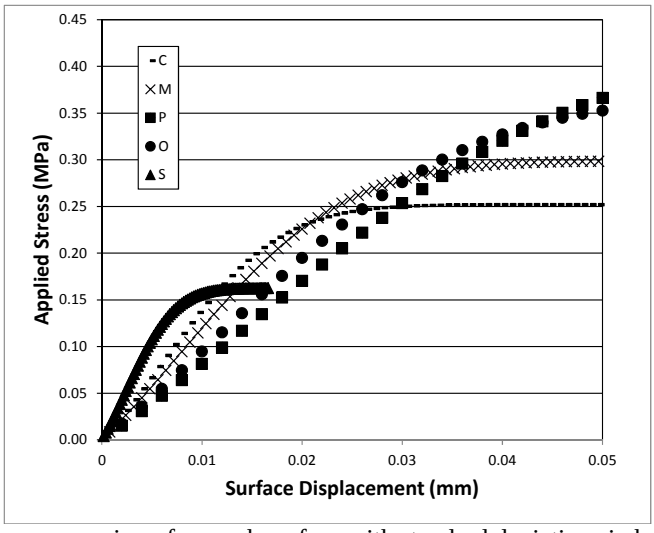

Figure 8: GW model of the compression of a rough surface with standard deviations in heights corresponding to the individual tissue samples. The model clearly shows the smoothest samples are the least compressible (steepest slope).

Softness appears to be more a function of the fine scale variability in the surface consistent with individual fibers extending from the surface. The compression of a single fiber is very similar to the compression of an individual beam, cf. **Figure 9**. **Figure 10** below shows the force deflection curve record for a single softwood fiber compressed on its end using an atomic force microscope. The fiber deflects much like a beam. Thus, it is reasonable to model the compressive behavior of a fiber much like that of a column. The load/deflection behavior for a cantilevered column is directly dependent on the elastic modulus of the material and moment of inertia of the column, and inversely dependent on the length of the column. From this one can determine that to increase the compressibility of the surface one can reduce the moment of inertia of the fibers extending from the surface, or extend the fibers further from the surface of the tissue sheet. Changing the moment of inertia may be accomplished by fiber selection, while creating fibers well extended from the surface is more a function of the processing method used.

4 CONCLUSIONS

Results indicate that the softness scores as determined through a panel evaluation were related to the surface characteristics of the tissue sheets. Image analysis showed that large, repeating patterns were perceived to be ineffective in creating softness. Small scale variability in the surface roughness showed a better relationship to the softness. This was linked to the compression of individual fibers, which extended from the surface of the sheet. Thus, while short, hardwood fibers may be well suited for creating a compressible bulk structure, it is more likely that lightly bonded softwood fibers that extend

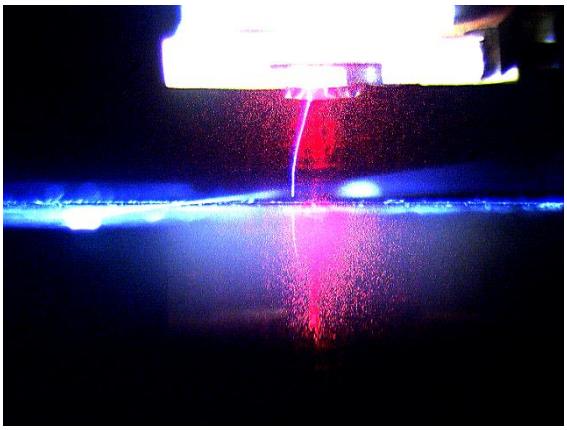

Figure 9: Image of fiber being deflected under compression in AFM. (courtesy, Tracy Meranda, NCSU)

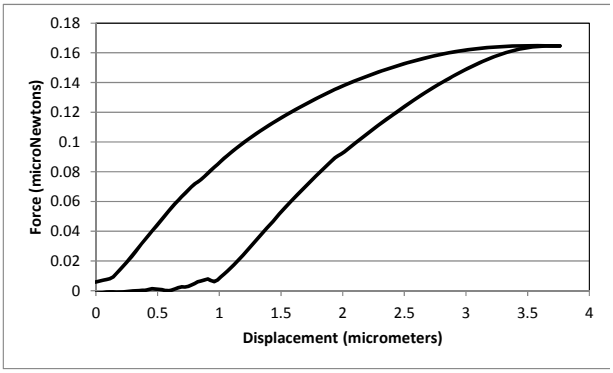

Figure 10: Force-Displacement curve of a softwood fiber compressed using an AFM. (courtesy, Tracy Meranda)

significant distances from the surface are more important for creating a compressible surface that is perceived as being soft. This work emphasizes the importance of processing techniques to modify the structure of the tissue sheet to effectively use softwood to create a soft surface. These results are contrary to traditional papermaking and tissue making where forming and creping are the only significant means to alter sheet structure and it is accepted that hardwood fiber creates a softer sheet.

5 ACKNOWLEDGEMENTS

The authors would like to thank Tracy Meranda, and Dr. M. K. Ramasubramanian for the contributions and collaboration on the single fiber compression. The authors would also like to thank Dr. Richard Venditti for inspiring this work.

6 REFERENCES

Chen, Y. Collier, B., Hu, P., Quebedeaux, D., 2000, "Objective Evaluation of Fabric Softness", Textile Research Journal 70:443.

Hollmark, H., and Ampulski, R.S., 2004, "Measuremtn of tisdsue paper softness: A literature review", Nordic Pulp and Paper Research Journal, 19:3 345-353.

Greenwood, J.A. and Williamson, J. B. P., 1966, " Contact of nominally flat surfaces." Proc. R. Soc. London Ser. A 295, pp. 300–319

Liu, J., Hseih, J., 2004, "Charaterization of facial tissue siftness", Tappi Journal 3(4):3-8.

Norman, b, Wahren, D., 1973, "Mass distribution and sheet properties of paper", Trans, of the 5th Fundamental Research Symposium, Cambridge.

Pan, Y.L., Habeger, C.C., Biasca, J.E., 1991, "Ultrasonic evaluations of tissue softness", Tappi Tissue Runnability Seminar (Seattle) 197-205.

Parker, I.H., 1975, "Frequency analysis in the paper industry, Appita 28:6.

Pawlak, J.J., 2001 "Local compressive properties of paper in relation to paper friction", PhD Dissertation, SUNY College of Environmental Science and Forestry, Syracuse, NY, USA.

Pawlak, J.J., and Keller, D.S., 2005, "The compression of a stratified fibrous structure", Mechanics of Materials, 37(1):1132-1142.

Tappi Test Methods, 1999, "Thickness (caliper) of paper, paperboard, and combined board," T411 om-97.

Mapping the Compressive Properties of Low Density Fibrous Web Materials

D. STEVEN KELLER,YAN HUANG,
JAKE HYLAND

Department of Chemical and Paper Engineering,
Miami University, Oxford, OH 45056, USA,

kellerds@muohio.edu

1 Abstract

The compressibility of tissue and towel grades is recognized as an important property that influences many of the important product qualities such as softness, flexibility and roll density. The usual method for determining the compressibility of tissue and towel grades involves measure the normal force required to compress a stack of samples. This method is adequate for most practical applications, but lacks the sensitivity to fully characterize the complex structure that is purposely engineered into these materials. This presentation will describe an investigation that focuses on the mapping of the compressibility at various in-plane spatial scales. It was hypothesized that the various inherent and induced features that comprise the structure of paper towels manufactured by different processes would exhibit different behavior under localized compression. For example, regions that were wet creped or those that were densifed under embossing would provide different characteristic compression functions. Likewise, the densified and bulked regions generated by different through air drying processes would show differences, at different locations, when mapped. An important aspect of this research was distinguishing between the collapse of out-of-plane features, i.e. flattening of embossments, and the localized compression of the web.

The method introduced in this investigation uses flat platen cylinders that approach the web simultaneously from opposing sides until the sample is initially contacted on each surface. The compressive stress on both sides is then recorded simultaneously as compressive strain is applied. Compressive response is determined at each location within a region as the in-plane position is raster scanned and the compression process is repeated. The dimensions of the array and the platen diameter are selected to examine specific sub-millimeter features that are present in the samples.

The nonuniformity of the compressive response obtained from the maps for a given region are then compared with thickness maps generated using the noncontact method from twin laser profilometry. By developing this method for mapping the micro-scale compressibility of towel and tissue samples over substantial regions, the effects of specific design patterns and processing techniques may be revealed.

Posters

Pulping and Stock Preparation

Cyclic loading and fatigue of wood

LAURI I SALMINEN[1], ARI SALMI[1,2], BIRGITTA A ENGBERG[3], TOMAS BJÖRKQVIST[4], EDWARD HÆGGSTRÖM[2], MIKAEL LUCANDER[1]

[1]VTT Technical Research Center Finland, P.O.B. 1000, FIN-02044 VTT, Finland
[2]Electronics Research Laboratory, Department of Physics, Division of Materials Physics, P.O.B. 64, FIN-00014 University of Helsinki, Finland
[3]Fibre Science and Communication Network (FSCN), Department of Natural Sciences, Engineering and Mathematics, Mid Sweden University, SWE-85170 Sundsvall, Sweden
[4]Department of Automation Science and Engineering, Tampere University of Technology, P.O.B. 692, FIN-33100 Tampere, Finland

lauri.salminen@vtt.fi

1 INTRODUCTION

Production of papermaking fibres by mechanical pulping, grinding or refining, involves wood deformation at high frequencies in processes that are energy demanding, typically 1000-3000 kWh (4 to 10 GJ) per ton of pulp. It is believed that energy can be saved by introducing fatigue [1] -structural changes - into wood using cyclic compression. Despite the common faith only one concept has been reported to save some 30% of energy [2] the reason for the saving still remaining unknown.

In any of its forms mechanical pulping process is a compromise between the energy consumption and pulp quality namely fiber bonding ability and fiber length. Poor quality mechanical pulp requires more of expensive chemical pulp to maintain the printing paper or package strength. To exploit the route towards energy efficient processing, one needs to know more about the mechanical response of the raw material (wood) to cyclic loading. Therefore wood deformation of was studied at high frequencies and at high strain rates.

Emphasis of the disquisition is on large i.e. inelastic compression and changes of wood cellular structure at the level of annual rings. We address the physics of our unexpected and unexplained results of unequal yield deformation.

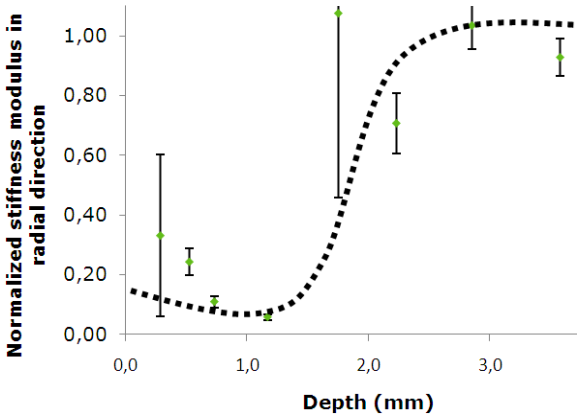

Figure 1. Stiffness modulus along the depth direction (into the sample) measured using ultrasonic depth profiling technique [5]. Dry wood sample, 15 000 fatiguing pulses.

2 METHODS

A custom built modulated loading device [3] at VTT was employed to fatigue [4,5] the samples of fresh Norway spruce. The modulated loading device resembles the physical situation at industrial grinding process, in particularly that of the energy efficient grinding [2]. The consequences of 24000 unipolar (constrained compression and free relaxation) loading cycles with a 0.75 mm nominal amplitude at 500 Hz frequency were quantified first by ultrasound at University of Helsinki. Ultrasonic analysis describes the small deformation elasticity and the stiffness of a sample is proportional to the square of the ultrasonic time of flight multiplied by the sample density.

The samples were after the non-destructive ultrasonic testing evaluated by impulsive loading experiments carried out in an encapsulated Split-Hopkinson device developed at Mid Sweden University. Impulsive loadings, which extended into the yield and plastic deformation region (compression phase duration typically 200 µs), were performed at four temperatures: 20, 65, 100 and 135°C. High-speed photography (50000 frames per second and 10 µs exposure time) and image analysis was applied to monitor local deformations at the sample. As fresh wet wood is partly transparent the samples were painted white and spotlighted with Ar:Ion laser light (wavelengths 488-489 and 511 nm). Unfortunately the painting prevented us for analyzing high-speed photographs below the resolution of annual rings.

3 RESULTS

The cyclic compressions caused plastic changes in the wood material, which was evidenced ultrasonically as a decreased stiffness of the samples. Ultrasonic measurements also revealed the presence of a fatigued 1-2 mm thick layer (localized

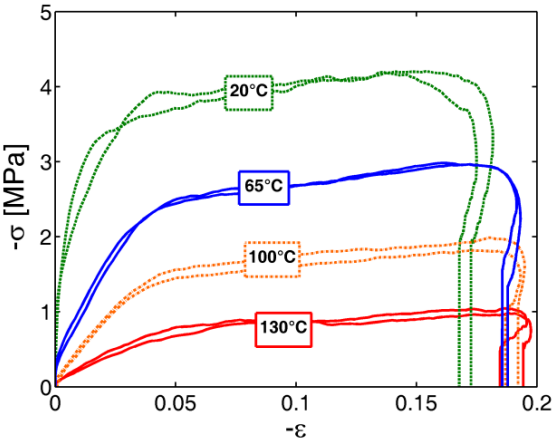

Figure 2. Stress-strain behaviour of native fresh wood [5].

plastic deformation) near the impacted surface (fig. 1). The mechanism behind this uneven change is unknown, simple mechanical attenuation cannot account for it [6].The results of Split-Hopkinson trials show that wood behaves as a general cellular material during fast compression [8]. In the stress-strain curves the elastic region is followed by distinct yield point and wide region of cell wall collapse (fig. 2 and 3). This plateau starts at 5 to10 % compressive strain (fig. 3) and extends up to cell densification. However the expected densification behaviour at 66 % compressive strain was not studied by split-Hopkinson trials. Other slower compression experiments have shown densification in both fatigued and native wood. Large variation in measurement results is a clear drawback and thought to originate from sample inequality.

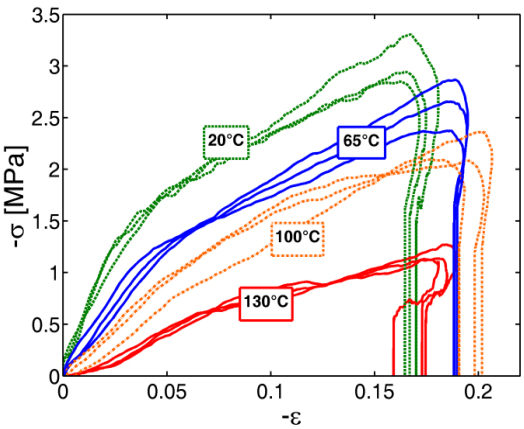

Figure 3. Stress-strain behaviour of fatigued wood [5]. Note unequal scales of ordinates on figures 2 and 3.

The following results were achieved:

- Fatigue was observed both in ultrasonic measurements and in impulsive loading
- Fatigue propagation is probably limited by the fatigue itself, therefore the thickness of the fatigue layer to seem to be only 1-2 mm.

4 DISCUSSION

We propose two mechanisms to contribute to the deformation localization behaviour:

- Compressive energy accumulation followed by eventual wood cell collapse that generates a mechanical shockwave. Shockwave means that highly nonlinear propagating deformation can dissipate energy rapidly [7].
- Deformation localization due to viscous heating and crack growth at lignin rich wood components. This mechanism cannot initialize the deformation localization.

In general the description of fatigue mechanism of wood in cyclic compression is incomplete. Novel concepts of strongly heterogeneous material mechanics like nonlinear mesoscopic elasticity[9] cannot be ruled out. We believe that at mechanical pulping research it is not enough to analyze wood structure as set of elastic beams [8]. Instead cellular solids like wood should be considered as consolidated materials whose mechanical properties are a consequence of their assembly. The elasticity can be dominated by the contacts (in wood: middle lamella) between the rigid elements (in wood: fibres) [9].

Mechanical pulping is not the only method to produce fibres for paper and board products. The alternative is the chemical pulping, where wood fibres are released by dissolving the lignin. Chemical pulping provides lower wood yield, typically 50 %, and if the dissolved material is burned the process is energy generative. Moreover the fiber length of chemical pulp is higher than that of the mechanical pulp and therefore many of the hardwoods cannot be utilized by mechanical pulping.

The effects on single wood fiber due to the fatigue are unknown although plastic yield deformation of cell walls (scale 10 µm) is indeed evitable. The observed temperature dependence suggests that lignin, having the lowest softening point (60-90°C depending on moisture content and deformation rate) of polymers of wood, is strongly linked in

general mechanical response of wood. Therefore one could conclude the phenomena of mechanical defibration are phenomena of lignin thermoplasticity.

The interesting observation by split-Hopkinson is that in fatigued wood the slope of the plateau region differs from that of native wood. In general cellular mechanics [8] this slope is expected to originate from gas being compressed inside the closed cells. That cannot be the origin in case of fatigued wood; instead we propose a primitive model describing the existence of the slope. We thereby assume that fatigue makes the fibres more flexible which helps them withstand high defibration forces without breaking. Therefore, fatigue is expected to have a beneficial effect on mechanical pulping energy consumption by enabling harsh grinding. This scheme supports a previous hypothesis about wood behaviour, which was utilized to develop the concept of energy efficient surface (EES) grinding [5].

REFERENCES

[1] L. Salmén, The Effect of the Frequency of a Mechanical Deformation on the Fatigue of Wood, Journal of Pulp and Paper Science, 13(1):J23-J28 (1987).

[2] M. Lucander, T. Björkqvist, New Approach on the Fundamental Defibration Mechanisms in Wood Grinding, Proceedings of International Mechanical Pulping Conference, Oslo, 149 – 155, (2005).

[3] M. Lucander, S. Asikainen, T. Pöhler, E. Saharinen and T. Björkqvist, Fatigue Treatment of Wood by High-Frequency Cyclic Loading, Journal of Pulp and Paper Science, 35(3-4):81-85 (2009).

[4] A. Salmi, L. Salminen, E. Hæggström, Quantifying fatigue generated in high strain rate cyclic loading of Norway spruce, Journal of Applied Physics, 106(10), 104905 (2009).

[5] A. Salmi, Lauri I. Salminen, Birgitta A. Engberg, Tomas Björkqvist and E. Hæggström, Unipolar cyclic compression causes localized plastic deformation in wood, submitted to Journal of Applied Physics (2011).

[6] T. Björkqvist, A Design Method for an Efficient Fatigue Process in Wood Grinding – an Analytical Approach, PhD thesis, Tampere University of Technology (2002).

[7] P.J. Tan, S.R. Reid, J.J. Harrigan, Dynamic Compressive Strength Properties of Aluminium Foams. Part I - Experimental Data and Observations, Journal of the Mechanics and Physics of Solids, 53(10):2174-2205, (2005).

[8] L.J. Gibson, M.F. Ashby, Cellular solids – Structure and properties, Cambridge University Press (1997).

[9] R.A. Guyer and P.A. Johnson, Nonlinear Mesoscopic Elasticity: Evidence for a New Class of Materials, Physics today, April (1999).

Effect of dry milling on physical and chemical properties of pulp

YANG-JIN, JOUNG, TAEYOUNG, KIM
SONG-MIN, LEE

KOMSCO, 54 Gwahang-no, Yuseong-gu, Daejeon
305-713, Korea
ktaey@komsco.com

Keywords: cellulose, dry milling, crystallinity index, viscosity, cotton linter pulp

ABSTRACT

Several kinds of cotton linter pulps and wood pulps were milled by dry process. Laboratory, pilot and mill scale cutter were chosen for dry milling. Intrinsic viscosity, fibre properties such as average length, width and fines content, and crystallinity index by PXRD and alpha cellulose content were measured and evaluated.

At first we could find that scale of milling operation was more important factor to dry milling than milling time itself.

Contrary to wood pulp, intrinsic viscosity of cotton linter pulp was decreased by dry milling itself and there was a very big reduction by mill scale milling. It was assumed that main reasons were high fines content and fibril like shape of fines.

Crystallinity index of each pulp was decreased by dry milling and there was no distinct relationship between intrinsic viscosity and crystallinity index, between size or fibre length and crystallinity index.

According to mill conditions such as knife type and milling weight per hour, properties of milled powder were altered and it was important to adopt proper or effiencient milling process.

We could find that alpha cellulose content was decreased by dry milling.

Finally, reduction of intrinsic viscosity and fibre length was increased and more fines happened with increase of apparent density within about 0.70 g/cm^3..

BACKGROUNDS

It is well known that wood pulp (dissolving pulp) or cotton linter pulp has been used as chemical cellulose for cellulose derivatives and regenerated fiber. At the first stage of chemical cellulose utilization, activation process such as milling is necessarily included for smooth chemical reaction [1]. Some researchers reported that crystallinity was decreased and DP (degree of polymerization) was reduced by dry milling [1, 2, 3, 4]. But, there was few papers dealing with effects of scale of milling cutter, pulp types such as wood and cotton pulp, and fractionation on dry milling.

1 MATERIALS AND METHODS

1.1 Materials

Several kinds of commercial cotton linter pulp or wood pulp imported from USA or China were chosen. Basically these pulps were used as chemical cellulose and specification such as viscosity and brightness was different with each other.

Table 1. Specifications of cotton linter pulps

	Intrinsic viscosity (cPs)	Brightness (%)	Apparent density (g/cm^3)
CLP_1	214.0	88.7	0.56
CLP_2	248.5	79.5	0.47
CLP_3	224.1	75.8	0.55
CLP_4	290.7	79.0	0.52
CLP_5	220.8	81.1	0.58
CLP_6	258.6	80.3	0.51

Table 2. Specifications of wood pulps

	Intrinsic viscosity (cPs)	Brightness (%)	Apparent density (g/cm^3)
WP_1	70.0	80.5	0.57
WP_2	5.2	86.2	0.72
WP_3	71.3	86.6	0.56

CED(cupriethylenediamine, 1M) solution was used for measuring viscosity of pulp.

1.2 Methods

Dry milling was executed by laboratory, pilot and mill scale continuous type cutter. In case of pilot and mill scale cutter, temperature sensor was installed inside of cutter. Pilot scale cutter was operated within 60 degree of Celsius and mill scale cutter was operated within 90 degree of Celsius.

Intrisic viscosity was measured accorting to Tappi test method T-230. CED solution was used as solvent and efflux time of 0.5% cellulose solution was measured with Ubbelohde type capillary viscometer.

Fiber properties of sheets or powders of pulp was measured by FIBER TESTER(L&W). Average fibre length, width and fines content were measured for analysis.

Particle size of milled powders were anaylzed by Particle size anayser Malvern Mastersizer 2000.

Crytallinity index of sheet or powders of each pulp was measured by PXRD(powder x-ray reflection diffractometry, 2theta=10~30). Crystallinity index was calculated by peak height ratio(Segal's equation).

Sieve shaker was used for fractionation of milled pulp powders. 80, 100, 120, 140 and 200 mesh sieves were installed. 150g of milled powders were added and operation time was 90minutes.

Apparent density of pulp was controled with laboratory calender.

2 RESULTS AND DISCUSSIONS

2.1 Effects of milling type on properties of pulp powder

In this study three scales of continuous type dry milling cutter were used for milling of pulp. Labolatory, pilot and mill scale cutter were used.

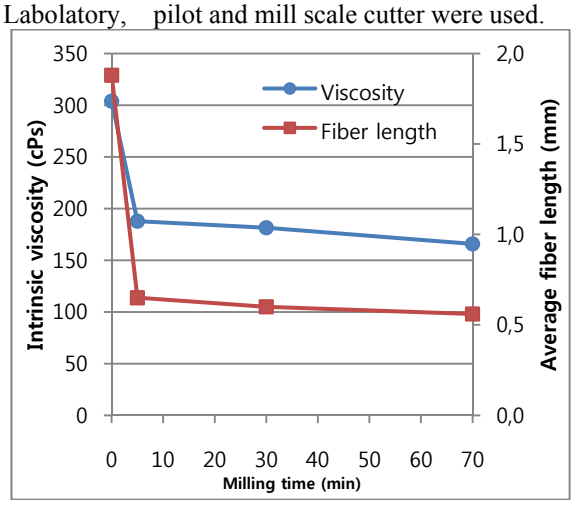

Figure 1. Intrinsic viscosity and fibre length as a function of milling time (lab. Scale cutter).

At first, effect of milling time on milling process was considered. According to figure 1, viscosity and fiber length was drastically changed but milling time itself was not an important factor. Increase of milling time after 5 minutes had small effect on viscosity and fiber length. In case of crystallinity index and alpha cellulose content, 0.77 and 97.6% was almost maintained after 5 minutes milling. But, after pilot scale milling, 0.68 and 95.3% were measured and initial vale were 0.84 and 99.5% respectively.

As a reference, laboratory scale milling was done with mixer and we could see the results on figure 2. Contrary to cutter, action of mixer was too weak to adjust for using to pulp milling. We could see that easily from viscosity reduction after 5 minutes milling between cutter (fig. 1) and mixer (fig. 2).

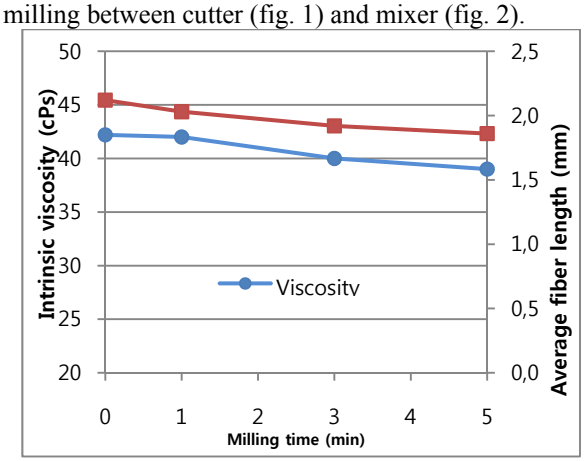

Figure 2. Viscosity and fibre length as a function of milling time (laboratory mixer).

That is to say, scale of milling operation was more important factor to dry milling than milling time itself. So, we determined to execute experiments as a function of laborotory, pilot and mill scale cutter. 3 kinds of cotton linter pulp and 1 kind of wood pulp were used as fiber soures.

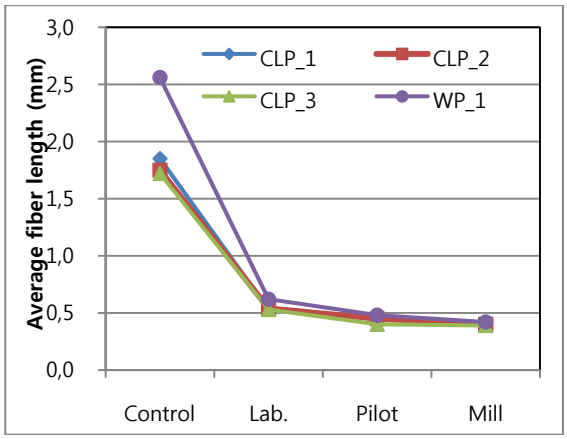

Figure 3. Average fibre length as a function of dry milling (laboratory, pilot and mill scale).

According to figure 3, fibre length was dramatically reduced by milling. We could guess harsh actions were caused in the cutter. Among laboratory, pilot and mill scale milling, there was a slightdifference In case of wood pulp, fibre length reduction ratio was higher than that of cotton linter pulp. It was assumped that intrinsic strength of fibre was an factor.

Particle size of milled powders were measured and shown on figure 4. Particle size was decreased by milling in the same way as fibre length.

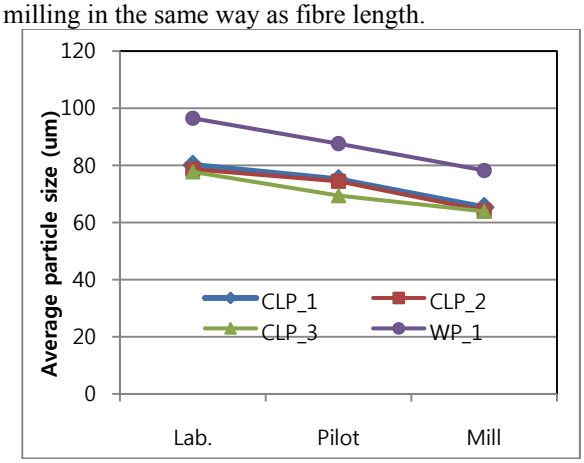

Figure 4. Particle size of milled powders as a function of dry milling (laboratory, pilot and mill scale).

Intrinsic viscosity of each sheet and milled powder was measured and shown on figure 5. There was a big difference between physical (fibre length) and chemical property (intrinsic viscosity). In case of intrinsic viscosity, we could find difference among laboratory, pilot and mill scale milling contrary to fibre length.

We could find that intrinsic viscosity of cotton linter pulp was decreased by dry milling itself and there was a very big reduction with mill scale milling from figure 4. But very slight decrease of viscosity was happened to wood pulp.

From figure 5, we could get a very important thing that milling is critical matter for chemical cellulose industry. Initial viscosity of CLP_3 and WP-1 was very different but, after mill scale milling, their viscosities were almost similar.

Among cotton linter pulps, CLP_2 showed the least reduction of intrinsic viscosity with milling. One difference among cotton linter pulps was apparent density (Table 1) and effects of density on milling operatios will be discussed later.

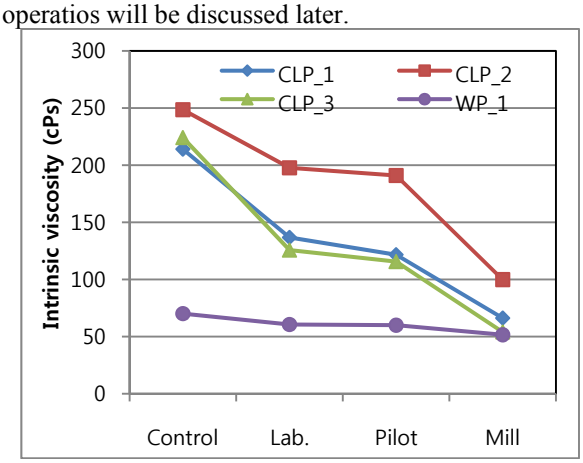

Figure 5. Intrinsic viscosity as a function of dry milling (laboratory, pilot and mill scale).

Considering several aspects, we could assume that content and shape of fines were closely related with viscosity reduction in dry milling.

At first we measured fines content of each sheet and powders. Basically, number of fines was increased by dry milling and fines content of wood pulp was smaller than those of cotton linter pulps. We could also find the highest fines contents among three kinds of milling in mill scale dry milling.

It was assumed that the first reason of small viscosity reduction of wood pulp was small fines content.

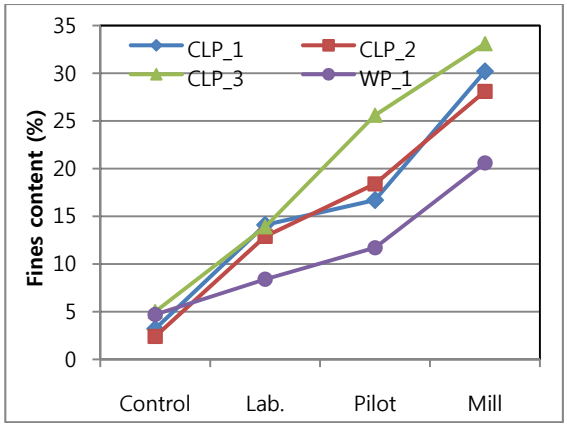

Figure 6. Fines content as a function of dry milling (laboratory, pilot and mill scale).

Subsequently we observed surface of milled pulp powders through SEM. We could find very interesting phenomena. In case of milled wood pulp powders, small fragments which preserved original fibre width were seen frequently (Fig. 7(a)). But, in case of cotton linter pulp powders, fibril or thread like small fractions which lose their original shape were observed mainly (Fig. 7(b)).

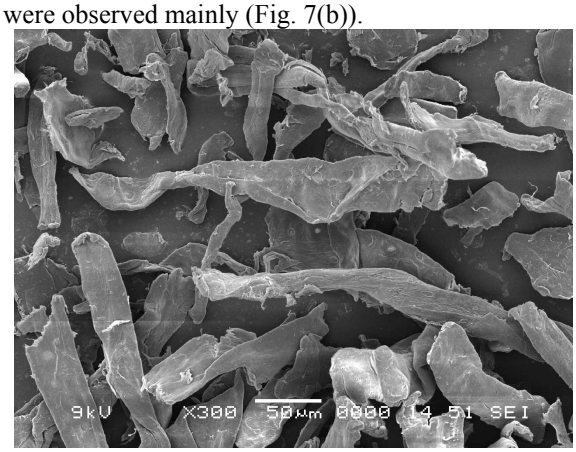

(a) WP_1

(b) CLP_1

Figure 7. SEM images of pulp powders (×300).

We observed enlarged milled cotton pulp powders more closely. From SEM image it was assumed that at the beginning or mild milling stage, surface of fibril (Fig. 8(a)) was produced and at harsh milling or later half of milling inside cleavage such as Fig. 8(b) was happened. These phenomena lead to decrease intrinsic viscosity and degree of polymerization, and finally increase reactivity of chemical cellulose.

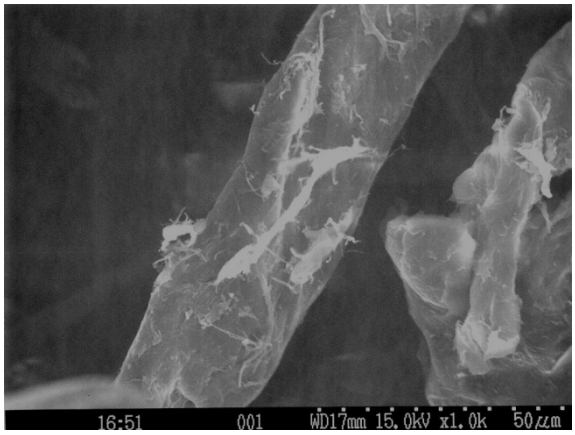

(a) Surface fibril (laboratory scale)

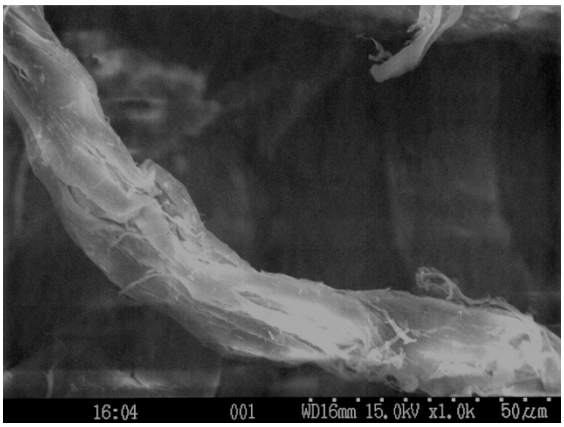

(b) Inside cleavage (mill scale)

Figure 8. SEM images of pulp powders (×100).

Generally we found similar results in wet milling such as beating or refining [1Cotton pulp needs more beating time to get same freeness [5] and it was reported that more fibrils were produced.

In the aspect of degree of polymerization or viscosity, it was assumed that there was small reduction of viscosity through width preserved fragments from wood pulp contrary to fibril like fragments from cotton linter pulp.

So, we could assume that the second reason of small viscosity reduction of wood pulp was related with the shape of fines.

In other words, production of fibril like fraction was more related with viscosity reduction by dry milling than fibre shortening itself.

We could get related results from fractionation. According to figure 9, almost no reduction of viscosity was happened in wood pulp but, viscosity of cotton linter pulp was continually decreased by fractionation. These results were related with degree of polymerisation or length of cellulose chain.

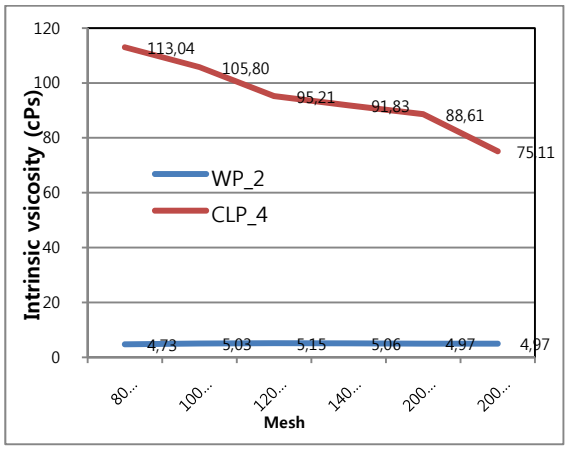

Figure 9. Intrinsic viscosity as a function of fractionation.

We measured crystallinity index of each sheet and powders. Crystallinity index of pulp sheet was shown on figure 10. Crystallinity index of cotton linter pulps and wood pulps were about 0.85 and 0.68~0.76 respectively.

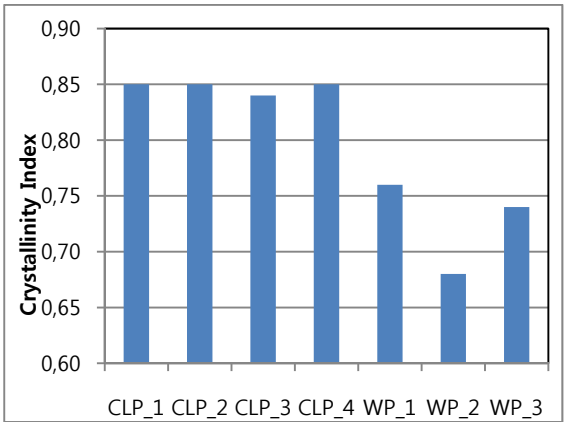

Figure 10. Crystallinity index of pulp sheet.

According to figure 11, crystallinity index was almost linearly decreased by dry milling. Cotton linter pulp was dropped into about 0.70 and wood pulp was dropped into 0.58. In case of wood pulp, crystallinity index was linearly reduced by dry milling contrary to intrinsic viscosity.

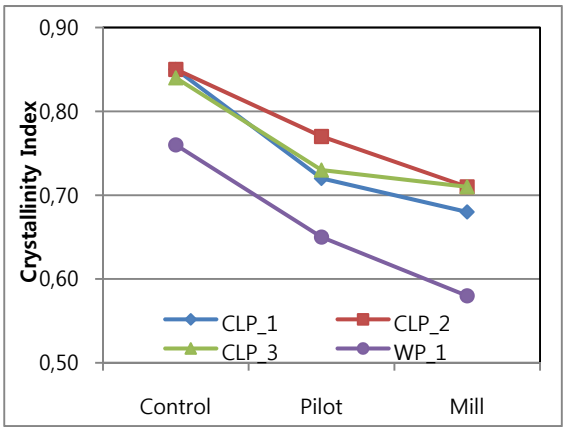

Figure 11. Crystallinity index as a function of dry milling (laboratory, pilot and mill scale).

We could find the change of crystalline region by milling from figure 12.

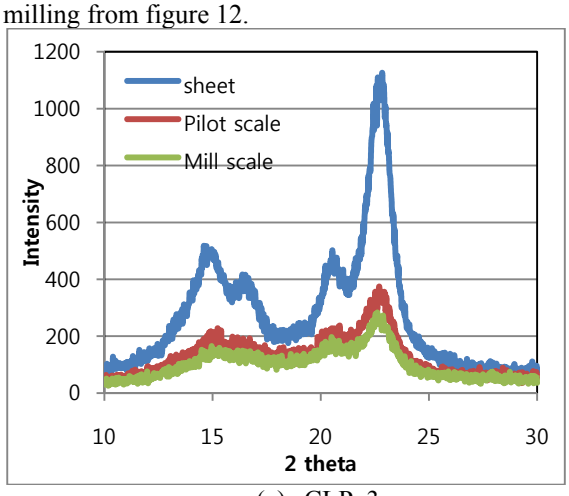

(a) CLP_3

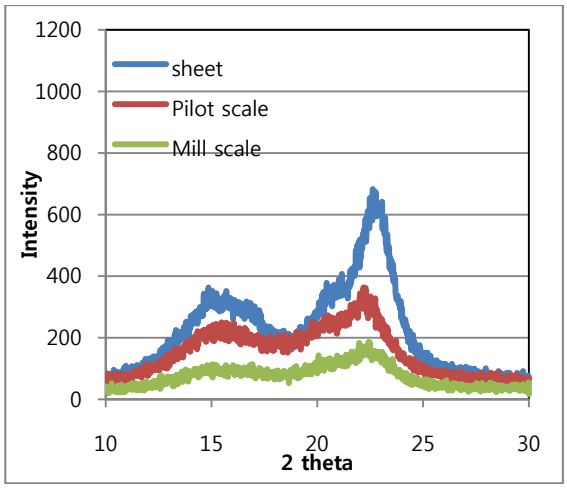

(b) WP_1

Figure 12. Intensity as a function of 2 theta with scale of milling (pilot and mill scale).

We measured crystallinity index of each fractions after fractionation by sieve shaker. As shown on figure 11, there was no distinct relation between fractions and crystallinity. That is to say, size or length of milled powder was not a critical factor to crystallinity index. Maybe intra structure of fibre and fibre fragments was an important factor.

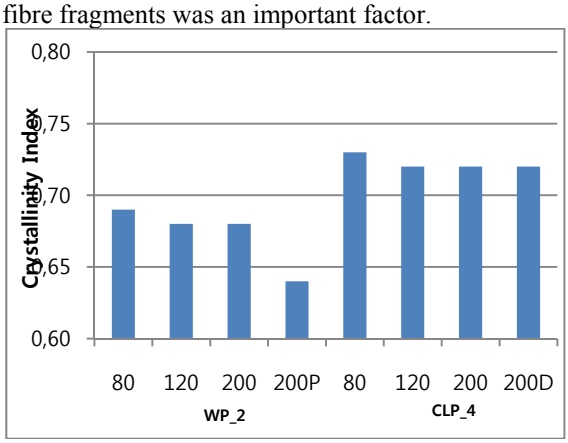

Figure 13. Crystallinity index as a function of fractionation of milled powder.

2.2 Effects of milling condition on properties of pulp powder

In this section, same wood or cotton linter pulp was milled by 2 kind of pilot cutters (S company and K company) respectively. Milling operations are done under routine conditions in both of two companies, even though it is not easy to explain each conditoins precisely. Cutter knife type and milling weight per unit hour were not the same.

2 kinds of cotton linter pulps and 1 kind of wood pulp were used. According to figure 12, pilot K and S showed different action on milling operation. Apparent difference between K and S could be seen in cotton linter and wood pulp. This was because wood pulp showed small reduction of viscosity by dry milling (Fig. 5).

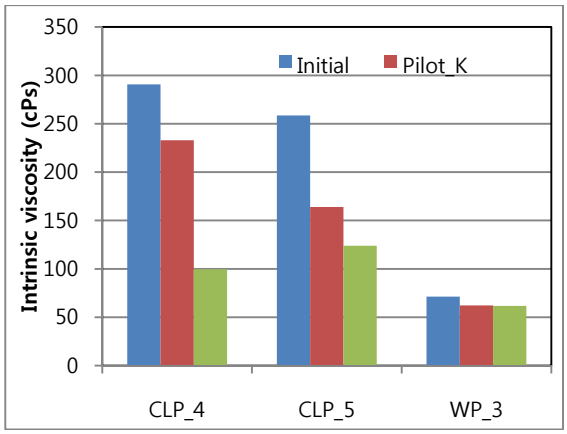

Figure 14. Intrinsic viscosity of sheet and milled powders (pilot_K vs. pilot_S).

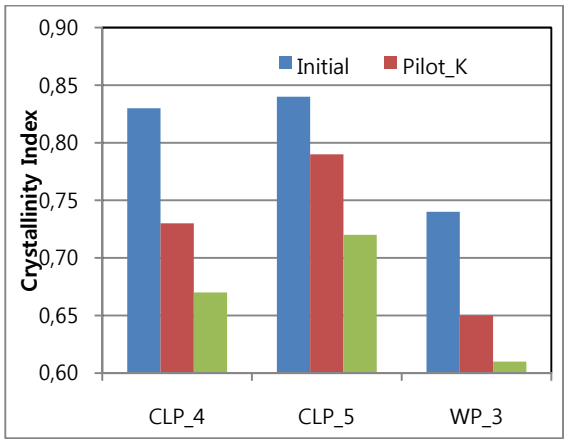

Figure 15. Crystallinity index of sheet and milled powders (pilot_K vs. pilot_S).

In case of crystallinity index and fines content, we could find a difference between K and S cutter.

These results inevitaly will cause chemical reactivity difference between milled powders. Productivity and performance of end products will be influenced also.

So, we could find that cutter type and operation conditions were very important factors to chemical cellulose treatment.

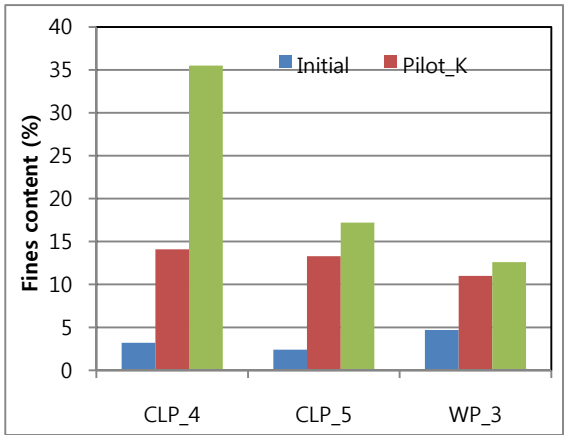

Figure 16. Fines content of sheet and milled powders (pilot_K vs. pilot_S).

2.3 Effects of dry milling on alpha cellulose content

We could find that alpha cellulose content of pulp was decreased by dry milling. We got a similar results when electonic beam was adopted to cotton linter pulp [6]. Intrinsic viscosity was dramatically decreased with increase of electronic beam dosage. Alpha cellulose was decreased also with electronic beam dosage.

After fractionation, we measured alpha cellulose of each fractions. But, there was no relationship between fractions (that is to say, size of powders) and alpha cellulose.

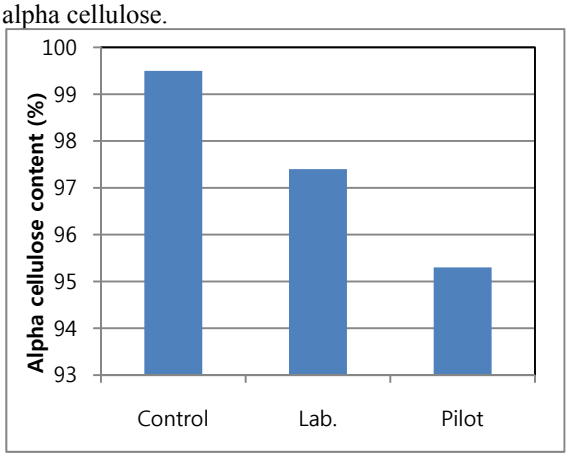

Figure 17. Fines content of sheet and milled powders (pilot_K vs pilot_S).

2.4 Effects of pulp density on properties of pulp powder

From figure 5, we found that CLP_2 showed the least reduction of intrinsic viscosity with milling and one difference among cotton linter pulps was apparent density.

One cotton linter pulp (CLP_6) was chosen and apprarent density of that pulp was changed into 5 levels by laboratory calendering (figure 18).

These pulps were firstly cutted into small pieces whose dimensions were 15mm by 15mm and secondly milled by laboratory cutter. Change of intrinsic viscosity and fibre properties with density were measured and shown on figures 19~21.

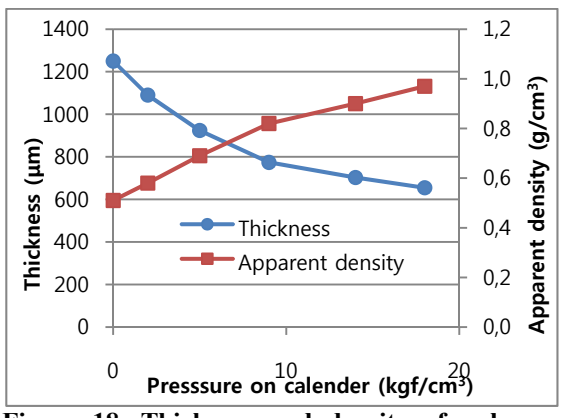

Figure 18. Thickness and density of pulp as a function of calendering.

According to figures 19~21, reduction of intrinsic viscosity and fibre length was increased and more fines happened with increase of apparent density within about 0.70 g/cm^3. But, above that point there was no linear relationship. It was assumed that another factor other than density was intervened.

To understand the effect of density on dry milling process, it was judged that profound study was needed.

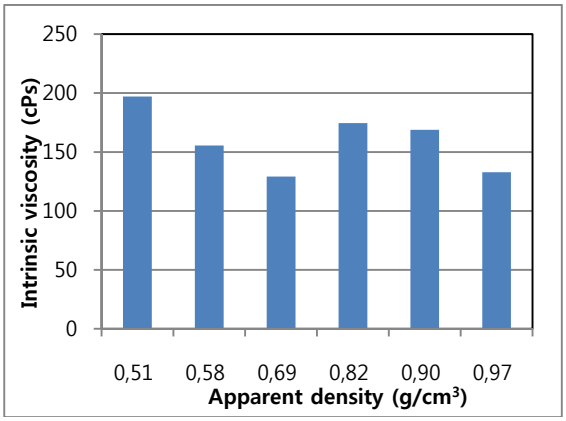

Figure 19. Intrinsic viscosity as a function of apparent density (laboratory scale).

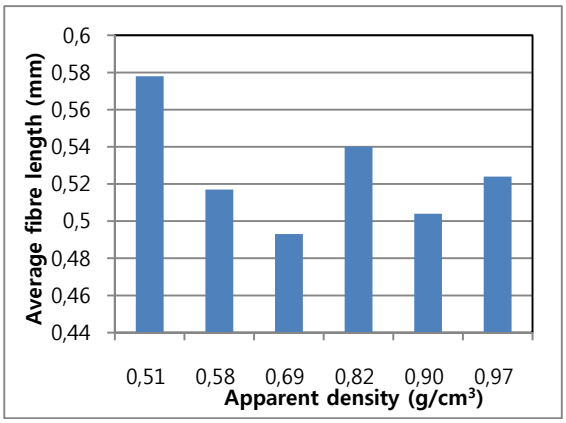

Figure 20. Fibre length as a function of apparent density (laboratory scale).

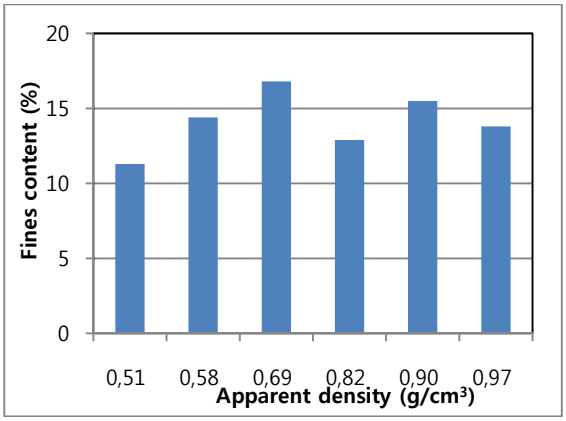

Figure 21. Fines content as a function of apparent density (laboratory scale).

3 CONCLUSIONS

Several kinds of cotton linter pulps and wood pulps were milled by dry process. Laboratory, pilot and mill scale cutter were chosen for dry milling. Intrinsic viscosity, fibre properties such as average length, width and fines content, and crystallinity index by PXRD and alpha cellulose content were measured and evaluated.

At first, we could find that scale of milling operation was more important factor to dry milling than milling time itself.

Contrary to wood pulp, intrinsic viscosity of cotton linter pulp was decreased by dry milling itself and there was a very big reduction by mill scale milling. It was assumed that main reasons were high fines content and fibril like shape of fines.

Crystallinity index of each pulp was decreased by dry milling and there was no distinct relationship between intrinsic viscosity and crystallinity index, between size or fibre length and crystallinity index.

According to mill conditions such as knife type and milling weight per hour, properties of milled powder were alterend and it is important to adopt proper or effiencient dry milling process.

We could find that alpha cellulose content was decreased by dry milling.

Finally, reduction of intrinsic viscosity and fibre length was increased and more fines happened with increase of apparent density within about 0.70 g/cm^3.

REFERENCES

[1] H.A.Krazzig, Cellulose; structure, accessibility and reactivity, Gordon and Breach Science Pulishers (1993)

[2] A. Lejeune and T. Deporez, Cellulose; structure and proeperties, derivatives and industrial uses, Nova Science Publishers (2003)

[3] A. Isogai, Advanced Technologies of cellulose utilization (2008)

[4] J. Wertz, O. Bedue and J. P. Mercier, Cellulose science and technology, EPFL Press (2010)

[5] K. Taeyoung, Effects of fibre properties, fibre treatment and impregnation process on crumpling tendency of paper, PPPS 2008, Helsinki, Finland (2008)

[6] Internal Publication (2011)

Influence of Beating and Chemical Modification on the Structural Characteristic of Cellulose

M. FILIPI, V. HEJLOVÁ

Department of Wood, Pulp a Paper, University of Pardubice, 532 10 Pardubice, Czech Republic, michaela.filipi@upce.cz, +420 466 038 015

Keywords: cellulose, oxycellulose, microtomography, X-ray diffraction

ABSTRACT

The both chemical and mechanical influences upon supermolecular structure of cellulose represented by oxidative-hydrolysis process of oxycellulose preparation and beating of bleached linters, respectively, were studied by use of X-ray diffraction and X-ray computed microtomography methods. In order to elucidate a role of fines, hydrocolloids and dissolved substances in this context, the beating experiments were conducted with and without separation of these ones and the samples of paper sheets were prepared by usually drainage papermaking methods and by drying of pulp slurries at Petri dishes as well as. Received results suggest an increase of crystalline portion of cellulose during beating of native cellulose followed by deeply changes in their qualities in the case of oxycellulose. In contradiction with native cellulose, the crystalline structure of oxycellulose was changed due to oxidative-hydrolysis process taking place during its preparation from cellulose I to more amorphous cellulose II being further changed by beating to polymorphs II and IV_{II} in the case of intensively oxidized cellulose (15 % and 19 % of COOH groups) and to polymorph IV_I for carefully oxidation of bleached linters (3,5 % of COOH groups). The explanation of this behaviour is described following of a concept of mutually structuralised hydration attractive-repulsive forces among cellulosic chains, microfibrils, fibrils etc.

1. Introduction

The unique properties and recent universal focus on natural material resources put also this group of cellulose derivates to the position of intensive scientific effort and consequently to the attention of industrial companies. Knowledge of macrostructure of the cellulose chains, i.e. supermolecular and hypermolecular structure of cellulose, accompanied by changes during its chemical or mechanical treatment is important not only for technical or biomedical applications, but predominantly, as a novel approach to better understand and control the aging of cellulose materials, e.g. in paper and paper products. Amorphous and crystalline parts are of course playing their key role in supermolecular structure of cellulose.[10] It is well known an influence of acid hydrolysis upon increase of crystalline parts of cellulose. Accessible amorphous and non-accessible crystalline parts of cellulose are indicated by peeling off model of kinetic of acid hydrolysis taking place during oxidative-hydrolysis process of oxycellulose preparation.[15] Whilst the usual acid hydrolysis of native cellulose takes place predominantly in accessible amorphous domains, i.e. more topochemically, the degradation of native cellulose during its oxidation is faster and more intense but this one also takes place in orientated crystalline domains of cellulose but not so intensive. Moreover, by application of external mechanical tension the acid hydrolysis is more extensive resulting in more homogeneous but more degraded cellulose material.

Cellulose fibres must be subjected to mechanical treatment before they can be made into paper. This treatment may be applied in a number of different ways, but it ordinarily includes a bruising, rubbing, or crushing action on the fibres. Certain pulps will develop some strength by simply agitating at high speeds with a stirrer, but most pulps require a more vigorous action.[1]

The term "beating" is used in the paper industry to describe the operation of mechanically treating of pulp fibres. Refining usually refers to a fibre separation and fibre cutting, whereas beating action may include these two effects, and also a fibrillating or bruising effect on the fibre. Sometimes, however, beating is referred to as refining in a general way, as it is one step in the refining of the pulp for paper.[1]

Beating is probably the most fundamentally important process in papermaking. Paper made from unbeaten stock is low in strength, fluffy, porous, and unfit for most uses, whereas paper made from beaten stock is strong, dense, and hard in texture. Well-beaten fibres can be readily formed into a uniform sheet of paper of quite high density, whereas unbeaten fibres cannot. The old maxim, "Paper is made in the beater," is still as basically true today as it was over two hundred years ago. In fact, the original Hollander beater has undergone very few improvements since its development in the eighteenth century.[1]

The aim of this study was to better understand to supermolecular structural changes of cellulose during chemical and mechanical treatments. Especially, does it change the supermolecular structure of cellulose during its beating?

2. Materials and Methods

2.1 Materials

Hydrogen peroxide bleached cotton linter pulp (Alpha cellulose content 97 – 98 %, P. TEMMING AG, Germany) made from 100% second cut cotton linters was used as the raw material for an acid process of N_2O_4-mediated cellulose oxidation. The resulting H-form of oxycellulose in fibrous form was used in all beating experiments[3]. Oxidized bleached cotton linter (OC) developing samples OKCEL HL 242/05, OKCEL HL 4/08,. (Synthesia Pardubice,Czech Republic), common characteristic of OC: carboxyl content 15-20wt. % were used.

2.2 Methods

2.3 Topography - Microtomography beamline

X-Ray computed microtomography (μCT) consists in recording a number of projections from an object, with different angle of views, and reconstructing from these projections a 3D image with the help of an adapted algorithm. The applications are based, as far as absorption imaging is concerned, on the very broad choice available in the photon energy (typically between 6 and 120 keV), which makes it possible to improve the contrast, on the improved spatial resolution (on the order of the μm), and on the quantitative data evaluation allowed by the monochromatic and parallel character of the beam. The very small source size provides, in an instrumentally simple way, phase images that reveal phenomena that are difficult to evidence by other means. This technique can be used for 2D or 3D imaging, either qualitatively for singularity edge detection (pores, inclusions), or quantitatively, through phase reconstruction complemented by tomographic reconstruction, in the approach called holotomography.[17, 20]

Beamline ID19 and microtomography

ID19 is a multi-purpose long (145 m) imaging beamline for radiography (absorption and phase contrast imaging) microtomography, and diffraction imaging (topography, analyzer-based imaging) experiments.[17] The beamline is installed on a low-beta section of the storage ring in ESRF, Grenoble, France.

Synchrotron X-ray is provided by the deviation of electrons through periodic arrays of magnets. On ID19, this deviation is ensured by one of the three insertion devices: two adulators and ine wiggler. They consist in a succession of magnets whose sizes and periodicity govern the characteristics (size and brilliancy) of the provide beam. This device forces the electrons to oscillate along their way. The created beam is the superposition of all the beams created by each magnet. Wigglers created a beam whose energy spectrum is continuous and whose intensity depends on the numbers of magnet. The magnets in adulators are smaller than the ones in wiggler. The inversion of the magnetic field is consequently more frequent. Beams created by these oscillations can interact. The resulting spectrum is not continuous any more and present maximum for some energies. The choice of the source depends on the experiment requirements.[17, 20]

This device has a small source size (30 μm vertical x 120 μm horizontal). Three insertion devices are located in the ID19 straight section (two undulators and one wiggler) the choice of one of them as source being a function of the experiment requirements. Long beamline coupled with the small source size allows us

1) exploiting the coherence properties of the beam, and

2) having either a wide and homogeneous beam when needed, or a focus spot below 100 nm when required.[17]

Energy range and monochromators

• The beamline can work in the energy range 6 to 100 keV, but most of the experiments are performed in the 10-35 keV range.

• The monochromatic beam can either originate from a double Si 111 crystals monochromator (ΔE/E 10-4) or a state of the art multilayer (ΔE/E 10^{-2}).[17]

Experimental setups

Various setups designed for the different imaging techniques are permanently installed in the experimental hutch of ID19. They are

• A microtomograph designed to perform absorption microtomography and, by varying the sample-to-detector distance, phase microtomography

• A « horizontal » diffractometer, designed for experiments requiring white beam and/or bulky sample environment (furnaces, cryostats, magnets, …)

• A « vertical » diffractometer that includes the possibility of using and analyzer crystal, for very accurate monochromatic beam imaging and diffraction.[17]

During most of the experiments carried out on paper samples, the udulator is set at an energy of 20,5 keV as this device present a maximum of brilliancy for this energy. The beam is

monochomatised by multiplayer. To meet reconstruction, beamline parameters are optimised.

The sample is place on a high precision rotation-translation stage that aligns the three main components: beam, sample and detector accurately. Sample preparation is discussed later on in the dedicated section. A scintillator converts the transmitted beam into visible light which is recorded by a camera. This 2048x2048 pixels detector has a large dynamic range, low noise and a short read-out time. It plays a crucial role in the acquisition time and data quality.

2.4 Sample preparation

Small pieces are extracted form the sheet of interest. To cut the sample, gloves were wearied to hold the paper sheet and use a pair of scissors. The gloves limit the moisture transfer from hands to paper, which could modify paper structure. The scissors were preferred to the blade razors as the induced modifications can not be seen on reconstructed data. Square of about 1,6x1,6 mm are extracted. The also prevent the structure from strain. One may recall here that microtomography techniques are said to be non-destructive.[20]

The studied sample is set on a capillary which is fixed on the rotation stage of the microtomograph during data acquisition. The used technique to hold the sample on the capillary must avoid glue penetration ad prevent the sample from moving. Several protocols were tested. The one presented hereafter gives the best results.[20]

3. Results and discussion

Beating and refining or mechanical treatment of fibres in water is an important step in using pulps for papermaking. It is an energy intensive process. The purpose of the treatment is to modify fibre properties to obtain the most desirable paper machine runnability and product properties. During beating and refining, fibres randomly and repeatedly undergo tensile, compressive, shear and bending forces. During the beating process, fibres are subjected to a mechanical action, and in the presence of water they swell. Carbohydrates and lignins in the swollen fibres can be leached from the cell wall and transferred to the surrounding solution. In the case of oxycellulose samples with different ratio of oxidation, it was found that samples with higher contents of COOH groups in starting pulp are characterized by a significantly lower specific beating energy consumption needed to achieving the same sizes of particles. Thus, the tenacity of pulp is decreased with intensity of oxidation which is characterized by content of COOH groups.

3.1 Microtomography analysis

In-plane original slices of two paper grades (on cellulosic and only oxycellulose basis) and their corresponding histograms following of microtomography measurements are presented in Figs. 1 and 2. Logically, the histogram of printing paper composed of calcium carbonate filler and bleached wood pulp has typical bimodal character and the histogram of paper composed of pure oxidised cellulose is typically unimodal but carefully evaluation of this histogram suggests more complicated supermolecular state of oxycellulose.

Gauss probability function $f_i(x) = a_i.\exp(-(\mu_i - x)^2 / 2.\sigma_i^2)$ was used for histogram data verification where μ_i and σ_i are the mean and the dispersion values of this probability function, respectively. The histogram of pure oxidised cellulose is composed of two Gauss theoretical probability functions (compare Figs. 3 - 4) with both different mean values (μ_1 = 116 and μ_2 = 127) and dispersions (σ_1 = 24 and σ_2 = 50). In reality the matter of oxidised cellulose is not homogeny involving of two parts of cellulosic supermolecular structure – the oriented crystalline part and the non-oriented amorphous part of cellulose. Obviously, a more compact crystalline part is characteristic with higher X-ray absorption, i.e. high grey value and lesser chemical reactivity. Due to typical topochemical reaction during the cellulose oxidation[15] the probability function $f_2(x)$ is so broadly distributed across the grey values. The high value of F_2/F_t (0,633) suggests a relative high amount of crystalline parts in oxycellulose concluding that the oxidation of cellulose has resulted in increase of crystalline parts of cellulose matter. Crystalline part of oxycelluloses with 15% and 19% COOH characterized by X-ray diffraction analysis are 11,73% and 28,22%, respectively.

The general shape of the histogram is independent of the X-ray energy but does not correspond to the expectations. Namely, as paper can be considered in a first approach as a two phase material (a pore phase and a solid phase), we could easily imagine that the histogram of the grey levels of such a material would be bimodal and would have two separated distributions but only in non-regularly distributed systems. However, if paper is consisted of three sorts of particles of different density the probability regularly distribution of these ones rapidly decreases. But, the amount of verified data is also important. With amount of data increase the histogram is more unimodal with smaller dispersion and vice versa. We have experienced that optimal data collection resulted in maximal distinction of these micro-objects has to be around 10^6 items. This comes from the fact that paper is mainly constituted

Figure 1: Printing Paper,OP Olšany, Polar bright, 50 g/cm^{2}OC

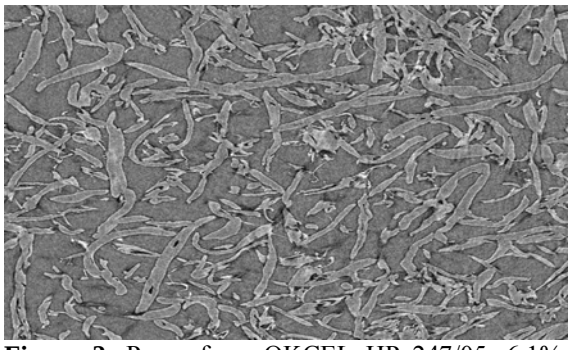

Figure 2: Paper from OKCEL HP 247/05, 6,1% COOH, 105 g/cm^2

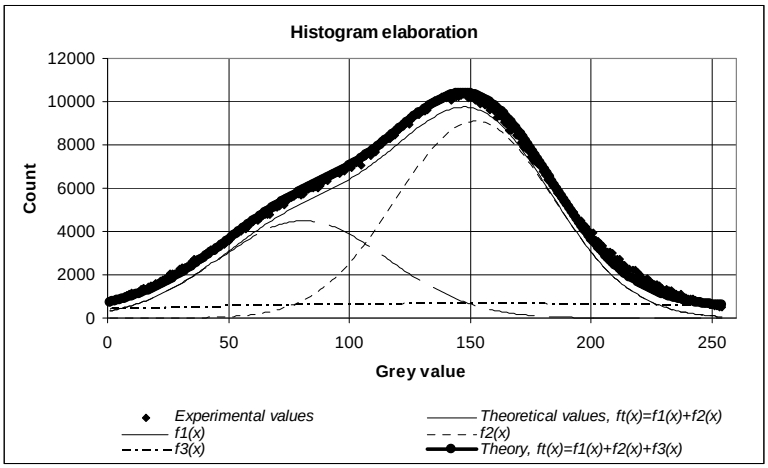

Figure 3: Printing paper, OP Olsany, 50 g/m^2, filled with chemical precipitated $CaCO_3$. $f_1(x)$: Mean = 81; Dispersion = 35; $f_2(x)$: Mean = 152; Dispersion = 32,5; $f_3(x)$: Mean = 152; Dispersion = 160. $F_1/F_t = 0{,}305$; $F_2/F_t = 0{,}579$; $F_3/F_t = 0{,}116$ if $\int_1^{255} f_i(x)dx = F_i$ and $\sum F_i = F_t$.

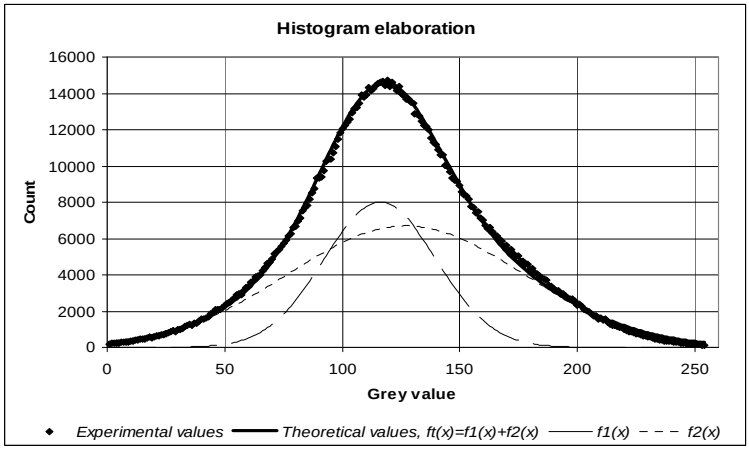

Figure 4: Paper from oxidized cellulose fibres OKCEL HP 247/05, 6,1 % COOH, 105 g/m^2 $f_1(x)$: Mean = 116; Dispersion = 24; $f_2(x)$: Mean = 127; Dispersion = 50.

$F_1/F_t = 0{,}367$; $F_2/F_t = 0{,}633$, if $\int_1^{255} f_i(x)dx = F_i$ and $\sum F_i = F_t$.

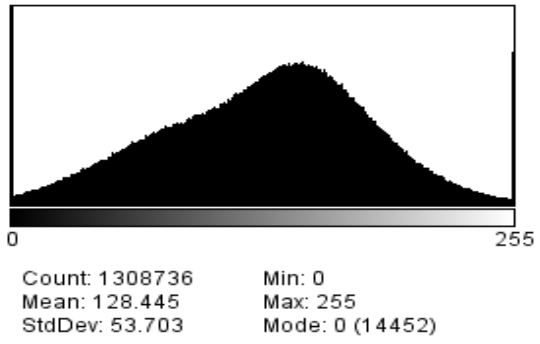

(a) Printing Paper,OP Olšany, Polar bright, 50 g/cm^2 OC

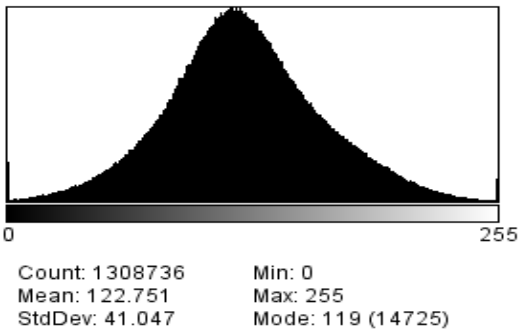

(b) Paper from OKCEL HP 247/05 , 6,1% COOH, 105 g/cm^2

Figure 5: This figure has two subfigures (a) and (b) In-plane original slices of two paper grades (on cellulosic and oxycelluloses basis) and their corresponding histograms, Synchrotron X-ray microtomography on ID19 multi-purpose beamline, ESRF, Grenoble 320x320 μm.

of light chemical elements that do not evoke distinctly changes in the coefficient of absorption in the range of energies classically used on this beam line. Therefore the characteristics of the grey level distributions are independent of the energy in the particular case of paper samples.
In order to ensure maximal objectivity of the data evaluation we have compared only data objects with the same amount of pixels.

In contradiction with filler particle (chemical precipitated $CaCO_3$) fibre cross profile measurements demonstrate a complicated profile of fibre wall because complicated well-known fibre wall morphology. It seems that due to erosive hydrolyse-oxidative process during oxycellulose preparation[15] the width of cellulosic fibre is decreased and the fibre cross profile gets more regular form.

3.2 Beating influence upon structure of cellulose

As expected, the lateral size of beated cellulosic fibres was significantly smaller then fibres only gently defibrillated in defibrillator. This observation indicates the beating of fibres in toroidal beating machine MSO as to be typical fibrillation process.

Paper prepared from these fibres, i.e. by dewatering of fibrous slurry followed by its drying, is distinguished by widely histogram of micro-matter distribution characterised by X-ray absorption. Histogram of paper prepared from gently defibrillated fibres is less homogeny – the histogram is typical bimodal – relatively to paper prepared from beated fibres. This observation suggests the paper matter is being composed of different three sorts (really two sorts) of cellulosic matter – one sort is characteristic with lesser X-ray absorbability ($\mu_1 = 97$), second one with higher X-ray absorbability ($\mu_2 = 158$) and small amount of third one is characteristic with high dispersion of numerical pixel distribution ($\sigma_3 = 160$).

For the paper prepared from the beated cellulosic fibres is characteristic practically unimodal histogram but with a broad dispersion. However, analysing this histogram by use of Gauss probability function it has been demonstrated that in reality the histogram curve is also bimodal composed of two similar probabilities functions with different mean values ($\mu_1 = 97$ and $\mu_2 = 155$). Obviously, the results confirm well known existence of two structural forms of cellulose: crystalline oriented part ($\mu_2 = 155$ - 158) and amorphous non-oriented part of cellulose ($\mu_1 = 97$). According to received results, the crystalline oriented part of cellulose is increased surprisingly by wet beating as was confirmed by X-Ray diffraction analysis. Aside from the facts that a lot of fine parts of cellulose fibres - especially so called crill - are separated from pulp slurry during paper preparation, i.e. during sheet dewatering, it is interesting to look in a closer way at the areas in the fibre that may have different level of supermolecular matter organisation.

First of all, what does a paper sheet prepared by merely drying of pulp slurry look like?

3.3 Mechanism of cellulose crystalline state increase during fibrillation pulp beating

The interesting cellulose behaviour during its beating is possible to explain by use the SCHL (Structural Changes in Hydration Layers) concept [12, 13] of hydration attractive – repulsive forces acting among hydrated nano-sites of both the oriented crystalline and the non-oriented amorphous parts of

cellulose in wet pulp state. If we assume a rush mechanical action during pulp beating in water, the plasticised cellulosic fibres are kneaded evoking so a mutually friction of microfibrils particularly in amorphous structural micro-regions of cellulose. With respect to this fact, interstitial mutually movement of hydrated cellulosic chains, microfibrils, fibrils etc. is evoked accompanied by formation of new hydration bonding abilities among them. The all process results then in decrease of inner energy connected with an increase of oriented part of cellulose.

4. Conclusions

The received results reveal that supermoleculare structure of cellulose is changed by chemical and mechanical treatment. The oxidative-hydrolysis process taking place during oxycellulose preparation has a qualitative influence upon crystalline domains of cellulose. Primary cellulose I is changed to more amphoteric polymorph cellulose II being change further by beating to polymorphs II and IV_{II} in the case of intensively oxidized cellulose (15 % and 19 % of COOH groups) and to polymorph IV_I for carefully oxidation of bleached linters (3,5 % of COOH groups). For native cellulose is typical only quantitative change of this supermoleculare structure due to intensive beating. Intensively fibrillation beating leads to increase of amount the crystalline domains in cellulose.

All these changes are evoked because a peculiar character of water molecules forming a weaker hydration bonding system of cellulose in wet state of cellulose as well as. The supermoleculare complex structure of wet cellulose, i.e. formed by weak hydration bonding system among cellulosic chains, is establishing from the hydrogen bonding system of cellulose in dry state. It is primary influenced by chemical composition of hydrophilic cellulose and secondary by mechanical action, e.g. by beating. As shown, the chemical changes are accompanied predominantly by qualitatively supermolecular structural changes. The rush mechanical action is influencing particularly the quantity of crystalline portion of cellulose by virtually mutual movement of cellulosic chains, microfibrils, fibrils etc.

Acknowledgements

All the data presented in this work were acquired at the ESRF located in Grenoble, France. The authors thank Dr. Sabine Rolland, prof. Jean-Francis Bloch from Université Joseph Fourier and assoc. prof. Ludvík Beneš form University Pardubice.

We also thank the Ministry of Education of the Czech Republic for financial support. This research was supported by Grant INGO LA 10010.

References

1. James P. Casey Pulp and paper 1952
2. Cloetens P., PhD thesis, Vrije Universiteit Brussel, Faculteit Toegepaste Wetenschappen, March 1999
3. Cloetens P., Ludwig W., Baruchel J., Van Dyck D., Van Landuyt J., Guigay J.P., Schlenker M., Appl. Phys.Lett. 75, 2912-2914 (1999)
4. Cloetens P., Pateyron-Salomé M., Buffière J.Y., Peix G., Baruchel J., Peyrin F, Schlenker M., J. Appl. Phys. 81, 5878-5886 (1997)
5. Espeso J.I., Cloetens P., Baruchel J., Härtwig J., Mairs T., Biasci J.C., Marot G., Salomé-Pateyron M., Schlenker M., Journal of Synchrotron Radiation, **5**, 1243-1249 (1998)
6. P. Havelka, T. Sopuch, V. Hnatowicz, P. Suchý, R. Masteiková, M. Bajerová, J. Gajdziok, M. Milichovský and V. Švorčík, Cellulose: Structure and Properties, Derivatives and Industrial Uses Chapter 6 chemistry, technology and applications of oxidized celluloses
7. Jaganathana, S., H. Vahedi Tafreshib, E. Shima, B. Pourdeyhimia , A study on compression-induced morphological changes of nonwoven fibrous materials, Colloids and Surfaces A: Physicochem. Eng. Aspects 337 (2009) 173–179
8. Jaganathana, S., H. Vahedi Tafreshib,, B. Pourdeyhimia , Arealistic approach for modeling permeability of fibrous media: 3-D imaging coupled with CFD simulation, Chemical Engineering Science 63 (2008) 244 – 252
9. Jaganathana, S., H. Vahedi Tafreshi b, B. Pourdeyhimi a, Modeling liquid porosimetry in modeled and imaged 3-D fibrous microstructuresS., Journal of Colloid and Interface Science 326 (2008) 166–17
10. Le Moigne N., Navard P. (2010) Dissolution mechanisms of wood fibres in NaOH-water. Cellulose 17:31-45
11. Mancini Lucia, PhD thesis, Université Joseph Fourier - Grenoble, June 1998
12. M. Milichovský, "A new concept of chemistry refining processes," TAPPI J., vol. 73, no. 10, October 1990, pp. 221-232.
13. M. Milichovsky, "Water- A Key Substance to Comprehension of Stimuli-Responsive Hydrated Reticular Systems", Journal of Biomaterials and Nanobiotechnology, Vol. 1, 2010, pp. 17-30.
14. Milichovsky M., Milichovska Sv. (2008) Characterization of oxidized cellulose with ultraviolet- visible spectroscopy . Journal

of Applied Polymer Science 107, 3, 2045-2052
15. Milichovsky M., Sopuch T., Richter J. (2007) Depolymerization during nitroxide-mediated oxidation of native cellulose. J. Appl. Polym. Sci. 106:3641-3647
16. Mocella Vito, PhD thesis, Université Joseph Fourier - Grenoble, June 1999
17. Official web ESRF: http://www.esrf.eu/
18. Rajinder S. Seth, Beating and refining response of some reinforcement pulps , VOL. 82: NO. 3 TAPPI JOURNAL 147 - 155 TAPPI JOURNAL MARCH 1999
19. Jean-Christophe Remigy, Martine Meireles, Assessment of pore geometry and 3-D architecture of filtration membranes by synchrotron radiation computed microtomography, Desalination 199 (2006) 501–503
20. Rolland du Roscoat S. Cnotribution á la quantification 3D de réseaux fibreux par microtomographie au rayonnement synchrotron: Applicasions, THESE 2007
21. S.Rolland du Rocsoat, J-F Bloch and X Thibault, Synchrotron radiation microtomog
22. S.Rolland du Roscoat(a), M. Peralba (b) , M.L. Jeuch (b) , P. Dumont (b) , J-F.Bloch (b) poster , In-situ analysis of microstructural evolution of papers under humidity by synchrotron X-Ray microtomography
23. W. Sauer, M. Streibl, T. H Metzger, A. G. C. Haubrich, S. Manus, A. Wixforth, J. Peisl, A. Mazuelas, J. Härtwig, and J. Baruchel, Appl. Phys. Lett. **75**, 1709 (1999)
24. Thygesen A., Oddershede J., Lilholt H.: On the determination of crystallinity and cellulose content in plant fibres; Celluse 12, (2005) 563-576
25. J.-P. Vassal, L. Orgéas,* D. Favier, and J.-L. Auriault, Upscaling the diffusion equations in particulate media made of highly conductive particles. II. Application to fibrous materials, PHYSICAL REVIEW E 77, 011303 _2008
26. Xiaoping Zhao,* Lars/3dberg, and Gunnel Risinger, Beating of wheat-straw pulp:dissolved carbohydrates and lignins,fiber swelling, and f'mes generation January 1992 TappiJI 153-161
27. Zugenmaier P.: Crystalline cellulose and derivatives. Characterization and Structure, Chapter 5. Cellulose, Springer Series in Wood Science, Ed.: Timell T. E., Sommer R., Springer-Verlag Berlin Heidelberg 2008

Effect of Recycling on Fibre Morphology

Imtiaz ALI, Raphaël PASSAS and Jean-Françis BLOCH

LGP2-Grenoble INP
461 rue de la Papeterie BP 65 - 38400 Saint Martin d'Hères, France
imtiaz.ali@lgp2.grenoble-inp.fr

1 BACKGROUND

Recycled pulp is considered as an important secondary raw material for the production of paper and paper-board. Replacement of virgin with recycled pulp is increasing day by day. The increased use of recycled pulp is partly caused by the increased price of the virgin pulp and partly by the enforcement of rigorous regulations from the environmental protection agencies in order to establish low-carbon and waste-free society.

Recycling rate is an indicator used to express the recycling of recovered paper and paper-board. In 2006, European recycling rate was 63.4% which reached ever highest 72.2% in 2009. In 2010, it was slightly lowered to 68.9% [1]. Similarly, recovery rate of U.S. consumed paper reached ever highest 63.5% in 2010 [2]. The term recycling rate in the European Declaration [3] is comparable to the term recovery rate used in U.S.

In past few decades, substantial amount of research in the field of paper recycling had been carried out. The main focus was to improve its properties by mechanical and/or chemical treatments so that the end product should conform to the acceptable quality standards. Indeed, recycling tends to modifies fibre morphology. In order to introduce recovered fibres in high value paper it is required to better understand morphological changes and the phenomenon of fibre hornification associated with recycling.

2 SUMMARY

In this study, bleached softwood pulp was 10 times recycled. Fibres were extracted from repeatedly recycled pulp. Morphological analysis of extracted fibres revealed no major changes in average fibre lengths and their average frequency distributions as expected. Average fibre width decreased during recycling which was mainly caused by the drop in widths of early-wood fibres. The fibre width shrinkage was more pronounced after first recycle of never dried pulp fibres where an overall drop of 7% in average fibre width was recorded. Fibre width shrinkage decayed exponentially. Repeated recycling reduced curl and kink in fibres thus making them straighter.

Image analysis of in-situ drying of recycled fibres under ESEM confirmed the width shrinkage. However, no quantitative conclusion can be drawn on the evolution of fibre width shrinkage while drying with recycling due to a higher standard deviation.

Drainability measured in terms of SR, drainage rate and water retention value (WRV) are important parameters from papermakers point of view. Drainability and drainage rate of the fibrous suspension remained unaffected by repeated recycles depicting no change in permeability of the fibrous suspension and mat.

Fibre hornification, a drop in WRV, after pressing and drying of never dried softwood pulp fibres was 67% of the total hornification cumulated at the end of 10th cycle. The contribution of later cycles of recycling towards fibre hornification followed a first order exponential decay. (cf. Figure 1)

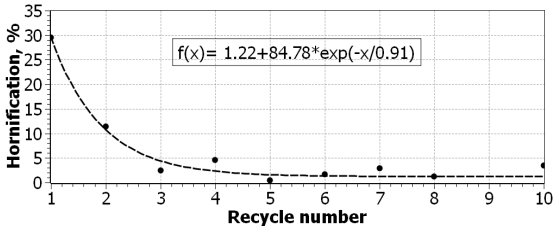

Figure 1. Evolution of fibre hornification with recycle number

REFERENCES

[1] European Recovered Paper Council, (ERPC). Five Years of Raising the Bar in Paper Recycling. http://www.paperrecovery.org/uploads/Modules/Newsmanager/erpc-monitoring-report-2010-final.pdf (Accessed: 7 July 2011)

[2] Paper Industry Association Council. Paper & Paperboard Recovery. http://www.paperrecycles.org/stat_pages/recovery_rate.html (Accessed: 7 July 2011)

[3] European Recovered Paper Council, (ERPC). European Declaration on Paper Recycling, 2006-2010. http://www.recoveredpaper-id.eu/uploads/MonitReport09.pdf (Accessed: 7 July 2011)

Effects of Enzymatic Deinking of Mixed Office Wastes on the Deinked Pulp Mechanical Properties

M. H. ARYAIE MONFARED AND
H. RESALATI

Gorgan University of Agricultural Sciences and Natural Resources (GUASNR), Gorgan, Iran.

Aryaie@gau.ac.ir

Keywords: Enzymatic deinking, Chemical deinking, Cellulase, Physical Properties, Strength Properties.

Abstract

Mixed office waste (MOW) deinking by conventional chemical process, other than having higher chemical consumption and considerable emission of environmental pollutions, has relatively lower deinking efficiency. On the other hand, enzymatic deinking increases deinking efficiency even at reduced environmental pollutions, but it may reduce the strength properties of deinked pulp. At present paper, the physical and strength properties of MOW enzymatic deinked pulps using commercial cellulase from Aspergillus niger, were compared with the chemical deinked and the reference samples. The results showed that, the enzymatic deinked pulps had lower caliper and bulk without having any significant differences with chemically deinked pulps, in terms of the strength properties. As a result, because of having better deinking efficiency and acceptable physical and strength properties, enzymatic deinking was recommended for deinking MOW instead of conventional chemical deinking process.

1 Introduction

Deinking is a term describing a process for detaching and removing printing inks from recycled fibers to improve optical characteristics of pulp and paper using recovered printed material. It is the most important process stage in processing of recovered paper as a raw material for the production of deinked pulp primarily used for manufacturing different papers [4].

Mixed office waste (MOW) is the most difficult raw material to deink. A large portion of these fibers are printed using photocopiers and laser printers that fuse ink to the fibers, making ink removal difficult by conventional methods. MOW is a large, virtually untapped source of high quality fiber that could be used for fine papers and many other products if the deinking process could be improved [7].

Most copiers and laser printers rely on the xerographic process of forming a latent charged image on a photoreceptor using visible or infrared light (via a laser diode). Dry toner is then developed on the latent image, which is subsequently transferred to paper and fused at high temperatures (>160°C) to fix the image. These toners are colored powders containing particles of approximately 7 to 11µm in size, and comprising about 80 to 95 per cent by weight of a thermoplastic resin, about 5 to 20 per cent by weight of pigment (*ie* carbon black), and less than about 2 per cent by weight of additives to control the powder flow and electrical properties of the toner. Unlike other inks, such as offset and flexographic inks, which have no dominant thermoplastic binders, xerographic images do not disintegrate well when the wastepaper is re-pulped in the first step of recycling [1].

Clearly, ink removal remains a major technical obstacle to greater use of noncontact printed recycled papers. Many of the conventional deinking processes require large quantities of chemicals, resulting in high wastewater treatment costs to meet environmental regulations [7]. Enzymatic treatment is a recent process which gives better performance to reach desired deinked performance to reach desired deinked pulp properties [8].

2 Material and Methods

The office papers was printed in 50 % of its surface with Sharp copier machine and used as raw material for deinking experiments. The commercial cellulase enzyme from *Aspergillus niger* with 1.02 U/mg activity was purchased from Fluka (japan). Poly sorbet 80 an Oleiec acid soap was used as Surfactant. Other chemicals used were: NaOH, Hydrogen peroxide, calcium chloride, sodium silicate and EDTA as chelating agent all purchased from Merck.

2. 1 Pulping

After one hour soaking of samples at 50 º C in warm water bath, the pulping was performed in the standard disintegrator at 2400 rpm using 0.2 percent surfactant for 10 min at 8 percent consistency.

2. 2 Enzymatic treatment

Enzymatic treatment was performed with 25, 50 and 100 U per mg bone dry pulp for 2 different treatment times of 10 and 15 minutes. During treatment the mechanical action was done for better fraction between fibers. The medium pH in this trial was around 8 (natural pH of waste papers pulp).

2. 3 Chemical treatment

Pulp chemical treatments were done with 1 % NaOH, 1 % H_2O_2 , 0.2 % sodium silicate and 0.3 % chelating agents (EDTA). The control trial was performed without any chemical treatment.

2. 4 Flotation

The flotation process was performed at 0.8 % consistency using 0.33 % calcium chloride in a 20 liter local made flotation cell. The selected enzymatic deinked pulps, in terms of optical properties, was choosen for mechanical tests (table 1).

Table 1. The selected enzymztic treatments

Treatment codes	conditions
E_0T_2	Control without any chemical and enzyme
C_1T_2	Chemical treatment for 15 min
E_2T_2	50 U enzyme for 15 min
E_2T_1	50 U enzyme for 10 min

2. 5 Mechanical tests

Physical and mechanical tests were measured according to TAPPI test methods: Thickness (T411om-89), Tensile (T404om-92), Burst (T403om-97) and Tear (T414om-88).

3 Results and discussion

It is interesting to note that enzymatic treatment of E_2T_1 has thicker sheets than the chemical and control ones, but the differences between this treatments and E_2T_2 were not statistically significant (figure 1).

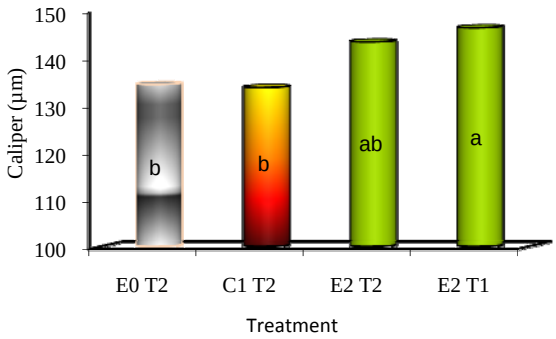

Figure 1. Effect of different deinking treatments on the sheet caliper

As can be seen in figure 2, the bulk of sheet was increased in the enzymatic treatment in comparison with control and chemical samples. Enzymatic treatment can remove the microfibrils from the fiber surface which reduces the bonds between fibers and as a result, caliper and bulk will be increased. According to the literatures [2, 3] using small amounts of cellulase can increase sheet density without causing any negative effects on strength properties that aren't compatible with our results.

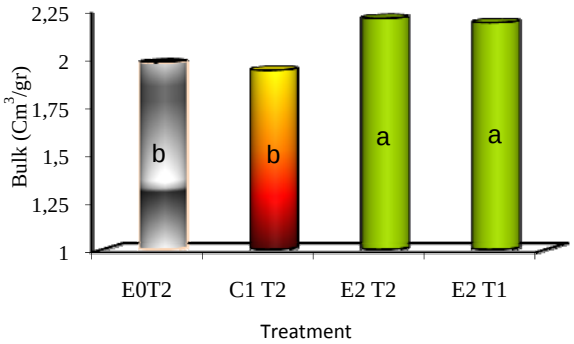

Figure 2. Effect of different deinking treatments on the sheet bulk

Enzymatic and chemical treatments significantly reduce tensile index of samples compared with control samples (Fig 3). The reduction is more severe in enzymatic treatment of E_2T_2 that had the lowest tensile index. The removal of microfibrils from surface of fibers can be a cause of fiber bond reduction and deterioration of cellulosic chains and reduction of DP that finally reduces the tensile strength [9, 10].

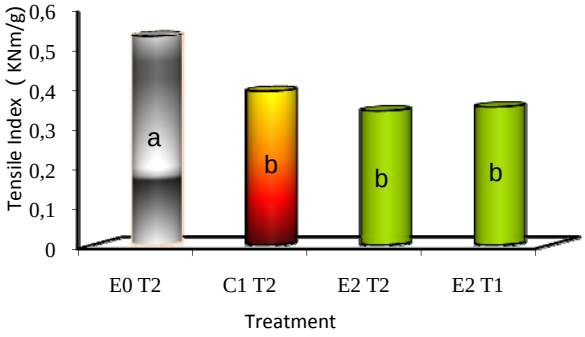

Figure 3. Effect of different deinking treatments on tensile strength

Enzymatic treatment, as compared with chemical ones, caused burst index to reduce, but the reduction was not statistically significant (figure 4). Similar to tensile, removal of surface microfibriles and reduction of DP may be the reasons for burst reduction in enzymatic treatments [10].

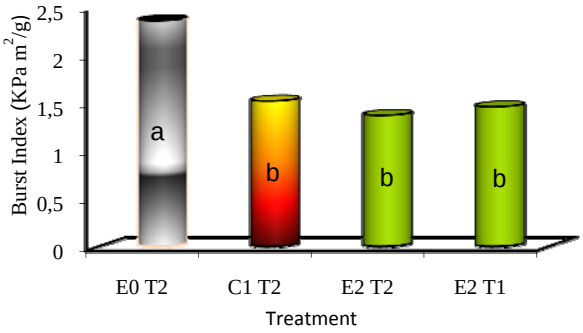

Figure 4. Effect of different deinking treatments on burst strength

As is shown in figure 5, the enzymatic treatment can reduce the tear index as compared with chemical ones, but the differences were not statistically significant. The control sample had higher tear strength than other treatments. The effect of cellulase on DP reduction can reduces single fiber strength which caused reduction of tear strength [5, 7].

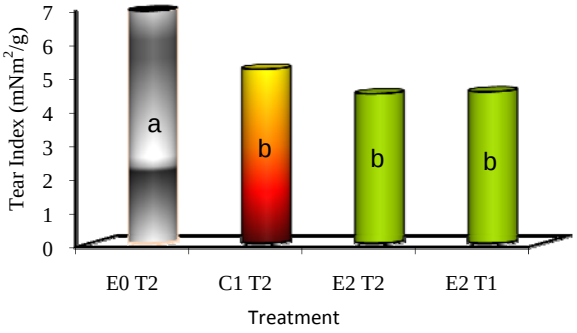

Figure 5. Effect of different deinking treatments on tear strength

4 Conclusion

Enzyme deinked pulps had higher brightness, opacity and bulk than chemical samples which may leads to better printability. Although enzymatic deinked pulps, because of partial degradation of cellulosic chains, had lower strength properties than chemically deinked pulp but the differences were not statistically significant and these results are in agreement with the works of [6]. With respect to numerous environmental benefits such as reduction of waste water toxicity, energy consumption and also better printability [7], enzymatic deinking of mixed office wastes could be recommend as an alternative for conventional chemical deinking.

References

[1] G. Sacripante and S. Kittelberger. describe how new inks will make feasible the recycling of high quality office paper, Worth of the paper (2001).

[2] H. Pala. M. Mota. and F. M.Gama. Enzymatic versus chemical deinking of non-impact ink printed paper. Journal of biotechnology 108: 79-89 (2004).

[3] H. Pala. M. Mota. and F. M. Gama. Factors influencing MOW deinking: laboratory scale studies. Enzyme and Microbial Technology 38: 81-87 (2006).

[4] J. Behi. And Sh. Vahed. Effect of alkyl chain in alcohol deinking of recycled fibers by flotation process. Colloids and Surfaces A: Physicochem. Eng. Aspects, 1-11 (2006).

[5] M. A. Hubbe, R. A. Venditti and O. J. Rojas. What Happens to Cellulosic Fibers During Papermaking and Recycling? A Review. BioResources. 2(4): 739-788 (2007).

[6] M, Qin. P, Gao. Q, Yinbo. Y, Fu. Z, Shao and W, Quan. Physical characteristics of enzymically modified fiber from old newsprint. Proc Int Symp Emerging Technol Pulping Papermaking Fast-Grow Wood, 462-73, (1998).

[7] P. Bajpai, and P. K. Bajpai. Deinking with enzymes: a review. TAPPI J. 81(12): 111-117 (1998).

[8] P. Puneet, B. Nishi K and S. Ajay K . Enzymatic deinking of office waste paper: an overview. IPPTA. J. vol 22(2): 83-88 (2010).

[9] Rutleg-Cropsey, K., Abubakr, S. M., and Klungness, J. H. Drying effects secondary fiber on papermachine runability, TAAPI Papermakers Conference Proceedins, Chicago. 311-317, (1995).

[10] T. Welt. Enztmatic deinking effectiveness and mechanisms.Doctoral dissertation. The Institute of Paper Science and Technology, Atlanta, Georgia (1996).

Posters

Fiber Suspensions and Paper Making

Furnish composition of newsprint - Effects on pressability, paper and print quality

Ø. ERIKSEN[*)], K. AASARØD[*)], G. CHINGA-CARRASCO[*)] and Ø. W. GREGERSEN[**)]

[*)] Paper and Fibre Research Institute (PFI)
[**)] Norwegian University of Science and Technology (NTNU)
Høgskoleringen 6B, 7041-NO Trondheim, Norway
oyvind.eriksen@pfi.no

1 INTRODUCTION

A major challenge for the pulp and paper industry is to develop more energy effective processes. With respect to environmental considerations the industry must address its impact on climate changes and focus their efforts on lowering the energy consumption globally. In addition, the principle of sustainable development is driving the paper industry towards more efficient use of energy and raw materials. These developments are reinforced in many countries by legislation and end-user demands.

The energy consumption is and will be even more crucial for the profitability of a paper mill as the electricity prices are increasing. A consequence is that the paper mills may focus on pulp dryability as an important quality parameter of each component in a given paper furnish.

The drying section is by far the highest consumer of steam in a paper mill. The steam consumption depends on e.g. the type of paper grade, internal sizing, the amount of flow through steam, surface condense and sheet basis weight. The amount of steam needed also depends on the ingoing dry content of the paper, and naturally a higher dry content after pressing gives a reduction in steam consumption.

The purpose of the present study is to investigate the effect of newsprint furnish composition on pressability, paper and print quality, aiming for a reduction in the steam energy consumption in the drying section.

2 EXPERIMENTAL

2.1 Furnish components

TMP, DIP and $CaCO_3$ slurry were collected from a Norwegian newsprint mill. The TMP was made from Norway Spruce and was collected from the last pulp tower in the pulp mill (100 CSF).The DIP was made from newsprint and magazine paper. The $CaCO_3$ was prepared on site and had a dry content of 40 %.

2.2 Handsheets

8 series of handsheets were made with recycling of the filtrate according to the furnish compositions shown in Table 1. The basis weight of the sheets was 45 g/m^2.

Table 1: Overview of the different handsheet series.

Code	TMP [%]	DIP [%]	$CaCO_3$ [%]
Reference	100	-	-
DIP-10/$CaCO_3$-4	86	10	4
DIP-10/$CaCO_3$-8	82	10	8
DIP-20/$CaCO_3$-4	76	20	4
DIP-20/$CaCO_3$-8	72	20	8
DIP-30/$CaCO_3$-4	66	30	4
DIP-30/$CaCO_3$-8	62	30	8
DIP-20/$CaCO_3$-6	74	20	6

After forming, the sheets were conditioned to 20 °C and 90 % RH and calendered 4 times in a soft/hard nip with temperature 60°C, line load 120 kN/m and 5 m/min speed.

2.3 Dewatering properties

The dewatering ability of the different furnish compositions was measured using a Voith FiberXPress apparatus. The temperature during the measurements was 20 °C, the pressure 6 bar and the pressing time 400 seconds.

In addition, the water retention value (WRV) was measured at room temperature according to ISO 23714.

2.4 Paper physical properties

The physical properties of the handsheets were measured according to the parameters shown in Table 2.

Table 2: Overview of physical properties

Property	Standard
Basis weight	ISO 536
Thickness	ISO 534
Density	ISO 1988
Surface roughness, PPS	ISO 8791/4
Brightness	ISO 2470
Opacity	ISO 2471
Light scattering and light absorption	ISO 9416
Tensile strength	ISO 1924-2

2.5 Printing

The 8 series were printed with a Prüfbau laboratory printing press and using a granite black cold-set ink.

For print-through assessment, samples were printed to a print density of 1.1 using 800 N nip load.

Set-off was measured using a print density of 1.1. The applied nip loads were 1000N and 400N for the printing unit and ink-receiving unit, respectively.

3 RESULTS AND DISCUSSION

3.1 Dewatering properties

The FiberXPress and WRV measurements are shown in Figure 1.

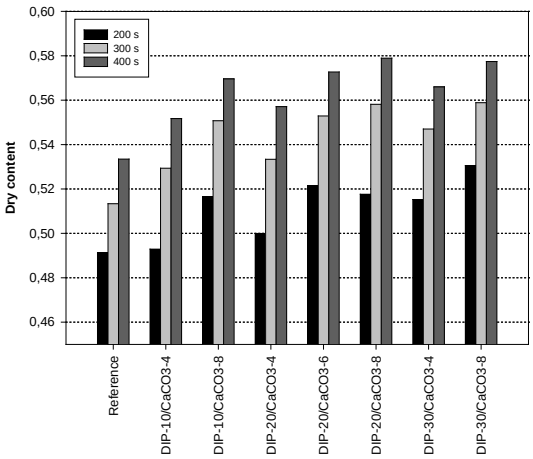

(a) Dry content of the different series as measured with FiberXPress.

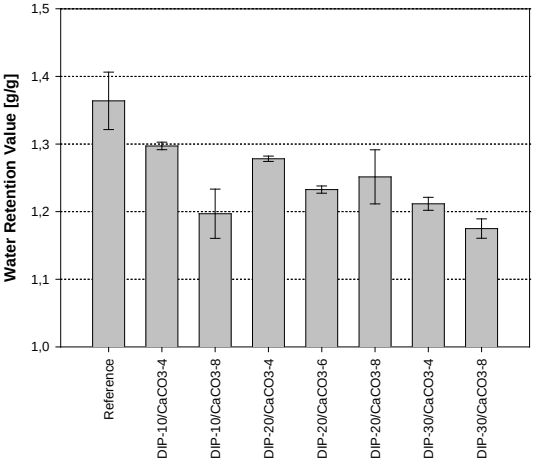

(b) WRV measurements for the different series.

Figure 1. FiberXPress (a) and WRV (b) measurements.

As seen in Figure 1a, after 300 s and up both additions of $CaCO_3$ and DIP have a significant effect on the measured dry content, and more $CaCO_3$ and DIP gives as expected a higher dry content as measured with the FiberXPress.

Figure 1b shows that addition of DIP and $CaCO_3$ to the furnish give a reduction in WRV. As the water retention value is highly negative correlated to ash in the pulp mixture, the effect of the $CaCO_3$ is larger than the effect of the lower ash containing DIP. For the data presented here, ash has a significant effect on the WRV at the 99 % confidence level, and the effect of the $CaCO_3$ addition is 5 times larger than the effect of DIP addition.

3.2 Paper physical properties

Figure 2 shows the density measurements and PPS readings for the different series.

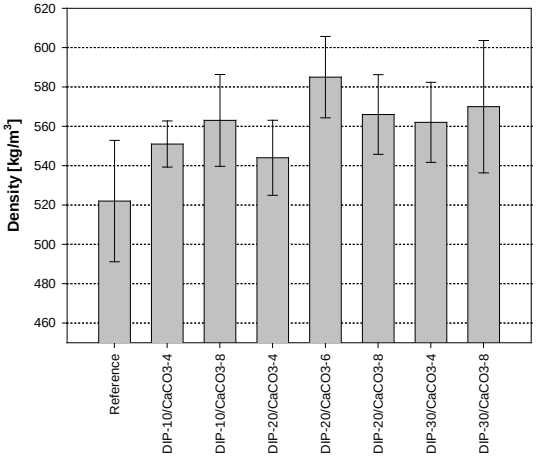

(a) Density measurements for the different series.

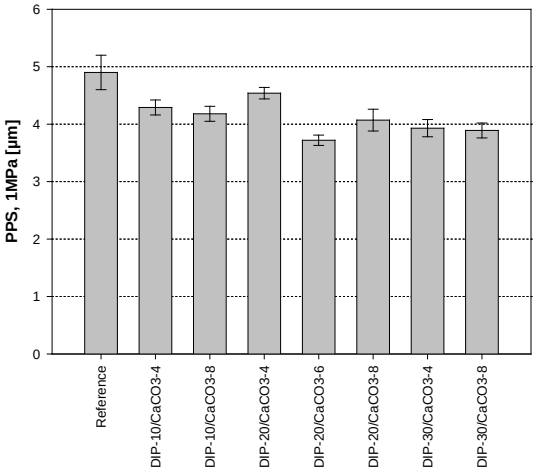

(b) PPS readings for the different series.

Figure 2. Density and PPS readings.

Both addition of $CaCO_3$ and DIP to the TMP furnish gives an increased density of the produced laboratory sheets. As for the ash measurements and the WRV, the effect of the $CaCO_3$ addition is greater than for the DIP addition. Multiple linear regression shows that the addition of $CaCO_3$ has a significant effect on the density at the 99 %

confidence level, while the DIP does not have a significant effect on the density for the data presented here.

Neither additions of DIP nor $CaCO_3$ have a direct significant effect on the PPS readings. For the samples presented here, PPS will be more affected by the calendering (and thus the density) than the actual furnish composition.

Figure 3 shows the light scattering coefficients for the different series. Addition of $CaCO_3$ gives an increase in the light scattering coefficient.

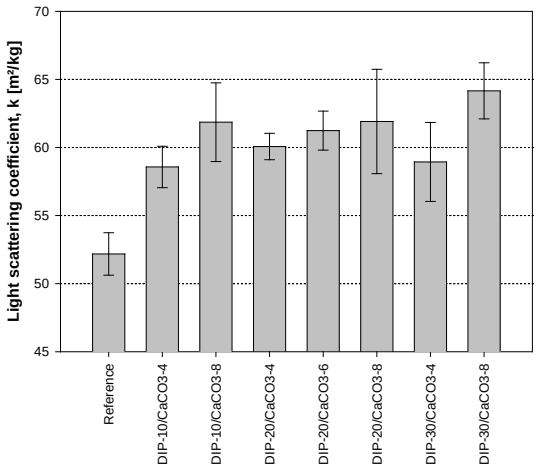

Figure 3. Light scattering coefficient for the different series.

3.3 Print quality

Figure 4 shows the print-through and set-off measurements for the different furnish comporsitions.

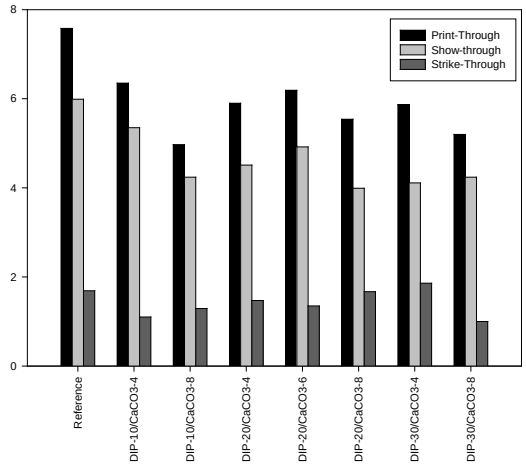

(a) Print-through, show-through and strike-through measurements of the different series.

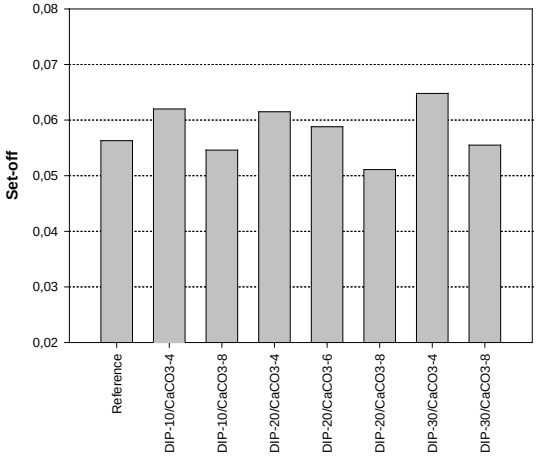

(b) Set-off measurements for the different series.

Figure 4. Print-through and set-off measurements.

For print-through, the results indicate that increasing the amount of $CaCO_3$ reduces the print-through with 1-2 units (between 15-30% reduction) compared to the reference sheet. The reduction is most probably due to the increase in light scattering of the corresponding sheets (Figure 3). Such effect is also confirmed by the development of the show-through levels as the $CaCO_3$ addition was increased.

The results indicate minor effects of the furnish composition on the set-off levels. In addition to the surface roughness, the surface compressibility may also affect the set-off levels.

4 CONCLUSION

The dewatering measurements showed that small variations in ash contents could cause differences in final dry content. Increasing ash content in the furnish increased the dry content.

Increased filler content in the furnish gave an increased density and light scattering coefficient and a decreased roughness of the produced handsheets. Also, increased ash content reduced the print-through values of the handsheets.

Results from this study give information of what to expect when changing the furnish composition regarding pressability, paper and print quality.

ACKNOWLEDGEMENT

The activities were performed as part of the PFI project “Energy efficient paper production of wood containing paper for next generation printing presses”. The authors thank our industry partners and The Research Council of Norway for funding.

A new method for characterizing turbulent mixing in semi-concentrated suspensions

PAUL KROCHAK and LARS THOMSSON

Innventia AB
Drottning Kristinas väg 61
114 86, Stockholm Sweden
paul.krochak@innventia

Keywords: Mixing, fibre suspension, turbulence

ABSTRACT

A new method for characterizing turbulent mixing and dispersion during the flow of semi-concentrated suspensions at arbitrary flow rate is presented here. A high frequency conductivity probe is used in conjunction with advanced signal processing to measure the turbulent fluctuations of a passive scalar, namely a saline solution, injected into semi-concentrated, monodispersed suspensions consisting of either 2 mm rayon fibres or 130 µm micro-spheres. The probe is mounted in a pipe flow such that its radial position can be adjusted manually. A saline solution is injected into the centreline of the pipe at a specified velocity relative to the suspension flow. The mean conductivity signal gathered with this tool enables estimation of the local concentration of salt at a given point in the flow, i.e. the mean spatial dispersion of the dosed component. Further analysis of the high frequency fluctuating signal enables characterization of the local mixing energy and turbulent spectrum, i.e. the spectral mixing scales available in the suspensions under a given set of conditions. The conductivity probe and results presented here should provide producers of paper and board products new insights into minimizing unwanted variability in the final paper properties which may result from poor mixing of stock components, from the uneven addition of chemical additives, or due to dilution of the thick stock prior to the headbox.

1 INTRODUCTION

Mixing of different pulp streams and mixing of chemicals into the furnish are basic unit operations in papermaking. The quality of mixing in the approach flow affects the uniformity of the stock composition, and subsequently the uniformity of the paper web. Mixing quality can also affect the performance of chemical additives such as retention aids. For example, large scale consistency variations in the furnish prior to the headbox can appear as unstable MD-CD grammage streaks in the final product. Small scale variability in the distribution of retention aids contributes to formation, dewatering and runnability issues [1]. On the other hand, a well mixed stock forms the basis for a uniform paper web, improved retention of fine particles in the forming section, and allows for the possibility to form the same product with fewer fibres, i.e. savings in production cost.

Mixing of multiple streams into a papermaking stock depends on the dynamics of the local flow, in particular the ratio between the inner (dosed) and outer (stock) velocities [2], the rheological properties of the inner and outer flows [3], and characteristics of the fibre suspension, i.e. fibre length, stiffness, coarseness and concentration [4]. The process is complicated by the tendency for fibres to form flocs. High shear and turbulence levels are generally needed to disrupt these fibre flocs, while turbulence is required to enhance dispersion at various scales. However, the presence of even the smallest amount of particles in a flow can strongly alter the turbulence, rheology and transport properties that are responsible for good mixing. Further, the size, shape and morphology of the solids particles can have significantly different effects on the turbulence [5].

Despite this very basic understanding of stock mixing, qualitative relationships between mixing conditions and mixing quality are still poorly understood. One major difficulty is that characterizing mixing at a spectral level in these suspensions is difficult. This is due to the inherently high solids concentration, the broad particle size distributions, and in particular, the opacity of the papermaking suspensions. Thus, traditional measurement techniques, i.e. laser and/or optical methods, rarely work within these suspensions.

Conductivity based measurements provide one class of measurement technique that can be used in almost any type of suspension under arbitrary flow conditions. The measurement principle with conductivity sensing probes is based upon detecting local variations of electrical conductivity (or resistivity) in a flow. Low resolution conductivity probes have previously been used to study the mean dispersion characteristics of a saline solution, injected concentrically into turbulent pulp suspensions by [6]. In this work, large effects of the pulp fibres on the mean, spatial dispersion of the saline solution were reported. Specifically, the local concentration of saline was found to decrease rapidly upon injection into the pulp suspensions compared with that into pure water. However, the spectral detail of the turbulent dispersion was not obtained with this method. Therefore the effect of pulp fibres on the spectral character of the turbulence was not determined.

In considering the turbulence of a conductive stream, it has been shown that the spectrum of a fluctuating passive scalar, e.g. conductivity in a turbulent flow, has the same wave-number dependence as the velocity spectrum itself [7]. Therefore the possibility should exist to exploit the high frequency fluctuations in local conductivity as a means to estimate the turbulence spectrum in an arbitrary flow. With this in mind, we have implemented a single-tip conductivity probe in conjunction with advanced signal processing to fully characterize mixing quality in semi-concentrated suspensions, including both the mean and spectral characteristics of the mixing. We do so for mono-dispersed suspensions consisting 130 µm micro-spheres, and for rayon, 2 mm length, 60 µm diameter (aspect ratio, r = 33) for flow at water based Reynolds numbers of 57 000 and 11400. Details of the experimental system are described in Section 2, followed by and evaluation of the system in Section 3. Also included in this section is a comparison of the turbulent spectra of the different suspensions considered.

2 Experimental Detail

The experiments were performed in the re-circulatory pipe flow facility of Innventia AB. A schematic diagram of this facility is shown in Figure 1. The main part of this facility consists of two long sections of cylindrical Perspex pipe, with length 3.0 m and inner diameter 57 mm. The flow loop is constructed in a modular manner such that different piping and experimental set-ups can easily be studied. The fluid is re-circulated from an open reservoir, approximately 1 m^3 in volume, which is mixed continuously with a 40 cm diameter impeller. The bulk suspension flow is driven by an ITT 4.2 kW variable frequency drive centrifugal pump (Flygt pumpp 3102- 152 mm impeller). Flow is measured through the device with an ABB magnetic flow meter (Fisher & Porter, model no. 10DS3111). Pressure sensors are mounted on either end of the pipe (Fuji FKCX22, 6 kPa and FKCX35, 130 kPa), specifically positioned at 0.25 m and 2.5 m. Velocity profiles can be obtained with a MetFlo DUO ultrasonic Doppler velocimetry profiler (UVP) with probes mounted 1.0 m downstream from the upper elbow, at an incident angle of 30 degrees. Average conductivity is measured in the reservoir and at the end of the test section using a Hach, HQ40D mutli-parameter measurement probe. Temperature was also monitored with this tool. A long brass pipe, 6 mm inner diameter, 8 mm outer diameter is used for injection of a high conductivity saline solution. It is inserted through the centre of the 90 degree elbow, and its axial-position adjusted manually. Flow of the salt dosage is controlled manually with pressurized air and monitored with an ABB magnetic flow meter, (Fisher & Porter, model no. 10DS2112A). The high resolution conductivity probe is mounted 50 cm downstream from the upper elbow. It should be pointed out that this distance represents only 10 pipe diameters downstream from the 90 degree elbow. Therefore, one must bear in mind that there exists a high risk of swirl, and other asymmetries in the flow. The radial position of the probe can be adjusted manually. A brass reference electrode is flush mounted along the inside of the pipe, approximately 20 cm upstream of the conductivity probe. All data is logged continuously while the facility is in operation using LABVIEW.

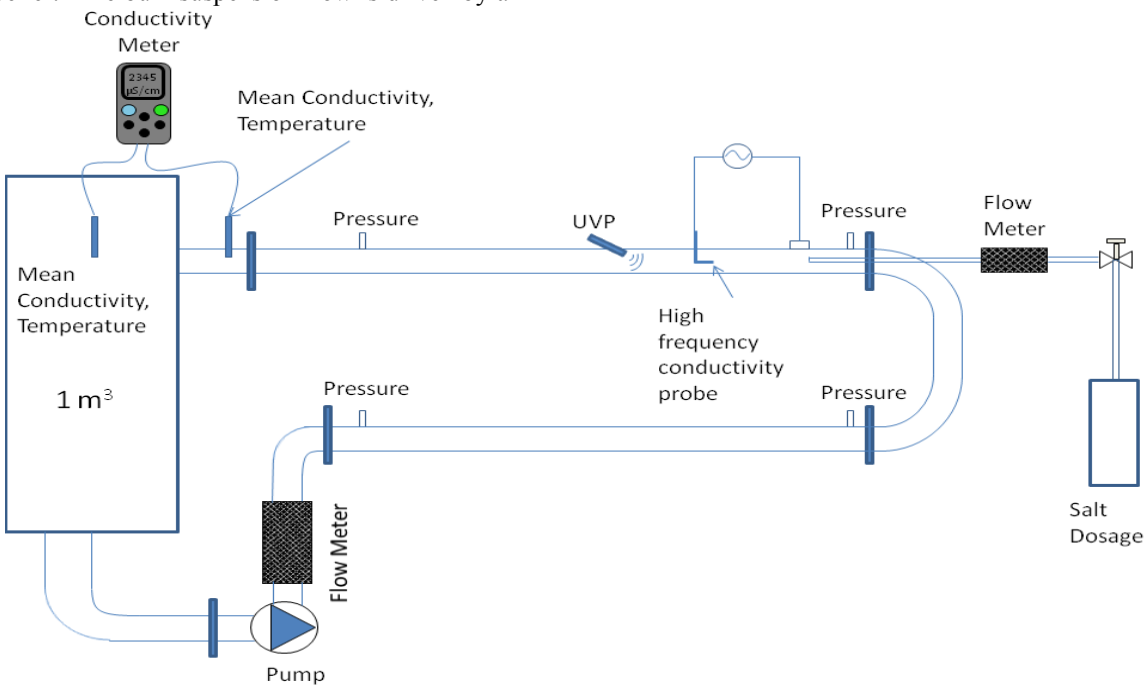

Figure 1. Overview of the Innventia flow loop facility.

2.1 Conductivity probe

Local conductivity measurements are made with a single tip conductivity probe and a copper counter electrode mounted upstream and made flush with the pipe wall. The measurement electrode, which is made by a 25 µm diameter platinum wire, is embedded in a fine ceramic capillary and glued with a UV-curing capsule resin. The platinum wire is cut in level with the resin just leaving a 25 µm diameter point visible at the probe tip. The ceramic capillary is in turn glued into a stainless steel tube and fitted into a brass holder that provides strength and a manageable interface with the external equipment. An electrically insulated wire soldered to the platinum wire runs through the probe holder and connects it to the measurement circuit. The probe design is roughly sketched in Figure 2. Complete details of the construction and performance of the probe can be found in [8].

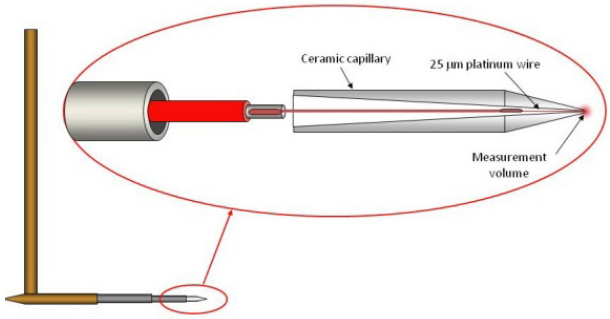

Figure 2. The conductivity micro-probe with a 25 µm platinum tip measuring electrode.

2.2 Signal Processing

The probe is excited with a 20 kHz sinusoidal analogue signal, ± 2 V, and sampled at a rate of 800 kHz. The small scale fluctuations in the local conductivity are detected as modulations in the amplitude of the 20 kHz response signal, see Figure 3.

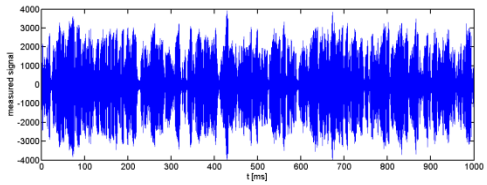

Figure 3: Example the raw signal as measured by the conductivity probe. The case shown here is for flow with rayon fibres, 1 m/s, Re_w = 57 000.

Fluctuations in the local conductivity are determined from the modulated amplitude of the sampled signal. In order to detect the modulated signal, a sine wave, with the same frequency but different phase and amplitude, is fit to each period of the sampled signal, i.e.

$$A(t) = A_i(t)\sin(\omega t + \varphi_i), \qquad (1)$$

where $A(t)$ is the measured amplitude modulated signal, $A_i(t)$ and φ_i are the amplitude and phase shift of the ith wave of the response signal. In order for conductivity measurements to be comparable to each other, the measured values are normalized according to the equation

$$\overline{C}(r,t) = \frac{C(r,t) - C_{outer}}{C_{inner} - C_{outer}}, \qquad (2)$$

where $C(r,t)$ is the local conductivity measured by the micro-probe, C_{inner} is the mean conductivity measured by the micro-probe placed in a bath of the dosed saline solution, and C_{outer} is the mean conductivity measured by the commercial probe placed at the end of the test pipe. It is further assumed that the conductivity signal can be expressed as a mean and fluctuating signal, C_m and c' respectively, i.e., $\overline{C} = C_m + c'$.

At each measurement point, the mean and fluctuating conductivity measurements are collected for approximately 30 seconds. The turbulent spectrum, $\Phi(f)$ is then computed from the Fourier transform of the square of the fluctuating signal, c'.

2.3 Experimental Conditions

Two types of particles were considered, at two different concentrations each. The first suspension consisted of polystyrene micro-spheres (Dynoseeds), with diameter, d_s = 130 µm, and specific gravity, SG_s = 1.05, suspended in tap water. The second suspension consisted of rayon fibres, with mean length, L_f = 2.0 mm, mean diameter, d_f = 60 µm, and specific gravity, SG_f = 1.50, suspended in tap water. The aspect ratio of these fibres, $r_f \approx 33$. Two concentrations were considered for each particle type, namely 0.1% and 1.0% volume fraction. For the fibre suspensions, these concentrations correspond to crowding factor values of 84 and 840 respectively. The Reynolds numbers considered here, based pipe diameter, D = 57 mm, mean suspension flow velocity and on the density and viscosity of water, were Re_w = 57000 and 114000 (corresponding bulk velocities, v_b = 1 m/s and 2 m/s respectively). A saline solution, consisting of table salt dissolved in tap water, 50 g/l in concentration, was used as the passive conductive tracer. The saline solution was injected into the suspensions with relative velocities of 80%, 100% and 120% of the bulk suspension velocity, which was controlled manually by pressurized air and monitored with a magnetic flow meter. In all cases, the saline solution was injected along the pipe centreline, 10 cm upstream from the conductivity probe.

3 Results

Conductivity measurements were made with the probe positioned at three different radial positions, namely along the pipe centreline, r = 0, and at radial

distances r = 5 mm, and r = 20 mm from the centreline. Presented first are profiles of the mean conductivity levels for the different suspension flows, see Figure 4. Variations in these measurements represent the mean dispersion of the dosed stream in response to the suspension contents. It should be mentioned that the statistical error in these measurements was extremely small due to the large number of samples collected at each point (approximately 30 seconds of sampling x 20 000 samples per second), therefore error bars are not included these plots.

The first observation to be made from the mean conductivity profiles is that the saline stream is highly concentrated about the pipe centreline for both the water and microsphere suspensions. This is clear from the large peak in conductivity at r = 0, and the relatively low and near constant values in conductivity at larger radial distances. However, with the fibre suspensions, the saline stream is found to disperse to at least as far as r = 5 mm, as indicated by the near equal, and relatively larger values of conductivity at r = 0 and r = 5 mm. This result is interesting and will be commented on further after investigating the turbulence spectra. The general effect of the solids phase is to suppress the mixing of saline solution in the flow direction. A greater suppression of mixing is also noted at higher solids concentration, i.e. lower conductivity levels are measured along the centreline at higher solids concentrations. It can also be seen that the suppression of mean conductivity is far greater in the fibre suspensions compared to that in the microsphere suspensions. An increase in the conductivity along the centreline is also noted at higher bulk suspension velocity. This is an effect of increased convection at higher velocity, which therefore leads to better transport of the saline solution.

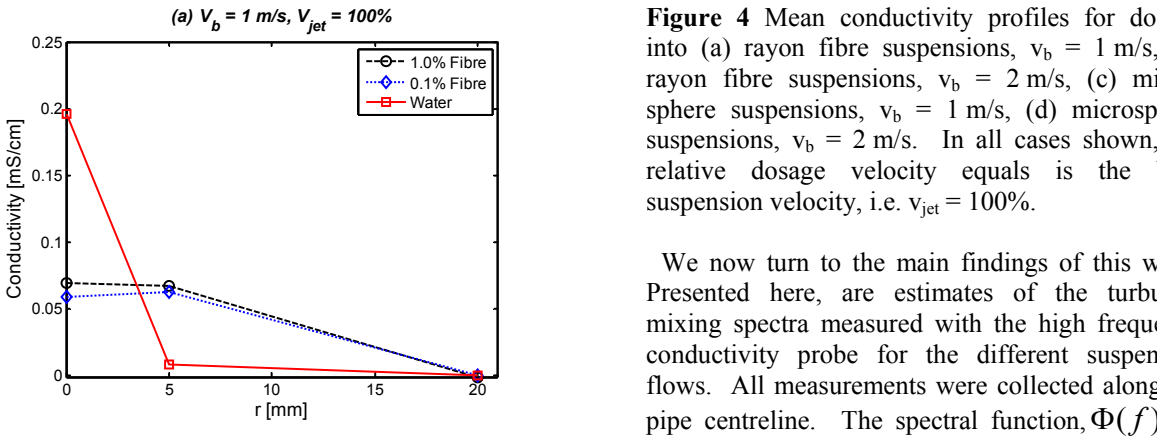

Figure 4 Mean conductivity profiles for dosage into (a) rayon fibre suspensions, v_b = 1 m/s, (b) rayon fibre suspensions, v_b = 2 m/s, (c) microsphere suspensions, v_b = 1 m/s, (d) microsphere suspensions, v_b = 2 m/s. In all cases shown, the relative dosage velocity equals is the bulk suspension velocity, i.e. v_{jet} = 100%.

We now turn to the main findings of this work. Presented here, are estimates of the turbulent mixing spectra measured with the high frequency conductivity probe for the different suspension flows. All measurements were collected along the pipe centreline. The spectral function, $\Phi(f)$, is defined as the Fourier transform of the square of the modulated conductivity signal, computed in frequency space, *f*. For convenience, we map the frequency based spectral function $\Phi(f)$ to wavelength space, where the wavelength λ, is defined in terms of the frequency and bulk

suspension velocity, i.e. $\lambda = v_b/f$. Using this definition of wavelength, the wavelength-based spectral function, $\Psi(\lambda)$, can be defined as follows [9]

$$\Psi(\lambda) = \frac{f^2}{v_b}\Phi(f). \qquad (3)$$

Estimates of the turbulent spectra for relative dosage velocity v_j = 100%, of the bulk suspension velocities, v_B = 1 m/s, and 2 m/s, along the pipe centreline are shown below, see Figures 5.

In general, the turbulent spectra are found to be clustered around a definite wavelength value and decay exponentially at both higher and lower wavelengths. The wavelength spectra are also noted to be skewed toward small wavelengths. However, the character of turbulent spectra is found to be highly dependent on the solids content. For example, with the rayon fibre suspensions, the large wavelength (low frequency) fluctuations are enhanced, while the small wavelength (high frequency) fluctuations are in fact damped. Also observed is a significant shift in the wavelength, corresponding to the spectral peak, to a larger wavelength value than that observed with pure water. These finding suggest that, in fibre suspensions, mixing predominantly takes place over large wavelength/low frequency scales, while the small wavelength/high frequency mixing eddies are damped by the fibre phase. This observation supports the character of the mean conductivity profiles measured in the fibre suspensions. Recall from Figure 4 (a) and (b), where we noted near equal mean conductivity levels at the position r = 0 and r = 5 mm. In light of the turbulent spectra, it would appear that the enhanced large wavelength mixing scales are able to better advect the saline solution radially in the fibre suspensions. However, one should be aware of the implications these results might have for mixing in papermaking fibre suspensions, where it should be desirable to achieve mixing at all scales. In particular, the high frequency mixing (small length scale) are believed to be of great importance, since these are the scales most likely to penetrate into fibre flocs and create dispersion at scales at or below that of the fibre length, e.g. when dosing a stock flow with retention aid polymers. Therefore, from a papermaking perspective, additional means may be necessary in order to enhance the high frequency scales of turbulence during concentric mixing. As an added observation, the higher concentration suspensions are found to result in slightly lower overall turbulence levels.

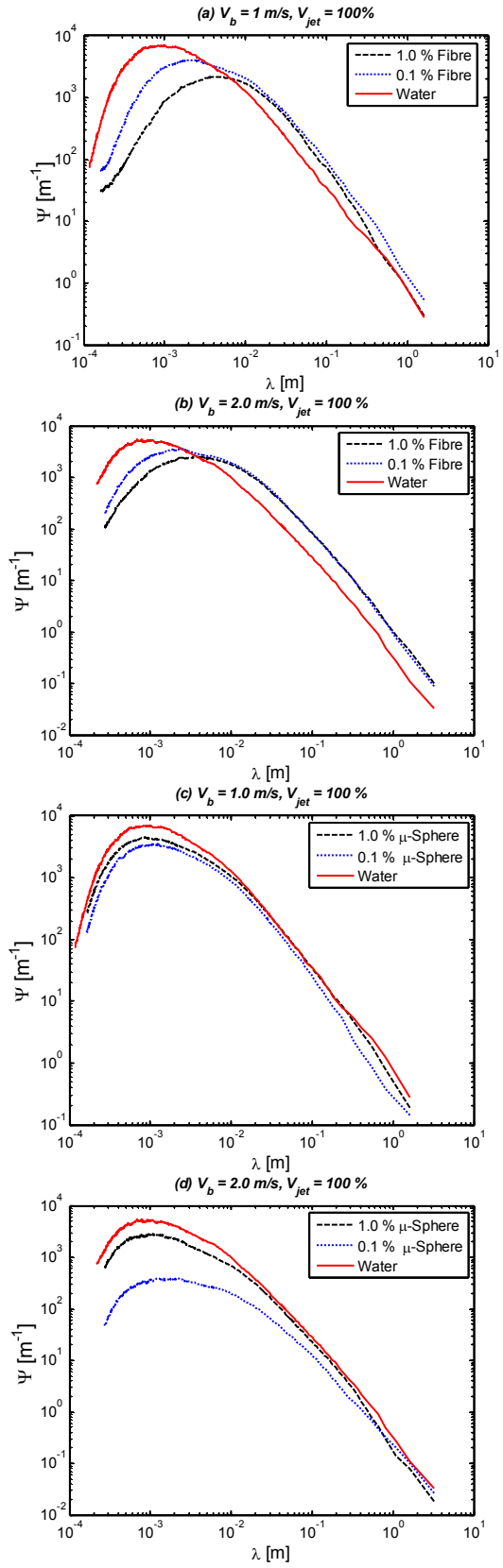

Figure 5 Estimates of the turbulent spectra along the pipe centreline for dosage into (a) fibre suspensions with bulk velocity v_b = 1 m/s, (b) fibre suspensions with bulk velocity v_b = 2 m/s, (c) micro-sphere suspensions with bulk velocity v_b = 1 m/s, (d) micro-sphere suspensions with bulk velocity v_b = 2 m/s. In all cases the relative dosage velocity is v_j = 100% of the bulk suspension flow.

The microspheres are found to have a rather different effect on the turbulence spectra. Specifically, the microspheres are found to damp the overall turbulent fluctuations at all scales and to have a negligible effect on the wavelength associated with the spectral peak. In general, the overall level of turbulent fluctuations tends to be lower with low concentration microsphere suspensions, opposite to what was observed in the fibre suspensions. In general, the behaviour of the turbulent spectrum in the microsphere suspension appears to be preferable to that in the fibre suspensions. From an industrial viewpoint, this result would suggest it may be possible to improve mixing quality if mixing is performed prior to introduction of the fibre phase.

A general analysis is presented now in order to investigate the effect of relative dosage velocity on turbulent mixing. To do so, we consider the mean-square of the fluctuating conductivity signal, c', which we henceforth refer to as the pseudo-turbulent energy, E, defined as follows

$$E = \langle c'c' \rangle . \qquad (4)$$

Plots of the pseudo-turbulent kinetic energy are presented in Figure 6. It should be mentioned that data is not available for v_j = 120% in the 1.0% fibre suspensions.

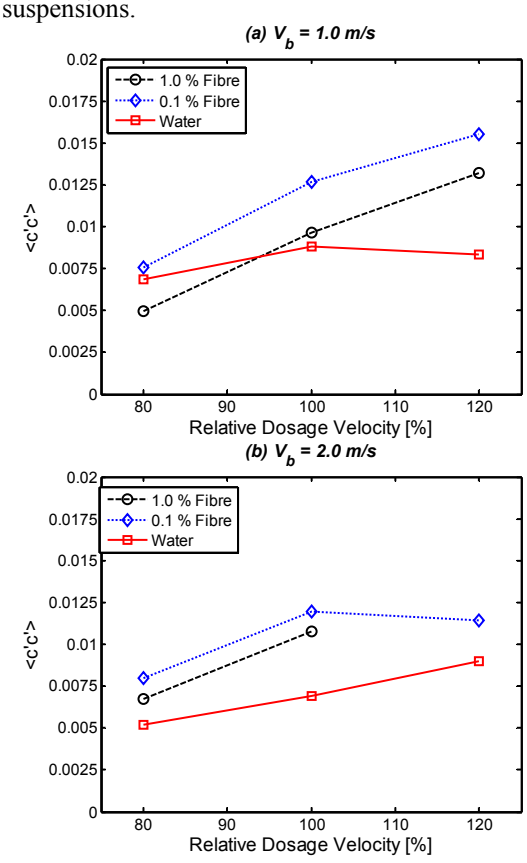

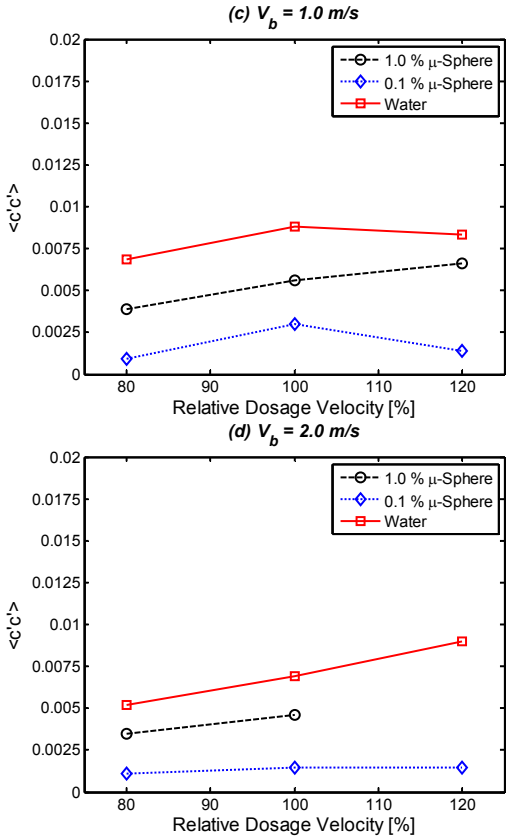

Figure 6 Plots of the pseudo.kinetic energy vs. relative dosage velocity for dosage into (a) rayon fibre suspensions, v_b = 1 m/s, (b) rayon fibre suspensions, v_b = 2 m/s, (c) micro-sphere suspensions, v_b = 1 m/s, (d) microsphere suspensions, v_b = 2 m/s.

Figure 6 shows that the pseudo-turbulent energy increases with saline dosage velocity in all cases. This relationship is generally found to be monotonic yet slightly non-linear. The effect is also shown to be highly dependent on particle type. For example, with the fibre suspensions, E increases significantly with dosage velocity. However with the microsphere suspensions, E increases gradually with dosage velocity. The case with pure water represents an intermediate region between the fibre and micro-sphere suspensions. The pseudo-turbulent energy is also found to decrease as the solids concentration increases in the fibre suspensions, whereas it is found to increase with solids concentration in the microsphere suspensions.

The effect of dosage velocity on the pseudo-turbulent energy observed in this study is similar to those presented by [2], where the effect of relative dosage velocity of a dyed fibre suspension, mixed into water, was studied through high speed imaging. They showed a similar trend, i.e. improved spatial mixing with increased relative dosage velocity. Comparison of the results of [2] with the results presented in this work, would suggest that the pseudo-turbulent energy, as measured with these conductivity probes, might

serve as a useful global measure of mixing quality in high concentration suspensions.

4 Conclusion

A new method for fully characterizing turbulent mixing and dispersion of a dosage stream in semi-concentrated suspension flow has been presented. A high frequency conductivity probe was used in conjunction with advanced signal processing to measure the turbulent fluctuations of a saline solution injected into semi-concentrated, mono-dispersed fibre and microsphere suspensions. The mean conductivity signal gathered with this tool was used to estimate the local concentration of the added saline stream at a given point in the flow, i.e. the mean spatial dispersion of the dosed stream. Analysis of the high frequency fluctuating conductivity signal allowed for characterization of the local mixing energy and turbulent spectrum, i.e. the spectral mixing scales available in the suspensions for a given set of flow conditions.

It was shown that the fibre phase effectively increased the low frequency turbulence in the suspension, attenuated the high frequency turbulent scales, and had the general effect to increase the overall turbulence energy in the dosed saline stream. The microspheres were shown to effectively damp the overall turbulence in the saline stream at all scales. The effect of concentration was shown to be opposite in the fibre suspensions and microsphere suspensions. The overall turbulence in the saline stream was characterized by the pseudo-turbulent kinetic energy, which was shown to increase monotonically with dosage velocity in all suspension and in pure water.

ACKNOWLEDGEMENTS

The authors wish to express their gratitude for the support by the financing companies in the Web Structure and Runnability Research Cluster in the Research Program 2009 – 2011 at Innventia. Founding from Energimyndigheten, The Swedish Energy Agency, is gratefully acknowledged.

REFERENCES

[1] M. Hubbe, H. Nanko, and M. McNeal. Retention aid polymeric interactions with cellulosic surfaces and suspensions: A review, BioResources, 4, 850-906, (2009).

[2] B. Norman, Å. Tegengren. Mixing of thick stock and white water. EUCEPA, 1988 Harrogate conference centre, Harrogate UK, Vol 1,52–56, (1988).

[3] L. Forney. Jet injection for optimum pipeline mixing. Encyclopedia of Fluid Mechanics Vol 2 – Dynamics of Single Fluid Flows and Mixing, Gulf Publishing Co., Houston, 660-690, (1986).

[4] R. Kerekes, C. Schell. Characterization of fibre flocculation regimes by a crowding factor, Journal of Pulp and Paper Science, 18, 32 – 38, (1992).

[5] G. Hetsroni. Particle-turbulence interaction. Int. J. Multiphase Flow 15, 735-746 (1989).

[4] Kulick J.D., Fessler, J.R., Eaton, J.K. 1994. Particle response and turbulence modification in fully developed channel flow. J. Fluid Mech. 277, 109–134.

[5] Rogers C.B., Eaton, J.K. 1991. The effect of small particles on fluid turbulence in a flat-plate, turbulent boundary layer in air. Phys. Fluids A, 3, 928–937.

[6] C. Luettgen, L.D. Lindsay, and R.A. Stratton. Turbulent dispersion in pulp flow: Preliminary results and implications for the mechanisms of fibre-turbulence interactions. IPST technical paper series, 408, Georgia Institute of Technology, Atlanta Georgia (1991).

[7] G. K. Batchelor. Small-scale variation of convected quantities like temperature in turbulent fluid. Part 1. General discussion and the case of small conductivity, J. Fluid Mech., **5**, 113-133 (1959).

[8] M. Fällman. Turbulence measurements in fibre suspensions: experimental methods and results. PhD thesis, Royal Institute of Technology, Stockholm (2009).

[9] B. Norman and D. Wahren, A descriptive method for the description of mass distribution in sheets and flocculation and turbulence in suspensions., Svensk Papperstidning., 75, 807-818, (1972).

Microstructure Simulation of Early Paper Forming Using Immersed Boundary Methods

A. MARK[1,⋆], E. SVENNING[1],
R. RUNDQVIST[1], F. EDELVIK[1],
E. GLATT[2], S. RIEF[2], A. WIEGMANN[2],
M. FREDLUND[3], R. LAI[4],
L. MARTINSSON[5], U. NYMAN[6]

[1]Fraunhofer-Chalmers Centre, Gothenburg, Sweden
[2]Fraunhofer ITWM, Kaiserslautern, Germany
[3]Stora Enso, Karlstad, Sweden
[4]Eka Chemicals, Bohus, Sweden
[5]Albany International, Halmstad, Sweden
[6]Tetra Pak Packaging Solutions AB, Lund, Sweden

⋆Correspondence to:
andreas.mark@fcc.chalmers.se

Keywords: Fluid Structure Interaction, Immersed Boundary Methods, Paper forming

ABSTRACT

Paper forming is the first step in the paper machine where a fiber suspension leaves the headbox and flows through a forming fabric. Understanding this process is important for the development of improved paper products because the configuration of the fibers during this step has a large influence on the final paper quality.

The simulation framework includes IBOFlow, a state-of-the-art Navier-Stokes solver, and PaperGeo, the virtual paper structure generator in GeoDict. Immersed Boundary Methods are used to resolve the flow around the fibers. The fibers are modeled with a finite element discretization of the Euler-Bernoulli beam equation in a co-rotational formulation. The contact model is based on a penalty method and includes friction as well as elastic and inelastic collisions.

The fiber model and the contact model are validated against demanding test problems from the literature with excellent result. The fluid-structure interaction in the model is examined by simulating an elastic beam oscillating in a cross flow. Finally, a simulation of initial paper forming is performed, which demonstrates the capabilities of the simulation framework.

1 INTRODUCTION

Paper forming is the first step in the paper machine where a fiber suspension leaves the headbox and flows through a forming fabric. A fiber web is gradually built up when the fibers land on the fabric. Understanding this process is important for the development of improved paper products, because the orientation and distribution of fibers during this step have a large influence on the final paper quality.

Simulation of paper forming offers huge challenges since it involves transient fluid flow with many immersed solid objects subjected to large displacements. The fibers are buoyant, which results in strong coupling between the fluid and the fibers. Contact phenomena play an important role because the fiber web is kept together only by contact forces and fluid forces. Therefore, the stability of the fiber model needs special attention.

Different methods for simulation of fiber suspensions are described in the literature. Yamamoto and Matsuoka [19] modeled a fiber as a chain of spheres connected with springs. Ross and Klingenberg [15] attempted to reduce computation times by modeling a fiber as a chain of prolate spheroids, thus allowing a fiber to be modeled with fewer elongated bodies. Lindström [8] developed a model where a fiber is treated as a chain of rigid rods and used the model to study paper forming. This model includes contacts between fibers as well as two-way coupling between the fibers and the fluid. However, the flow around the fibers is not resolved. The model proposed in [8] is not based on a beam theory, the derivation starts with Newton's second law and expressions for the bending moments in the joints are inserted.

Understanding the phenomena occuring on the length scale of a single fiber requires DNS simulations where the flow around every fiber is resolved. Furthermore, the fiber model should be based on a rigorous beam theory. Therefore, an implementation of more accurate methods is necessary.

In the present work, the flow around the fibers is resolved with Immersed Boundary Methods. The fibers are modeled as Euler-Bernoulli beams in a co-rotational formulation and discretized with the Finite Element Method. The nonlinear system of equations is solved with Newton's method and Hilber's α-method is used for the temporal discretization. The fiber-fiber and fiber-fabric contacts are modeled with a penalty method and elastic/inelastic contacts as well as friction is taken into account.

The fiber model and the contact model are validated

against demanding problems described in the structural mechanics literature. The interaction between a slender object and a fluid is investigated by simulating a flexible beam in a cross flow. Finally, an example of a paper forming simulation is given, demonstrating that the model is robust enough for this demanding problem.

2 GOVERNING EQUATIONS

2.1 Fluid model

The motion of the fluid is governed by the Navier-Stokes equations:

$$\nabla \cdot \vec{u} = 0 \tag{1}$$

$$\rho_f \frac{\partial \vec{u}}{\partial t} + \rho_f \vec{u} \cdot \nabla \vec{u} = -\nabla p + \mu \nabla^2 \vec{u} \tag{2}$$

In the equations above, $\vec{u}$ is the fluid velocity, ρ_f is the fluid density, p is the pressure and μ is the dynamic viscosity.

The CFD solver IBOFlow [5] is used to solve the incompressible Navier-Stokes equations (1) and (2). IBOFlow (Immersed Boundary Octree Flow Solver) is based on a Finite Volume discretization and the Immersed Boundary Method is used to model the presence of arbitrary moving objects in the flow. The solver uses a Cartesian octree grid that can be dynamically refined and coarsened, enabling adaptive grid refinements to follow moving bodies with almost no extra computational cost. The octree grid allows grid refinements to be created without deterioration of the mesh quality.

IBOFlow solves the Navier-Stokes equations in a segregated way and the velocity and pressure fields are coupled with the SIMPLEC [2] method. All variables are stored in a co-located arrangement and Rhie-Chow interpolation [14] is used to prevent pressure oscillations.

The forming fabrics studied in the present work have complex geometries which cannot be described analytically. The geometries are described numerically by voxelizations generated with GeoDict [3], these voxelizations are used to set boundary conditions on the fluid and to detect collisions between the fibers and the forming fabric. The voxelizations are based on CAD geometries from Albany International.

2.2 Fluid-structure coupling

Immersed boundary methods are used to study the flow around arbitrary moving objects without the need of a body-fitted mesh. In the present work, the hybrid immersed boundary method [10] is used to model the presence of fibers in the flow. This method extends the mirroring immersed boundary method [9, 11] by adding extrapolation points at the immersed boundary.

Application of the immersed boundary method requires that a cell type is assigned to each cell in the fluid domain. The cells are marked as *fluid cells, internal cells, mirroring cells* or *extrapolation cells* depending on the position relative to the immersed boundary.

The velocity in the internal cells is set to the velocity of the immersed object with a Dirichlet boundary condition. For the mirroring cells, an exterior normal point $\vec{p}_e$ is defined as [10]:

$$\vec{p}_e = \vec{p}_{mi} + 2.0\left(\vec{p}_{ib} - \vec{p}_{mi}\right) \tag{3}$$

In the equation above, $\vec{p}_{mi}$ is the center of the mirroring cell and $\vec{p}_{ib}$ is the closest point on the immersed boundary. For extrapolation cells, an exterior point is defined as:

$$\vec{p}_e = \vec{p}_{ib} + 2.0\left(\vec{p}_{ex} - \vec{p}_{ib}\right) \tag{4}$$

In the equation above, $\vec{p}_{ex}$ is the cell center of the extrapolation cell. Figure (1) illustrates the definition of these points.

The boundary condition for a mirroring cell is:

$$\frac{\vec{u}_{mi} + \vec{u}_e}{2} = \vec{u}_{ib} \tag{5}$$

The boundary condition for an extrapolation cell takes the following form:

$$\frac{\vec{u}_{ib} + \vec{u}_e}{2} = \vec{u}_{ex} \tag{6}$$

The velocity in the point $\vec{p}_e$ is interpolated and inserted into the immersed boundary condition. As a result, (5) and (6) become implicit boundary conditions which can be added to the matrix in the discretized equations. This results in a fictitious fluid velocity field inside the immersed object. Mass conservation is ensured by excluding the fictitious velocity field in the discretized continuity equation. The result is a robust method that is second order accurate in space [10, 11].

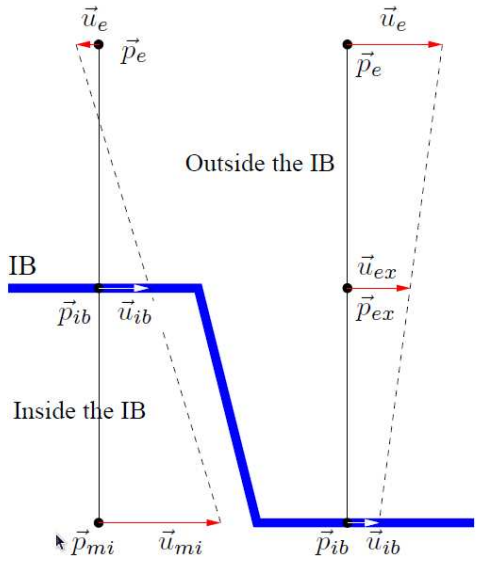

Figure 1: Two-dimensional visualization of an immersed boundary.

2.3 Fiber model

The fibers are modeled as slender beams with hollow elliptical cross section. The strong form of the equations of motion for a beam are given in [1]:

$$\frac{\partial \vec{k}}{\partial t} = \vec{f}_{ext} + \frac{\partial}{\partial x}\left(\underline{\underline{E}} \cdot \vec{f}_{int}\right) \tag{7}$$

$$\frac{\partial \vec{\pi}}{\partial t} = \vec{m}_{ext} + \frac{\partial \vec{r}}{\partial x} \times \left(\underline{\underline{E}} \cdot \vec{f}_{int}\right) + \frac{\partial}{\partial x}\left(\underline{\underline{E}} \cdot \vec{m}_{int}\right) \tag{8}$$

Following the notation in [1], $\vec{k}$ is the linear momentum and $\vec{\pi}$ is the angular momentum. $\vec{f}_{ext}$ is the externally applied body force and $\vec{m}_{ext}$ is the externally applied body moment. $\underline{\underline{E}}$ is the transformation from local to global coordinates, $\vec{f}_{int}$ is the internal force in a point and $\vec{m}_{int}$ is the internal moment in a point.

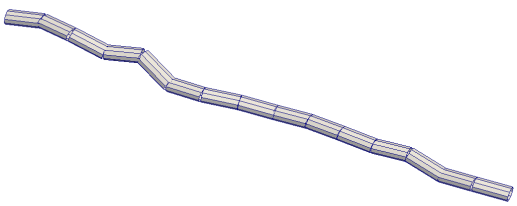

Figure 2: A typical fiber divided into several elements.

The equations in (7) and (8) governing the motion of the fibers are discretized with the Finite Element Method. A fiber is discretized by dividing it into several elements as shown in figure (2) and each element is associated with two nodes, a node at the start point and a node at the end point. Every node has 6 degrees of freedom: translation in 3 directions and rotation about 3 axes. Hence a beam element has 12 degrees of freedom. A local coordinate system is fixed to each element and this coordinate system is defined in such a way that the local $\vec{e}_x$ axis is always aligned with the centerline of the element. The $\vec{e}_y$ and $\vec{e}_z$ axes are perpendicular to the centerline. The effect of large rotations is included with the method of co-rotational frames as described by Nour-Omid and Rankin [12, 13]. The essence of this method is that the linear Finite Element model is formulated in a coordinate system that moves with the element. In this way, geometric nonlinearities are included through the motion of the coordinate system. The inertia terms are computed as described by Crisfield et al. [1] and the bending terms are computed according to the Euler-Bernoulli beam theory. The nonlinear system of equations is solved with Newton's method and Hilber's α-method is used for the temporal discretization.

The contacts are modeled with a penalty method. Elastic and inelastic collisions are modeled by introducing the coefficient of restitution directly into the expression for the normal force as suggested by Harmon [4]. Friction is modeled with a square root regularization of Coulomb's law as described by Wriggers [18].

3 NUMERICAL RESULTS

To validate the implementation of the beam model, large amplitude oscillations of an L-shaped cantilever beam are studied. The contact model is validated by simulation of a spinning rod impacting a table. Comparisons are made with results from the literature.

The fluid-structure coupling is examined by simulation of a flexible beam oscillating in a cross flow. A comparison is made with a simplified one-way coupling simulation and a Fourier series expansion of the Euler-Bernoulli beam equation.

Finally, the capabilities of the software are demonstrated by performing a simulation of paper forming.

3.1 Oscillation of an L-shaped beam

The first test case investigates the dynamic response of an elastic beam and has been studied by several authors. Simo and Vu-Quoc [16] analyzed the problem

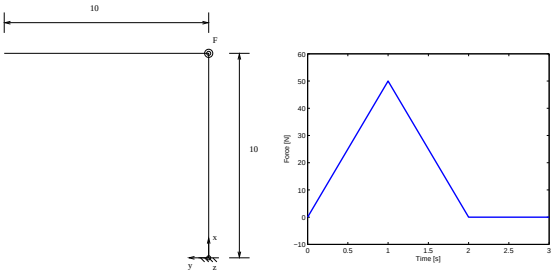

Figure 3: Geometry of the L-shaped beam considered in the first test case (left) and loading history (right).

with a fully nonlinear, geometrically exact finite strain beam model. It was later studied by Ibrahimbegović and Mikdad [6], who used a geometrically exact beam model based on the Reissner beam theory. In this problem, the L-shaped cantilever beam shown in figure (3) is studied. A point force is applied in the out-of-plane direction at the elbow. Figure (3) shows the time history of the force, which has a maximum value of 50 N and is applied for two seconds. The cross section of the beam has the following properties:

- $GA_y = GA_z = EA = 10^6\ N$
- $EI_y = EI_z = GJ = 10^3\ Nm^2$
- $A\rho = 1\ kg/m$
- $I\rho_x = 20\ kgm$
- $I\rho_y = I\rho_z = 10\ kgm$

It should be noted that in the present work, a model based on the Euler-Bernoulli beam theory was used, which implicitly assumes $GA_y = GA_z = \infty$. As will be seen, this assumption does not have a noticeable effect on the results for this test case. The reason for this is most likely that the structure studied in this problem is indeed very slender and therefore the Euler-Bernoulli assumption is justified. The beam is discretized with 20 elements and a time step size of $\Delta t = 0.25\ s$ is used.

The beam is initially at rest and starts to deflect when the external force is applied. After the force has been removed, the structure performs free vibrations with large magnitude. As noted in [6] and [16], the amplitude of the vibration is of the same order of magnitude as the length of the structure. Therefore, this problem is a good test of the models capability of handling transient problems involving large rotations and displacements.

Figure (4) shows the z-displacement of the elbow and the tip as a function of time. Values predicted by Ibrahimbegović and Mikdad [6] as well as by Simo and Vu-Quoc [16] are also shown for comparison. The agreement is very good even though different beam models were used in the present work and the reference solutions [6, 16]. The results shown in figure (4) were obtained with the same time step size as used by Simo and Vu-Quoc: $\Delta t = 0.25\ s$, but 20 elements were used for the spatial resolution. The solution presented by Simo and Vu-Quoc was obtained with ten elements with quadratic base functions, and in that study it was not investigated whether the solution obtained was grid-independent or not. This lack of grid-independency is probably the reason for the discrepancy observed for the deflection of the elbow at $t \approx 17\ s$. Here, the result from the present study agrees well with the results predicted by Ibrahimbegović and Mikdad while slightly different results are given by Simo and Vu-Quoc.

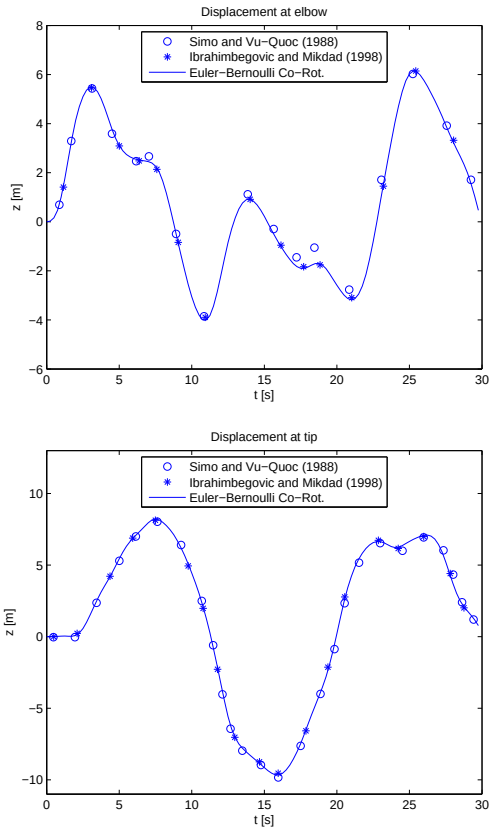

Figure 4: Out-of-plane displacement of the elbow (top) and the tip (bottom).

3.2 Impact of spinning rod

The second test case is a spinning rod falling onto a table. This problem, which involves fricton and in-

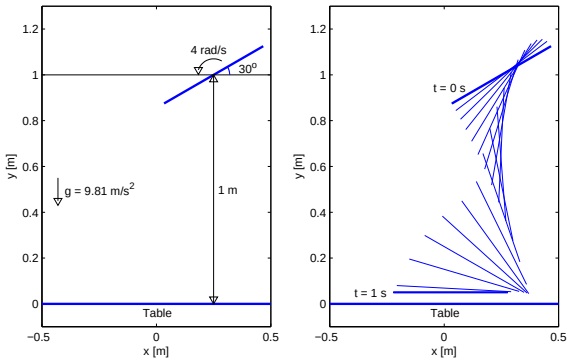

Figure 5: Geometry of a rod impacting a table (left) and the location of the rod at different instants in time (right).

elastic contact, was previously studied by Stewart and Trinkle [17]. The rod shown to the left in figure (5) is released from a height of 1 m with an angle of 30^o to the horizontal. Initially, the center of mass of the rod has no translational velocity, but the initial angular velocity is 4 rad/s about the center of mass. Gravity causes the rod to fall downwards and impact the table located at $y = 0$. The table is rigid and the coefficient of friction for the contact between the rod and the table is $\mu_{fr} = 0.6$. The impacts are considered to be inelastic with $e_{cor} = 0$. The length of the rod excluding the rounded ends is $l = 0.5$ m and it has a radius of $r = 0.05$ m. The mass of the rod is 1 kg and its moment of inertia with respect to the center of gravity is $J = 0.002$ kgm^2. Stewart and Trinkle studied a rigid rod. The code developed in the present work deals with elastic problems and cannot simulate perfectly rigid objects. Instead, the rod was meshed with one element and the material parameters of steel were used ($E = 210$ GPa, $\nu = 0.3$). In this way, the rod will behave as almost rigid in the simulations.

The initial angular velocity causes the rod to rotate as it falls towards the table. The rod impacts the table with one of its ends and continues to rotate towards the table with its other end. Eventually the other end hits the table and the rod comes to rest. The right figure in (5) shows the centerline of the rod at different instants in time as it falls towards the table. Note that the rod has a radius of $r = 0.05$ m and therefore the centerline of the rod stops at a distance of 0.05 m from the table.

Figure (6) shows a comparison with the results given by Stewart and Trinkle [17]. The agreement between the penalty method used in the present work and the reference solution is good. Note that this good agreement was achieved even though a regularization of Coulomb's law was used in this simulation.

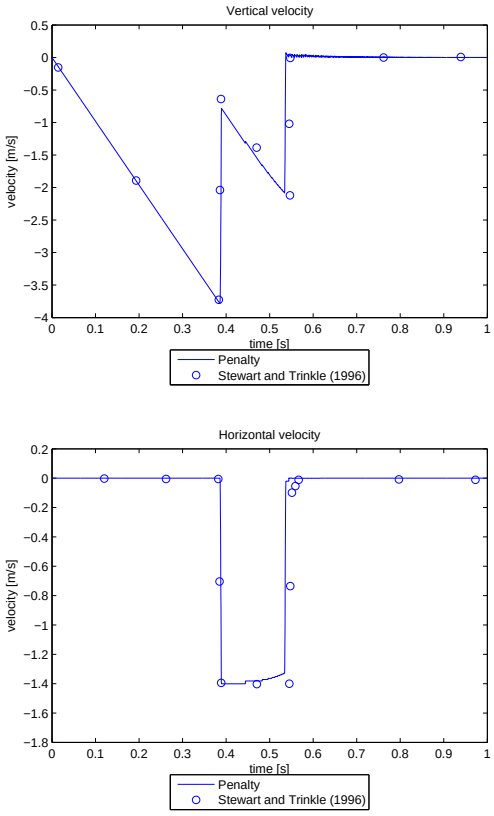

Figure 6: Vertical (top) and horizontal (bottom) velocity of a rod impacting a table. The velocity was sampled at the center of mass of the rod.

3.3 Oscillating beam in cross flow

The first FSI problem investigates the interaction between a fluid flow and a slender structure. An elastic beam is clamped at the wall in a domain filled with a Newtonian, incompressible fluid. The beam is initially at rest, but the forces from the fluid cause the beam to deflect and start oscillating. These oscillations are gradually damped out by the fluid and a wake develops due to the presence of the beam. The problem has been studied with three methods: a DNS simulation with two-way coupling, a simulation with one-way coupling and a Fourier series expansion.

The beam is surrounded by water with viscosity $\mu_f = 1.0 \cdot 10^{-3}$ Pas and density $\rho_f = 1000$ kg/m^3. The fluid domain is bounded by its lower corner $\vec{p}_{lc} = (0,\ 0,\ 0)$ mm and its upper corner $\vec{p}_{uc} = (0.5, 3.0, 1.0)$ mm. The beam is made of a linear elastic material with Young's modulus $E = 1.0 \cdot 10^7$ Pa and Poisson's ratio $\nu_s = 0.3$. The density of the beam material is $\rho_s = 5000$ kg/m^3. The beam has a circular cross

section and its geometry is defined by the start point, the end point and the radius:

- Start point: (0, 1.0, 0.5) *mm*
- End point: (0.15, 1.0, 0.5) *mm*
- Radius: $r = 0.01$ *mm*

15 elements are used for the discretization of the beam. The time step length was set to $\Delta t = 0.3125$ μs, resulting in a CFL number of roughly 0.5 on the finest grid. The end time of the simulation was set to $t_{end} = 2$ *ms* and the inlet velocity was set to one meter per second: $v_{in} = (0,\ 1,\ 0)$ m/s. The fluid boundary conditions and the location of the beam are illustrated in figure (7). Symmetry boundary conditions are employed on the z^- and z^+ surfaces.

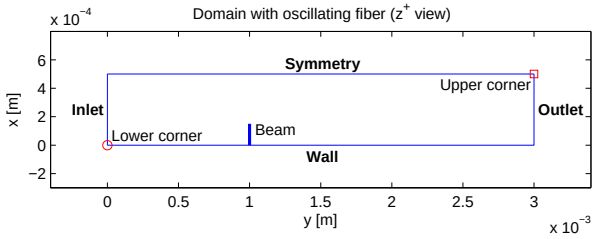

Figure 7: Fluid domain seen in z^+ direction.

Simulations were performed with several different grids and the deflection of the beam tip was monitored. The beam was kept fixed for the first $1.0 \cdot 10^{-4}$ *s* in all the simulations in order to allow the boundary layer around the beam to develop. Five different grids were used, ranging from 3 refinements and $2.8 \cdot 10^4$ cells to 6 grid refinements and $2.0 \cdot 10^5$ cells. The first order upwind scheme was used for the convective terms and the implicit Euler scheme was used for the temporal discretization in the fluid simulation. DNS simulations were performed, hence no turbulence model was used. Hilber's α-method with $\alpha = -0.05$ was used for the temporal discretization of the Finite Element equations describing the motion of the beam.

The oscillation of a beam in a fluid was also studied with modal analysis. A Fourier series expansion of the Euler-Bernoulli beam equation was computed and the influence of the surrounding fluid was included as a distributed load under the assumption of one-way coupling. The flow field was assumed to be uniform and a drag correlation for long cylinders was used to estimate the fluid force.

Figure (8) shows the velocity field around the beam during the first oscillation and when the beam has settled in its steady state configuration. The deflection of

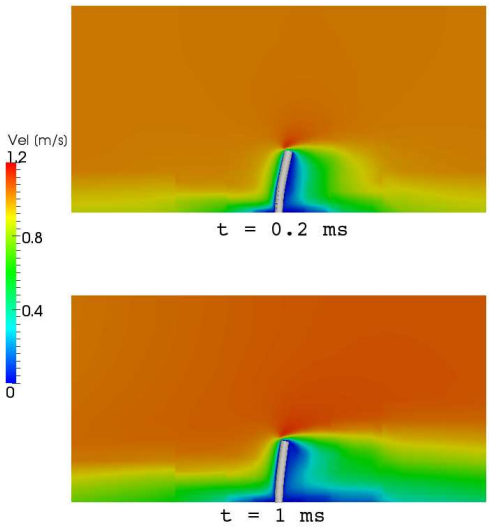

Figure 8: Flow field around an oscillating beam during the first oscillation (top) and when the beam has reached steady state (bottom).

the beam as well as the development of the wake can be seen in the figure.

Figure (9) shows a comparison between the results obtained with the Fourier series analysis, the DNS simulation and the simulation with one-way coupling. The solution obtained from the Fourier series expansion is nearly identical to the simulation with one way coupling. This is expected, because both of these computations use the same assumption for the fluid force: one way coupling is used and it is assumed that the drag force is the only important force. The small difference between the Fourier series solution and the one-way coupling simulation can be attributed to the fact that the Fourier series expansion assumed a uniform flow field while the one-way coupling simulation sampled the fluid velocity from the simulated flow field. This simulated flow field is not perfectly uniform due to the effect of the wall, even though the boundary layer is thin compared to the length of the beam. The DNS simulation predicts oscillations with larger amplitude than the simplified methods, especially during the first period. The reason for this is most likely that the DNS simulation accounts for the history force and the added mass force, which were neglected in the simplified analysis. Furthermore, the DNS simulation predicts a slightly larger period time due to the strong coupling with the fluid. It is interesting to note that all three methods approach the same steady state value. This is also expected, because the simplified analysis included the stationary force but neglected some transient forces.

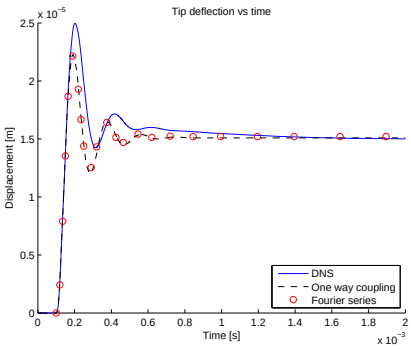

Figure 9: Tip deflection in y-direction of a beam oscillating in a fluid: comparison of results obtained with DNS, simulation with one way coupling and Fourier series analysis.

3.4 Initial simulation of paper forming

The last numerical example investigates the possibilities of simulating paper forming with the modeling framework developed in the ISOP (Innovative Simulation of Paper) project [7]. The simulation starts with a cloud of fibers randomly distributed in the fluid domain as shown in figure (10). Adaptive grid refinements are added around the fibers and the forming fabric. The fluid flows from the inlet in the top of the domain through the forming fabric to the outlet in the bottom of the domain. The fibers follow the fluid and therefore gradually fall down onto the forming fabric where they start to form a fiber web. This process is visualized in figure (11).

Figure (12) shows the solution when all fibers have come to rest on the forming fabric. The solution is stable even though the fiber web is kept together only by contact forces and fluid forces.

4 CONCLUSIONS

A simulation framework for microstructure simulation of early paper forming has been developed. The simulation framework includes the Navier-Stokes solver IBOFlow [5], the virtual paper structure generator PaperGeo in GeoDict [3] and a fiber model based on a Finite Element discretization of the Euler-Bernoulli beam equation in a co-rotational formulation.

The fluid-structure interaction is handled with the Immersed Boundary Method, which allows the flow around every fiber to be resolved.

Fiber-fiber and fiber-fabric contacts are modeled with a penalty method. Elastic and inelastic collisions as well as friction are taken into account.

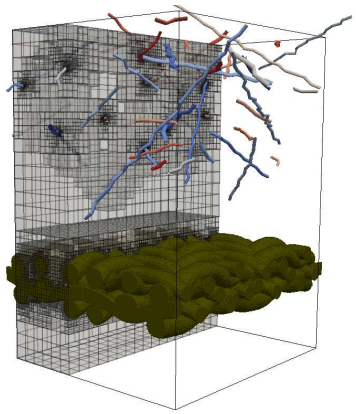

Figure 10: Simulation setup for initial simulation of paper forming: a cloud of fibers is randomly distributed in the fluid domain. As can be seen, the representation of the forming fabric has been constructed by mirroring a smaller part of the true geometry. The geometrical description of the forming fabric used in this study is therefore an approximation.

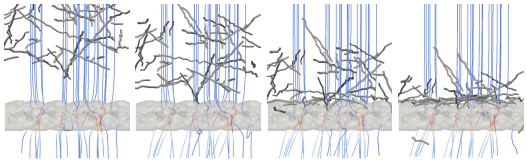

Figure 11: 50 fibers falling down on a forming fabric. The streamlines are colored by the fluid velocity.

The fiber model has been validated against test problems described in the literature with excellent result. The code is very robust and it can be concluded that the modeling framework can be used to simulate paper forming. The results obtained with the resolved simulations could be used to derive better macroscale models for the phenomena governing paper forming.

Future work includes more advanced interaction models that e.g. take chemicals and surface charges into account. So far only fibers have been simulated but fillers and fines will also be included. Models for how the chemicals affect the retention of fillers and fines in the sheet formed on the fabric will be developed.

5 ACKNOWLEDGEMENTS

This work was part of the ISOP project with industrial partners Albany International, Eka Chemicals, Stora Enso and Tetra Pak. It was supported in part by the Swedish Foundation for Strategic Research (SSF) through the Gothenburg Mathematical Modeling Centre (GMMC).

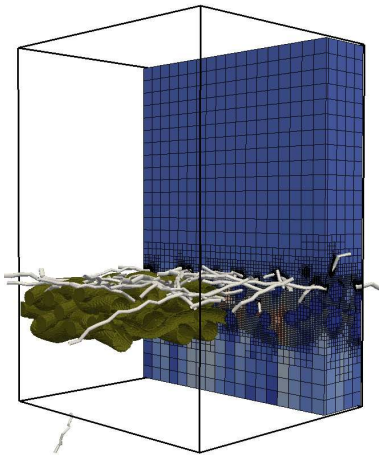

Figure 12: Fibers resting on the forming fabric. The grid is colored by the fluid velocity.

References

[1] M.A. Crisfield, U. Galvanetto, and G. Jelenić. Dynamics of 3-d co-rotational beams. *Computational Mechanics*, 20:507–519, 1997.

[2] J.P. Van Doormaal and G.D. Raithby. Enhancements of the SIMPLE method for predicting incompressible fluid flows. *Num. Heat Transfer*, 7:147–163, 1984.

[3] GeoDict. `http://www.geodict.com`.

[4] D. Harmon. *Robust, Efficient and Accurate Contact Algorithms*. PhD thesis, Columbia university, 2010.

[5] IBOFlow. `http://www.iboflow.com`.

[6] A. Ibrahimbegović and M.A. Mikdad. Finite rotations in dynamics of beams and implicit time-stepping schemes. *International Journal for Numerical Methods in Engineering*, 41:781–814, 1998.

[7] ISOP. http://www.fcc.chalmers.se/comp/projects/innovative-simulation-of-paper.

[8] S.B. Lindström. Simulations of the dynamics of fiber suspension flows, 2007. Lic. Thesis, Fiber Science and Communication Network, Department of Natural Sciences, Mid Sweden University, Sundsvall.

[9] A. Mark, J.E.S. Oliveira, and B.G.M. van Wachem. A new novel implicit second-order finite-volume immersed-boundary method. In *Int. Conf. on Multiphase Flow ICMF 2007*, pages 9–13, Leipzig, Germany, 2007.

[10] A. Mark, R. Rundqvist, and F. Edelvik. Comparison between different immersed boundary conditions for simulation of complex fluid flows. *Fluid Dynamics & Materials Processing*, 7(3), 2011.

[11] A. Mark and B.G.M van Wachem. Derivation and validation of a novel implicit second-order accurate immersed boundary method. *J. Comput. Phys.*, 227:6660–6680, 2008.

[12] B. Nour-Omid and C.C. Rankin. The use of projectors to improve finite element performance. *Computers and Structures*, 30:257–267, 1988.

[13] B. Nour-Omid and C.C. Rankin. Finite rotation analysis and consistent linearization using projectors. *Computer Methods in Applied Mechanics and Engineering*, 93:353–384, 1991.

[14] C.M. Rhie and W.L. Chow. Numerical study of the turbulent flow past an airfoil with trailing edge separation. *AIAA J1*, 21:1527–1532, 1983.

[15] R.F. Ross and D.J. Klingenberg. Dynamic simulation of flexible fibers composed of linked rigid bodies. *J. Chem. Phys.*, 106(7), 1997.

[16] J.C. Simo and L. Vu-Quoc. On the dynamics in space of rods undergoing large motions - a geometrically exact approach. *Computer Methods in Applied Mechanics and Engineering*, 66:125–161, 1988.

[17] D.E. Stewart and J.C. Trinkle. An implicit time-stepping scheme for rigid body dynamics with inelastic collisions and Coulomb friction. *International Journal for Numerical Methods in Engineering*, 39:2673–2691, 1996.

[18] P. Wriggers. *Computational Contact Mechanics*. Springer Berlin Heidelberg New York, 2006.

[19] S. Yamamoto and T. Matsuoka. Viscosity of dilute suspensions of rodlike particles: A numerical simulation method. *J. Chem. Phys*, 100(4), 1994.

High and Low Speed Fourdriniers: New aspects to consider

J. CECCHINI, J. MUHONEN, A. POIKOLAINEN AND A. PUURTINEN

Metso Paper Inc.
P.O. Box 587, 40101-Jyväskylä, Finland
juan.cecchini@metso.com
jukka.muhonen@metso.com
antti.poikolainen@metso.com
ari.puurtinen@metso.com

ABSTRACT

In this study, a new approach to the Fourdrinier Former has been taken.

A new type of Forming Board, a vacuum assisted (non-pulsating or very low pulsating one) has been introduced combined together with hydraulic headbox. The combination of such tools has granted new possibilities either on high and low speed.

A wide machine speed range has been studied (600-1550 m/min) at pilot scale with vacuum assisted forming board. Compared to traditional forming board, the vacuum assisted forming board allows higher machine speed at higher headbox jet activity without stock jump.

Independently from machine speed, the vacuum assisted forming board allowed to operate at high jet to wire speed differences than those at traditional Fourdriniers equipped with conventional forming board. Continuous drainage pressure takes place over the vacuum assisted forming board and simultaneously applied shear forces create together a paper structure with desired orientation degree. Controlled drainage stabilizes the fiber mat and makes the sheet immune for other shear forces applied on the remaining sections of the former (e.g.: foils pulsations), thus formation remains at excellent level also at high jet to wire speed differences. Other interesting aspects and considerations have pop up from new running approaches.

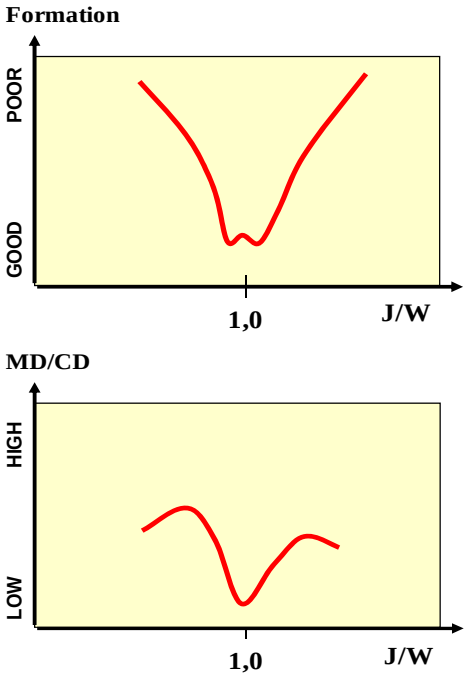

Figure 1. Schematic representation of Beta-Formation and tensile orientation (MD/CD ratio) responses of Fourdriniers equipped with traditional Forming Board as function of jet-to-wire ratio.

REFERENCES

[1] O. F. Sodergren and J. A. Neun. Developments in activity generation on Fourdriniers. Tappi J. Peer review paper, October 2000.

[2] D. W. Bousfield and V. Wildfong. Activity generation on single wires table. 2003 Tappi Spring Technical Conference and Trade Fair.

[3] R. Herzig and D. B. Johnson. Investigation of Thin Fiber Mat Formed and High Velocity. Tappi J. Peer review paper, NO.1, Vol.82, January 1999

[4] J. A. Neun. High Vacuum Dewatering of Newsprint. Tappi J., NO.9, Vol. 79, September 1996

[5] K. O. Räisänen, H. Paulapuro and S. J. Karrila. The effect of retention aid, drainage conditions and pretreatment of slurry on high vacuum dewatering: a laboratory study. Tappi J., NO.4, Vol. 78, April 1995.

[6] M. Odell. Customizing Roll and Blade Formers for different applications. The 10th Valment Paper Machine Days, 1996.

[7] A-L. Erkkilä, P. Pakarinen and M. Odell. Sheet Forming Studies using layered orientation analysis. CPPA Annual Conference, 1996.

[8] S. Zahrai, F. H. Bark and B. Norman. An analysis of blade dewatering in a Twin-wire paper machine. Journal of Pulp and Paper Science, Vol. 23, September 1997

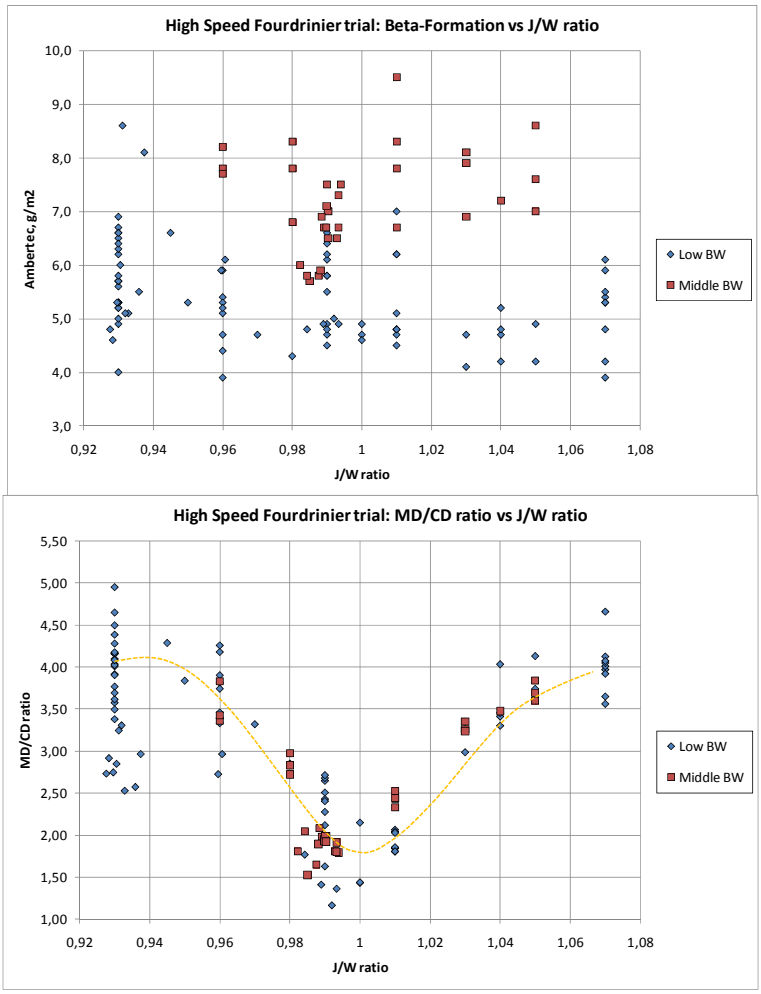

Figure 2. Results of Beta-Formation and tensile orientation (MD/CD ratio) responses of Fourdriniers equipped with Vacuum Assisted Forming Board as function of jet-to-wire ratio.

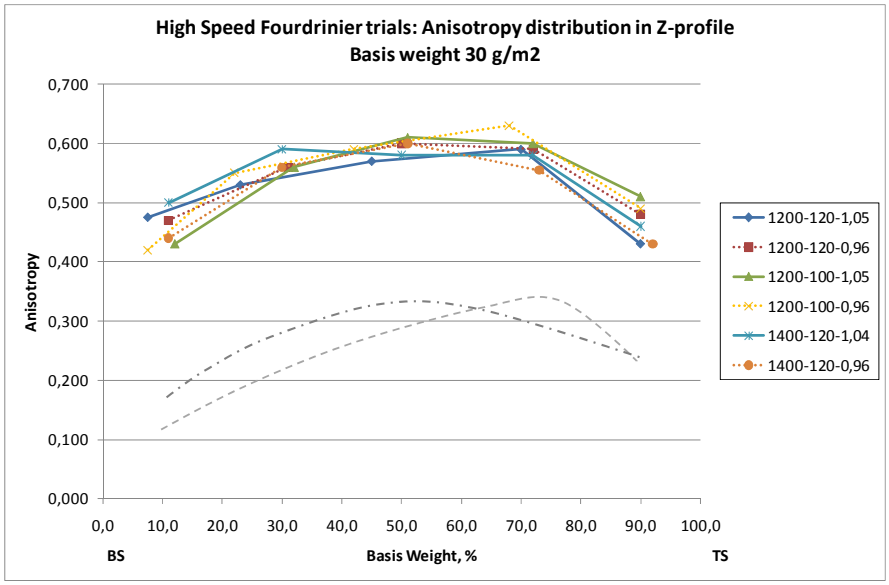

Figure 3. Anisotropy distribution in Z-profile (Fiber Layer Orientation) responses of Fourdriniers equipped with Vacuum Assisted Forming Board (coloured lines) as function of jet-to-wire ratio in rush and drag conditions. The dashed grey lines give a typical anisotropy response from Fourdrinier equipped with traditional forming board

FiberXPress - A new device for evaluating the press dewatering ability of furnish

S. PLOBNER[1], A. EICHLER[1]
J. KRITZINGER[2] and W. BAUER[2]

[1]Voith Paper GmbH
Linzer Straße 55, A-3100 St.Pölten
andreas.eichler@voith.com
[2]Institute for Paper, Pulp and Fiber Technology,
TU Graz, Kopernikusgasse 24/II A-8010 Graz.

Keywords: pressing; laboratory; dewatering

ABSTRACT

A new device and method for characterizing of furnish with respect to its dewatering characteristics in the press section of a paper machine is presented. Unlike other methods not only a single value is used for the furnish characterization, but rather the development of the dry content over time is recorded. Pressing parameters as pressure profile, temperature, dwell time, grammage can be varied within a wide range.

Several examples for the impact of pressure, dwell time, incoming dry content and grammage on the dry content for a variety of different furnishes are presented and discussed.

1 Introduction

The dry content at the exit of the press section is one of the most important but at the same time least known key performance indicators of a paper machine. It determines the amount of steam necessary for drying the paper and is crucial for the wet web strength at the entrance of the drying section.

The maximum dry content that can be achieved is determined by many factors. Among the most important are: the press arrangement, the linear nip loadings, the speed of the paper web, the grammage of the paper, the dry content of the web at the entrance of the press section, the web temperature, press felts and chemistry.

FiberXPress (see Fig. 1) is a measuring device that was designed to characterize the dewatering process of a given furnish by taking into account most of these parameters. An arbitrary pressure profile is applied on a furnish sample. During the pressing process the water which is pressed out of the furnish sample is weighed continuously in order to determine the actual dry content at every time step during the process.

Hence, in contrast to conventional methods (water retention value,…) not only a single point along the dewatering process (final dry content) is chosen for the characterization, but rather the whole dewatering curve can be recorded.

In order to operate on time scales which are easily accessible the sample grammage is increased to 1000-3000 g/m². In that way the flow speed of the water is reduced according to Darcy's law and the dewatering process becomes observable.

In this paper a new method is introduced and applied to the investigation of the dependencies of various pressing parameters on dry content for several furnishes. After a description of the laboratory device in the next chapter, follows a brief theoretical discussion on pressing parameters in general and their representation in FiberXPress. In the main part of the paper (chapter 4) the influence of several pressing parameters on dry content is presented and discussed. Most results were taken from two diploma theses [1, 2].

2 Technical Description

2.1 The Apparatus

In order to fill a big gap in furnish quality testing, a pneumatic press for furnish characterization regarding press dewatering was designed (see Fig. 1); partly by combining earlier approaches [3,4], partly by new functionalities. The pressing device is operated with pressurized air at 6 bar (4). The pressure is amplified by a pneumatic cylinder (1), so that in the sample chamber (2) (filling volume: 200 ml; diameter: 50 mm) a pressure of up to 10 MPa can be applied onto the furnish sample. The water pressed out of the furnish passes a wire, which holds back fibers and fines. This wire ensures also a lateral flow towards the small syringe through which the water flows and is collected on a scale (5,6). After the pressing process, the moist pellet is taken out of the device, weighed and dried in an oven. From the mass balance between the squeezed out water and the oven dry fiber mass the dry content of the pellet throughout the pressing process can be derived. The whole measuring process is controlled from and recorded with a MS Excel spreadsheet with embedded VBA code.

Besides its basic functionality FiberXPress is equipped with additional features: computer aided control of the pressure transducer (3) allows the simulation of arbitrary pressure profiles over time. The pressing chamber can be heated by a heating clamp (7). Finally, a potentiometric displacement transducer (8) was integrated with which the thickness of the sample can be measured during the pressing process and hence information on compressibility and spring-back behaviour of a furnish can be derived.

2.2 The Measurement Procedure

All measurements presented in this paper were performed at room temperature (21°C). The fiber suspension is filled into the pressing chamber at a

consistency of around 1-4% and dewatered at low pressure (0.05 MPa) up to a typical dry content at the entrance of the press section (20 %) after which the pressure was increased and the actual measurement starts. For all results reported in this paper a rectangular pressure pulse (constant pressure over time) was used for simplicity and convenience.

The furnishes used throughout this study are additionally described by their water retention value (WRV) [10] and their Schopper-Riegler (SR) value.

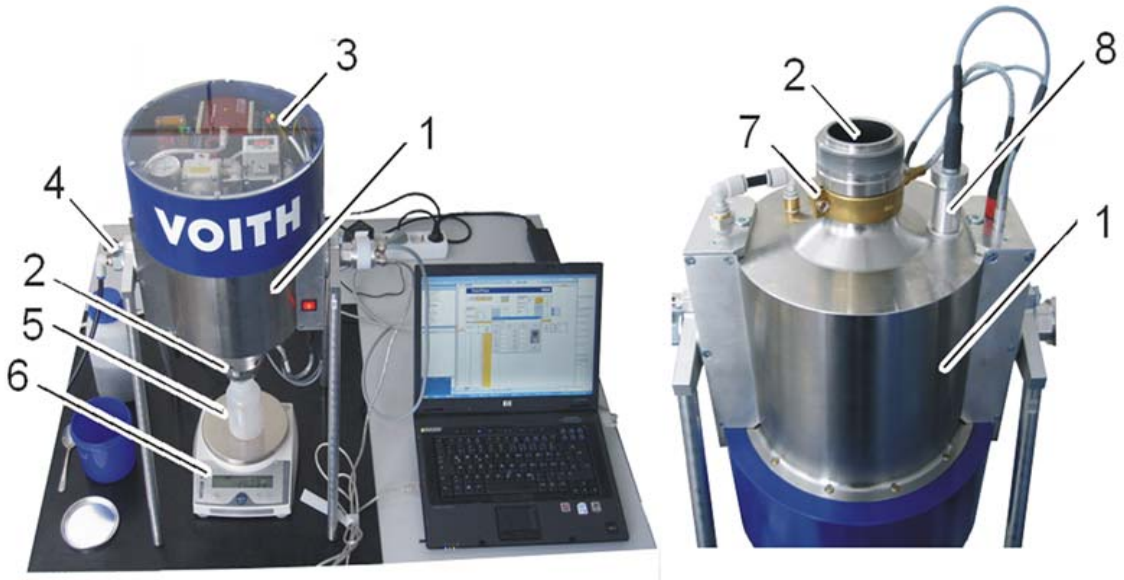

Figure 1. Measurement Setup of FiberXPress: FiberXPress (1), pressurized furnish chamber (2), pressure controller (3), pressurized air (4), water collector (5) scale (6), heating clamp (7), displacement transducer (8).

3 Theory

3.1 Parameters influencing the press process

The main quantity in the description of the pressing process is traditionally the dry content or consistency of the paper web *dc* (%), defined as the solid mass fraction of the total mass of the sheet. Another related quantity, which is closer connected to the amount of water in the sheet is the so-called moisture ration *mr*, telling the water mass per kg solids. Both quantities are related by

$$mr = (1 - dc) / dc \,.$$

The wet pressing process itself is determined by a number of physical parameters, some of which can be influenced by the paper maker, others are determined by the product or the press section.

The *pressure profile* p(t) is determined by the geometry of the nip and the linear-load, partly as well by the hardness of the roll covers, press felts, etc.

The *dwell time* t (s) is determined by the length of the nip and the machine speed

Time and pressure are often combined in their impact on the dewatering process in the *press impulse* $I = \int p(t)dt$. In the case of a constant pressure this reduces simply to $I=p \cdot t$. This quantity is directly related to the linear load *LL*(N/m) of the press and the machine speed *v*(m/s) by $I=LL/v$.

Grammage W (kg/m²)

The *Temperature T* influences mainly the viscosity of the water. However there are probably effects beyond that as well, mostly related to a change in the fiber properties itself [5].

The *dry content* before the nip dc_S.

The press felt has a major influence on the pressing process too. A positive one in the sense that it transfers the pressure onto the paper and takes the water which is pressed out of the paper, but also a negative one: since a small portion of the water that was pressed out of the paper is transferred after the nip from the felt back into the paper, an effect called *rewetting*. In the easiest approach this fact is accounted by a constant rewetting term R in kg water per m².

Further influencing parameters are e.g. roll surfaces and covers or chemistry.

3.2 Representation of pressing parameters in FiberXPress measurements

In FiberXPress most of the parameters can be simulated in a realistic manner suitable for the description of a press section:

The dry content of the pellet immediately after the pressing process is determined in the usual gravimetric way, by determining the fraction of the wet and the oven dry weight of the pellet. The dry content at any time during the pressing process is calculated based on this value and the water mass pressed out.

The dry content before the press is - at the beginning of the measurement - estimated on the basis of the consistency of the furnish at filling and the squeezed out water. At the end of the measurement, it is calculated as well on the basis of the dry weight after pressing. (The retention of solid matter is assumed to 100 %, soluble substances are ignored)

The temperature of the pressing chamber can be adjusted by the heating clamp between room temperature and about 80°C. Temperate effects can be taken into account in FiberXPress, but are not reported in this paper. For some results see [1,5].

The pressure is applied pneumatically and the pressure profile can be freely modeled over time. However, in most cases, a simple rectangular profile is the most adequate one.

A compromise had to be made only regarding grammage and dwell time. In reality typical paper-weights are between 50 g/m² and 200 g/m² with residence times in a press nip of below 1s. However, in these short time intervals, it is impossible, to observe the pressing process over the time. In order to enlarge this time span, the basis weight is increased significantly (~1000-3000 g/m²) which moves the time window comparable to the paper machine pressing process into the range of 5-100 s. Consequently, also typical press impulses have to be stretched by 1-2 orders of magnitude compared to the paper machine. A more analytical description of the consequences is given below.

The influence of the felt is deliberately neglected, in order to characterize the furnish alone and not the furnish/felt combination. However, the use of a wire in the device induces similar effects: as it is responsible for the pressure distribution over the paper surface and for rewetting.

Finally, chemical or furnish related effects can of course be investigated with FiberXPress.

3.3 Grammage dependence on pressing

The central and most used equation to describe press dewatering is Darcy's law, which was designed to describe the flow through porous media, mostly applied in geology for water travelling through soil or sand:

$$\frac{q}{A} = -\frac{k}{\mu} \cdot \frac{\Delta P}{L}$$

The equation describes how a volumetric flow q (m³/s) passes through a cross sectional area A (m²), driven by a pressure drop of ΔP (Pa) over a distance L (m). The proportionality between resulting flow and driving pressure drop is the permeability k (m²) divided by the dynamic viscosity μ (Pa s).

Transferred to wet pressing, the term q/A divided by the water density ρ describes the dewatering speed of the paper web in kg/m² per second. This dewatering speed induces a change in moisture ratio (dryness), which is proportional to the basis weight: $q \sim W \Delta mr \sim -W \Delta dc$.

The pressure drop ΔP on the right hand side is applied by the press nip, while the distance L is the actual thickness of the paper and hence correlates with the basis weight of the sheet as well.

These two dependencies on basis weight lead to a quadratic relationship between the change in dry content with basis weight: $\Delta dc \sim -1/W^2$

However, some shortcomings in this transfer are more or less obvious:

- Water does not only travel through the paper web, but water is released there, by pressing it out of the fiber walls.
- The permeability changes during the pressing process, since the paper web gets dryer and compressed.
- Also the thickness changes significantly during the pressing process, since water leaves the sheet.
- The dewatering process is determined by at least two different permeabilities, which differ by orders of magnitude: water flow through the paper web and water flow out of the fiber walls. The ratio of these two contributions changes throughout the pressing process.

Nevertheless, the equation describes the dewatering process in a satisfying manner and the absence of better descriptions explains its general application in almost all models [6,7,8].

4 Parameter Dependency

4.1 Dwell Time

The development of the dry content over dwell time comes as a direct result of a single measurement. This is shown in Fig. 2 for DIP (WRV=111.8, SR=44) at four different pressure levels (1.5, 3.0, 6.2, and 9.0 MPa). The well-known pseudo logarithmic development of the dry content with time can be observed for each of the curves [9]. In that way a unique fingerprint of a furnish can be derived, which characterizes completely the dewatering potential of the furnish for any press section. While for other techniques only the dry content after the pressing or centrifuging event can be used for the fiber characterization, with FiberXPress it is possible to monitor the evolution of the dry content over time.

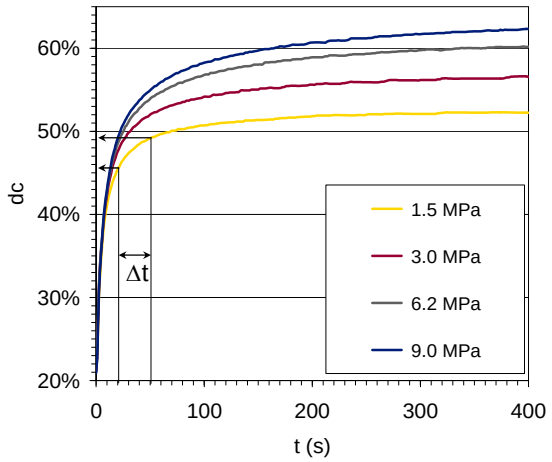

Figure 2. Development of dry content (dc) over dwell time (t) after applying a constant pressure (1.5, 3.0, 6.2 and 9.0 MPa); 1500 g/m², DIP.

4.2 Incoming Dryness

Although in this section the influence of the incoming dry content, i.e. the dry content before press shall be discussed, we will again deal with the same measurements as already discussed above. However, this time we will use a different way of representation. Since a single measurement contains the continuous result over the whole time span, a simple transformation leads to another valuable representation of the measurement results, which shows the dependency on dry content before press (Fig. 3).

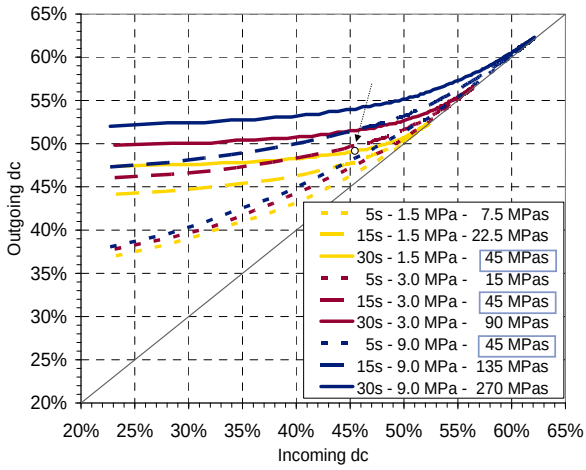

Figure 3. Dry content (outgoing dc) after applying a given pressure (1.5/3.0/9.0 MPa) for a certain time (5/15/30s) vs. dry content before the pressing event (incoming dc). The arrow marks the point corresponding to the time interval indicated in Fig. 2

This is possible by the following procedure: All pairs of points from the curves in Fig. 2 with the same vertical distance (dwell time) are connected by the same pressing event which transforms the left point (lower dry content) into the right one. Hence, by drawing - for a given vertical time distance Δt - the dry content of the right end versus the dry content of the left end, a curve is derived describing the dependence of the outgoing dry content from the incoming dry content for that specific impulse, determined by the product Δt×pressure. The procedure is illustrated for 1.5 MPa and Δt=30s in Fig. 2, resulting in the point 45.5/49.0% in Fig. 3 (small circle, marked by an arrow). Fig. 3 shows the result of this procedure for time intervals of 5/15/30 s and pressures of 1.5/3.0/9.0 MPa. The outcome compares well to what is known from the literature for the relationship between dryness before and after press [9]. For longer dwell times, the curves are characterized by a rather long horizontal part, which means that the final dry content is independent of the incoming dry content. Shorter dwell times move the curves closer to the x=y line, which means that a certain advantage in dry content from before the press can be carried through the press and results in a similar advantage after the pressing event.

The shape of these curves gives a good insight into the behavior of a given furnish in a press under various conditions. As an example we pick out the three lines representing different pressure events of same press impulse (45 MPa s). It can be seen, that for low incoming dry contents the pulses with low pressure, but high pressing time are most efficient (1.5 MPa for 30 s), while the situation gets inverted for high incoming dry contents, where first the 3 MPa/15 s and finally the 9 MPa/5 s curve lead to the highest dry content. For practical purposes, this means that an optimum pressure profile should start with low pressure and increase the pressure gradually with dry content. This is e.g. realized in the shoe profile of a shoe press. However, the ideal shape depends on the furnish. We will discuss this phenomenon in more detail below.

4.3 Pressure

In order to make an analysis of the pressure dependence of the dry content easier, the measurements from above are now presented in a third way. The dry content reached after a certain dwell time (starting again from 20 %) is plotted against the applied pressure (Fig. 4). While the curves for short dwell times are quite flat, the curves for the longer dwell times exhibit a pronounced increase with pressure. This reflects the fact that at the beginning of the pressing process the pressure is not that important; dewatering is dominated by the velocity of the water flowing out of the fiber web. However, at increasing dry content, the structural pressure has to be overcome in order to dewater the web and higher pressures become more and more important. This general behavior can be described quite well by a potential law (comp. e.g. [8]), as can be seen by the dashed lines in Figure 4: $dc(p) = dc(p = 1\text{MPa}) \cdot p^{\alpha}$, where the exponent α increases with dwell time. In the actual case $\alpha = 0.022 \cdot \ln(t) - 0.022$ would be an

appropriate description of the exponent for different dwell times t.

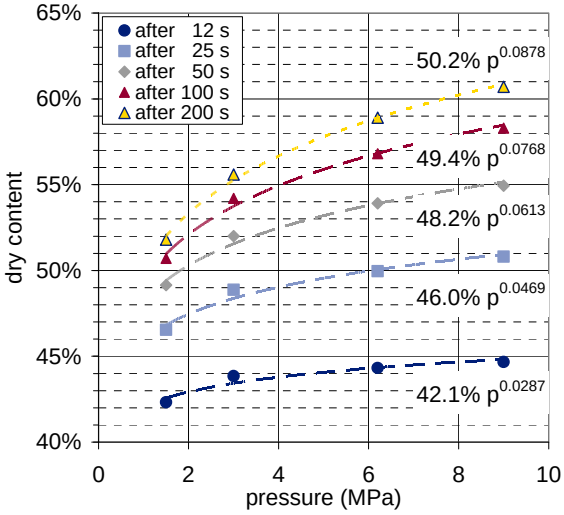

Figure 4. Variation of dry content with pressure in MPa for selected dwell times. Dashed lines represent analytical fits to these data (comp. equations).

4.4 Press Impulse

For a rectangular press impulse, as it is used throughout the studies presented in this paper, the press impulse is given as the product of pressure and dwell time; hence, it increases during the measurement linearly with time. In Fig. 5 the evolvement of the dry content with press impulse at three different pressure levels (3, 6 and 9 MPa) is shown for four different furnishes. Qualitatively all furnishes behave in a similar way: in the first regime, pressing with high pressure is the least effective at a given press impulse. As dry content increases, the low pressure curve starts to level out, while the curves for higher pressure levels reach higher dry content. However, the crossing points and the pressure dependence are quite different for the investigated furnishes:

The LF+DIP mixture exhibits a very slow dewatering due to its high refining (65SR) and high water retention value. The curves do not cross at all within the range displayed here and the dewatering depends almost exclusively on time (and not on pressure): e.g. after 30 s pressing (points marked with a long arrow) the dry content is always ~39%. Similarly, after 40 s (points marked with a short arrow) the dry content is around 40-41%. The 9 MPa curve is always slightly slower, probably due to a pressure induced reduction of the permeability.

For all other furnishes, the curves cross within the first 400 MPa s: e.g. for DIP the 6 MPa curve crosses the 3 MPa curve after 100 MPa (50% dry content) and at much higher longer press impulse (350 MPa s, 53%) finally the 9 MPa curve takes the lead. For OCC the picture is very similar, but now the difference between 6 and 9 MPa is much smaller and the crossings happen earlier (~120 and 200 MPa s).

The dewatering characteristics for the unbleached kraft pulp (UBKP) can almost completely be described by the press impulse alone: the three curves do almost overlap in this representation. Only in the first 50 MPa s the low pressure curve gives up to 5% better dewatering.

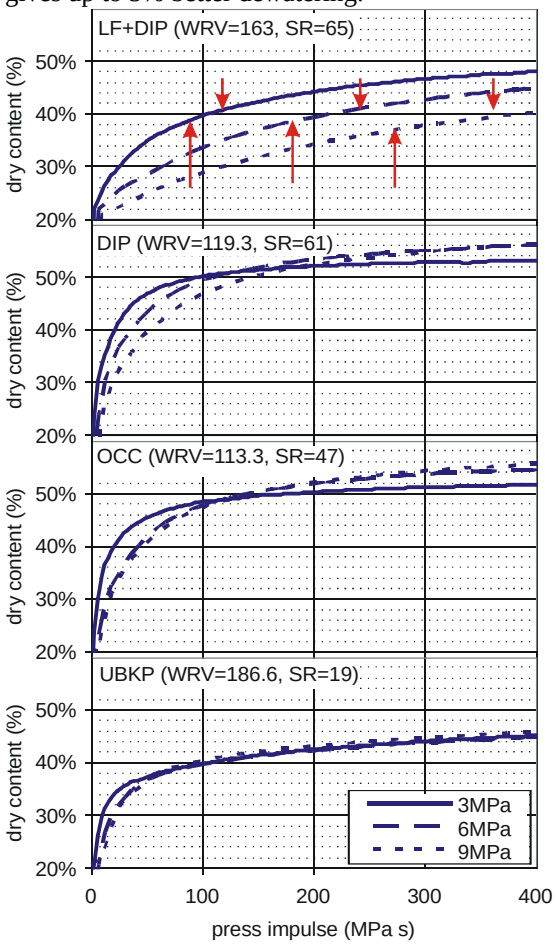

Figure 5. Dry content vs. press impulse for 4 different furnishes. Measurements were obtained for 1000 g/m² at 3 different pressure levels: 3 MPa (full lines), 6 MPa (dashed lines) and 9 MPa (dotted lines). Long (short) arrows for L+F furnish denote points after 30 s (40 s) of pressing.

4.5 Grammage Dependency

The high grammage regime which can be investigated in FiberXPress is beyond what is typically produced on paper machines. This is the price that has to be paid for making the dewatering observable. However, trends of the dewatering properties with basis weight can help to bridge the gap down to more realistic weights.

The LF+DIP mixture was investigated at different refining levels. For each mixture measurements were performed at 6 grammages between 750 and 3000 g/m². In the upper panel of Figure 6 the time required to reach 35% dryness (starting again from 20%) with a pressure of 6 MPa is shown. Together with the data points, analytical curves $t=t_0 \cdot W^m$ are drawn, which were fit to the data points. t_0 can be

interpreted as time required to dewater a sheet with 1 g/m² from 20 to 35% dryness, while the exponent *m* describes the dependence on the basis weight W. As expected from Darcy's law, the exponential is around 2, while the prefactor decreases from 10 µs (80 SR) to 1 µs (46 SR). The dewatering of the 29 SR furnish was too quick for accurate measurements and good data quality.

The lower panel of Fig. 6 shows the time required to increase the sample dryness further up to 40%. Although the amount of water is now six times less than before, the dewatering times are quite similar. However, at this higher dry content, more water has to be pressed out of the fiber walls than out of the fiber mat and hence the slope of the curves in the log-log representation (exponent m) is lower for all curves.

In both cases, the dependency on grammage follows over a wide grammage range strictly the analytical representation, which makes an extrapolation into the low basis weight range possible.

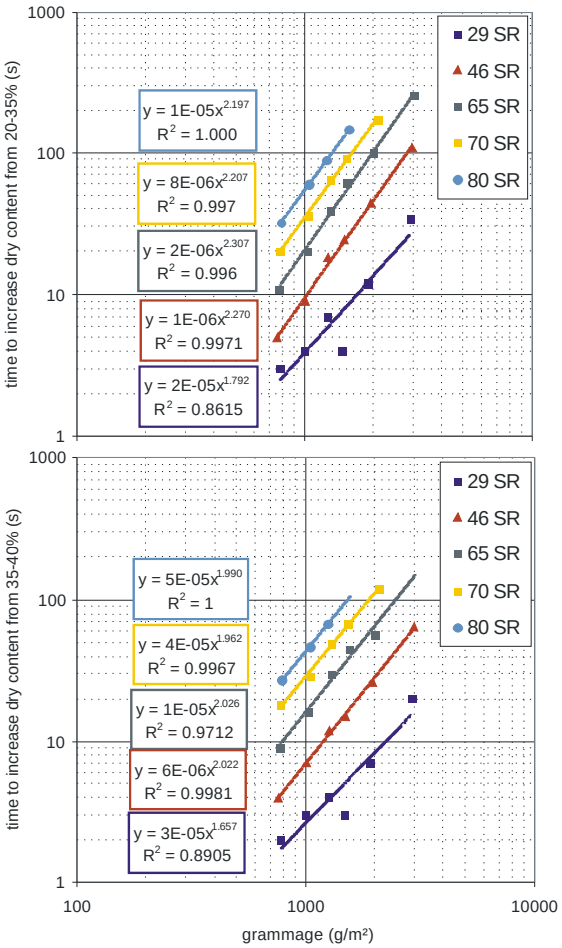

Figure 6. Dewatering times for reaching a certain dry content level at pressure of 6 MPa as function of grammages for various refining levels of a 40% long fiber + 60% DIP mixture. Upper panel: 20% to 35% dryness, lower panel: 35%-40% dry content.

In Fig. 7 a comparison of 4 different furnishes is given (the same as discussed above for the press impulse), this time with focus on the dependence on basis weight. The Figure shows the moisture ratio that was reached after 12 s, 50 s and 200 s.

Similar to before, the furnishes exhibit all a qualitatively similar behavior, although in different degrees:

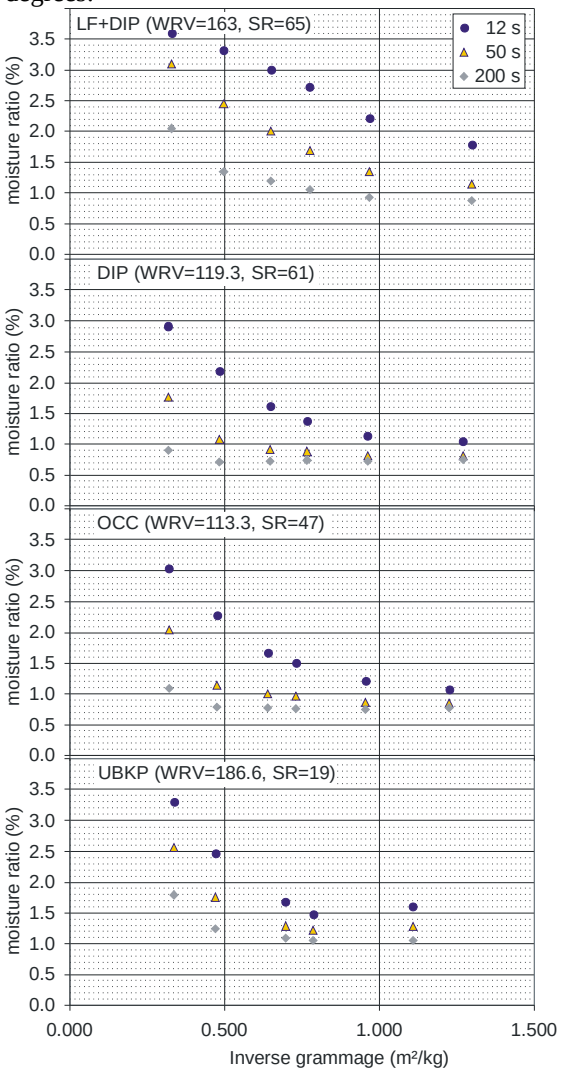

Figure 7. Dry content reached at 6 MPa pressing after 12 (blue circles), 50 (grey diamonds) and 200s (yellow triangles) for four different furnishes as a function of grammage.

After short dewatering times (12 s) the points have just left the initial mr=4 (dc=20%). The higher the basis weight, the closer the points come towards mr=4, which would be reached for infinite grammage on the left hand side of the chart. With increasing dwell time, the furnishes reach asymptotically their limited consistency: lighter basis weights earlier, heavier sheets later.

The two extremes can be found for the 12 s at the LF+DIP (65 SR) mixture and the 200 s curve of the DIP: in the first case, (LF+DIP, 12s) not much has happened after 12 s of pressing. All sheets have lost approximately the same amount of water, leading to an almost linear characteristic of the curve. The other extreme can be seen in the 200 s curves of the fast dewatering furnishes (e.g. DIP). There the

maximum dry content for the applied 6 MPa (mr=0.75, dc=~58%) is reached for almost every grammage; only the 3000 g/m² sample is still slightly wetter. In this case the dewatering starts to get pressure limited - no further water can be squeezed out with 6 MPa.

All other curves represent a stage somewhere in between these two extreme cases

5 Comparison to Water Retention Value

Finally we want to close with a comparison with the established water retention value (WRV) [10]. The WRV is obtained by centrifuging a certain amount of furnish for a well defined time. The final resulting moisture ratio of the sample after this procedure is called WRV. The pressure level resulting from the centrifugal forces is much lower than typical press pressures, which is compensated by comparably long residence times in the centrifuge, so that in most cases something like a limiting dryness for low pressures is obtained.

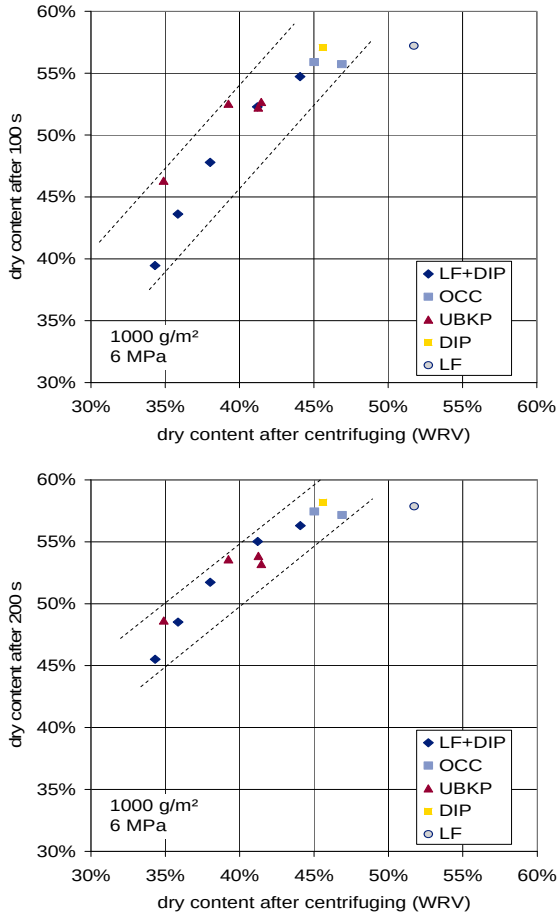

Figure 8. Correlation between dry content after FiberXPress dewatering of several furnishes after 100 s (upper panel) and 200 s (lower pannel) with WRV (converted into a dry content).

However, in some cases, especially for slowly dewatering furnish, it can happen, that the final value is not reached at the end of the process. Hence, the WRV value gives an estimate on the dewatering potential, but cannot account for the much more complicated facets of the furnish. Fig. 8 shows a comparison between the WRV-value and the dry content after pressing the furnish (1000 g/m²) for a certain time (100 s upper panel / 200 s lower panel) at 6 MPa for 13 different furnishes. Clearly a correlation between the values can be seen. For longer dwell time (200 s) the correlation becomes better in two respects: first the width becomes smaller, second the slope of the correlation becomes approximately one. In the second panel the slowly dewatering furnishes on the lower left end of the diagram could still improve their dryness significantly.

However, the remaining width of the distribution still remains about 5% dryness. This is comparably to a correlation Busker found for the correlation between WRV and a roll nip press [9].

A last example in Fig. 9 shows the dewatering characteristics (1000 g/m², 6 MPa) of two furnishes (BKP and LF+DIP) with almost the same WRV. While both reach the same dry content after about 100 s in FiberXPress, there dewatering speed differs significantly; e.g. after around 10 s the two curves differ by about 5% dryness. On the other hand, the LF+DIP will probably reach significantly higher dryness for longer dwell time than the BKP (compare also the corresponding points in Fig.8 at around 41% dryness after centrifuging (WRV)). This difference in dewatering speed is reflected by the SR-value as well.

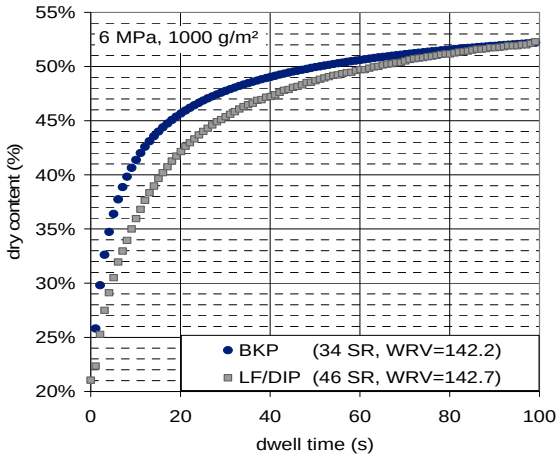

Figure 9. Dry content over dwell time curves for two furnishes with almost identical WRV values.

6 Summary

Summarizing, with FiberXPress a new laboratory technique could be established, which enables a very detailed characterization of the pressing process for a given furnish, which goes far beyond the possibilities of conventional methods.

REFERENCES

[1] C. Wendt. Rohstoffcharakterisierung hinsichtlich Pressenentwässerung mittels einer pneumatischen Presse (in German). Diploma Thesis, Fachhochschule München (2007).

[2] S. Plobner. Rohstoffcharakterisierung hinsichtlich Pressenentwässerung mittels einer pneumatischen Presse sowie die Ermittlung charakteristischer Parameter zur Beschreibung des Entwässerungsverhaltens (in German). Diploma thesis, Graz University of Technology (2011).
[3] G. Carlsson, T. Lindström, C. Söremark. Expression of water from cellulose fibers, In Fiber–Water Interactions in Paper-Making, Trans. VIth Fund. Res. Symp. Oxford, 1977, (Fundamental Research Committee, ed.), 389–402, FRC, Manchester (1977).
[4] G.V. Laivins, A.M. Scallan, A.M. Removal of water from pulps by pressing. Part I: Inter- and Intra-wall water. Tappi Engineering Conference 1993, 741-748 (1993).
[5] A. Eichler, C. Wendt. FiberXPress - A new device for evaluating the press dewatering ability of furnish. Papermaking Research Conference, Kuopio (2009).
[6] R.J. Clos, L.L. Edwards, I. Gunavan. A limited consistency model for pulp dewatering and wet pressing; *Tappi Journal*, **77**: 179 (1994).
[7] J. D. McDonald, R.J. Kerekes, R.J.; A decreasing permeability model of wet pressing with rewetting. *Tappi Journal* **78**(11), 107 (1995).
[8] G.H.J. Holstege. Press dewatering new life for an old concept. *Tappi Journal*, **81**(6) 115, (1997).
[9] The Paper Machine Wet Press Manual, Ed. Reese, R.A., Chapter 8, Tappi Press, Atlanta (1999) and references therein.
[10] Verein der Zellstoff- und Papier-Chemiker und -Ingenieure, Bestimmung des Wasserrückhaltevermögens von Zellstoffen. Merkblatt IV/33/57 (1957).

Simulation of Press Dewatering

STEFAN PROBST-SCHENDZIELORZ[1],
STEFAN RIEF[2], ANDREAS WIEGMANN[2],
HEIKO ANDRÄ[2] AND
MATTHIAS W. SCHMITT[1]

[1]Voith Paper Fabric and Roll Systems, St. Pöltener Str. 43, 89522 Heidenheim, Germany
Stefan.Probst-Schendzielorz@voith.com
[2] Fraunhofer ITWM, Fraunhofer-Platz 1, 67663 Kaiserslautern, Germany
Stefan.Rief@itwm.fraunhofer.de

Dewatering of pulp in a paper machine is a well established process. Nevertheless, it is far from being fully understood. One of the major steps in this process is the mechanical dewatering within the press section. It is achieved by applying large mechanical loads on the wet paper web while at the same time providing an escape route for the excess water. The quality of this process is influenced by many parameters.

Besides the press nip parameters like pressure, roll diameters and press type (roll or shoe press), also other factors contribute to the mechanical dewatering performance. Among these factors the press felts, that transport the paper web through the press nip, are a major influence. Besides dewatering pulp, press felts govern also the papers smoothness and printability.

Two-scale simulation

We study the dewatering process in the press nip with particular attention to different felt designs using a two-scale simulation approach [1].

Hence we analyse and simulate the two major parameters for press felts which influence the dewatering of the paper web: the flow properties, the rheological properties and the combination of both on the felt scale and on the nip scale.

Press felt simulation

On the micro-scale (or felt-scale, see Fig. 1) we simulate the flow through press felts in machine direction and through direction. The simulation details reveal the flow properties of individual felt layers. The analysis is performed on 3D scans of existing felts and is also applicable to virtually created press felt structures, i.e. it does not require manufacturing the felt first.

The dynamical rheological behaviour of felts is analysed with a state-of-the-art measurement procedure. The resulting viscous-elastic model predicts the dynamics of press felts for arbitrary pressure impulses.

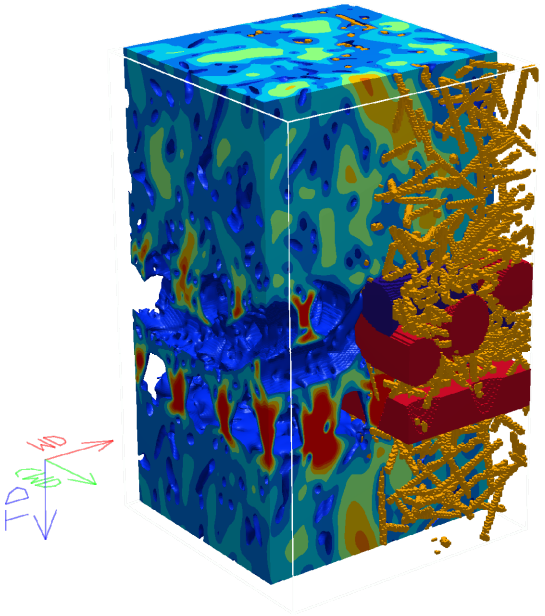

Figure 1. Simulated flow velocity of water through a virtual press felt structure.

Nip simulation

On the macro scale (or nip-scale, see Fig. 2), these simulated properties combined with other press parameters are used to simulate the dewatering process in the press nip.

The simulation predicts the saturation of the flow in the roll cover-felt-paper sandwich, as well as the deformation of these different layers. On the one hand, it yields the dry solid contents for different

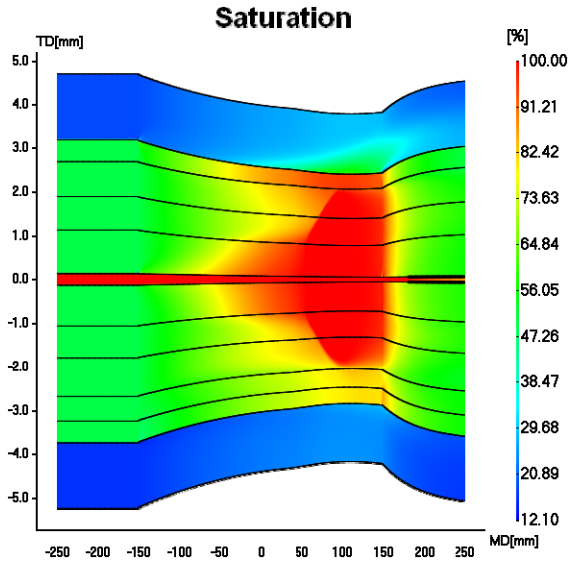

Figure 2. Simulation of paper dewatering in a shoe press nip. The felt, the paper and the roll cover are modelled by 12 different layers. The middle layer represents the paper. Before the press, the simulated dry solid content of the paper is 24 % and after the press, the dry solid content is 47 %.

felt designs. The dry solid content is used to differentiate between felts without requiring expensive trials on paper machines. On the other hand, simulations give a better understanding of the process of wet pressing itself. This will help to optimize all aspects of the paper dewatering process in future developments.

We present the micro-scale and the macro-scale methods of this multi-scale simulation approach. The results for different press felt designs are compared with laboratory data and paper machine measurements.

REFERENCES

[1] S. Rief Nonlinear Flow in Porous Media; PhD thesis, University of Kaiserslautern, (2005)

Modeling and optimization of paper drying for optimum strength properties

MOHAMMAD HASSAN EKHTERA, KLAUS VILLFORTH and SAMUEL SCHABEL

Chair of Paper Technology and Mechanical Process Engineering, Technische Universität Darmstadt
Alexanderstr. 8, 64283 Darmstadt, Germany
ekhtera@papier.tu-darmstadt.de

Keywords: Strength Properties, Strain, Stress, Elastic Modulus, Drying, Free Draw, Bonding

ABSTRACT

Mechanical forces acting on the paper web during drying have a big effect on the final quality properties of paper like strength properties. The development of the web's mechanical properties in the paper machine is essential for the quality of packaging papers and graphic papers. At the end of this research a scientific model will show the relationship among the most process variables, especially drying in free draw, inter-fibre bonding and mechanical properties.

1 STRESS-STRAIN BEHAVIOR OF PAPER DURING DRYING

The stress – strain behaviour of paper changes with moisture content. At low moisture content, paper is stiff and brittle. It fails at low strain values. At high moisture content during drying, the elastic modulus and stress levels are lower than at low moisture content. At the molecular level, the effect of moisture on the mechanical properties paper comes from the softening of the hemicellulose. Fibres and especially inter-fibre bonds gradually loose mechanical rigidity as moisture increases [1,2,3,4,5,7].

This work shows experimentally and theoretically how drying (or moisture) influences the elastic modulus of fibres and paper. At low moisture content below approximately 5 %, the elastic modulus depends only very weakly on the moisture content [1,2,3,4,5].

In wet paper, the elastic modulus and tensile strength are much lower than in dry paper. The elastic modulus increases with increasing dry content [1,2,3,4,5].

The elastic modulus is an important property because it controls the behaviour of paper in printing and converting. For example, the elastic modulus determines how web tension depends on the speed difference in open draws in printing presses. The elastic modulus can also be an indicator of other paper properties such as various strength and dimensional stability. The relationship between the elastic properties and structure of paper is much better understood than other mechanical properties. Elastic modulus is sensitive to the drying shrinkage and wet straining of paper and fibre orientation [1,2,3,4,8].

In this work the elastic modulus will be used as a very good indicator for showing properties of paper during drying.

2 INFLUENCING FACTORS ON INTER-FIBRE BONDING

2.1 Beating

Unbeaten fibres can not form strong paper, at least if not mixed with other pulps. The concept of fibre bonding, ever since the beginning of papermaking history, is related to development of strength properties. Beating clearly promotes inter-fibre bonding. Contact between fibres increases, and the surface of fibres changes physically. In addition to this, refining increases bond strength. The most significant effect of beating is an increment of flexibility through delamination, swelling, and dislocation within individual fibres. This permits adjacent wall segments and fibres to mould and conform to one another during pressing and drying [1,6,7,8,12,19].

Interaction effect of drying conditions and beating on inter-fibre bonding and strength of paper is not very clear. Therefore this work tries to find a good model for describing relation among them.

2.2 Fibre fines

In mechanical pulps, the fines content has a strong influence on the structure and properties of fibre network. The primary effect of fines on the paper network is an increase in density, which results in an increased number of bonds and in that way, improves tensile strength properties of the sheet [6,8,19,20,21].

Different amount of fines are used in this research for the evaluation of fines effects on inter-fibre bonding and strength of paper during drying. It is assumed that fines act as a bridge among fibres, this work investigates the accuracy of this belief.

2.3 Additives

Additives that affect inter-fibre bonding positively are high molecular weight, hydrophilic colloids, either natural or synthetic, such as starch, proteins, vegetable gums and water-soluble resins. They act by adsorption onto fibre surfaces, where fibre-to-binder-to-fibre bonds can evolve and contribute to bond and sheet strength [8,21].

Addition of dry strength chemicals is an ideal way of improving inter-fibre bonding and tensile strength of paper but the optimum amount of additives for different furnish of pulp is not very

clear, so this work tries to investigate different amount of additives during variable drying conditions for finding relation among them and finally increasing quality of paper.

2.4 Drying stresses

The mechanical properties of bonds and bonded fibre segments are closely coupled with the drying stresses that act across every inter-fibre bond. During drying, the shrinkage of component fibres causes contraction of the whole fibre network and creates internal stresses in the paper. Fibre shrinkage influences various properties of paper, such as sheet structure, mechanical properties, and hygroscopic behaviour. Drying of previously undried virgin pulp fibres under axial tension increases considerably the tensile strength and decreases the breaking strain. Laboratory experiments have even shown that an 8% increase in strain from -4% (shrinkage) to +4% (stretch) can yield a tensile stiffness five times the original [1,3,8,9,10, 11,13,19,22].

3 METHOD

The draws are also responsible for web breaks in the paper machine, which diminish the productivity of paper mills. The adjustment of web tension in free draws for best mechanical properties at a tolerable frequency of web breaks is very important [4,10].

The problem is strongly related to the shrinkage of fibres in the paper web while drying in the drying section after dewatering in sheet forming section and after pressing. Groups of steam heated cylinders are used to evaporate the water in the web. The web is guided by fabrics to insure a good contact with drying cylinders and to prevent web deformation. At free draws between the drying groups, the web is elongated in machine direction (MD) and shrinks in cross machine direction (CD) [6,9,14,15]. **Figure 1** illustrates a free draw between two drying cylinders.

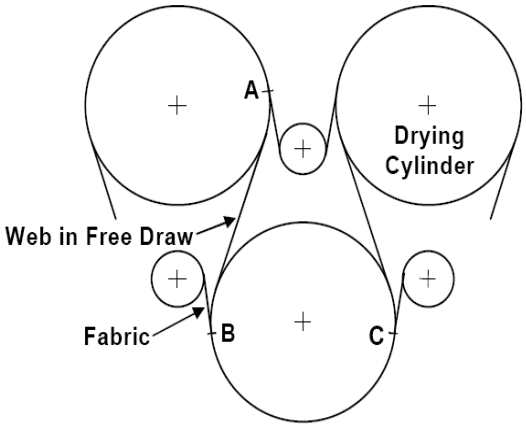

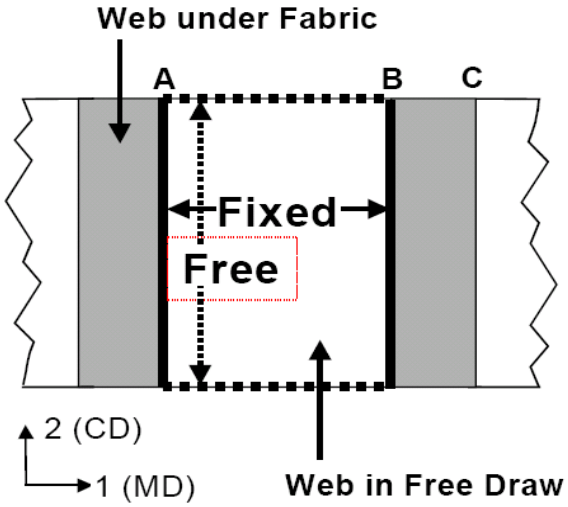

Figure1. Paper web in free draw and cylinder contact

In free draw sections, the elastic modulus decreases in cross machine direction due to fibre shrinkage, but increases in machine direction by web elongation. While web elongation is controlled by the paper machine, web shrinkage arises from local changes in the plain strain [1,10,13,14,16].

With a new measurement set up we can measure the local deformation of paper during drying with a high resolution and investigate the effect of different draws during different phases of paper drying processes on final properties. **Figure 2** and **Figure 3** show the principle design of the test rig. It comprises a programmable tensile testing machine Zwick/Roell Z010, which simulates the free draws, a powerful high-speed radiant heater, an electronic balance to measure the evaporation rate and a high-resolution CCD-camera, which traces local web deformation.

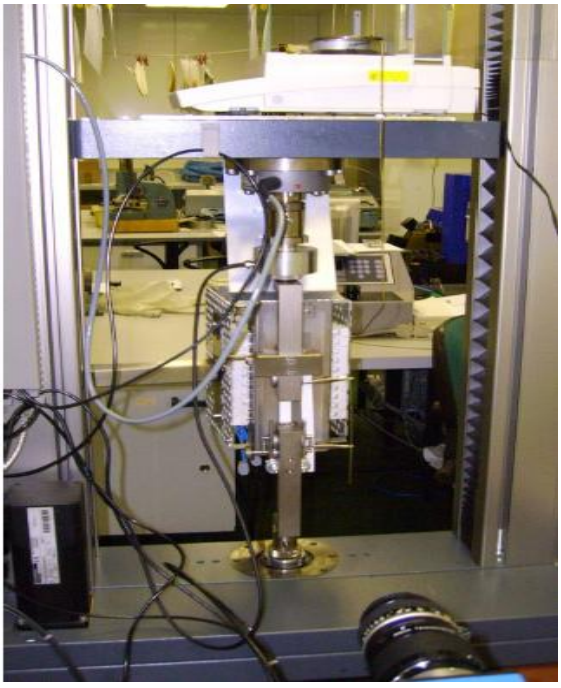

Figure2. Test rig

A PC with MATLAB controls the components and the test procedure. Local shrinkage and elongation are measured by online image analysis with high accuracy [17].

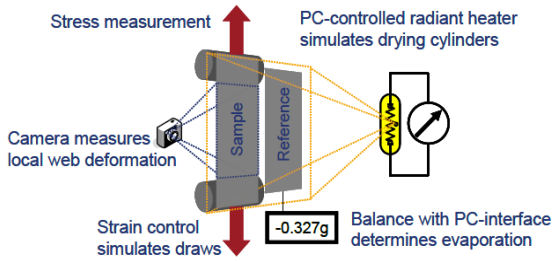

Figure 3. Test rig simulating paper machine's drying section

The performance of the test rig has been demonstrated by pre-trials with mixtures of mechanical and chemical pulp, which differ significantly in their drying behaviour. **Figure 4** illustrates the development of the elastic modulus in the drying process for pulps with increasing capability for fibre-to-fibre bonding. The fibres of stone ground wood (SGW) are shorter and more rigid than fibres from pine kraft pulp (KiSa). The latter has been beaten to a freeness (Schopper-Riegler) of 20° SR, 40° SR and 60° SR to increase fibre flexibility and fibrillation leading to improved fibre bonding. The figure shows the effect of the fibre treatment on the development of the tensile stiffness in machine direction.

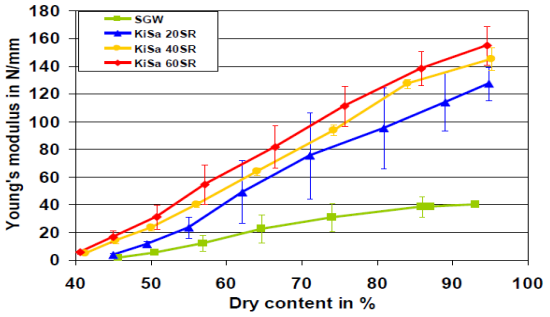

Figure 4. Development of tensile stiffness in the drying process with 7 free draws

Samples of paper are tested by Scott bond strength test after drying. Scott bond strength test represents the z-directional tensile bond strength and it shows internal bond of fibres. Tensile strength (the breaking force per cross-sectional area) and Breaking strain (the point where the load elongation curve ends) are done by Zwick-machine for measuring the strength properties of papers.

4 OBJECTIVES

The objectives of this work are to examine properties of paper during free draw with the help of laboratory scale analyses.

This research investigates:

1. The relation between shrinkage (deformation) of paper and strength properties of paper during free draw.
2. Differences in the papermaking process affect shrinkage of paper during free draw.
3. The relation of fibre bonding and shrinkage of paper: which factors affect bonding and finally change shrinkage?
4. The effect of drying and drying stress on bonding and shrinkage of paper, and in turn, the effect of bonding on drying and drying stress and shrinkage of paper.

The fibre treatment also affects the swelling and shrinkage of fibre, which in turn determines web shrinkage and tensile stiffness in cross machine direction. The effect of fibre shrinkage on the paper quality is evident but not fully understood.

In this work experimental investigations have to be carried out based on the existing pre-trials in order to better understand the effect of relevant parameters like fibre type, freeness of fibre and process parameters on the drying behaviour of paper. The design of the experiments have to be systematic in that way that the results can be utilized for modelling the development of paper strength properties during drying taking into account the forces introduced by draws in paper machines.

REFERENCES

[1] K. Niiskanen. Paper Physics. Book 16, Book Series Paper Science and Technology, FAPET Oy, Helsinki, (1998).

[2] H. Nauko and J. Wu. Mechanisms of paper shrinkage during drying. International Paper Physics Conf., CPPA, Montreal, 103-113 (1995).

[3] M. Karlsson. Papermaking Part II – Drying. Book 9, Book Series Paper Science and Technology, FAPET Oy, Helsinki, (1998).

[4] H. Holik. Handbook of paper and Board. Wiley-VCH, (2006).

[5] M. Östlund, S. Östlund, L. A. Carlsson, and C. Fellers. The influence of drying conditions on residual stress build-up in paperboard. J. Pulp Pap. Sci. 30(11):312-316 (2004).

[6] M. Östlund, S. Östlund, L. A. Carlsson, and C. Fellers. The influence of drying restraints and beating degree on resisual stress build-up in paperboard. J. Pulp Pap. Sci. 30(11):289-293.

[7] A. Vainioand and H. Paulapuro. The effect of wet pressing and drying on bonding and activation in paper. Nordic Pulp and Paper Research journal 22(4), 403-408. (2007).

[8] A. K. Vainio and H. Paulaporo. Interfiber bonding and fiber segment activation in paper. Bioresources J. 2(3):442-458(2007).
[9] T. Wahlström. Influence of shrinkage and stretch during drying on paper properties. Paper Technology Journal. 41(6):39-46(1999).
[10] R. Wathén. Characterizing the influence of paper structure on web breaks. Licentiate Thesis, Helsinki University of technology, (2003).
[11] D. H. Page and P. A. Tydeman. A new theory of the shrinkage, structure and properties of paper. The Formation and Structure of Paper, Transactions of the Symposium held in Oxford, 1961, London 397 – 421 (1962).
[12] A. Lundh, T. Wahlström, T. Hansson and C. Fellers. Biaxial straining of handsheets during drying – Effect on delamination properties. International Paper Physics Conference, September 26-30, San Diego, CA (1999).
[13] H. Nauko, and J. Wu. Mechanisms of paper shrinkage during drying. Int.Paper Physics Conf., CPPA, Montreal, 103-113, (1995).
[14] C. Green. Some effect of paper shrinkage on properties. PTN49 (1999).
[15] P. Lipponen, T. Leppänen and J. Hämäläinen. On the role of drying induced cross-machine shrinkage on paper cockling phenomenon. Nordic Pulp and Paper Research journal. 24(1): 60-64 (2009).
[16] L. I. Salminen and M. J. Alava. Simulation of network shrinkage. Nordic Pulp and Paper Research Journal. 17(2):105-110 (2002).
[17] K. Villforth and S. Schabel. Analyse und Ursachen plastischer Dehnungsprofile von Papierbahnen bei der Papierherstellung und Verarbeitung. Final Report on AiF-Project 13365N. Darmstadt, Techn. Univ., FG Papierfabrikation u. Mech. Verfahrenstechnik. Bericht (2005).
[18] D. Arnold and K. Lautenschläger. Die Dimensionsstabilität von Papier und Karton. Zellstoff und Papier J. 24(1) :15 – 19(1975).
[19] E. Hiltunen. On the beating of reinforcement pulp. Doktoral thesis. Helsinki University of technology, Espoo (2003).
[20] K. Lukko and H. Paullapuro. Mechanical pulp fines: Effect of particle size and shape. Tappi J. 82(2), 95-101 (1999).
[21] M. A. Hubbe. Bonding between cellulosic fibers in the absence and presence of dry strength agents. Bioresources J. 1(2): 281-318 (2006).
[22] M. Htun, A. De Ruvo and C. Fellers. The dynamic mechanical behaviour of paper during drying. J. Applied Polymer Science.30:1597-1604 (1985).

Model-based optimization in papermaking process design

MIKKO LINNALA[1*], JARI HÄMÄLÄINEN[2]

[1]University of Eastern Finland,
P.O.Box 1627, FI-70211 Kuopio, Finland.
mikko.linnala@uef.fi

[2]Lappeenranta University of Technology,
P.O.Box 20, FI-53851 Lappeenranta, Finland.
jari.hamalainen@lut.fi

*Corresponding author

Keywords: Model-based optimization, Simulation, Process design, Papermaking process

ABSTRACT

Model-based optimization is a very useful design tool for different kinds of papermaking processes. The method is extended from unit process design and single-level optimization to simultaneous design of process structure and operations. This is enabled using a bi-level optimization problem. That way, unnecessary iterations between the process and automation designs can be avoided. Here, the bi-level optimization approach is studied from multiobjective optimization and decision making point of view. The method is illustrated by a case study in which the broke system structure and operations are optimized simultaneously.

1 INTRODUCTION

Few past years have proved that paper industry needs new production systems as well as new products to deal with economical strain. Therefore, investments in new mills and rebuilds of the old ones are necessary. In order to do that, new process design methods and tools are needed as well. New process types and structures can be designed cost effectively using more effective design methods. A model-based optimization is one method which has been already used in the paper industry for headbox design [1] and in broke system studies [2], for example.

Paper industry is seeking large production volumes, good runnability and high product quality. At the same time, they are interested in minimal capital costs as well as minimal raw material costs and other operational costs. That is possible only with excellent process structure and the best operation practices. Traditionally, the process has been built first based on the product and production volume specifications. After that, rationalization of the operation practices is taken under examination.

In model-based optimization, the process structure and the process operation are designed simultaneously which is enabled by a bi-level optimization [3, 4]. There, the upper-level consists of structural design optimization and the lower-level consists of operational optimization. Hence, a solution of the bi-level problem is optimal process structure (design) with optimal process operation. In practice, we know the operational principles and control methods already before the process is even built [5, 6].

Here, different types of process models are exploited as in traditional process design too. The type of process model used is a compromise between model accuracy and computational time. Results are very realistic but the solution process can take several days when a detailed model is used. However, those can be used as verification model and the computational time can be decreased using simplified models in the lower-level optimization where the numerous simulations are required. In this study, the main focus is on the multiobjective nature of the optimization problem and decision making related to that. Hence, the modelling issues are not handled largely.

The challenge in bi-level optimization, as in multiobjective optimization in general, is conflicts between the objectives which lead to a set of Pareto optimal solutions [7]. They are mathematically equally good solutions, what means that decision making is needed. The best solution to be implemented as an investment should be selected somehow. Usually, decision maker is a person who has expert knowledge about the current process, in this case about the papermaking, but is not necessarily familiar with optimization methods. Therefore, one major aim in this study is to develop methods to produce such information that the decision making is easier for the papermaking experts. This can be made by visualization of trade-off analyses in which different conflicting objectives are compared between each other, for example.

Simultaneous optimization of process structure and operation is a new way for cost efficiency process design. Bi-level optimization enables examination of large and complicated optimization problems including dynamic and multiobjective problems of papermaking applications. Anyway, the optimization is based on the process models and therefore reliability of the results depends on accuracy of the models used. Overall, it is very important that this kind of engineering tool is able to produce such information that the decisions about incoming investment are possible to do.

2 MODEL-BASED OPTIMIZATION AS A PROCESS DESIGN TOOL

Traditionally, the industrial processes are designed in turn between the structural design (e.g. process flow sheet and equipment dimensioning) and automation design (e.g. control system and control logics). Model-based optimization enables combining of these design stages so that the process

structure and the control principles can be achieved simultaneously [8].

Now, a process model and a mathematical optimization algorithm are combined with two-way interaction. Process model can be even a steady-state model or a dynamic model, depending on the current process application. Similarly, optimization algorithm applied depends on the formulation of the optimization problem. Usually, the optimization problems related to the papermaking industry are multiobjective and dynamic ones. That is because the process itself is complicated and dynamic, and therefore the problems cannot be described only with single objective.

The optimization problem can be formulated as a bi-level problem when the process design consists of structural design and operational design. There, the upper-level problem (structural optimization) is a leader and the lower-level problem (operational optimization) is a follower. In practice, optimal solution for the upper-level problem requires optimal solution for the lower-level problem. Two-way coupling between the optimization levels and the process models are illustrated in Figure 1.

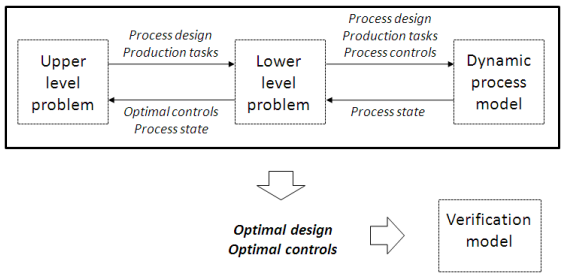

Figure 1. Two-way coupling between the optimization levels and the process models.

Bi-level optimization procedure begins by defining some process design candidate and possible production tasks (e.g. break, grade change) on the upper level. Then, the optimal process controls for that current process design candidate are defined on the lower level where the solution is based on the simulations with the process model. After the optimal process controls are defined, the controls and the process state data are returned on the upper-level optimization where the next design candidate is defined and fed to the lower-level optimization. This kind of optimization-simulation loop is repeated until the optimal process design with optimal controls is achieved.

Bi-level optimization procedure requires numerous repeated simulations which sets requirements for the process models used. There is a possibility to use several models with different accuracy and details. It is reasonable to use more detailed model as a verification model and execute the optimization procedure with a simplified model. Hence, after the optimal process design and controls is achieved, the solution can be tested with verification model in order to get more realistic simulations data.

3 DECISION MAKING

Optimization problems related to the papermaking are multiobjective ones, and therefore, a decision making is needed [9]. Several conflicting objectives cannot be satisfied simultaneously because, if the value of one objective function can be decreased (in case on minimization problem), a value of another objective function increases. This leads to a set of Pareto optimal or non-dominated solutions (Figure 2) which are equally good from mathematical point of view [7]. Still, in practical investment case, only one solution should be able to be picked out as the best one.

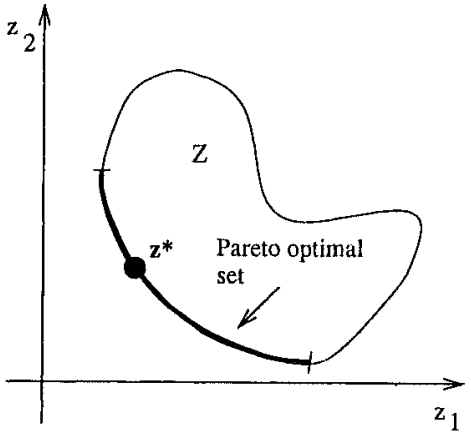

Figure 2. Principle of Pareto optimality in the minimization task of two objectives, z_1 and z_2 [7].

Conflicts are possible also between the upper-level objectives and the lower-level objectives when studying bi-level optimization problems. An example from the previous studies proves that capital costs of broke system cannot be minimized on the upper level simultaneously to the maximization of broke dosage on the lower level as can be seen in Figure 3.

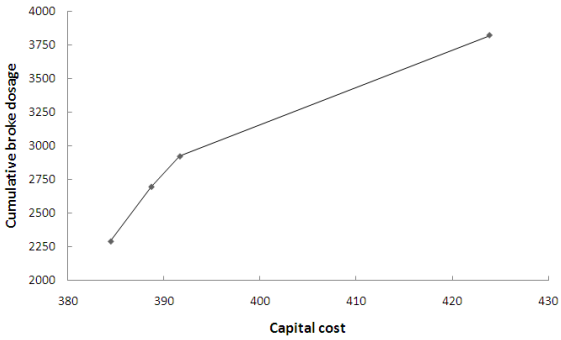

Figure 3. Example of trade-offs between upper-level and lower-level objective functions [8, modified by M. Linnala].

Although a set of optimal designs with optimal controls is able to achieve by a bi-level optimization procedure, the most optimal solution should be selected somehow. Sometimes, selection can be made with scalarization function but the most suitable way is to use a human decision

maker. Based on his/her expert knowledge of the current process application and information produced in optimization, that person should be able to make the final decision. Anyhow, one interesting question is what that information includes and how it should be presented to the decision maker?

4 CASE STUDY: A BROKE SYSTEM

Next, the bi-level optimization is illustrated by a case study in which the broke system of a LWC (light-weight coated) papermaking line is studied.

4.1 Background

Papermaking line studied and modelled included all main components from the raw material inputs to the net production as presented in Figure 4.

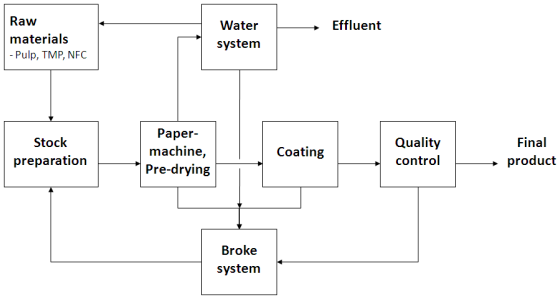

Figure 4. Main components of the papermaking line modelled.

As mentioned above, the papermaking processes as well as the process models are usually very complicated. Using comprehensive and very detailed process model, computational time increases too much in the optimization procedure. This can be avoided using different models in different places according to Figure 1. In this case study, the simplified process model used in the optimization procedure was constructed with Matlab™ software. That way the computational time was able to keep short enough. The model was mainly a set of material balance equations that formed a continuous process through the flow sheet presented in Figure 4. First, the initial state was calculated backward from the gross production to the raw material inputs. Then, the dynamic simulation was calculated forward from the raw material feeds to the final product.

Instead, the verification model was constructed with Apros™ software [10] which is more detailed and realistic dynamic simulator than Matlab™. The verification model was built in Technical Research Centre of Finland. Usually, the more detailed model can also offer some additional information for the decision making process. Anyhow, both models should be such a similar that also the optimization results achieved with a simplified model are reliable. In this case study, the main focus was on the multiobjective optimization and the decision making problems. Hence, the verification simulations were led out of examination.

4.2 Broke system

The broke system of LWC papermaking line was divided in two lines, one for uncoated broke and another for coated broke. Broke was generated in three positions in the main papermaking line as presented in Figure 5.

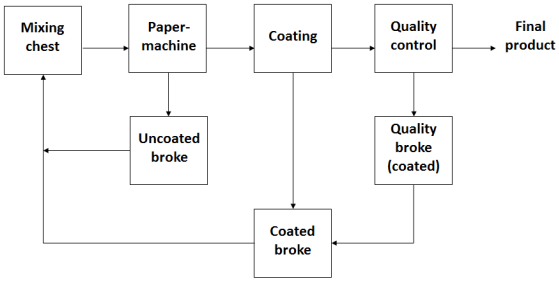

Figure 5. Broke system of the papermaking line modelled.

First position existed in the paper machine after the wet pressing (43 % dry solid content). There, the breaks occurred randomly and were defined using a strength model which was based on the raw material composition and the current base paper basis weight according to Equations 1 and 2.

$$s = IBW_{bp} \tag{1}$$

where I is a strength index (Equation 2) and BW_{bp} is a base paper basis weight.

$$I = \frac{\sum s_i x_i}{s_{ref}} \tag{2}$$

where s_i is a nominal strength of component i, x_i is a mass fraction of component i and s_{ref} is a reference value of strength.

Second position for the breaks existed after the coating unit (96 % dry solid content). There, the breaks occurred randomly as well. Approximated break frequency was 0.88 breaks/day and duration of one break 31 minutes. Third broke source existed in final product quality control where 8 % of gross production was rejected randomly (96 % dry solid content).

Uncoated and coated broke were diluted to 3.5 % dry solid content before the storage towers but the quality broke was stored without dilution at first (illustrates paper rolls). Quality broke pulpering was controlled and diluted broke was fed to the storage tower of coated broke. Both broke types could be dosage to the mixing chest, so that, the total broke dosage and the proportion of uncoated broke were controlled.

4.3 Bi-level optimization problem

The bi-level optimization problem consisted of the structural design of the broke towers (upper level)

and optimization of the broke system operations (lower level). Following objective functions (F) and decision variables (a) were studied on the upper level:

F_1: Cost of uncoated broke tower ($V^{0.7}$)
F_2: Cost of coated broke tower ($V^{0.7}$)
F_3: Cost of quality broke storage ($V^{0.7}$)
a_1: Volume of uncoated broke tower
a_2: Volume of coated broke tower
a_3: Volume of quality broke storage

Instead on the lower level, following objective functions (f) and decision variables (u) were studied:

f_1: Variation in fill-% of uncoated broke tower
f_2: Variation in fill-% of coated broke tower
f_3: Variation in fill-% of quality broke storage
f_4: Cumulative broke dosage
f_5: Cumulative production loss
u_1: Total broke dosage
u_2: Proportion of uncoated broke
u_3: Feed (pulpering) of quality broke

All objective functions were minimized and the search spaces of the decision variables were constrained with box constraints. The bi-level optimization problem was solved on both levels with differential evolution algorithm [12]. Because the lower-level problem was multiobjective and the optimization procedure took so long, instead of human decision maker there was scalarization function implemented (l_2-metric [13]) which selected the best solution.

5 RESULTS

After the bi-level optimization problem was solved, a set of Pareto optimal process designs were achieved. Optimal broke tower volumes (a) and corresponding values of the objective functions (F) are presented in Tables I and II.

Table I. Optimal values for the decision variables of the upper-level optimization problem.

	Volume uncoated broke [m^3]	**Volume** coated broke [m^3]	**Volume** quality broke [m^3]
Design 1	2763.8	4358.1	3475.8
Design 2	3364.5	3793.9	2837.2
Design 3	5681.2	1588.5	2601.0
Design 4	6091.5	3279.4	2447.1
Design 5	6896.0	1663.4	2058.4
Design 6	3581.9	3378.2	3358.8

* Initial values: 3000, 3000, 3000.
** Limits: 1500/7500, 1500/7500, 1500/4500.

Table II. Values for the objective functions of the upper-level optimization problem.

	Cost uncoated broke	**Cost** coated broke	**Cost** quality broke
Design 1	256.48	352.79	301.12
Design 2	294.33	320.15	261.23
Design 3	424.72	174.06	245.81
Design 4	445.97	289.11	235.54
Design 5	486.43	179.76	208.67
Design 6	307.52	295.18	293.99

As Tables I and II shows, it is not obvious which one of these six designs is the best one. To help decision making between the designs, it is useful to visualize the results somehow. In Figure 6, normalized objective function values are presented in a spider-web diagram.

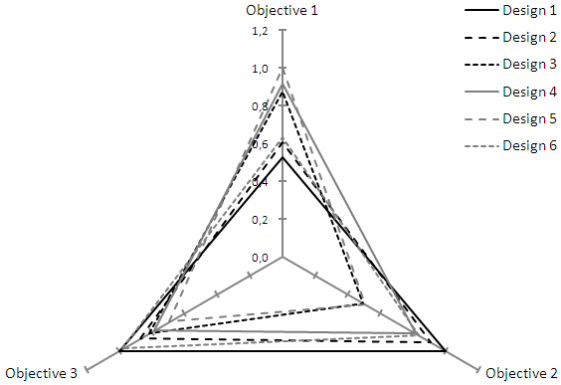

Figure 6. Normalized objective function values of the upper-level optimization.

Graphical representations of different process parameters over the simulation horizon are also useful information because the process model was dynamic one and the breaks occurred randomly. Fill percentages of the uncoated broke tower is presented in Figure 7.

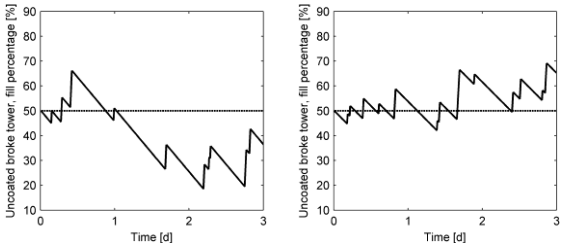

(a) Fill percentages of uncoated broke tower. Left: Design 1 (2763.8 m^3), right: Design 2 (3364.5 m^3).

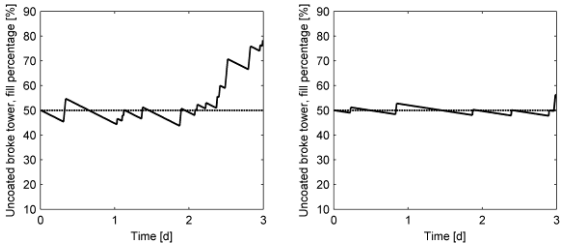

(b) Fill percentages of uncoated broke tower. Left: Design 3 (5681.2 m^3), right: Design 4 (6091.5 m^3).

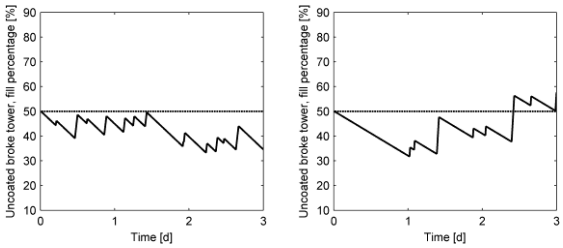

(c) Fill percentages of uncoated broke tower. Left: Design 5 (6896.0 m^3), right: Design 6 (3581.9 m^3).

Figure 7. Fill percentages of uncoated broke tower. (a) Designs 1 and 2, (b) Designs 3 and 4, (c) Designs 5 and 6.

Figure 7 shows that the process stability varies very much between the designs. In Design 4, the tower volume is high and the fill percentage is stabile. But then, in Design 5, the tower volume is even higher and the fill percentage is unstable. Hence, it might be useful look at also the fill percentages of the coated broke tower and quality broke storage presented in Figures 8 and 9.

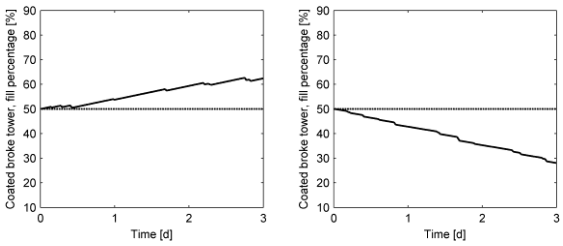

(a) Fill percentages of coated broke tower. Left: Design 1 (4358.1 m^3), right: Design 2 (3793.9 m^3).

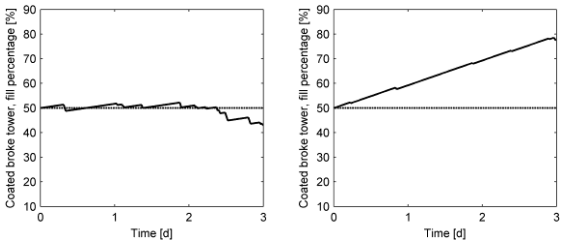

(b) Fill percentages of coated broke tower. Left: Design 3 (1588.5 m^3), right: Design 4 (3279.4 m^3).

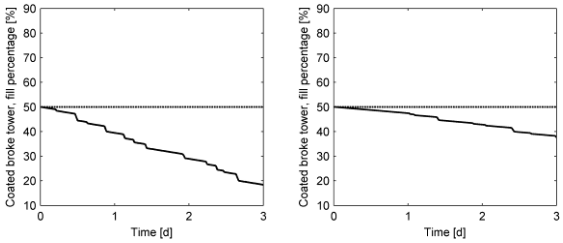

(c) Fill percentages of coated broke tower. Left: Design 5 (1663.4 m^3), right: Design 6 (3378.2 m^3).

Figure 8. Fill percentages of coated broke tower. (a) Designs 1 and 2, (b) Designs 3 and 4, (c) Designs 5 and 6.

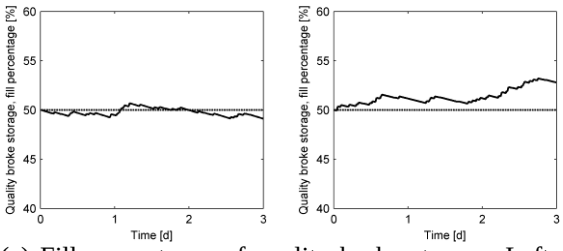

(a) Fill percentages of quality broke storage. Left: Design 1 (3475.8 m^3), right: Design 2 (2837.2 m^3).

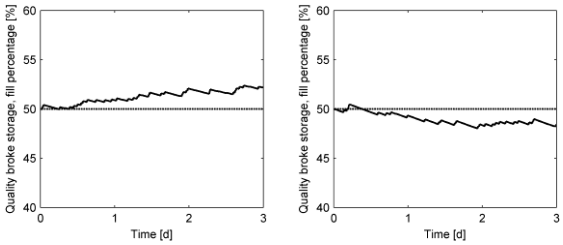

(b) Fill percentages of quality broke storage. Left: Design 3 (2601.0 m^3), right: Design 4 (2447.1 m^3).

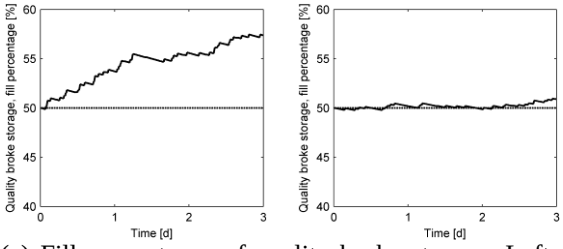

(c) Fill percentages of quality broke storage. Left: Design 5 (2058.4 m^3), right: Design 6 (3358.8 m^3).

Figure 9. Fill percentages of quality broke storage. (a) Designs 1 and 2, (b) Designs 3 and 4, (c) Designs 5 and 6.

Figures 7-9 illustrate very well the numerical values of the objective functions. Each design is better than another if only one or two broke towers are compared, but if all three towers are compared, situation comes complicated. In this kind of cases, requirements for the decision maker's knowhow are high.

Combining the optimal controls to analyse of six process designs, random nature of the breaks comes up. The optimal values for the decision variables (u) are presented in Table III.

Table III. Optimal values for the decision variables of the lower level optimization problem.

	Total broke dosage [%]	Uncoated broke proportion [%]	Quality broke dosage [%]
Design 1	13.64	48.96	9.29
Design 2	12.67	53.10	6.21
Design 3	11.28	54.55	6.31
Design 4	9.54	42.71	7.83
Design 5	14.64	68.94	5.01
Design 6	10.65	50.53	5.84

* Initial values: 9.9, 31.4, 7.98.
** Limits: 5/15, 5/95, 3/12.

As can be seen, values of all the decision variables vary a lot between the designs. That was because the breaks occurred dissimilarly between the simulations as presented in Figure 10.

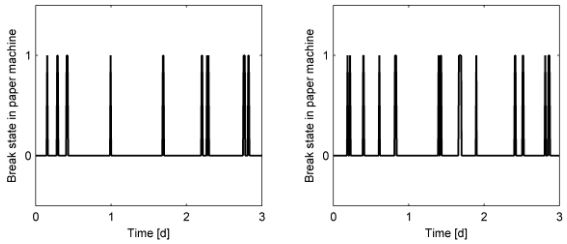

(a) Break history over the simulation horizon, 1 = break, 0 = not break. Left: Design 1, right: Design 2.

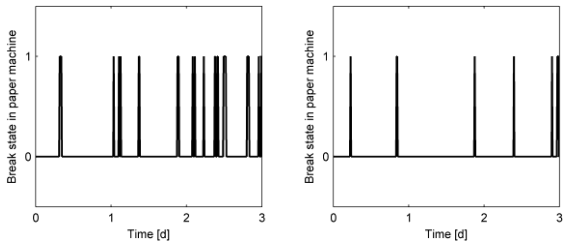

(b) Break history over the simulation horizon, 1 = break, 0 = not break. Left: Design 3, right: Design 4.

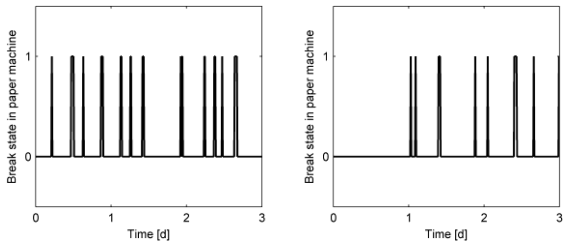

(c) Break history over the simulation horizon, 1 = break, 0 = not break. Left: Design 5, right: Design 6.

Figure 10. Break history over the simulation horizon. (a) Designs 1 and 2, (b) Designs 3 and 4, (c) Designs 5 and 6.

The scalarization function was implemented to make the final selection from the Pareto optimal sets on the lower-level optimization. Scalarization methods have their advantages and disadvantages. In this case, the computational time decreased when human decision maker was not used in both levels. But then, the selected solution is highly depended on the reference point selected in l_2-metric method. If the reference point would be selected otherwise, the results would be different.

The lower-level objective function values (*f*) are also taken into account in the decision making process. That information can be presented similar to the upper-level objective functions, by a spider-web diagram presented in Figure 11, for example.

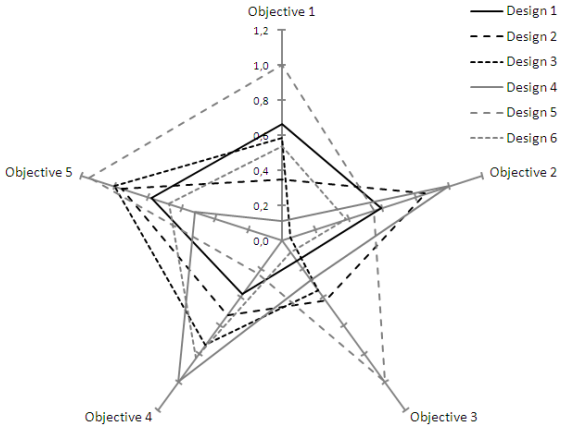

Figure 11. Normalized objective function values of the lower-level optimization.

Figure 11 shows that comparison of different solutions comes more difficult when the number of objective functions increases. But then, the visualizations have more important role in information offered to the decision maker.

6 CONCLUSIONS

Global pulp and paper industry needs new innovations for both the manufacturing processes and the products. In order to realize the innovations, new methods and tools for the process design are needed as well. Here, the model-based optimization is presented as a process design tool. In place of single-objective optimization and limited applicability, model-based optimization can be extended using bi-level optimization and large process models. That approach is demonstrated by a case study in which the broke system dimensioning and process control optimization were made simultaneously. The results show that the bi-level optimization can be applied to the papermaking, but because of complicated and multiobjective nature of the application, selection of the best solution is difficult.

Multiobjective optimization problems lead to a set of mathematically equally good solutions and therefore decision making is needed. In a bi-level case, some scalarization method can be used in the lower level, but human decision maker is needed to make the final selection. Different methods to produce information for the decision maker were presented also in the case study. Visualization of

the objective function values as well as the graphical representations of the simulation time series are very illustrative information. Anyhow, in case of complicated industrial processes, such as papermaking, expert knowledge of the decision maker itself counts very much.

AKNOWLEDGEMENTS

Authors wish to thank all the research partners of Finnish Forestcluster Ltd. EffNet-program for their co-operation as well as Finnish Forestcluster Ltd. and Finnish Funding Agency for Technology and Innovation (TEKES) for financial support.

REFERENCES

[1] J.P. Hämäläinen, K. Miettinen, P. Tarvainen and J. Toivanen. Interactive solution approach to a multiobjective optimization problem in a paper machine headbox design. Journal of Optimization Theory and Applications **116**(2):265-281 (2003).

[2] M.Dabros, M. Perrier, F. Forbes, M. Fairbank and P.R. Stuart. Model-based direct search optimization of the broke recirculation system in a newsprint mill. Journal of Cleaner Production **13**(15):1416-1423 (2005).

[3] B. Colson, P. Marcotte and G. Savard. Bilevel programming: A survey. 4OR: A Quarterly Journal of Operations Research **3**(2):87-107(2005).

[4] J. Fliege and L.N. Vicente. Multicriteria approach to bilevel optimization. Journal of Optimization Theory and Applications **131**(2):209-225 (2006).

[5] V. Bansal, J.D. Perkins, E.N. Pistikopoulos, R. Ross and J.M.G van Schijndel. Simultaneous design and control optimization under uncertainty. Computers and Chemical Engineering **24**(3):261-266 (2000).

[6] V. Bansal, J.D. Perkins and E.N. Pistikopoulos. A case study in simultaneous design and control using rigorous, mixed-integer dynamic optimization models. Industrial and Engineering Chemistry Research **41**(4):760-778 (2002).

[7] K. Miettinen. Nonlinear multiobjective optimization. Kluwer Academic Publishers, (1999).

[8] M. Linnala and J. Hämäläinen. Improvement of the cost efficiency in papermaking with optimization tools, PaperWeek Canada, Montreal, 95-98, (2011).

[9] J. Hämäläinen, E. Madetoja and H. Ruotsalainen. Simulation-based optimization and decision support for conflicting objectives in papermaking. Nordic Pulp and Paper Research Journal **25**(3):405-410 (2010).

[10] VTT, Technical Research Centre of Finland, Apros Overview, available from: http://www.apros.fi [Cited 15 June 2011], (2011).

[11] K. Price, R. Storn and J. Lampinen. Differential evolution – a practical approach. Springer, (2005).

[12] K. Deb. Multi-objective optimization using evolutionary algorithms. John Wiley & Sons Ltd., (2001).

Posters

New Pulp and Paper Products

MULTI-SCALE MODELING OF CELLULOSE NANOFIBERS IN PAPER-LIKE APPLICATIONS

J. KETOJA[1], E.K.O. HELLÉN[1], J. LAPPALAINEN[1], J. SORVARI[1], A. KULACHENKO[2], A. PUISTO[3], M. ALAVA[3], A. PENTTILÄ[4], K. LUMME[4], S. PAAVILAINEN[5], L. MCWHIRTER[5], T. RÓG[5], I. VATTULAINEN[5], D. VIDAL[6], T. UESAKA[6]

[1] VTT Technical Research Centre of Finland, P. O. Box 1000, FI-02044 VTT, Finland
[2] Royal Institute of Technology (KTH), Sweden
[3] Aalto University, School of Science and Technology, Department of Applied Physics, P.O. Box 4100, FI-02015 TKK, Espoo, Finland
[4] Department of Physics, P.O. Box 64, 000014 University of Helsinki, Finland
[5] Department of Physics, Tampere University of Technology, P.O. Box 692, FI-33101 Tampere, Finland
[6] FPInnovations, Pointe-Claire, 570 St-Jean Blvd., H9R 3J9, Québec, Canada

Jukka.Ketoja@vtt.fi

Cellulose nanofibers show a great potential in expanding the use of sustainable raw materials in forest products industry. Here we introduce a set of multi-physics simulation tools that enable model-aided analysis of industrial nanocellulose applications. These tools have been developed as a joint effort of several research groups. They describe structural, mechanical and optical properties of paper-like structures based on particle-level models, which cover materials and structures from nano to macro scale, i.e., from atomistic simulations to macroscopic product properties (figure 1). In addition to the detailed description of material characteristics, there is a possibility to vary physical and chemical process conditions while forming the structures.

Each simulation tool can be used independently but the maximum advantage is gained by combining several solvers together into a multi-scale and multi-physics approach. The simulation tools are integrated with the help of Simantics platform developed recently at VTT [1]. We demonstrate the use of this platform in terms of multi-scale simulation analysis of experimental high-filler-content nanocellulose sheets.

[1] https://www.simantics.org

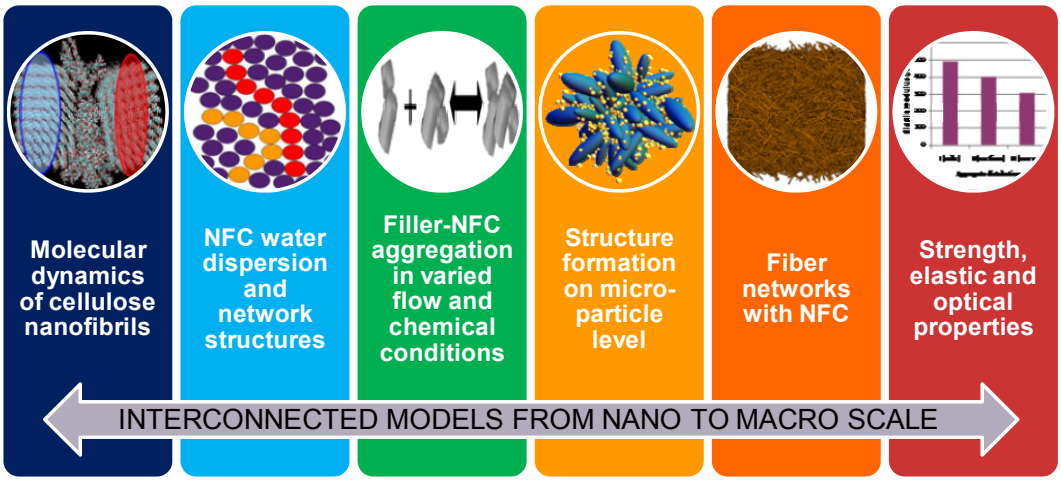

Figure 1. Combining several models enables multi-scale analysis ranging from atomistic simulations to macroscopic product properties.

Vulcanized fiber as a high-strength construction material for highly loaded construction units

KÜNNE, B.; WILLMS, U.; STUMPF, C.

Faculty of Mechanical Engineering, Department of Machine Elements, Dortmund University of Technology, Germany

1 The raw material

Within the range of natural products vulcanized fiber belongs to the high-strength fiber materials. Vulcanized fiber is a material, which is producible from cellulose in the form of several layers of specialty paper by effect of concentrated zinc chloride solution or concentrated sulfuric acid. Within the layers of paper and between these a more or less strong welding of the cellulose fibers takes place [1].

2 Momentary application

Shuttles in the field of textile industry, coat-hangers, threaded pipes, abrasive pads and folders are made of vulcanized fiber [2]. Seals from vulcanized fiber are used for industrial applications and in the sanitary area. In the electrical industry vulcanized fiber is used because of the good isolating characteristics and because of the transmit-deleting behavior e. g. as insulator in circuit-breakers and contactors. Vulcanized fiber is used as backing material for the production of grinding wheels. Therefore it is coated with resins and pasted with abrasive materials. For the production of welder´s face shields the method of deep-drawing is applied. Due to the not existing static rechargeableness vulcanized fiber is also used in highly combustile ranges in place of metals or plastics. Beyond that, if a hydrophobic material behavior is not compellingly necessary, vulcanized fiber is used for the production of thread guides and spinning cans in the field of textile industry [3].

3 Material properties

Vulcanized fiber possesses very good mechanical characteristics, for example a strong fiber connection, a high impact strength, an abrasion and an oil as well as a fat stability and an electric insulation. Since the material is to be called almost pure cellulose fiber, it can be spoken of a functional organic raw material with a biologically degradable character [4]. Vulcanized fiber is corrosion resistant and is characterized by a long life span. It does not fatigue under static or changing tensions and possesses a high tensile strength and a high tear strength. Beyond that the material can be connected easily with the surfaces of other materials, exhibits arc-deleting characteristics and shows up uninfluenced by vibrations [4]. Vulcanized fiber is characterized by high impact resistance, hardness, low heat conductivity and low density [1]. It is toughly, flexibly, hardly inflammable, statically not rechargeable and exhibits during a mechanical destruction no fragments or sharp breaking edges [3]. Vulcanized fiber can be cut, sawn, bored, planed, milled, lathed, grinded, polished, pressed, punched, bended, folded and deep-drawn [1].

Table 1. Material properties in clear representation [1]

Density [g/cm^3]	1.1 to 1.45
Tensile strength longitudinal [N/mm^2]	up to 120
Tensile strength lateral [N/mm^2]	up to 75
Bending strength longitudinal [N/mm^2] (thickness: 10 mm)	up to 125
Bending strength lateral [N/mm^2] (thickness: 10 mm)	up to 100
Impact strength [kJ/m^2] (thickness: 10 mm)	up to 120
Notch impact strength [kJ/m^2] (thickness: 10 mm)	up to 30
Ball hardness [N/mm^2]	up to 100
Dielectric strength [kV/mm] (thickness: 0.3 mm, 4 days, relative humidity: 50 %)	up to 8
Young´s modulus [N/mm^2]	up to 8030
Wrought material costs [€/kg] (starting from a delivery volume of 50 tons)	4

4 Research project

In a research project worked on at present the structure of the vulcanized fiber is adapted in such way and/or changed that in the future the product will exhibit the following characteristics:

- Dimensional stability due to a resistance against humidity
- High firmness and rigidity
- High heat resistance

5 The approach

In a first step the actual raw materials of the vulcanized fiber, a mixture of cotton linter pulp and cellulose, are variegated. Hemp and flax are applied because they contribute to an increase of firmness. By a change of the freeness of the raw materials a stronger fiber composite can be obtained and thus the firmness can be increased additionally.

Further the influence of a variation of the parameters of the production process of the specialty paper, as for example the concentration of the suspension or the packing pressure, is examined with regard to the purposes of the project. The application of ecologically compatible chemical additives, as for example sizing agents or wet strength agents, particularly contributes to an increase of the firmness and the rigidity, to a minor degree also to an increase of the hydrophobicity.

For further increase of firmness and heat resistance it is intended to integrate reinforcing fibers into the matrix of the fibers of the cellulose sheetings, as for example glass fibers, polyphenylene sulfide fibers or aramide fibers. For the achievement of a hydrophobic material behavior it is intended to create a surface functionalization by the use of silanes or resins.

6 The demonstrator objects

It is a purpose of the project to be able to use vulcanized fiber in the range of the automotive industry after detailed optimization. For the market sighted which shall be entered a covering within the range of the B-pillar of a motor vehicle, a heat shield of a turbocharger and a door lining are selected. The products are made of a vulcanized fiber plate by exercising deep-drawing as first draw with help of a clamping frame.

(a)

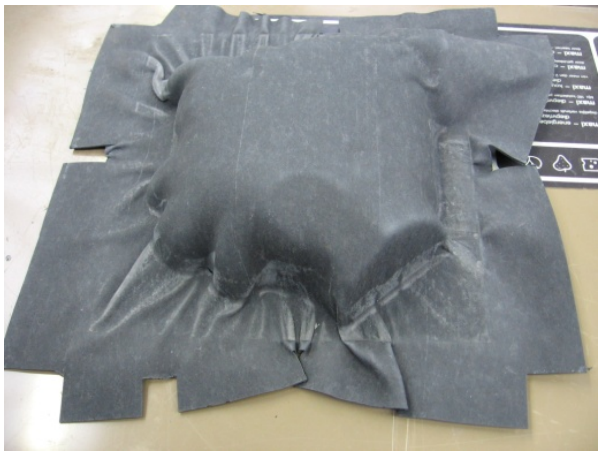

(b)

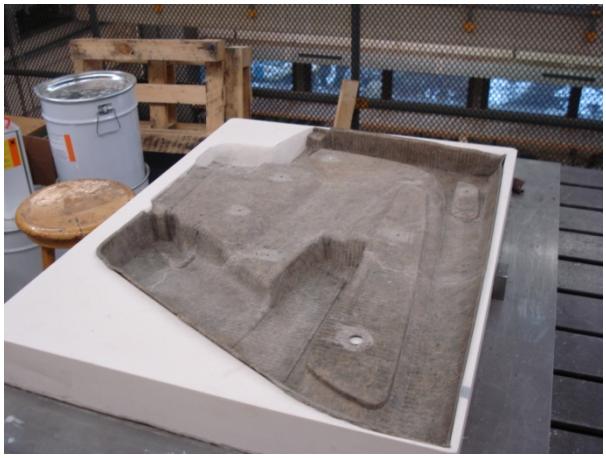

(c)

Figure 1. (a) Covering within the range of the B-pillar of a motor vehicle. (b) Heat shield of a turbocharger. (c)Deep drawing tool for a door lining

7 Results

The selected demonstrator objects can be deep-drawn well and coated afterwards to achieve a hydrophobic material behavior. The finished products are characterized by small formation of wrinkles and high accuracy to size. The best deep-drawing results can be received after a conditioning of the vulcanized fiber plates in a water quench, accomplished before.

References

[1] Bartholome´, E.; Biekert, E.; Hellmann, H.; Ley, H.; Weigert, M.; Weise, E.: Textilhilfsmittel bis Vulkanfiber, Ullmanns Encyklopädie der technischen Chemie, 4., neubearbeitete und erweiterte Auflage, Band 23, Verlag Chemie, Weinheim; Deerfield Beach, Florida; Basel, 1983

[2] Suzuki, K.: Production and characteristics of vulcanized fiber produced from the raw materials of nonwood fiber, Kami, Parupu Gijutsu Taimusu/Japanese Journal of Paper Technology 47 (6), pp. 42-47, Tokyo, 2004

[3] Joseph, M.: Vulkanfiber, Renaissance eines alten Werkstoffes. Vulcanized fibre – renaissance of a known material, naro.tech, Internationales Symposium, Werkstoffe aus Nachwachsenden Rohstoffen, 3rd International Congress, Materials made Renewable Natural Resources, 3, (2001), Seite 1-4, Erfurt, 2001

[4] Vulcanised fibre- a key to reliable electrical insulation, Electrical Review, 188 (1971) 15, S. 482-3, London, 1971

3D-forming of double-curved paperboard structures for packaging applications

SÖREN ÖSTLUND, MAGNUS ÖSTLUND[1] and SVETLANA BORODULINA

BiMaC Innovation
Department of Solid Mechanics
KTH, Royal Institute of Technology
SE-100 44 Stockholm, Sweden
soren@kth.se

ABSTRACT

Experiments were made with a laboratory apparatus for 3D-forming of paper and board sheets into complex-shaped structures. The objective was to learn more about design criteria. The influence of forming parameters such as moisture was studied and the performance of some common pulps as raw materials for the paper sheets was evaluated.

1 INTRODUCTION

Plastics have an advantage over paperboard in the possibility to form shell structures of an arbitrary shape without losing structural integrity.

Two types of complex-shaped paperboard structures already exist. Pulp can be sprayed on to a mould, which in general leads to packages with limited mechanical properties. Also, flat paperboards may be deep-drawn, but such paperboards are typically pre-creased and the final structures lack some esthetical appeal.

Here, 3D-forming from flat paperboard blanks is explored. Although deep-drawn products are common there is very little published in the scientific literature on deep-drawing of paperboard. In [1] plentiful examples from the Iggesund paperboard company are given, and 50 mm is indicated as a maximum drawing depth for the material. Some information may be learned from patent applications such as [2] and two theses also exist [3,4].

2 MATERIALS AND METHODS

To form complex-shaped paper specimens, the laboratory apparatus shown in Fig. 1 was developed. Pressure is applied on a rubber membrane to make it inflate like a balloon above the paper specimen. Below it is a heated mould against which the paper specimen is pressed. Some degree of restraint is enforced on the edge of the paper specimen by pressure from the ring outside the balloon against the mould (Figure 2). Circular specimens with a diameter of 15.5 cm were used. A piston induces a small deflection at the centre of the specimen prior to balloon inflation. Positioning of a specimen symmetrically on the typically hot mould along with applying the piston and clamping implies a delay of about 20 s between subjecting a specimen to heat and actual forming.

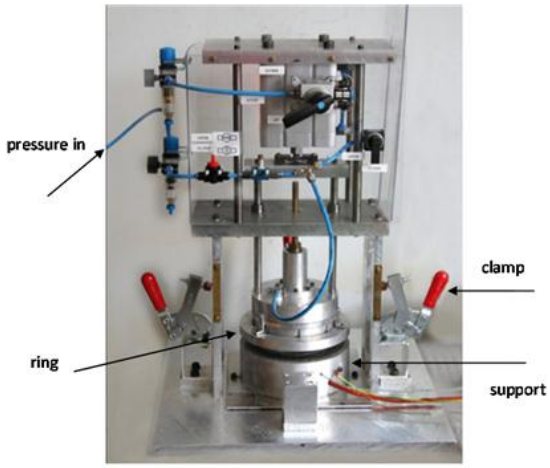

Figure 1. Laboratory forming equipment

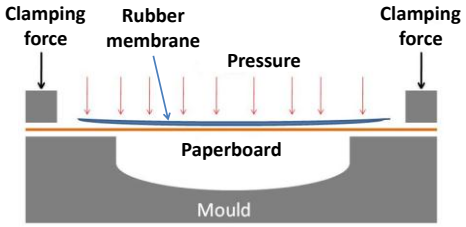

Figure 2. Forming principle

The moulds used in this work are shown in Fig. 3. The first two are spherical and the third is convex/concave with nominal strains (supposing homogeneous strain and no material flow into the mould) of 6, 12 and 21 %, respectively.

Figure 3. Moulds with a diameter of 100 mm

Typical process parameters are moisture, temperature, forming pressure, flow rate of pressure application and duration of the specimen in the mould. The influences of these parameters are investigated in [5]. Here we will discuss moisture in some detail. It can decrease the bending stiffness and increase the strain at break of paper materials. Water was typically applied by spraying. For paperboard specimens it was difficult to obtain a weight increase of more than 70 % by spraying

[1] Now at Tetra Pak Packaging Solutions AB, Lund, Sweden

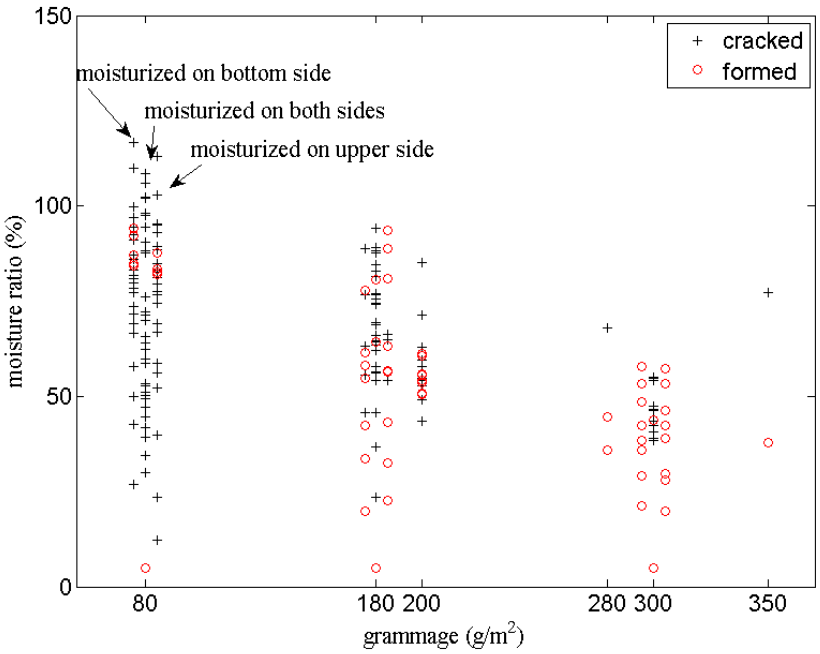

Figure 4. Forming attempts using the shallow mould (6 % nominal strain) with different grammage papers at varying moisture ratio

and moisture application was by immersion in a water bath in some cases. The moisture ratio was calculated by normalizing the wet weight by the weight after oven drying at 105 °C.

After removing the specimens from the mould, they were left to take on the ambient climate in the laboratory. Cracks in the specimens, wrinkling, non-flatness of the specimens and the spring back effect were observed over time after forming. Tensile testing of the formed and unformed paper sheets was performed to evaluate damage during forming.

3 RESULTS

The moisture ratio was varied for commercial papers and paperboards (grammage: 80, 180, 200, 280, 300 and 350 g/m^2).

3.1 Moisture content

In Fig. 4, the outcome of the forming using the shallow mould is shown for the various grammages and moisture levels. The temperature of the mould was between 130 °C and 170 °C.

Forming of 80 g/m^2 was successful only for a small interval in initial moisture ratio and only for one-sided moisturizing. For higher grammages, there were more successful results and the advantage of one-sided moisturizing is even clearer.

3.2 Wrinkles

Figure 5 shows the two major types of wrinkling encountered. The left specimen was formed dry and exhibits a handful of randomly placed wrinkles. The right specimen was formed with significant amounts of water applied to its upper surface before forming. It exhibits a sort of waviness, or short wavelength buckling, at the edge.

Figure 5. Two types of wrinkles: formed dry (left) and formed with significant amounts on water on upper surface (right)

3.3 Effects of specimen furnish

In [6] a range of well-characterized laboratory made boards were formed with minimal restraint at the edge at 130 °C and a moisture content of 30 % to check the correlation between forming results and paperboard properties.

Boards from hardwood pulp were prone to cracking in the forming process. This may be related to short fibres and defect sensitivity. Also, the board from mechanical pulp (CTMP) showed unexpectedly good forming results. This material has both low strength and strain at break.

Cracking during the forming process was in the experiments always by fibre pull-out. In all, defect sensitivity may be critical to good formability.

Tensile tests were done on successfully formed specimens to evaluate the damage to the material from the forming (Figure 6). Strain at break was lower than in the unformed material as expected. There was also some decrease of tensile strength

and a large decrease in tensile stiffness. This might suggest that the successfully formed specimens had

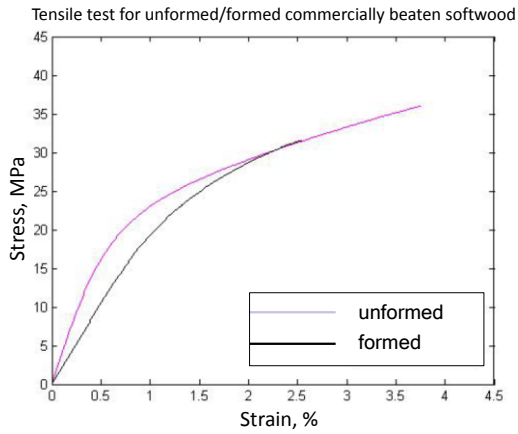

Figure 6. Stress-strain curves for formed and un-formed samples of commercially beaten softwood

been quite close to failure during forming. As to the loss of tensile stiffness, the bending stiffness is much higher for double curved paperboards for geometrical reasons, so it may not be a problem at the package level.

Inspired by the relative success of the initial 3D-forming trials more advanced trials were made. Examples of promising trials using sheets from mechanical and chemical pulps, respectively, are shown in Figures 7 and 8.

Figure 7: Paperboard from mechanical pulp (HT-CTMP) formed in the deep mourld (12 % nominal strain)

Figure 8: Paperboard from sized oxygen-bleached softwood chemical pulp formed in the convex/concave mould (21 % nominal strain)

4 SUMMARY AND CONCLUSIONS

In this project, the interest was to determine the best forming criterion to have specimens free of holes and cracks, observe the difference in mechanical properties of unformed and formed samples, to evaluate the materials' degree of damage and hence formability, and perhaps to choose which type of paperboard is more promising in continuation work.

This study has shown that it is possible to form 3D shapes using a wide range of paperboards. A wide range of moisture levels could also be used without cracking of the specimens, provided that moisture was applied to only one side of the specimen. A possible interpretation of this requirement is that a dry fibre layer was necessary to achieve high enough strength.

If the edge of the specimen is restrained during forming, the material in the formed region must stretch and therefore strainability should be an important property. If forming is accomplished by letting material from the edge flow into the formed region, strength is probably more significant for the material to overcome the frictional force at the edge. Wrinkling might be an issue with this latter type of forming.

Finally, this research shows that important knowledge on the complex relations between forming outcome, material properties and forming parameters is still to a large extent missing. Research activities to accomplish such knowledge include modifications of properties of the fibres and fibre network as well as advanced modelling.

Acknowledgements

The authors gratefully acknowledge the financial support for this project from BiMaC Innovation.

REFERENCES

[1] Kirwan, M. J., ed., Paper and Paperboard Packaging Technology, Vol.1, Blackwell Publishing Ltd (2005).

[2] Cross, G.H., Bernier, R.T., Method and apparatus for forming rigid paper products from wet paperboard stock, US Patent nr. 3305434 (1967).

[3] Scherer, K., Untersuchungen über die Ziehfähigkeit und den Ziehvorgang von Pappe (In German), PhD thesis, TU Dresden (1932).

[4] Hauptmann M. Die gezielte Prozessführung und Möglichkeiten zur Prozessüberwachung beim mehrdimensionalen Umformen von Karton durch Ziehen (In German), PhD Thesis, TU Dresden (2010).

[5] Östlund M, Borodulina S, Östlund S. Influence of paperboard structure and processing conditions on forming of complex paperboard structures. *Packag. Technol. Sci.*, in press, DOI: 10.1002/pts.942 (2011).

Improvement of conductivity of paper through Layer-by-Layer multilayering of PEI and PEDOT:PSS

HYE JUNG YOUN, JEGON LEE, JAEHO RYU, KYUJEONG SIM, and HAK LAE LEE

Dept. of Forest Sciences, Seoul National University
1, Gwanak-ro, Gwankak-gu, Seoul, 151-921
KOREA
page94@snu.ac.kr

1 INTRODUCTION

Paper is a representative insulating material with relative low cost. It has been used for cables or coil windings. Becuase it has characteristics such as low cost, excellent specific mechanical properties and chemical stability, however, its use can be extended to various industry fileds like electronic field. One of the approaches to enhance the application of paper is to modify the surface of paper using functional materials. A layer-by-layer multilayering technology is known as the versatile and simple method for surface modification [1].

Conductive paper can be made through Layer-by-Layer (LbL) mulitlayering of conductive polymer to pulp fibers. Because poly (3,4-ethylenedioxythiophene) : poly(sodium 4-styrene sulfonate) (PEDOT:PSS) has high affinity to water and anionic charge, it can be adsorbed on to pulp fibers by the aid of cationic polymer. Agarwal et al [2] produced a conductive fiber with conductivity of 1 – 10 S/cm through LbL multilayering of PEDOT:PSS and polycation. Conductive paper with nanocomposite of carbon nanotubes and conductive polymers was also reported [3]. This combination resulted in the paper with higher conductivity. The adsorption of PEDOT:PSS on fibers was characterized by SPAR or XPS [4,5]. The conductivity of the paper was dependent on the polycation type and multilayering conditions. In this study, the effect of salt concentration (ionic strength) during multilayering process was investigated to make a conductive paper. In addition, the influence of the sheet densification by calendering on the conductivity was also examined to increase the conductivity of paper.

2 EXPERIMENTAL

Bleached Eucalyptus kraft pulp was disintegrated in a Valley beater and washed to remove colloidal and dissolved materials. PEDOT:PSS was used as a conductive polymer and polyethyleneimine (PEI) was used to help PEDOT:PSS to be adsorbed on the pulp fibres and form a multilayer. The ionic strength of the pulp suspension was controlled using NaCl solutions of 2.5 mM, 5.0 mM, and 10.0 mM. The pH of the suspension was adjusted using HCl or NaOH solution. The PEI was firstly added to the 0.5% pulp slurry and mixed for 20 min. After adsorption of PEI, the pulp fibers were washed twice using deionized water to remove the unadsorbed polymer. The PEDOT:PSS was then adsorbed for 20 min and rinsed again. The successive adsorption of PEI and PEDOT:PSS forms a 1 bi-layer. The pulp fibers were treated upto 10 layers (5 bi-layers). The adsorption behavior and the amount of PEDOT:PSS and PEI were evaluated using quartz crystal microbalance (QCM) and by elemental analysis of paper sheet.

Handsheets with grammage of 100 gsm were prepared using untreated and LbL multilayered fibers. They were calendered under different pressure conditions. After preconditioning at the constant relative humidity and temperature, the physical properties and conductivity of the handsheets were measured.

3 RESULTS

3.1 Effect of salt concentration

In this study, the multilayering of PEI and PEDOT:PSS was conducted upto 10 layers. The handsheests were made from the multialyered fibers with PEDOT:PSS in the outmost layer (even layer). The conductivity of the handsheet was depicted in Figure 1. The conductivity of the paper increased with an increase in the number of layers. In the earlier layer (2 layer), the paper conductivity was higher when the salt concentration was increased. On the other hand, it was in inverse proportional to the salt concentration at higher number of layers. In the case of 10 layers, the handsheet which was prepared at 2.5 mM NaCl condition showed 1.2×10^{-4} S/cm, which was three times higher compared to that of 10 mM NaCl condition.

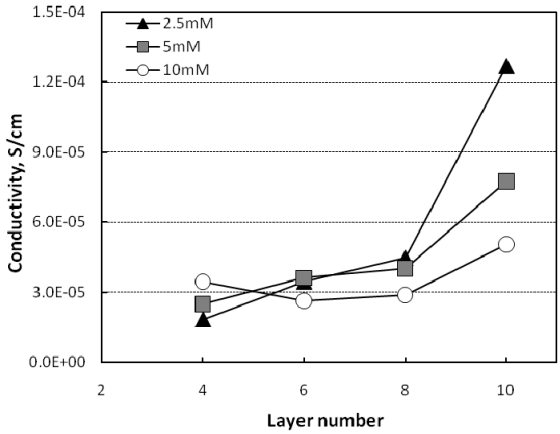

Figure 1. Conductivity of handsheet made of PEI/PEDOT:PSS multilayered fibers.

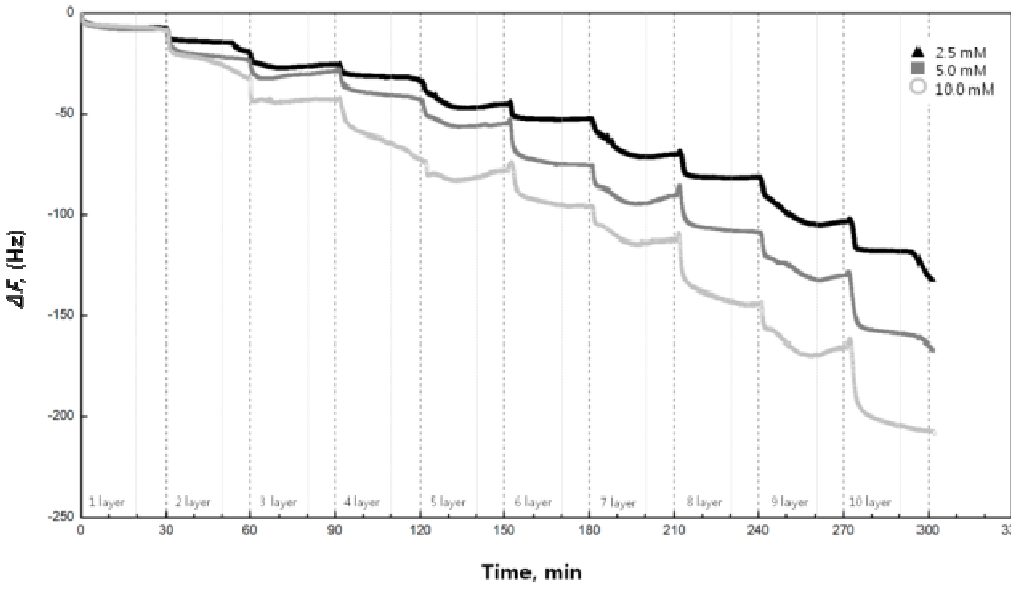

Figure 2. Frequency change during the layer-by-layer multilayering of PEI/PEDOT:PSS on cellulose film.

The adsorption behavior of PEDOT:PSS was evaluated. Figure 2 showed the frequency change during the adsorption of PEI and PEDOT:PSS which was measured using QCM. The negative change of frequency indicated the adsorption of the material on the substrate. The cellulose model film was used as a substrate. The multilayering process which consisted of 20 min adsorption and 10 min washing stages was carried out until 10 layers. As the number of layers increased, the adsorption amount of polymers increased. Also, the adsorbed amount of the polymers increasaed at high ionic strength condition because of the screening effect of electrolyte.

The amount of PEDOT:PSS which existed on the pulp fibers was quantified as the sulfur content of the paper using calibration curve. The sulfur content was measured using inductively coupled plasma optical emission spectrometer (ICP-OES). The cumulative adsoprtion amount of PEDOT:PSS was represented in Figure 3. The trend was similar to the QCM result.

It suggested that the conductivity is affected by the adsorption amount in the earlier layer (2 layer). When the pulp fibers were multilayered at low salt concentration, however, the paper had higher

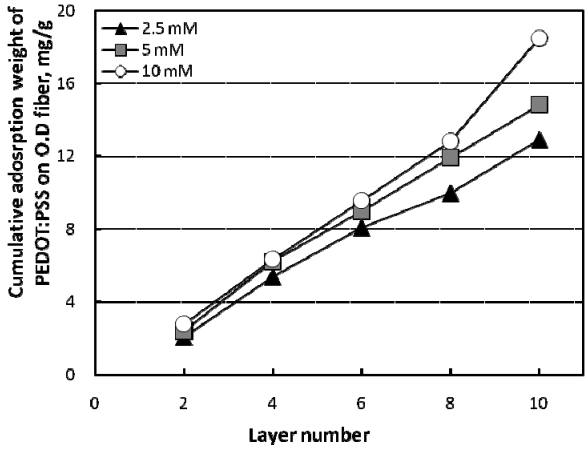

Figure 3. Cumulative adsorption amount of PEDOT:PSS on fibers.

conductivity with the increase in the number of layers. In other to say, the relative low adsorption amount of PEDOT:PSS showed better conductivity at a higher number of layers. It indicated that the structure of the polymer layer was more critical factor to develop the conductivity of the paper at higher layer number.

3.2 Effect of calendering

The calendering is a representative process to reduce the thickness. The sheet densification by calendering was considered to improve the conductivity of the paper. The conductivity of the paper could be increased by about twice through calendering (Figure 4). The change of paper structure by calendering seemed to be good for improving the electrical conductivity.

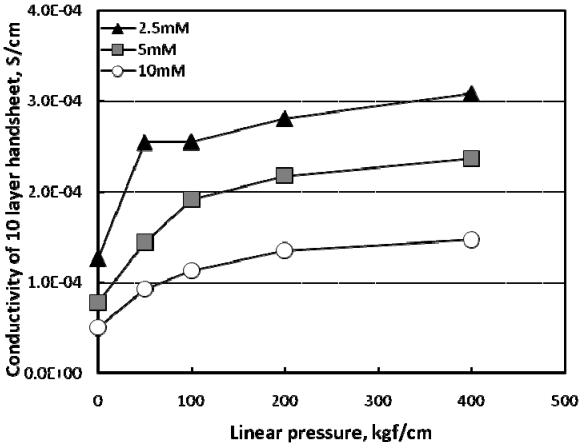

Figure 4. Effect of calendering on the conductivity of the handsheet (10 layers).

4 CONCLUSIONS

A conductive paper was prepared through layer-by-layer multilayering of PEDOT:PSS and PEI, and the effects of salt concentration and calendering were investigated. The conductivity of the paper increased with an increase in the number of layers. In the earlier layers, the conductivity was affected by the adsorption amount. When the pulp fibers were multilayered at low salt concentration, the paper had higher conductivity at a higher number of layers. In other to say, the relative low amount of polymer adsorbed showed better conductivity at a higher number of layers. The structure of the polymer layer was more critical factor to develop the conductivity of the paper at higher layer number. The conductivity of the paper could be increased by calendering.

5 ACKNOWLEDGEMENT

This work was supported by Mid-career Researcher Program through NRF grant funded by the MEST (R01-2007-000-10791-0).

REFERENCES

[1] Decher, G., Hong, J.D., and Schmitt, J., Buildup of ultrathin multilayer films y a self-assembly process: III. Consecutively alternating adsorption of anionic and cationic polyelectrolytes on charged surfaces, *Thin Solid Films*, **210/211**:831-835 (1992).

[2] Agarwal, M., Lvov, Y., and Varahramyan, K., Conductive wood microfibers for smart paper through layer-by-layer nanocoating, *Nanotechnology*, **17**:5319-5325 (2006).

[3] Agarwal, M., Xing, Q., Shim, B.S., Kotov, N., Varahramyan, K., and Lvov, Y., Conductive paper form lignocelluloses wood microfibers coated with a nanocomposite of carbon nanotubes and conductive polymers, **20** (2009).

[4] Montibon, E., Järnström, L., and Lestelius, M., Characterization of poly(3,4-ethylenedioxythiophene)/poly(styrene sulfonate) (PEDOT:PSS) adsorption on cellulosic materials, *Cellulose*, **16**:807-815 (2009).

[5] Wistrand, I., Lingström, R., and Wågberg, L., Preparation of electrically conducting cellulose fibres utilizing polyelectrolyte multilayers of poly(3,4-ethylenedioxythiophene):poly(styrene sulphonate) and poly(allyl amine), *European Polymer J.*, **43**:4075-4091 (2007).

Posters

Paper Properties

2D fibre and filler grammage maps using movable radiation emitters and detectors

MARCO LUCISANO, PAUL KROCHAK, ÅKE HANSSON, LARS THOMSSON, JON LOFTHUS and BO NORMAN

Innventia AB
Box 5604, SE-11486 Stockholm (Sweden)
marco.lucisano@innventia.com

Keywords: Measurement technique, grammage, paper structure, filler content, variability.

ABSTRACT

We have designed a scanning equipment to map total grammage and filler grammage with 2 – 5 mm resolution in large paper samples. The equipment has been integrated with a pilot-scale winding machine at Innventia, to allow automatic scanning of samples of arbitrary length and maximum width 400 mm. Sensors for total grammage and for filler grammage move across the paper while the sheet is kept stationary. The sheet is advanced to the next position after each scan.

The data generated by the system can be analyzed in a stand-alone program by which colour-coded maps can be plotted for total grammage as well as for fibre and filler grammage. Additionally it is possible to evaluate variability within any subregion in the data set.

1 INTRODUCTION

Current and ongoing needs of producers of paper and board products focus largely on improving product quality and reducing the consumption of raw material and energy. Excessive variability in the web structure degrades the web properties and therefore requires increased grammage levels in order to deal with problem zones.

A paper web may have high levels of variability in local grammage as well as in web structure, including the local fibre orientation, the distribution of filler, fines and chemical additives. Variability is due largely to process deficiencies, for example uneven raw material mixing coupled with fibre flocculation effects, instabilities in headbox flow and disturbances during dewatering. If variability could be reduced, this would allow a reduction in mean grammage, i.e. savings in fibre consumption and therefore also in energy consumption, combined with improved product quality and improved runnability.

One key aspect in research efforts aimed at improved homogeneity is the capacity to acquire large data sets describing the structure of paper. Therefore we have developed new scanning equipment that complements the measurement capabilities already available to papermakers.

1.1 On-line variability measurements

Modern paper machines are equipped with on-line systems to characterize paper quality. Grammage, moisture, filler content, caliper and surface roughness are some of the properties that are commonly measured. Because of the high cost of quality control sensors for on-line applications, the measurement unit is typically moving across the web to record both MD (machine direction) and CD (cross-machine direction) information. The separation of MD variation from CD variation is a classic problem in paper machine control and reviews on the subject are available in the literature, e.g. [1]. Although this approach is well-known and widely used, its descriptive value is limited by the fact that only a very small fraction of the total web area is scanned.

Recently, a full width camera-based system has been described that enables variations in light transmissions to be determined online at the wet end of paper machines [2]. These variations can be interpreted as variation in web fibre mass distribution, if one is aware of the limits imposed by the necessary assumptions [3]. The experience from mill installations with this system suggests that paper machines tend to have a very high level of high-frequency formation variations. Therefore it is likely that new investigations of variability in paper structure performed with tools capable of scanning large areas at high resolutions might provide new insights, which have previously been unattainable because of the limited capability of available measurement equipment.

1.2 Characterizing variability in large paper samples

The structural variability in paper samples of large dimensions has been measured with the ATPA system (The Advanced Total Paper Analyser) at Stora Enso (Kvarnsveden paper mill, Sweden) [4, 5]. Composed of a modified rewinder and of a standard traversing quality control system, the ATPA scans paper samples stepping both in MD and CD. The resolution is reported to be 1 cm at best and typically 5 cm. The ATPA is a unique tool since it generates 2D descriptions of the structure of very large samples, frequently several km in length.

Laboratory scale devices that can acquire large amount of data along a single line are commercially available for quality control purposes, e.g. [6]. Here, MD or CD strips are passed under one or more sensors to measure a variety of properties, e.g. grammage, caliper, filler content.

1.3 Variability studies at laboratory scale

A large variety of laboratory techniques for characterization of web structures and variability in

paper samples is described in the literature. These techniques span from standardized procedures, such as the beta-radiation based methods to characterize grammage and formation [7], to research tools to study the distribution of fillers [8]. Whereas the availability of laboratory methods for studies of web structure is practically unlimited and their resolution satisfies all requirements, the surface area that can be analyzed is often small, at the most in the order of magnitude of one A4 sheet. Thereby, measurement methods developed for laboratory use are impractical when acquiring large data sets to describe the structural variability of the web caused by the papermaking process.

This article presents a new scanning system to map local fibre and filler grammage in large paper samples. The equipment allows automatic scanning of samples of arbitrary length and maximum width 400 mm. Sensors for total grammage and for filler grammage move across the paper sheet, which, in its turn, is moved forward between two successive scans. The device is now used as a research tool in projects aiming at improving the structural uniformity of paper as well as for characterization of samples of commercial origin for quality assessment and troubleshooting.

2 METHOD

2.1 Principle of operation

The measurement device is integrated with Linda, a pilot winding machine at Innventia used for dynamic studies of moving paper webs. Initially, the paper reel to be tested is mounted onto the unwinding and winding stations of the machine (Figures 1 and 2). These are used both to feed the sample to the measurement frame under controlled tension and to reel up the web after the measurement. The longitudinal movement of the sample (C in Figure 1) is controlled by a servo motor connected to one soft nip (E) on the Linda machine.

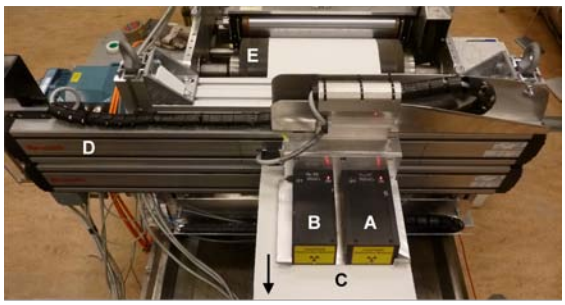

Figure 1. The scanning equipment: Pm-147 (A) and Fe-55 source (B); detectors are placed below the sample (C); frame and linear translation units (D); soft nip (E).

Two sensors, one each for grammage and filler (A and B in Figure 1), are moved across the width of the sample on an O-frame connected to the frame of the Linda machine. The transversal movement of the sensors is generated by a servo motor connected to two linear translation units mechanically connected to each other, in order to maintain alignment between the source and the detector of each of the two sensors.

A LabVIEW-based system controls the longitudinal and transversal movements, acquires the signals from the two sensors and handles calibration issues. Depending on the purpose of the investigation, scanning can be performed in a point-by-point fashion or in a continuous mode, the details of which are presented in Section 2.3.

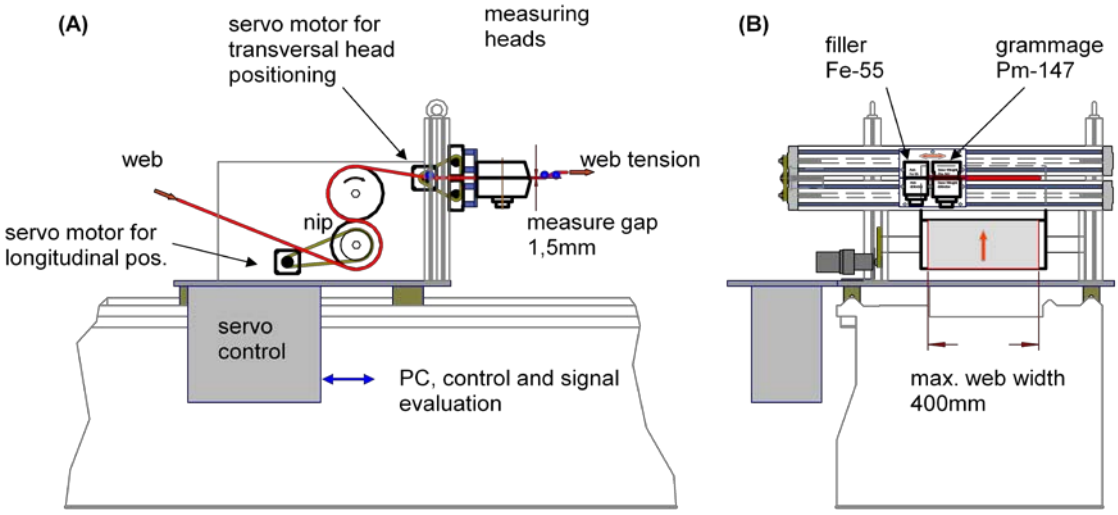

Figure 2. Schematic of the scanning unit mounted on Linda (A) side view and (B) front view.

2.2 Sensors

The measurement system is based on sensors used in commercial instruments (Tapio Oy, Espoo, Finland), where they are implemented as stationary sensors through which a narrow reel of paper (oriented in CD or MD) is moved [6]. Each sensor consists of one radiation source and one radiation detector, placed on opposite sides of the sample to be measured. The sensors have been supplied with a mechanical aperture just before the detectors, limiting the measured area to a circle with either 2 mm or 5 mm in diameter. The system is set up and calibrated following the original strategies and formulas supplied by Tapio Oy, which have been implemented in a LabVIEW program. Due to the statistical nature of the behaviour of the radioactive sources, smaller apertures lead to higher noise levels in the measurement, or, for a fixed noise level, to a longer integration time. The 2 mm and 5 mm apertures represent a reasonable compromise between spatial resolution, noise level and measurement speed.

Total grammage

The sensor for total grammage consists of promethium-147 (Pm-147) as the source for beta radiation (electrons) and a solid state detector. The activity of the Pm-147 source is 500 mCi, with a half-life of 2.62 years. The beta radiation from Pm-147 is rather soft and its intensity is halved after passing a sheet of paper with a basis weight of approximately 140 g/m^2 which makes it suitable for basis weight measurements in the basis weight range of about 30–240 g/m^2.

The calibration of the total grammage sensor is based on three standard samples of known grammage (Tapio Oy), as well as on a measurement of the detector-side offset performed with the measurement gap blocked by a metal shutter. Curve fitting is performed according to the Lambert-Beer law of absorption. Two independent calibration procedures are performed for each of the two aperture diameters, 2 mm and 5 mm.

Filler

The sensor for filler grammage is based on iron-55 (Fe-55) to generate X-ray radiation. The activity of the Fe-55 source is 100 mCi, with a half-life of 2.74 years. The X-rays employed are considerably "harder" than the beta radiation and are, as a first order effect, blocked by the inorganic substances in the sheet, while passing through the organic components. Yet, all components in the sheet attenuate the radiation to some extent, an effect that needs to be accounted for in the processing of measurement data. A further degree of complexity is caused by the fact that different fillers are associated with different levels of attenuation of the incoming radiation, which can be described by a mass attenuation constant (MAC). The MAC of water and of most organic constituents is approximately 0.002 whereas traditional fillers in the papermaking practice have higher values: kaolin and talcum exhibit a MAC of 0.009 (4.5 times the MAC of the organic constituents). Gypsum and $CaCO_3$ exhibit a MAC about twice that of the previous group, 0.018. TiO_2, is associated with the highest MAC: 0.03, almost twice again.

In order to account for these complications, the software asks the user for an estimate of the global filler content and of the composition of the inorganic material. The program then calculates the MAC separately for the inorganic and organic components (MAC_{inorg} and MAC_{org}, respectively). The total mass attenuation constant for the entire structure is calculated with Lambert-Beer law, given the attenuation measured with the Fe-55 sensor and the total grammage measured with the Pm-147 sensor. K_{inorg}, the fraction of the total grammage that can be attributed to fillers, is then calculated as:

$$K_{inorg} = \frac{MAC - MAC_{org}}{MAC_{inorg} - MAC_{org}},$$

from which the local fibre grammage and local filler grammage are calculated.

The filler sensor requires the total grammage sensor to over scan by the inter-detector distance (110 mm), in order to measure filler content on the last measurement point on the sheet. Therefore, considerable time may be saved (especially when the scan width is narrow) if data acquisition for filler measurement is suppressed when not needed. As an example, when the required measurement width is 220 mm, the total scanning width including the ash measurement is 330 mm (a 50% increase in scanning time as compared to measuring the total grammage alone).

2.3 Scanning mode

The scanning unit has been designed to acquire high resolution maps of local fibre and filler grammage with good accuracy and acceptable measurement speed. Although the movement of the sensors can be programmed for any arbitrary scanning pattern over the surface of the sample, we have restricted our study to two scanning modes: either (A) point-by-point operation or (B) continuous mode (Figure 3). In both operation modes, the spatial resolution was set to either 2 mm or 5 mm, chosen as the diameter of the two mechanical shutters of the detectors. Therefore the longitudinal stepping distance between two consecutive scanning lines was set to either 2 mm or 5 mm, depending on the actual resolution.

In the *point-by-point mode*, the sensors move to the new measuring point and stop there while integrating the measurement signals. There are several advantages to this measurement mode. Due to its sequential nature it absorbs any time delays

generated by the operating system ensuring that the intended area is measured every time. Further, there is no spatial smoothing. On the down side is that the continuous acceleration and deceleration needed to move from point to point consume time.

In the point-by-point mode, where the points are placed side by side (i.e. the stepping distance equals the aperture diameter) just under 80% of the sheet area is assessed. The remaining area falls between the measured circles.

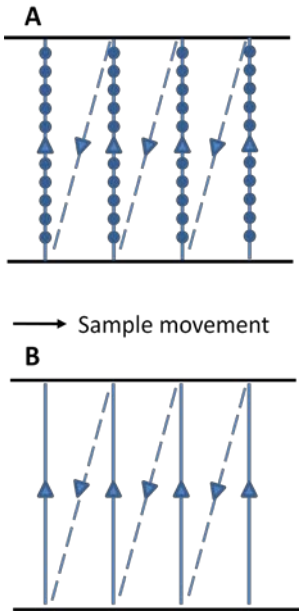

Figure 3. Schematic of the scanning path of the measurement sensors. In the point-by-point mode (A) dots indicate the centre of the measurement points. In the continuous mode (B) information is sampled along the solid lines only. The broken lines represent movements with no data acquisition. Drawing not to scale.

In the *continuous mode*, the sensors traverse across the sheet at a constant speed. Due to the uncertainties in the timing of the operating system there is no way to know with certainty where the scanning heads are positioned at each specific moment. Therefore the software is designed under the assumption that the heads move at a constant speed. Dead reckoning is used to estimate at what specific time the next integration should start to match the position of the next grid point. The integration and all house-keeping function should be completed in time before the next grid starting point is reached.

When working in continuous mode, the optimum combination of scanning speed and integration time needs to be determined for each specific case, taking into account that a longer integration time leads to better signal-to-noise ratio, but also reduces the spatial resolution and increases the risk of not being ready for the next measurement point when that grid point is reached.

In principle, close to 100% sheet coverage may be obtained in this mode, but at a cost of substantial spatial averaging and considerable overlap between measurement points.

In both operation modes, when the measurement heads reach the back-side edge, they are returned at highest speed available to the scan start point (broken lines in Figure 3). It was decided not to measure on the return movement in order to avoid problems with asymmetrical time delays which easily could result in more complex measurement tuning parameters.

2.4 Software for data handling

The output of the measurement unit is in the form of tabbed data files that can be handled with any conventional software. To simplify the evaluation of data, we have prepared a stand-alone MATLAB program which reads the raw measurement data, prepares graphic representation of the measured parameters and performs basic statistical evaluation (Figure 4). In the software, the user can generate 2D-maps of total grammage, fibre grammage, filler grammage and local filler content. Additionally the software calculates the mean value, the standard deviation and the coefficient of variation of the data, it plots histograms, identifies outliers and performs FFT analysis. Yet another useful feature of the software is the possibility to perform the analysis on user-selected subsets of the measurement data.

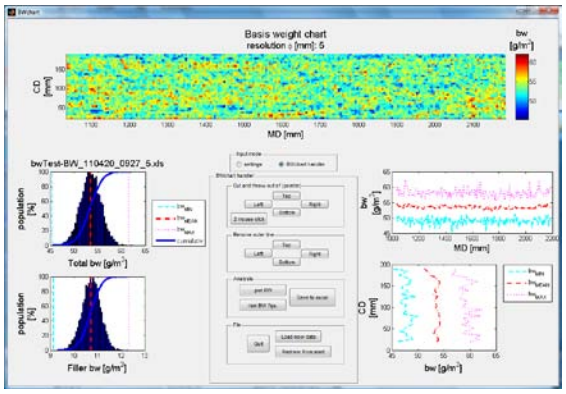

Figure 4. Graphical user interface of the data handling program.

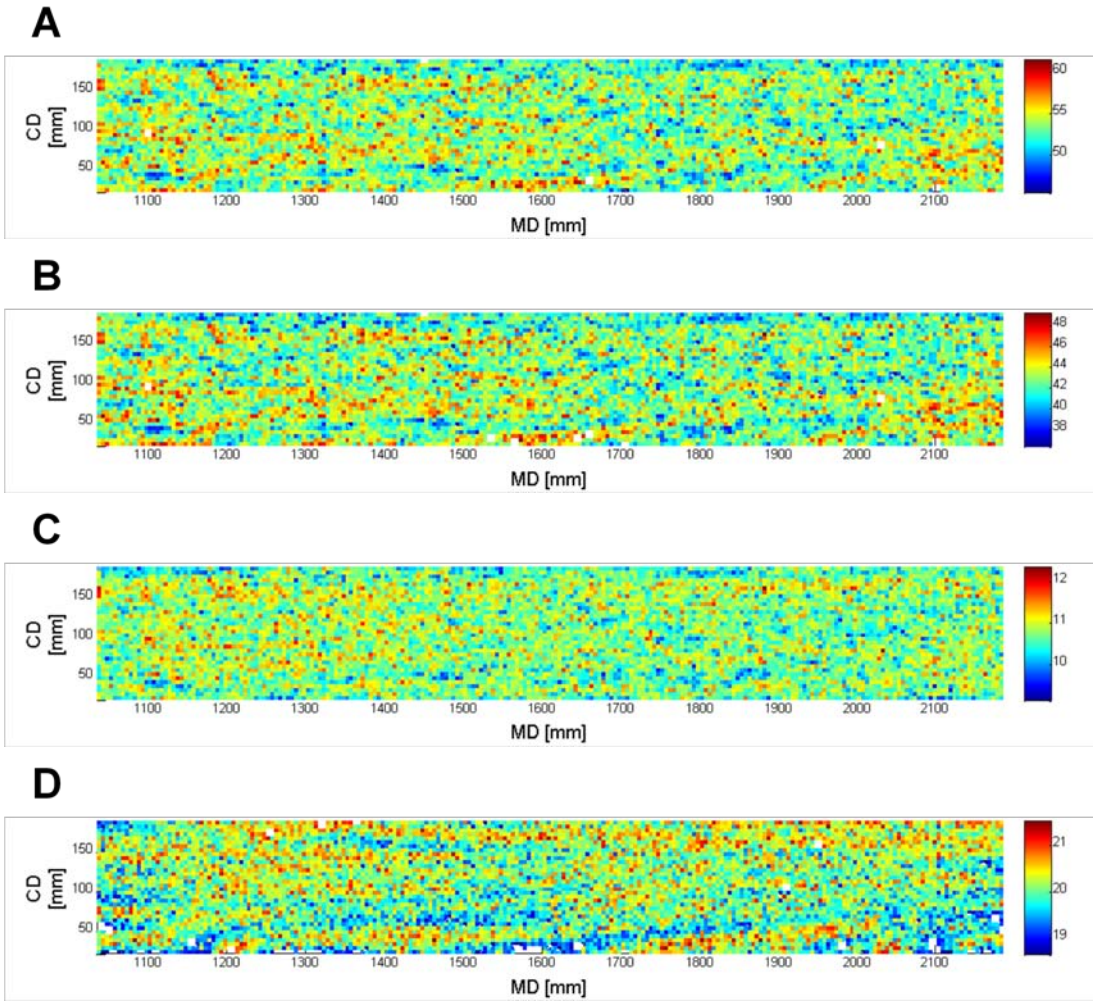

Figure 5. Sample measurement result for a sample of 200 mm (CD) × 1200 mm (MD), with mean total grammage 55 g/m^2, and mean filler content 20%. The sub images show 2D-maps of (A) the total grammage, (B) the fibre grammage, (C) the filler grammage and (D) the percentage filler proportion.

3 RESULTS

This article introduces and describes a new system to characterize variability in the structure of paper, specifically variations in total grammage and filler grammage. The new measurement unit consists of two sensors mounted on a frame, which gives linear translations. The frame has been integrated on Linda, a pilot scale dynamic web testing machine at Innventia. The system automatically measures the total grammage and the filler grammage of samples of arbitrary length and maximum width 400 mm. The spatial resolution in is set to either 2 mm or 5 mm.

The raw data files from the systems are in the form of 2D matrices with local measurements of total grammage and filler grammage. In our studies of variability in paper structures we have found that four different modes of representation give valuable information: (A in Figure 5) total grammage, (B) fibre grammage, (C) filler grammage and (D) percentage filler proportion.

2D maps of total grammage

The analysis of 2D maps of total grammage is common both in research and development and in the industrial practice of papermaking. These investigations are traditionally performed at laboratory scale on samples of limited size. The only notable exception described in the literature is the Advanced Total Paper Analyser, ATPA, which allows measurement of samples of arbitrary length over the full width of a paper machine [4, 5].

In this respect, the difference between our equipment and the ATPA is found in the balance between the resolution and the width of the samples: the spatial resolution of the system presented here is higher than in the ATPA, yet the maximum width of the samples is limited to 400 mm.

2D maps of total grammage can be used to study variability in industrial papermaking processes. When measuring 4 m of a sample of commercial origin, we could identify two bands of high grammage, extending 200 – 300 mm in MD and spaced approximately 2200 mm from each other (Figure 6). This occurrence would have been unnoticeable to most traditional laboratory scale

measurement methods, with the exception of scanning techniques analogous to that in [5], on which our work is based. Therefore Figure 6 can be interpreted as an illustration of the difficulties of obtaining reliable measurement on a material with the structural complexity of paper. It is easy to realize that two samples originating respectively at MD = 500 mm and at MD = 3500 mm in Figure 6 would provide completely different information for quality control.

We have used 2D grammage maps as a tool in our research and development work on the mechanisms influencing the generation of structural non-uniformity in paper. In one set of experiments we introduced a variety of controlled defects in paper produced with the FEX pilot paper machine at Innventia. The paper samples were later characterized with respect to structural variability and mechanical properties. One of the cases we studied was the effect of a local dilution flow in different positions in the headbox. Figure 7 illustrates one of these experiments, where the dilution defect appears as a very sharp streak essentially parallel to the MD.

2D maps of filler grammage

Whereas investigations of in-plane 2D variations of total grammage are a well known practice in the papermaking industry, separate mapping of fibre grammage and filler grammage for large paper samples are a new feature. Figure 8 presents a 2D filler grammage map for a commercial paper sample of 400 mm (CD) × 950 mm (MD).

We envision that the availability of detailed 2D-descriptions of the local filler grammage could evolve into a valuable new tool for development of products and processes in papermaking. Some examples of possible fields of application might include (i) troubleshooting of industrial processes; (ii) studies of the relationship between the nature of the papermaking process and the small-scale structure of the product, in particular (iii) studies of the mechanisms determining the relationship between formation and retention in paper.

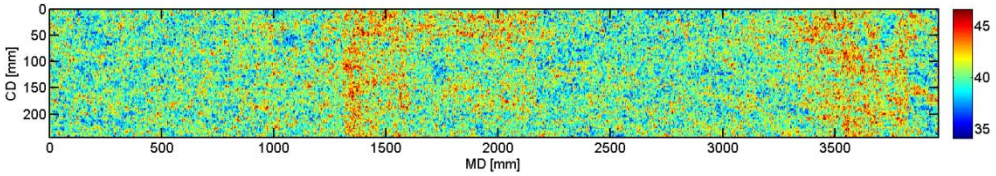

Figure 6. Total grammage map of a commercial sample of 250 mm (CD) × 4000 mm (MD). Grammage is colour-coded in g/m^2.

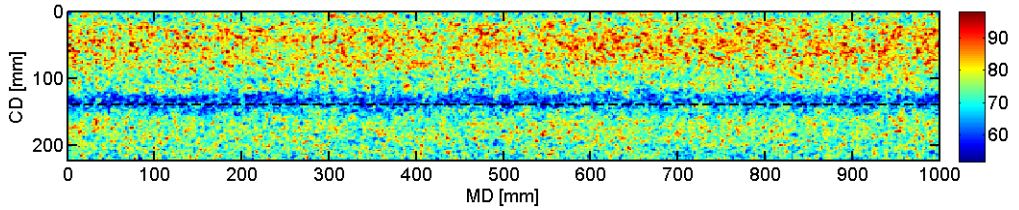

Figure 7. Total grammage map of a sample of 210 mm (CD) × 1000 mm (MD). Grammage is colour-coded in g/m^2. The highly localized low-grammage streak was generated in a pilot-scale run with extreme local dilution.

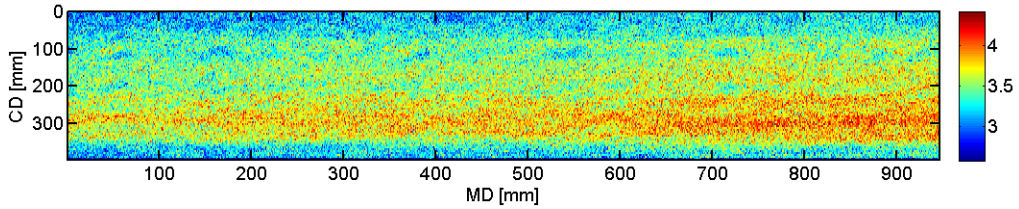

Figure 8. Filler grammage map of a streaky area in a commercial sample of 400 mm (CD) × 950 mm (MD). Local filler grammage is colour-coded in g/m^2.

4 FUTURE DEVELOPMENTS

Transversal positioning and movements

In the current implementation of both scanning modes, the heads are set up to scan the sheet on a measurement grid with the point distances made equal to the selected measurement aperture size (i.e. no gaps between measurement points). The measurement grid is fixed in relation to the measurement frame, implying that the sheet edges should also be transversally fixed vis-à-vis the measurement frame.

It has proven hard to accurately control the transversal position of the sheet with reference to the measurement frame. Therefore future implementations may include a scanning mode that adapts to the relative movement of the actual edge of the sample.

Longitudinal positioning

One major advantage of the equipment presented here is that the system automatically scans samples of arbitrary length with no interaction with its operator. The longest trial that we have performed involved uninterrupted scanning for three weeks. The availability of a structural description of a sample opens new opportunities for selecting the optimal sampling position for specimens to be used to characterize any additional property. Yet, we have realized that identifying specific spots in a reel that can have a length of several meters is impractical. Therefore we are in the process of installing an ink-jet printing head to print regular position markers on the sample, at the same time as the grammage scanning proceeds.

New sensors

The system was designed to allow future extensions to include scanning of other properties, for which a 2D mapping over the surface of the sample might provide new insight. One example, which might be added in a future upgrade is the OptiTopo, a non-contact system that provides three-dimensional images of a paper surface [9, 10]. Additional sensors with a measurement time comparable to or shorter than the present implementation of the two radioactive sensors would not imply any significant delay in the scanning performance.

ACKNOWLEDGEMENTS

Margareta Bäckström at Innventia is thanked for managing the installation and start-up of the measurement system.

The authors wish to express their gratitude for the support from the companies financing the Web Structure and Runnability Research Cluster in the Research Program 2009 – 2011 at Innventia. Funding from Energimyndigheten, The Swedish Energy Agency, is gratefully acknowledged.

REFERENCES

[1] Figel, K., John, G., Machattie, R., Nuyan, S. and Tippet, J. Paper machine quality control systems, Vol. 1: Measurement systems and product variability, TAPPI (2010).

[2] Söderberg, D., Wiberg, A. and Jonhed, L. Real-time measurements of basis weight variations across the full machine-width of individual plies in board production, Control Systems ’10, Stockholm, SPCI (2010).

[3] Norman, B., Overview of the physics of forming, 9th Fundamental Research Symposium, vol. 3, pp. 73-149 (1989).

[4] Hiertner, M., Basis weight varies faster than on-line systems can measure. Control Systems ‘98, Porvoo, Finland, Finnish Society of Automation, 307–313, (1998).

[5] Hjertner, M., Profiling cross machine basis weight – Measurement and characterization, Scientific and Technological Advances in the Measurement and Control of Papermaking, Edinburgh, UK, Pira, (2000).

[6] Hilden, K. and Perento, J. Paper analysis: the key to optimizing and troubleshooting paper machines. Pulp Paper Can. 101(7):37–42 (2000).

[7] Norman, B. (ed.) Beta-radiation based grammage formation measurement – Radiogram methods applicable to paper and light weight board. Nordic Standardization Program Report 5 (2009).

[8] Lucisano, M.F.C. Measuring the local distribution of fillers in paper: A new method for false 3D-studies of filler retentions. Progress in Paper Physics Seminar, FPInnovation, Montreal (2010).

[9] G.G. Barros and P.-Å. Johansson. The Optitopo technique for fast assessment of paper topography: limitations, applications and improvements. J. Imag. Sci. Tech. 49(2):170-178 (2005).

[10] P. Hansson and P.-Å. Johansson. A New Method for the simultaneous measurement of surface topography and ink distribution on prints. Nord. Pulp Pap. Res. J. 14(4):314-319 (1999).

Advanced Wire Marks Analysis – A Powerful Tool for Paper Inspection

KLAUS VILLFORT and SAMUEL SCHABEL

Chair of Paper Technology and Mechanical Process Engineering, Technische Universität Darmstadt
Alexanderstr. 8, 64283 Darmstadt, Germany
villforth@papier.tu-darmstadt.de

Keywords: Digital image processing, Image analysis, Wire mark, Paper structure, Hydraulic marks, Topographic marks, High resolution colour imaging, Tensile stiffness index.

ABSTRACT

Detection of quality variations in paper webs is always an important aspect of paper testing. Non-destructive test methods are essential for quality control, optimization and trouble shooting. Measuring tensile stiffness orientation (TSO) by ultrasonic wave propagation and optical formation analysis give indication for inhomogeneity in paper webs. Advanced wire marks analysis is a new supplementary tool to get an insight into paper structures.

As stand-alone unit, wire marks analysis quantifies all web deformations since sheet forming by analysis of periodic structures in paper due to dewatering on a forming fabric or between two forming fabrics (top and bottom wire).

Advanced wire marks analysis can distinguish between topographic marks caused by the contact of the fibre mat with the forming fabric's fine paper side and hydraulic marks caused by the coarse weave pattern of the wear side. Intensity variations of hydraulic marks show differences in dewatering, which affect local retention and formation. Intensity variations concerning top and bottom wire represent the hydraulic balance regarding two sidedness.

Colour imaging gives further information about local distribution of fibres and fines. Fibres show a high contrast in the blue component of the three RGB primary colours. The green component represents a balanced visual impression while the red component is dominated by fillers due to the low contrast of fibres. Advanced wire marks based on colour imaging provides information about the distribution of fibre components in the paper web.

1 INTRODUCTION

Paper structures originate mainly from dewatering of fibre suspensions in the paper. While dewatering paper fibres flocculate and form stochastic structures called cloudiness or formation. On a forming fabric fibre flocks, single fibres and fines form a filter mat, which may retain more or less mineral fillers and fibre fines. Fibres store the characteristic topography of the underlying fabric. Fines however, follow local flow and pulsations cause fines to collect at the wire sides. Both effects combine to form hydraulic marks.

Intensity and pattern of these hydraulic marks depend mainly on the design of a paper machine's wet end, the fabric structure, the settings of machine parameters and the structure of the fibre mat. Drainage elements such as suction rolls can also leave their own characteristic marks in the paper structure.

After sheet forming in paper machine's wire section, felts remove the water squeezed out of the paper web in the press nip. Hereby, the felt base may leave felt marks in the paper web. These felt marks have a hydraulic component, since some of the fines are removed together with the water.

Strain in machine direction (MD) and web shrinkage in cross machine direction (CD) are basic characteristics of a drying section. Configuration of the dryer, fibre properties, fibre orientation and spatial web tension lead to specific shrinkage profiles with high values at the edges. Wire marks analysis detects shrinkage profile and web deformation with high accuracy [1].

Every paper machine is unique due to differences in its design, machine clothing (fabrics and felts), machine settings (manner of operation), and paper grade. In this respect, paper structure can be seen as an individual fingerprint of a specific paper machine. In the produced paper, several marks interfere with each other. They can be revealed by image analysis methods.

Preferably different methods are combined to get a deeper insight into paper machine processes such as sheet forming, dewatering, pressing and drying. Ultrasonic measurement of tensile stiffness in combination with formation and wire marks analysis based on high resolution colour imaging give substantial information about local differences in paper structure.

1.1 Determination of Tensile Stiffness

The ultrasonic based measurement of tensile stiffness index (TSI) in MD and CD direction is a well known method performed by Lorentzen & Wettre TSO Tester [2]. The $TSI_{MD/CD}$ ratio shows a strong relation to local shrinkage measured by wire marks analysis.

1.2 Determination of Wire Marks

The detection of wire marks is based on their periodic structure. First, an image of the paper sample has to be taken in transmitted light. After being filtered in spatial domain, the image is transformed into the frequency domain. High-pass filters suppress the low frequency signals caused by the paper's formation. Basic algorithms and their

application are published in detail since the late eighties [3,4,5,6,7].

A new fuzzy cluster algorithm for the analysis of periodic paper structures was developed at the TU Darmstadt in the frame of the AiF research project 13365 N [8, 9]. The cluster algorithm detects autonomously wire marks of any weave pattern. In the frequency domain, the pattern of a wire mark can be represented by set of two base vectors. This set can be seen as least common multiple of a forming fabric's weave pattern. Linear combinations of these base vectors point to all peaks of a wire mark. Once detected, weft and warp peaks provide basic information concerning web elongation and shrinkage as well as forming fabric's distortion. The latter retards dewatering locally and affects hydraulics in z-direction (two sidedness) in gap formers.

In case of multilayer fabrics, the weave pattern of the fine paper side differs from subjacent weaves like the coarse wear side. Advanced wire marks analysis makes use of differences in weave pattern in order to distinguish topographic from hydraulic marks.

2 METHODS

Improved hardware and new software features enhance the classical image analysis approach. Homogeneous illumination by electroluminescent foils, high resolution colour imaging with digital SLR cameras, and high performance computing by use of graphics processing units (GPU) are basic technical advances for the last years. Restrictions on image size are obsolete. Enhanced algorithms e. g. for Fast Fourier Transformation (FFT) process images of arbitrary aspect ratio. All these improvements contribute to advanced wire marks analysis.

2.1 Image acquisition and processing

The images are taken in transmitted light. The resolution of 508 dpi corresponds to a spatial resolution of 50 µm/pixel. The image size is 4,288 x 2,848 pixels (214.4 mm x 142.4 mm) which is approx. DIN A5. An electroluminescent foil (DIN A4) of 0.4 mm thickness powered by 140 V @ 400 Hz illuminates the paper sample in transmitted light. A digital SLR camera takes colour images with 3 x 14 bit resolution (16,384 gray values per colour channel). The offset between camera and the centre of the ultrasonic sensor device of L&W TSO Tester is 200 mm. **Figure 1** illustrates the camera setup.

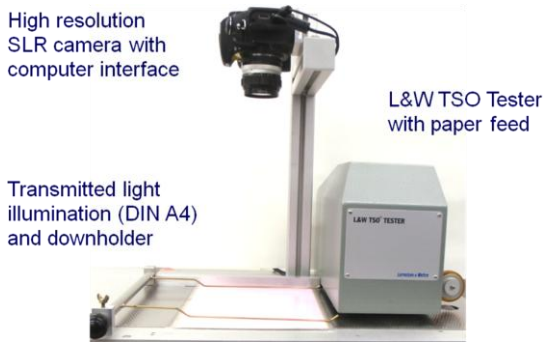

Figure 1. TSO Tester with digital SLR camera.

Windows Image Acquisition (WIA) provides the camera interface. Microsoft's driver model can be used by many programs such as MATLAB of MathWorks Inc.

A MATLAB program captures an image when TSO Tester's paper feed stops for an ultrasonic measurement. Stored images are converted without losses from raw format into portable pixmap format (PPM). MATLAB imports the 3 x 16 bit RGB PPM images and TSO data for advanced wire marks analysis.

A NVIDIA GeForce GTX 460 graphic processing unit with 2 GByte RAM provides sufficient computing power to analyse a colour image within 6 s in order to keep step with TSO Tester measuring cycle. The MATALB program uses GPU parallel computing power by a freeware library named GPUmat from GP-you Group.

The program processes the red, green, and blue colour channels of the RGB images separately. **Figure 2** exemplifies the big differences caused by the light absorption of fibres at short wavelength. The blue component shows an intensive formation. The red component is dominated by fillers due to the low contrast of fibres.

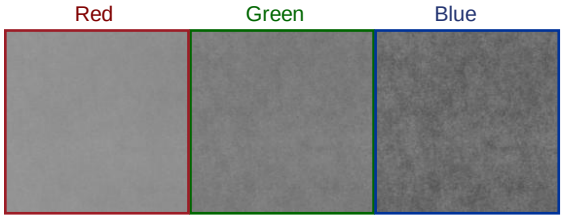

Figure 2. Fibres get more apparent at shorter wavelength.

A two-dimensional cosine window filter ensures the periodicity of the image. The filter prevents the fringe effect and provides accurate peaks in the frequency domain. **Figure 3** shows an image in the spatial and frequency domain.

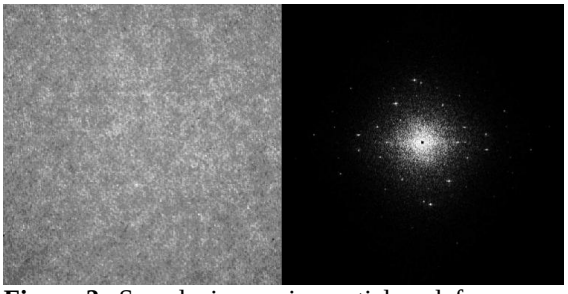

Figure 3. Sample image in spatial and frequency domain.

2.2 Clustering of Periodic Structures

The clustering method has to assign the peaks of the power spectrum to a certain wire mark. Fuzzy clustering is used, because peaks can belong to none, one or to more forming fabrics. Fuzzy clustering assigns variable degrees of cluster memberships to the peaks, where cluster prototypes represent the wire marks.

The overlay of peaks happens rather often, especially when top wire and bottom wire have the same design. The Fuzzy clustering splits the variance of an overlaid peak according to its membership values. This enables a reliable measurement of the wire marks' intensity.

Fuzzy clustering algorithms group element by a distance criterion. The distance between cluster centre and cluster members is optimised iteratively by moving the cluster centre and updating the memberships. The wire mark peaks are spread over the power spectrum, forming a regular but incomplete periodical pattern. The underlying pattern W can be defined as a transformation of integers by matrix a_{ij}:

$$W = \left\{ y \in \Re^2 : y_i = a_{ij} t_j : t_j \in Z^2 \right\} \qquad (1)$$

Matrix a_{ij} is modified for minimal distance between actual and calculated position of clustered peaks [8]. The sequence provides the best possible results, because all harmonics contribute to the method's precision. **Figure 4** shows pattern of two wire marks wit their base vectors.

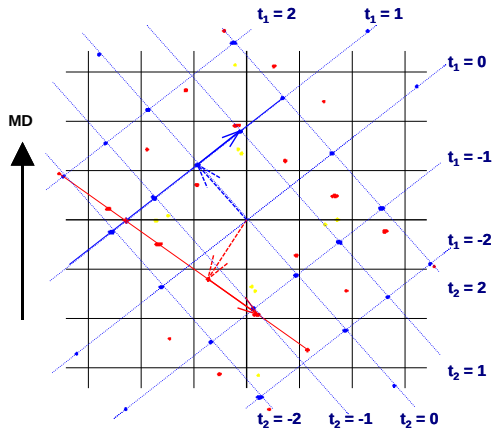

Figure 4. Structure of two wire marks (blue and red peaks) in the frequency domain.

2.3 Evaluation of Web Deformation

Web deformations are derived from positions of weft and warp peaks. The distortion of forming fabric reduces the nominal warp density. This distortion has to be compensated before evaluating web deformation [1]. An indicator for the fabric's distortion is the weft angle, which in turn changes with the web deformation. An iterative approach solves the problem [9].

Initially, the web elongation profile is estimated from weft density and weft angle. The shrinkage profile is approximated as a function of warp density and weft angle. Based on the shrinkage profile, the weft angle is adjusted. The last two steps converge in an iteration loop.

3 RESULTS AND DISCUSSION

The wire marks analysis can be used to determine reversible and irreversible web deformations by measuring rewetting dry paper samples. The rewetted state shows the irreversible deformation. The difference to the dry sample is the reversible part, as shown in **Figure 5** and **Figure 6**.

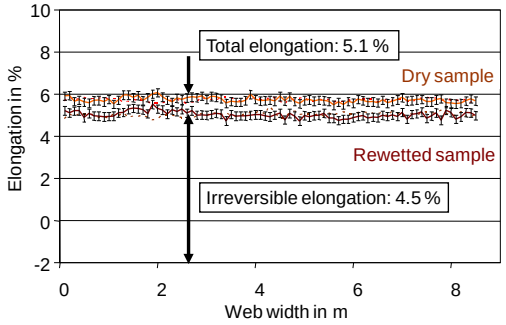

Figure 5. Profiles of reversible and irreversible web elongation.

Only a small portion of the elongation releases while rewetting paper samples, as seen in **Figure 5**. Paper shrinkage in cross direction vanishes almost completely. **Figure 6** illustrates the decrease of the shrinkage profile by rewetting. Only at the edges irreversible portions can be detected.

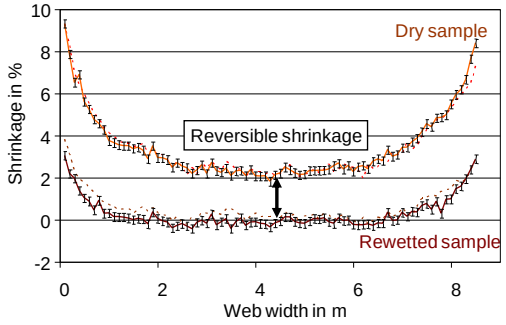

Figure 6. Profiles of reversible and irreversible web shrinkage.

The Wet Stretch Dynamics Analyzer (WSD) determines the behavior of paper materials by means of one-sided liquid contact in order to provide information about the composition of papers. **Figure 7** illustrates the strong correlation between wet stretch and reversible part of the shrinkage. The WSD wet stretch shows higher values due to the applied tension.

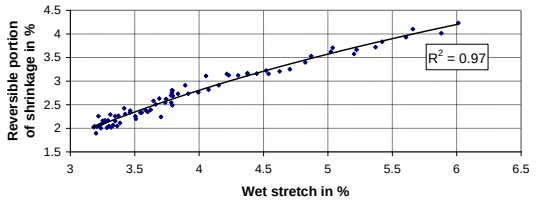

Figure 7. Correlation between Wet Stretch Dynamics Analyzer (WSD) and reversible part of the web shrinkage.

There is also a strong correlation between $TSI_{MD/CD}$ ratio and local shrinkage measured by wire marks analysis. **Figure 8** shows a shrinkage profile and the corresponding $TSI_{MD/CD}$ ratio.

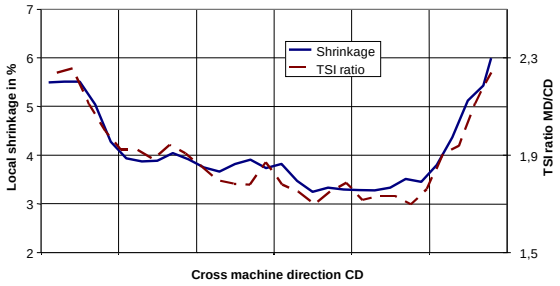

Figure 8. Shrinkage profiles and tensile stiffness.

The correlation between $TSI_{MD/CD}$ ratio and local shrinkage is specific for tested paper machines and furnish, as **Figure 9** demonstrates. The points with lower shrinkage are from the middle of the web while the higher shrinkages are measured at the edges.

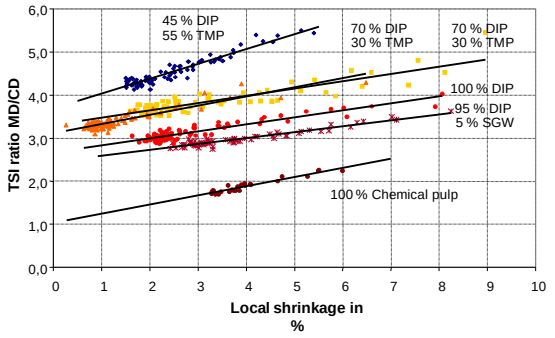

Figure 9. Correlation between local shrinkage and $TSI_{MD/CD}$ ratio.

Figure 10 gives an idea about the fuzzy cluster algorithm's ability. It separates wire marks from the triple layer forming fabric (blue peaks) and the fabric of the dandy roll (red peaks) from other markings (yellow peaks). The weave pattern of the forming fabric consists of visible blue peaks as well as hidden peaks below detection threshold. The set of two base vectors references all peaks of the forming fabric independently from detection threshold. Thus, the Inverse Fast Fourier Transformation (IFFT) can be used in order to visualise the whole forming fabric's weave pattern.

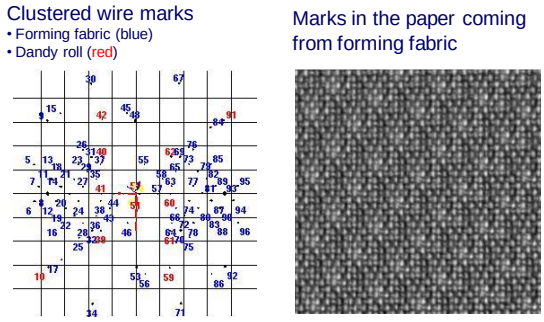

Figure 10. Visualisation of selected wire marks.

Furthermore, the plain weave of the paper side can be separated from overall weave pattern. **Figure 11** shows the topographic and hydraulic fractions in the paper structure caused by the forming fabric.

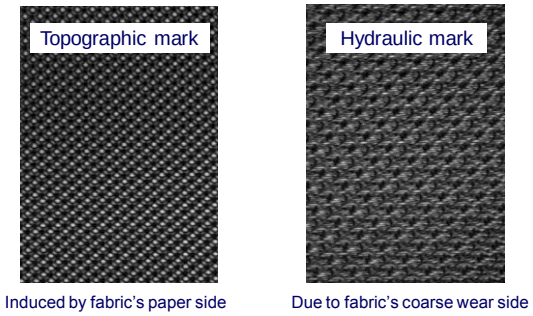

Figure 11. Extraction of topographic und hydraulic wire marks.

4 CONCLUSION

The introduced fuzzy clustering based method replaces the manual isolation of wire marks in the spectrum. The method finds punctiform periodic structures like the peaks of weaving patterns in the frequency domain. Associated with a high resolution, the dimensional stability of forming fabrics and the web deformation can be measured from paper samples.

To split the web deformation profiles in reversible and non-reversible parts is the key for a better understanding of the papermaking process. After a single-sided bath and couching, the paper sample is analysed again as part of the developed method. While the shrinkage in cross direction is almost reversible, the elongation in machine direction remains more or less constant.

Ultrasonic measurements of tensile stiffness index show a linear correlation between $TSI_{MD/CD}$ ratio and shrinkage in CD direction. This correlation

enables shrinkage compensated estimation of TSI which may be used as diagnostic tool to adjust mechanical properties and fibre orientation at the headbox.

Advanced wire marks analysis evaluates the complex structures of modern forming fabrics. Depending on the local dewatering conditions, a multilayered fabric leaves a distinctive mark in the web. The new method resolves such a wire mark into fractions origin from the fine weave structure of fabric's paper side and its coarse wear side. Topographic marks indicate the pattern caused by the web's contact with the fabric's surface. Hydraulic marks describe the portion dominated by currents through the entire fabric.

Mobility and retention of particles depend on their size and dewatering condition such as thickening and filtration. Fibres, fines and fillers show specific effects on turbulence, drainage speed and retention aids. Colour imaging makes differences in spatial particle distribution visible, because fibres and fillers differ in their spectral light scattering and adsorption power. From red, green and blue components (RGB), fibre fraction is unremarkable in red but dominant in blue.

REFERENCES

[1] S. J. I'Anson, R. P. A. Constantino, S. M. Hoole and W. W. Sampson. Estimation of the Profile of Cross-Machine Shrinkage of Paper. Meas. Sci. Technol. 19 (2008) 015701.

[2] G. Lindblad and T. Fürst. The Ultrasonic Measuring Technology on Paper and Board. Lorentzen & Wettre, (2007), ISBN 91-973781-0-0.

[3] H. Praast and L. Göttsching. Analyse der Siebmarkierungen im Durchlicht. In: Das Papier; Darmstadt; **41**(3):110ff. (1987).

[4] H. Praast. Deterministische und stochastische Papierstrukturen – ihre bildanalytische Quantifizierung. Dissertation Technische Hochschule Darmstadt, Inst. f. Papierfabrikation, 1990.

[5] S. J. I'Anson. Identification of periodic marks in paper and board by image analysis using two-dimensional fast Fourier transforms – Part 1: The basics. Tappi J. **78(**3):113–119 (1995).

[6] S. J. I'Anson. Identification of periodic marks in paper and board by image analysis using two-dimensional fast Fourier transforms – Part 2: Forming and press section marks. Tappi J. **78**(7):97–106 (1995).

[7] M. R. Dowling, S. J. I'Anson, R. W. Hoyland and S. M. Hoole. Predicting the Strength of Periodic Press Section Marks in Paper. Norcross, Georgia, USA, Tappi 2004.

[8] K. Villforth and S. Schabel. Clustermethoden für die Analyse von Siebmustern in der Papierfabrikation. In: 14. Workshop Fuzzy-Systeme und Computational Intelligence, Mikut, R. and Reischl, M. (Hrsg.) Universitätsverlag Karlsruhe, 33 – 41 (2004).

[9] K. Villforth and S. Schabel. Analyse und Ursachen plastischer Dehnungsprofile von Papierbahnen bei der Papierherstellung und Verarbeitung. Abschlussbericht zum AiF-Forschungsvorhaben 13365N. Darmstadt, Techn. Univ., FG Papierfabrikation u. Mech. Verfahrenstechnik. Bericht (2005).

Direct Measurement of calendar blackening

JÖRG-KARL BÖSNER and SAMUEL SCHABEL

TU Darmstadt / Fachgebiet Papierfabrikation und Mechanische Verfahrenstechnik
Alexanderstr. 8
64283 Darmstadt
joerg.boesner@papier.tu-darmstadt.de

1 Introduction

For good printability, the surface of the paper must be smooth. To achieve this, the paper can be calendared. This also leads to unwanted side effects, such as the calendar blackening.

In this paper, we present a new method for directly measuring the calendar blackening by combining the high resolution measurements of the optical properties and the local thickness. From this method we can derive one simple dimensionless number J characterising smoothness and optical quality[1].

1.1 Cause of calendar blackening

To understand calendar blackening, we have to take a look at the light's path though the paper:

White light consists of electromagnetic radiation with different wavelength. This radiation can be absorbed, reflected or refracted:

- Absorption will occur when the electromagnetic wave excites an electron in a molecule; the energy is dissipated as heat.
- Reflection will occur in either direct (like in metals) or diffuse way (like in paper)
- Scattering will occur when an electromagnet wave hits a surface with a different refraction index.

All these effects occur on a microscopic base (fig. 1). To ease the view, only fibres in MD are shown.

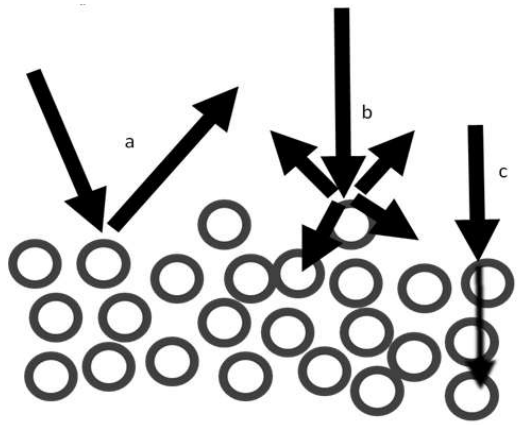

Figure 1, Scheme of an uncalendared paper sheet cut in MD (a) Reflection of a light beam, (b) a light beam is scattered, (c) a light beam is absorbed

When the paper sheet gets calendared, the properties will change, because the fibres collapse and the lumen disappears. Therefore, the interfaces between the fibres' wall and the lumen cannot scatter light anymore. The paper gets transparent at these places (fig. 2).

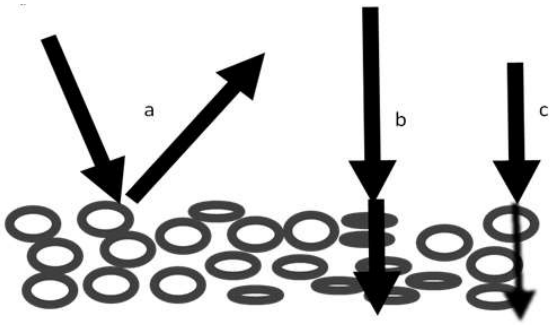

Figure 2: Light is not scattered in (b) anymore because the air/fibre interfaces disappear when the lumina collapse.

In this case, the black printing from the back side is visible.

2 The used measurements

As mentioned above, the new method uses a new way to measure the local thickness and a simple camera based way to get the optical properties.

2.1 Local thickness – principle

The local thickness is measured by the combination of the surface profiles from the top face and the rear face. To map the two sides to one another, two marks are punched into the paper (fig. 3). The hole in the lower left corner is defined as hole no. 1.

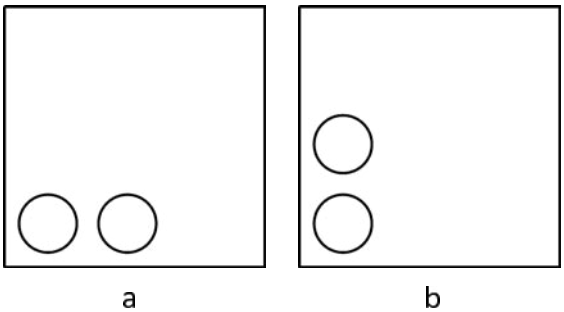

Figure 3: Schema of the sample (a) top view, (b) bottom view. The sample is turned via the diagonal from the lower left to the upper right corner for measuring the bottom side.

2.2 Surface profile

The surface profiles are recorded with a Nanofocus µscan device[2], which uses a focused laser beam to detect the local elevation. This is

done by moving the measurement head by scanning the surface sequentially over the surface. The height at the actual point is the distance the optical system in the head has to travel to get back into focus (fig. 4).

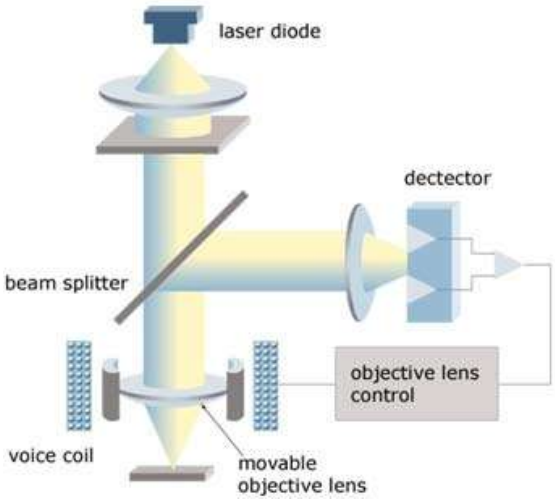

Figure 4: The optical components of the Nanofocus µscan [3]

The sample is put on a vacuum table made of sintered brass and held down during the measurement.

2.3 Defluting of the scan

Even if the paper is sucked tightly to the surface, it is still fluting. To get a realistic view of the topology, it is necessary to remove the long distance variations. This is done by a 2D high pass filter. An image of an ideal plane and the topology is shown in fig. 5.

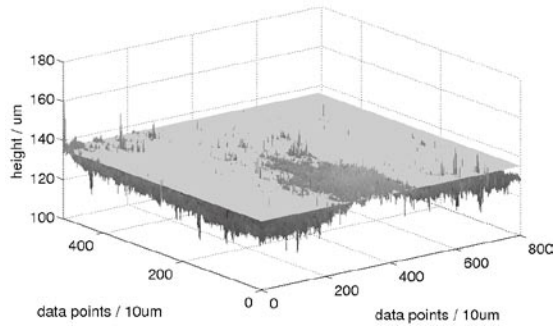

Figure 5: An unfiltered topology cut by an ideal plane

2.4 Putting the pieces together

The centres of the two holes were determined by cross correlation: Two disks of the same size as the marker holes were correlated. The two local maxima are taken as the centre of the holes for each of the both sides. The correctness of the recognition is checked by the comparison of the two holes' distances. The outer part of the picture shows artefacts from the cross correlation. These are discarded (fig. 6).

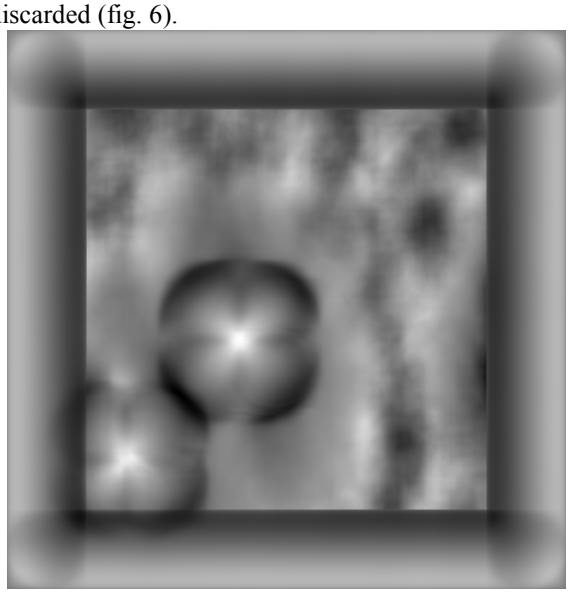

Figure 6: Cross correlation of a round disk with the surface profile of a SC paper

2.5 Calculating the local thickness

The local thickness is calculated by the difference between the top (p_{top}) and the bottom (p_{top}) profile. To get only positive values, an offset is added. For handy values, it is recommended to use the macroscopic thickness as offset:

$$d = p_{top} - p_{bottom} + d_{macroscopic}$$

2.6 Measuring the local optical properties

The paper is based on a black surface and observed via a microscope in reflected white light from a regular light bulb. The scale is adjusted by the distance of the marking holes.

To get a homogenous light distribution, it is assumed, that the optical inhomogeneities of the sample are small compared to the derivation of the illumination. Therefore, the greyscale of the paper is normed by forming the quotient between image and blurred image:

$$g = \frac{I}{I_{blurred}}$$

This can be seen in figure 7.

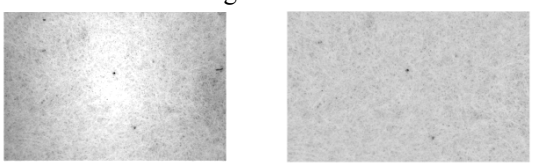

(a) (b)

Figure 7: Optical properties bevor and after compensating the inhomegeneities of the illumination

In this setup, calendar blackened parts of the paper get translucent and appear dark.

3 Displaying the results

The results are plotted in a Cartesian diagram. Each pair of data (the local thickness and the corresponding grey value) is displayed as a single point at the corresponding coordinates, the x coordinate being d, the y coordinate g The points form a cloud and the size gives information about the papers' structure:

- The bigger the variation in y direction, the more optical inhomogeneities occur
- The bigger the variation in x direction, the rougher is the paper
- The shift after calendaring to darker values gives information about calendar blackening.
- The decrease of the variations in thickness shows a smoother paper.

3.1 Calculating J

J is introduced as a parameter for opto-mechanical quality of a paper; it is calculated by the variations of thickness and optical appearance:

$$J = v_d \times v_g - a \times g_{center\ of\ cloud}$$

To get comparable results, the conditions for the measurements have to be the same. To adjust the range of J to feasible values, a parameter a can be introduced. Lower values of J represent a smoother paper and/or one, which is more prone to calendar blackening. $g_{center\ of\ cloud}$ is the arithmetic average of all grey values measured.

4 Conclusions

In this paper, a new measurement method for rating the opto-mechanical quality of paper has been introduced. It is not dependant on special measurement devices, but can be used with all devices getting surface profiles and greyscale images. It has the advantage that from now on, only one characteristic number has to be taken into account.

5 Outlook

To establish a new industrial standard, the measurement of the optical properties must be normed and a useful value for a must be introduced. The results have to be tested with different papers and the values for an ideal J have to be identified with printing tests.

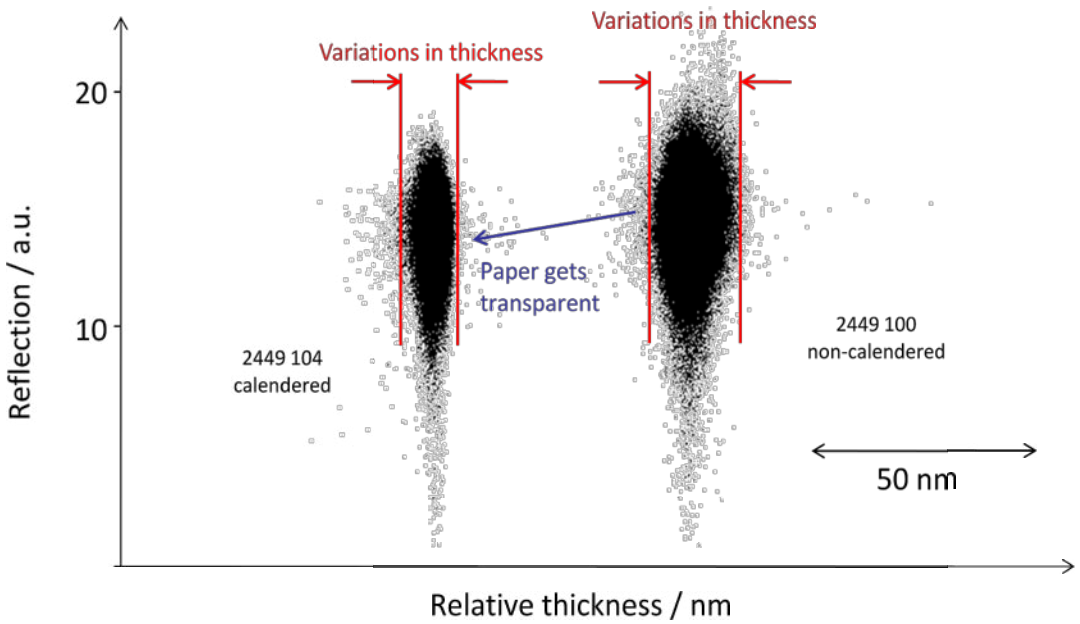

Figure 8: A piece of calendared and uncalendared paper. The two clouds are plotted with a horizontal offset to increase visibility.

REFERENCES

[1] U. Elbert et al., Bildanalytische Bewertung der Schwarzsatinage (in German). Das Papier 2/1996, 1996

[2] Nanofocus AG, Betriebsanleitung Nanofocus µscan

[3] Nanofocus AG, Promotional Photo, http://nanofocus.de/ (2007)

Ink penetration in uncoated paper using immuno-gold labeling: Intra-fiber diffusion and wicking.

B. A. ARTHUR[1], R.P. SMITH[2], S. LAVRYKOV[1] and B.V. RAMARAO[1]

1 Department of Paper and BioProcess Engineering, Empire State Paper Research Institute
SUNY College of Environmental Science and Forestry (ESF), Syracuse, NY 13210
bapeters@syr.edu
bvramara@esf.edu
lavrykov@esf.edu

2 N.C. Brown Ultrastructure Center, SUNY College of Environmental Science and Forestry, Syracuse, NY 13210
rpsmith@esf.edu

Keywords: Computational methods in fluid dynamics, Paper ultrastructure, Ink penetration, Immuno-labeling, electron microscopy

ABSTRACT

Ink penetration in paper is influenced by the structure of the inter- and intra-fiber void spaces of the medium and the surface characteristics of the fibers. Some new techniques to determine the impact of the fiber surfaces and the cell wall internal structure on ink spreading and penetration are described in this paper. The location and penetration of ink is demonstrated by optical (OM), scanning electron (SEM), confocal laser scanning (CLSM) and transmission electron (TEM) microscopy methods. A comparison of ink penetration as determined by each of these methods is shown. The hemicellulosic nature of the fiber's internal surfaces can be determined by immunochemical labeling in conjunction with TEM imaging. This is demonstrated through the use of primary monoclonal antibodies with specificity for hemicellulose with a secondary colloidal gold marker (18 nm). This technique offers a way of visualizing the location of hemicelluloses inside the cell wall pore structure and on the surfaces of nanopores inside the fiber cell wall.
Combining paper structure with fluid spreading and wicking models allows us to determine parameters describing the influence of fiber surfaces and the cell wall on drop imbibition. A representative model using dual porosity fields for drop imbibition is presented.

INTRODUCTION

It is well known that the mechanisms involved in the imbibition of ink drops into paper are considerably complex. Pore spaces in the paper exist not only between the fibers (inter-fiber or macro pores of the order of a few micrometers) but also within the cell walls themselves, on a nanometer scale. Imbibition of ink drops can occur by capillary action in the inter-fiber pores, wicking into the intra-fiber and fiber cell wall nanopores and spreading along the surface of the fibers. Ink jet drops are in the picoliter range and as a consequence, intrafiber wicking is the most significant absorption phenomenon coupled to the spreading along the fibers. Earlier studies of ink penetration have focused mostly on the penetration of the inter-fiber pore space [Dubé et al. [1,], Starov et al. [2, 3,4]]. Dubé et al found that picoliter ink droplets penetrate the interfiber pores and tend to spread along the fibers. However, capillary action by the fiber cell walls tends to retard this spreading. This capillary action depends on the nanocapillary sizes, network topology and fiber surface energetics. It is the aim of the present work to demonstrate techniques that are suitable for locating and quantifying the ink spread and penetration into the fiber cell walls by immunoelectron microscopy to show both chemical constitution of the nanopores surfaces and their location inside the cell wall. Our technique employs gold nanoparticles as labeling markers tagged to xylan antibodies and their subsequent detection by scanning and transmission electron microscopy [5]. This technique can display ink penetration distribution into fibers.

A detailed analysis of the physics of spreading and absorption into porous media was given by Starov et al. [2,3,4] and by Alleborn and Raszillier [6]. Starov's model in essence uses the laws of Darcy, Cassie-Baxter and Tanner to describe the dynamics of the viscous dissipation within the drop by the lubrication approximation from hydrodynamic theory. Alleborn and Raszillier then expand Starov's model considerably, including the effect of the precursor film through a disjoining pressure equation and also obtaining a numerical solution to the complete penetration problem in two dimensions. In addition, Alleborn and Raszillier's work considered the problem of interference of two drops placed close to each other on the surface. Results for the penetration time, drop shape on top of the surface as well as that inside the porous medium and how it interacts with a second drop are given in this work. For these reasons, this model will be used as the basis for our effort in understanding the behavior of ink drops in paper. [7]
The critical drawback to the aforementioned models for

drop spreading is the understanding and treatment of capillary action of the ink into the paper media. Current models are not capable of displaying the extent of penetration of the ink into the paper and, do not give the distribution of ink across the interface as it spread within the sheet. [8] This work describes our best efforts to quantify these current concepts into our proposed model.

1. MATHEMATICAL MODEL OF INK PENETRATION INTO PAPER

We consider the paper sheet as a porous medium with pores on two size scales (dual porosity). Therefore there are two porosity fields ε_1 and ε_2 corresponding to the inter- and intra- fiber pore spaces. The secondary porosity field contains nanoscale pores and is responsible for water uptake due to the hygroscopicity of the fibers.
Consider a drop on the surface of a paper sheet as described in Fig 1. The spreading of the drop radius is modeled by the following equation (1) where the first term represents spreading due to surface tension and the second is the effect of capillary suction into the medium.

$$\frac{dr}{dt} = \frac{\gamma}{3\omega\mu}\left(\frac{4V}{\pi}\right)\frac{1}{r^9} + \frac{1}{\pi\theta^* r^2}\frac{dV}{dt} \qquad (1)$$

The suction rate can be determined by solving a non-linear parabolic equation for the saturation field S inside the paper which was first developed by Ramaswamy and Ramarao [7] for modeling water absorption by paper materials. The saturation S represents the local void fraction filled with water.

$$\frac{\partial S}{\partial t} = \nabla.D(S).\nabla S - \nabla.\left(\frac{K_r K_s}{\mu}\rho g\vec{z}\right) + k_i(1-\alpha S) \qquad (2)$$

We denote the moisture content of the fibers by q. The following equation describes water movement by diffusion (D) and capillary wicking (k_i) in the fibers.

$$\frac{\partial q}{\partial t} = \nabla.D.\nabla q - k_i(1-\alpha S) \qquad (3)$$

At the surface of the sheet, wicking results in ink transfer to the sheet described by the integral of the flux over the base area of the drop. This is given by

$$\frac{\partial V}{\partial t} = -\int_0^{r(t)} D(S)\nabla S dr \qquad (4)$$

The key parameters in the above model are the diffusivity D(S) representing capillary action and k_i representing wicking or absorption into the fibers. The physical basis of the complete model and its solution will be given elsewhere.

2. METHODS

One of our goals was to determine the local composition in the paper structure and hemicelluloses are a key component impacting the surface energetics. Hence, techniques that can identify the topochemical nature of the intra-fiber pore surfaces are necessary if wicking is to be understood. The chemical nature of the interfiber surfaces can be determined by combining immunochemical techniques with electron microscopy. We opted to employ smaller gold spheres (10 nm) in the ink that would conceptually allow for liquid penetration through the paper voids on and into the fiber surfaces and cell wall nanopores. Holmstad et al [9] determined that interfiber pores to be in the range of 1-5 μm. Maloney et al [10] determined the cell wall nanopores sizes as between 10-100 nm. Not only would quantification of the ink penetration into small pores help elucidate paper penetration modeling equations [11] , but may answer some unknown relationships between surface chemistry and micro pore structures in fibers. After the application of the ink laden with the smaller gold particles, they were then enhanced with silver to a larger size to allow for easier detection using both Scanning Electron Microscopy and Transmission Electron Microscopy techniques to determine visually that antibody binding has occurred. Paper samples were sectioned to a fresh face using a sliding microtome and steel knife. Light micrographs were taken on a Nikon SMZ 1500 using a spot software camera to measure ink penetration in paper. (Fig.2)

3.1 Electron Microscopy and Confocal Laser Scanning Microscopy Imaging

A JEOL 5800 SEM operating at 20 kV was used in the secondary and backscatter mode to image samples. The ink colorants had too low electron densities rendering them invisible under electron or CL illuminations [12]. Silver nanoparticles (AgNP) (ranging from 50-250nm) mixed in the ink were used as tracers [13]. Paper samples with ink drops were sectioned and imaged in the z direction by SEM (Fig.1,4) in atomic number backscatter mode to locate the AgNPs.
CLSM [as described by Ozaki et al, 14] was used to obtain similar images along the z directional thickness. A Zeiss LSM510 with a 488 nm laser was used. Fluorescent filters separate the AgNP areas and appear as green areas against a blue background coloring (see Fig. 3). Images clearly indicated the location of the ink drop and were correlated with the images of the ink drops using optical microscopy and verified using SEM x-ray analysis of silver. (not shown)
For TEM, paper samples were placed directly into epoxy resin and polymerized overnight at 60C into

Fig 1. A SEM image control paper using SEM atomic number backscatter. No Ag tracer present. Paper filler is bright white

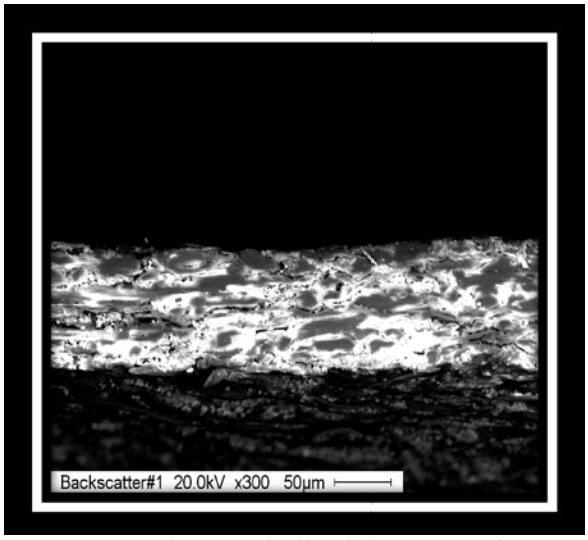

Fig 1.b SEM image of silver/ink tracer using SEM atomic number backscatter. AG tracer appears bright along and includes metal containing filler.

blocks. Ultrathin sectioning was performed on a LEICA EM UC6 microtome using a Diatome 35° angle diamond knife. The sections were stained with Uranyl Acetate and viewed on a JEOL 2000EX at 100 keV.

3.2 Antibody Staining followed by Transmission Electron Microscopy

A wide range of molecular probes, such as monoclonal antibodies (mABs) have proven very effective in locating plant cell wall components, especially polysaccharides [15,16]. Two monoclonal antibodies, LM 10 and LM11, have been demonstrated to bind to polysaccharides. LM 10 in particular, bound only to unsubstituted or low substituted xylans and did not bind to arabinoxylan. LM11, in contrast, bound strongly to arabinoxylan in addition to low-substituted xylans [17]. Both of these were obtained for the purpose of this study (supplied by PlantProbes, Leeds LS29 JT UK). Although the mABs can bind to hemicelluloses, the specific location of binding can be obtained only under microscopic observation. Since the mABs and other components cannot be directly detected under electron beam illumination, it is necessary to attach suitable inert tags to ensure their visibility. Secondary gold nanoparticle tags have been used with mABs for this purpose.

3.3 Immuno-gold labeling-TEM

A recent review by Ruel et al [18] identified immunochemical labeling as a precise way for locating and visualizing hemicelluloses in plant cell walls. This post embedding technique [19] consisted of floating the ultrathin sections of paper on a series of drops of blocking agents [Phosphate-buffered saline (PBS) containing 1% bovine serum albumin (PBS BSA), and PBS containing 1% cold water fish gelatin and then a 1:20µl dilution of the antibody (mABs) in PBS BSA for 15 minutes each. The samples were then washed and subsequently, floated in a dilution of 1:20 µl of 18 nm gold in Anti-rat IgG. (secondary marker) (Jackson ImmunoResearch Laboratories, West Grove PA) The sections were fixed, rinsed in water, stained with uranyl acetate and visualized by TEM.

3. RESULTS

4.1 SEM, Optical and CLSM Results

Figure 1.a shows an SEM of the cross-section of the paper without the **AgNPs**. The paper filler containing titanium, shows as white particle areas. Fig 1.b shows an SEM of the same sample with ink laced with AgNPs. The silver nanoparticles show as bright white regions comingled with some of the filler particles. Furthermore, the micrographs show evidence of the ink following the inter-fiber voids clearly. Fig 2 shows an image of a cross-section of a paper sample with an ink drop. The sample was sectioned in the z-direction using a microtome and imaged in an optical microscope at 500 X magnification.

Paper samples with and without AgNPs were imaged in the CLSM using both XYZ and XZY scan modes. The sequenced XY images taken at an interval of 1µm in the z-direction were stacked to provide a reconstruction of the ink drop inside the paper. The CLSM pictures were compared with like Z direction optical images of inked paper. Figs 3.a and 3.b show two sample CLSM images. The blue regions indicate the uninked portions within the

paper structure. The bright green regions indicate the AgNP ink due to the strong fluorescence the silver has under the green filter. This technique allows for visualization of the relative amounts of ink onto and around the paper components particularly in comparing varying fiber types and fillers.

Both the optical and CLSM images showed the same drop quite clearly in terms of drop size, boundary and location. The drop images were also compared to those obtained by secondary SEM imaging and SEM imaging using the backscatter mode (shown in Fig. 4). The ink spread observed in the samples under optical condition spread (2.2mm) and depth of (.15 mm) compared to CLSM imaging (2.35mm) and depth of (.18mm) verifying the two techniques. The structure of the **AgNP** inked papers was identified by CLSM. Differentiating the liquid from the fiber/void areas can help quantify ink penetration into the structures because the AgNP tracer showed well under the green filter. Additionally, it is possible to image the same position for verification purposes first using the CLSM followed by the SEM using this non-destructive technique.

Two SEM micrographs obtained under normal and backscatter conditions are shown in Fig 4.a and 4.b. Normal imaging (4.a) shows a fiber cross section with its lumen directly visible. Backscatter however results in illumination of the AgNPs (on account of the high atomic mass of Ag) coating the fiber as a background.

4.2 Attachment of Tagged Xylan Antibodies Followed by TEM

TEM images obtained after conducting the immuno-assay with nanoparticle gold as described in the methods section are shown in Figs 5 and 6. The xylan antibody tagged gold nanoparticles appear as bright white spheres

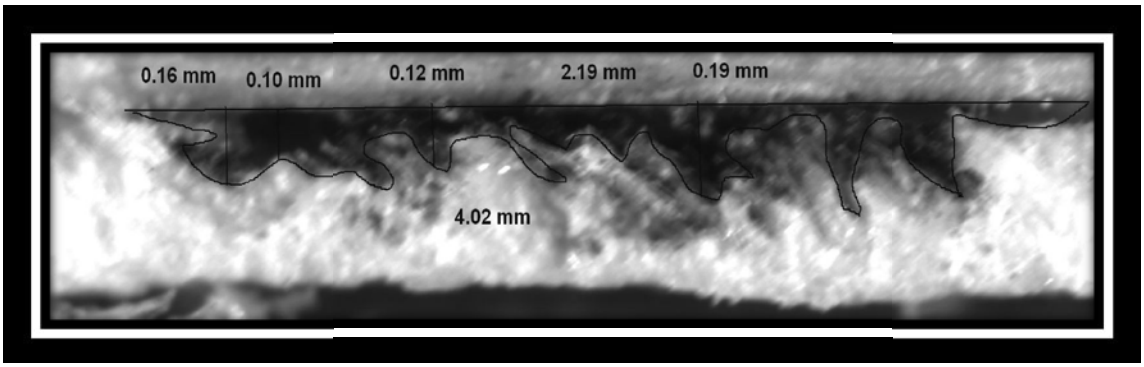

Figure 2. Optical images taken of microtomed sections of dry inked paper in the z direction showing measured ink drop penetration

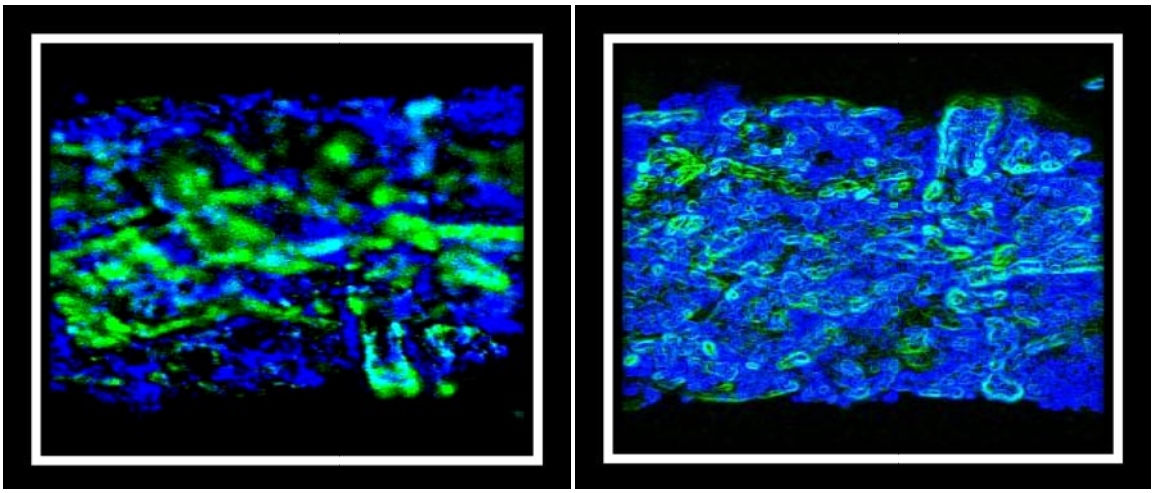

Figure 3. CLSM Z-stack images of AgNPs tracer using Plan Neufluar 10x objective. Ink shows green, un-inked paper fibers are blue using two filters BP480-520IR and LP 560 at 488 nm wavelength at 19% stacked image.

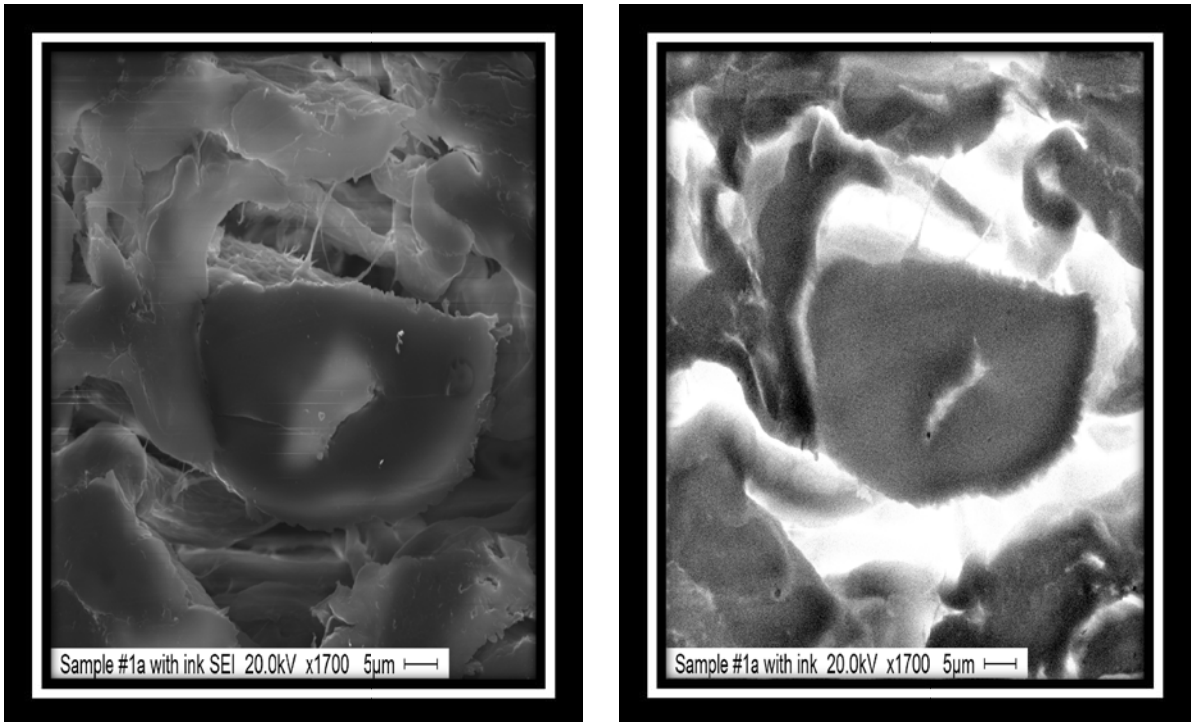

Figure 4. SEM images of Ag tracer using SEM. The left image shows inked paper under secondary conditions. The right image shows AgNP inked paper under atomic number backscatter conditions.

in these images. The labeling appears to have been successful and the gold nanoparticles attach themselves to the appropriate hemicellulose components (un or substituted xylans depending on the antibody considered). Ag NP ink is bright white.Figure 6 shows an ultrathin section of paper with the fiber structure (lumen, pits and fibrous matter). The secondary gold label shows the location of the hemicelluloses in the fiber and is observed to be especially heavy in regions bordering the lumen and inside the fibrous structures. The gold label can only be taken to be representative of the quantity of hemicelluloses in an approximate sense [see, 19]. Labels around the edges of the fibers likely represent hemicellulose that is on the fiber surface but is separated by the length of the IgG molecules on the primary and secondary antibody. The TEM image in Fig. 6 clearly shows two different types of bright spots. The hemicellulose tag is similar to that in Fig 5, and is concentrated around the edge of the fiber cavity. The second spots correspond to the AgNPs within the fiber and are in the proximity of the hemicellulose tags. The AgNPs have clearly penetrated the cell wall carried by the ink.

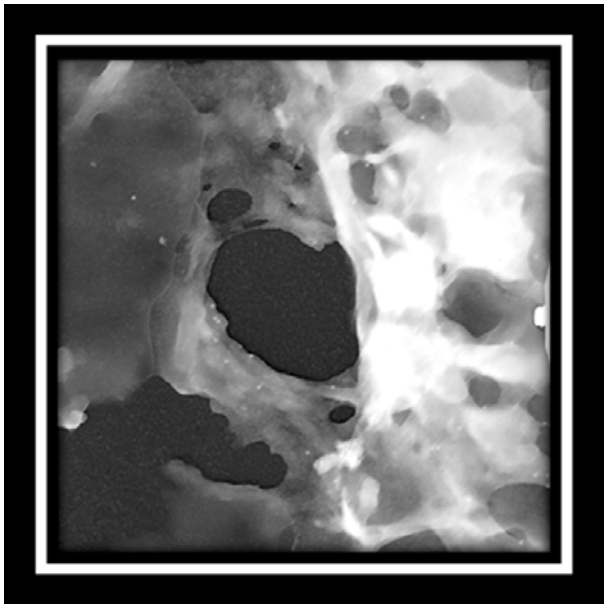

Figure 5. TEM image of thin sectioned monoclonal antibody LM 10 labeled paper with secondary 18 nm gold label showing hemicellulose presence within the paper fiber and around a hardwood vessel. 30,000x

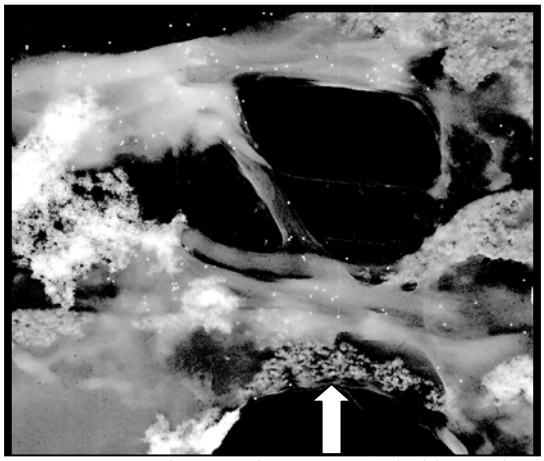

Figure 6. TEM image of AgNP traced, thin sectioned, LM 10 monoclonal antibody labeled paper. Tracer within the fiber sporadically overlaps the hemicelluloses tag. Large arrow shows AgNP tracer. Smaller brighter spheres are the hemicellulose label.

4. CONCLUSION

We have demonstrated a viable method of locating paper fibers and their sub-cellular components (Fig.6). The ink path can be quantified using AgNPs. Bound primary mABs with secondary gold labels identified the location of hemicellulose components of the paper fibers more efficiently than previous methods. Correlation of the AgNPs to the hemicellulose label clearly shows penetration into the cell walls. Labeling with antibodies possessing high specificity hemicellulosic polysaccharides allows identification of xylan and other fiber components. A subcellular understanding of ink penetration might possibly lead to an ink and paper recycling savings.

Acknowledgement

We thank the member companies of the Empire State Paper Research Institute and Dr. Kapil Singh of International Paper Co., for support of this project. Dr. Arvydas Matiukas (SUNY-Upstate Medical Center) is acknowledged for his kind help in confocal imaging and Dr. Paul Knox (PlantProbes, Leeds, UK) for the donation of the antibodies used in this study.

REFERENCES

[1] M.Dubé, F.Drolet, C.Daneault, and P. J. Mangin. Drop penetration in paper. Papermaking Research Symposium. Kuopio, Finland. (2009)

[2] V.M. Starov, S. R. Kostvintsev, V. D. Sobolev, M.G. Velarde, and S.A. Zhdanov. Spreading of liquid drops over dry porous layers: complete wetting case. *J. Coll. Int. Sci*. **246**(2):372-397 (2002a).

[3] V.M. Starov, M.G. Velarde, and S.A. Zhdanov. Spreading of liquid drops over dry porous layers: complete wetting case. *J. Coll. Int. Sci*. **252**(2):397-408 (2002b).

[4] V.M. Starov, M.G. Velarde, and S.A. Zhdanov. Spreading of liquid drops over thick porous layers: complete wetting case. *Langmuir.* **18**: 9744-9750 (2002c).

[5] M. Kaneda, K. Rensing and L. Samuels. Secondary cell wall deposition in developing secondary xylem of poplar. *Journal of Integrative Plant Biology.* **52**(2):234-243 (2010).

[6] N. Alleborn and H. Raszillier. Spreading and absorption of a droplet on a porous substrate. *Chem. Engng. Sci.* **50:**2071-2088 (2004).

[7] B. V. Ramarao, A. Massoquete, S. Lavrykov and S. Ramaswamy. Moisture transport in paper materials in the hygroscopic range and characteristics of diffusion parameters. A review. *DRT - Drying Technology*. **21**(10) 2007-2056 (2003)

[8] B. Arthur, S. Lavrykov, B.V. Ramarao. Modeling and experimental investigation of the effect of surface roughness on spreading of ink drops on paper. Tappi 2010 Progress in Paper Physics Conference, Montréal, Quebec, Canada (2010).

[9] R. Holmstad, S. Ramaswamy, A. Goel, Ø.W. Gregerson and B. V. Ramarao. Comparison of 3D structural characteristics of high and low resolution X-ray microtomographic images of paper and board. International Paper Physics Conference, Victoria, B.C. Canada, 65-69 (2004).

[10] T.C. Maloney and H. Paulapuro. The Formation of Pores in the Cell Wall. *Journal of Pulp and Paper Science.* **25**(12):430-436 (1999).

[11] J. Hyväluoma, P. Raiskinmäki, A. Jäsberg, A. Koponen, M. Kataja, and J. Timonen. Simulation of liquid penetration in paper. Department of Physics, University of Jyväskylä, FI-40014 Jyväskylä, Finland. *Phys. Rev*. **73**(3): 036705 (2006).

[12] L. Yang, A. Fogden, N. Pauler, O. Savborg, and B. Kruse. A novel method for studying ink penetration. *Nordic Pulp Pap. Res. J*. **20**:399-404 (2005).

[13] S.P. Wu, K.C Yung, L.H. Xu, and X.H. Ding. Fabrication of Polymer Silver conductor Using Inkjet Printing and Low Temperature Sintering

Process. *IEEE Transactions of Electronics Packaging,Manufacturing*. **31**(4):291-296 (2008).

[14] Y. Ozaki, D. W. Bousfield, and S. M. Shaler. Three-Dimensional Characterization of Ink Vehicle Penetration by Laser Scanning Confocal Microscopy. *J.Pulp Paper Sci.* **31**(1):48-51 (2005).

[15] K. Ruel, V. Chevalier-Billosta, F. Guillemin, J. Berrio-Sierra and J-P Joseleau. The wood cell wall at the ultrastrucutural scale formation and topochemical organization. Maderas.Ciencia y tecnología. **8**(2): (2006).

[16] C. Altaner, J.P. Knox, and M.C. Jarvis. In situ detection of cell wall polysaccharides in sitka spruce (Picea sitchensis (Bong.) Carrière). *Wood ti'Scientific Commons,* **2**(2):284-296 *(*2007).

[17] L. McCartney, S. Marcus, and J.P. Knox. Monoclonal Antibodies to Plant Cell Wall Xylans and Arabinoxylans. *Journal of Histochemistry and Cytochemistry*. **53(**4):543 – 546 (2005).

[18] K. Ruel. Immunochemical probes for microscopy study of the plant cell walls. In: Mendez-Vilas A, ed. *Science, technology and education of microscopy: an overview (ed A.)*. **1**(2):445-454 (2003).

[19] C. Griffith. Fine Structure Immunocytochemistry. Springer-Verlag, New York (1993).

Influence of accelerated aging on properties of office copy paper

KATARINA ITRIĆ, VESNA DŽIMBEG-MALČIĆ, TOMISLAV CIGULA and ŽELJKA BARBARIĆ MIKOČEVIĆ

Faculty of Graphic Arts / University of Zagreb
Getaldićeva 2, 10000 Zagreb, Croatia
kitric@grf.hr

Keywords: accelerated ageing, FTIR, photo ageing, thermal ageing

ABSTRACT

In this article the investigation was done on Navigator office paper, the most used photocopier paper in Croatia. Research was carried out by photo and thermal accelerated aging of paper.

The moleculare changes in the paper structure are detectable through IR spectra (FTIR spectroscopy), and optical caracteristics through visible spectra. Experimental results show differences in some parts of spectra, which point out the changes in the paper structure.

1 INTRODUCTION

Office papers are widely used in everyday life, not just in photocopying purposes, but for handwriting and printing documents used for archiving. Due to their mass use, they need to have certain suitable characteristics, such as water resistance, dimensional and optical stability. Those characteristics are obtained by adding adequate substances during paper production. Except cellulose fibres, which can be virgin or recycled by origin, there are many other organic and inorganic compounds that are added in the paper network structure like fillers, adhesives, pigments, binders, etc. According to paper type these materials are added in bigger or smaller quantities, so office papers available on market are different in their chemical composition. Paper products are an important part of everyday life (households, offices and industry). Nowadays there is an increasing requirement in quality production of writing paper as well as printing paper. The main priority is to achieve physical-chemical characteristics which will give them the best printing, writing and optical quality. Effective agents for increasing of whiteness impression of paper are Fluorescent whitening agents (FWA). FWA's are organic materials which absorb the UV radiation and transform it to visible light. When papermakers add this agent to the paper reflectivity drops in the NIR where the energy is absorbed and in the blue part of the spectrum where EM radiation is emitted reflectivity exceeds 100% [1]. To improve the optical characteristics of paper the blue-lilac dye with absorption from 500 nm to 650 nm is often used in fine paper.

The process of natural paper ageing is too slow to permit observing changes in a reasonable time frame. The purpose of an accelerated aging test is to duplicate the physical and chemical changes occurring naturally in a material in a relatively short time frame.

2 EXPERIMENTAL

The investigation was done on white Navigator 80 g/m^2 office paper. Samples included new and old paper sheets. New sheets were taken from a closed ream and old sheets were taken out from an open ream, naturally aged for three years.

Two different accelerated ageing cycles (thermal ageing and photo ageing) were set up with the goal of simulating different degradation processes that naturally occur in cellulosic materials.

Thermal ageing was carried out on the new samples of paper at 160 ˚C in the oven in the intervals of 24h, 48h and 72h. Thermal oxidation which accompanies this process induces the breakage of chemical bonds in cellulose and the formation of carbonyl, carboxyl and hydro peroxide groups [2].

In the photo ageing process the samples were exposed in solarbox 1500e equipped with a Xenon light source for 24h, 48h, 72h, 96h and 120h. Irradiation was kept at a constant power of 550W/m^2 and at a temperature of 65 ˚C. Xenon lamp simulates natural daylight on a paper surface with the light flux that is substantially greater than in normal indoor conditions of paper exposure. Photo oxidative reactions results in an increase of carbonyl content, carboxyl and hydroperoxide groups [3]

All of the samples (naturally aged, artificially aged and not aged) were evaluated by means of visible and IR spectroscopy as well as contact angle measurements. Reflectance measurements in the visible region (370-750nm) were acquired using USB4000 Miniature Fiber Optic Spectrometar at a 45˚ angle. Each spectrum is the average of 10 individual scans. IR absorption spectra were acquired on FTIR Iraffinity-21 spectrometer in Attenuated Total Reflection (ATR) mode with a Silver Gate accessory equipped with a diamond ATR crystal. A total of 15 scans were taken for each sample with a resolution of 4cm^{-1}.

Measurement of contact angle was used to observe any changes in the surface characteristics of the investigated paper. Contact angle measurement was made with Dataphysics' OCA 30 measuring unit. This measuring unit is computer controlled and enables high precision measurement.

The unit is equipped with automatic dosing unit that enables measurement with defined volume of fluid. Measurements were conducted using Sessile drop method. Used liquid for measurements was glycerol (Surface free energy mNm^{-1}, viscosity 1412 mPas). As contact angle changes in time, all measurements were made at one second after initial contact between solid and liquid phase.

3 RESULTS

3.2 FTIR analysis

Figure 1 shows the results of FTIR-ATR measurements for thermally aged, naturally aged and unaged samples, while Figure 2 displays the results for photo aged, naturally aged and unaged samples.

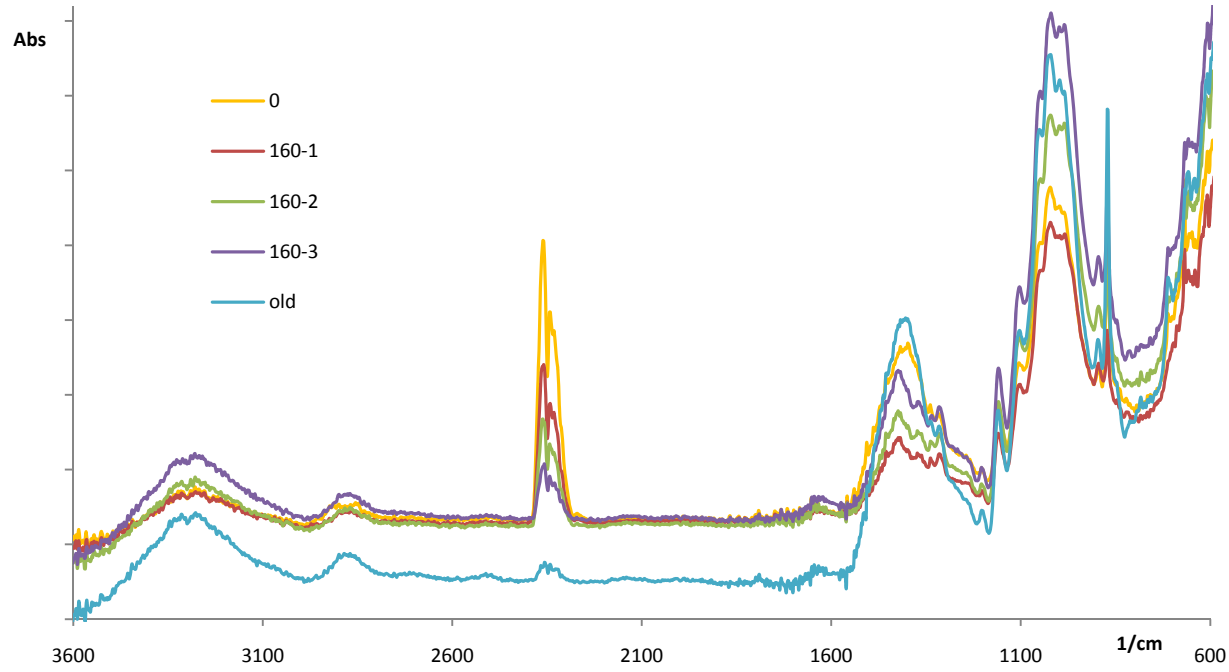

Figure 1. Absorbance measurements in the IR region (old-three years old paper, 0-unaged paper, 160-1..3 thermally aged paper)

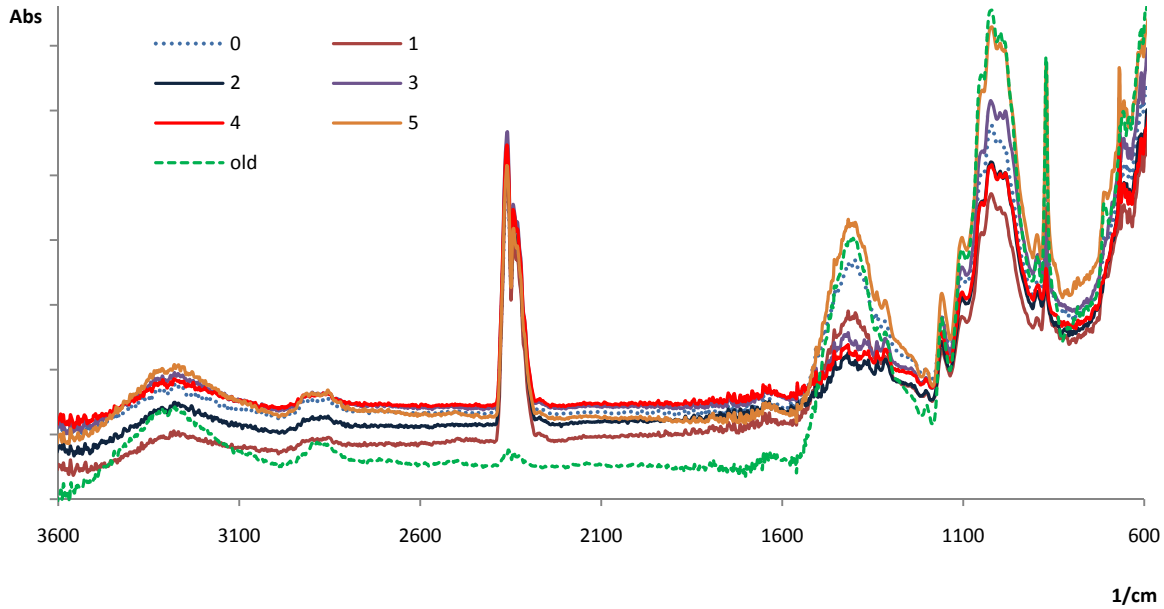

Figure 2. Absorbance measurements in the IR region (old-three years old paper, 0-unaged paper, 1-5 photo aged paper)

These spectra are due to two main components: cellulose, which is polymeric matrix which constitutes paper and calcium carbonate, much used inorganic filler added to improve optical and physical characteristics of paper. It can be seen that the most interesting and characteristic absorption features of paper compounds are located in these three regions: 800-1700 cm^{-1}, 2200-2400 cm^{-1}, 2700-3600 cm^{-1}.

In the first region there are several most expressive bands: $CaCO_3$ shows strong absorption bands at about 1420 cm^{-1} and 880 cm^{-1} ; cellulose is characterized by a main band composed of several peaks at 1160 cm^{-1} , 1107 cm^{-1} , 1055 cm^{-1} , 1030 cm^{-1}; there is some overlap between the $CaCO_3$ band at 1420 cm^{-1} and some minor peaks of cellulose in the same region [4] ; clay materials are characterized with sharp peaks at 1000 cm^{-1} and 910 cm^{-1}.

Second and third region is characterized with the peaks due to OH groups which are much dependent on water content of the samples. In that way they are function of the storage history which can hardly be controlled [4].

When we compare the third region on Figure 1 and on Figure 2 we can see broadening of band at 3300 cm^{-1} only on samples aged in solarbox.

In the second region, as we can see from Figure 3 and Figure 4, there are big differences in absorbance intensities of samples due to different type of aging. Samples obtained by thermal ageing (Fig. 4) show the decreasing absorption with increasing time interval with tendency of reaching the natural aged sample. This behaviour is not obtained with the photo ageing of samples (Fig. 3). This can be explained by the process of dehydration of samples subjected to high temperatures (160°C) in the oven.

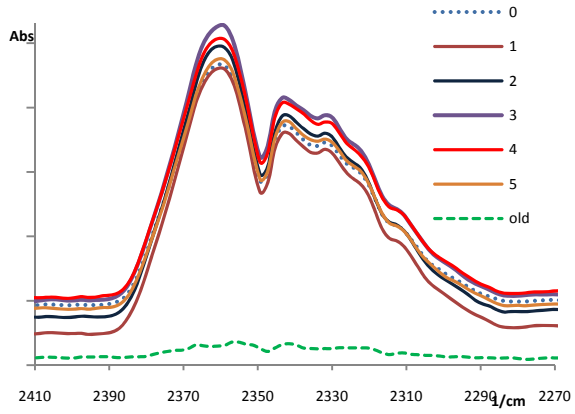

Figure 3. Absorbance measurements in the IR region 2270-2410 cm^{-1} (old-three years old paper, 0-unaged paper, 1-5 photo aged paper)

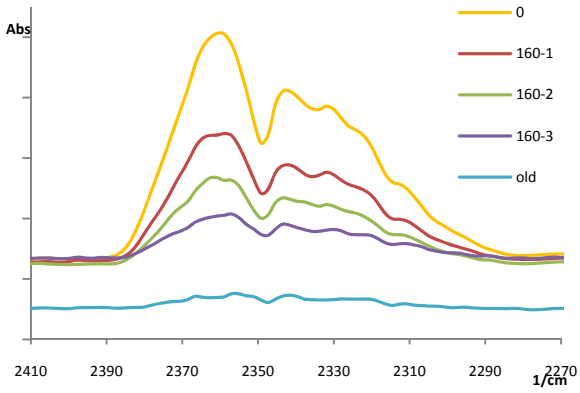

Figure 4. Absorbance measurements in the IR region 2270-2410 cm^{-1} (old-three years old paper, 0-unaged paper, 160-1..3 thermally aged paper)

$CaCO_3$ band with the peak at 1420 cm^{-1} shows different behaviour which depends on the type of ageing. This peak shows reproducibility during exposure to Xenon lamp (Figure 5).

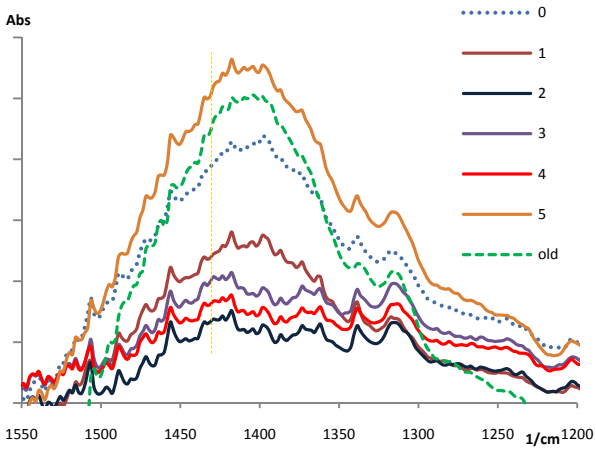

Figure 5. Absorbance measurements in the IR region 1200-1550 cm^{-1} (old-three years old paper, 0-unaged paper, 1-5 photo aged paper)

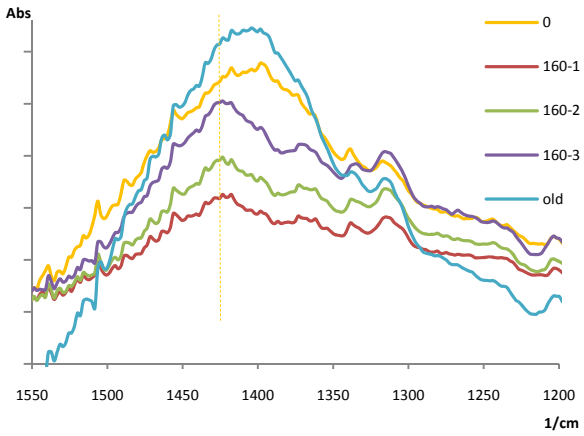

Figure 6. Absorbance measurements in the IR region 1200-1550 cm^{-1} (old-three years old paper, 0-unaged paper, 160-1..3 thermally aged paper)

Contrary, from Figure 6 we can conclude that $CaCO_3$ is thermally dependent (there is no peak after three days in the oven). Also thermally depended behaviour can be seen at 1000 cm^{-1} -clay materials (Figure 1).

Appearing of band at approx. 1000 cm^{-1} is characteristic for plane paper and we can follow the changes in peak intensity which achieved its maximum at the fifth day of photo ageing (Figure 7). This maximum value is very close to the value achieved by natural ageing.

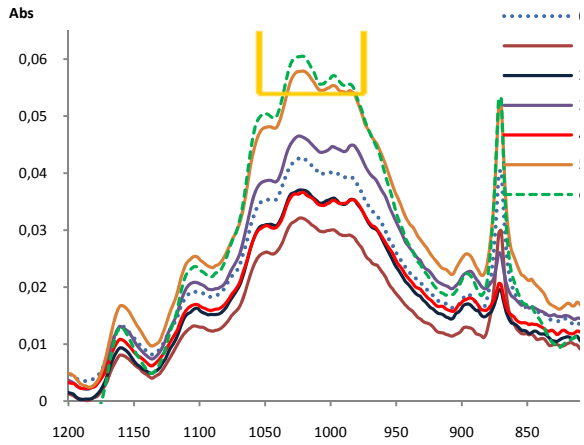

Figure 7 Absorbance measurements in the IR region 800-1200 cm^{-1} (old-three years old paper, 0-unaged paper, 1-5 photo aged paper)

Since maximum differences in FTIR spectra occurred in the samples obtained by photo ageing we decided to investigate possible changes that might appear in contact angle (Figure 8). By ageing contact angle decreases what we can interpret with increasing of free surface energy.

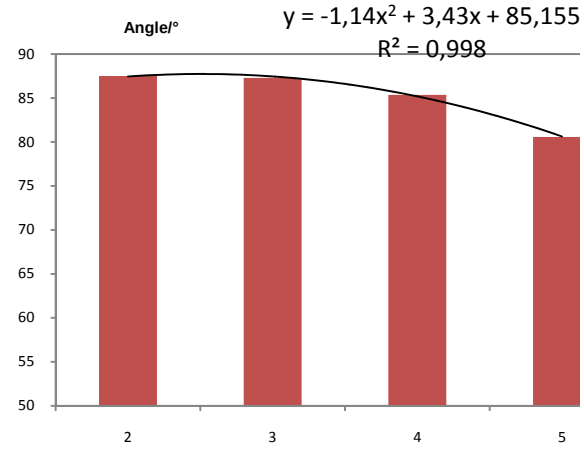

Figure 8. Contact angle measurments

3.2 Analysis of the reflectance measurements in the visible region

Figure 9 shows the results of reflectance measurements in the blue-green part of the visible region of EM radiation for all samples. The changes in the reflectance values were most emphasized in that part of spectrum.

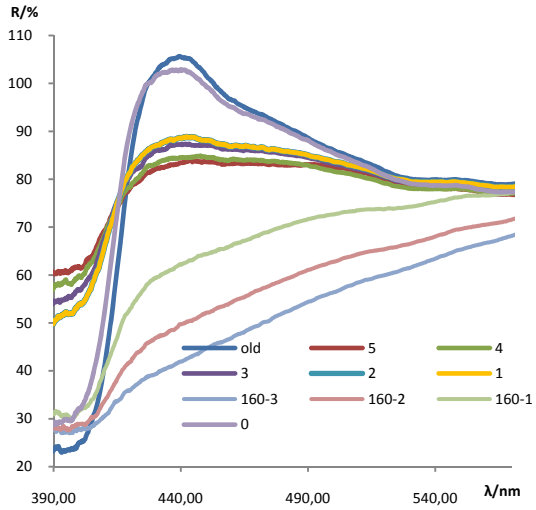

Figure 9. Reflectance measurements in the visible region for all samples (old-three years old paper, 0-unaged paper, 1-5 photo aged paper, 160-1..3 thermally aged paper)

As we can see from Figure 9 for unaged and naturally aged paper samples reflectivity possess maximum value (≈110%) at 440 nm and minimum value (≈25%) at 380 nm, while for accelerated aged samples this differences between extreme values are much smaller. For the samples aged in the solarbox, absorption is not so pronounced and becomes smaller during ageing. After the first day reflectance value is approximately 45% and after the fifth day it is around 60%, while reflectance in the visible part of spectrum during aging becomes smaller.

Accelerated ageing without EM radiation, only under high temperature of 160°C, has even more influence on optical characteristics of paper in the blue part of the spectrum. FWA isn't efficient anymore; this agent is obliviously thermally unstable and pronounced absorption in visible part of spectrum (400-650 nm) could be originated from lignin. [1]

CONCLUSION

With the aim of determining the influences of photo, thermal and natural ageing, Navigator office paper was investigated by means of IR and visible electromagnetic radiation. Since the biggest changes occurred in the bands of cellulose and $CaCO_3$ we focused on those regions in more details.

It was found that accelerated thermal ageing processes significantly modify the structure and the properties of the examined samples in the visible region. Evidently the absorption of electromagnetic radiation in the blue part of the spectrum causes degradation in the optical characteristics (yellowness).

Photo ageing processes influenced mostly the bands of cellulose and $CaCO_3$.From this results we can conclude that trigger time of irradiation was 5 days.

It would be interesting to conduct further research for longer periods of ageing and to investigate the behaviour of the samples with Raman spectroscopy.

REFERENCES

[1] N. Pauler. Paper Optics. AB Lorentzen and Wettre. Sweden (2001).

[2] J. Rychlý, L. Matisová-Rychlá, M. Lazár, K. Slovák, M. Strlič, D. Kočar, J. Kolar. Thermal oxidation of cellulose investigated by chemiluminescence.The effect of water at temperatures above 100 °C. *Carbohyd. Polym*. **58**:301–309 (2004)

[3] J. Malesic,J. Kolar, M. Strlic, D. Kocar , D. Fromageot, J. Lemaire, O. Haillant. Photo – induced degradation of cellulose. *Polym. Degrad. and Stability* **89**: 64-69 (2005).
Conference Proceedings Reference

[4] V. Causin, C. Marigo, A. Marigo, R. Casamassima, G. Peluso. Forensic differentiation of paper by X-ray diffraction and infrared spectroscopy. *Forensic Science International* **197:** 70-74 (2010)

Posters

Paper Mechanics

Numerical simulation of tensile testing using stochastically produced fibre networks of paper

JAN MATHEAS, MONIQUE ERDT
and SVEN ALTMANN

Papiertechnische Stiftung, Methodology-Design-Simulation
Pirnaer Str. 37, 01809 Heidenau, Germany,
Jan.Matheas@ptspaper.de

1 1 GEOMETRY OF STRUCTURE

The development of continuum mechanical models to simulate the behaviour of natural fibre materials under mechanical loads requires in-depth knowledge regarding the characteristics of the individual fibres, in particular their morphology, situation in the network, strength, stiffness and their qualities at the fibre contact areas. A consideration at the micro mechanical level is therefore necessary. The material structure of special paper grades can be realistically recreated on a numerical basis by the parameter-controlled generation of fibre networks with stochastic distributions of geometrical properties, e.g. taking the anisotropy of the machine direction into consideration by using a sieve-jet difference in velocity and the statistics of the resulting orthogonal strengths linked with it, see fig. 2a). Above all, this generic micro structure contains the fibre walls, metric and curvature information on their surfaces, hollow cavities within fibres, information about neighbouring fibres for contact, and where appropriate additional particles and pigments. This will make modelling possible in different physical areas, e.g., optics, continuum mechanics and fluid dynamics with one model. Depending on the respective objectives pursued by the simulation, idealisations must be made which lead to more or less abstracted models.

2 2 MECHANICAL MODEL

2.1 Discretisation with finite elements

Special studies of the mechanical behaviour at small network extracts can be made with discretisation of the fibre walls with shell elements. Investigations were carried out with surface-related multi-director finite shell elements which are applicative in particular for contact, see [1, 3]. Fig. 2b) shows a derived mechanical model of the same fibre network like in 2a), in which the fibre centre line (brown) and fibre bonds (blue), which form between the fibre walls of touching fibres in real geometry, are represented by different beam models. Their material models take viscoplasticity and failure in particular into consideration in each case. The image of additives and particles is taken into account indirectly by qualities in the fibre contact zones and fibre bond discretisation, respectively.

2.2 Fibre Bonding

Bonding between fibres plays an important role in the network deformation process, particularly affecting the ultimate loads the network can sustain. Factors which are important for the bonding mechanical properties are particularly geometry of the bonds, the shape of the bonded area, material and surface properties in the bonded region. Modelling on this scale is used to systematically study the contribution of each factor into the deformation process. In order to capture all the details of the bonding, it is necessary to create a detailed, parameterised model of the bond between two fibres considering mechanical contact and adhesion, see fig. 1. The development of the bond should be understood with the reference to the manufacturing processes, including forming, pressing and drying.

The information extracted on the fibre bond level are used in the mechanical fibre network model for changing the investigation level in order to can maximize the desired properties of paper.

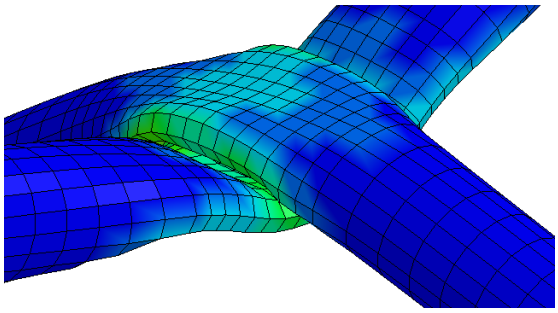

Figure 1. Two-fibre contact model, outer fibre surface discretised with shell elements. Lighter and green colouring shows high plastic strains.

3 3 TENSILE TESTING

In this case, the model shows a paper fibre network consisting of 500 fibres (0.5mm to 0.75mm in length) on a surface area of 1mm² with a height of 0.09mm and a sheet density of 0.6g/cm³. Nine material identity curves could be obtained with aid of several stochastic realisations of this model, e.g. by an accurate numerical evaluation of the stress-strain relationships in the case of normal and shear loads of this representative volume element (RVE) in all spatial directions for a completely three-dimensional orthotropic material

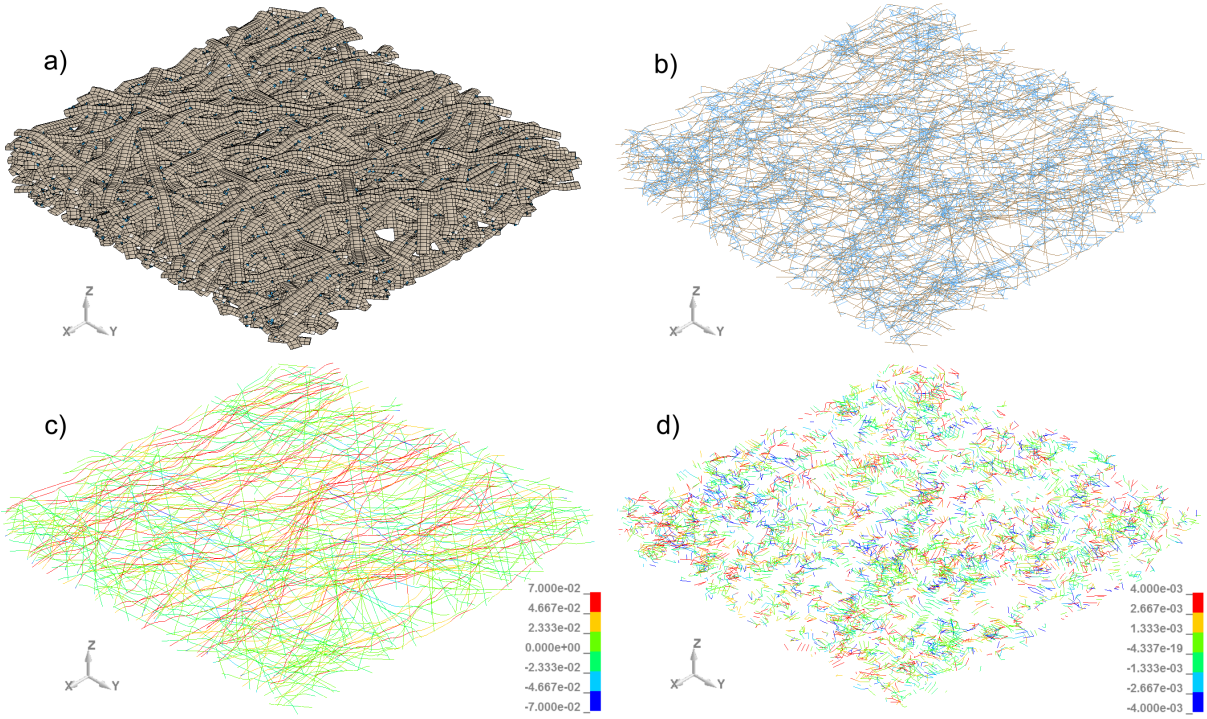

Figure 2. a) Numerically created paper fibre network on a surface area of 1mm² with a height of 0.09 and a sheet density of 0.6g/cm³; **b)** A mechanical model of the same fibre network; brown: centre fibre line, blue: idealised fibre bonds; **c)** longitudinal fibre forces in N when the network is stretched by 2% in the x-direction (tensile test); red: tension; blue: pressure; **d)** bonding forces of the idealised fibre bonds in N when the network is stretched by 2% in the x-direction corresponding to c.

law. This can be used directly to simulate the mechanical behaviour of larger structures, e.g. on the mesoscopic scale, see [2], or in product simulations, to the overall description of the material paper as a so-called homogenised material law. Failure only should be considered in simultaneous multi level simulations to make sense.

The results are presented here for only one of the huge number of necessary simulations, i.e. the normal load expressed as tension in the x-direction (machine direction) at a strain rate of 0.01/s and an achieved strain of 2.0% for one stochastic realisation, i.e. immediately before system failure. A parameter fitting of the model was carried out with varying strain rates even in this tension test and in the cross direction. The transferability to a direction perpendicular to the sheet is of fundamental importance, e.g. when simulating calandering, and is the object of future studies.

Fig. 2c) shows the distribution of forces in the longitudinal direction of the fibres with high longitudinal tension forces (orange to red) in fibres which form a small angle with the x-axis and high pressure forces (light blue to blue) in fibres with corresponding large angles. The resultant force at the front ends of the RVE where x=0.0 and x=1.0 amounts to 4.7 N which corresponds to 52 N/mm² accordingly to tensile tests. Fig. 2d) shows the distribution of the tension and pressure forces occurring in the fibre bonds. An elasticity module for an isotropic fibre wall of 42000 N/mm² and initial plasticity of the bonds at 130 N/mm² and their failure strain of 0.2% were used as the basis. It should be noted that the forces calculated for the fibre bonds cannot be interpreted directly as contact forces. A conclusion about the bonding forces can only be drawn by an in-depth two-fibre contact model.

REFERENCES

[1] J. Matheas. Entwicklung von Finiten Schalenelementen zur Berechnung von Verstärkungen aus Textilbeton bei Flächentragwerken. kid - Konstruktiver Ingenieurbau Dresden, 9 (2007)

[2] J. Schreiber, J. Matheas, P. Haller, *Zur Verteilung der Dichte an Fichtenpressholz - Tomografie und Simulation*. Holztechnologie, 4:8-13 (2010)

[3] J. Matheas, Delamination/Bruch in der Grenzfläche von Beton und Textilbeton mit Kontakt und Reibung. In: Bundesanstalt für Materialforschung und -prüfung, Berlin (ed.): *MP Materials Testing,* Hanser-Verlag, München 49/10: 554-559 (2007)

On the Fracture Behavior of Paper

DOUGLAS W. COFFIN AND KUN LI
Miami University
Department of Chemical and Paper Engineering
64 Engineering Building
Oxford OH 45056 USA
coffindw@muohio.edu

1 INTRODUCTION

The work reported here was a small part of an investigation into the end-use performance of tissue grades of paper. Tearing and fracture are not typically used to characterize tissue papers. Instead for example with tensile properties, tensile strength (TS), tensile energy absorption (TEA), and stretch (ε_f) or modifications of these properties are used. For end-use applications of paper towels and toilet paper durability is important and TS, TEA, and ε_f cannot always be correlated to performance. One often observes tears forming in the paper prior to or at failure. In order to improve durability predictions, tearing and fracture resistance of tissue papers was investigated. In this paper, some preliminary results of an investigation into fracture resistance are reported.

The fracture resistance of paper has received much attention in the literature and good reviews of the subject were given by Kortschot [1] and Mäkelä [2]. The use of properties such as fracture toughness, J-Integral, essential work of fracture were considered as potential parameters.

An objective of the present work was to determine if a simple test could be developed to evaluate the notch sensitivity of tissue papers with the test results used to rank different commercial products. The results of such a test should rank the papers differently than a ranking based on TS, TEA, or ε_f.

The results presented here are limited to assessing notch sensitivity of load limits for various papers using double edge-notched tensile (DENT) specimens. Comments to the effects of structural features and plasticity on inherent size scales are given. In the spirit of the purpose of the progress in paper physics seminars the ideas presented herein represent work in progress with the intent of gaining insightful comments from the community.

2 ANALYSIS

Most papers exhibit sensitivity to cracks or notches, but tend to be relatively tough materials. Notch sensitivity can typically be attributed to a concentration of stresses near the tip of the notch. There is typically a zone around the notch where the material has yielded and plastic deformation occurs. At some level of loading the material fails typically at the notch. The maximum load could correspond to the point when the notch length begins to increase or shortly after that event.

Consider the DENT specimen shown in Figure 1. The sample of length, L, width a_0, and thickness t, has two edge notches such that the central ligament is of length a. The sample is loaded in tension with a load P. Across the ligament a, the net tensile force must still equal P, but if stresses are higher at the notch tip the load limit ratio, P/P_0, achieved in a DENT test likely will be lower than the in proportional ligament length change a/a_0. Thus, DENT test results can be utilized to determine notch sensitivity.

Seth and Page [3] used DENT samples to determine critical stress intensity factors using linear elastic fracture mechanics [LEFM] including the Irwin addition of a localized plastic zone. Tanaka and Yamauchi [4] estimated the plastic deformation zone using DENT specimens and found good comparison between measured values and those based on LEFM; at least for less ductile papers.

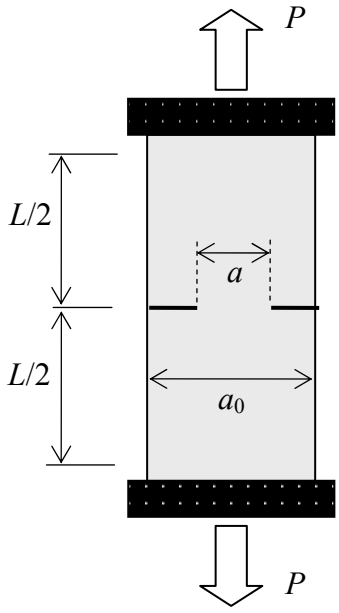

Figure 1. Double edge-notched tensile test.

Utilizing limit loads would provide a simple method to characterize notch sensitivity. Bither and Waterhouse [5] showed that notch sensitivity as indicated by limit loads varied dramatically with changes in refining and somewhat with changes in pressing. The sensitivity of a material to notching depends on the sample size because the characteristic zone length for stress concentrations would have more influence with smaller width samples [6].

Swinehart and Broek [7] made a strong argument for the use of stress concentration factors to characterize paper fracture and showed good correlation between limit load and notch length.

Thus, it was decidePd to begin with limit loads and characterize them with LEFM before moving on to more complex methods.

Notch sensitivity can be obtained by comparing the ratio of ultimate load of the notched specimen, P, to that of the un-notched specimen, P_0. The criteria is

$$\frac{P}{P_0} < \frac{a}{a_0} \text{ implies specimen is notch sensitive.} \quad (1)$$

An equality sign in Equation (1) would imply no sensitivity to the notch, and a greater than sign would imply the notch is stronger than a sample having a width equal to the ligament length.

Consider a linear elastic material that is notch sensitive. For the DENT specimen the stress intensity factor can be expressed as [1,2]

$$K_I = \sigma\sqrt{\pi(a_0 - a)/2}\, f(a/a_0) \quad (2)$$

where

$$f(a/a_0) = \left[1 + 0.122\cos^4\left(\tfrac{\pi}{2}(1 - a/a_0)\right)\right]\sqrt{\frac{\tan\left(\frac{\pi}{2}(1 - a/a_0)\right)}{\frac{\pi}{2}(1 - a/a_0)}} \quad (3)$$

and σ is the far field stress. Equation (3) is the same expression used in [4].

Assume that paper has an inherent characteristic zone length, α, such that the un-notched limit load can be written as

$$P_0 = \frac{K_I a_0 t}{f(\alpha/a_0)\sqrt{\pi\alpha}} \quad (4)$$

where t is the specimen thickness. Then the limit load ratio for at any notch can be written as

$$\frac{P}{P_0} = \frac{f(\alpha/a_0)}{f(a/a_0 + \alpha/a_0)}\sqrt{\frac{1}{(a/\alpha + 1)}} \quad (5)$$

Equation (5) provides a one-parameter model to predict the relationship between the measured values of a DENT test and the notch depth. Thus, besides using a simple ratio of limit loads, Equation (5) could be used to determine a characteristic zone length for the material.

Figure 2 illustrates some curves using equation (5) with various values of α/a_0. If the characteristic zone length is a plastic zone radius then the curves in Figure 2 would approach the solid line for small ligament lengths instead of going to zero for ligaments lengths less than 2α.

The figures show that if the characteristic zone length is small compared to the width the notch sensitivity is more pronounced. For the same sample size, ratios of limit load or the characteristic length could be used to indicate notch sensitivity.

For a network structure one would expect that the edges would not be as effective at carrying load and for small notches there would be little or no drop in limit load. This can be accounted for by reducing the effective width of the sample. An example is given as the dashed curve in Figure 2.

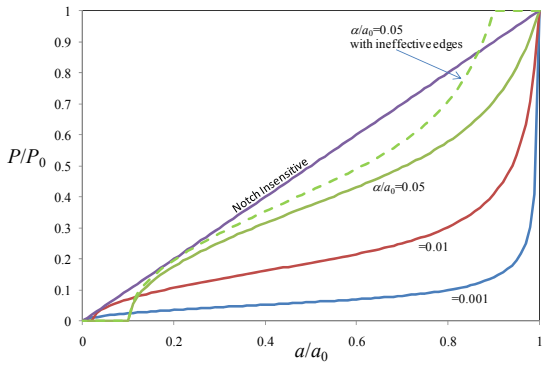

Figure 2. Various notch sensitivities using Equation (5)

As the width of the sample is increased the sensitivity to notches would be more apparent because the relative value of α/a_0 would decrease. On the other hand, ineffective edges would be more observable as the sample width decreases. Whether the curves approach the notch insensitive line or approach zero strength at some finite ligament length could indicate whether plasticity or network structural features dominate the characteristic zone length.

3 RESULTS AND DISCUSSION

Figures 3 and 4 provide results for DENT tests of several papers and cellophane for sample widths of 76 mm and lengths of at least 150 mm. At this specimen size, the cellophane exhibits the highest sensitivity to notches while the tissue papers exhibit the least. As one would expect, CD notch sensitivity is less than MD sensitivity.

Equation (5) was fit to the data with an edge defect included for the tissue papers. The fits are shown as solid lines in Figures 3 and 4. Equation (5) which is modified from Linear Elastic Fracture Mechanics (LEFM) provides an adequate fit for all the data. This gives some justification that a ranking of notch sensitivity can be obtained for various commercial papers. For tissue papers, the standard tensile test specimen is 76 mm as used in the present results. Although it would be better to use wider samples to enhance the notch sensitivity [6], this may not be possible with all tissue papers. For example, commercial toilet paper typically is found in 100 mm wide rolls. Also many towels and toilet papers are perforated into sections limiting the length in MD.

For the 76 mm wide sample, the present results suggest that a ligament length ratio of a/a_0=0.75 would be appropriate for a single notch test. If the

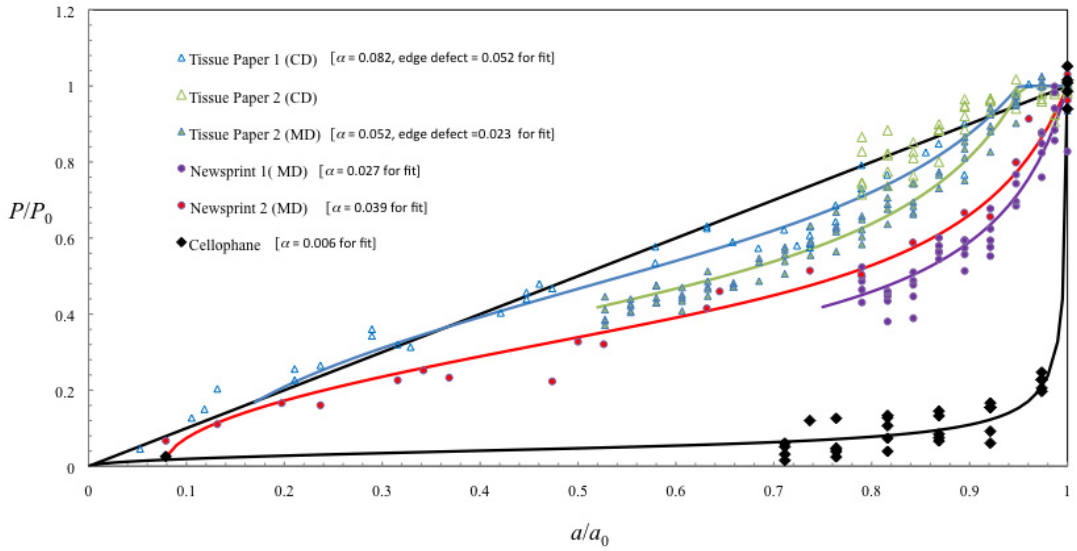

Figure 3. Relative Strength ratio versus relative ligament length for various papers and cellophane

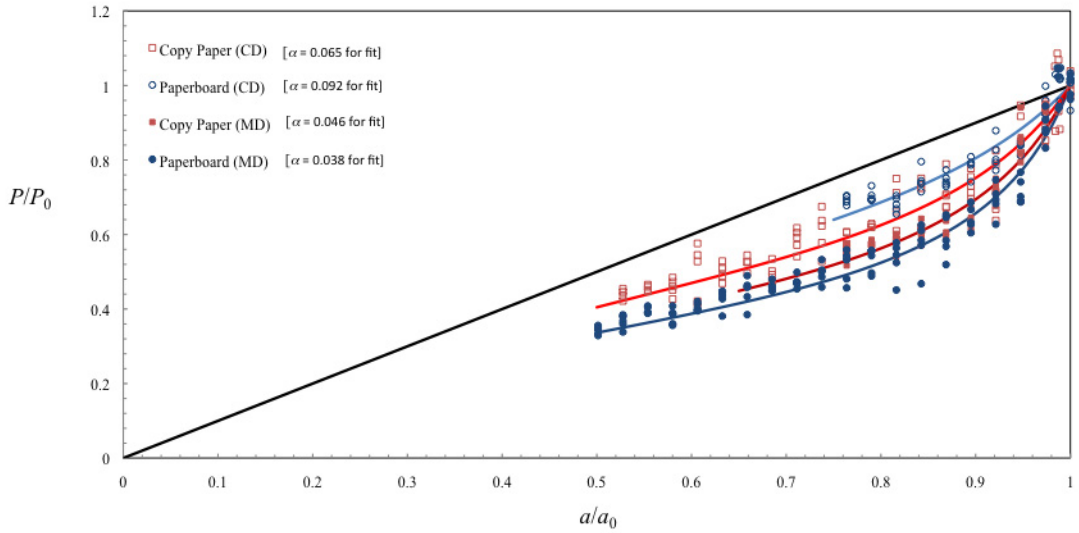

Figure 4. Relative Strength ratio versus relative ligament length for copy paper and paperboard.

ratio was chosen to be less than 0.5 the ligament could be fully loaded at failure and the notched test would not be indicative of notch sensitivity.

For the tissue grades of papers it appears that accounting for under-loaded edges is important with cuts of 2 mm having little effect on the load limit. In fact, tests show that for samples with notch lengths less than 2 mm many samples did not fracture at the cuts but rather at some other inherent flaw along the edge. In addition it may be that network characteristics are more important than material plasticity for notch sensitivity of tissue grades.

Figure 5 provides an example of the results of DENT tests for two narrow widths of a paper towel tested in the MD direction. Equation (5) does not fit this data well, but the results show two important aspects. First for notches less than about 1.5 mm there is no appreciable decrease in strength indicating again that the edges of the sample are not effective in carrying load. Second, as the ligament length decreases the narrower width sample

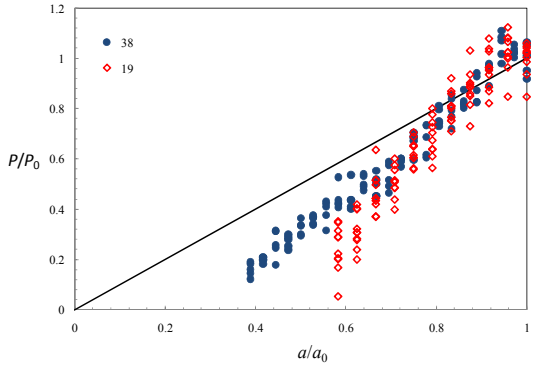

Figure 5. Effect of sample width on notch sensitivity for a paper towel in MD direction.

experiences a larger drop in limit load. In addition, the load is diverging away from the notch insensitivity line. This suggests that network characteristics are such that the inherent length scale needed to distribute load and develop stress concentrations is significantly large for some tissue papers. If one extrapolated the curves in Figure 5 to zero load, this towel would have a length scale feature of approximately 7.5 mm.

Although more work is required to validate these ideas and refine the concepts the approach seems promising. The fact that Equation (5) can be used to fit to the data suggests that tensile strength and notch sensitivity are governed by a characteristic zone length and the concept of an unflawed paper is unrealistic. For low grammage sheets and bond failure dominated sheets the relative notch insensitivity may arise from an inability of the network to create large stress concentrations. Larger width samples would need to be evaluated to extend the characteristic length from specimen to sample.

Although Equation (5) does not fit the small width tissue samples shown in Figure 5, the curves are suggestive of in inherent flaws in the material. At these widths it is probably necessary to account for post damage behaviors, material heterogeneity, and other scale issues.

Not all the variability shown in the data is due to experimental error. Due to the heterogeneity of paper the notch sensitivity will vary. In fact, for some engineered tissue structures one can separate out two distinct curves of $P(a)$ depending on where the notches are placed relative to certain structural features.

4 SUMMARY

It may be fruitful to use load limit ratios from notched samples as a property to rank papers. For tissue grades it appears that the characteristic zone lengths are sufficiently large that significant notch sensitivity may only be observable using larger samples than would be found in converted products. Although even at a width of 76 mm some notch sensitivity can be observed. More interesting is that tissue papers appear to have significant inherent edge flaws and the actual characteristic zone lengths may not be much different than those of higher grammage papers.

A simple LEFM based equation with the inclusion of a characteristic zone length of the paper was able to match load limit ratios for a large range of notch sizes and a wide range of cellulosic-based materials. This suggests that paper is an inherently flawed material and the same characteristic zone length that describes the notch sensitivity relates to the un-notched tensile strength.

More work needs to be completed with specimens of various widths to gain a better understanding of the dependency of the characteristic zone length on specimen size. Perhaps by studying the fracture behavior of paper one can more easily differentiate the role of material plasticity versus network characteristics on the mechanical behavior of paper.

REFERENCES

[1] M. T. Kortschot. “Fracture of Paper”, in *Handbook of Physical Testing of Paper*, editors R. E Mark, C. C. Habeger, J. Borch, and M. B. Lyne, Marcel Dekker, vol. 1, edition 2, 429-480, (2001).

[2] P. Mäkelä, “On the fracture mechanics of paper,” *Nordic Pulp and Pap Res J.* **17**(3):254-274 (2002).

[3] R. S. Seth and D. H. Page, “Fracture Resistance of Paper, *J Mats Sci* **9**:1745-1753 (1974).

[4] A. Tanaka and T Yamauchi, “Size Estimation of Plastic Deformation Zone at the Crack Tip of Paper Under Fracture Toughness Testing,” *J Pack Sci Tech* **6**(5)”268-277 (1997).

[5] T. Bither and J. F. Waterhouse, “Strength development thought refining and pressing,” *Proceedings of the TAPPI 1991 International Paper Physics Conference* 89-107 (1991).

[6] T. Uesaka, “Specimen Design for Mechanical Testing of Paper and Paperboard,” *Handbook of Physical Testing of Paper*, editor R. E Mark, Marcel Dekker, vol. 1, edition 1, 429-480, (1983).

[7] D. Swinehart and D. Broek, “Tenacity and Fracture Toughness of Paper and Board,” *J of Pulp and Pap Sci*, **21**(11):J389-J397 (1995)

Development of tensile tester with liquid applicator and dryer unit

JARMO KOUKO

VTT Technical Research Centre of Finland,
FI-40101, Jyväskylä, Finland
Jarmo.Kouko@vtt.fi

1 INTRODUCTION

Water is applied to the surface of paper in many sub-processes of papermaking and paper converting, such as through the application of coating colour, surface sizing solutions, printing inks, etc. The resulting increased moisture content alters the dimensions and tensions of the paper and has an immediate impact on runnability. In sizing and offset printing processes, the moisture content of paper can reach around 25%. On-line web tension and moisture content are not commonly measured in real process conditions. In order to study the tensile properties of moisturized paper samples, a liquid applicator was developed for a C-Impact tensile tester fitted with a dryer unit [1].

2 APPARATUS

In this work, an apparatus was developed to attain an even moisture content in the xy-direction of paper samples, with target moisture contents corresponding to those of industrial coating, sizing and printing processes.

The moisturizer assembly consists of an ultrasonic (US) atomizer, water container and mechanics for precision movement of the atomizer. The US atomizer (Lechler type no. 710.070.16.60) has a very low volume flow of between 0.03–0.3 mL/s and a viscosity range from 0 to 20 mPas [2]. The jet forms a full cone with a 30 degree angle. The width of the moisturized area can be accurately controlled by adjusting the distance between the US atomizer and the paper.

The average droplet diameter can be adjusted from 10 to 60 microns by power adjustment of a high frequency oscillator [2]. The amount of liquid applied to the target surface can be adjusted by adjusting the sweep time of the US atomizer and the volume flow. The sweep velocity ranges from 30–550 mm/s and the volume flow was set at a range of 0.1–0.2 mL/s. For example, the sweep time across a 100 mm long paper strip is 180 ms. The US atomizer has a theoretical minimum moisture application level of 11 g/m^2, however the actual amount of water absorbed by the paper is 50–75% of this amount due to scatter and droplet evaporation.

Figure 1 shows the C-Impact tensile tester with US moisturizer and water container. Figure 2 shows the US atomizer spraying water.

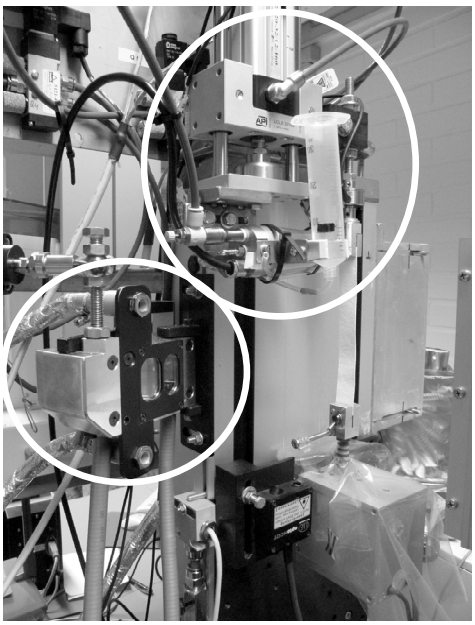

Figure 1. Ultrasonic atomizer and water container (circled top right) attached to a C-Impact tensile tester; and IR moisture and temperature sensors (circled bottom left).

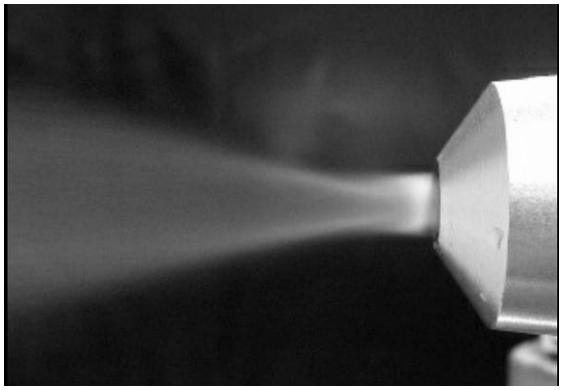

Figure 2. The ultrasonic atomizer spraying water.

The C-Impact tensile tester records the tensile force and the strain during the moisturizing phase and the drying phase. In addition, the paper surface temperature and moisture can also be measured with IR devices (circled bottom left in Figure 1). The C-Impact tensile tester can strain paper strips at speeds up to 100 mm/s, i.e. close to the speed of industrial papermaking and printing processes. Drying can be performed by blowing air heated to 95–125 °C (typical range) onto the paper sample with a dryer unit attached to the C-Impact tensile tester (the dryer unit is not shown in Figure 1).

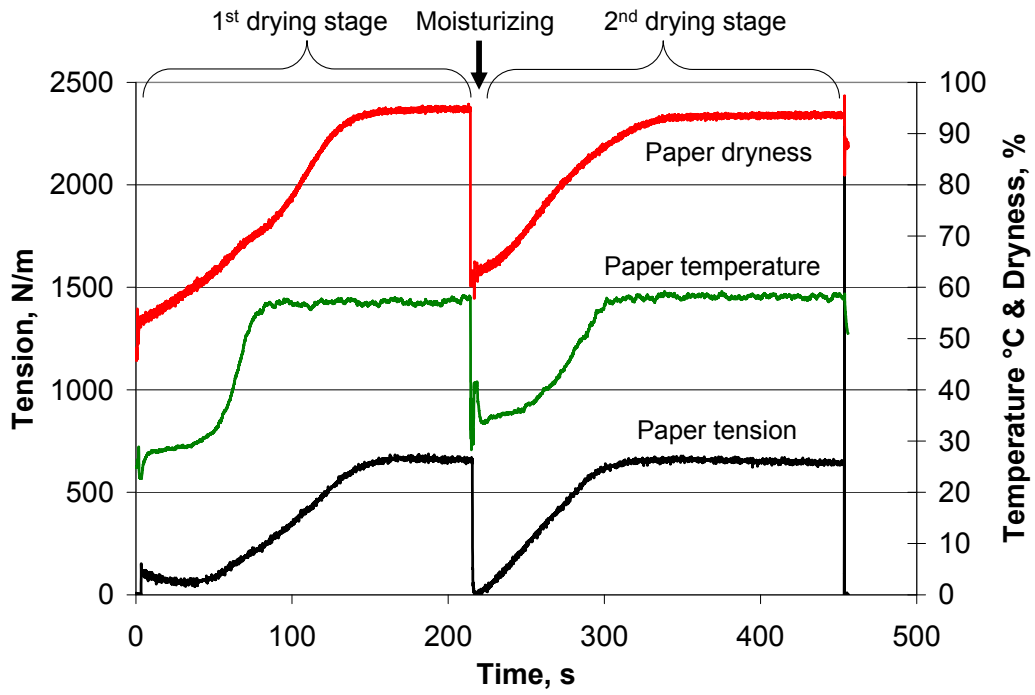

Figure 3. Fine paper sample with initial dryness of 50%, the 1st drying stage, moisturizing to 63% dryness, and the 2nd drying stage.

3 RESULTS

During the drying and moisturizing phases the strain level of the paper strip can be adjusted and the tension can be controlled. Figure 3 shows tension, dryness and temperature data for a never-dried fine paper sample dried and moisturized using the C-Impact tensile tester. Initial straining of 1% and a tensile test at the end of the 2nd drying stage were performed. The paper tension, temperature and dryness decreased sharply due to moisturizing.

Figure 4 shows an example of tensile strength and tensile stiffness after moisturizing. The samples were initially dry fine paper handsheets with a grammage of 60 g/m^2. Decreased dryness led to an almost exponential decrease in tensile strength and tensile stiffness. The results are consistent with the generally known behaviour of paper [3].

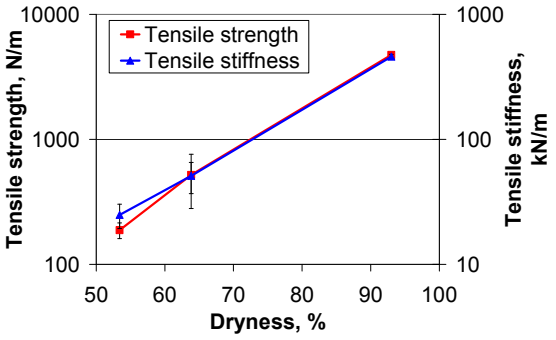

Figure 4. Tensile strength and tensile stiffness after moisturizing as a function of dryness.

4 CONCLUSION

A liquid applicator was developed for a C-Impact tensile tester fitted with a dryer unit. The modified C-Impact tensile tester can simulate dynamic process conditions having liquid application and drying phases, and can measure tensile properties in all phases of the process. The tension levels, dryness and temperature of the paper samples were realistic compared to industrial processes.

The tensile properties of paper are highly dependent on dryness. In further studies, liquid application could be performed with liquids of varying viscosity. In addition, the influence of re-moisturizing and re-drying cycles on paper tensile properties could be studied.

REFERENCES

[1] J. Kouko and P. Kekko. Multi-stage tensile straining during drying of SC paper. 11th International Conference on Web Handling. Stillwater, Oklahoma, (2011).

[2] Lechler. Ultrasonic atomizer, 2005.

[3] K. Niskanen. Paper Physics. Chapter 8. Rheology and moisture effects. Fapet Oy, (1998).

Numerical Investigation of Paperboard Folding

HUI HUANG, AND MIKAEL NYGÅRDS

BiMaC Innovation, Solid Mechanics, Kungliga Tekniska Högskolan, Stockholm, Sweden
huih@kth.se
nygards@kth.se

1 Introduction

Folding process is the last stage of making a package. A good folding can result a high quality package, which means no crack on the folded corner at out-side of paperboard. Certainly, creasing process makes the folding easier because of introducing internal damage between the piles. But the mechanism of folding is still not fully understood. In this work, authors used numerical method to simulate and study a four-ply commercial paperboard folding, material mapping method and double notch shear test were used to determine the material parameters for the model.

2 Material and Methods

The finite element model was aimed to mimic the creasing and folding setups, and to represent paperboard as a combination of continuum and cohesive models using Abaqus/Standard [1]. The four plies were represented by plane strain continuum elements (CPE4), and the three interfaces were represented by a surface formulation using the cohesive behaviour functionality in ABAQUS [1].

The continuum model used is an elastic-plastic model, available in ABAQUS [1], with orthotropic linear elasticity, Hill's yield criterion and isotropic hardening. The interface model was described by an orthotropic elastic-plastic cohesive law which related the interface tractions to the opening and sliding. The material model detail is explained in the creasing analysis in reference [2].

2.1 Mapping of continuum material properties

From the characterization of material data for the top, middle and bottom plies [3], it is obvious that the different plies have different properties. For further investigation of this variation, a 260 mm long paperboard was ground with a tilted groove; the paperboard was put on movable tilted surface where difference in height was 0.4 mm. Thereafter the paperboard was ground in small increments, roughly 0.01 mm/pass. The resulting surface will then show the thickness profile of the paperboard, as show in Figure 1. In the picture, two transition zones between top-middle piles and middle-bottom plies were not sharp straight boundaries. It is obvious that the interfaces between the continuum plies are not uniform and smooth. The fibres from the plies can interact between two plies randomly. Based on this observation, a second order polynomial conversion of the measured material property of paperboard along the thickness direction was assumed and used to define the continuum material data, which is illustrated schematically in Figure 2. Hence, instead of having uniform properties through the plies, we assigned different properties to each element row in the finite element model. The mapping of data was made such that the average value of the ply would still coincide with the measured value. Moreover, the properties across the interfaces were assumed continuous. This mapping was applied on the elastic moduli, initial yield stresses and the hardening modulus.

Figure 1. Picture of vertical view of a declined slop groove which was ground on the top surface of the paperboard. The squared dash-lines point out the transition zone between the plies. (Direction of top surface to bottom surface is from right to the left side of this picture.)

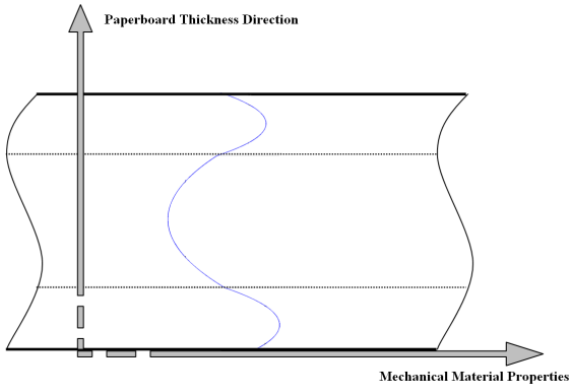

Figure 2. Schematic illustration of the paperboard mechanical property distribution in the through thickness direction. The two horizontal dashed lines represent the ply boundaries of outer plies.

2.2 Interface properties

In reference [4], it was observed that the out-of-plane shear strength through thickness profile of paperboard varies. The shear profile is also more localized when short shear zone length (5 mm) is used, compared to long zone (15 mm) that is commonly used to characterize shear properties in paperboard. During creasing and folding, the paperboard is locally loaded, and the short shear zone length would be more appropriate to use. Hence, the shear strength profiles for the paperboard analyzed in this study were determined using a shear zone length of 5 mm. In reference [2], the interface properties of all three interfaces were defined same parameters. However, the actual shear strength profiles in the MD and CD directions are

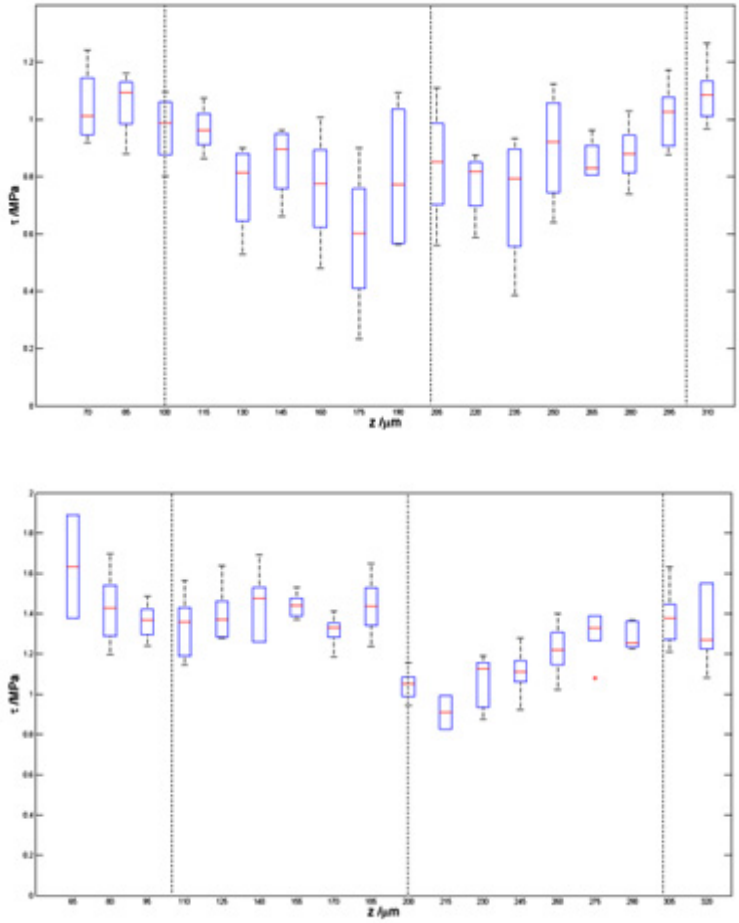

Figure 3. Box plot of shear stress with 5 mm long shear zone length for CD tests (top) and MD tests (bottom).

presented in Figure 3. In this picture, the three interfaces shear strengths are varied. Therefore, these measured shear strengths were used to set the new out-of-plane initial damage shear tractions of interfaces.

2.3 Folding experiment setup

The folding experiment was executed on the L&W creasability tester (AB Lorentzen & Wettre, Stockholm, Sweden), as Figure 4 shows. This apparatus is widely used for industrial converting quality control measurements. Figure 5 explains the experiment principle. The paperboard test piece is clamped on one side of the crease line by a rotation clamp, and a loadcell is located on the other side 10 mm away from crease line. When the test machine is activated, the clamp will rotate 90 degree. Meanwhile, the loadcell records the reaction force produced by this rotation process. The experiments were performed at a constant room temperature 23 °C with relative humidity of 50%.

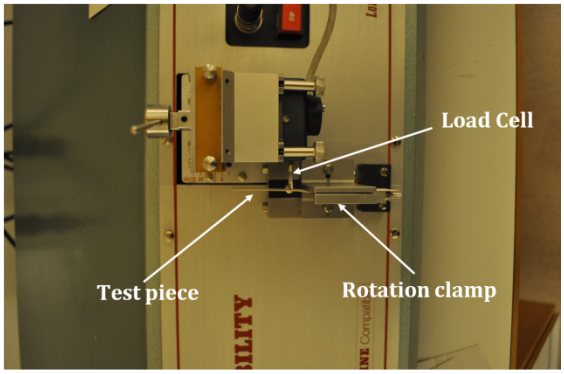

Figure 4. L&W creasability tester was used to perform folding experiments.

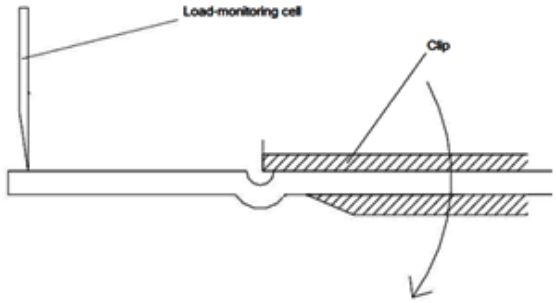

Figure 5. 2D schematic illustration of the L&W creasability tester.

3 Results

For this folding investigation, the four-ply commercially produced paperboard was tested and simulated both in machine direction (MD) and cross machine direction (CD) with crease depth d = 0.0 mm and d = 0.2 mm, respectively.

Figure 6 shows the microscopic structure and simulation contour plots of the creased and folded zones of two test specimens. In the picture, the four-ply paperboard is thoroughly delaminated in both simulation and experiment. The shallow creased sample ended up with triangle-shape deformation, and while the deeper creased sample got a more trapezium-shape deformation. Figure 7 displays the bending moment-angle curve comparison between experiment and simulation.

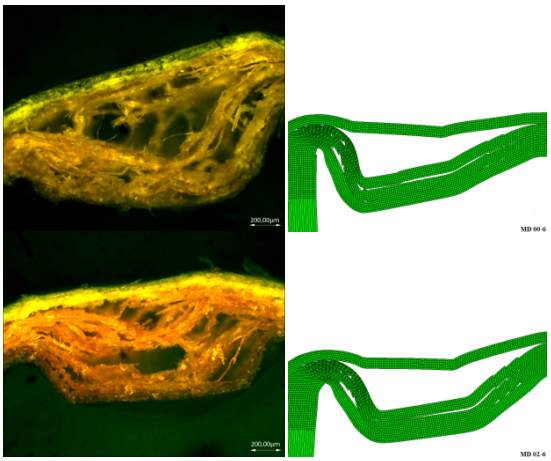

Figure 6. Microscopic picture and contour plot of the crease zone in a MD sample after folding. The pictures on the top were the folding results from crease depth d = 0.0 mm, while the pictures on the bottom were the folding results from crease depth d = 0.2mm.

The simulation results predict the experimental results well. From this moment-angle curve, the peak value of bending moment is lowered with deeper creasing. Moreover, the bending moment reaches its peak value after 25 degrees. At this stage, the interfaces of top ply and middle ply are totally separated, which further on enables an excessive bulging of the different plies. Thus, after peak value, the interfaces have opened up so much that the strength of the interfaces are becoming smaller and smaller, and the properties of the cohesive interface do no contribute to the slope of the moment–angle curve. Besides, for deeper creased paperboard, the folding profile is smoother, with a lower peak value, since interfaces have been damaged to a larger degree during the creasing operation. In addition, the difference in bending stiffness between d = 0.0 mm and d = 0.2 mm, is more pronounced than the difference between MD folding and CD folding.

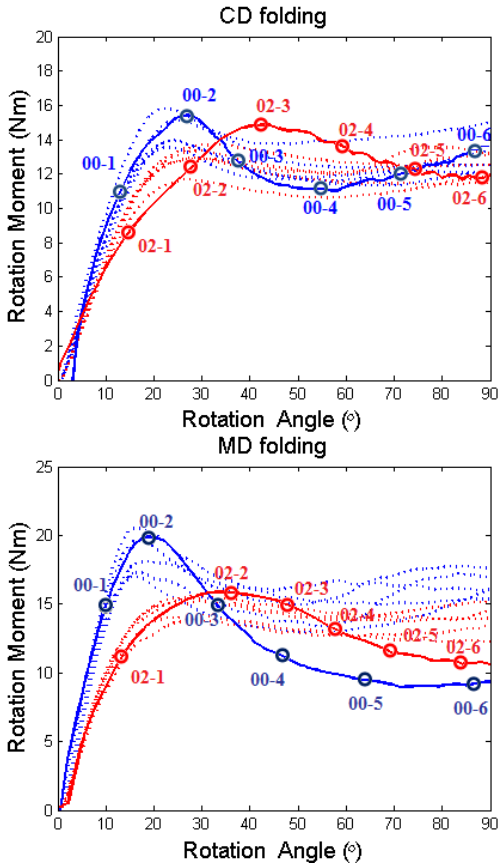

Figure 7. Bending moment-angle curve for folding. Solid lines represent the simulation results; dashed lines represent the experiment results. Blue lines represent samples with crease depth d = 0.0 mm, and red lines represent samples with crease depth d= 0.2 mm.

4 Conclusion

In this study, in order to predict the mechanical behavior of paperboard folding four novelties was accounted for in the model formulation, namely:

1. The use of an anisotropic elastic model, using a Hill yield surface with isotropic hardening in the continuum model.
2. A mapping procedure that accounted for observed mixing of different plies was used to assign continuum properties.
3. The use of a combined cohesive and contact formulation for the elastic-plastic interfaces.
4. The tilted double notched shear test with 5 mm long shear zones was used to assign interface shear strengths.

According to this improved model, folding analyse obtained good results. The simulation results captured folding behaviour well, which included a reduced the bending moment with deeper crease depth.

Finally, a fairly simple model with more realistic material parameters were used to simulate the folding operations and it gave good results. The simulation results helped us to understand the folding mechanism better and it also opened the possibilities to do more research to identify the importance of different material properties and the effect of crease depth. This is an important step in order to better understand paperboard damage and deformation mechanisms. However, there are still many unknown properties and phenomena remaining to be studied related to folding of multiply paperboard, such as the deformation and damage mechanisms can e.g. be better related to the network structure.

REFERENCES

[1] ABAQUS. User's Manual. Abaqus Inc, Providence, RI, USA, 6.8 edition, (2008).

[2] H. Huang and M. Nygårds, A simplified material model for finite element analysis of paperboard creasing*, Nord. Pulp Paper Res. J*. **25**(4) 505, (2010).

[3] M. Nygårds, Experimental techniques for characterization of elastic-plastic material properties in paperboard, *Nord. Pulp Paper Res. J.* **23**(4):432, (2008).

[4] M. Nygårds and H. Huang, The dependency of shear zone length on the shear strength profiles in paperboard, Technical Report no. 501, KTH, Solid Mechanics, (2011).

The effect of polyethylene on hygroexpansion of PE coated papers and boards

SARA PAUNONEN, ØYVIND GREGERSEN

Department of Chemical Engineering/ Norwegian University of Science and Technology (NTNU)
Sæm Sælandsvei 4 (Kjemiblokk 5),
N-7491 Trondheim, Norway
sara.paunonen@chemeng.ntnu.no

1 INTRODUCTION

Packaging papers and boards show hygroexpansion when they get into contact with moisture during the lifetime of the package. The magnitude and rate of hygroexpansion affects the dimensions of a transport box or carton, which in turn affects the package's storage properties.

Polyethylene (PE) is commonly used as a moisture barrier coating on packaging boards. The effect of PE is twofold. First, it restricts the moisture penetration to the base paper material, and forces the moisture diffusion inside the material to mainly occur in the in-plane directions. Secondly, the PE film mechanically restricts the expansion of the wood fiber-based substrate, and has no hygroexpansion itself. The hygroexpansive properties of the coated board emerge as a combination of mechanical properties of all plies including the PE coating and the hygroexpansive properties of the plies in the substrate board.

1.1 Transient hygroexpansion

Development of the hygroexpansive strain after a change in relative humidity (transient hygroexpansion) has been less studied than the equilibrium hygroexpansion of paper materials. Niskanen et. al. [1] studied transient hygroexpansion of paperboards that had grammages from 127gsm to 336gsm. In general, the strain rates depend on basis weights, stress state of the fiber network, and rate of change of the ambient moisture steps [1]. They noticed that CD strain development in absorption is slower than developments of CD strain in desorption and both MD strains (absorption and desorption).

Niskanen et al. [1] used two measurement methods that differed in how the samples interacted with ambient humidty: In the one method, air flow was forced across and though the sample. In the other method, no forced air flow was applied. Also, humidity steps with either ramp or "square wave" form were used.

Coupling between the sample and the environment affects the observed hygroexpansion transient. Even a small forced air flow around the sample increases the observed hygroexpansion rates compared to the non-moving air situation. As a result, comparisons of results obtained by different measurement methods should be done carefully. In addition, stabilisation times of moisture content and hygroexpansion strains are not equal. In desorption, the moisture content changes roughly at the same rate as as strains do [1]. In absorption on the other hand, the moisture content changed faster than the slow CD strains.

Lavrykov et al. [2] continued the studies on transient hygroexpansion, and proved with their model that the inclusion of residual stresses in MD was enough to explain the slower CD hygroexpansion strain rates.

Mechanical properties of several hundreds of commercial crystalline polyethylene polymers vary considerably, and also the extrusion coating process affects the properties of the resulting coating by introducing anisotropy to the film [3]. In addition, polymers are generally considered as viscoelastic materials, and thus mechanical properties of PE are dependent on the testing conditions. The properties of the PE coating on a paperboard should therefore be tested directly.

1.2 Aim

This work shall answer to two questions. The first question is weather the slow CD strain development can be observed in PE coated materials, and how the PE coating affects the phenomenon. It will also be studied how the capacity of the polyethylene to restrict the hygroexpansion can be described. The first approximation assumes that the restriction arises solely from the elastic modulus of the polyethylene film.

2 EXPERIMENTAL

The following polyethylene coated paper and board grades will be studied: i) kraft paper, 60gsm with 17gsm LDPE coating (the codes used in figures: k60 and k60PE), ii) sack paper, 70gsm with 20gsm LDPE coating (s70 and s70PE), iii) liquid packaging board, 265gsm, 14gsm and 25gsm LDPE coatings on each side (265gsm, 265gsmPE), iv) liquid packaging board, 370gsm, on one side 14gsm and 25gsm LDPE coating on the other side (370gsm, 370gsmPE)

Hygroexpansion tests were carried out with a Lorentze&Wettre type 3-2 micrometer system (Neenah type tester) and a Fibro DST tester (digital correlation type tester). The thin materials (i-ii) were tested with Fibro. The samples were relaxed before the testing by exposing them to the following moisture cycling: 30%, 80%, 30%, 80%, 30% RH with one hours hold times. The moisture cycling in the hygroexpansion test was as follows: 30%, 50%, 80%, 50%, 30%, 50% RH with two hour hold times.

Thick materials (iii-iv) will be tested with the Lorentze&Wettre micrometer system.

Changes in moisture content were measured by weighing one sample in varying intervals after a step change in relative humidity. The sample sizes were: 74mm × 74mm for materials (i-ii), 15mm × 210mm for materials (iii-iv). The 80% RH was created in a climate box. Samples were transferred to 50% RH climate controlled room conditions to create the 80% to 50% RH step. The step from 50% to 80% RH was created by putting the samples from the climate controlled room to the 80% RH climate box. The stabilization time before the step change was 5 days.

PE coatings were separated from the substrate paper by base treatment. The coated sack and kraft paper samples were soaked in 20% w/w NaOH solution for 30min, rinsed with tap water and gently brushed to remove the fibers from the surface. The liquid board samples were torn to two halves, and most of paperboard material was manually torn away. The remaining layers were soaked, rinsed and brushed as before. Stress-strain behaviour of the separated PE films was measured with Zwick tensile tester (free length 100mm, test speed 13.9%/min) in cyclic tests. Test pieces were strained to 0.6mm, 1.2mm, 1.8mm, 2.5mm in CD, and to 0.2mm, 0.4mm, 0.8mm, 1.2mm in MD. The strain was brought to zero in between the strains mentioned above.

The tensile stiffness of the samples without PE (k60, s70, gsm265, gsm370) will be measured with L&W tensile tester according to ISO 1924-3:2005, but three climates will be used: 30%, 50%, and 80% RH.

3 PRELIMINARY RESULTS AND DISCUSSION

Paper materials have a variable response rate to changes in environmental moisture. The rate of moisture content change depends on i) intrinsic absorption of moisture to the paper surface, ii) bulk moisture diffusion inside paper, iii) on the interaction and coupling between the test piece and the ambient environmental conditions, and iv) the shape of relative humidity step. **Figure 1** shows how the materials respond to step changes in relative humidity in conditions where there is no forced air flow. A model was fitted to the data. The best fit was obtained with an "exponential rise to max" model structure which has two parts:

$$\Delta mc = a(1-e^{-bt})+c(1-e^{-dt}) \qquad (1)$$

The structure of the model suggests that there are two co-acting underlying mechanisms of moisture sorption and desorption. The figure shows that the higher the basis weight is, the more time it takes to reach the equilibrium moisture content.

Figure 2 shows the hygroexpansion response of PE coated and non-coated kraft paper measured with a Fibro DST tester. In the beginning of the curve there is moisture cycling between 40% and 80% RH for the stress relaxation. The experiment starts at 6 hours from 30% RH. Figure 2 shows that the polyethylene restricts the hygroexpansion in CD. In MD, there seems to be no difference between the coated and not coated samples. The comparisons with the moisture content development are to be done.

Figure 3 shows that there is a lot of variation in the hygroexpansion of PE coated materials measured with the Fibro DST tester. The same problem is also seen throughout the experiment in Figure 2. The curve s70PE-1MD (Figure 3) also shows shrinkage after an initial expansion after an increasing step in relative humidity. Based on these preliminary results, it seems best to measure hygroexpansion of all PE coated materials with the Lorenzen&Wettre micrometer system or other testers that measure elongation (Neenah type).

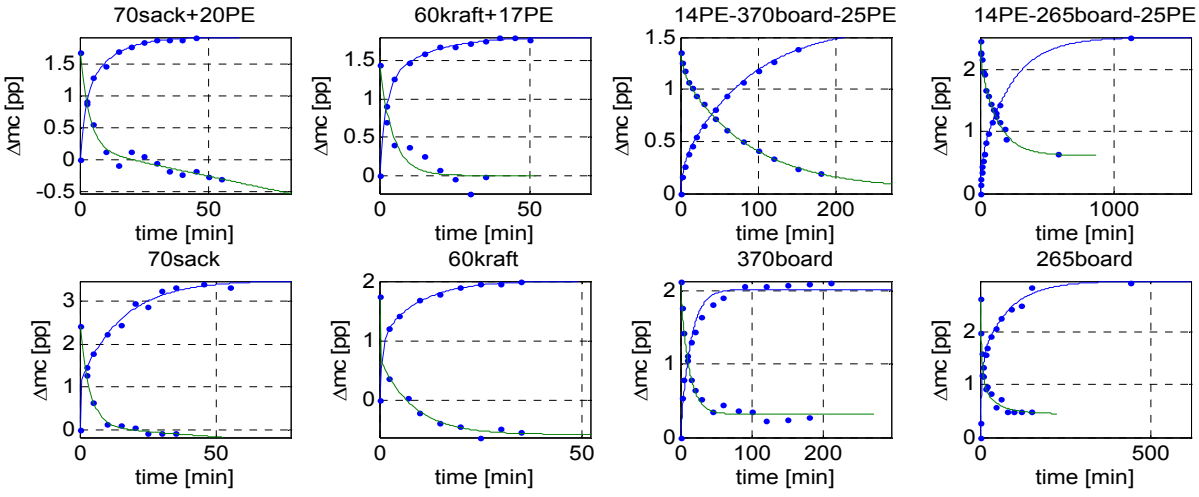

Figure 1. Moisture content change of the test pieces after two step changes in RH (50%→80%→50% RH).

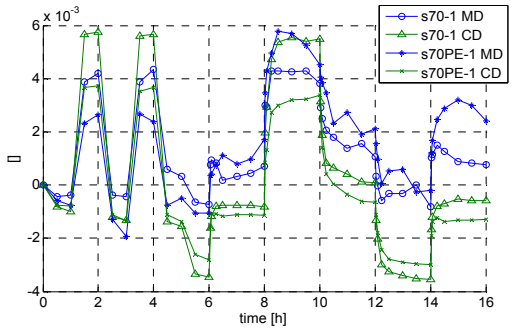

Figure 2. Hygroexpansion of sack paper (s70) and PE coated sack paper (s70PE).

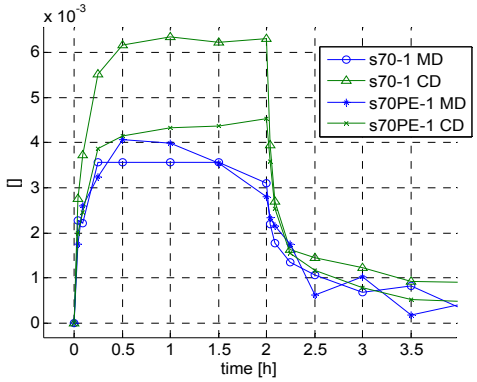

Figure 3. The section 50%→80%→80% RH from Figure 2.

Pulkkinen et al. [4] have reported that hygroexpansion measurement results obtained by elongation and image based methods generally are not comparable. They suspect that the differences arise from local variations in thickness, fibre orientation and grammage. The shape and size of the test piece were not enough to explain the differences. The present work shows that the image based method is not suitable for measuring PE coated boards, possibly due to buckling of the sample caused by moisture gradients during testing..

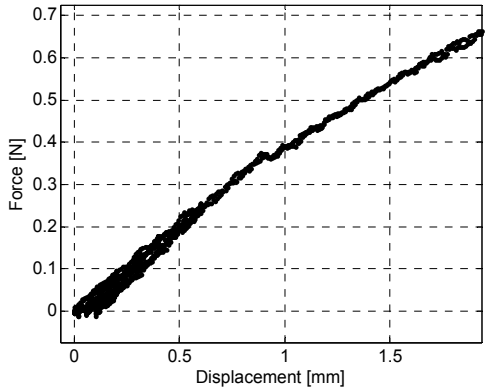

Figure 4. Stress strain curve of PE film separated from the sack paper substrate (PE film form s70PE, MD). L_o=100mm.

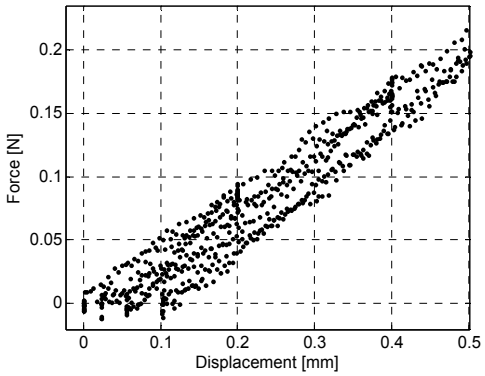

Figure 5. The range 0..0.5mm from Figure 4. PE film from s70PE, MD, L_o=100mm.

The PE films separated from samples k60PE and s70PE were stress-strain tested in order to understand share elastic and plastic response during the hygroexpansion (Figure 4 and Figure 5). The cycle to 0.4mm corresponds roughly the hygroexpansion that PE coated sack paper experience during a step from 50% to 80% RH. The figure shows that permanent deformation accounts for approximately 12% of the total displacement in each cycle. In the next phase of this work, it will checked if the difference in the hygroexpansion of coated and non-coated boards can be explained by the tensile stiffness of the coatings.

4 CONCLUSION

The work is in progress and not all the results are available. So far it can be said that the Fibro DST tester is not optimal for hygroexpansion measurement of polyethylene coated papers and boards. For sack paper measured with Fibro DST, we did not find a significant difference in MD and CD hygroexpansion rate, however an elongation type tester should be used to verify the result. For sack paper, the PE coating restricted expansion more in CD.

REFERENCES

1. Niskanen, K.J., S.J. Kuskowski, and C.A. Bronkhorst, *Dynamic hygroexpansion of paperboards.* Nordic Pulp & Paper Research Journal, 1997. **12**(2): p. 103-110.
2. Lavrykov, S.A., B.V. Ramarao, and O.L. Lyne, *The planar transient hygroexpansion of copy paper: Experiments and analysis.* Nordic Pulp and Paper Research Journal, 2004. **19**(2): p. 183-190.
3. Brydson, J.A., *Plastics Materials*. 7th ed. 1999, Oxford Boston : Butterworth-Heinemann: Elsevier. xxvii, 920.
4. Pulkkinen, I., J. Fiskari, and V. Alopaeus, *The effect of sample size and shape on the hygroexpasion coefficient: a study made with advanced methods for hygroexpansion measurement.* TAPPSA Journal, 2009. **March 2009,**: p. 26-33.

Visions become reality

Today´s visions are driving solutions for tomorrow.
Every day, engineers and scientists at Voith Paper work toward the great challenge of enhancing efficiency for the future of papermaking. Increases in productivity and quality, as well as reductions in energy and water consumption, are just a few of our focus areas. Our R&D engineers are targeting advancements in the complete integrated system – the entire papermaking process from raw material to the final product.

At Voith Paper, we are driven by continuous innovations and the urge to turn visions into reality.

www.voithpaper.com

VOITH
Engineered Reliability

ANDRITZ
Pulp & Paper

From the first piece to last.

We give you a complete solution.

ANDRITZ Paper Technology - get your high-quality paper production line from one supplier. Unified design - from stock prep to the reel - and guaranteed performance are certainties when you partner with ANDRITZ for your paper/board production line. Why puzzle over the right supplier when ANDRITZ Paper Technology offers the most cost-effective technology, service and performance?

www.andritz.com

We accept the challenge!

Strength when you need it

Our strength is continuous innovation. FennoBond™ 3000 and 4000X are the newest technologies in our FennoBond product line. FennoBond 3000 synthetic polymer backbone is structured to provide the papermaker with increased fiber to fiber bonding and significant dewatering improvements, allowing enhancements in refining and formation. FennoBond 4000X is a new hydrogel dry strength solution that is particularly formulated for recycled fiber. Its' tolerance to high calcium and conductivity levels make it the strength solution as paper mills close their water loops.

If your need is wet strength, our FennoBond functional promoters significantly improve wet strength efficiency while maintaining system charge balance.

Kemira's innovative products and application expertise strengthen your papermaking processes

Kemira Chemie Ges.mbH
Hafenstrasse 77
A-3500 Krems, Austria
Tel. +43 2732 711550
www.kemira.com/fennobond


VOITH
Engineered Reliability


kemira


XERIUM
TECHNOLOGIES, INC.
STOWE
WEAVEXX
HUYCK.WANGNER


ANDRITZ
Pulp & Paper


BYK
Additives & Instruments


OMYA


AGRANA
STARCH


bio
Montan


BTG
RAISING YOUR PRODUCTIVITY